frontiers | Research Topics

Women in remote sensing 2022

Edited by
Jane Southworth, Kelley Crews, Erin Bunting and Hannah Victoria Herrero

Published in
Frontiers in Remote Sensing

ISSN 1664-8714
ISBN 978-2-8325-4707-6
DOI 10.3389/978-2-8325-4707-6

About Frontiers

Frontiers is more than just an open access publisher of scholarly articles: it is a pioneering approach to the world of academia, radically improving the way scholarly research is managed. The grand vision of Frontiers is a world where all people have an equal opportunity to seek, share and generate knowledge. Frontiers provides immediate and permanent online open access to all its publications, but this alone is not enough to realize our grand goals.

Frontiers journal series

The Frontiers journal series is a multi-tier and interdisciplinary set of open-access, online journals, promising a paradigm shift from the current review, selection and dissemination processes in academic publishing. All Frontiers journals are driven by researchers for researchers; therefore, they constitute a service to the scholarly community. At the same time, the *Frontiers journal series* operates on a revolutionary invention, the tiered publishing system, initially addressing specific communities of scholars, and gradually climbing up to broader public understanding, thus serving the interests of the lay society, too.

Dedication to quality

Each Frontiers article is a landmark of the highest quality, thanks to genuinely collaborative interactions between authors and review editors, who include some of the world's best academicians. Research must be certified by peers before entering a stream of knowledge that may eventually reach the public - and shape society; therefore, Frontiers only applies the most rigorous and unbiased reviews. Frontiers revolutionizes research publishing by freely delivering the most outstanding research, evaluated with no bias from both the academic and social point of view. By applying the most advanced information technologies, Frontiers is catapulting scholarly publishing into a new generation.

What are Frontiers Research Topics?

Frontiers Research Topics are very popular trademarks of the *Frontiers journals series*: they are collections of at least ten articles, all centered on a particular subject. With their unique mix of varied contributions from Original Research to Review Articles, Frontiers Research Topics unify the most influential researchers, the latest key findings and historical advances in a hot research area.

Find out more on how to host your own Frontiers Research Topic or contribute to one as an author by contacting the Frontiers editorial office: frontiersin.org/about/contact

Women in remote sensing: 2022

Topic editors
Jane Southworth — University of Florida, United States
Kelley Crews — The University of Texas at Austin, United States
Erin Bunting — Michigan State University, United States
Hannah Victoria Herrero — The University of Tennessee, Knoxville,United States

Citation
Southworth, J., Crews, K., Bunting, E., Herrero, H. V., eds. (2024). *Women in remote sensing: 2022*. Lausanne: Frontiers Media SA. doi: 10.3389/978-2-8325-4707-6

Table of contents

frontiers | Frontiers in Remote Sensing

TYPE Editorial
PUBLISHED 22 March 2024
DOI 10.3389/frsen.2024.1369697

OPEN ACCESS

EDITED AND REVIEWED BY
Jean-Pierre Wigneron,
Institut National de recherche pour l'agriculture, l'alimentation et l'environnement (INRAE), France

*CORRESPONDENCE
Jane Southworth,
jsouthwo@ufl.edu

RECEIVED 12 January 2024
ACCEPTED 29 February 2024
PUBLISHED 22 March 2024

CITATION
Southworth J, Bunting E, Herrero HV and Crews K (2024), Editorial: Women in remote sensing: 2022.
Front. Remote Sens. 5:1369697.
doi: 10.3389/frsen.2024.1369697

Editorial: Women in remote sensing: 2022

Jane Southworth[1]*, Erin Bunting[2], Hannah V. Herrero[3] and Kelley Crews[4]

[1]Department of Geography, University of Florida, Gainesville, FL, United States, [2]Department of Geography, Environment, and Spatial Sciences, Michigan State University, East Lansing, MI, United States, [3]Department of Geography and Sustainability, University of Tennessee, Knoxville, TN, United States, [4]Department of Geography and the Environment, University of Texas, Austin, TX, United States

KEYWORDS

women, remote sensing, breaking boundaries, theoretical advancements, practical applications

Editorial on the Research Topic
Women in remote sensing: 2022

In a world where less than 30% of researchers are women, with similar proportions reflected in the remote sensing community, this Research Topic of Frontiers in Remote Sensing stands as a beacon of change and diversity. This collection of 15 papers led by women researchers offers a panoramic view of the remarkable contributions of women across the spectrum of remote sensing research. With over 28,000 views as of January 2024, these studies not only showcase scientific excellence but also serve as a testament to the crucial role of gender equality in driving sustainable development. This goal is underscored by the United Nations Educational, Scientific and Cultural Organization (UNESCO), a world leader dedicated to fostering global peace and security, sustainability, and gender equality through the encouragement of international collaboration in the fields of education, the arts, sciences, and cultural endeavors.

The scope of this issue spans from theoretical advancements to practical applications, addressing global challenges through a multifaceted lens. Together, these papers weave a rich tapestry of innovation, diversity, and scientific rigor. They not only demonstrate the invaluable contributions of women in remote sensing but also chart a course for future research in this dynamic field. As we stand at the intersection of technology, environmental science, and gender equality, this Research Topic marks a significant milestone in our collective journey toward a more inclusive and sustainable future. Highlighting the themes, synergies, and connections among the 15 works in this Research Topic on Women in Remote Sensing demonstrates the diversity and collaborative potential within the field. Broadly speaking, these manuscripts, together with the participants in and sponsors of the 6-part Women in Remote Sensing presentation sessions, the Remote Sensing Specialty Group Highlight Session, the mentoring reception, and the community-building dinner at the 2023 American Association of Geographers (AAG) illustrate the breadth and depth of foundational contributions that span: 1) data/data collection devices and protocols, 2) methodological and analytical approaches, 3) a variety of regions and units of analysis, and 4) many topical areas of study, while at the same time highlighting the community building, mentoring, and inclusivity inherent in this collaborative approach to science (Figure 1).

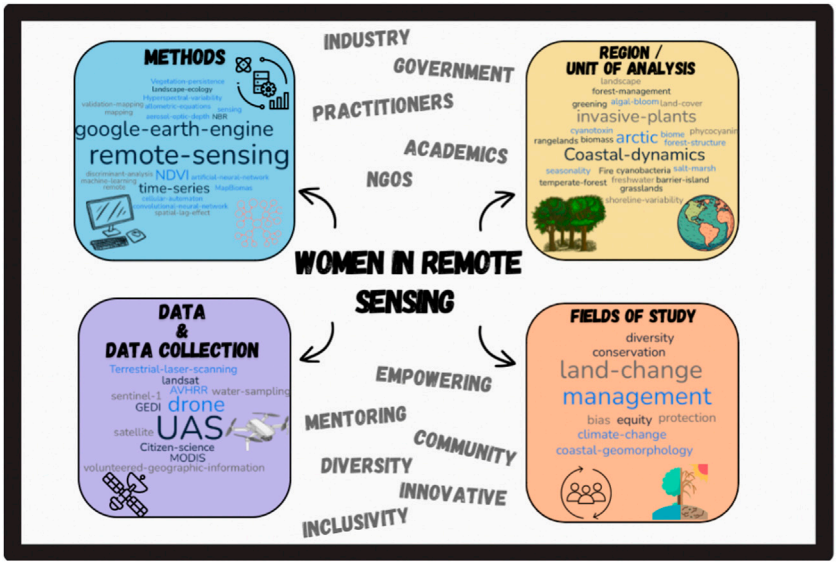

FIGURE 1
This thematic concept map represents the keywords for each of the articles in this special issue of Women in Remote Sensing. The keywords are grouped similarly to the list of key themes and include methods of analysis, data/data collection approaches, fields of study, region/unit of analysis in addition to the characteristics of the Women in Remote Sensing ethos, which is open to all remote sensing practitioners.

1. Technological Innovation and Methodological Advances: Several papers, like those by Mattilio et al., Herrmann et al., and Krause et al., demonstrate innovative applications of machine learning and terrestrial laser scanning (TLS). These technological advancements underscore the common theme of leveraging cutting-edge tools to address ecological and environmental challenges.
2. Environmental Monitoring and Conservation: Carvalho et al., Rivarola et al., and Digiacomo et al. focus on different aspects of environmental monitoring. While analyze coastal morphological changes, assess the effectiveness of protected areas, and evaluate coastal wetland habitats using Unoccupied Aircraft Systems (UAS). Collectively, these studies highlight the critical role of remote sensing in environmental conservation and management.
3. Climate Change and Ecosystem Dynamics: The contributions by Southworth et al., Parkinson, and Vogeler et al. share a common thread in studying the effects of climate change. Work on global biome shifts, Parkinson's research on Arctic Sea ice, and assessment of forest structure are all crucial to understanding and responding to climate change impacts.
4. Urbanization and Land Use Change: Fontana et al. and Yang et al. explore urban development and land use transitions. Urbanization predictions in Brazil and study of forest management strategies in the U.S. both address how land use changes impact the environment, offering insights for sustainable development.
5. Data Integration and Interdisciplinary Approaches: The works by Karale and Yuan. and Hanlon et al. represent the integration of various data sources, such as satellite data with ground measurements and drone-based water sampling, to improve environmental monitoring. This integration reflects a broader theme of interdisciplinary approaches to addressing complex environmental issues.
6. Policy Implications and Conservation Strategies: Several studies, including those by Herrmann et al., Rivarola et al., and Vogeler et al., have direct implications for policy and conservation strategies. Collectively, these papers contribute to a better understanding of how scientific research can inform and shape environmental policy and practice.
7. Diversity and Inclusivity in Science: The paper by Joyce et al. stands out for addressing the meta-theme of diversity in the scientific community, particularly within editorial boards. This paper connects to the broader issue of gender representation and inclusivity in science, technology, engineering, and mathematics (STEM) fields, which is a central theme of the Research Topic.
8. Synergies in Remote Sensing Applications: The works by Huelsman et al. and Digiacomo et al. both utilize unoccupied aerial vehicles (UAVs), showcasing the synergy in remote sensing applications across different environmental contexts. Their research highlights the versatility and potential of remote sensing technologies.

Each contribution in this Research Topic underscores the diversity of thought and high level of rigor in remote sensing, with Joyce et al. initiating the discourse by examining the composition of editorial boards in remote sensing journals. Their audit exposes a striking lack of diversity, shedding light on the implicit biases and citation disparities faced by underrepresented communities. They propose an action plan aimed at fostering inclusivity within the field, paving the way for a more diverse and equitable research environment.

In a blend of geospatial analysis and environmental science, Carvalho et al. delve into the morphological dynamics of a tropical

barrier island. Utilizing Landsat imagery and Google Earth Engine, they unravel the complex interplay of erosional trends and seasonal shifts, providing valuable insights into coastal processes along the southeastern coast of Brazil. This study not only contributes to our understanding of coastal morphology but also underscores the importance of long-term environmental monitoring.

Rivarola et al. shine a light on the effectiveness of protected area zoning, employing remote sensing to evaluate conservation strategies in Nahuel Huapi National Park, Argentina. Their work highlights the need for critical evaluation of conservation goals, and emphasizes the role of remote sensing in large-scale environmental management.

Taking a step into the realm of global ecology, Southworth et al. harness the power of the normalized difference vegetation index (NDVI) time series to decipher patterns of vegetation change over 3 decades. Their findings not only reveal the impact of climate and land-use change on global biomes but also underline the utility of statistical time series analysis in ecological research.

In a demonstration of precision agriculture, Mattilio et al. present a novel application of machine learning to map leafy spurge infestations. Their work, rooted in high-accuracy classification models, offers a glimpse into the potential of technology to manage invasive species—a critical aspect of sustainable land management. The theme of machine learning continues with Herrmann et al. who apply these techniques to the regulatory landscape of highland grassland fires in Brazil's Atlantic Forest Biome. Their findings reveal significant discrepancies between authorized and actual burned areas, offering evidence to inform policy revision and environmental governance.

Krause et al. bring a technological edge to forestry research by employing terrestrial laser scanning for biomass estimation. Their work challenges existing methodologies, offering more accurate assessments that have significant implications for carbon quantification and forest management. Vogeler et al. investigate the potential of satellite data, particularly the Global Ecosystem Dynamics Investigation (GEDI), in generating predictive models of forest structure. Their study evaluates the utility of GEDI data in biodiversity assessments and wildlife habitat modeling, contributing to our understanding of forest ecosystems. Yang et al. explore the intersection of forest management, land use transitions, and citizen science in the southeastern United States. Their integration of crowdsourced data underscores the value of public participation in scientific research, particularly in the context of regional land change dynamics.

Digiacomo et al. assess the utility of UAS for monitoring coastal wetland habitats. Their work not only addresses the need for methodological standardization but also demonstrates the potential of UAS in large-scale ecological assessments. In the field of water quality, Hanlon et al. introduce an innovative drone-based method for sampling harmful algal blooms. This approach, which overcomes the limitations of traditional sampling methods, offers a timely and precise tool for monitoring and managing aquatic ecosystems. Huelsman et al. utilize drones for species identification, shedding light on the capabilities of UAV-based spectroscopy in differentiating between invasive plant species. Their findings contribute to the advancement of remote sensing techniques in biodiversity conservation.

Parkinson (2022) presents a comprehensive record of Arctic Sea ice changes over 43 years, utilizing satellite passive microwave data. Her work provides crucial evidence of long-term trends in sea ice coverage, and reinforces the role of satellite observations in climate change research. In urban studies, Fontana et al. examine land use and land cover changes in the Metropolitan Region of Porto Alegre, Brazil. Their integration of historical Landsat data and spatial modeling not only paints a picture of urban expansion but also provides a forecast of future developments, serving as a valuable tool for urban planning and policy formulation. Finally, Karale and Yuan improve the estimation of particulate matter (PM) concentrations in PM2.5 by integrating satellite data with ground measurements. Their approach, which uses a Convolutional Neural Network, not only improves air quality monitoring but also opens new avenues for environmental health research.

In summary, this Research Topic, diverse in approach, topical foci, and occupational roles of the authors, collectively emphasizes the importance of technological innovation, environmental stewardship, climate change research, urban and land use studies, data integration, policy impact, and the promotion of diversity in the field of remote sensing. This Research Topic not only contributes significantly to the scientific literature but also reinforces the vital role of women in advancing remote sensing research and its applications for an inclusive, collaborative, and sustainable future.

Author contributions

JS: Writing–review and editing, Writing–original draft, Conceptualization. EB: Writing–review and editing, Writing–original draft, Visualization. HH: Writing–review and editing, Writing–original draft. KC: Writing–review and editing, Writing–original draft.

Conflict of interest

The authors declare that the research was conducted in the absence of any commercial or financial relationships that could be construed as a potential conflict of interest.

Publisher's note

frontiers | Frontiers in Remote Sensing

ORIGINAL RESEARCH
published: 08 June 2022
doi: 10.3389/frsen.2022.901463

Assessing Protected Area Zoning Effectiveness With Remote Sensing Data: The Case of Nahuel Huapi National Park, Argentina

María Daniela Rivarola[1], Jacob Dein[2], Daniel Simberloff[1] and Hannah Victoria Herrero[2]*

[1]Ecology and Evolutionary Biology Department, University of Tennessee, Knoxville, TN, United States, [2]Geography Department, University of Tennessee, Knoxville, TN, United States

Protected areas (PAs) remain the most important tool to prevent biodiversity loss and habitat degradation worldwide, but the formal creation of a PA constitutes only the first step. In recent decades, concerns about PA effectiveness have arisen, and several PAs have been evaluated using different methods. Results show that while some PAs are achieving their conservation goals, others have been less effective. Particularly, assessing broadscale outcomes is a method that allows us to monitor change over time at a large scale, using remote sensing data. In this study, we evaluated the effectiveness of Nahuel Huapi National Park, with particular attention to its three protection categories: Strict Natural Reserve (SNR), National Park (NP), and National Reserve (NR) (IUCN categories Ia, II, and VI respectively). We compared changes in Normalized Difference Vegetation Index (NDVI) among sites in these categories and between them and neighboring unprotected areas, over the period 2000–2020. Overall, habitat degradation was low, and we found no difference among the four categories evaluated. Nevertheless, a greening process has been conspicuous in the entire area, with higher values both in the SNR and in the unprotected area. We propose possible explanations as we consider variables such as dominant tree species, precipitation, temperature, elevation, and wildfires. This study supports the importance of NHNP at the regional and national levels, particularly its SNR areas.

Keywords: conservation, NDVI, protection categories, temperate forest, time series analysis

OPEN ACCESS

Edited by:
Gabriel Pereira, Universidade Federal de São João del-Rei, Brazil

Reviewed by:
Yosio Edemir Shimabukuro, National Institute of Space Research (INPE), Brazil
Louis Reymondin, Alliance Bioversity International and CIAT, France

****Correspondence:***
María Daniela Rivarola
mrivarol@vols.utk.edu

Specialty section:
This article was submitted to Remote Sensing Time Series Analysis, a section of the journal Frontiers in Remote Sensing

Received: *22 March 2022*
Accepted: *18 May 2022*
Published: *08 June 2022*

Citation:
Rivarola MD, Dein J, Simberloff D and Herrero HV (2022) Assessing Protected Area Zoning Effectiveness With Remote Sensing Data: The Case of Nahuel Huapi National Park, Argentina. Front. Remote Sens. 3:901463. doi: 10.3389/frsen.2022.901463

INTRODUCTION

Some consider the biodiversity loss occurring nowadays to be the worst biological disaster since the last mass extinction 65 million years ago (Soulé, 1987). Although protecting certain areas or ecosystems is not enough to stop and reverse this trend, the creation of protected areas (PAs) remains one of the most important measures in conservation biology (Hunter & Gibbs, 2007), as shown by the fact that protected area coverage rapidly achieved the goal of 17% of land and inland water protected set by the Convention of Biological Diversity in 2010 (CBD, 2010; WDPA, 2021).

Establishing a PA is the first step toward ecosystem conservation; however, creating a PA does not by itself guarantee its effectiveness at achieving its conservation and management goals. The need to assess PA effectiveness has been widely noted, resulting in a growing number of studies addressing the outcome from different perspectives (Bruner et al., 2001; Nagendra, 2008; Leverington et al.,

2010a; Coad et al., 2015; Barnes et al., 2016; Barnes et al., 2017; Coad et al., 2019). Leverington et al. (2010a) summarized different approaches used to assess PA effectiveness as follows: Coverage–studies biodiversity representation within PAs, also known as Gap Analysis (Scott et al., 1993; Armenteras & Villareal, 2003; Chape et al., 2005; Rodríguez-Cabal et al., 2008); Broadscale Outcomes–compares environmental changes within and outside protected areas, generally using remotely sensed data (Nagendra et al., 2013; Herrero et al., 2016); Protected Area Management Effectiveness Assessments (PAME)—uses the scoring framework developed by the IUCN (Hockings, 2003; Coad et al., 2015) or a similar approach; and lastly, Detailed Monitoring–generally reports animal population trends, vegetation conditions, or socioeconomic impacts of a particular PA (Barnes et al., 2016; Geldmann et al., 2018). These different approaches are complementary, as each addresses the outcome from a singular perspective (Hockings et al., 2006).

The term "protected area" comprises areas known by different names, often referring to different types of management. The International Union for Conservation of Nature (IUCN) recognizes six management categories organized from more to less strict as follows: Ia-Strict nature reserve, Ib-Wilderness area, II-National Park, III-Natural monument or feature, IV-Habitat/species management area, V-Protected landscape or seascape, and VI-Protected area with sustainable use of natural resources (Dudley, 2013). While extractive use is forbidden or minimal in categories from I to IV, the restrictions are reduced in categories V and VI. The idea that a stricter management category will yield better habitat preservation has been widely explored in a variety of environments, with contrasting results. A study conducted in Bolivia, Costa Rica, Indonesia, and Thailand found that, although deforestation was generally lower inside the strictest PAs, it was unclear whether this outcome was related to the management category or instead to the remote location of most of the strict PAs (Ferraro et al., 2013). The Royal Chitwan National Park in Nepal allows use by and involvement of local residents, while Celaque National Park in Honduras has a more traditional management approach in which local residents do not participate in this endeavor. Although deforestation rate was lower inside both PAs, the regeneration and conservation of the buffer zones surrounding the PAs were better where local residents were involved, suggesting that regulated use of PAs could be more effective in the long run (Nagendra et al., 2004). Fire incidence in tropical forest located in strict PAs in Latin America and Asia was lower than in the unprotected area; however, multi-use PAs in these continents sustained an even lower fire incidence (Nagendra, 2008).

While most studies looked at entire units belonging to one particular management category, the division of a PA into zones with differing categories of protection has been less studied (Hull et al., 2011). A common management approach is subdividing a PA into more than one management category, resulting in more strictly regulated areas surrounded by less regulated categories acting as buffer zones between the most highly protected area and the unprotected area (Geneletti & van Duren, 2008). This is the situation in Nahuel Huapi National Park (NHNP), located in the northern portion of the temperate forests in Patagonia, Argentina. This protected area, originally created in 1922 as National Park (formerly Southern National Park, then Nahuel Huapi National Park; NP category II IUCN), was later subdivided into National Reserve (NR; category VI IUCN) and Strict Nature Reserve (SNR; category I IUCN) (Rivarola et al., 2021a). The National Reserve was established in 1970 as a buffer zone between the National Park (west) and the unprotected area (east); furthermore, most of the private properties that existed at the time were included in this new (lower) category, allowing for regulated extractive use. Finally, in 1990 pristine and remote areas within the National Park were declared Strict Nature Reserve with no human intervention allowed (Martin & Chehébar, 2001; Rivarola et al., 2021a). NHNP has one city and two small towns on its borders, accounting for a total population of approximately 170,000 people. This region had a low human population density for most of the 20th century, a situation that changed in the 1980s. The population growth rate between 1980 and 1991 reached 101.58%, and it peaked again between 2001 and 2005 (74%), resulting in an unplanned and unregulated urbanization expansion in which social and economic inequity are evident, pressing on natural resources in a complex manner (Madariaga, 2007).

The economic development of this region was historically based on agriculture, livestock, and logging but later switched to tourism, the main source of income nowadays (Schlüler, 1994; Nuñez & Vejsbjerg, 2010). Three biomes are protected by NHNP: high Andes, Patagonian temperate forests, and steppe, with Patagonian temperate forests accounting for the largest extent (Monjeau et al., 2005). These forests have been isolated from other temperate forests since the mid-Tertiary Period (Axelrod et al., 1991; Villagrán and Hinojosa, 1997), and, as a result, 90% of the woody species are endemic (Arroyo et al., 1996) and the region is characterized by one of the highest known rates of plant-animal mutualisms (Aizen & Escurra, 1998). Despite the existence of multiple PAs incorporating Patagonian forests in Chile and Argentina (Armesto et al., 1998; Burkart, 2005), more than 1/3 of the Patagonian forests have been lost since the arrival of Europeans in the 19th century (Tecklin et al., 2002). The assessment of NHNP effectiveness in preserving its biodiversity is crucial. Integral and pluralistic approaches are needed in order to assess PA performance (Caro et al., 2009). Three of the effectiveness assessment methods suggested by Leverington et al. (2010a) have been implemented in this PA. The first was a PAME assessment that found that NHNP management falls in the fairly satisfactory category (Rusch, 2002). Secondly, a coverage study concluded that the hotspot of Patagonian biodiversity is not fully covered by the current PAs (Rodríguez-Cabal et al., 2008). Lastly, a detailed monitoring of the small mammal community of NHNP concluded that there is no clear evidence that a stricter category preserves this community better, with the exception of the endemic marsupial *Dromiciops gliroides* (Rivarola et al., 2021b). The fourth type of PA effectiveness assessment, broadscale outcome, has not yet been performed, and it is the main goal of the present study.

Ecological applications of satellite remote sensing (SRS) can potentially improve environmental management by providing verifiable and standardized data at a large temporal and spatial scale (Pettorelli et al., 2014). For decades, access to SRS data was very expensive, limiting its use in many countries and regions. The shift toward free SRS databases provided the opportunity for better and wider use of these data (Woodcock et al., 2008). Concomitantly, advances in processing methods have allowed such data to be used in a more comprehensive manner (Hansen & Loveland, 2012). An increasing number of studies have used SRS to assess PA broadscale outcomes, facilitating the evaluation of large areas that would not have been possible to assess from the ground (Nagendra et al., 2004; Buchanan et al., 2008; Wiens et al., 2009). Among all sensors, Landsat provides the longest consistently calibrated data set registering surface changes since 1972 (Markham & Helder, 2012), providing an excellent source of data for habitat monitoring, allowing detection of habitat fragmentation and disturbances in PAs (Nagendra et al., 2013).

Several vegetation indices have been developed in order to draw inferences about vegetation structure, photosynthetic capacity, and leaf water content among other ecological data. Normalized Difference Vegetation Index (NDVI) is the most widely used index and is defined as the ratio of the difference between the spectral reflectance in near-infrared (NIR) and the red (RED) wavelengths divided by the sum of both, where NIR and RED are the light reflected by the vegetation in the NIR and RED wavelength bands, respectively (Gandhi et al., 2015; Yengoh et al., 2016). This index is based on the fact that chlorophyll absorbs RED, while the mesophyll disperses NIR (Pettorelli et al., 2005), and its values range between −1 and +1, where negative values correspond to unvegetated areas (Myneni et al., 1995). This index is highly sensitive to changes in canopy photosynthetic activity, and such changes can be used as an early warning of habitat modification (Leisher et al., 2013; Nagendra et al., 2013). In terrestrial ecosystems, the amount and distribution of vegetation directly influence the abundance and distribution of resident and migrant animals; thus, NDVI is a valuable tool not only for assessing photosynthetic activity but also to infer overall ecosystem status at a large spatial and temporal scale (Pettorelli et al., 2005). Time series analysis of NDVI has been used to assess PA effectiveness, allowing researchers to differentiate between seasonal and yearly changes (Waylen et al., 2014; Herrero et al., 2016; Southworth et al., 2016; Herrero et al., 2020).

The research reported here explores vegetation status of NHNP among its three protection categories along with a neighboring unprotected area. We aimed to assess the effectiveness of the three levels of protection in the NHNP during the 21st century by comparing NDVI time series from 2000 to 2020 of areas under each level of protection to that for "matching" (or "apples-to-apples") unprotected areas in order to reduce variation associated with different land characteristics (Joppa & Pfaff, 2011). Variation in NDVI can be associated with variables including land cover, precipitation, temperature, and elevation; therefore, we incorporated these factors in our analysis. Using NDVI as a comprehensive metric for all change in vegetation aimed to identify overall trends while serving to suggest influential land change processes for further analysis.

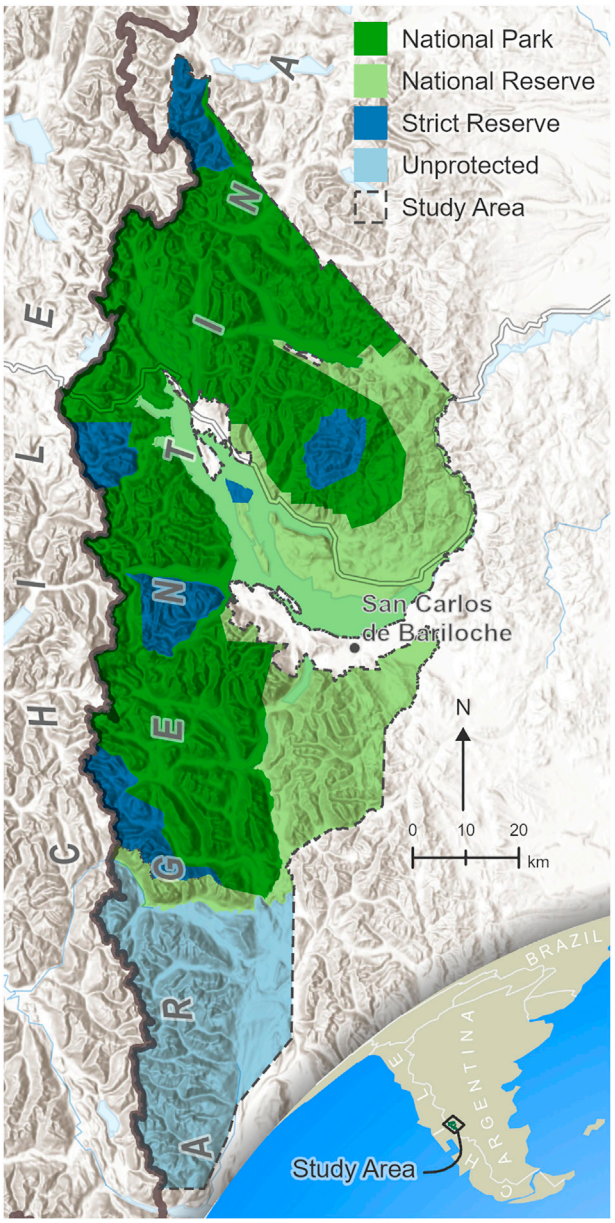

FIGURE 1 | Map of Nahuel Huapi National Park. Levels of protection indicated by different colors.

METHODS

Study Area

Nahuel Huapi National Park is located between parallels 40° 08′ 18″ and 41° 35′ 19″ South and longitudes 71°50′ 52″ and 71° 04' 45" West (**Figure 1**). It is bordered in the west by Chile, in the north by Lanín National Park, in the east by the Patagonian steppe (a small area of which is included within NR), and in the south by the Manso river. Its total area of 7,172.61 km^2 is subdivided into different management categories. The eastern 2,253.8 km^2 are designated National Reserve (NR), IUCN category VI. This area contains several private properties,

where authorized livestock and logging are frequent. Furthermore, this category allows more intensive use and the development of infrastructure related to tourism (hotels, sky resorts). The western 4,918.81 km^2 are designated National Park (NP), IUCN category II (WDPA, 2021). There are fewer private properties in this region, and although livestock and logging are forbidden by law in a category II PA, these activities are still common. More extensive use is also allowed, such as campsites and low-impact developments. In 1990, pristine areas within the National Park were declared Strict Nature Reserve (SNR, IUCN category Ia), covering 755.25 km^2; and later in 1994, a new subdivision of the NP was proclaimed Wilderness Natural Reserve (WNR, IUCN category Ib). Information regarding the decision process that led to selection of those areas to be included under the strictest category level is unavailable, other than that they were pristine areas, remotely located, with difficult or no ground access. Consequently, several are located at higher elevations (where conflicts with human uses are minimal) or in areas accessible only by boat. This category does not allow any use, other than patrolling and scientific research (Rivarola et al., 2021a). In this study, we investigated NR, NP, and SNR, insofar as we lacked access to spatial data that included WNR. Additionally, we evaluated 2,423.8 km^2 of unprotected area located south of the Manso river, using the same NHNP longitudinal range (**Figure 1**).

NHNP lies within the Valdivian Ecoregion, where High Andean, Patagonian Forests, and Steppe biomes are represented (Burkart et al., 1999). It has a mean annual precipitation of 1,800 mm, with a marked west-east gradient (from above 2,000 mm to approximately 200 mm) owing to the shadow effect of the Andes Mountains (Cabrera, 1976). Most of the NHNP is covered by forest dominated by evergreen or deciduous species of the genus *Nothofagus* (*N. pumilio*—Lenga, *N. antarctica*—Ñire, *N. dombeyi*—Coihue, *N. betuloides*—Guindo, and *N. nitida*—Coihue de Chiloé) and *Araucaria araucana* (Araucaria) in the northern area, and *Austrocedrus chilensis*—cypress along the eastern fringe in the ecotone between forest and steppe (Cabrera, 1976).

Data Collection

To quantify NDVI change in the study area in relation to significant environmental variables, we collected satellite imagery, precipitation, and temperature data from available remote sensing products from years 2000–2020, leveraging the resources of Google Earth Engine (Gorelick et al., 2017). While limited remote sensing data are available before 2000, sufficient data available starting in year 2000 allowed us to analyze vegetation change one decade after the strict reserves were first established. In addition to remote sensing data, we also acquired fire history (Mermoz et al., 2005), land cover provided from CIEFAP (Centro de Investigación y Extensión Forestal Andino Patagónico), and tourism data from APN (Administración de Parques Nacionales).

We created cloudless composites using Landsat data by selecting the "greenest" pixel from all scenes captured between December 1 and March 1 of each summer season. We selected only summer data because the presence of evergreen and deciduous forests prevents us from evaluating photosynthetic activity in fall and winter, while frequent presence of snow during the spring would also bias our analysis. The greenest pixel was taken to be that with the highest NDVI, which we computed for each available scene during each season. At least 25 scenes were available for each season.

Composites before 2013 were created using Landsat 7 scenes (Landsat 7 Collection 1 Tier 1 TOA Reflectance courtesy of the U.S. Geological Survey), and composites 2013 and after were created using Landsat 8 (Landsat 8 Collection 1 Tier 1 TOA Reflectance courtesy of the U.S. Geological Survey).

Selecting the greenest pixel allowed for the best interseason NDVI comparisons. However, while the method works well for creating cloudless composites in areas with vegetation present,

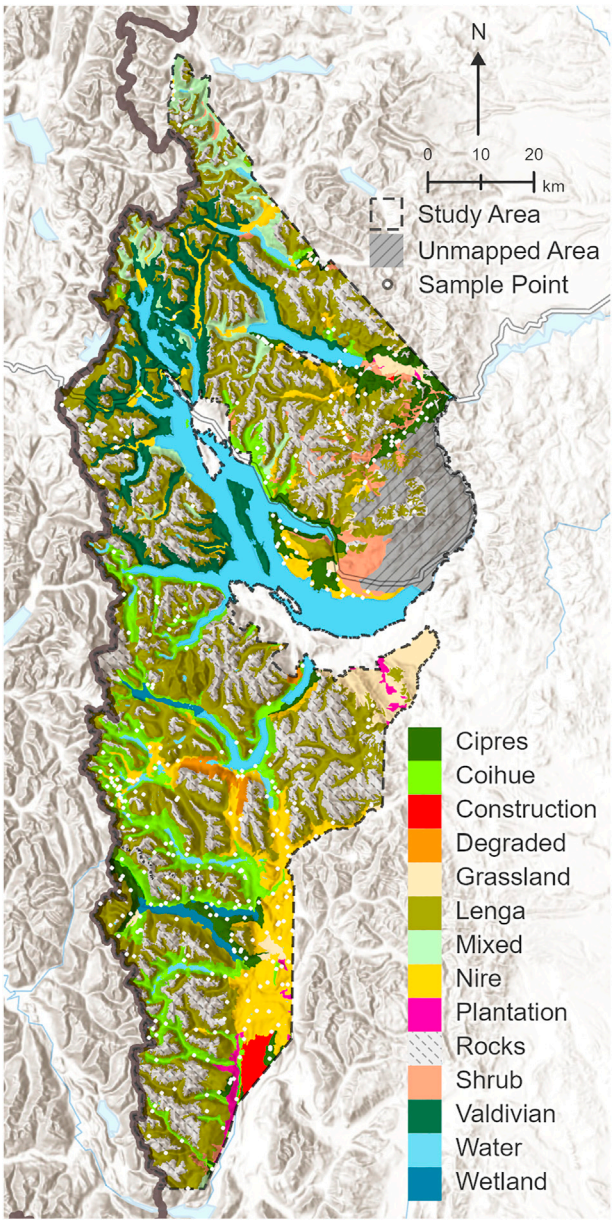

FIGURE 2 | Land cover of NHNP and neighboring area.

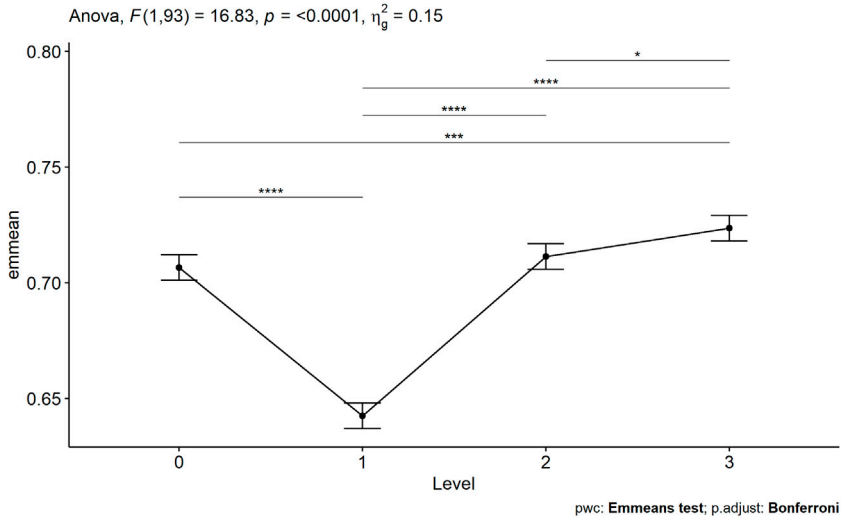

FIGURE 3 | Variation in mean NDVI at different levels of protection (0: Unprotected area, 1: National Reserve, 2: National Park, 3: Strict Nature Reserve). Horizontal lines on top indicate statistical differences between levels of protection (pairs).

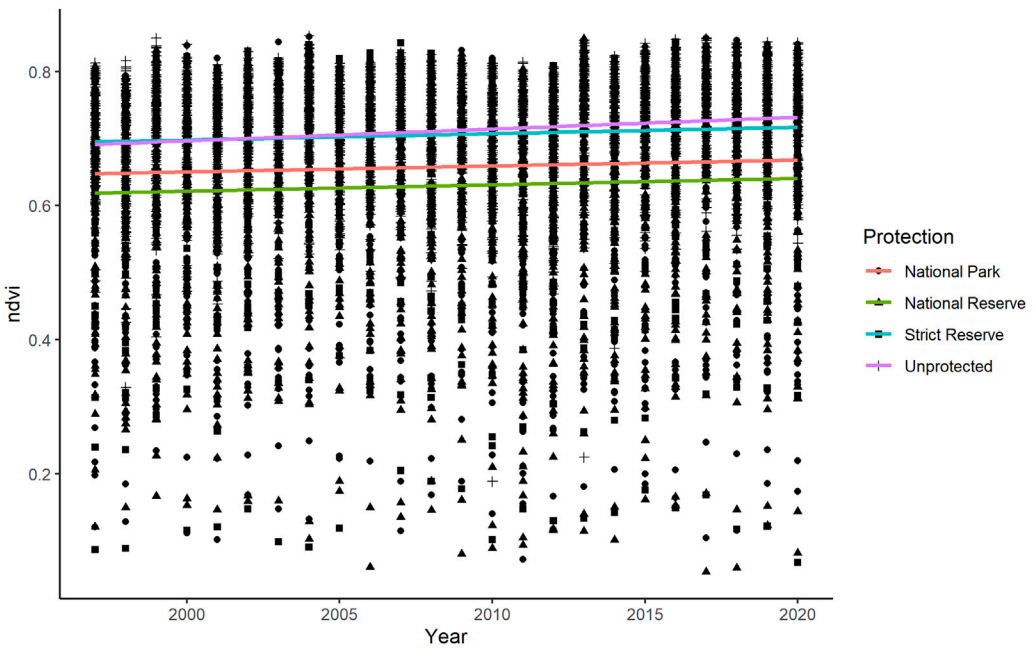

FIGURE 4 | NDVI values over time recorded for a total of 375 random points equally distributed among the four levels of protection and four dominant tree species (*Nothofagus dombeyi*, *N. antarctica*, *N. pumilio*, and *Austrocedrus chilensis*).

pixels containing clouds are often selected over areas with low NDVI values, such as water bodies, urban areas, and areas above the tree line. Because these areas contained little vegetation (e.g., sparse ground vegetation growing above the tree line) or no vegetation (water bodies, rocks, bare ground), they were irrelevant to our analysis, and we masked them from the resulting composites to exclude them from analysis. The mask was taken from land cover data provided to us by CIEFAP (Centro de Investigación y Extensión Forestal Andino Patagónico) and shown in **Figure 2**.

We collected precipitation data within the study area from the Global Precipitation Measurement (GPM) Integrated Multi-satellitE Retrievals for GPM (IMERG) dataset (Huffman et al., 2019). IMERG provides total precipitation for every month at 0.1 × 0.1° (approximately 11.1 × 11.1 km) spatial resolution and calibrates multiple satellite estimates with ground sources.

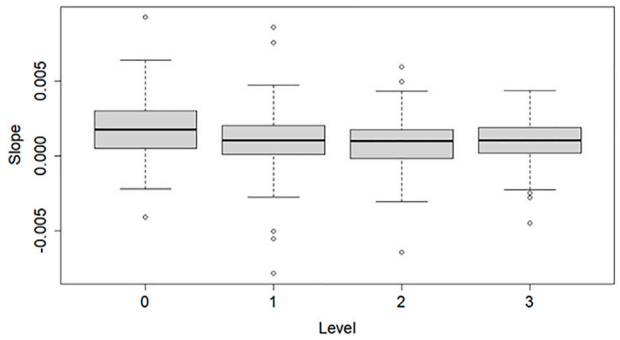

FIGURE 5 | Comparison of the NDVI increases over time, indicated as positive slope values, among the different levels of protection (DF = 3, 368, F = 4.366, p = 0.005). 0: unprotected area, 1: National Reserve, 2: National Park, and 3: Strict Nature Reserve.

We collected temperature data within the study area from the MOD11A1 V6 product derived from data collected by satellites equipped with the Moderate Resolution Imaging Spectroradiometer (MODIS) instrument (Wan et al., 2015). The data provide daily (one daytime and one nighttime) land surface temperature estimates at 1 × 1 km resolution. We computed the mean daytime temperature for every year (Jan 1st-December 31st) for use in analysis.

Data Analysis

We calculated the mean NDVI per austral summer from 2000 to 2020 at each level of protection (SNR, NP, NR, Unprotected). We evaluated the synergistic effect of protection and time on changes in mean NDVI using an analysis of covariance (ANCOVA), followed by a post hoc Bonferroni adjustment test. Level of protection and years (2000–2020) were the categorical and continuous variables, respectively. Since differences in NDVI among the levels of protection do not necessarily mean healthier vegetation, but rather could be related to differences in dominant species cover (e.g., NP mostly dominated by *N. dombeyi* vs. NR mostly dominated by *A. chilensis*), precipitation, elevation, or temperature, in a second step we selected random points in each of the Unprotected, NR, NP, and SNR levels. Using the available data regarding dominant species cover across NHNP (Margutti & Arosteguy, 2019), we selected 25 random points per area dominated by one of the four most common dominant tree species: *N. dombeyi*, *N. antarctica*, *N. pumilio*, and *A. chilensis*, accounting for a total of 100 random points each for NP, NR and Unprotected area, and 75 random points for SNR, because no area is dominated by *A. chilensis* within this category (**Figure 2**). For these 375 random points we extracted the elevation, and their NDVI values, temperature, and precipitation from 2000 to 2020.

For each random point we ran a linear regression in which we evaluated NDVI change over time, resulting in a total of 375 linear regressions. From each linear regression, we extracted the slope, as it provided us with information regarding the general trend of NDVI change per level of protection. Lastly, we ran an ANOVA test to evaluate if the slopes (indicating NDVI change over time) varied among the four levels of protection, followed by a Tukey HSD test.

Nothofagus dombeyi, *N. antarctica*, *N. pumilio*, and *A. chilensis* respond differently to disturbances such as wildfire, drought, livestock, and windstorm (Raffaele et al., 2014). To investigate if these species experienced a different trend among the levels of protection, we ran a two-way ANOVA test, grouping by level of protection and dominant species and using as dependent variable the 375 slopes from the random points mentioned above, followed by a Bonferroni test.

Previous studies have indicated that precipitation plays an important role in determining NDVI (Herrero et al., 2020). Other characteristics, such as elevation and temperature, might also affect the NDVI values. In order to reduce the number of physical variables used to explain changes in NDVI, we used Pearson's

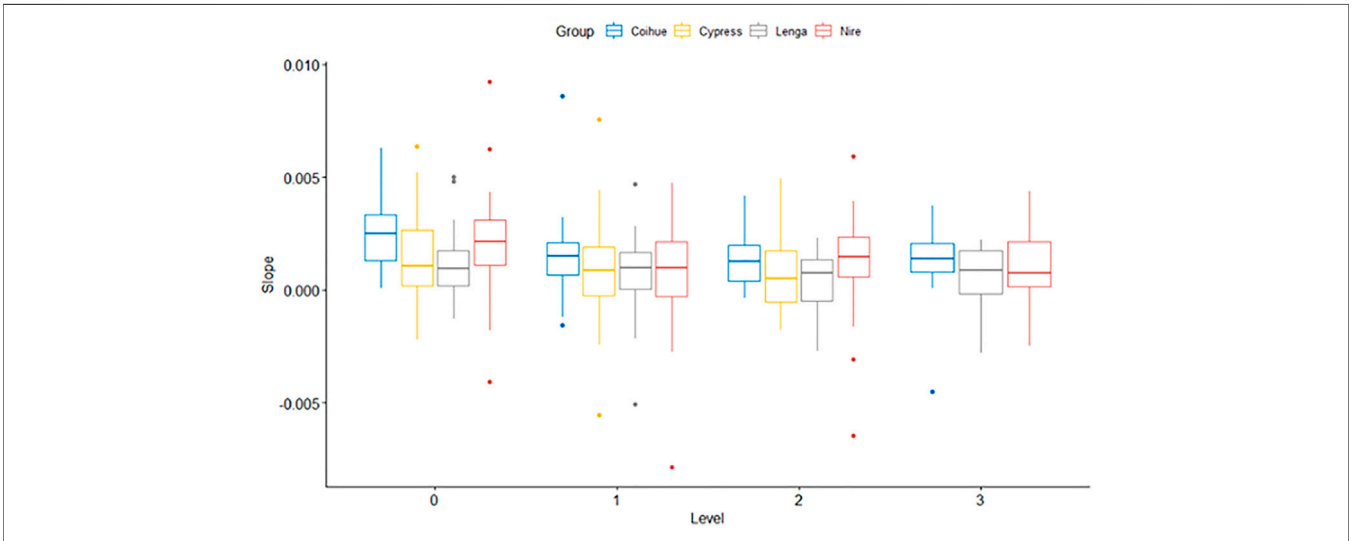

FIGURE 6 | Comparison among the NDVI increases over time, indicated as positive slope values, for each of the four most common dominant tree species, among the different levels of protection. 0: unprotected area, 1: National Reserve, 2: National Park, and 3: Strict Nature Reserve.

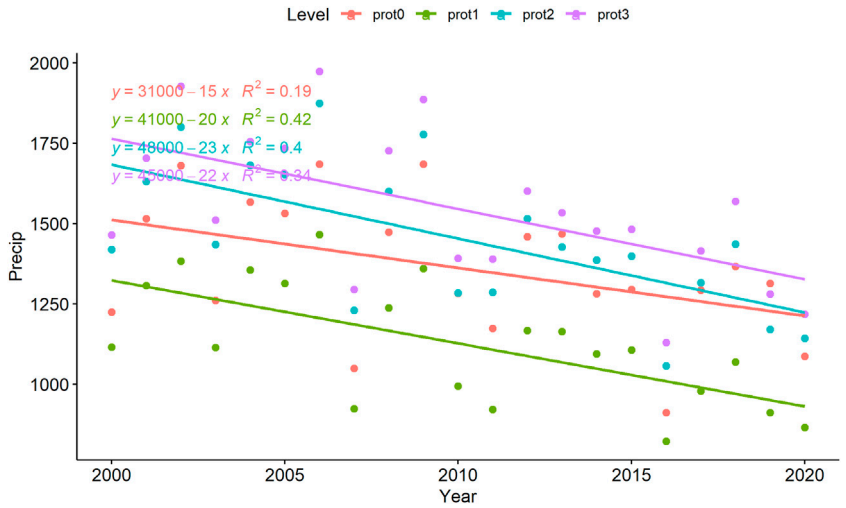

FIGURE 7 | Annual precipitation change for each level of protection. prot0: unprotected area, prot1: National Reserve, prot2: National Park, prot3: Strict Nature Reserve.

TABLE 1 | Results from a Bonferroni test indicating differences between changes in annual precipitation at each protection category. Statistical significance is indicated by ∗.

Levels Compared	DF	F	p
Unprotected vs. NR	79	4.28	5.16e-5 ***
Unprotected vs. NP	79	−1.66	0.100
Unprotected vs. SNR	79	−3.35	1.24e-3 **
NR vs. NP	79	−5.97	7.07e-8 ****
NR vs. SNR	79	−7.63	4.5e-11 ****
NP vs. SNR	79	−1.69	0.096

product-moment correlation to evaluate the correlation between precipitation and elevation (t = 2.16, df = 7,810, p-value = 0.03) and correlation between precipitation and temperature (t = −36.20, df = 7,810, p-value=<1.1e-16). We ran a linear regression to evaluate if annual precipitation in the studied area affected its NDVI. We transformed NDVI values using a Box-Cox transformation to satisfy the normality assumption, then evaluated by ANCOVA whether different levels of protection differed in annual precipitation.

To identify areas where changes in NDVI over the 20-year period were more notable, we filtered those pixels where values changed by more than 1 standard deviation (1 SD = 0.05) in both positive and negative directions. We ran a linear regression to evaluate if increases in NDVI were related to the level of protection, and we ran a second linear regression to analyze the relation between NDVI decreases and level of protection. As mentioned above, total area differs among levels of protection. To standardize the measure among them, we used the percent of area (of each level of protection) where NDVI changed by more than 1 SD. While an increase in NDVI is associated with vegetation growth, this does not necessarily mean that natural vegetation is thriving; in fact, several undesired landscape modifications can induce that change, such as land abandonment and agriculture expansion (Pan et al., 2018). On the other hand, a decrease in NDVI in areas dominated by a particular tree species could reflect disturbances with negative effects on that species. To investigate this situation further, we conducted an ANOVA test to evaluate if decreases in NDVI were related to the type of forest.

We performed the statistical analyses using R 4.0.3 (R Core Team, 2014).

The study area is highly visited during the summer months, when the risk of wildfire is higher owing to low seasonal precipitation. Campsites distributed in NP, NR, and in the neighboring unprotected area receive thousands of visitors, increasing the risk of wildfires. We performed a colocation analysis to determine if fires were more likely to occur near designated campsites. Colocation analysis yields a colocation quotient for each fire centroid, where values less than 1 indicate isolation and values greater than 1 indicate spatial correlation (Leslie & Kronenfeld, 2011). We performed the analysis using the Spatial Statistics toolbox in ESRI ArcGIS Pro version 2.8 using the four nearest neighbors. Fire data were provided by INIBIOMA (Instituto de Investigaciones en Biodiversidad y Medioambiente) and campsite data were provided by NHNP.

RESULTS

We performed an ANCOVA to determine the effect of level of protection on NDVI after controlling for time (years). There was a statistically significant difference in NDVI between the groups (F (3,91) = 170.43, $p < 0.0001$). Mean NDVI in the Strict Nature Reserve (0.724 ± 0.003) significantly exceeded that in the National Park (0.711 ± 0.003), Unprotected area (0.707 ± 0.003), and National Reserve (0.642 ± 0.003), $p < 0.001$ (**Figure 3**).

Linear regressions based on the 375 random points showed an overall NDVI increase over time (**Figure 4**). We analyzed differences in slope among protection categories by ANOVA. The greening process (NDVI increase over time) was significantly higher in the

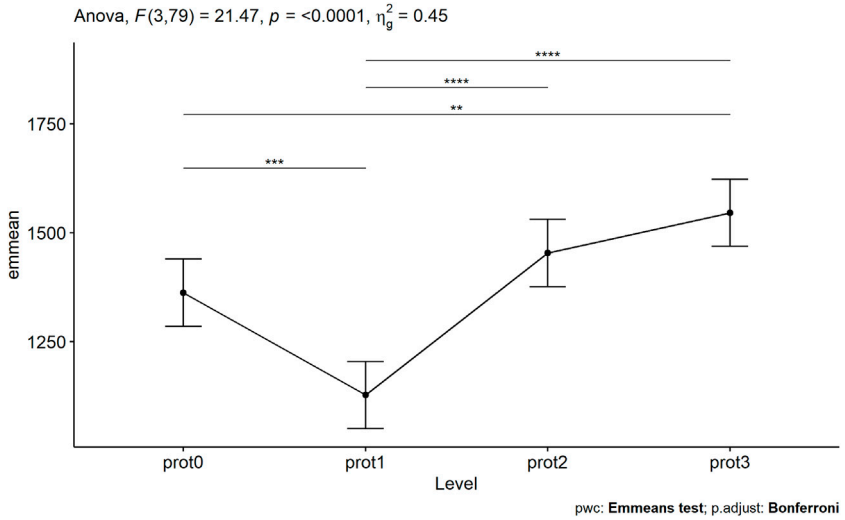

FIGURE 8 | Estimated mean annual precipitation for each level of protection based on 20 years of precipitation data (period 2000–2020). Statistical differences among the protection categories are indicated with *. prot0: unprotected area, prot1: National Reserve, prot2: National Park, prot3: Strict Nature Reserve. Horizontal lines on top indicate statistical differences between levels of protection (pairs).

unprotected area than in the Natural Reserve ($p = 0.022$), the National Park ($p = 0.01$), and the Strict Nature Reserve ($p = 0.03$) (**Figure 5**).

We further investigated if dominant tree species had a different trend of NDVI change over time in each protection category with a two-way ANOVA. The interaction term between level of protection and dominant tree species was not significant (DF = 8, 357, F = 0.283, $p = 0.971$), indicating that the tree species did not follow different trends over time in different protection categories (**Figure 6**). Nevertheless, the "Group" term indicated that different species did follow a different trend without accounting for the protection level (DF = 3, 357, F = 4.036, $p = 0.008$). We then computed a pairwise comparison using a Bonferroni test and found that the trend of NDVI change over time was more pronounced in *N. dombeyi* than in *N. pumilio* ($p = 0.0009$), with no differences among the other species.

Precipitation and temperature were negatively correlated (t = −36.198, df = 7,810, p-value < 2.2e-16, r = −0.38), and areas with higher temperature had lower NDVI. On the other hand, precipitation and elevation were positively correlated (t = 2.1616, df = 7,810, p-value = 0.03, r = 0.02). We further analyzed the effects of precipitation on NDVI, since it was the physical variable that explained the highest fraction of the variation. We found a positive correlation between annual precipitation and NDVI (F (1,82) = 17.87, $p = 6.1e-05$). We conducted an ANCOVA in order to determine if annual precipitation has changed in the studied area, and furthermore, if this change is consistent among the different levels of protection. We found an overall decrease in annual precipitation (F (1,79) = 38.428, $p = 2.42e-08$), although this decrease differed among levels of protection (F (3,79) = 21.469, $p = 2.88e-10$) (**Figure 7**). In addition, a post-hoc Bonferroni analysis showed that estimated mean annual precipitation in the National Reserve was significantly lower than in the other three categories and that the estimated mean precipitation in the Strict Nature Reserve was higher than in the unprotected area (**Table 1**; **Figure 8**).

Areas where NDVI changed by more than 1 standard deviation (both positive and negative) are indicated in **Figure 9**. The percent of greening areas in the unprotected area significantly exceeded that in the NR (Adj. R-squared = 0.435, F (4, 91) = 19.26, $p = 1.666e-11$), while no significant differences with and among the other categories were found (**Figure 10**). On the contrary, the same analysis applied to percent of areas with a decreased NDVI yielded no relationship with years or level of protection (Adj. R-squared = 0.001, F (4, 91) = 1.039, $p = 0.392$) (**Figure 11**).

To evaluate if negative changes in NDVI were more frequent in forests dominated by a particular tree species, we conducted an ANOVA. We found a significant difference between the number of pixels with a decreased NDVI and the type of forest (F (4,15) = 3.922, $p = 0.023$). Forests dominated by *N. pumilio* contained larger proportional areas with a decreased NDVI than did mixed forests ($p = 0.0339$) and forests dominated by shrub species ($p = 0.026$) (**Figure 12**).

As shown in **Figure 13** and **Table 2**, colocation analysis suggests that some fires were more likely to occur near campsites than if they were randomly distributed. However, none of the quotients are statistically significant, which could be due to the low number of both fires (n = 23) and campsites (n = 28). Overall, approximately 1.7% of the land within the study area burned between 2000 and 2020.

DISCUSSION

Remote sensing data provide an excellent opportunity to evaluate land surface changes over time at different scales, from local to

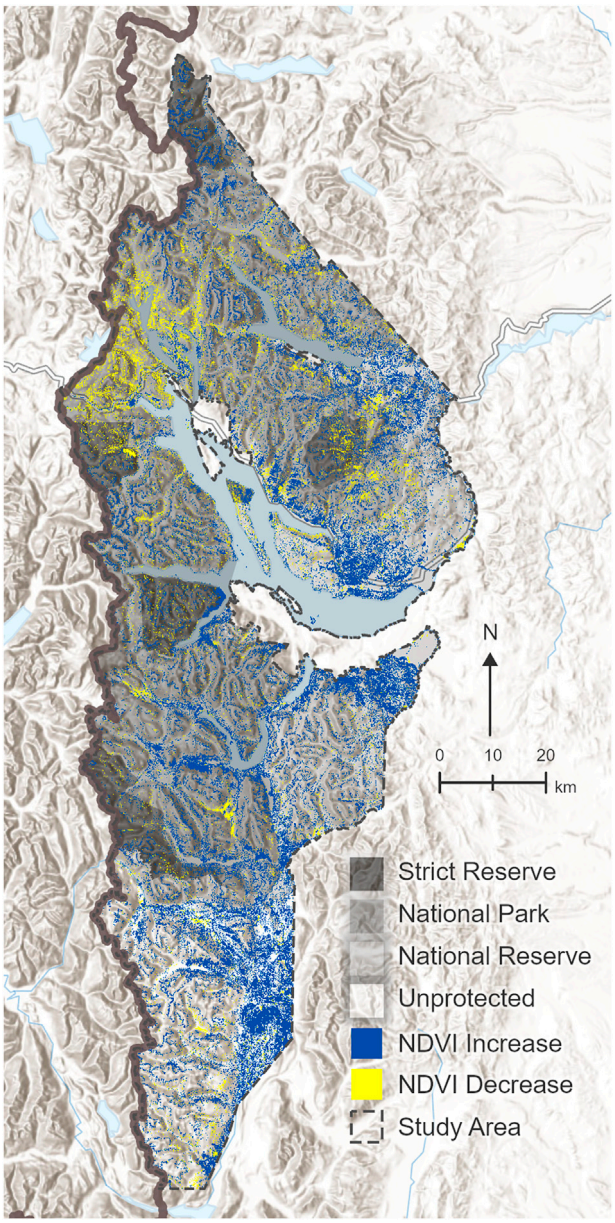

FIGURE 9 | Map with areas with NDVI increase (blue) and decrease (yellow) in the period 2000–2020.

global assessments, and they have been widely used to evaluate fragmentation and degradation within protected areas (Nagendra et al., 2013). Leisher et al. (2013) analyzed land and forest degradation in 1,788 PAs in Latin America between 2004 and 2009, concluding that the rate of degradation increased from 0.04 to 0.10% per year, resulting in 1,097,618 ha degraded. They evaluated 166 Argentinean PAs, concluding that almost 20% of them have experienced land and forest degradation, despite having a funding level three times the average for the Latin American countries (US$ 8.60 versus US$ 2.50 per hectare). In this study, we evaluated in detail the conservation status of the oldest and one of the largest of the Argentinean PAs, Nahuel Huapi National Park (NHNP). The second NHNP Management Plan published in 2019 (Margutti & Arosteguy, 2019) highlighted the importance of unifying the criteria used to subdivide the PA following its formal and legal delimitation between different conservation categories (Strict Nature Reserve, Wilderness Natural Reserve, National Park, National Reserve; IUCN categories Ia, Ib, II and VI respectively) rather than by zoning categories based on its uses, as the first management plan proposed (Gil et al., 1986). Because the strictest category was created in 1990, our study spanning from 2000 to 2020 provides the best up-to-date evidence at a broad scale regarding the effectiveness of this high conservation category. NDVI values were consistently higher in the SNR compared to the other protection categories and the unprotected area with an assessment based on the average NDVI per category per year.

This result would provide an optimistic assessment of the effectiveness of the strictest category. However, differences in area, location (affecting precipitation, temperature, elevation), and dominant tree species among the protection categories might bias our understanding of differences among them in effectiveness. To address this problem, we re-evaluated NDVI changes based on the selection of 375 random points, with an equal representation of different dominant tree species among the four levels. Surprisingly, with this second analysis, the unprotected area shows the highest values of NDVI, which differ statistically from those values reported in the three categories inside the PA. A common approach is to compare vegetation inside and outside PAs. However, the border of a PA may coincide with a natural change in habitat type leading to misinterpretation regarding the effectiveness of such a PA (Mas, 2005; Joppa & Pfaff, 2011; Ferraro et al., 2013). We purposely selected as unprotected area the neighboring southern region based on landscape, climatic conditions, and floral similarities with the PA, since the eastern area transitions into steppe and the western area is in a different nation, Chile. Finally, NDVI values within NHNP coincided with the levels of protection (NDVI values SNR > NP > NR).

The general NDVI change trend was positive for all four categories. We found similar results with both assessments (average NDVI per category and using 375 pixel values). The observation of increasing NDVI values agrees with the greening phenomenon reported globally (Zhu et al., 2016). However, interpreting positive NDVI changes remains challenging because no rigorous method has yet been validated (Leisher et al., 2013). Greener does not necessarily mean better conserved. Seasonal or annual changes in NDVI could be associated with an increase in leaf size, number of leaves per plant, plant density, and crop grown per year, but it can also reflect replacement of natural ecosystems by agricultural lands, or non-native species colonization after disturbances (Piao et al., 2020). We selected the widespread NDVI as a comprehensive metric to assess overall vegetation trends between levels of protection. Established land change detection algorithms, such as LandTrendr (Kennedy et al., 2018) and CCDC (Arévalo et al., 2020), for example, could be used to study specific land change processes, such as forest degradation/regeneration (e.g., Piffer et al., 2022), in more detail. However, algorithms designed to detect abrupt changes may not identify land change processes,

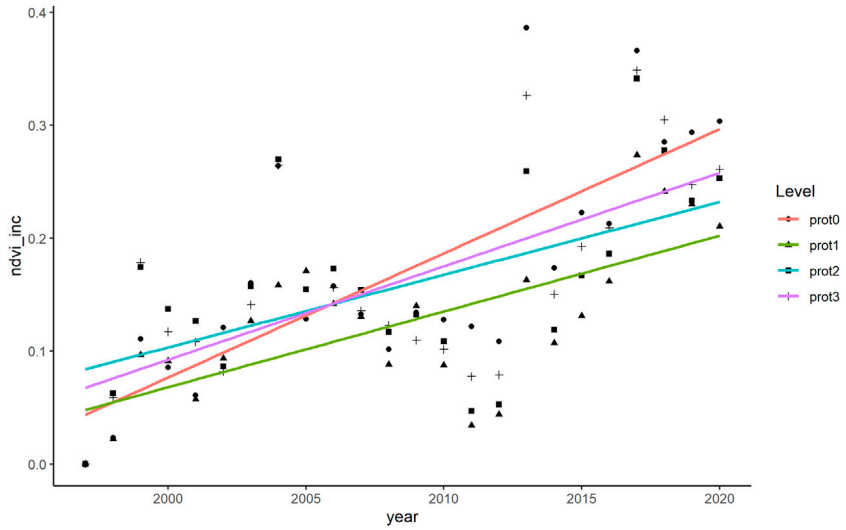

FIGURE 10 | Percent of area with an increase in NDVI, per level of protection, over time. prot0: unprotected area, prot1: National Reserve, prot2: National Park, prot3: Strict Nature Reserve.

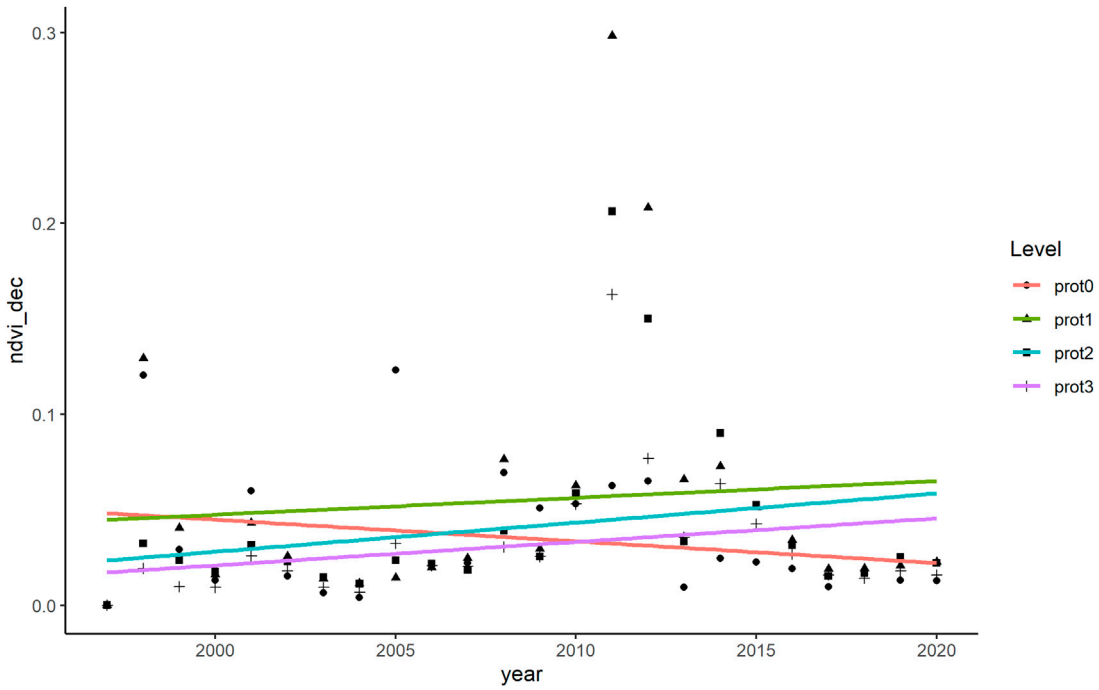

FIGURE 11 | Percent of area with a decrease in NDVI, per level of protection, over time. prot0: unprotected area, prot1: National Reserve, prot2: National Park, prot3: Strict Nature Reserve.

such as the spread of invasive species or global greening. In the case of NHNP, no forest has been replaced by agricultural land, but rather more gradual land change processes of livestock grazing and spread of non-native species were identified as main threats to the PA, along with the more abrupt disturbances of logging and wildfire (Margutti & Arosteguy, 2019). While a compelling body of evidence depicts negative effects associated with non-native plant species in NHNP (Simberloff et al., 2002; Nuñez, 2008; Svriz et al., 2013; Franzese & Ghermandi, 2014), where 25% of the plant species are non-native (Raffaele et al., 2014), further studies are needed to evaluate if this colonization is related to the increased NDVI

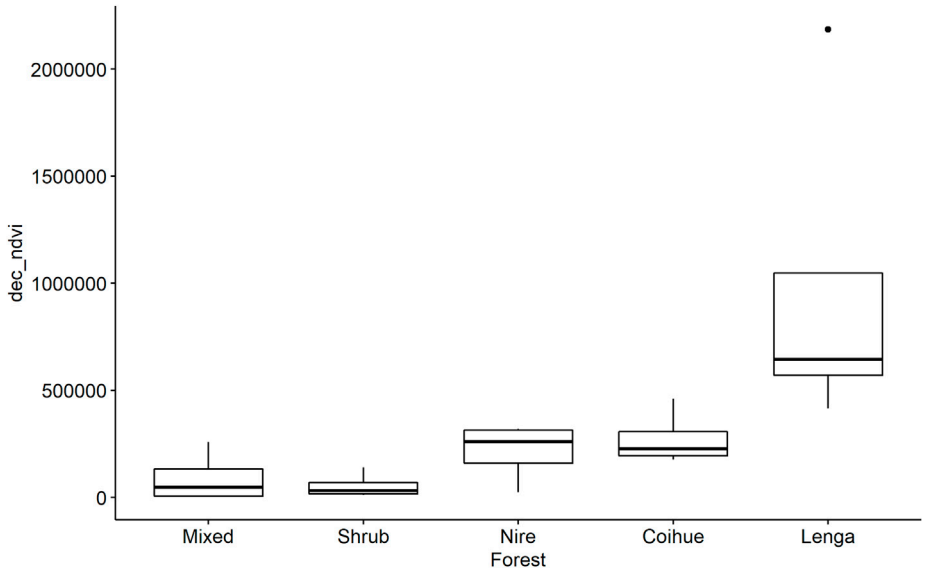

FIGURE 12 | Total number of pixels where NDVI decreased over a 20-year period for each type of forest.

TABLE 2 | Colocation Analysis Summary: relation between wildfires and campsites.

ID	Year	Area (ha)	Colocation Quotient	*p*-value	Colocation Label
2	2013	201.2	1.4	0.5	Colocated
3	1999	99.4	0.0	0.06	Isolated
4	2002	14.8	1.1	0.96	Colocated
9	1999	593.8	1.2	0.86	Colocated
10	1999	2.1	1.4	0.76	Colocated
11	1999	145.0	0.3	0.2	Isolated
12	1999	3,830.6	1.4	0.48	Colocated
13	1999	513.4	0.0	0.06	Isolated
15	2002	191.8	1.4	0.42	Colocated
19	2015	459.9	0.9	0.74	Isolated
20	1999	123.1	1.4	0.72	Colocated
21	1999	8.6	1.4	0.52	Colocated
1	1999	1933.2	Not analyzed	—	—
22	1999	177.8	Not analyzed	—	—
23	2004	272.4	Not analyzed	—	—
5	2013	1.0	Not analyzed	—	—
6	2006	246.8	Not analyzed	—	—
7	2012	322.3	Not analyzed	—	—
8	2009	2160.0	Not analyzed	—	—
14	2012	39.6	Not analyzed	—	—
16	2002	2364.4	Not analyzed	—	—
17	2002	317.0	Not analyzed	—	—
18	2004	278.6	Not analyzed	—	—

values reported here. Furthermore, introduced animals impact forest structure and regeneration in NHNP (Barrios-Garcia & Simberloff, 2013; Nuñez et al., 2013; Rodríguez-Cabal et al., 2013; Martin-Albarracin et al., 2015). Land change processes can interact to produce complex outcomes. For example, the combination of cattle and wildfires negatively affected regeneration of *Nothofagus dombeyi - Austrocedrus chilensis* mixed forests in NHNP, facilitating a post-fire transition from forest to bamboo-dominated shrubland (Blackhall et al., 2008), which could increase NDVI values (Franco et al., 2020). Specific studies addressing this question are needed and could be aided by land cover classification in combination with established land change detection algorithms.

We found a positive relationship between NDVI and precipitation, supporting previous findings (Herrero et al., 2020). Furthermore, the variation in precipitation among the

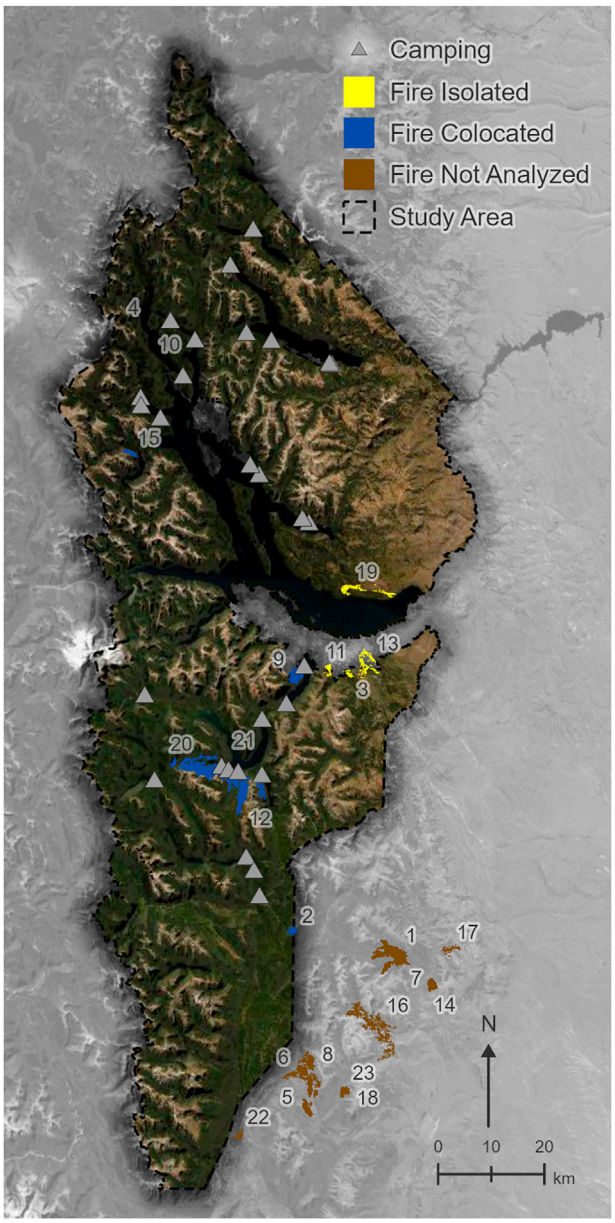

FIGURE 13 | Fires and campsites within the study area.

levels of protection resembles the differences found among their NDVI values (SNR > NP > Outside > NR, see **Figure 3** and **Figure 8**), suggesting that precipitation might be the cause of these differences in NDVI rather than levels of protection. However, mean annual precipitation fluctuated over time across this region, but the overall trend manifests a decreasing pattern. Precipitation therefore cannot explain the increasing NDVI trend.

In addition to identifying the general greening pattern explained above, we further investigated this process by extracting pixels where the NDVI changed more than 1 SD during the period studied. The unprotected area accounted for a larger increase compared to the NR, while this difference was not evident between unprotected and NP, unprotected and SNR, or within the three levels of protection inside NHNP. As stated above, interpretation of increasing NDVI is difficult; however, as a similar pattern or tendency was observed inside and outside the PA, the greening process could be a consequence of a global phenomenon such as climate change and increased CO_2 (Ogunkoya et al., 2021), further exacerbated in the unprotected area where extensive livestock and logging are common.

Negative NDVI change could be more easily related to degradation and habitat fragmentation (Morton et al., 2005; Leisher et al., 2013). We found no evidence that degradation was more extensive in the unprotected area compared to that in areas under any level of protection. However, during the year 2012 there was a peak in the percentage of area with a negative NDVI change inside the PA (NR ~ 30%, NP ~ 20%, SNR ~16%), but this value remained low in the unprotected area (~5%). This result could be explained by the massive ash deposit as consequence of the Puyehue-Cordón Caulle volcanic eruption that dispersed about 100 million metric tons of ash, covering 7.5 million ha in Patagonia (Wilson et al., 2013). While the central and northern areas of NHNP were severely affected by ash deposition, the southern portion of NHNP and the unprotected area evaluated in this study remained free of ash. The area more severely affected by ash deposition (Bignami et al., 2014) coincides with the yellow area observed in the NW section of **Figure 9**.

Fragmentation or degradation were more striking in areas dominated by *Nothofagus pumilio* (both inside and outside the PA) compared to areas dominated by mixed forests and shrublands. *Nothofagus pumilio* forests are distributed at high elevations along approximately 3,000 km of the southern Andes Mountain chain (Mathiasen & Premoli, 2010). A previous study found a positive correlation between *N. pumilio* growth and precipitation, and a negative correlation with mean annual temperature (Lara et al., 2005). Severe droughts in the 20th century following relatively wet and cool years have been associated with a persistent decline in *N. pumilio* growth, suggesting that current and future trends with lower precipitation and higher temperatures associated with climate change would further promote the decline of these forests (Rodríguez-Catón et al., 2016). Furthermore, wildfires have historically affected forests of *N. pumilio* by direct burning (Veblen et al., 2003) and also by reducing root ectomycorrhizal colonization after fire (Longo et al., 2011).

Wildfires in the region are common between September and April, with record numbers in January and February, due to the combination of low precipitation and high temperatures during the austral summer. The causes of most of these wildfires remain unknown owing to lack of trained personnel and low budgets. However, human activities are thought to be closely related to their occurrence (Monjeau et al., 2005; Margutti & Arosteguy, 2019). Although tourists arrive in NHNP throughout the year, more than 23% of the total annual visitation occurs during the summer months (Área Técnica y Estadística, 2015). Campsites are distributed in NP, NR, and the unprotected area, and camping during summer is one of the favorite activities for both residents and tourists. Since the establishment of campsites within the PA

is regulated by the APN (National Park Administration), we explored if the locations of wildfires were associated with the authorized campsites. We used available data (date, location, and area burnt) for 22 wildfires that occurred between 1999 and 2015 within NHNP. Although we found no relationship between these two variables, it is important to notice that there were a total of 239 fires recorded in this period, most of which (150) affected less than 0.5 ha (Margutti & Arosteguy, 2019), and no location data were available, so we could not include such data in our analysis. Furthermore, illegal campfires are common across the region, and the low number of personnel and lack of appropriate vehicles make it difficult for authorities to prevent them (Rivarola et al., 2021a). On the other hand, the combination of the current trend of warmer and drier summers following unusually dry springs (phenomena associated with La Niña events), uncommon electrical storms during the summer, and the massive accumulation of fuel material in the forests constitutes a permanent threat for these forests, across all levels of protection. The remote and isolated location of most SNR areas makes them particularly vulnerable to fires, since ground access is difficult, preventing prompt response to many fires, resulting in thousands of hectares affected. On 7 December 2021, lighting ignited a wildfire in the southern area of NHNP, within the SNR. The initial, small fire could not be controlled because firefighters could not access the area. The wildfire is spreading and remains active at the time this manuscript is being written, 1.5 months after the initiation of the fire. It is estimated that more than 6,000 ha of pristine native forests within NHNP (both in SNR and NP) have been burned (ADN, 2022; Sala de Noticias, 2022).

Effectiveness assessments should be performed regularly, using multiple and complementary approaches, which would provide crucial information to update management plans as needed, and ultimately, would secure PA conservation goals. The inclusion of PA protection categories, reports regarding effectiveness assessments implemented in those PAs with multiple categories, and current and past management plans within WDPA (the global databases on PAs) would allow a consistent evaluation at the local and global scale. Effective management of PAs is essential to conserve natural ecosystems. Their role in ecosystem services and preserving biodiversity goes beyond the limits of a PA, and they constitute a substantial fraction of a country's national capital, supporting national sustainable development and human well-being (Bovarnick et al., 2010). The Argentinean PA system has a long history, and despite political and economic instability in the country, the general trend of PA establishment and management by the APN is promising (Rivarola et al., 2021a). Weaknesses and threats were well identified in the latest management plan for NHNP, and general and specific goals were established for both the short and the long term. This study provides new information that stakeholders in NHNP could take into account to better assess the conditions and changes occurring in this PA and act accordingly. NHNP is an emblematic PA at the national and international level, and its successful management would benefit not only the natural ecosystems represented in the area but also people who are directly or indirectly connected to this PA.

DATA AVAILABILITY STATEMENT

The raw data supporting the conclusions of this article will be made available by the authors, without undue reservation.

AUTHOR CONTRIBUTIONS

MR developed the idea, obtained local data, did the literature review, analyzed the data, created the graphs, and wrote the manuscript. JD obtained, cleaned, and organized the data, and made the maps. DS revised and edited the manuscript. HH provided ideas, revised and edited the manuscript.

REFERENCES

Adn, S. U. R. (2022). *ADN Sur Agencia de Noticias*. Chubut, Argentina: Comodoro Rivadavia. https://www.adnsur.com.ar.Río Negro: el incendio cerca del Lago Steffen ya afectó unas 5.438 hectáreas

Aizen, M., and Escurra, C. (1998). High Incidence of Plant-Animal Mutualisms in the Woody Flora of the Temperate Forest of Southern South America: Biogeographical Origin and Present Ecological Significance. *Ecol. Austral* 8, 217–236.

Arévalo, P., Bullock, E. L., Woodcock, C. E., and Olofsson, P. (2020). A Suite of Tools for Continuous Land Change Monitoring in Google Earth Engine. *Front. Clim.* 2, 576740. doi:10.3389/fclim.2020.576740

Armenteras, D., Gast, F., and Villareal, H. (2003). Andean Forest Fragmentation and the Representativeness of Protected Natural Areas in the Eastern Andes, Colombia. *Biol. Conserv.* 113, 245–256. doi:10.1016/s0309-1740(03)00100-110.1016/s0006-3207(02)00359-2

Armesto, J. J., Rozzi, R., Smith-Ramírez, C., and Arroyo, M. T. K. (1998). Conservation Targets in South American Temperate Forests. *Science* 282, 1271–1272. doi:10.1126/science.282.5392.1271

Arroyo, M. T. K., Riveros, M., Peñaloza, A., Cavieres, L., and Faggi, A. M. (1996). "Phytogeographic Relationships and Regional Richness Patterns of the Cool Temperate Rainforest Flora of Southern South America," in *High-Latitude Rainforests and Associated Ecosystems of the West Coast of the Americas: Climate, Hydrology, Ecology, and Conservation*. Editor R. G. Lawford, et al. (New York, NY: Springer New York), 134–172. doi:10.1007/978-1-4612-3970-3_8

Axelrod, D. I., Kalin Arroyo, M. T., and Raven, P. H. (1991). Historical Development of Temperate Vegetation in the Americas. *Rev. Chil. Hist. Nat.* 64, 413–446.

Barnes, M. D., Craigie, I. D., Dudley, N., and Hockings, M. (2017). Understanding Local-Scale Drivers of Biodiversity Outcomes in Terrestrial Protected Areas. *Ann. N.Y. Acad. Sci.* 1399, 42–60. doi:10.1111/nyas.13154

Barnes, M. D., Craigie, I. D., Harrison, L. B., Geldmann, J., Collen, B., Whitmee, S., et al. (2016). Wildlife Population Trends in Protected Areas Predicted by National Socio-Economic Metrics and Body Size. *Nat. Commun.* 7, 1–9. doi:10.1038/ncomms12747

Barrios-Garcia, M. N., and Simberloff, D. (2013). Linking the Pattern to the Mechanism: How an Introduced Mammal Facilitates Plant Invasions. *Austral Ecol.* 38, 884–890. doi:10.1111/aec.12027

Bignami, C., Corradini, S., Merucci, L., de Michele, M., Raucoules, D., De Astis, G., et al. (2014). Multisensor Satellite Monitoring of the 2011 Puyehue-Cordon Caulle Eruption. *IEEE J. Sel. Top. Appl. Earth Obs. Remote Sens.* 7 (7), 2786–2796.

Blackhall, M., Raffaele, E., and Veblen, T. T. (2008). Cattle Affect Early Post-fire Regeneration in a Nothofagus Dombeyi-Austrocedrus Chilensis Mixed Forest in Northern Patagonia, Argentina. *Biol. Conserv.* 141, 2251–2261. doi:10.1016/j.biocon.2008.06.016

Bovarnick, A., Fernandez Baca, J., Galindo, J., and Negret, H. (2010). *Financial Sustainability of Protected Areas in Latin America and the Caribbean: Investment Policy Guidance*. New York, NY and Arlington, VA: United Nations Development Program (UNDP) and The Nature Conservancy (TNC).

Bruner, A. G., Gullison, R. E., Rice, R. E., and da Fonseca, G. A. B. (2001). Effectiveness of Parks in Protecting Tropical Biodiversity. *Science* 291, 125–128. doi:10.1126/science.291.5501.125

Buchanan, G. M., Butchart, S. H. M., Dutson, G., Pilgrim, J. D., Steininger, M. K., Bishop, K. D., et al. (2008). Using Remote Sensing to Inform Conservation Status Assessment: Estimates of Recent Deforestation Rates on New Britain and the Impacts upon Endemic Birds. *Biol. Conserv.* 141, 56–66. doi:10.1016/j.biocon.2007.08.023

Burkart, R. (2005). "Las Áreas Protegidas de la Argentina," in *La Situación Ambiental Argentina 2005*. Editors A. Brown, U. Martinez Ortiz, M. Acerbi, and J. Corcuera (Buenos Aires, Argentina: Administracion de Parques Nacionales), 399–431.

Burkart, R., Barbaro, N. O., Sanchez, R. O., and Gomez, D. A. (1999). in *Eco-Regiones de la Argentina* (Buenos Aires, Argentina: Presidencia de la Nacion), 45. Administracion de Parques Nacionales, S. d. R. N. y. D. S.

Cabrera, L. A. (1976). *Regiones Fitogeográficas Argentinas*. Buenos Aires: ACMA.

Caro, T., Gardner, T. A., Stoner, C., Fitzherbert, E., and Davenport, T. R. B. (2009). Assessing the Effectiveness of Protected Areas: Paradoxes Call for Pluralism in Evaluating Conservation Performance. *Divers. Distributions* 15, 178–182. doi:10.1111/j.1472-4642.2008.00522.x

CBD (2010). *Decision Adopted by the CoP to the CBD at its 10th Meeting (UNEP/CBD/COP/DEC/X/2*. Montreal: Secretariat of the CBD.

Chape, S., Harrison, J., Spalding, M., and Lysenko, I. (2005). Measuring the Extent and Effectiveness of Protected Areas as an Indicator for Meeting Global Biodiversity Targets. *Phil. Trans. R. Soc. B* 360, 443–455. doi:10.1098/rstb.2004.1592

Coad, L., Leverington, F., Knights, K., Geldmann, J., Eassom, A., Kapos, V., et al. (2015). Measuring Impact of Protected Area Management Interventions: Current and Future Use of the Global Database of Protected Area Management Effectiveness. *Phil. Trans. R. Soc. B* 370, 20140281. doi:10.1098/rstb.2014.0281

Coad, L., Watson, J. E., Geldmann, J., Burgess, N. D., Leverington, F., Hockings, M., et al. (2019). Widespread Shortfalls in Protected Area Resourcing Undermine Efforts to Conserve Biodiversity. *Front. Ecol. Environ.* 17, 259–264. doi:10.1002/fee.2042

Dudley, N. (2013). *Guidelines for Applying Protected Area Management Categories Including IUCN WCPA Best Practice Guidance on Recognising Protected Areas and Assigning Management Categories and Governance Types*. Gland: IUCN, 86.

Estadística, Á. T. Y. (2015). *Temporada Estival Enero Y Febrero, Comparación Anual*. San Carlos de Bariloche: Secretaría Municipal de Turismo, 16.

Ferraro, P. J., Hanauer, M. M., Miteva, D. A., Canavire-Bacarreza, G. J., Pattanayak, S. K., and Sims, K. R. E. (2013). More Strictly Protected Areas Are Not Necessarily More Protective: Evidence from Bolivia, Costa Rica, Indonesia, and Thailand. *Environ. Res. Lett.* 8, 025011. doi:10.1088/1748-9326/8/2/025011

Franco, M. G., Mundo, I. A., and Veblen, T. T. (2020). Field-validated Burn-Severity Mapping in North Patagonian Forests. *Remote Sens.* 12, 214. doi:10.3390/rs12020214

Franzese, J., and Ghermandi, L. (2014). Early Competition between the Exotic Herb Rumex acetosella and Two Native Tussock Grasses with Different Palatability and Water Stress Tolerance. *J. Arid Environ.* 106, 58–62. doi:10.1016/j.jaridenv.2014.03.004

Gandhi, G. M., Parthiban, S., Thummalu, N., and Christy, A. (2015). Ndvi: Vegetation Change Detection Using Remote Sensing and GIS - A Case Study of Vellore District. *Procedia Comput. Sci.* 57, 1199–1210. doi:10.1016/j.procs.2015.07.415

Geldmann, J., Coad, L., Barnes, M. D., Craigie, I. D., Woodley, S., Balmford, A., et al. (2018). A Global Analysis of Management Capacity and Ecological Outcomes in Terrestrial Protected Areas. *Conserv. Lett.* 11, e12434. doi:10.1111/conl.12434

Geneletti, D., and van Duren, I. (2008). Protected Area Zoning for Conservation and Use: A Combination of Spatial Multicriteria and Multiobjective Evaluation. *Landsc. Urban Plan.* 85, 97–110. doi:10.1016/j.landurbplan.2007.10.004

Gil, J., Malvarez, I., and Martín, C. (1986). *Plan de Manejo del Parque Nacional Nahuel Huapi*. Editor A. d. P. Nacionales (Bariloche - Argentina: APN).

Gorelick, N., Hancher, M., Dixon, M., Ilyushchenko, S., Thau, D., and Moore, R. (2017). Google Earth Engine: Planetary-Scale Geospatial Analysis for Everyone. *Remote Sens. Environ.* 202, 18–27. doi:10.1016/j.rse.2017.06.031

Hansen, M. C., and Loveland, T. R. (2012). A Review of Large Area Monitoring of Land Cover Change Using Landsat Data. *Remote Sens. Environ.* 122, 66–74. doi:10.1016/j.rse.2011.08.024

Herrero, H., Southworth, J., and Bunting, E. (2016). Utilizing Multiple Lines of Evidence to Determine Landscape Degradation within Protected Area Landscapes: A Case Study of Chobe National Park, Botswana from 1982 to 2011. *Remote Sens.* 8, 623. doi:10.3390/rs8080623

Herrero, H., Southworth, J., Muir, C., Khatami, R., Bunting, E., and Child, B. (2020). An Evaluation of Vegetation Health in and Around Southern African National Parks during the 21st Century (2000-2016). *Appl. Sci.* 10, 2366. doi:10.3390/app10072366

Hockings, M., Stolton, S. U. E., Leverington, F., Dudley, N., Courrau, J., and Valentine, P. (2006). *Evaluating Effectiveness. A Framework for Assessing Management Effectiveness of Protected Areas*. Gland, Switzerland and Cambridge, UK: IUCN The World Conservation Union.

Hockings, M. (2003). Systems for Assessing the Effectiveness of Management in Protected Areas. *BioScience* 53, 823. doi:10.1641/0006-3568(2003)053[0823:sfateo]2.0.co;2

Huffman, G. J., Stocker, E. F., Bolvin, D. T., Nelkin, E. J., and Tan, J. (2019). *GPM IMERG Final Precipitation L3 1 Month 0.1 Degree X 0.1 Degree V06*. Greenbelt, MD: Goddard Earth Sciences Data and Information Services Center (GES DISC.

Hull, V., Xu, W., Liu, W., Zhou, S., Viña, A., Zhang, J., et al. (2011). Evaluating the Efficacy of Zoning Designations for Protected Area Management. *Biol. Conserv.* 144, 3028–3037. doi:10.1016/j.biocon.2011.09.007

Hunter, M. L., and Gibbs, J. P. (2007). *Fundamentals of Conservation Biology*. Maden, MA, USA: Blackwell Publishing.

Joppa, L. N., and Pfaff, A. (2011). Global Protected Area Impacts. *Proc. R. Soc. B* 278, 1633–1638. doi:10.1098/rspb.2010.1713

Kennedy, R., Yang, Z., Gorelick, N., Braaten, J., Cavalcante, L., Cohen, W., et al. (2018). Implementation of the LandTrendr Algorithm on Google Earth Engine. *Remote Sens.* 105, 691. doi:10.3390/rs10050691

Lara, A., Villalba, R., Wolodarsky-Franke, A., Aravena, J. C., Luckman, B. H., and Cuq, E. (2005). Spatial and Temporal Variation in Nothofagus Pumilio Growth at Tree Line along its Latitudinal Range (35°40′-55° S) in the Chilean Andes. *J. Biogeogr.* 32, 879–893. doi:10.1111/j.1365-2699.2005.01191.x

Leisher, C., Touval, J., Hess, S., Boucher, T., and Reymondin, L. (2013). Land and Forest Degradation inside Protected Areas in Latin America. *Diversity* 5, 779–795. doi:10.3390/d5040779

Leslie, T. F., and Kronenfeld, B. J. (2011). The Colocation Quotient: A New Measure of Spatial Association between Categorical Subsets of Points. *Geogr. Anal.* 43, 306–326. doi:10.1111/j.1538-4632.2011.00821.x

Leverington, F., Costa, K. L., Pavese, H., Lisle, A., and Hockings, M. (2010a). A Global Analysis of Protected Area Management Effectiveness. *Environ. Manag.* 46, 685–698. doi:10.1007/s00267-010-9564-5

Longo, M. S., Urcelay, C., and Nouhra, E. (2011). Long Term Effects of Fire on Ectomycorrhizas and Soil Properties in Nothofagus Pumilio Forests in Argentina. *For. Ecol. Manag.* 262, 348–354. doi:10.1016/j.foreco.2011.03.041

Madariaga, M. (2007). *Interacción entre ambiente y población en San Carlos de Bariloche*. Bariloche, Rio Negro, Argentina: INTA, 40.

Margutti, L., and Arosteguy, C. (2019). "Plan de Gestión del Parque Nacional Nahuel Huapi," in *San Carlos de Bariloche*. Editor A. d. P. Nacionales.

Markham, B. L., and Helder, D. L. (2012). Forty-year Calibrated Record of Earth-Reflected Radiance from Landsat: A Review. *Remote Sens. Environ.* 122, 30–40. doi:10.1016/j.rse.2011.06.026

Martin, C. E., and Chehébar, C. (2001). The National Parks of Argentinian Patagonia - Management Policies for Conservation, Public Use, Rural Settlements, and Indigenous Communities. *J. R. Soc. N. Z.* 31, 845–864. doi:10.1080/03014223.2001.9517680

Martin-Albarracin, V. L., Nuñez, M. A., and Amico, G. C. (2015). Replacement of Native by Non-native Animal Communities Assisted by Human Introduction

and Management on Isla Victoria, Nahuel Huapi National Park. *PeerJ* 3, e1328. doi:10.7717/peerj.1328

Mas, J.-F. (2005). Assessing Protected Area Effectiveness Using Surrounding (Buffer) Areas Environmentally Similar to the Target Area. *Environ. Monit. Assess.* 105, 69–80. doi:10.1007/s10661-005-3156-5

Mathiasen, P., and Premoli, A. C. (2010). Out in the Cold: Genetic Variation of Nothofagus Pumilio (Nothofagaceae) Provides Evidence for Latitudinally Distinct Evolutionary Histories in Austral South America. *Mol. Ecol.* 19, 371–385. doi:10.1111/j.1365-294X.2009.04456.x

Mermoz, M., Kitzberger, T., and Veblen, T. T. (2005). Landscape Influences on Occurrence and Spread of Wildfires in Patagonian Forests and Shrublands. *Ecology* 86, 2705–2715. doi:10.1890/04-1850

Monjeau, A., Nazar Anchorena, S., Montoni, V., Marquez, J., Alcalde, D., D'Iorio, A., et al. (2005). Perfil del Área Protegida Argentina: Parque Nacional Nahuel Huapi. Available at: http://www.parkswatch.org/parkprofile.php?l=eng&country=arg&park=nhnp.

Morton, D. C., DeFries, R. S., Shimabukuro, Y. E., Anderson, L. O., Del Bon Espírito-Santo, F., Hansen, M., et al. (2005). Rapid Assessment of Annual Deforestation in the Brazilian Amazon Using MODIS Data. *Earth Interact.* 9, 1–22. doi:10.1175/ei139.1

Myneni, R. B., Hall, F. G., Sellers, P. J., and Marshak, A. L. (1995). The Interpretation of Spectral Vegetation Indexes. *IEEE Trans. Geosci. Remote Sens.* 33, 481–486. doi:10.1109/TGRS.1995.874602910.1109/36.377948

Nagendra, H. (2008). Do parks Work? Impact of Protected Areas on Land Cover Clearing. *AMBIO A J. Hum. Environ.* 37, 330–337. doi:10.1579/06-r-184.1

Nagendra, H., Lucas, R., Honrado, J. P., Jongman, R. H. G., Tarantino, C., Adamo, M., et al. (2013). Remote Sensing for Conservation Monitoring: Assessing Protected Areas, Habitat Extent, Habitat Condition, Species Diversity, and Threats. *Ecol. Indic.* 33, 45–59. doi:10.1016/j.ecolind.2012.09.014

Nagendra, H., Tucker, C., Carlson, L., Southworth, J., Karmacharya, M., and Karna, B. (2004). Monitoring Parks through Remote Sensing: Studies in Nepal and Honduras. *Environ. Manag.* 34, 748–760. doi:10.1007/s00267-004-0028-7

Nuñez, M. A. (2008), Experiments on Multiple Factors Affecting Pinaceae Invasions on Isla Victoria, Nahuel Huapi National Park, Argentina. *Ecology and Evolutionary Biology, PhD. Diss*. Knoxville, TN: University of Tennessee, 102.

Nuñez, M. A., Hayward, J., Horton, T. R., Amico, G. C., Dimarco, R. D., Barrios-Garcia, M. N., et al. (2013). Exotic Mammals Disperse Exotic Fungi that Promote Invasion by Exotic Trees. *PLoS One* 8, e66832. doi:10.1371/journal.pone.0066832

Nuñez, P., and Vejsbjerg, L. (2010). *Tourism between Economic Activity and Social Right*, 19. Nahuel Huapi National Park, 1934930–1955945.*Estud. Perspect. Tur.*

Ogunkoya, A., Kaplan, J., Whitlock, C., Nanavati, W., Roberts, D. W., and Poulter, B. (2021). Drivers of Recent Forest Cover Change in Southern South America Are Linked to Climate and CO2. *Landsc. Ecol.* 36, 3591–3606. doi:10.1007/s10980-021-01330-7

Pettorelli, N., Laurance, W. F., O'Brien, T. G., Wegmann, M., Nagendra, H., Turner, W., et al. (2014). Satellite Remote Sensing for Applied Ecologists: Opportunities and Challenges. *J. Appl. Ecol.* 51, 839–848. doi:10.1111/1365-2664.12261

Pettorelli, N., Vik, J. O., Mysterud, A., Gaillard, J.-M., Tucker, C. J., and Stenseth, N. C. (2005). Using the Satellite-Derived NDVI to Assess Ecological Responses to Environmental Change. *Trends Ecol. Evol.* 20, 503–510. doi:10.1016/j.tree.2005.05.011

Piao, S., Wang, X., Park, T., Chen, C., Lian, X., He, Y., et al. (2020). Characteristics, Drivers and Feedbacks of Global Greening. *Nat. Rev. Earth Environ.* 1, 14–27. doi:10.1038/s43017-019-0001-x

Piffer, P. R., Rosa, M. R., Tambosi, L. R., Metzger, J. P., and Uriarte, M. (2022). Turnover Rates of Regenerated Forests Challenge Restoration Efforts in the Brazilian Atlantic Forest. *Environ. Res. Lett.* 17 (4), 045009. doi:10.1088/1748-9326/ac5ae1

R Core Team (2014). *R: A Language and Environment for Statsitical Computing*. Vienna, Austria: R Foundation for Statistical Computing.

Raffaele, E., de Torres Curth, M., Morales, C. L., and Kitzberger, T. (2014). *Ecologia e Historia Natural de la Patagonia Andina*. Ciuddad Autonoma de Buenos Aires, Argentina: Fundacion de Historia Natural Felix de Azara.

Rivarola, M. D., Simberloff, D., and Leppanen, C. (2021a). History of Protected Areas in Argentina: A Seesaw of Shifting Priorities and Policies in a Developing Country. *Environ. Hist. camb* 27, 515–548. doi:10.3197/096734019X15740974883825

Rivarola, M. D., Simberloff, D., and Leppanen, C. (2021b). Nahuel Huapi National Park, Argentina: Conservation Effectiveness Assessment through Monitoring Small Mammal Communities. *PARKS* 27, 15–26. doi:10.2305/iucn.ch.2021.parks-27-2mdr.en

Rodríguez-Catón, M., Villalba, R., Morales, M., and Srur, A. (2016). Influence of Droughts on *Nothofagus Pumilio* Forest Decline across Northern Patagonia, Argentina. *Ecosphere* 7, e01390. doi:10.1002/ecs2.1390

Rodríguez-Cabal, M. A., Barrios-Garcia, M. N., Amico, G. C., Aizen, M. A., and Sanders, N. J. (2013). Node-by-node Disassembly of a Mutualistic Interaction Web Driven by Species Introductions. *Proc. Natl. Acad. Sci. U.S.A.* 110, 16503–16507. doi:10.1073/pnas.1300131110

Rodríguez-Cabal, M. A., Nuñez, M. A., and Martínez, A. S. (2008). Quantity versus Quality: Endemism and Protected Areas in the Temperate Forest of South America. *Austral Ecol.* 33, 730–736. doi:10.1111/j.1442-9993.2008.01841.x

Rusch, V. (2002). *Estado de Situacion de las Areas Protegidas de la porcion Argentina de la Ecoregion Valdiviana*. Argentina: Fundacion Vida Silvestre ArgentinaWWF, 98.

Sala de Noticias (2022). Incendios en Bariloche: ya hay más de 6.000 hectáreas afectadas y esperan la ayuda de la lluvia. El Noticiero Digital. Available at: https://elnoticierodigital.com.ar.

Schlüler, R. G. (1994). San Carlos de Bariloche: Costos y beneficios del ecoturismo. *Estud. Perspect. Tur.* 3, 149–196.

Scott, J. M., Davis, F., Csuti, B., Noss, R., Butterfield, B., Groves, C., et al. (1993). Gap Analysis: A Geographic Approach to Protection of Biological Diversity. *Wildl. Monogr.*, 3–41.

Simberloff, D., Relva, M. A., and Nuñez, M. (2002). Gringos en el bosque: introduced tree invasion in native *Nothofagus/Austrocedrus* forest. *Biol. Invasions* 4, 35–53. doi:10.1023/a:1020576408884

Soulé, M. E. (1987). History of the Society for Conservation Biology: How and Why We Got Here. *Conserv. Biol.* 1, 4–5. doi:10.1111/j.1523-1739.1987.tb00001.x

Southworth, J., Zhu, L., Bunting, E., Ryan, S. J., Herrero, H., Waylen, P. R., et al. (2016). Changes in Vegetation Persistence across Global Savanna Landscapes, 1982-2010. *J. Land Use Sci.* 11, 7–32. doi:10.1080/1747423X.2015.1071439

Svriz, M., Damascos, M. A., Zimmermann, H., and Hensen, I. (2013). The Exotic Shrub Rosa Rubiginosa as a Nurse Plant. Implications for the Restoration of Disturbed Temperate Forests in Patagonia, Argentina. *For. Ecol. Manag.* 289, 234–242. doi:10.1016/j.foreco.2012.09.037

Tecklin, D., Vila, A. R., and Palminteri, S. (2002). *A Biodiversity Vision for the Valdivian Temperate Rain Forest Ecoregion of Chile and Argentina*. Washington, D.C: WWF.

UNEP-WCMC and IUCN (2022). *Protected Planet: The World Database on Protected Areas (WDPA) and World Database on Other Effective Area-Based Conservation Measures (WD-OECM)*. Cambridge, UK: UNEP-WCMC and IUCN.

UNEP-WCMC (2017). *Protected Planet. Base de datos mundial sobre la efectividad del manejo de áreas protegidas Manual del usuario 1.0*. Cambridge, UK: UNEP-WCMC. Available at: http://wcmc.io/GD-PAME_User_Manual_ES.

Veblen, T. T., Kitzberger, T., Raffaele, E., and Lorenz, D. C. (2003). "Fire History and Vegetation Changes in Northern Patagonia, Argentina," in *Fire and Climatic Change in Temperate Ecosystems of the Western Americas*. Editor T. T. Veblen, et al. (New York, NY: Springer New York), 265–295.

Wan, Z., Hook, S., and Hulley, G. (2015). *NASA EOSDIS Land Processes DAAC*.MOD11A1 MODIS/Terra Land Surface Temperature/Emissivity Daily L3 Global 1km SIN Grid V006 [Data Set]

Waylen, P., Southworth, J., Gibbes, C., and Tsai, H. (2014). Time Series Analysis of Land Cover Change: Developing Statistical Tools to Determine Significance of Land Cover Changes in Persistence Analyses. *Remote Sens.* 6, 4473–4497. doi:10.3390/rs6054473

WDPA (2021). *World Database of Protected Areas - Protected Planet*, 2021.

Wiens, J., Sutter, R., Anderson, M., Blanchard, J., Barnett, A., Aguilar-Amuchastegui, N., et al. (2009). Selecting and Conserving Lands for Biodiversity: The Role of Remote Sensing. *Remote Sens. Environ.* 113, 1370–1381. doi:10.1016/j.rse.2008.06.020

Wilson, T., Stewart, C., Bickerton, H., Baxter, P., Outes, A. V., Villarosa, G., et al. (2013). Impacts of the June 2011 Puyehue-Cordón Caulle Volcanic Complex Eruption on Urban Infrastructure. *Agric. public health* 2012, 88. Institute of Geology and Nucelar Sciences; GNS Science.

Woodcock, C. E., Allen, R., Anderson, M., Belward, A., Bindschadler, R., Cohen, W., et al. (2008). Free Access to Landsat Imagery. *Science* 320, 1011. doi:10.1126/science.320.5879.1011a

Yengoh, G. T., Dent, D. L., Olsson, L., Tengberg, A. E., and Tucker, C., III (2016). *Future Trends, and Practical Considerations*. ChamNew York: Springer International Publishing AG.Use of the Normalized Difference Vegetation Index (NDVI) to Assess Land Degradation at Multiple Scales: Current Status

Zhu, Z., Piao, S., Myneni, R. B., Huang, M., Zeng, Z., Canadell, J. G., et al. (2016). Greening of the Earth and its Drivers. *Nat. Clim. Change* 6, 791–795. doi:10.1038/nclimate3004

Conflict of Interest: The authors declare that the research was conducted in the absence of any commercial or financial relationships that could be construed as a potential conflict of interest.

Publisher's Note: All claims expressed in this article are solely those of the authors and do not necessarily represent those of their affiliated organizations, or those of the publisher, the editors and the reviewers. Any product that may be evaluated in this article, or claim that may be made by its manufacturer, is not guaranteed or endorsed by the publisher.

frontiers | Frontiers in Remote Sensing

ORIGINAL RESEARCH
published: 01 July 2022
doi: 10.3389/frsen.2022.869291

Discovering Inclusivity in Remote Sensing: Leaving No One Behind

Karen E. Joyce[1], Catherine L. Nakalembe[2], Cristina Gómez[3,4], Gopika Suresh[5], Kate Fickas[6], Meghan Halabisky[7], Michelle Kalamandeen[8,9,10] and Morgan A. Crowley[11]*

[1]James Cook University Nguma-bada Campus, College of Science and Engineering/TropWATER, Cairns, QLD, Australia, [2]Department of Geographical Sciences, University of MD, College Park, MD, United States, [3]EiFAB-iuFOR, Campus Duques de Soria, Universidad de Valladolid, Soria, Spain, [4]Department of Geography and Environment, University of Aberdeen, Aberdeen, United Kingdom, [5]German Federal Agency for Cartography and Geodesy, Frankfurt Am Main, Germany, [6]Department of Environmental Conservation, Holdsworth Natural Resources Center, University of MA, Amherst, MA, United States, [7]School of Environmental and Forest Sciences, College of the Environment, University of WA, Seattle, WA, United States, [8]Department of Plant Sciences, University of Cambridge, Cambridge, United Kingdom, [9]Living with Lakes Centre, Laurentian University, Sudbury, ON, Canada, [10]Remote Sensing Lab, School of Earth, Environment and Society, McMaster University, Hamilton, ON, Canada, [11]Department of Natural Resource Sciences, McGill University, Sainte-Anne-de-Bellevue, QC, Canada

Innovative and beneficial science stems from diverse teams and authorships that are inclusive of many perspectives. In this paper, we explore the status of inclusivity in remote sensing academic publishing, using an audit of peer-reviewed journal editorial board composition. Our findings demonstrate diversity deficiency in gender and country of residence, limiting the majority of editors to men residing in four countries. We also examine the many challenges underrepresented communities within our field face, such as implicit bias, harsher reviews, and fewer citations. We assert that in the field of remote sensing, the gatekeepers are not representative of the global society and this lack of representation restricts what research is valued and published, and ultimately who becomes successful. We present an action plan to help make the field of remote sensing more diverse and inclusive and urge every individual to consider their role as editor, author, reviewer, or reader. We believe that each of us have a choice to continue to align with a journal/institution/society that is representative of the dynamic state of our field and its people, ensuring that no one is left behind while discovering all the fascinating possibilities in remote sensing.

Keywords: equity, diversity, inclusion, gatekeepers, editorial boards, bias, women in STEM, remote sensing

OPEN ACCESS

Edited by:
Kelley Crews, University of Texas at Austin, United States

Reviewed by:
Muhammad Imran, Pir Mehr Ali Shah Arid Agriculture University, Pakistan
Paige Wooden, American Geophysical Union, United States

****Correspondence:***
Karen E. Joyce
karen.joyce@jcu.edu.au

Specialty section:
This article was submitted to Remote Sensing Time Series Analysis, a section of the journal Frontiers in Remote Sensing

Received: *04 February 2022*
Accepted: *30 May 2022*
Published: *01 July 2022*

Citation:
Joyce KE, Nakalembe CL, Gómez C, Suresh G, Fickas K, Halabisky M, Kalamandeen M and Crowley MA (2022) Discovering Inclusivity in Remote Sensing: Leaving No One Behind. Front. Remote Sens. 3:869291. doi: 10.3389/frsen.2022.869291

1 SETTING THE SCENE

The rules of any game determine the winners and losers, whether it is in sports or academia. In academia, the definition of success includes who is talented, who is competent, who is brilliant, what research has potential, and what methods are innovative. However, this very definition of success has been and continues to be determined by a group incongruous with the demographic depth of the field. Yet rules defining success do not have to be static. Science, just like nature, is dynamic and must evolve, to provide the greatest opportunity for advancement. It is, therefore, time to examine the various stages in academic publishing to make them more inclusive and representative of the present state of our dynamic planet.

Perhaps the ultimate determinant of a journal´s success is its financial bottom line, and its ability to stay 'in business' and sustain a high impact factor. Contributions from editors, authors, reviewers, and the readership drives any journal as a business. These stakeholder groups are not mutually

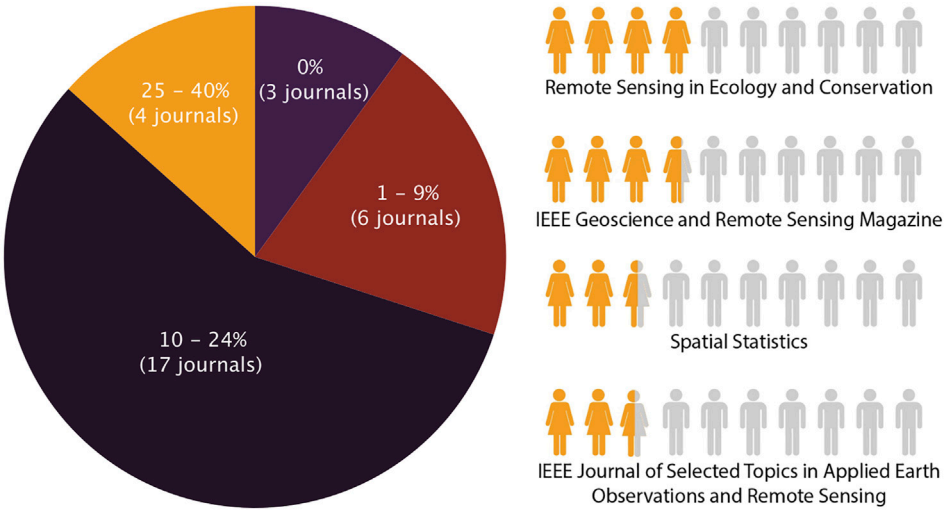

FIGURE 1 | Proportion of women on the editorial boards of 30 peer-reviewed journals in the remote sensing discipline audited as part of this article. The four journals with the highest proportion of women on their boards are also shown.

exclusive, and many people act in two or more of these roles at any given time. If large numbers of individuals within any of these groups disengage, the journal's 'success' may be in jeopardy. It is therefore beholden on a journal to keep its mission, publications, and management in line with stakeholders' desires, demands, or values. The stakeholders therefore have the power to shape the success of the journal. Including a diverse set of voices from a variety of communities and geographical locations into these stakeholder groups compels the journal to be representative of the current state of global research.

However, not all stakeholders hold equal power and weight in shaping the vision and trajectory of a journal. The editors - and to a lesser extent reviewers - act as gatekeepers, deciding which research is worthy of publication (Demeter, 2020; Schurr et al., 2020). Previous studies have shown marginalisation in research gatekeeping positions work against promoting research by women, especially women of colour (Davies S. et al., 2021; Davies S. W. et al., 2021) and a phenomenon known as the "Matilda Effect" where women's achievements are attributed to men. This Effect acknowledges and contributes to the gender gap in recognition, award winning, tenure, and citations for women, that clearly exists in scientific publishing (Lerchenmueller and Sorenson, 2018; Lincoln et al., 2012; Weisshaar, 2017). While these articles only studied the marginalisation of women, implicit bias and discrimination exist for all underrepresented genders, communities, and groups in science, technology, engineering, and mathematics (STEM) at every career stage (Larivière et al., 2013; Jones et al., 2014; Silbiger and Stubler, 2019; Chaudhary and Berhe, 2020; Huang et al., 2020; Berhe et al., 2022).

As scientists in the field of remote sensing, we must ask ourselves–Are the present publishing gatekeepers representative of the entire scientific community? We assert that in the field of remote sensing, the gatekeepers are not representative of the global society and that this lack of representation restricts what research is valued and published, and ultimately who becomes successful.

2 STATUS OF DIVERSITY IN REMOTE SENSING ACADEMIC PUBLISHING

To demonstrate the diversity deficiency in our discipline, we conducted a baseline audit of the editorial boards of 30 well -established peer reviewed journals within the remote sensing discipline based on Schurr et al. (2020), over the period September–November 2020. It was necessary to create our own editorial board audit for baseline demographics characteristics because this information was not easily accessible for a majority of the top remote sensing journals. Our findings indicate eight out of the top ten remote sensing journals (by impact factor) have editorial boards with more than 80% men (**Figure 1**). Three (10%) of the audited journals do not have any women on their editorial boards, and the largest percentage of women on any editorial board was just 40%. In fact, 84% of the journals had fewer than 20% women on their board. Our findings reinforce previous analyses in other scientific fields that there are fewer women in scientific journal editorial roles (Chawla 2018; Feeney et al., 2019). We also note that in a recent study of leading geoscience journals, women were identified as first author in 13–30% of publications (Pico et al., 2020), which is consistent with broader analyses of scientific authorship (Larivière et al., 2013; West et al., 2013). First author publications and editorial board roles seem to reflect each other in other fields (Dhanani and Jones, 2017; Helmer et al., 2017). As we advocate for diversifying editorial boards, we believe this will also result in more diverse authorship and more inclusive publication processes (Cho et al., 2014; Lerback and Hanson, 2017; Cheng et al., 2021), leaving no one behind.

Further documenting the gatekeeping countries, based on the affiliation of the editorial board members, we report that the majority of editors reside within just four countries. The United States (27%), China (11%), Italy (8%), and Germany (6%) represent 52% of the residence countries of editorial

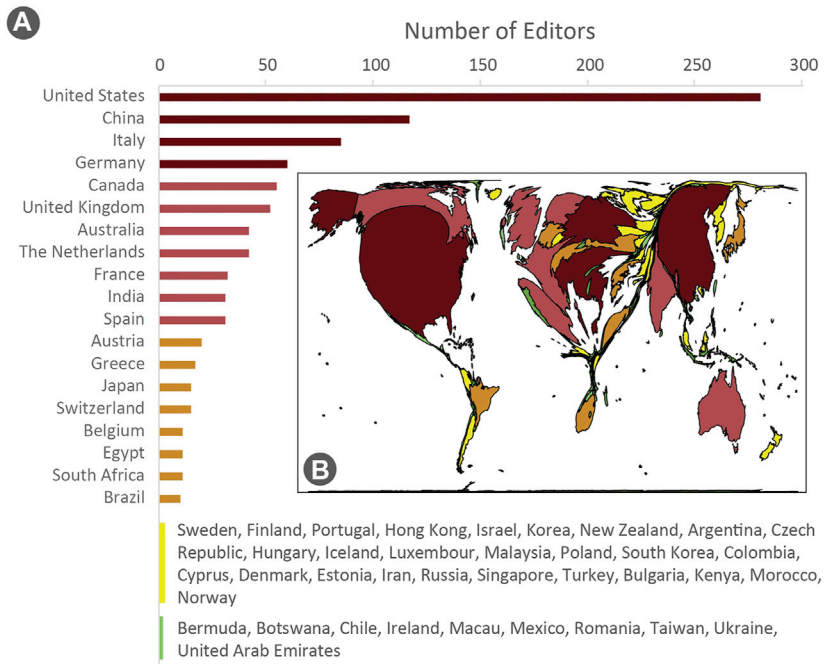

FIGURE 2 | Global distribution of editorial board members (n = 1055) within 30 peer reviewed journals in the remote sensing discipline. **(A)** Count of editors per country (including Special Administrative Regions). **(B)** World cartogram (Gastner et al., 2018) weighted by number of editors demonstrating the skew towards the United States, China, Italy, and Germany with negligible contribution from South America and Africa. Note that regions identified in yellow each have between two and eight editors identified, while those in green have one editor.

board members (**Figure 2**). While we bring to light gender and country of residence, these are not the only aspects of gatekeeping needing attention. In particular, there is a lack of survey data of other self-identification characteristics, like race, in the field of remote sensing. We suggest that future analyses could conduct direct surveys of editorial board members to gather stakeholder information and work towards reducing other disparities in the field of remote sensing. While we treat gender and country of residence as separate metrics, we acknowledge the complexity of privilege, exclusion, and intersectionality associated with these identities (e.g., Schurr et al., 2020), which could be examined in future survey analyses.

The lack of representation and diversity at this evolved stage of scientific publishing in fields like remote sensing restricts science from reaching its full potential (Murray et al., 2019; Schurr et al., 2020). Conversely, developing more gender and geographically diverse editorial boards will provide the opportunity to connect with research from around the globe, thereby aiding in considering global opinions and voices (Cheng et al., 2021). This will better represent different global, regional, or local communities and interests, and ultimately lead to superior science -based solutions to the world's most pressing problems like climate change or loss of diversity. By acknowledging and tackling implicit biases, we will benefit from more fair and balanced conversations and debates about what we as a remote sensing community value in our field.

The history of bias in remote sensing science is a two-fold problem. Like many other disciplines, remote sensing has historically been driven and shaped by the most dominant voices who hold positions of power, many of whom have acted as gatekeepers when they have consciously or unconsciously chosen to not recognise or act to rectify the implicit bias and lack of representation in the field. These dominant voices include the most frequently published authors, the members of technical science teams, and the most-funded principal investigators. Further, the remote sensing field has fewer marginalised voices in positions of power, and many describe feeling invisible or feel like their voices go unnoticed (Crowley, 2019; Adams et al., 2020; Crowley, 2020; Crowley et al., 2021a; Crowley et al., 2021b; Stéphenne et al., 2021; Vizireanu et al., 2021). It is the responsibility of every individual in our remote sensing community to proactively make our field's editorial boards more diverse and inclusive, but it is the duty of gatekeepers to act responsibly and promote underrepresented and diverse voices (Ryan 2022).

Gatekeeping occurs at every stage of science, and not just on editorial boards. Our remote sensing community consists of all of our combined excellence, with many gears that fit together and depend on one another. The success of a scientist depends on their host institution, faculties, co-investigators, affiliations, citations, number of publications, and other factors (van den Besselaar and Sandström, 2017; Davies S. et al., 2021; Davies S. W. et al., 2021). Our field is not exempt from implicit and explicit bias. Some of the authors on this article have suffered implicit bias, especially when submitting manuscripts to technical and

methods -oriented journals that have a larger gender gap, not only in the editorial or review boards, but also in the number of manuscripts submitted by first authors that are men. Our experience is that as authors who identify as women, we gain lesser visibility and increased risk due to biases from editors, reviewers, and readers throughout the publication process in many remote sensing journals, similar to what has been found in the field of ecology (Fox et al., 2016; Fox and Paine, 2019). Further, authors with non-western presenting names from underrepresented communities receive harsher reviews and fewer citations (Fejes and Nylander, 2017; Silbiger and Stubler, 2019). In addition to men self-citing their papers more than women (King et al., 2017), women's research is less likely to be cited by others, their ideas are more likely to be attributed to men, and women's solo-authored research takes twice as long to move through the review process (Dion et al., 2018). In a world where metrics and h-indices define the success of a scientist (Davies S. et al., 2021; Davies S. W. et al., 2021; Maas et al., 2021), this implicit bias against women and other minorities hinders their career forcing many to leave science (Bostwick and Weinberg, 2022; Huang et al., 2020; Larivière et al., 2013). The loss of scientists and their ideas has detrimental impacts on potential scientific innovations.

3 IT'S TIME TO DO BETTER

To reduce negative impacts incurred from bias, it is not enough for any organisation to claim to be 'champions of diversity and inclusion', without demonstrating actions towards achieving a goal. It takes active allies to put the work in turning the ship towards more diversity and inclusivity. To increase representation, institutions must actively increase visibility of their scientists, researchers, and authors from underrepresented and marginalised groups and communities. These could be by using social media platforms and professional networks such as the Ladies of Landsat, Sisters of SAR, Women in Copernicus, IEEE GRSS IDEA, Women+ in Geospatial, and other networks (Crowley et al., 2021a; Crowley et al., 2021b; Riedler et al., 2021; Stéphenne et al., 2021; Vizireanu et al., 2021) that aim to promote and support women in remote sensing. Actively nominating women for grants/awards, or by creating 'special issues' within a journal to amplify their work can also help to promote and support their research (Amon 2017; Van Oosten et al., 2017; Joyce et al., 2021).

Within the remote sensing community, we must assign roles with decision-making powers to researchers and scientists from previously underrepresented groups, actively and consciously. This must not be tokenistic, instead including them on editorial boards, in senior management and positions with power to make change. Focusing solely on empowerment programs does not change the system, because underrepresented groups do not need 'fixing' and rarely lead such programmes. They have the skills and knowledge but may lack the resources that enable visibility. They need to be heard, and we need to listen.

We suggest an action plan to change this, specifically within our remote sensing discipline.

1) Collect diversity data to learn and change: Publishers, professional societies, institutions, and individuals need to actively collect baseline demographic data over time and assess the extent of gender, racial, regional, and institutional bias and their impacts on remote sensing scientists (e.g. van Veelen et al., 2019) to enable change.
2) Journals and gatekeepers must act responsibly: Gatekeepers and journals should actively make their editorial and review boards more representative and inclusive, and with modesty enable regional experts to evaluate what is relevant work in specific areas. These efforts can be achieved through policies that support more diverse editorial and review boards (Cho et al., 2014; Cheng et al., 2021; Maas et al., 2021).
3) Editorial boards must strive for internal diversity: This will drive change from the top, create visible pathways for junior academics, and encourage diverse perspectives and expertise in areas sought for special issue publications (Cheng et al., 2021; Cho et al., 2014; Emerald Publishing, n.d.; Lerback and Hanson, 2017; Squazzoni et al., 2021).
4) Double blind reviews or fully open reviewing to tackle bias and harsh reviews: Given the bias observed towards accepting papers from authors considered 'similar' to the editors and reviewers (Helmer et al., 2017; Murray et al., 2019), we should investigate more widespread double blind reviews (Darling 2015), or alternatively fully open reviews where all are accountable for their words and decisions. We must also continue to provide clear guidelines for reviewers to produce constructive and fair reviews to avoid negative impacts on authors from underrepresented groups (Silbiger and Stubler, 2019).
5) Actively promote work undertaken by underrepresented or marginalised remote sensing scientists: This might include promoting the work and authors once published, but also in actively seeking out/inviting work from these authors in the first place (Maas et al., 2021) and offering language or financial support where required. We also recognise that there are further accessibility challenges regarding publishing fees and gaining access to the articles once published. Open access publications help to remove the barrier of access to publications, and initiatives supporting fee waivers for minoritised groups help to provide financial support by reducing or removing article-processing charges (Valenzuela-Toro and Viglino, 2021; Ross-Hellauer, 2022).
6) Accept and encourage ideas and manuscripts that are multidisciplinary, transdisciplinary, and different from the established norm: By promoting and inviting these types of articles in remote sensing and special collections, especially from minoritised scientists, we can contribute as a field towards reaching global targets such as the Sustainable Development Goals and the Sendai Framework.
7) Ensure that local communities/institutions are credited appropriately and benefit from "successful publications" conducted in their geographic regions: This includes collaborating with local representatives and organizations and recognizing their contributions to the remote sensing

research to avoid "helicopter" science and increase the impact of remote sensing articles (Abbasi and Jaafari,2013).

Systemic change will not happen overnight. However, our audit shows that the remote sensing literature is driven by and largely contains the voice of primarily men from a minority of countries. Can we afford to let only a narrow scientific community make a majority of the editorial decisions in the field of remote sensing? As a result, is the field of remote sensing limiting the inclusion of remote sensing scientists from the rest of the world (Maas et al., 2021)? It is the responsibility of the privileged, including established institutions, journals, and scientists to help create the platform and spaces for underrepresented and marginalised groups and communities to be in line with the motto of Agenda 2030 of "leaving no one behind". Therefore, more journals must update their editorial boards and policies. Creating diverse and inclusive organisations includes more than doing what is right for individuals and underrepresented groups: it is vital that we make large-scale structural changes to the system. The data clearly demonstrate that we see more innovative and beneficial science that stems from diverse teams and authorships that are inclusive of many perspectives (Abbasi and Jaafari, 2013; Freeman and Huang, 2014; AlShebli et al., 2018). This is a change we must embrace to excel our discipline.

4 OUR CALL TO ACTION

It is difficult to translate individual desire or demand into systemic change, particularly at a discipline level. That is where the power of the collective is increasingly important. We can choose to continue to 'hold our stake' in journals whose mission aligns with our own values, and advocate for others to do so with us. As a community, we can strive to create enough noise in hope that it will 1 day resonate loud enough to be heard.

As an individual, consider your role as an editor, author, reviewer, or reader. Is the journal you select or represent demonstrating their worth as an active ally in creating a diverse and inclusive remote sensing discipline? You have the choice to continue aligning with that journal, or you can seek alternatives and be the change you wish to see, leaving no one behind.

As the all-women team of co-authors on this paper, we invite all active allies to join us for a more inclusive future in our discipline.

DATA AVAILABILITY STATEMENT

The raw data supporting the conclusion of this article will be made available by the authors, without undue reservation.

AUTHOR CONTRIBUTIONS

All authors have contributed substantially to every aspect of conceptualization, data curation, writing, reviewing, and editing. All authors have read and agreed to the published version of the manuscript.

ACKNOWLEDGMENTS

As co-authors of this article, we each pay our respects to the traditional custodians of the land, sea, and sky country from the diverse parts of the world from where we live, breathe, work, and play.

REFERENCES

Abbasi, A., and Jaafari, A. (2013). Research Impact and Scholars' Geographical Diversity. *J. Inf.* 7, 683–692. doi:10.1016/j.joi.2013.04.004

Adams, E. C., Crowley, M. A., Casey, K., and Halabisky, M. (2020). *Gender and Social Inclusion in Climate Data Services and Analyses I Posters*. Washington, DC: American Geophysical Union. Available at: https://agu.confex.com/agu/fm20/meetingapp.cgi/Session/104606 (Accessed May 3, 2022).

AlShebli, B. K., Rahwan, T., and Woon, W. L. (2018). The Preeminence of Ethnic Diversity in Scientific Collaboration. *Nat. Commun.* 9, 5163. doi:10.1038/s41467-018-07634-8

Amon, M. J. (2017). Looking through the Glass Ceiling: A Qualitative Study of STEM Women's Career Narratives. *Front. Psychol.* 8, 236. doi:10.3389/fpsyg.2017.00236

Berhe, A. A., Barnes, R. T., Hastings, M. G., Mattheis, A., Schneider, B., Williams, B. M., et al. (2022). Scientists from Historically Excluded Groups Face a Hostile Obstacle Course. *Nat. Geosci.* 15, 2–4. doi:10.1038/s41561-021-00868-0

Bostwick, V. K., and Weinberg, B. A. (2022). Nevertheless She Persisted? Gender Peer Effects in Doctoral STEM Programs. *J. Labor. Econ.* 40 (2), 397–436.

Chaudhary, V. B., and Berhe, A. A. (2020). Ten Simple Rules for Building an Antiracist Lab. *PLoS Comput. Biol.* 16, e1008210. doi:10.1371/journal.pcbi.1008210

Cheng, S. J., Zaringhalam, M., Carvalho, A. P. S., Barnes, R. T., Goldman, G., Simonis, J. L., et al. (2021). *Moving Scientific Publishing toward Social Justice*. Washington, DC: Times Higher Education. Available at: https://www.insidehighered.com/advice/2021/09/09/call-action-more-socially-just-publishing-opinion (Accessed May 3, 2022).

Cho, A. H., Johnson, S. A., Schuman, C. E., Adler, J. M., Gonzalez, O., Graves, S. J., et al. (2014). Women Are Underrepresented on the Editorial Boards of Journals in Environmental Biology and Natural Resource Management. *PeerJ* 2, e542. doi:10.7717/peerj.542

Crowley, M. A., de Souza Mendes, F., Fickas, K. C., and Halabisky, M. (2021a). *Celebrating International Day of the Girl with Ladies of Landsat*. Washington, DC: USAID. Available at: http://www.agrilinks.org/post/celebrating-international-day-girl-ladies-landsat (Accessed May 3, 2022).

Crowley, M. A. (2020). *How Small Acts Became Big Movements towards Inclusivity*. Mountain View: Google Earth and Earth Engine. Available at: https://medium.com/google-earth/how-small-acts-became-big-movements-towards-inclusivity-9ba5cedc8db5 (Accessed May 3, 2022).

Crowley, M. A. (2019). *Ladies of Landsat Builds Inclusivity in the Geosciences*. Google. Available at: https://blog.google/products/earth/ladies-of-landsat/ (Accessed May 3, 2022).

Crowley, M. A., Fickas, K., and Halabisky, M. (2021b). *Ladies of Landsat*. Ottawa, Canada: Women in Wood. Available at: https://www.womeninwood.ca/single-post/ladies-of-landsat (Accessed May 3, 2022).

Darling, E. S. (2015). Use of Double-Blind Peer Review to Increase Author Diversity. *Conserv. Biol.* 29, 297–299. doi:10.1111/cobi.12333

Davies, S., Putnam, H., Ainsworth, T., Baum, J., Bove, C., Crosby, S., et al. (2021). Shifting Our Value System beyond Citations for a More Equitable Future.

Available at: https://www.preprints.org/manuscript/202102.0493/v1 [Accessed May 3, 2022].

Davies, S. W., Putnam, H. M., Ainsworth, T., Baum, J. K., Bove, C. B., Crosby, S. C., et al. (2021). Promoting Inclusive Metrics of Success and Impact to Dismantle a Discriminatory Reward System in Science. *PLoS Biol.* 19, e3001282. doi:10.1371/journal.pbio.3001282

Demeter, M. (2020). "Gatekeepers of Knowledge Dissemination: Inequality in Journal Editorial Boards," in *Academic Knowledge Production and the Global South: Questioning Inequality and Under-representation* (Cham: Springer International Publishing), 137–151. doi:10.1007/978-3-030-52701-3_6

Dhanani, A., and Jones, M. J. (2017). Editorial Boards of Accounting Journals: Gender Diversity and Internationalisation. *AAAJ* 30, 1008–1040. doi:10.1108/AAAJ-08-2014-1785

Dion, M. L., Sumner, J. L., and Mitchell, S. M. (2018). "Replication Data for: Gendered Citation Patterns across Political Science and Social Science Methodology Fields," in *Harvard Dataverse V1*.

Emerald Publishing. (n.d.). What Is Preventing Diversity on Editorial Boards? Available at: https://www.emeraldgrouppublishing.com/opinion-and-blog/what-preventing-diversity-editorial-boards [Accessed May 3, 2022].

Feeney, M. K., Carson, L., and Dickinson, H. (2019). Power in Editorial Positions: A Feminist Critique of Public Administration. *Public Admin Rev.* 79, 46–55. doi:10.1111/puar.12950

Fejes, A., and Nylander, E. (2017). The Economy of Publications and Citations in Educational Research: What about the 'Anglophone Bias'? *Res. Educ.* 99, 19–30. doi:10.1177/0034523717740146

Fox, C. W., Burns, C. S., and Meyer, J. A. (2016). Editor and Reviewer Gender Influence the Peer Review Process but Not Peer Review Outcomes at an Ecology Journal. *Funct. Ecol.* 30, 140–153. doi:10.1111/1365-2435.12529

Fox, C. W., and Paine, C. E. T. (2019). Gender Differences in Peer Review Outcomes and Manuscript Impact at Six Journals of Ecology and Evolution. *Ecol. Evol.* 9, 3599–3619. doi:10.1002/ece3.4993

Freeman, R. B., and Huang, W. (2014). Collaboration: Strength in Diversity. *Nature* 513, 305. doi:10.1038/513305a

Gastner, M. T., Seguy, V., and More, P. (2018). Fast Flow-Based Algorithm for Creating Density-Equalizing Map Projections. *Proc. Natl. Acad. Sci. U. S. A.* 115, E2156–E2164. doi:10.1073/pnas.1712674115

Helmer, M., Schottdorf, M., Neef, A., and Battaglia, D. (2017). Gender Bias in Scholarly Peer Review. *eLife* 6, e21718. doi:10.7554/eLife.21718

Huang, J., Gates, A. J., Sinatra, R., and Barabási, A.-L. (2020). Historical Comparison of Gender Inequality in Scientific Careers across Countries and Disciplines. *Proc. Natl. Acad. Sci. U.S.A.* 117, 4609–4616. doi:10.1073/pnas.1914221117

Jones, T. M., Fanson, K. V., Lanfear, R., Symonds, M. R. E., and Higgie, M. (2014). Gender Differences in Conference Presentations: A Consequence of Self-Selection? *PeerJ* 2, e627. doi:10.7717/peerj.627

Joyce, K. E., Anderson, K., and Bartolo, R. E. (2021). Of Course We Fly Unmanned-We're Women!. *Drones* 5, 21. doi:10.3390/drones5010021

King, M. M., Bergstrom, C. T., Correll, S. J., Jacquet, J., and West, J. D. (2017). Men Set Their Own Cites High: Gender and Self-Citation across Fields and over Time. *Socius* 3, 2378023117738903. doi:10.1177/2378023117738903

Larivière, V., Ni, C., Gingras, Y., Cronin, B., and Sugimoto, C. R. (2013). Bibliometrics: Global Gender Disparities in Science. *Nature* 504, 211–213. doi:10.1038/504211a

Lerback, J., and Hanson, B. (2017). Journals Invite Too Few Women to Referee. *Nature* 541, 455–457. doi:10.1038/541455a

Lerchenmueller, M. J., and Sorenson, O. (2018). The Gender Gap in Early Career Transitions in the Life Sciences. *Res. Policy* 47, 1007–1017. doi:10.1016/j.respol.2018.02.009

Lincoln, A. E., Pincus, S., Koster, J. B., and Leboy, P. S. (2012). The Matilda Effect in Science: Awards and Prizes in the US, 1990s and 2000s. *Soc. Stud. Sci.* 42, 307–320. doi:10.1177/0306312711435830

Maas, B., Pakeman, R. J., Godet, L., Smith, L., Devictor, V., and Primack, R. (2021). Women and Global South Strikingly Underrepresented Among Top-publishing Ecologists. *Conserv. Lett.* 14, e12797. doi:10.1111/conl.12797

Murray, D., Siler, K., Larivière, V., Chan, W. M., Collings, A. M., Raymond, J., et al. (2019). Author-Reviewer Homophily in Peer Review. *bioRxiv*. 400515.

Pico, T., Bierman, P., Doyle, K., and Richardson, S. (2020). First Authorship Gender Gap in the Geosciences. *Earth Space Sci.* 7, e2020EA001203. doi:10.1029/2020ea001203

Riedler, B., Stéphenne, N., Aguilar-Moreno, E., Jagaille, M., Monfort-Muriach, A., Fiore, G., et al. (2021). "Towards Gender Equality in Education and Career in the Earth Observation and Gi Sector," in *The International Archives of the Photogrammetry, Remote Sensing and Spatial Information Sciences* (Nice, France: ISPRS), 21–27. doi:10.5194/isprs-archives-XLIII-B5-2021-21-2021

Ross-Hellauer, T. (2022). Open Science, Done Wrong, Will Compound Inequities. *Nature* 603, 363. doi:10.1038/d41586-022-00724-0

Ryan, M. (2022). To Advance Equality for Women, Use the Evidence. *Nature* 604, 403. doi:10.1038/d41586-022-01045-y

Schurr, C., Müller, M., and Imhof, N. (2020). Who Makes Geographical Knowledge? the Gender of Geography's Gatekeepers. *Prof. Geogr.* 72, 317–331. doi:10.1080/00330124.2020.1744169

Silbiger, N. J., and Stubler, A. D. (2019). Unprofessional Peer Reviews Disproportionately Harm Underrepresented Groups in STEM. *PeerJ* 7, e8247. doi:10.7717/peerj.8247

Singh Chawla, D. (2018). Huge Peer-Review Study Reveals Lack of Women and Non-westerners. *Nature* 561, 295–296. doi:10.1038/d41586-018-06678-6

Squazzoni, F., Bravo, G., Farjam, M., Marusic, A., Mehmani, B., Willis, M., et al. (2021). Peer Review and Gender Bias: A Study on 145 Scholarly Journals. *Sci. Adv.* 7, eabd0299. doi:10.1126/sciadv.abd0299

Stéphenne, N., Riedler, B., a Aguilar-Moreno, E., Jagaille, M., Monfort-Muriach, A., Fiore, G., et al. (2021). "Women in Copernicus: Recommendations from Women Testimonials," in 2021 IEEE International Geoscience and Remote Sensing Symposium IGARSS, Brussels, Belgium, 11-16 July 2021 (IEEE), 33–36. doi:10.1109/IGARSS47720.2021.9554567

Valenzuela-Toro, A. M., and Viglino, M. (2021). How Latin American Researchers Suffer in Science. *Nature* 598, 374–375. doi:10.1038/d41586-021-02601-8

van den Besselaar, P., and Sandström, U. (2017). Vicious Circles of Gender Bias, Lower Positions, and Lower Performance: Gender Differences in Scholarly Productivity and Impact. *PLOS ONE* 12, e0183301. doi:10.1371/journal.pone.0183301

Van Oosten, E. B., Buse, K., and Bilimoria, D. (2017). The Leadership Lab for Women: Advancing and Retaining Women in STEM through Professional Development. *Front. Psychol.* 8, 2138. doi:10.3389/fpsyg.2017.02138

van Veelen, R., Derks, B., and Endedijk, M. D. (2019). Double Trouble: How Being Outnumbered and Negatively Stereotyped Threatens Career Outcomes of Women in STEM. *Front. Psychol.* 10, 150. doi:10.3389/fpsyg.2019.00150

Vizireanu, A.-M., Wagemann, J., Szeto, S. H., and Vrinceanu, C.-A. (2021). "Women in Geospatial+ - Changing the Status Quo by Creating a Strong Network of Women+ Leaders and Changemakers," in 2021 IEEE International Geoscience and Remote Sensing Symposium IGARSS, Brussels, Belgium, 11-16 July 2021, 46–48. doi:10.1109/IGARSS47720.2021.9554033

Weisshaar, K. (2017). Publish and Perish? an Assessment of Gender Gaps in Promotion to Tenure in Academia. *Soc. Forces* 96, 529–560. doi:10.1093/sf/sox052

West, J. D., Jacquet, J., King, M. M., Correll, S. J., and Bergstrom, C. T. (2013). The Role of Gender in Scholarly Authorship. *PLOS ONE* 8, e66212. doi:10.1371/journal.pone.0066212

Conflict of Interest: The authors declare that the research was conducted in the absence of any commercial or financial relationships that could be construed as a potential conflict of interest.

Publisher's Note: All claims expressed in this article are solely those of the authors and do not necessarily represent those of their affiliated organizations, or those of the publisher, the editors and the reviewers. Any product that may be evaluated in this article, or claim that may be made by its manufacturer, is not guaranteed or endorsed by the publisher.

frontiers | Frontiers in Remote Sensing

TYPE Original Research
PUBLISHED 24 August 2022
DOI 10.3389/frsen.2022.949052

OPEN ACCESS

EDITED BY
Hannah Victoria Herrero,
The University of Tennessee, Knoxville, United States

REVIEWED BY
Elif Sertel,
Istanbul Technical University, Turkey
Susannah Leahy,
Queensland Government, Australia

*CORRESPONDENCE
David G. Schmale,
dschmale@vt.edu

SPECIALTY SECTION
This article was submitted to Unoccupied Aerial Systems (UASs and UAVs),
a section of the journal
Frontiers in Remote Sensing

RECEIVED 20 May 2022
ACCEPTED 19 July 2022
PUBLISHED 24 August 2022

CITATION
Hanlon R, Jacquemin SJ, Birbeck JA, Westrick JA, Harb C, Gruszewski H, Ault AP, Scott D, Foroutan H, Ross SD, González-Rocha J, Powers C, Pratt L, Looney H, Baker G and Schmale DG (2022), Drone-based water sampling and characterization of three freshwater harmful algal blooms in the United States.
Front. Remote Sens. 3:949052.
doi: 10.3389/frsen.2022.949052

Drone-based water sampling and characterization of three freshwater harmful algal blooms in the United States

Regina Hanlon[1], Stephen J. Jacquemin[2], Johnna A. Birbeck[3], Judy A. Westrick[3], Charbel Harb[4], Hope Gruszewski[1], Andrew P. Ault[5], Durelle Scott[6], Hosein Foroutan[4], Shane D. Ross[7], Javier González-Rocha[7,8], Craig Powers[1,4], Lowell Pratt[8], Harry Looney[8], Greg Baker[8] and David G. Schmale[1]*

[1]School of Plant and Environmental Sciences, Virginia Tech, Blacksburg, VA, United States, [2]Lake Campus, Wright State University, Celina, OH, United States, [3]Lumigen Instrument Center, Wayne State University, Detroit, MI, United States, [4]Civil and Environmental Engineering, Virginia Tech, Blacksburg, VA, United States, [5]Department of Chemistry, University of Michigan, Ann Arbor, MI, United States, [6]Biological Systems Engineering, Virginia Tech, Blacksburg, VA, United States, [7]Aerospace and Ocean Engineering, Virginia Tech, Blacksburg, VA, United States, [8]Lake Anna Civic Association, Mineral, VA, United States

Freshwater harmful algal blooms (HABs), caused mostly by toxic cyanobacteria, produce a range of cyanotoxins that threaten the health of humans and domestic animals. Climate conditions and anthropogenic influences such as agricultural run-off can alter the onset and intensity of HABs. Little is known about the distribution and spread of freshwater HABs. Current sampling protocols in some lakes involve teams of researchers that collect samples by hand from a boat and/or from the shoreline. Water samples can be collected from the surface, from discrete-depth collections, and/or from depth-integrated intervals. These collections are often restricted to certain months of the year, and generally are only performed at a limited number of collection sites. In lakes with active HABs, surface samples are generally sufficient for HAB water quality assessments. We used a unique DrOne Water Sampling

Abbreviations: Anatoxin-a (ANA), a neurotoxin produced by cyanobacteria including (but not limited to) *Anabaena*, *Planktothrix*, and *Raphidiopsis*; Chlorophyll a (Chl a), a green pigment found in both cyanobacteria (prokaryotes) and in the chloroplasts of algae (photosynthetic eukaryotes) and plants (eukaryotes); Cyanobacteria, prokaryotic aquatic bacteria that carry out photosynthesis; Cyanotoxins, toxins produced by cyanobacteria; Cylindrospermopsin (CYN), a hepatotoxin and protein synthesis inhibitor produced by cyanobacteria including (but not limited to) *Anabaena*, *Aphanizomenon*, and *Cylindrospermopsis*; Harmful Algal Bloom (HAB), rapid growth of cyanobacteria to levels that can harm people, animals, or the local ecology; Microcystin (MC), a hepatotoxin with many variations, or congeners produced by freshwater cyanobacteria including (but not limited to) *Anabaena*, *Microcystis*, and *Planktothrix*; Nodularin (NOD), a protein phosphatase inhibitor produced by the cyanobacterium *Nodularia*; Phycocyanin (PC), a protein pigment in cyanobacteria that vary in color from blue to green; Potentially TOXigenic Cyanobacteria (PTOX), cyanobacteria that have the potential to produce various cyanotoxins; Recreational Use Value (RUV), a recommended limit of exposure; Saxitoxin (STX), a neurotoxin and paralytic shellfish toxin that is produced in both marine and freshwater environments by dinoflagellates (eukaryotes) and cyanobacteria (prokaryotes).

SystEm (DOWSE) to collect water samples from the surface of three different HABs in Ohio (Grand Lake St Marys, GLSM and Lake Erie) and Virginia (Lake Anna), United States in 2019. The DOWSE consisted of a 3D-printed sampling device tethered to a drone (uncrewed aerial system, or UAS), and was used to collect surface water samples at different distances (10–100 m) from the shore or from an anchored boat. One hundred and eighty water samples (40 at GLSM, 20 at Lake Erie, and 120 at Lake Anna) were collected and analyzed from 18 drone flights. Our methods included testing for cyanotoxins, phycocyanin, and nutrients from surface water samples. Mean concentrations of microcystins (MCs) in drone water samples were 15.00, 1.92, and 0.02 ppb for GLSM, Lake Erie, and Lake Anna, respectively. Lake Anna had low levels of anatoxin in nearly all (111/120) of the drone water samples. Mean concentrations of phycocyanin in drone water samples were 687, 38, and 62 ppb for GLSM, Lake Erie, and Lake Anna, respectively. High levels of total phosphorus were observed in the drone water samples from GLSM (mean of 0.34 mg/L) and Lake Erie (mean of 0.12 mg/L). Lake Anna had the highest variability of total phosphorus with concentrations that ranged from 0.01 mg/L to 0.21 mg/L, with a mean of 0.06 mg/L. Nitrate levels varied greatly across sites, inverse with bloom biomass, ranging from below detection to 3.64 mg/L, with highest mean values in Lake Erie followed by GLSM and Lake Anna, respectively. Drones offer a rapid, targeted collection of water samples from virtually anywhere on a lake with an active HAB without the need for a boat which can disturb the surrounding water. Drones are, however, limited in their ability to operate during inclement weather such as rain and heavy winds. Collectively, our results highlight numerous opportunities for drone-based water sampling technologies to track, predict, and respond to HABs in the future.

KEYWORDS

drone (uncrewed/unmanned aerial vehicle), cyanobacteria, cyanotoxin, phycocyanin, freshwater (health/environment), harmful algal bloom (HAB), water sampling methods

Introduction

Harmful algal blooms (HABs), caused mostly by toxic cyanobacteria, have been observed around the world (Anderson et al., 2002). Different HAB-associated cyanobacteria produce a range of toxins called cyanotoxins that impact human health, including microcystins (MCs), saxitoxin (STX), anatoxin-a (ANA), and cylindrospermopsin (CYN) (Zurawell et al., 2005; Du et al., 2019; Ballot et al., 2020). HABs appear to be increasing in prevalence and severity around the world (Anderson et al., 2002; Schmale et al., 2019; Wells et al., 2020), and new information is necessary to understand the fate and transport of HABs and their associated toxins (Stumpf et al., 2016; Topp et al., 2020; Ross et al., 2022). Research is needed to understand threats, manage risks, mitigate incidents, develop capabilities, and strengthen collaborations for water quality (Topp et al., 2020). This information is critical for determining time-sensitive health advisories for drinking water and recreation in water bodies impacted by HABs (US EPA, 2016; Oregon Health Authority, 2019).

The first known report of cyanotoxins was documented in Australia in 1878. In the United States, from 1882 to 1946, five states reported an occurrence of cyanotoxins [MN, CO, MT, IA, and ND (Yoo, 1995)]. These numbers have increased by orders of magnitude in recent years, leading to HABs being increasingly characterized as one of the largest threats to food and water resources in the future (Anderson, 2012; Graham, 2016). In 2014, the municipal water supply in Toledo, Ohio was contaminated with MC levels above the US EPA adult health advisory limit for drinking and resulted in non-potable water for 400,000 people (Jetoo et al., 2015; Qian et al., 2015). The maximum recommended recreational use value (RUV) for canine exposure is 0.2 ppb MC (CFR, 2022) (Table 1). The United States Environmental Protection Agency (US EPA) 10-day health advisory limit for infants is 0.3 ppb MC, and for 6 years old to adult is 1.6 ppb (MC) for drinking water (US EPA, 2019) (Table 1). The US EPA recommended RUV limits for MC and CYN toxin in recreational waters is 8 and 15 ppb, respectively (US EPA, 2016; US EPA, 2019).

Two of the lakes in our study, GLSM and Lake Erie in Ohio, have a long history of HABs. One of the lakes, Lake Anna in Virginia, has only recently experienced a HAB, offering a unique look at a freshwater lake near a tipping point. GLSM experiences a HAB for most of the year and is nature's example of an extreme

10.3389/frsen.2022.949052

TABLE 1 Water quality index table with nomenclature to denote water quality based on concentration metrics for microcystin (MC), phycocyanin (PC), and phosphorus. This classification table is an expansion of the Trophic State Index (TSI) table in Carlson (Carlson 1977) that defined a range of total phosphorus concentration in freshwater lakes as oligotrophic, mesotrophic, eutrophic, and hypereutrophic (healthy to unhealthy). MC and PC concentration ranges have been defined here to create a more inclusive water quality index. The color bands denote water quality conditions relative to toxin load. Microcystin (MC) toxin concentration value ranges from 0.0–0.2 ppb are classified as Dog recreational use value (Dog RUV) (blue), 0.21–1.60 ppb are classified as Adult Drinking health advisory (HA) (green), 1.61–8 ppb are classified as below toxin RUV (yellow), and >8ppb is Toxin >8 ppb (orange) for MC. (EPA 820-R-15-100 (2015), EPA 822-R-10-001 (2019), Oregon Health Authority (2019). PC concentration ranges of 0–1.9 ppb (blue), 2.0–4.9 ppb (green), 5.0–49.4 ppb (yellow), and 49.41–800 ppb (orange) are denoted as Alert level 1, Alert level 2, Alert level 3, and Action level, respectively (Izydorczyk et al., 2009; Cotterill et al., 2019).

Microcystin (ppb)	Advisory level	Phycocyanin (ppb)	Advisory level	Total Phosphorus (mg/L)	Trophic state	TSI
0.00	No advisory	0.0	Alert level 1	0.00075	Oligotrophic	0
0.10	Below dog RUV (MC)	1.9	Alert level 1	0.0015	Oligotrophic	10
0.20	Dog RUV (MC)	1.9	Alert level 1	0.003	Oligotrophic	20
0.20	Dog RUV (MC)	1.9	Alert level 1	0.006	Oligotrophic	30
0.20	Dog RUV (MC)	1.9	Alert level 1	0.012	Oligotrophic	40
0.21	Above dog RUV (MC)	2.0	Alert level 2	0.017	Mesotrophic	45
0.30	Infant drinking HA (MC)	2.0	Alert level 2	0.017	Mesotrophic	45
1.60	Adult drinking HA (MC)	4.9	Alert level 2	0.024	Mesotrophic	50
1.61	Below RUV (MC)	5.0	Alert level 3	0.030	Eutrophic	53
8.00	Below RUV (MC)	49.4	Alert level 3	0.048	Eutrophic	60
8.10	Toxin >8 ppb (MC)	50	Action level	0.096	Hypereutrophic	70
15	Toxin >8 ppb (MC)	75	Action level	0.192	Hypereutrophic	80
18	Toxin >8 ppb (MC)	150	Action level	0.384	Hypereutrophic	90
21	Toxin >8 ppb (MC)	800	Action level	0.768	Hypereutrophic	100

HAB environment. GLSM is classified as a hypereutrophic system and has been designated as a distressed watershed since 2011 (Jacquemin et al., 2018). The West section of Lake Erie (including the southern basin) has been classified as Eutrophic on the trophic state index (TSI) scale since 1999 (Lake Erie Forage Task Group, 2020). Lake Anna is a recent location of concern with the potential to experience a seasonal HAB. Forty-eight water samples were collected in Lake Anna in 2018 by the Virginia Department of Environmental Quality (DEQ) and potentially toxigenic cyanobacterial cell counts were recorded by the Virginia Department of Health (VDH). Twenty-seven percent (13/48) of these samples had potentially toxigenic cyanobacteria counts above 100,000 (personal communication with VDH, 2021). All three of these lakes serve as unique locations that vary in their temporal and spatial distribution of HABs.

Nutrient runoff from agricultural and industrial sites that has been linked to the overall health of aquatic environments (Fraterrigo and Downing, 2008; Anderson, 2012). An increase in phosphorus content could push a population of cyanobacteria to be nitrogen-limited and shift toxin production from one congener of microcystin to another (MC-RR to MC-LR) (Maliaka et al., 2021). MC-LR is ten-fold more toxic than MC-RR (Zurawell et al., 2005). The TSI for lakes was developed to categorize lakes on a scale of 0–100 with each multiple of 10 representing a doubling of biomass (Carlson, 1977). TSI can be used to categorize lakes into oligotrophic (TSI 0–40), mesotrophic (TSI 41–50) eutrophic (TSI 51–60), and hypereutrophic (TSI 61–100) (Carlson, 1977) (Table 1). Oligotrophic lakes have a low level of nutrients and high level of water clarity, while eutrophic lakes have high nutrient levels, and a low level of water clarity. Hypereutrophic lakes have an extreme overload of nutrients, usually greater than 0.1 mg/L of phosphorus and 40 μg/L of chlorophyll. Lakes can transition between trophic states (Scheffer et al., 1993).

Collection guidelines for freshwater lakes and reservoirs differ based on the research objective. Reconnaissance studies usually address the presence of cyanobacteria, toxins, and compounds associated with taste and smell (Graham et al., 2008). Interpretive studies are generally long-term studies that assess environmental factors that affect the occurrence of cyanotoxins. Depth-integrated studies are continuous or discontinuous with equal intervals of collections. The potential location and vertical distribution of cyanobacteria in the water column has been described as having six general configurations in lakes and reservoirs (Graham et al., 2008). Open water accumulation, surface scum, and photic zone distributions were shown to have cyanobacteria present at the surface and evenly distributed below the surface at least halfway to the lake bottom (Graham et al., 2008). Discoloration is usually obvious in such locations (blue-green, or brown, or red), and filaments or large colonies may be visible at or near the surface. Cyanobacteria sample collections for recreational areas are typically collected as surface samples or integrated photic zone samples. Our study was a reconnaissance type study carried out in three recreational freshwater lakes that had a history of HABs, visible discoloration

at the time of sampling, with occasional scum or large clumps of cells near the shoreline.

Within the last decade, a variety of remote sensing tools have been used to study freshwater HABs. Stumpf et al. (2016) used satellite images to map distributions of cyanobacteria and predict MCs. The relationship between MC and cyanobacterial pigments was analyzed using data from three different lake studies. Derivative algorithms were determined to be the most robust predictors of cyanotoxins. Mishra et al. (2021) took satellite-based measurements one step further and compared detection of cyanobacteria to MC data. Data were collected from 30 different lakes in 11 states, and the authors showed that their algorithm could be used as a pre-screening tool to identify areas most likely to experience a HAB. A variety of measurements used in multiple linear regression models were accurate above 80% of the time when site-specific locations were tested in Ohio (Francy et al., 2020). Accuracy above 90% was achieved when continuous monitoring data was used in the models to forecast toxin levels over the action threshold. Correlations between pigment measurements (e.g., phycocyanin, PC and Chl-a) and cyanotoxins are difficult to predict, and studies thus far have focused on specific locations with historic water quality data that extends over several seasons (or years). Recently, drone imagery was used to detect and characterize rhodamine dye (a surrogate HAB) in the ocean (Filippi et al., 2021). This method could find use in freshwater lakes to pinpoint areas of sample collection that would be most useful in determining water quality metrics in lakes with a history of HABs.

Traditional water sampling methods collected by hand are labor intensive, arduous, and require the use of various pump technologies in conjunction with water sampling devices (e.g., Wilde et al., 1998). For example, inertial, peristaltic, pneumatic, and bladder pumps have been used and some of these require compressors on site to run these pumps. The United States Geological Survey (USGS) has used devices such as the Kemmerer sampler, the Van Dorn, and a double check-valve bailer for water sampling (Wilde et al., 1998). Primary disadvantages of these samplers are the care needed to prevent cross-contamination between samples, time needed to implement these monitoring protocols, often narrow spatial coverage of possible sampling, and requisite personnel expertise to maintain sampling consistency. Thus, new tools and accessible technologies with quick turn-around times are needed to understand the fate and transport of HABs and their associated toxins. Recent advances in uncrewed robotic systems offer one solution to many of these problems and have allowed researchers to conduct environmental research in aquatic systems at an unprecedented level of detail (Powers et al., 2018a; Powers et al. 2018b; Powers et al., 2018c; Ribas-Ribas et al., 2019). Aerial and aquatic robots have been used to collect and characterize microorganisms (Powers et al., 2018b) and detect and track fluorescent dyes (surrogates for hazardous agents) in lakes (Powers et al., 2018a) and the ocean (Filippi et al., 2021). Ore et al. (2015) developed a pump-driven drone water sampling platform for water quality measurements in a variety of aquatic environments. Benson et al. (Benson et al., 2019) used the DrOne Water Sampling SystEm (DOWSE) to collect water and study microorganisms from eight remote Alpine lakes in Austria. Drones have also been used to collect samples from hazardous pit lake environments (Castendyk et al., 2020). Koparan et al. (2020) developed adaptive water sampling approaches for bathymetry and turbidity maps at Lake Issaquena, SC. In recent years, water quality sampling equipment has become easier to manage with faster sampling times and autonomous systems have enabled the collection of environmental samples in remote or dangerous locations. The ability of the DOWSE to collect numerous samples at different distances from shore or boat and the quick turnaround time for preliminary water quality data highlight the potential for predicting and tracking HABs to inform citizens and establish possible mitigation protocols.

The overall goal of this work was to use drone-based water sampling methods to characterize cyanotoxins, phycocyanin, and nutrients in three freshwater lakes in the United States that had active HABs. We chose water quality metrics with specific measurements to provide indicators for human and animal health (cyanotoxins), the presence of cyanobacteria (phycocyanin), and the extent of anthropogenic influence (nutrients). This study was specifically designed to quickly gather small-volume samples and produce a rapid turnaround of measurable water quality using a small set of metrics. The specific objectives of our work were to 1) collect surface water samples using a drone-based water collection system (DOWSE) at different distances (10–100 m) from the shore and from an anchored boat in GLSM, Lake Erie, and Lake Anna and 2) characterize cyanotoxins, phycocyanin, and nutrients in drone water samples from each of the lakes while establishing improved understanding of the relationships among these parameters. Our work demonstrates the potential for drone-based water sampling technologies to be used by public health and water quality experts to provide critical and timely information for regulatory decisions and health advisories.

Materials and methods

Lake collections using the DrOne water sampling SystEm

The DOWSE (Benson et al., 2019) was used to collect water samples from three freshwater lakes with active HABs. Briefly, a Phantom 4 quadcopter (DJI, Shenzhen, China) outfitted with a carbon fiber mount on the landing gear was used to gather water samples by attaching the 3D printed water sampler apparatus to the quadcopter with a 4.6 m tether line (Figure 1). The water

sampler was lowered to the surface until the sample tube filled with water. Once the water sample was at the surface, a picture was taken from the drone showing the sampler in the water. Each drone image contains metadata that ultimately allows the precise location of the sampler in the lake to be determined (Filippi et al., 2021). This method was repeated for each sampling point along a 100-m transect (10–100 m) [e.g., transects as highlighted in (Benson et al., 2019)] from land or from an anchored boat until 10 samples were collected for each flight. The average time span between the first (10 m) and last (100 m) collection along the transect was 12 min. Ten water samples spaced 10 m apart from each other, and collected in a short time frame, allowed for variability of water quality metrics to be compared across a 100 m transect. A freshly opened sterile tube was inserted into the water sampling device immediately before each collection. As each sample was returned *via* the drone tether (to shore or boat), the filled sample tube was replaced with a freshly opened sterile collection tube while the drone hovered in place to allow for sample tubes to be switched quickly. Following the ten sample collections for each flight, a 50 ml control tube was filled with sterile water and flown out to the furthest collection point (100 m from the shore or boat), held at an altitude greater than 4.6 m above the lake surface, and then returned *via* the tether to be capped and stored with each flight sample set of ten tubes. To avoid potential cross contamination among lakes, a new tether was used for each of the lakes and the sampling devices were soaked in a dilute solution of sodium hypochlorite. Water samples were held on ice in a cooler in the dark until all samples were collected for each sampling day.

FIGURE 1
The DrOne Water Sampling SystEm (DOWSE) returning a water sample collected in 2019 at GLSM in Celina, OH **(A)**. The DOWSE collects water samples at the surface **(B)**, and a drone returns the filled sample tube in the sampler on a 4.6 m nylon tether **(C)**.

Lake study sites

Field experiments were conducted at GLSM, Celina, OH, Lake Erie at Maumee Bay OH, and Lake Anna, Mineral, VA (Figure 2). Seasonal HAB conditions persist at both GLSM and Lake Erie during August. Lake Anna is a recent concern for HABs so August and September provided two temporal measurements when potential toxins could be measured toward the end of the season when cyanobacterial accumulation and or cell death could provide a scenario of increased toxin production at levels that could be detected, especially in a lake that has recently been identified as a potential HAB concern. Samples were collected from GLSM (August 5–6), Lake Erie (August 8), and Lake Anna (August 23, and September 10) during the 2019 HAB season. GLSM covers 13,500 acres and is a shallow (5–7 feet in depth) man-made reservoir lake constructed from 1837 to 1845. The Celina Water Plant began testing intake water from GLSM for MC in 2009 and continues to test weekly for the presence of toxins as part of the water purification process. Lake Erie is the 11th largest lake globally and covers over six million acres. For over 20 years, Lake Erie has been plagued with HABs that produce MC and in 2014 the Toledo water crisis left half a million people without safe water. Lake Anna is another inland reservoir lake that covers 13,000 acres. The lake bottom was cleared, and the North Anna River dam was completed in 1972. Cyanobacterial cell counts of potentially toxigenic taxa have been reported as above recreational advisory thresholds at Lake Anna since 2018 (>100,000 cells/ml). These freshwater lakes were sampled in field year 2019 and are shown in Figure 2. Freshwater samples were collected from a single location at GLSM and Lake Erie. The GPS location in decimal degrees (DD) for GLSM (40.544873, −84.510843) is shown with a green map marker and for Lake Erie (41.702472, −83.463598) with a red marker. Collections at Lake Anna (Lake Anna) were carried out at 12 unique locations (Figure 2). GPS locations for Lake Anna are listed in Table 2. These locations were selected based on the predictable incidence of annually occurring HABs (GLSM, Lake Erie) and/or high cyanobacteria cell counts, >100,000 cells/ml of potentially toxigenic species, or >40,000 cells/ml of *Microcystis* species (Lake Anna).

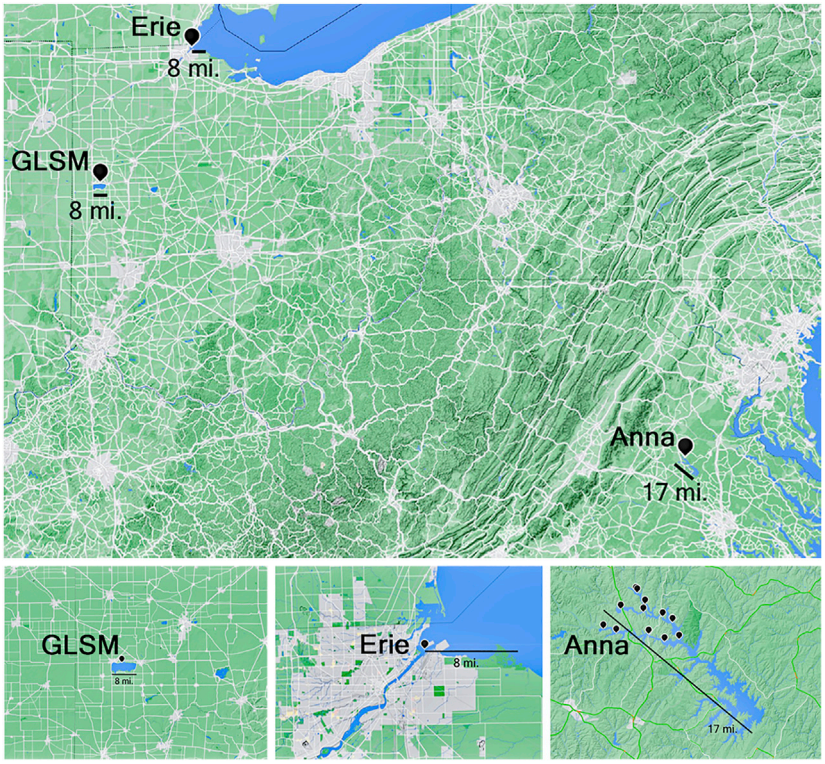

FIGURE 2
Three freshwater lakes with known HABs were sampled in the US in 2019. Locations are marked as follows: Grand Lake Saint Mary's (GLSM), Celina, OH (40.544873, −84.510843), Lake Erie at Maumee Bay, OH (41.702472, −83.463598), and Lake Anna, Mineral, VA (multiple sampling locations, with 38.10642, −77.84076 designating the location near the "splits" at the State Park). GLSM, was sampled on August 5–6, Lake Erie was sampled on August 8, and Lake Anna was sampled on August 23 and September 10.

Handling of water samples

Water samples were aliquoted on the day of collection. Tubes were labeled for toxin analysis and nutrient determination for all flight samples (Figure 3). Tubes for downstream toxin analysis were frozen at −20°C. The remaining sample tubes were held at 4°C prior to processing.

Cyanotoxin analysis with LC-MS/MS

Water samples from the three lakes were analyzed for the presence of putative cyanotoxins (Table 3) with the most abundant toxins in each lake shown in Figure 4. Toxin analysis was performed at the Lumigen Instrument Center, Wayne State University, Detroit, MI. The 15 cyanotoxins analyzed include 12 microcystins (MCs), nodularin, anatoxin-a, and cylindrospermopsin. The internal standard C_2D_5 MC-LR* was run with the suite of MC toxins and nodularin, whereas, two internal standards, L-Phenylalanine-D_5** and Uracil-D_4** were analyzed in the anatoxin-a and cylindrospermopsin suite. Sample aliquots of 5 ml were subjected to three freeze-thaw cycles and analyzed by LC-MS/MS with controls to determine toxin concentrations. The Lumigen Instrument Center tested for cyanotoxins using two methods. One method included 12 MC congeners and nodularin (NOD), and the second method cylindrospermopsin and anatoxin-A.

The detection of MCs and nodularin using LC-MS/MS was completed using the method described in Birbeck et al. (2019). Briefly, samples were analyzed by an online concentration method using a Thermo Scientific TSQ Altis™ triple quadrupole mass spectrometer (Thermo Scientific, Waltham, MA, United States) with an EQuan MAX Plus™ system. An injection volume of 1 ml of sample was injected onto the loading column (Thermo Scientific Hypersil GOLD aQ 2.1 × 20 mm, 12 µm particle size) using an HTC PAL autosampler (CTC Analytics, Zwingen, Switzerland). Analytes were then separated on a Thermo Accucore aQ, 50 × 2.1 mm, 2.6 µm particle size column. Mass spectrometry analysis was performed using an electrospray ionization source in positive ion mode.

The detection of anatoxin-a and cylindrospermopsin were analyzed using a Thermo Scientific TSQ Altis™ triple quadrupole mass spectrometer (Thermo Scientific, Waltham, MA,

TABLE 2 Details for each of the drone flights including date of collection, lake (Grand Lake St Mary's, Erie, or Anna), time (24-h), GPS location of launch site on ground or from boat, Nitrate-N (mg/L), total phosphorus (mg/L), and N/P ratio.

Flight	Date	Est	Lake	GPS location	Mean NO3-N mg/L ± SE	Mean TP -P mg/L ± SE	N/P ratio
FLIGHT01	5-Aug-19	09:40–09:53	GLSM	(40.544873, −84.510843)	0.13 ± 0.01	0.33 ± 0.01	0.41
FLIGHT02	5-Aug-19	13:31–13:44	GLSM	(40.544873, −84.510843)	0.14 ± 0.01	0.27 ± 0.01	0.53
FLIGHT03	6-Aug-19	09:36–09:46	GLSM	(40.544873, −84.510843)	0.10 ± 0.01	0.39 ± 0.01	0.26
FLIGHT04	6-Aug-19	13:47–13:58	GLSM	(40.544873, −84.510843)	0.12 ± 0.01	0.37 ± 0.01	0.32
FLIGHT05	8-Aug-19	12:36–12:46	Erie	(41.702472, −83.463598)	2.48 ± 0.02	0.11 ± 0.01	23.04
FLIGHT06	8-Aug-19	14:31–14:41	Erie	(41.702472, −83.463598)	3.27 ± 0.10	0.14 ± 0.01	24.14
FLIGHT07	23-Aug-19	08:18–08:28	Anna	(38.148070–77.892803)	0.09 ± 0.01	0.09 ± 0.02	1.01
FLIGHT08	23-Aug-19	09:04–09:15	Anna	(38.138523, −77.894524)	0.08 ± 0.01	0.06 ± <0.01	1.21
FLIGHT09	23-Aug-19	09:48–09:59	Anna	(38.132604, −77.864658)	0.07 ± <0.01	0.03 ± <0.01	2.27
FLIGHT10	23-Aug-19	10:40–10:52	Anna	(38.125945, −77.849134)	0.08 ± 0.01	0.03 ± <0.01	2.72
FLIGHT11	23-Aug-19	12:01–12:13	Anna	(38.106428, −77.804766)	0.09 ± 0.01	0.03 ± <0.01	3.35
FLIGHT12	23-Aug-19	12:46–13:01	Anna	(38.102509, −77.863082)	0.10 ± 0.01	0.03 ± <0.01	3.14
FLIGHT13	23-Aug-19	13:39–13:50	Anna	(38.111752, −77.886401)	0.09 ± 0.01	0.05 ± <0.01	1.89
FLIGHT14	23-Aug-19	14:26–14:38	Anna	(38.113106, −77.936464)	0.12 ± 0.01	0.10 ± <0.01	1.16
FLIGHT15	10-Sept-19	08:22–08:34	Anna	(38.161642, −77.903738)	0.10 ± 0.01	0.04 ± 0.01	2.45
FLIGHT16	10-Sept-19	08:59–09:11	Anna	(38.161476, −77.903289)	0.10 ± 0.01	0.05 ± 0.01	2.06
FLIGHT17	10-Sept-19	10:17–10:30	Anna	(38.140964, −77.928508)	0.14 ± 0.02	0.10 ± 0.01	1.36
FLIGHT18	10-Sept-19	12:26–12:38	Anna	(38.118197, −77.954825)	0.07 ± 0.01	0.11 ± 0.01	0.69

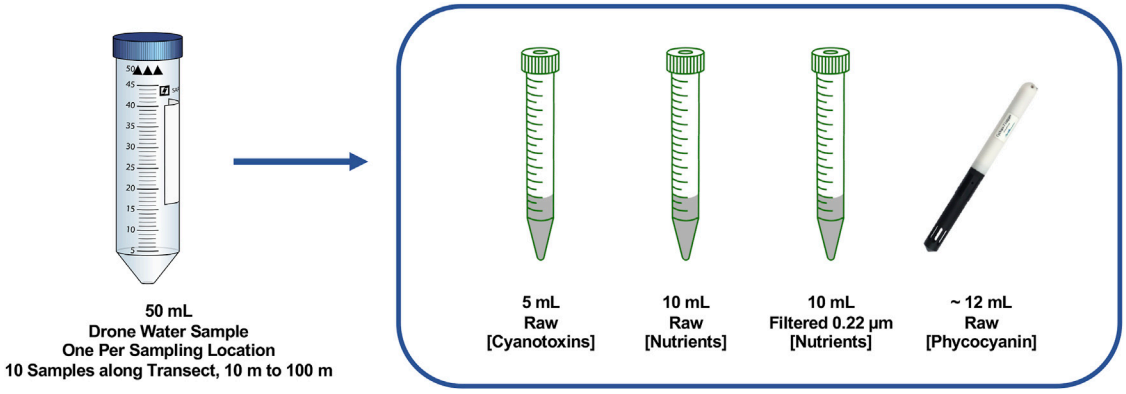

FIGURE 3
Schematic illustrating how samples were processed for each 50 ml drone water sample. Aliquots were made for toxin analysis (5 ml), nutrient analysis (10 ml), and filtrate nutrient analysis (</ = 0.45 µm) (10 ml), for all flights. One milliliter was aliquoted for flow cytometry (1 ml) from Lake Anna collections (Flight 07–Flight 18). The remaining volume in the 50 ml collection tube was adjusted to 12 ml and used for phycocyanin (PC) readings with the Cyclops-7 sensor from Turner Designs, Inc. (Sunnyvale, CA) on the day of collection. PC data was recorded with the Precision Measurement Engineering data logger (Vista, CA).

United States) with an EQuan MAX Plus™ system. Samples were separated on a Hypersil GOLD™ aQ C18 columns, 2.1 × 100 mm, 1.9 µm. Mobile phases for the step gradient were (A) 100 mM acetic acid in LC-MS grade water and (B) 100 mM acetic acid in LC-MS grade methanol. The flow rate was set at 0.4 ml/min and gradient started at 0% B from 0 to 0.1 min, stepped to 10% B from 0.1 to 2.7 min, then stepped to 95% B from 2.7 to 4.7 min. At 4.71 min the gradient was stepped back down to 0% B until 7.5 min for re-equilibration. Sample injection volume was 10 µl, and the column temperature was held constant at 30°C. All analysis was in positive ion mode, and the mass spectrometer settings were as follows: positive ion voltage at 3500 V, sheath gas

TABLE 3 List of 15 cyanotoxins analyzed in drone water samples. Toxins not detected are noted as ND. The MCs present at a mean above 0.05 ppb at GLSM and Lake Erie are noted in bold and shown in Figure 4 for two flights from each lake. At Lake Anna three MC were detected in addition to Anatoxin-a. These toxins are noted in bold and shown for two flights from Lake Anna (Figure 4).

Analyte	Quantifier ion (m/z)	Qualifier ion (m/z)	GLSM mean (ppb)	Lake Erie mean (ppb)	Lake Anna mean (ppb)
[D-Asp^3]-MC-RR	135.07	498.91	**12.79**	<0.05	ND
MC-RR	135.07	212.94	<0.05	**0.89**	ND
MC-YR	135.00	213.03	**1.66**	**0.31**	ND
MC-HtyR	135.05	1031.46	ND	<0.05	ND
MC-LR	135.07	155.08	**0.08**	**0.58**	**0.009**
[D-Asp^3]-MC-LR	135.01	213.03	**0.44**	<0.05	ND
MC-HilR	135.00	155.08	ND	<0.05	ND
MC-WR	135.03	626.25	ND	>0.05	ND
MC-LA	776.41	375.16	ND	**0.054**	**0.010**
MC-LY	868.42	494.18	<0.05	<0.05	**0.0001**
MC-LW	517.18	446.17	<0.05	<0.05	ND
MC-LF	852.41	478.17	ND	<0.05	ND
Nodularin	135.00	389.16	ND	ND	ND
C_2D_5 MC-LR *	135.09	163.08			
Anatoxin-a	149.000	131.000	ND	ND	**0.098**
Cylindrospermopsin	194.058	176.040	ND	ND	<0.10
L-Phenylalanine-D_5 **	125.040				
Uracil-D_4 **	98.000				

(arb units) at 45, aux gas (arb units) at 13, sweep gas (arb units) at 1, ion transfer tube temperature (°C) at 342, and vaporizer temperature (°C) at 358. Transitions that were used for the cyanotoxins are listed in Table 3. Data were analyzed using TraceFinder™ EFS 4.1 where retention time, and quantitative and qualitative ion qualifications were set and monitored to ensure proper cyanotoxin identification.

Phycocyanin concentration using the Cyclops-7 sensor

Freshwater cyanobacteria produce phycocyanin, and the presence of this pigmented protein can be measured to give an indication of the concentration (i.e., estimate of biomass) of cyanobacteria in a collected water sample. The biomass of cyanobacteria does not have a direct correlation to cyanotoxin production or toxin concentration (Christensen et al., 2019; Christensen et al., 2022). The use of the word biomass in this manuscript is not critically defined but used as a common language word in reference to its relationship with nutrient levels, its use in the description of trophic lake state values, and its use as a possible indicator of elevated PC pigments. This objective measure of PC can be recorded as parts per billion (ppb) or micrograms per liter (μg/L) in a water sample and these values can be used to assign risk levels to areas of HAB concern (Cotterill et al., 2019; Thomson-Laing et al., 2020). Alert level 1 and 2 indicates a state of surveillance while alert level 3 indicates the need for repeat testing. Action level indicates that advisories should be posted by authorities to inform citizens that a specific aquatic environment is a potential human health hazard. Last year in Virginia total potentially toxigenic cyanobacterial counts at or above 100,000 cells/ml or total MC species counts at or above 40,000 cells/ml were used as the action level advisory limit for posting HAB warning signs (US EPA, 2019). A Precision Measurement Engineering data logger outfitted with a Turner Instruments Cyclops-7 PC sensor (Model No: 2110-000) was used to collect PC measurements (Figure 5). Water samples were moved to room temperature 20 min prior to PC measurements. For all collections, the sensor was submerged into approximately 12 ml of lake water and held in place 2.4 cm from the bottom of a 50 ml conical tube. The sensor collected PC concentration in ppb at 5-s intervals in the dark for a minimum of 30 s. The PC sensor was rinsed with distilled water and wiped with a Kimwipe between each sample. Distilled water blanks were measured prior to, and after completion of, sample readings.

Phycocyanin sensor calibration

The Cyclops-7 PC sensor (Model No: 2110-000) was calibrated with the *Cyclops* Solid Standard (Turner, cat # 2100-900, rev. J). The rhodamine WT (water tracing), 400 ppb (cat # 6500-120) liquid calibration standard was diluted to

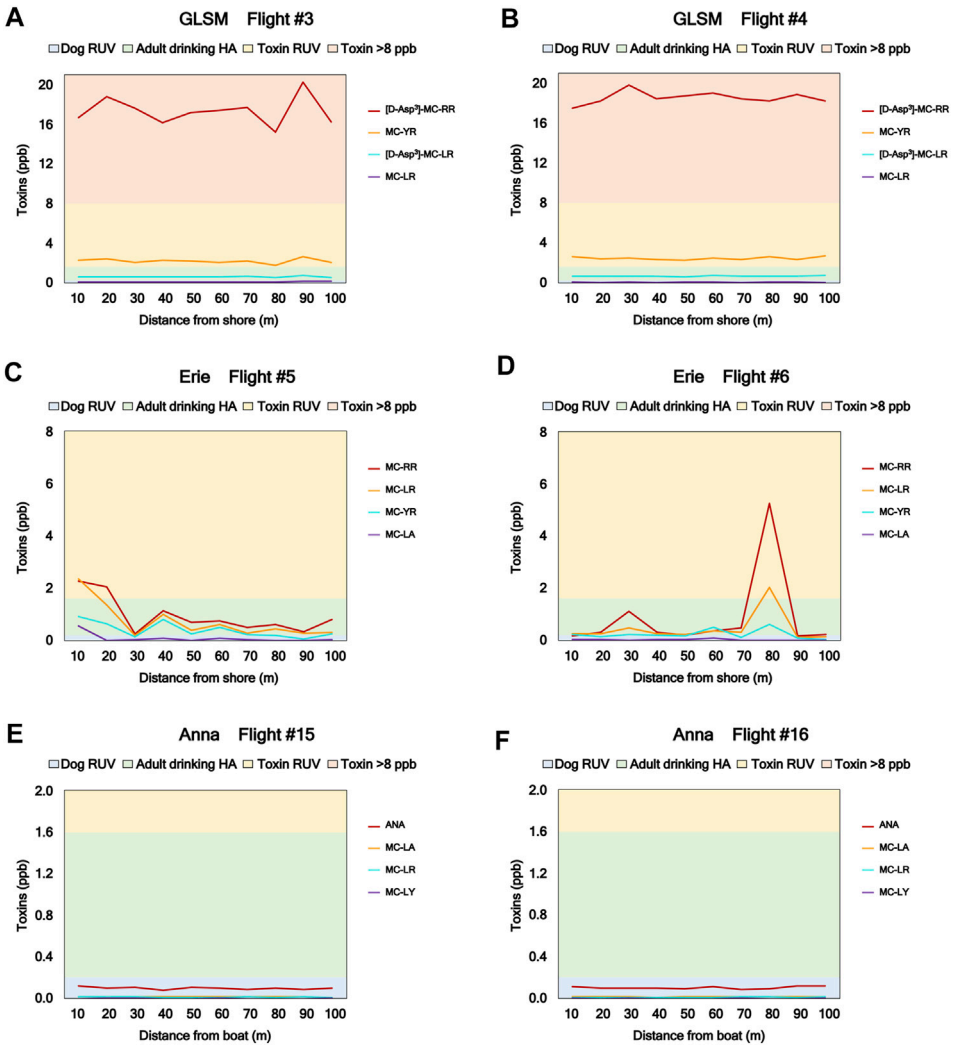

FIGURE 4
Graphical summary of toxins from two flights collected from each lake. The data shown for GLSM **(A,B)**, Lake Erie **(C,D)**, and Lake Anna **(E,F)** were collected in consecutive flights. Distance across the 100 m transect is shown on the x-axis. Toxin concentration in ppb is shown on the y-axis. The color bands denote water quality conditions relative to toxin load. Water quality metrics for MC toxin concentrations are shown in Table 1 and correspond to the trophic state lake classifications of oligotrophic (blue), mesotrophic (green), eutrophic (yellow), and hypereutrophic (orange).

200 ppb and the sensor calibration set point was equilibrated to 260 ppb PC as per manufacturers specifications.

Nutrient analyses for phosphorus and nitrogen

Phosphorus and nitrate concentrations (mg/L) were determined for all lake collections. These small volume samples were designed to provide a rapid turnaround of measurable nutrients. To this end, we analyzed samples for nitrate-N and not for total Kjeldahl nitrogen. Analyses were performed at the Wright State University Lake Campus, Celina, OH. Upon collection, a portion of the water was immediately filtered (</ = 0.45 µm), at which point both samples were kept in the dark at 4°C prior to nutrient analyses. All samples were analyzed within 24 h to 2 weeks of collection. The raw (unfiltered) sample was used to determine total phosphorus (0.025 mg/L MDL) following acid-persulfate sample digestion while the filtered portion of the samples was used to determine dissolved reactive phosphorus (Ortho-P 0.025 mg/L LOD) and nitrate-N (NO_3-N 0.15 mg/L MDL) concentrations. Due to sample volume limitations, it was not possible to analyze samples for total Kjeldahl nitrogen (and thus total nitrogen as a function of TKN + NOx). Phosphorus concentrations were assessed using ascorbic acid methods (EPA 365.1; www.ecfr.gov/)

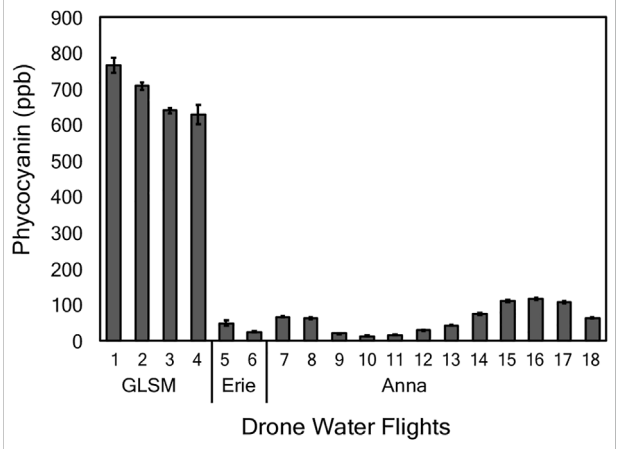

FIGURE 5
Phycocyanin (PC) values shown in parts per billion (ppb) for the 18 flights collected at the three lakes in field year 2019. Four flights were collected from GLSM, two from Lake Erie, and 12 from Lake Anna. The mean PC concentration at GLSM, Erie, and Anna was 687, 38, and 62 ppb, respectively. The error bars represent standard error of the mean (n = 10) for the ten transect tubes collected for each flight.

while nitrate was measured using the dimethylphenol method (EPA 40 CFR 136; www.ecfr.gov/) using a benchtop visible spectrum spectrophotometer (HACH DR 3900). A series of blanks, analytical duplicates, field duplicates, premixed standards, and spikes were run concurrent with every 20-sample batch. Specific to these QA/QC checks for this study, no instances of any appreciable variations greater than 10% from "expected" values were detected.

Results

Lake collections using the DrOne water sampling SystEm

A total of 180 water samples was collected across 18 flights at three freshwater lakes in 2019. Forty samples were collected from GLSM, 20 samples from Lake Erie, and 120 from Lake Anna. Each drone-based water sampling mission was comprised of a 10-tube transect over distances of 10–100 m. Temporal differences between sample sites ranged from 2 h to 18 days. Drone-sampling missions at GLSM and Lake Erie were performed from the shore at a single GPS location. Drone-sampling missions at Lake Anna were performed from an anchored boat at 12 different locations at 11 unique sites on the lake. Two drone samples at Lake Anna were collected within close spatiotemporal parameters; both transects were collected inside a 49-min time span, and within a lake surface area of 200 m^2. Each sample site location was given a unique flight number, Flight 01–Flight 18 (Table 2). Flight 16, collected at Lake Anna on 10 September 2019 departed from a traditional line transect to target a visual pattern of floating expected on the surface of the lake.

Our collections incorporated ten measurements along a distance of 100 m in an effort to examine the potential variability of water quality metrics in a spatially repeatable sampling regime. Each flight was able to collect ten samples in a short time frame (12 min). Water quality metrics at GLSM and Lake Erie were repeated at the same location with various increments of time among collections. Since these lakes were experiencing late summer HAB conditions (i.e., August), the flights were able to explore high resolution temporal variation with repeated sample collections at the same site. The second sampling date at Lake Anna allowed for a spatial extension of water quality metrics in the three northern branches of the lake: Terry's Run, Upper Pamunkey, and North Anna. The back-to-back sampling flights shown in Figures 4, 6, 7 were an example of the difference between morning and afternoon sampling times (when were able to conduct flights safely around inclement weather) for GLSM and Lake Erie. Lake Anna Flights 15 and 16 were collected in close spatial proximity since we were following visual scum on the lake surface. Consequently, the Lake Anna flights were both collected in the morning.

Cyanotoxin analysis with LC-MS/MS

Cyanotoxins were present in all three of the freshwater lakes. Graphical summaries of the four most abundant cyanotoxins in each lake are represented by two flights from each lake and are shown in Figure 4. The two flights from each lake represent measured variation across a 100 m transect with the same spatial location taken on the same day with little temporal variation. Three MC congeners were present in Lake Anna, seven in GLSM, and 12 in Lake Erie. Anatoxin-a (ANA) was only detected at Lake Anna, and was present in 93% (111/120) of the samples. Cylindrospermopsin was detected in a single collection at Lake Anna. Nodularin was not detected in any of the lake samples. The highest individual MC congener toxin level was found at GLSM (D-Asp3-Dhb7-RR) and was present at a mean value of 17.97 ppb. This concentration is well above the RUV advisory level of eight total ppb for MC as a result of the D-Asp3-Dhb7-RR congener values alone. Cyanotoxins with the highest mean concentrations from Flight 03 and Flight 04 at GLSM were D-Asp3-Dhb7-RR (17.97 ppb), MC-YR (2.32 ppb), D-Asp3-LR (0.619 ppb), and MC-LR (0.0719 ppb). All 12 congeners of MC were detected in the western basin of Lake Erie in a total of two collections, Flight 05 and Flight 06. Ten MC congeners were detected in at least 65% (13/20) of the samples. MC-HtyR was detected in 30% of the samples (6/20) and MC-LF was detected in 10% (2/20) of the Lake Erie collections. The four toxins with the highest mean toxin concentration in Lake Erie were MC-RR

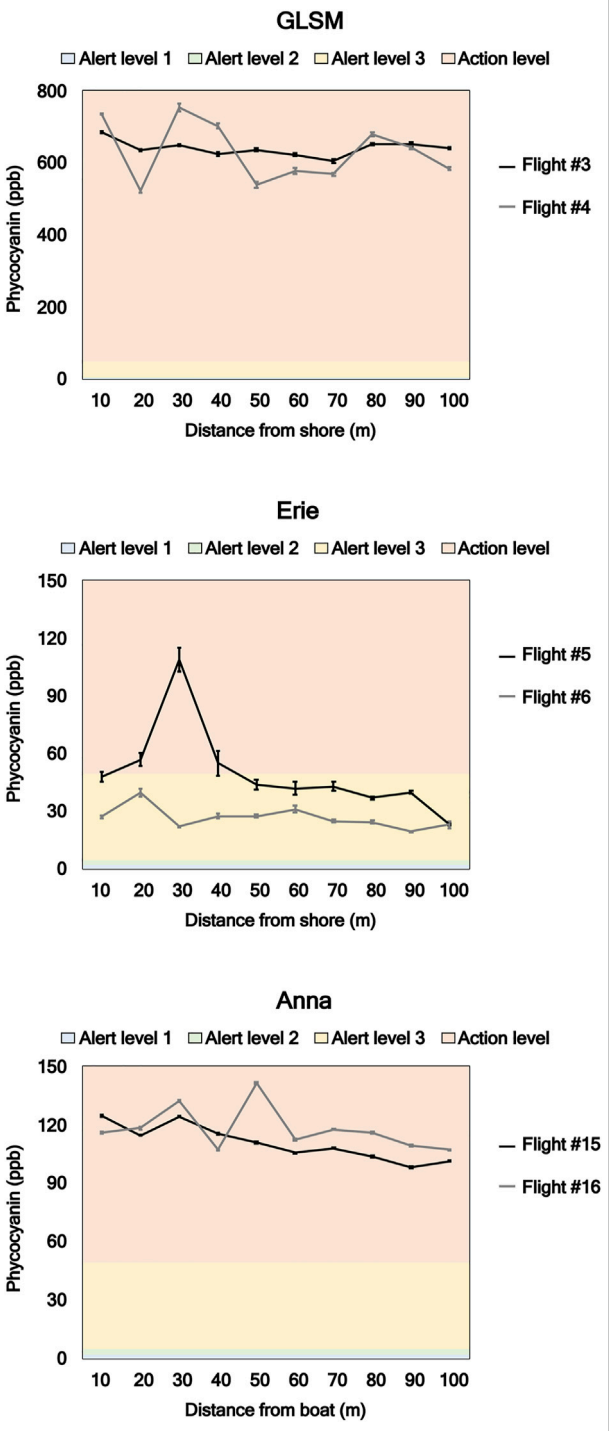

FIGURE 6
The concentration of PC from each transect location is shown for two consecutive flights from each lake. Distance across the 100 m transect is shown on the x-axis. PC concentration in ppb is shown on the y-axis with a scale of 0–800 ppb (GLSM), or a scale of 0–140 ppb (Lake Erie and Lake Anna). The color bands represent Alert level 1 (blue), Alert level 2 (green), Alert level 3 (yellow), and Action level (orange). The water quality metrics are shown in Table 1 and correspond to the trophic state lake classifications of oligotrophic, mesotrophic, eutrophic, and hypereutrophic.

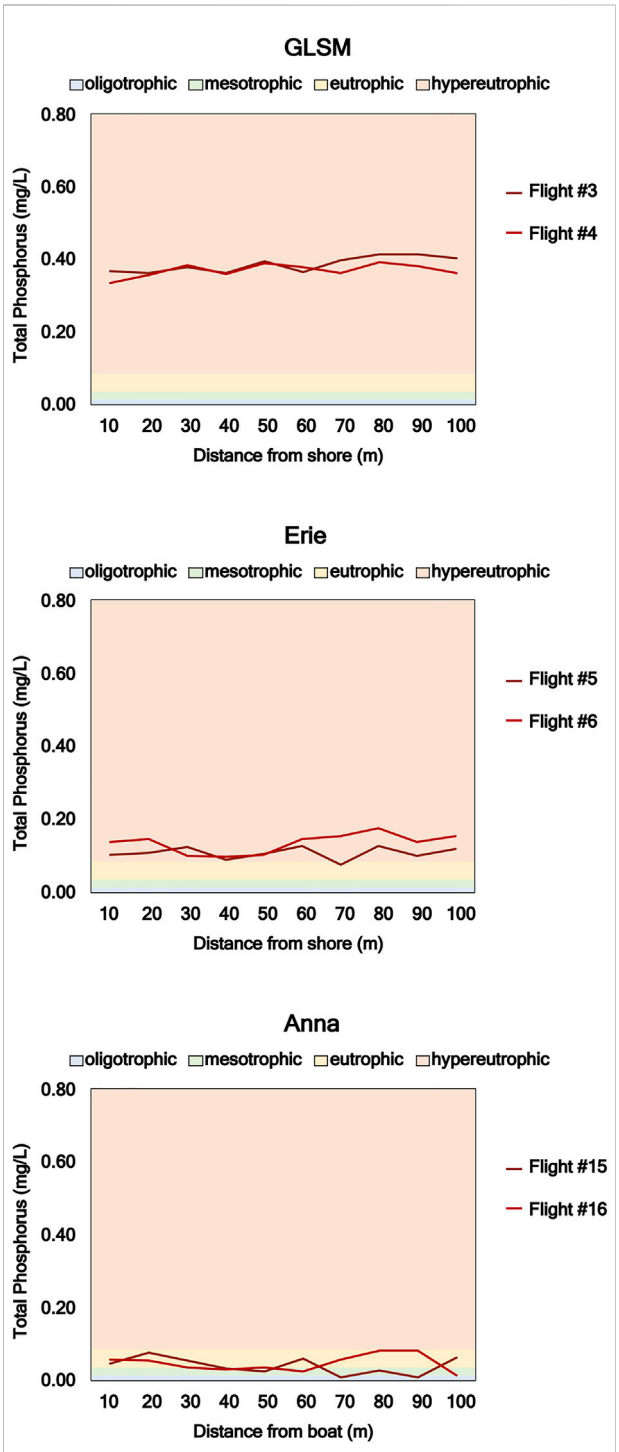

FIGURE 7
Graphical representation of total phosphorus from two consecutive flights collected on the same day, for each freshwater lake. The color bands denote lake water quality as oligotrophic (blue), mesotrophic (green), eutrophic (yellow), and hypereutrophic (orange) (Table 1). Trophic State Index (TSI) values for oligotrophic (TSI 0–40), mesotrophic (TSI 41–50), eutrophic (TSI 51–60), and hypereutrophic (TSI 70–100) follow the TSI table published by (Carlson, 1977). Collection points in 10-m increments are shown on the x-axis. Total phosphorus mg/L for both flights from each lake is shown on the y-axis. A total phosphorus concentration is 0–0.80 mg/L.

(0.893 ppb), MC-LR (0.579 ppb), MC-YR (0.310 ppb), and MC-LA (0.0544 ppb). Several samples from Lake Erie had MC concentrations above the adult drinking health advisory limit of 1.6 ppb (Table 1). Three of the 12 MC congeners were present in Lake Anna. MC-LA and MC-LR were identified in 77% (92/120) and 85% (102/120) of flight collections, respectively, while MC-LY was exclusively detected in Flights 15–16. The most abundant cyanotoxins identified in Lake Anna from Flight 15 and Flight 16 were ANA (0.0984 ppb), MC-LA (0.0124), MC-LR (0.00959), and MC-LY (0.00130). The US EPA RUV limit for MC and ANA is 8 ppb.

Phycocyanin

PC concentrations from the three lakes was measured for each of the 18 flights (Figure 5). GLSM had the highest PC values with a mean of 687 ppb for Flight 01–Flight 04. The mean PC from Lake Erie (Flight 05 and Flight 06) was 38 ppb. Lake Anna had a mean of 62 ppb for the 12 flights (Flight 07–Flight 18) collected on both sampling days, 23 August and 10 September 2019. A subset of six flights was chosen to analyze PC concentration at each 10 m interval (Figure 6) on a color band graph to show the alert level of PC as listed in Table 1 (Izydorczyk et al., 2009; Cotterill et al., 2019). The flights chosen for each lake were Flight 03–Flight 04 (GLSM), Flight 05–Flight 06 (Lake Erie), and Flight 15–Flight 16 (Lake Anna). The high PC concentrations in GLSM and Lake Anna place these lakes in the Action level. PC concentrations in Lake Erie declined between the morning Flight 5 (action level) to the afternoon Flight 6 (Alert level 3) in a time span less than 2 h.

Nutrient analyses for phosphorus and nitrogen

A graphical summary of total phosphorus mg/L concentration is shown for two drone-sampling missions for each lake in Figure 7 (Lake Erie Forage Task Group, 2020). Total phosphorus was the highest at GLSM, with a mean TP-P concentration of 0.378 mg/L (Flight 03 and Flight 04), placing GLSM in a hypereutrophic state (0.0481–0.768 mg/L) for phosphorus content as denoted in Table 1 (Carlson, 1977). Lake Erie was just above eutrophic levels for phosphorus with a mean TP-P concentration of 0.122 mg/L for Flight 05 and Flight 06. Flight 15 and Flight 16 from Lake Anna had a mean concentration of 0.043 mg/L TP-P, placing this lake in a eutrophic state (0.0241–0.048 mg/L) for phosphorus. Individual water samples for phosphorus in Lake Anna spanned both mesotrophic (0.0121–0.024 mg/L) and eutrophic lake state values. Dissolved reactive phosphorus (Ortho-P) was highest in GLSM with a mean of 0.139 mg/L (0.127–0.153 mg/L) followed by Lake Erie with a mean of 0.022 mg/L (BDL-0.046 mg/L) and Lake Anna with a mean of 0.01 mg/L (range BDL-0.021) mg/L). Nitrogen content measured as nitrate (NO_3-N) was the highest at Lake Erie with a mean of 2.875 mg/L (Flight 05 and Flight 06), placing Lake Erie in a hypereutrophic state (1.471–23.6 mg/L) for total nitrogen content even without total Kjeldahl nitrogen (TKN) measurements to add to these NOx values (Kratzer and Brezonik, 1981). GLSM (Flight 03 and Flight 04) and Lake Anna (Flight 15 and Flight 16) had mean nitrate concentrations of 0.111 and 0.097 mg/L NO_3-N, respectively (Table 2). It is worth noting that grab samples from GLSM around this time indicated TKN values between 3 and 4 mg/L (unpublished data), unsurprisingly, likely putting GLSM above Lake Erie or Lake Anna.

Discussion

New remote sensing tools and technology are needed to detect and monitor freshwater HABs. The distribution of cyanobacteria in aquatic habitats is influenced by a variety of anthropogenic and environmental factors that are in constant flux (Anderson, 2012; Graham et al., 2016). Not all cyanobacteria produce cyanotoxins, and limitations in testing capabilities further limit water quality assessments. We used a unique DrOne Water Sampling SystEm (DOWSE) to collect water samples from three HABs in three freshwater lakes in the United States. Drone water sampling technologies can be deployed quickly and can provide access to remote areas that are not easily accessible or typically monitored (Ore et al., 2015; Benson et al., 2019; Filippi et al., 2021). This study demonstrates the utility of a such a rapid water sampling system capable of obtaining water samples to assess the parameters one would require to better understand a HAB (e.g., concentrations of toxins, phycocyanin, and nutrients). In addition to quick sampling capabilities in remote aquatic locations, advantages of our drone-based water sampling approach include the ability to collect surface samples without disturbing the surrounding water and without entering a body of water on foot and wading out to grab a sample. Disadvantages include the need for drone equipment and a certified (and preferably skilled) drone pilot. Though GLSM and Lake Erie have a long history of HAB research, our work represents the first drone-based water sampling of these lakes. Moreover, our work is the first to report anatoxins in surface water samples of Lake Anna—a lake with a relatively new (young) HAB near its tipping point.

Cyanotoxins were measured from each of the samples because they provide an indication of a potential health hazard to humans and domestic animals. Representative congeners of the cyanotoxin MC were present in each of the lakes. GLSM was characterized by total MC levels that averaged 15 ppb, well above the RUV of 8 ppb (Figure 4). The total MC toxin levels at Lake Erie and Lake Anna were lower than GLSM, with mean values of 1.92 and <0.02 ppb, respectively. The MC

concentrations at Lake Erie were highly variable with concentrations both above and below the adult drinking health advisory limit (1.6 ppb) in the same flight (Figure 4). This variability of MC concentration within a distance of only 100 m highlights the importance of testing multiple water samples across space and time. Another example of spatial variability of MC toxins was observed in the Prespa Lakes, Greece during 2012–2014 (Maliaka et al., 2021). Concentrations of MC in Lesser Prespa ranged from 25 to 861 ug/L (ppb) in 2014. In addition to the spatial heterogeneity observed in MC toxin concentrations in Lake Lesser Prespa, a high variability was observed in the surface accumulation of cyanobacteria in 2012 (Maliaka et al., 2021). The cyanotoxin levels found in Lake Anna were much lower than the other lakes and were below the dog RUV level (Figure 4). Interestingly, Lake Anna was the only lake that showed the presence of the anatoxin-A (ANA) (the US EPA RUV limit for ANA is the same as MC at >8 ppb). Several cyanobacteria can produce ANA, including *Anabaena*, *Aphanizomenon*, *Cylindrospermum*, *Microcystis*, *Planktothirix*, and *Raphidiopsis* (Varner, 2018). Though the genus or genera of cyanobacteria in Lake Anna that are responsible for ANA production are presently unknown, the potentially toxigenic cyanobacterial genera with counts above 100,000 cells/mL as reported by VDH for Lake Anna in 2018 were *Microcystis*, *Cylindrospermopsis*, *Rahpidiospsis*, *Pseudoanabaena*, and *Planktolyngbya* (personal communication with VDH, 2021). *Anabaena*, *Aphanizomenon*, and *Planktothrix* were among the potentially toxigenic taxa identified at Lake Anna in 2018 (personal communication with VDH, 2021) at counts lower than the 100,000 cells/mL threshold for concern. A recent algal bloom assessment in 2021 listed *Pseudoanbaena*, *Raphidiopsis*, and *Planktolyngbya* as dominant species in the North Anna branch (Solitude Lake Management, 2022). High-use recreational areas with HABs need timely information regarding the presence of cyanotoxins above RUVs. This information should be used to keep citizens informed about how safe it might be to have their dog at the lake or if toxin levels could cause skin irritation.

Phycocyanin was analyzed because this pigment is a signature of cyanobacteria, and different sensors are available to measure PC and other pigments found in water due to the presence of living organisms. Phycocyanin was present above action levels in GLSM and Lake Anna. Although Lake Erie had a lower average PC, samples along 100 m drone water sampling transects ranged from Alert level 3 to Action level within a 2-h time interval. This highlights the need for quick remote sampling capabilities that could be used to provide health advisory data on a body of water that provides drinking water to a population of over 400,000 residents.

Phosphorus and nitrogen content was measured because these components contribute to growth and accumulation of cyanobacteria in freshwater environments. Phosphorus levels varied from oligotrophic (Anna) to hypereutrophic (GLSM) (Figure 7). The total phosphorus load measured at GLSM was extremely high and stable in the hypereutrophic range. Although our measurements were taken in a single month, the mean value of total phosphorus measured bimonthly in 2019 at GLSM (samples were collected by hand) was 0.30 mg/L (S. Jacquemin, unpublished observations). This value is hypereutrophic and in line with our drone sampling of GLSM. Lake Erie had phosphorus levels that were just above eutrophic, and Lake Anna ranged from oligotrophic to eutrophic. It is important that future studies ensure multiple species of nitrogen are measured to be able to calculate total nitrogen as well as phosphorus. Such measurements are important in the context of environmental changes required to improve water quality; after 2011 Distressed Watershed legislation limited allowable nutrient loads in the agricultural watershed the water quality improved tremendously (Jacquemin et al., 2018). Specifically, reductions were more notable during winter months when a ban on manure was implemented, and all parameters were decreased by 20%–60%. However, analyzing multiple species of nitrogen in a water sample requires increased sample volumes, which depending on the analytical methods used could be up to 150 ml. Should larger volumes of water be necessary for future work, our water sampling device could be modified to sample larger volumes of water. Such a design modification would need to consider the payload limits of the platform (for the drone used in this work, the sampling payload when full of water should not exceed 500 g for safe operations) and reduced flight times due to additional battery consumption to power the drone with a heavier payload.

Our work to characterize HABs in different freshwater lake environments could be enhanced by additional information from other technology platforms. We were able to quickly sample and characterize HABs in three freshwater lakes using a unique drone-based water sampling approach. Though we focused our analyses on cyanotoxins, phycocyanin, and nutrients, future work could include additional analyses such as cyanobacterial concentrations or other water quality parameters. Such analyses would likely require larger collection volumes; our current sampling method is limited to sampling 50 ml of water. Future work could include additional remote sensing tools such as the Cyanobacteria Monitoring Collaborative website (Cyanobacteria.org, 2021) or the new US EPA CyAN web application released July 2021 (US EPA, 2019). The EPA CyAN platform is free and designed to support real-time decisions regarding HABs based on the Copernicus Sentinel-3 European satellite. The CyAN imagery interface is a new web-based tool that could be used in future research efforts to add another layer of information to current tools and technology. For example, the CyAN could be used with real-time water quality measurements to observe changes in a HAB that was characterized by high levels of MC-RR and could shift to the MC-LR congener due to a decrease in total available nitrogen. In August 2019, the higher level of nitrogen content relative to

phosphorus at Lake Erie could favor the nitrogen rich congener, MC-RR over the more toxic congener, MC-LR (MC-RR was the most abundant congener with MC-LR the next abundant congener). A shift in nutrient content in the Western basin area of Lake Erie that would favor the MC-LR congener, could quickly pose a safety hazard to drinking water in the greater Toledo area. This is notable with regard to Lake Erie, because the MC congeners with the highest concentrations were MC-RR and MC-LR and several collections along the 100 m transect had total MC values above drinking advisory levels. A shift in conditions that would favor MC-LR as the prominent MC congener could quickly contaminate the drinking water supply to nearby citizens. The MC-LR variant showed a lethal dose response in mice at levels 10 to 40 times greater than the MC-RR congener (Zurawell et al., 2005). Late summer blooms in Lake Erie occur when the annual TN:TP input from the Maumee River is low and N is limited (Gobler et al., 2016). Cyanobacterial blooms have been studied to better understand communities with regard to abundance of biomass, the composition of species present, and the ability to produce toxins (Christensen et al., 2019, 2021, 2022; Chorus and Welker, 2021). Christensen et al. (2022) showed that similar water quality metrics from three spatially separate locations on Kabetogama Lake had differences in phytoplankton communities at the same locations.

Additional water quality research is needed to make accurate predictions about toxin levels in any area where cyanobacteria loads are elevated to a level of concern. Informing the public with accurate information on water quality and the presence of cyanotoxins is becoming an ever-increasing need in locations where cyanobacteria persist. As climate conditions shift to higher temperatures for longer periods of time, the danger of HABs producing toxins above the US EPA health advisory drinking limit for adults (1.6 ppb, MC) becomes more of a threat (Wells et al., 2020). The US EPA RUV limit for dogs (0.2 ppb, MC) is much lower, and MC toxins could become a deadly threat to dogs if climate conditions increase toxicity of HABs. Many factors influence the growth and accumulation of cyanobacteria in freshwater environments. Elevated cell counts are an indicator that a harmless HAB could become a toxic HAB. Comparing the dominant species of cyanobacteria in a specific area could indicate how a new HAB might behave relative to existing information on toxic HABs that have been characterized over several seasons. However, a myriad of environmental factors has been shown to influence the growth and accumulation of HABs. These factors influence the production of cyanotoxins from such HABs. Predicting the presence and level of cyanotoxins based solely on the abundance of cyanobacteria requires additional work and careful experimentation.

Chasing the visual clues of a potential toxin producing bloom are challenging due to the spatial complexity and highly variable conditions that can occur in a dynamic water environment (Janssen et al., 2014). Visual clues of a potential HAB location can disappear before samples can be collected or measured. Citizens rely on state sponsored collections and toxin testing or cell count information to be gathered, analyzed, and posted to make decisions about spending time in recreational waters. In some instances, monitoring efforts identify high concentrations of cyanobacteria but do not necessarily provide toxin information. Long-term datasets are needed to study the influence of climate change on the occurrence and severity of HABs (Wells et al., 2020). Remote sensing technologies have been used to gather data and test models related to water quality (Topp et al., 2020). There is a knowledge gap in using this information to turn methods and models into scientific characterization of inland water quality (Topp et al., 2020).

Spatial and temporal differences in water quality measurements highlight the need for new approaches to test water, determine quality, and use these measurements as a proxy to predict the likelihood of harmful toxins in lakes and other aquatic environments. Drones can be used to collect water samples from lakes with a long or even recent history of HABs. The spatial and temporal sampling regime determined at any freshwater lake can be successfully carried out by the DOWSE, provided environmental conditions are suitable to safe drone operations. It is important to note that our sampling of the three lakes in this study was designed to collect water quality data, not to establish a recommended sampling regime for a specific lake. Once a sampling regime has been determined at a specific lake, the DOWSE has the capability to collect water quickly and precisely at any time in any location with line of sight from the collection point. The collection ability of the DOWSE makes it a great tool for lakes that experience persistent HAB conditions since it can be deployed as often as needed, and in specific areas that require intensive sampling approaches. For freshwater lakes that experience HAB conditions seasonally, the DOWSE can be used as needed temporally and can sample in remote or new locations to help elucidate the extent of the HAB across the lake. Our work is important for informing coordinated sampling efforts with uncrewed robotic systems and providing critical and timely information to guide advisory decisions to provide quick and accurate information to citizens and stakeholders.

In conclusion, the sampling methods described here provide a precise and immediate sampling protocol for potentially dangerous surface waters on freshwater lakes. The DOWSE could help elucidate the temporal and spatial distribution of HABs in freshwater lakes that are under visual surveillance. This would allow HAB hazard notifications to be posted and sent to citizens and businesses near the HAB location. The drawbacks include the need for a competent and certified drone pilot, and the need for fair weather during flight operations.

Data availability statement

The raw data supporting the conclusion of this article will be made available by the authors, without undue reservation.

Author contributions

RH and DS conceived, planned, and conducted the field experiments at all of the lakes. RH coordinated and managed analyses for all of the samples, conducted calibration experiments in the laboratory, and analyzed data from all of the experiments. SJ conducted nutrient analyses. JB and JW conducted cyanotoxin analyses. CH assisted with phycocyanin measurements. HG assisted with processing water samples for downstream analyses. AA, HF, SR, and JG-R were part of campaigns at GLSM and Erie. CP designed the drone-based water sampling device. LP, HL, and GB assisted with data collection and analysis for Lake Anna. RH and DS led the writing of the manuscript. All authors provided feedback on the manuscript.

Funding

This research was supported in part by the National Science Foundation (NSF) under grant number NRI-2001119, the Institute for Critical Technology Applied Science at Virginia Tech under grant number ICTAS-178429, and Virginia Tech's DA-GSS under grant number 177908. Publication fees were provided by Virginia Tech's Open Access Subvention Fund (OASF).

Acknowledgments

We thank Wright State University for coordinating lodging and accommodations for our field campaigns at GLSM. We thank LP for providing lodging and accommodations for our field campaigns at Lake Anna. We thank LP and J. Marsh for the use of their boats at Lake Anna. We also thank members of the Lake Anna Civic Association (LACA) for their ongoing engagement in our work.

Conflict of interest

Authors LP, HL, and GB are members of the Lake Anna Civic Association.

The remaining authors declare that the research was conducted in the absence of any commercial or financial relationships that could be construed as a potential conflict of interest.

Publisher's note

References

Anderson, D. (2012). HABs in a changing world: A perspective on harmful algal blooms, their impacts, and research and management in a dynamic era of climactic and environmental change. *Harmful Algae 2012 (2012)* 2012, 3–17.

Anderson, D. M., Glibert, P. M., and Burkholder, J. M. (2002). Harmful algal blooms and eutrophication: Nutrient sources, composition, and consequences. *Estuaries* 25 (4), 704–726. doi:10.1007/bf02804901

Ballot, A., Swe, T., Mjelde, M., Cerasino, L., Hostyeva, V., and Miles, C. O. (2020). Cylindrospermopsin- and deoxycylindrospermopsin-producing Raphidiopsis raciborskii and microcystin-producing Microcystis spp. in meiktila lake, Myanmar. *Toxins* 12 (4), 232. doi:10.3390/toxins12040232

Benson, J., Hanlon, R., Seifried, T., Baloh, P., Powers, C., Grothe, H., et al. (2019). Microorganisms collected from the surface of freshwater lakes using a drone water sampling system (DOWSE). *Water* 11 (1), 157. doi:10.3390/w11010157

Birbeck, J. A., Peraino, N. J., O'Neill, G. M., Coady, J., and Westrick, J. A. (2019). Dhb microcystins discovered in USA using an online concentration LC-MS/MS platform. *Toxins* 11 (11), 653. doi:10.3390/toxins11110653

Carlson, R. E. (1977). A trophic state index for lakes1. *Limnol. Oceanogr.* 22 (2), 361–369. doi:10.4319/lo.1977.22.2.0361

Castendyk, D., Voorhis, J., and Kucera, B. (2020). A validated method for pit lake water sampling using aerial drones and sampling devices. *Mine Water Environ.* 39 (3), 440–454. doi:10.1007/s10230-020-00673-y

CFR (2022). 40 CFR Part 136 - guidelines establishing test procedures for the analysis of pollutants. Available at: https://www.ecfr.gov/current/title-40/chapter-I/subchapter-D/part-136.

Chorus, I., and Welker, M. (2021). in *Toxic cyanobacteria in water: A guide to their public health consequences, monitoring and management*. 2nd edn. Second edition (Boca Rataon: CRC Press, an imprint of Informa). doi:10.1201/9781003081449

Christensen, V. G., Maki, R. P., Stelzer, E. A., Norland, J. E., and Khan, E. (2019). Phytoplankton community and algal toxicity at a recurring bloom in Sullivan Bay, Kabetogama Lake, Minnesota, USA. *Sci. Rep.* 9 (1), 16129. doi:10.1038/s41598-019-52639-y

Christensen, V. G., Olds, H. T., Norland, J., and Khan, E. (2022). Phytoplankton community interactions and cyanotoxin mixtures in three recurring surface blooms within one lake. *J. Hazard. Mater.* 427, 128142. doi:10.1016/j.jhazmat.2021.128142

Christensen, V. G., Stelzer, E. A., Eikenberry, B. C., Olds, H. T., LeDuc, J. F., Maki, R. P., et al. (2021). Cyanotoxin mixture models: Relating environmental variables and toxin co-occurrence to human exposure risk. *J. Hazard. Mater.* 415, 125560. doi:10.1016/j.jhazmat.2021.125560

Cotterill, V., Hamilton, D. P., Puddick, J., Suren, A., and Wood, S. A. (2019). Phycocyanin sensors as an early warning system for cyanobacteria blooms concentrations: A case study in the rotorua lakes. *N. Z. J. Mar. Freshw. Res.* 53 (4), 555–570. doi:10.1080/00288330.2019.1617322

Du, X., Liu, H., Yuan, L., Wang, Y., Ma, Y., Wang, R., et al. (2019). The diversity of cyanobacterial toxins on structural characterization, distribution and identification: A systematic review. *Toxins* 11 (9), 530. doi:10.3390/toxins11090530

Filippi, M., Hanlon, R., Rypina, I. I., Hodges, B. A., Peacock, T., and Schmale, D. G. (2021). Tracking a surrogate hazardous agent (rhodamine dye) in a coastal ocean environment using *in situ* measurements and concentration estimates derived from drone images. *Remote Sens.* 13 (21), 4415. doi:10.3390/rs13214415

Francy, D. S., Brady, A. M., Stelzer, E. A., Cicale, J. R., Hackney, C., Dalby, H. D., et al. (2020). Predicting microcystin concentration action-level exceedances resulting from cyanobacterial blooms in selected lake sites in Ohio. *Environ. Monit. Assess.* 192 (8), 513. doi:10.1007/s10661-020-08407-x

Fraterrigo, J., and Downing, J. (2008). The influence of land use on lake nutrients varies with watershed transport capacity. *Ecosystems* 11, 1021–1034. doi:10.1007/s10021-008-9176-6

Gobler, C. J., Burkholder, J. M., Davis, T. W., Harke, M. J., Johengen, T., Stow, C. A., et al. (2016). The dual role of nitrogen supply in controlling the growth and toxicity of cyanobacterial blooms. *Harmful Algae* 54, 87–97. doi:10.1016/j.hal.2016.01.010

Graham, J. L., Dumbrovsky, N. M., and Eberts, S. M. (2016). Cyanobacterial harmful algal blooms and U.S. Geological Survey science capabilities. Open-File Report 2016-1174. doi:10.3133/ofr20161174

Graham, J. L., Loftin, K. A., Ziegle, A. C., and Meyer, M. T. (2008). Guidelines for design and sampling for cyanobacterial toxin and taste-and-odor studies in lakes and reservoirs. Available at: https://pubs.usgs.gov/sir/2008/5038/pdf/SIR2008-5038.pdf.

Izydorczyk, K., Carpentier, C., Mrówczyński, J., Wagenvoort, A., Jurczak, T., and Tarczyńska, M. (2009). Establishment of an Alert Level Framework for cyanobacteria in drinking water resources by using the Algae Online Analyser for monitoring cyanobacterial chlorophyll a. *Water Res.* 43 (4), 989–996. doi:10.1016/j.watres.2008.11.048

Jacquemin, S. J., Johnson, L. T., Dirksen, T. A., and McGlinch, G. (2018). Changes in water quality of Grand Lake St. Marys watershed following implementation of a distressed watershed rules package. *J. Environ. Qual.* 47 (1), 113–120. doi:10.2134/jeq2017.08.0338

Janssen, A. B. G., Teurlincx, S., An, S., Janse, J. H., Paerl, H. W., and Mooij, W. M. (2014). Alternative stable states in large shallow lakes? *J. Gt. Lakes. Res.* 40 (4), 813–826. doi:10.1016/j.jglr.2014.09.019

Jetoo, S., Grover, V. I., and Krantzberg, G. (2015). The Toledo drinking water advisory: Suggested application of the water safety planning approach. *Sustainability* 7 (8), 9787–9808. doi:10.3390/su7089787

Koparan, C., Koc, A. B., Privette, C. V., and Sawyer, C. B. (2020). Adaptive water sampling device for aerial robots. *Drones* 4 (1), 5. doi:10.3390/drones4010005

Kratzer, C. R., and Brezonik, P. L. (1981). A carlson-type trophic state index for nitrogen in Florida lakes. *J. Am. Water Resour. Assoc.* 17 (4), 713–715. doi:10.1111/j.1752-1688.1981.tb01282.x

Lake Erie Forage Task Group (2020). Report of the lake Erie forage Task Group. Available at: http://www.glfc.org/pubs/lake_committees/erie/FTG_docs/annual_reports/FTG_report_2020.pdf.

Maliaka, V., Lürling, M., Fritz, C., Verstijnen, Y. J., Faassen, E. J., van Oosterhout, F., et al. (2021). Interannual and spatial variability of cyanotoxins in the Prespa Lake area, Greece. *Water* 13 (3), 357. doi:10.3390/w13030357

Mishra, S., Stumpf, R. P., Schaeffer, B., Werdell, J., Loftin, K. A., Meredith, A., et al. (2021). Evaluation of a satellite-based cyanobacteria bloom detection algorithm using field-measured microcystin data. *Sci. Total Environ.* 774, 145462. doi:10.1016/j.scitotenv.2021.145462

Ore, J.-P., Elbaum, S., Burgin, A., and Detweiler, C. (2015). Autonomous aerial water sampling. *J. Field Robot.* 32 (8), 1095–1113. doi:10.1002/rob.21591

Oregon Health Authority (2019). Oregon harmful algae bloom surveillance (HABS) program recreational use public health advisory guidelines cyanobacterial blooms in freshwater bodies. Available at: https://www.oregon.gov/oha/PH/HEALTHYENVIRONMENTS/RECREATION/HARMFULALGAEBLOOMS/Documents/2019%20Advisory%20Guidelines%20for%20Harmful%20Cyanobacterial%20Blooms%20in%20Recreational%20Waters.pdf.

Powers, C., Hanlon, R., and Schmale, D. (2018a). Tracking of a fluorescent dye in a freshwater lake with an unmanned surface vehicle and an unmanned aircraft system. *Remote Sens.* 10 (2), 81. doi:10.3390/rs10010081

Powers, C., Hanlon, R., and Schmale III, D. G., III (2018b). Remote collection of microorganisms at two depths in a freshwater lake using an unmanned surface vehicle (USV). *PeerJ* 6, e4290. doi:10.7717/peerj.4290

Powers, C. W., Hanlon, R., Grothe, H., Prussin, A. J., Marr, L. C., Schmale, D. G., et al. (2018c). Coordinated sampling of microorganisms over freshwater and saltwater environments using an unmanned surface vehicle (USV) and a small unmanned aircraft system (sUAS). *Front. Microbiol.* 9, 1668. doi:10.3389/fmicb.2018.01668

Qian, S. S., Chaffin, J. D., DuFour, M. R., Sherman, J. J., Golnick, P. C., Collier, C. D., et al. (2015). Quantifying and reducing uncertainty in estimated microcystin concentrations from the ELISA method. *Environ. Sci. Technol.* 49 (24), 14221–14229. doi:10.1021/acs.est.5b03029

Ribas-Ribas, M., Battaglia, G., Humphreys, M. P., and Wurl, O. (2019). Impact of nonzero intercept gas transfer velocity parameterizations on global and regional ocean-atmosphere CO2 fluxes. *Geosciences* 9 (5), 230. doi:10.3390/geosciences9050230

Ross, S. D., Fish, J., Moeltner, K., Bollt, E. M., Bilyeu, L., and Fanara, T. (2022). Beach-level 24-hour forecasts of Florida red tide-induced respiratory irritation. *Harmful Algae* 111, 102149. doi:10.1016/j.hal.2021.102149

Scheffer, M., Hosper, S., Meijer, M. L., Moss, B., and Jeppesen, E. (1993). Alternative equilibria in shallow lakes. *Trends Ecol. Evol.* 8 (8), 275–279. doi:10.1016/0169-5347(93)90254-M

Schmale, D. G., Ault, A. P., Saad, W., Scott, D. T., and Westrick, J. A. (2019). Perspectives on harmful algal blooms (HABs) and the cyberbiosecurity of freshwater systems. *Front. Bioeng. Biotechnol.* 7, 128. doi:10.3389/fbioe.2019.00128

Solitude Lake Management (2022). *Algal bloom assessment and recommendations for part of lake Anna*. Virginia Department of Health.

Stumpf, R. P., Davis, T. W., Wynne, T. T., Graham, J. L., Loftin, K. A., Johengen, T. H., et al. (2016). Challenges for mapping cyanotoxin patterns from remote sensing of cyanobacteria. *Harmful Algae* 54, 160–173. doi:10.1016/j.hal.2016.01.005

Thomson-Laing, G., Puddick, J., and Wood, S. A. (2020). Predicting cyanobacterial biovolumes from phycocyanin fluorescence using a handheld fluorometer in the field. *Harmful Algae* 97, 101869. doi:10.1016/j.hal.2020.101869

Topp, S. N., Pavelsky, T. M., Jensen, D., Simard, M., and Ross, M. R. V. (2020). Research trends in the use of remote sensing for inland water quality science: Moving towards multidisciplinary applications. *Water* 12 (1), 169. doi:10.3390/w12010169

US EPA (2016). Draft human health recreational ambient water quality criteria and/or swimming advisories for microcystins and cylindrospermopsin. Available at: https://www.federalregister.gov/documents/2016/12/19/2016-30464/request-for-scientific-views-draft-human-health-recreational-ambient-water-quality-criteria-andor.

US EPA (2019). Recommended human health recreational ambient water quality criteria or swimming advisories for microcystins and cylindrospermopsin. Available at: https://www.epa.gov/sites/default/files/2019-05/documents/hh-rec-criteria-habs-document-2019.pdf.

Varner, Mia (2018). Using high frequency monitoring of environmental factors to predict cyanotoxin concentrations in a multi-use, inland reservoir. Varner, Mia: University of Cincinnati ProQuest Dissertations Publishing. Thesis.

VDH (2021). Guidance for cyanobacteria bloom recreational advisory management. Available at: https://www.vdh.virginia.gov/content/uploads/sites/178/2022/01/FINAL_SIGNED_Guidance_for_Cyanobacteria_Recreational_Advisory_Mgt.5Aug2021-1.pdf.

Wells, M. L., Karlson, B., Wulff, A., Kudela, R., Trick, C., Asnaghi, V., et al. (2020). Future HAB science: Directions and challenges in a changing climate. *Harmful Algae* 91, 101632. doi:10.1016/j.hal.2019.101632

Wilde, F. D., Radtke, D. B., Gibs, J., and Iwatsubo, R. T. (1998). Selection of equipment for water sampling. *Environ. Sci.* doi:10.3133/TWRI09A2

Yoo, R. S. (1995). *Cyanobacterial (Blue-Green algal) toxins: A resource guide*. Denver: Waterworks Association Research Foundation.

Zurawell, R. W., Chen, H., Burke, J. M., and Prepas, E. E. (2005). Hepatotoxic cyanobacteria: A review of the biological importance of microcystins in freshwater environments. *J. Toxicol. Environ. Health, Part B* 8 (1), 1–37. doi:10.1080/10937400590889412

frontiers | Frontiers in Remote Sensing

TYPE Original Research
PUBLISHED 24 August 2022
DOI 10.3389/frsen.2022.924969

OPEN ACCESS

EDITED BY
Jane Southworth,
University of Florida, United States

REVIEWED BY
Christine Angelini,
University of Florida, United States
Dongdong Shao,
Beijing Normal University, China

*CORRESPONDENCE
Alexandra E. DiGiacomo,
alexandra.digiacomo@stanford.edu

SPECIALTY SECTION
This article was submitted to Unoccupied Aerial Systems (UASs and UAVs), a section of the journal Frontiers in Remote Sensing

RECEIVED 21 April 2022
ACCEPTED 21 July 2022
PUBLISHED 24 August 2022

CITATION
DiGiacomo AE, Giannelli R, Puckett B, Smith E, Ridge JT and Davis J (2022), Considerations and tradeoffs of UAS-based coastal wetland monitoring in the Southeastern United States. *Front. Remote Sens.* 3:924969. doi: 10.3389/frsen.2022.924969

Considerations and tradeoffs of UAS-based coastal wetland monitoring in the Southeastern United States

Alexandra E. DiGiacomo[1]*, Ryan Giannelli[2], Brandon Puckett[3], Erik Smith[4], Justin T. Ridge[1] and Jenny Davis[5]

[1]Duke University Marine Laboratory, Division of Marine Science and Conservation, Nicholas School of the Environment, Duke University, Beaufort, NC, United States, [2]Consolidated Safety Services Inc, for National Oceanic and Atmospheric Administration, Fairfax, VA, United States, [3]North Carolina National Estuarine Research Reserve, Beaufort, NC, United States, [4]North Inlet Winyah Bay National Estuarine Research Reserve and University of South Carolina Baruch Institute, Georgetown, SC, United States, [5]National Centers for Coastal Ocean Science, National Oceanic and Atmospheric Administration, Beaufort, NC, United States

Coastal wetlands of the Southeastern United States host a high abundance and diversity of critical species and provide essential ecosystem services. A rise in threats to these vulnerable habitats has led to an increased focus on research and monitoring in these areas, which is traditionally performed using manual measurements of vegetative characteristics. As these methods require substantial time and effort, they are often limited in scale and infeasible in areas of dense or impassable habitat. Unoccupied Aircraft Systems (UAS) provide an advantage over traditional ground-based methods by serving as a non-invasive alternative that expands the scale at which we can understand these ecosystems. While recent interest in UAS-based monitoring of coastal wetland habitats has grown, methods and parameters for UAS-based mapping lack standardization. This study addresses variability introduced by common UAS study techniques and forms recommendations for optimal survey designs in vegetated coastal habitats. Applying these parameters, we assess alignment of computed estimations with manually collected measurements by comparing UAS-SfM mapping products to ground-based data. This study demonstrates that, with careful consideration in study design and analysis, there exists great potential for UAS to provide accurate, large-scale estimates of common vegetative characteristics in coastal salt marshes.

KEYWORDS

coastal monitoring, UAS, vegetation structure, biomass, salt marsh

1 Introduction

Estuarine intertidal habitats are rich in both species diversity and abundance (Noss et al., 2015). Tidal wetlands are used as foraging grounds, nursery habitat, and reproductive space for commercially and recreationally important fishery stocks (Barbier et al., 2011). Beyond providing critical habitat for fauna, vegetated

wetlands enhance coastal water quality by trapping sediments and filtering nutrients, are valued for their ability to sequester carbon, and can protect coastal communities by dampening wave energy and slowing the inland transfer of water during storm induced flood events (Morris et al., 2002; Barbier et al., 2011; Spalding et al., 2014). Intertidal wetlands occupy the narrow zone between upland and open water regions and as a result, are uniquely vulnerable to sea level rise. Salt marshes dominated by smooth cordgrass (*Spartina alterniflora,* recently reclassified as *Sporobolus alterniflorus* (Peterson et al., 2014)) are common along southeastern US coastlines. These systems serve as sentinels of coastal change and as a result, resource management agencies, academic researchers and non-profits expend considerable effort monitoring wetlands for change detection.

Despite the known ecological value of these habitats, tidal wetlands continue to suffer area loss and degradation (Jackson et al., 2001; Lotze et al., 2006). Erosion from storms, sea level rise, and coastal development threaten these vulnerable habitats (Morris et al., 2002; Meixler et al., 2018). The resultant losses in tidal wetlands have jeopardized coastal communities through increased exposure to flooding and diminished habitat for local fish stocks (Barbier et al., 2011; Spalding et al., 2014). In response, rapid and consistent monitoring of these wetland ecosystems has become a priority for coastal management efforts (Psuty et al., 2018). An example of these efforts is the National Estuarine Research Reserve System (NERRS) program. NERRS, funded by the National Oceanic and Atmospheric Administration (NOAA), was designed to produce research that informs and aids coastal managers seeking to conserve and restore coastal resources (Trueblood et al., 2019). The NERR system consists of 30 coastal US sites covering over 1.3 million acres of estuarine habitat (National Estuarine Research Reserve System, 2021). Monitoring these wetland habitats for change detection is central to understanding resilience to shifting environmental conditions and informing coastal management decisions within the NERRS and beyond.

Traditional marsh monitoring practices involve on-the-ground measures of vegetative structure (i.e. species presence and abundance, stem density, stem height, total standing biomass, percent cover, and often sediment surface elevation) (Roman et al., 2001; James-Pirri et al., 2002). While manual field surveys provide crucial information about plant community structure, they are time and labor intensive. As a result, manual surveys are limited in scale and often rely on several small (1 m^2) fixed monitoring plots to characterize the entire marsh. Moreover, some areas of these ecosystems are inaccessible by foot and trampling of wetland vegetation in the process of manual monitoring can have lasting negative impacts (Minchinton et al., 2019). Monitoring approaches that minimize boots on the ground and maximize spatial coverage of observations will allow for greater ability to detect change at scales that are meaningful to resource managers (MacKay et al., 2009).

Remote sensing can provide a non-invasive, scalable alternative to manual estimates of marsh properties (Roughgarden et al., 1991; Fennessy et al., 2007). Rapid monitoring regimes that minimize costs while maximizing coverage are increasingly recognized as essential for wetland assessment programs and effective resource management (Fennessy et al., 2007). The use of remote sensing to understand coastal ecosystems is well-established (Green et al., 1996). Satellite imagery has provided breakthroughs in the ability of researchers to understand and visualize ecosystem change (Pettorelli et al., 2018). Satellite remote sensing has improved management capabilities in coastal regions by facilitating large-scale mapping of critical habitats and associated ecosystem properties over time (McCarthy et al., 2017). However, limitations to satellite-based approaches include cloud cover obstruction, image resolution, and limited spatial and temporal coverage of available datasets (Pettorelli et al., 2018). Light Detection and Ranging (LiDAR) data can improve monitoring accuracy from satellite data by providing multi-temporal high spatial resolution imagery (Pham et al., 2019). Airborne and hyperspectral LiDAR have been used to map salt marsh vegetation height and bare earth elevation but the high cost associated with LiDAR collection is a barrier to widespread use (Klemas, 2013; Pham et al., 2019). Unoccupied Aircraft Systems (UAS), or drones, can provide an alternative to time and labor-intensive manual measurements with the benefit of fine-scale resolution that provides an edge over satellite-based imagery (Klemas, 2013; Whitehead and Hugenholtz, 2014). UAS have been applied to the study of salt marsh and estuarine habitats, providing large-scale, efficient monitoring of these habitats (Doughty and Cavanaugh, 2019; Farris et al., 2019; DiGiacomo et al., 2020; Thomsen et al., 2021). Structure-from-Motion (SfM) processing of overlapping UAS imagery make possible the 3-dimensional reconstruction of salt marsh habitats (DiGiacomo et al., 2020).

Though UAS-based methods are increasingly being utilized for monitoring coastal wetlands (Doughty and Cavanaugh, 2019; Farris et al., 2019; DiGiacomo et al., 2020; Thomsen et al., 2021), imaging protocols and analysis methods lack standardization amongst studies. Inter-sensor comparisons reveal differences in surface reconstruction and reflectance values between common consumer-grade UAS platforms (Sona et al., 2014; Yanagi and Chikatsu, 2016). Moreover, other studies have found differences in mapping products produced by different SfM software packages for forested (Fraser and Congalton, 2018; Kameyama and Sugiura, 2021) and unvegetated (Sona et al., 2014; Yanagi and Chikatsu, 2016) areas. Variability introduced by UAS flight protocols and UAS-SfM workflows for mapping dynamic coastal wetland environments has not yet been well explored. Identifying sources of uncertainty in mapping products is a critical first step to building standardized protocols that can generate rigorous

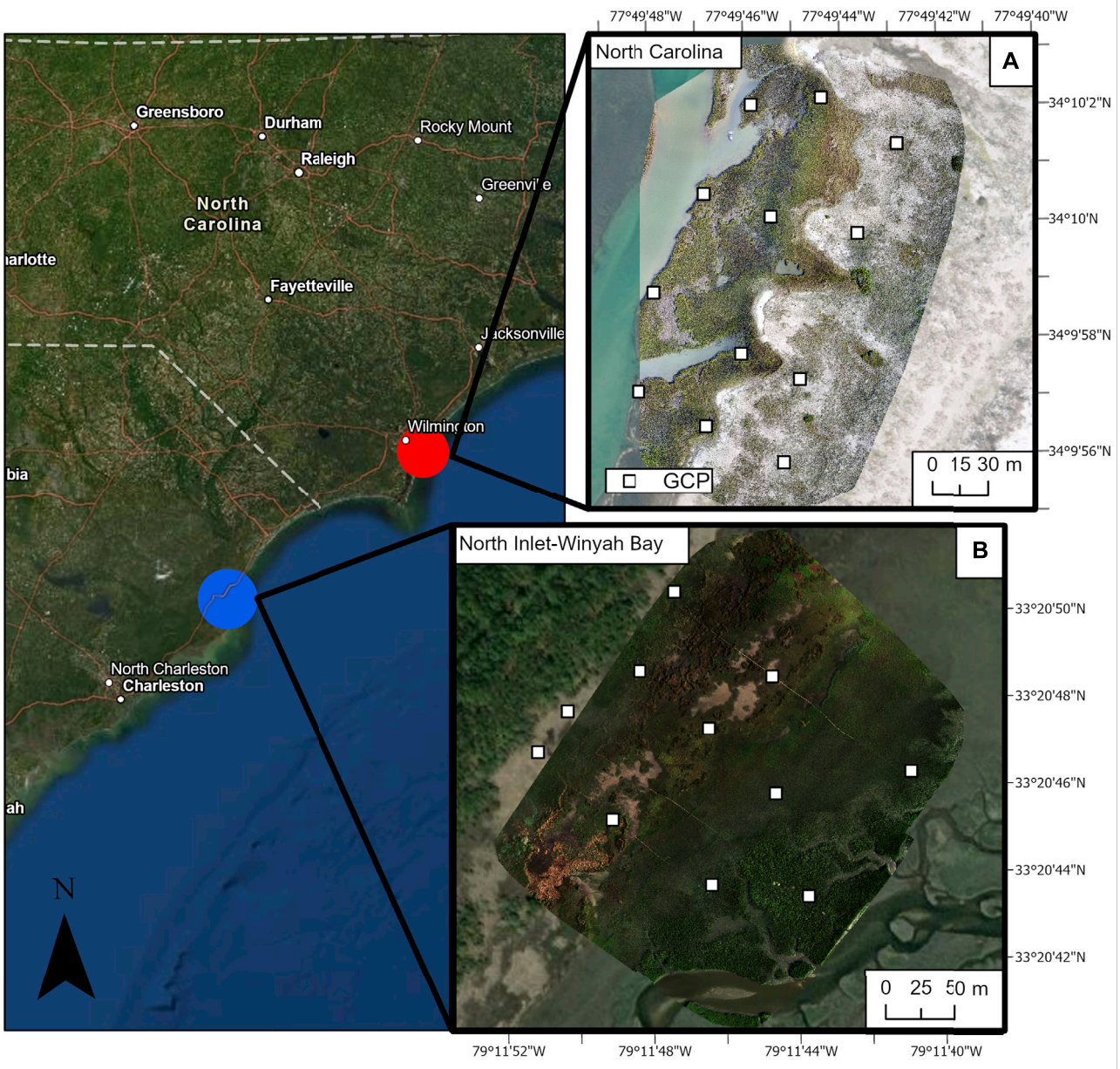

FIGURE 1
National Estuarine Research Reserve (NERR) field sites. **(A)** North Carolina NERR and **(B)** North Inlet-Winyah Bay NERR. Orthomosaic imagery from both sites was collected at 50 m altitude in September 2020.

estimates of coastal habitat metrics. For this purpose, this study evaluates the use of several UAS-SfM photogrammetry-based approaches for the estimation of standard wetland monitoring parameters. The specific goals of this study were to 1) conduct spatial error analyses exploring the impact of Ground Control Point (GCP) distribution and UAS operational parameters (ground sampling distance, sensor resolution, and sensor specifications) on horizontal and vertical error of UAS-based mapping products and use the results of which to 2) compare UAS-SfM computed vegetative characteristics to manually collected data (above ground biomass, canopy height, percent cover).

2 Materials and methods

2.1 Study site

A test site at Swan Island, Maryland (*38.005197, -76.044356*) was used before exploring the NERR sites to establish an initial

understanding of best practices to reduce spatial error. This site was recently restored with dredged sediments and largely devoid of vegetation.

The North Carolina (NC) NERR at Masonboro Island, NC and North Inlet-Winyah Bay (NIWB) NERR in Georgetown, SC were selected as the field sites for this study. Both sites are *S. alterniflora*-dominated salt marsh habitats in which NERR scientists annually document vegetative characteristics and marsh surface elevation at fixed, long-term monitoring plots (Figure 1). The NC NERR is a back-barrier island marsh system dominated by *S. alterniflora* with a ribbon of mixed species (*S. alterniflora, Salicornia* spp., *Distichlis spicata*) at its upland edge that transitions to a narrow ribbon of *Spartina patens*-dominated vegetation in the back-barrier dune system (Figure 1A). The NIWB NERR study site is a bar-built, ocean-dominated estuary characterized by expansive salt marsh habitat drained by a network of sub-tidal and intertidal creeks. The study area within NIWB NERR is the intertidal marsh platform in the western-most sub-basin of the North Inlet estuary, where the lower elevations are characterized by monoculture *S. alterniflora* which transition at mid-marsh elevations to a patchy mosaic of mixed species (*Salicornia* spp., *Distichlis spicata, Juncus romerianus*) surrounding areas of barren hyper-saline salt panne (Figure 1B).

2.2 Ground control

Ground control points (GCPs) were used to improve 3-dimension positional accuracies (X, Y, Z) of all UAS based mapping products. Expanding upon previous analyses of optimal GCP density (Haskins et al., 2021), this study explored the impact of GCP distribution in both horizontal and vertical space on model accuracy. It has been previously demonstrated that the optimal GCP density for maximizing efficiency and model accuracy is 2 GCPs/ha (Haskins et al., 2021).

Swan Island, the test site used for this GCP analysis, was largely devoid of vegetation at the time of sampling. Therefore, the bare-earth surface models produced by SfM processing were not influenced by the presence of vegetation and SfM-produced estimates of elevation were likely to represent the true ground surface. Twenty-four 5-gallon bucket lids painted with markers were randomly distributed as GCPs across the island. To assess horizontal and vertical error, true elevations were manually collected by surveying checkpoints (n = 115) across the expanse of the island using a Real-time Kinematic Global Navigation Satellite Systems (RTK-GNSS). Computed elevations were extracted from SfM-generated models of the site surface. These Digital Surface Models (DSMs) were generated at Swan Island using 3, 6, 12, and 24 GCPs, corresponding to approximately 0.25, 0.5, 1, and 2 GCPs/ha, respectively. For each GCP density explored, a "clustered" iteration, with GCPs clustered toward one end of the site, and a "spaced" iteration, with GCPs relatively evenly spaced, was performed. Computed elevations were extracted from UAS-SfM-derived surface models and compared to manually surveyed checkpoints. Vertical error was computed as the root mean square error (RMSE) of differences between computed elevation and true elevation. Horizontal error was computed by SfM softwares as the RMSE of horizontal differences in the XY plane given by each GCP in the process of fitting the DSMs. Results of this investigation were used to inform GCP density and placement for surveys at the NERR sites.

GCPs used at the NERR study sites included 0.25 m^2 high-density polyurethane black and white checkerboard tiles (NIWB NERR, n = 11), permanent structural features (NIWB NERR, n = 4), or 5-gallon bucket lids painted with point markers (NC NERR, n = 12). Each GCP contained a clearly defined center point which was surveyed with a survey-grade RTK-GNSS (NC: Trimble R8 Model 4, NIWB: Trimble R8s). These known locations were later incorporated into image processing by partial-automation using Structure-from-Motion (SfM) softwares. Horizontal data were referenced to the North American Datum 1983 State Plane (NAD 1983 North Carolina FIPS 3200, Meters) at NC NERR. At NIWB NERR, horizontal data were referenced to the World Geodetic Datum 1984 (WGS 1984) universal Transverse Mercator (UTM) Zone 17N. Vertical data were referenced to North American Vertical Datum of 1988 (NAVD88).

2.3 Flight information

At Swan Island, flights for GCP analysis were conducted in August 2019 with a DJI Phantom 4 Pro equipped with a 20 MP camera with 1 inch CMOS sensor. Images were collected from an altitude of 37 m with a neutral density polarizing filter (ND8-PL) to minimize glare.

At NIWB, aerial imagery was collected using a DJI Matrice 200 V2 quadcopter equipped with a Micasense Altum sensor (Table 1). At NC, optical (Red-Green-Blue; RGB) imagery was collected using a Hasselblad L1D-20c camera. Multispectral imagery was collected by a Sentera Double 4K sensor that uses Red Edge, Near-Infrared (NIR), and Red bands to produce Normalized Difference Vegetation Index (NDVI) and Normalized Difference Red Edge Index (NDRE) imagery. The Sentera Double 4K NDVI + NDRE sensor was mounted on a DJI mavic 2 Pro quadcopter with a Built-in Hasselblad camera (Table 1). At NIWB, Radiometric calibration of the Altum imagery was performed by imaging a Micasense-provided reflectance panel pre-and post-flight. The Altum is also equipped with an ambient light sensor (DLS2) that measures intensity and angle of incident light for each of the five bands of the sensor, allowing for at-sensor calibration of each image set acquired during flight. Sentera Double 4K and DJI Mavic 2 Pro

TABLE 1 UAS platforms and sensors used at each site. Optical sensors collect RGB images (Hasselblad and Phantom built-in) or individual Red (R), Green (G), and Blue (B) band imagery post-processed to composite RGB imagery (Altum). Multispectral sensors collect composite NDVI images (Sentera) or individual Red Edge (RE) and Near-Infrared (NIR) imagery post-processed to composite NDVI imagery (Altum). Optical and multispectral sensors are provided with the associated sensor resolutions derived from company-reported platform and sensor specifications.[31–33]

Site	Platform	Optical sensor	Multispectral sensor	Resolution	Radiometric calibration
Swan Island	DJI Phantom 4 Pro	Built-in DJI camera *RGB composite*	NA	20 MP CMOS	no
NC	DJI Mavic 2 Pro	Hasselblad L1D-20c *RGB composite*	Sentera Double 4K NDVI + NDRE *NDVI composite*	20 MP CMOS (Optical) 12 MP BSI-CMOS (Multispectral)	no
NIWB	DJI Matrice 200 V2	Micasense Altum *individual band imagery (R, G, B, RE, NIR)*		3.2 MP per band	yes

sensors lacked radiometric calibration capabilities. Optical and Multispectral imagery was collected simultaneously, with the exception of one multispectral flight (NC 9/14/20 at 25 m altitude) reflown due to camera malfunction on 10/15/20. Lithium-ion polymer batteries were used to power the aircraft.

Duplicate image datasets were collected at each of the NERRS sites during two sampling periods: September 2020, near annual peak marsh biomass, and February 2021, near annual minimum biomass (referred to herein as dormant season). The area of interest was flown three times during each sampling period at three different altitudes (25, 50, 120 m) to determine the influence of ground sampling distance on image-based product accuracy. An average of 286 (NC) and 574 images (NIWB) were collected during each sampling period, focusing on an area of approximately 2–3 ha. The ground sampling distance was between 0.5–6 cm resolution depending on flight altitude and sensor resolution. All flights were conducted in compliance with the Federal Aviation Administration 14 CFR Part 107 regulations. Ground-based aircraft launches and retrievals were performed at the Swan Island and NERR field sites and specialized launching equipment was not required. UAS details are provided in accordance with Barnas et al. (2020).

To further investigate the impact of sensor resolution and specifications on UAS-based mapping products, an additional set of test flights was conducted in May of 2021. In this case, both aircraft-sensor combinations were flown in succession at NC NERR. Both flights were conducted at an altitude of 50 m and images from both sensors were geolocated using the same GCPs.

UAS mission planning softwares were used to ensure consistent image overlap and monitoring of the same area among flights. Flight paths were developed by Drone Deploy (Swan Island), Pix4D Capture mapper application (NC) and DJI Pilot mission flight application (NIWB). The same flight path was used for all repeat flights to ensure that the same area was covered across altitudes and seasons. Optical imagery data was collected as 20-megapixel RGB images (Hasselblad, NC; 5,472 × 3,648 pixels) or 3.2-megapixel individual band imagery (Micasense Altum, NIWB; 2064 × 1,544 pixels) (Altum and MicaSense, 2021; Mavic 2, 2021). Multispectral imagery was collected by the 12-megapixel (Sentera Double 4K, NC) or radiometrically calibrated 3.2-megapixel (Micasense Altum, NIWB) sensor with imagery at 4,032 × 3,024 pixels and 2064 × 1,544, respectively (Altum and MicaSense, 2021; Double 4K Sensor - Sentera, 2021). All aircraft are equipped with onboard GPS recording geolocation data. Onboard SD cards recorded imagery data with associated aircraft metadata and were offloaded to computers during post-flight processing.

2.4 UAS-SfM processing

UAS imagery were stitched together using commercially-available Structure-from-Motion (SfM) softwares Agisoft Metashape (*v.1.6.1*) and Pix4Dmapper (*v. 4.6.4*) to generate continuous models of each site. All image data sets were processed using both software packages. Imagery was geolocated using GPS onboard the UAS aircraft, which attaches geotag information to each image, and georectified by incorporating GCP data in the SfM software processing workflow.

Pix4Dmapper. Using Pix4Dmapper, key points were extracted at the full imagery resolution and image matching was set up for an aerial grid or pre-planned flight path. The number of key points was automatically determined and the calibration method was set to standard. A minimum of five images per band were identified by partial-automation to register each GCP in UAS-SfM softwares.

Agisoft Metashape. In Agisoft Metashape, the software aligns imported images, approximating camera position and orientation to generate tie points in the form of a sparse point cloud. A high accuracy was chosen for the photo alignment such that tie points were extracted from the full-resolution images. After alignment, GCPs were manually picked in order to georeference all images. The software then grids the dense cloud and filters out erroneous points based on the angle and distance between points. The cloud was also filtered on the basis

of reconstruction uncertainty, projection accuracy, and reprojection error. Camera and point optimization was performed after each round of point filtering (Agisoft LLC, St. Petersburg, Russia).

Optical (RGB) data was used to generate orthomosaics of each site. RGB images were also used to generate Digital Surface Models (DSMs), 3-dimensional models of the marsh surface (including vegetation), and Digital Terrain Models (DTMs), 3-dimensional bare-earth elevation models. By default, DSMs, RGB orthomosaics, and NIR orthomosaics in Pix4D were generated at a pixel size of 1 x the Ground Sampling Distance (GSD) of the corresponding UAS flight. DTMs were generated by Pix4D at 5 x GSD. RGB and NIR orthomosaics in Agisoft were generated at a pixel size of 1 x the GSD, while DSMs and DTMs were generated at 2 x the GSD. All models were subsequently resampled to matching resolutions for analysis. Orthomosaics, DSMs, and DTMs were further analyzed in ArcGIS Pro Mapping Software version 2.7.3 (Esri Inc., Redlands, CA, United States).

2.5 Ground validation of vegetative characteristics

Field measurements of vegetative properties were recorded at fixed long term monitoring plots within each NERR project site in the 1–2 weeks following UAS flights. These data provide true metrics with which to validate UAS-SfM computed values.

Percent Cover. At NC NERR, percent cover of *S. alterniflora* was assessed through a point-intercept method (Roman et al., 2001). A thin rod was lowered perpendicular to the substrate at 50 equally spaced grid nodes within a 1 m^2 quadrat. Species intercepting the rod were recorded and their binary presence at each node was summed across the 50 nodes and multiplied by two for a percent cover estimate (0–100%). At NIWB NERR, percent cover was estimated visually for each species and recorded at 5% intervals. At both sites, estimates represent percent cover of *S. alterniflora* because only monospecific plots were included.

Canopy Height. In September, average maximum canopy height was estimated by recording the height above the sediment of the three tallest *S. alterniflora* stems observed in each sampling plot. The *S. alterniflora* stems were manually measured with a meter stick after stretching the stem to its full straight length. In February, average maximum canopy height estimates were derived from an average of the three maximum elevations reached by vegetation in each sampling plot and stems were not stretched vertically to their full straight-line length. In both seasons, plot centers were recorded by RTK-GNSS to align ground data with UAS-SfM products.

Biomass. Aboveground biomass was quantified by clipping standing vegetation to the soil surface within 0.25 m^2 plots proximal to the plots used for measuring percent cover and canopy height. In September, standing *S. alterniflora* biomass was mostly live (green) with very few senescent leaves. Dead stems without leaves, likely from previous years, were discarded before weighing. In February, much of the existing *S. alterniflora* biomass was dead (brown) or senescent (yellow). As a result, clipped biomass was separated into three categories (green, yellow, and brown) and each group was dried and weighed separately. Estimates of live above-ground biomass used for analysis were the total of green and yellow biomass (total biomass = green biomass + yellow biomass). After harvest, stems were washed, dried at 60 °C for 72 h, and weighed to the nearest 0.1 g to provide total standing biomass data. Total above-ground biomass (g) was standardized by area (g/m^2) by dividing biomass weight by the plot area (0.25 m^2). Plot centers were recorded by RTK-GNSS to identify these plots in UAS-SfM products.

2.6 Sensor comparison

There are a wide range of commercially-available UAS sensors and platforms with varying specifications. Considerations of cost, flight time, and multispectral capabilities are among the reasons that UAS platform and sensor choice varies among research groups. In this analysis, different UAS were used for data collection at NC NERR and NIWB NERR. The Sentera Double 4K, used to collect multispectral data at NC NERR, is a 12 Mega-Pixel (MP) non-radiometrically calibrated camera. The Micasense Altum, used at NIWB NERR, is a lower-resolution 3.2 MP sensor that is radiometrically calibrated. To understand whether site differences in multispectral products (NDVI rasters) were due to differences in sensors or true variability among sites, a comparative analysis was conducted using data collected in May 2021 when both platform-sensor combinations were flown at NC NERR during sequential flights. Sampling plots (n = 1,000) were randomly generated across the vegetated survey area in ArcGIS Pro to imitate 0.25 m^2 vegetation sampling plots collected in the manual analysis. Mean Normalized Difference Vegetation Index (NDVI; described below) values within the plots were extracted and compared across softwares and sensors.

2.7 Spatial error quantification

As the SfM softwares stitch individual 2-D images into a continuous 3-D surface, SfM-computed locations may differ slightly from true position. The quality of SfM-derived orthorectification was assessed by evaluating the differences between photogrammetrically-computed positions and true measured positions. True measured positions were surveyed by RTK-GNSS systems (see Section 2.2) with horizontal error of approximately 1–2 cm and a vertical error of approximately 2–4 cm. Projection error in UAS-SfM derived products was

assessed in the XY plane using visually-identified GCPs. XY error was derived directly from UAS-SfM software reports, which report GCP error as the difference between the true (RTK-GNSS-derived) position of the GCP center and the computed (SfM-derived) position as identified by the photogrammetry software in the orthomosaic. Vertical error (in the Z plane) was assessed using additional GNSS observations taken across the field sites referred to as checkpoints (CPs). Vertical estimates were computed by overlaying RTK-GNSS surveyed CPs onto SfM-derived Digital Surface Models (DSMs) and Digital Terrain Models (DTMs). CP elevation was extracted from elevation models in ArcGIS Pro via the Extract Values to Points tool and directly compared to true elevation.

2.8 Alternative terrain modeling

Vertical error from UAS-SfM models was compared to that of available LiDAR datasets accessed via the National Oceanic and Atmospheric Administration's (NOAAs) data access viewer (NOAA, 2021). LiDAR DEM data at NC NERR is derived from the 2018 United States Army Corps of Engineers (USACE) National Coastal Mapping Program (NCMP) Post-Florence Topobathy Lidar DEM collected in October 2018. This dataset was collected by the Joint Airborne Lidar Bathymetry Technical Center of Expertise (JALBTCX) at a cell size of 1 m and a reported vertical accuracy of 19.6 cm (OCM Partners, 2018). LiDAR DEM data at NIWB NERR is derived from the 2017 South Carolina (SC) Department of Natural Resources (DNR) Lidar DEM collected between December 2016 and March 2017. Raster DEMs have a cell size of 0.76 m and vertical accuracy of 5.8 cm (OCM Partners, 2017). LiDAR vertical elevation accuracy was assessed by overlaying ground-surveyed checkpoints on LiDAR DEMs in ArcGIS and computing the difference between LiDAR DEM elevation and GNSS-surveyed elevation. LiDAR DEM vertical checkpoint error was compared to that of UAS-SfM DTMs (computed as outlined in Section 2.7).

2.9 Image-based quantification of vegetative metrics

Products generated from SfM softwares (DSMs, DTMs, orthomosaics, and vegetation indices) were used to compute estimates of percent cover, canopy height, and biomass.

Above-ground Biomass. The relationship between SfM-computed vegetation indices and field-derived biomass was explored through a simple linear correlation analysis. Sampling plots were digitized in ArcGIS by generating a 0.25 m^2 square around each GNSS-recorded plot center point. The ArcGIS Zonal Statistics tool was used to extract the cell values of the corresponding vegetation index raster within each plot. The mean index raster value within each plot was computed and compared to field-recorded measurements of biomass.

Vegetation Indices. Alternative indices were tested for a relationship with biomass. The Near-Infrared (NIR) band was used in combination with the Red band (R) to generate NDVI rasters. NDVI has been widely used to identify and quantify vegetation (Adam et al., 2010). Additional vegetation indices Excess Green (ExG) and Vegetative Index Green (VIg) were calculated using combinations of the Green (G), Red (R), and Blue (B) bands to test for a relationship with biomass (Meyer and Neto, 2008). To do this, individual bands were extracted from RGB composite imagery collected by the Mavic 2 Pro at NC and image pixel values were normalized. Original imagery was used at NIWB, as Micasense Altum sensors collect individual band imagery. Indices were computed by combining individual bands using the raster calculator in ArcGIS according to the following equations:

$$\mathbf{NDVI} = (\mathbf{NIR} - \mathbf{Red})/(\mathbf{NIR} + \mathbf{Red}) \quad (1)$$

$$\mathbf{ExG} = \mathbf{2}*\mathbf{Green} - \mathbf{Red} - \mathbf{Blue} \quad (2)$$

$$\mathbf{VIg} = (\mathbf{Green} - \mathbf{Red})/(\mathbf{Green} + \mathbf{Red}) \quad (3)$$

Mean index value was computed as the average of all pixels that fell within the area of each ground-sampled biomass plot using Zonal Statistics in ArcGIS.

Canopy Height. Canopy height was computed as the difference between SfM-generated DSM and DTM elevations at monitoring plots according to the following equations:

Canopy Height =

$$\mathbf{max}(\mathbf{DSM}) - \mathbf{min}(\mathbf{DTM}) \quad (4a)$$

$$\mathbf{max}(\mathbf{DSM}) - \mathbf{mean}(\mathbf{DTM}) \quad (4b)$$

where the maximum value is represented by the maximum cell value of the corresponding elevation raster (DSM or DTM) within the area of the fixed monitoring plot. Accordingly, the minimum value is represented by the minimum cell value, and the mean value is represented by the average cell value. Raster values within digitized sampling plots were extracted using Zonal Statistics in ArcGIS. Prior to this analysis, elevation model rasters were resampled to the lowest resolution models within each site-season pair (DSM and DTM) and snapped to ensure proper overlay of raster cells. All computed canopy height metrics were compared to ground-validated values using the Tidyverse and Dplyr packages in R (v.1.3.1093). Canopy height analysis is broken down by season due to the differences in ground-based methodologies across seasons (see Section 2.5). R^2 and Root Mean Square Error (RMSE) were computed in R to assess the potential to use UAS-SfM data to provide canopy height estimates of *S. alterniflora*.

Percent cover. Training samples consisting of ground points (n = 30) and vegetated points (n = 30) were manually identified using the respective site orthomosaics. NDVI values were extracted at these points. A dynamic NDVI threshold was employed to distinguish bare ground from vegetation. While some studies have employed fixed thresholds to identify vegetation (Chen et al., 2016; Laengner et al., 2019), others have developed dynamic thresholds as NDVI has been shown vary in different environmental conditions (Lopes et al., 2020). In this study, after analyzing the distribution of NDVI values across ground and vegetated training samples, the vegetation threshold was set as the average of the minimum recorded NDVI value for vegetated training points and the maximum recorded value for ground training points. The threshold was set according to the following equation:

$$\textbf{Threshold} = [\textbf{min}(\textbf{vegetation NDVI}) + \textbf{max}(\textbf{ground NDVI})]/2 \quad (5)$$

Raster cell values within each of the plots were re-coded to a binary value (vegetated/non-vegetated) on a per-pixel basis using the corresponding threshold value. Percent vegetated cover was estimated as the % of pixels within the area of each fixed vegetation monitoring plot that were classified as vegetated with NDVI values above the threshold. Given the observed differences in NDVI values across sites and seasons, separate thresholds were computed for each site-season pair.

3 Results

3.1 Spatial error analyses

3.1.1 Ground Control Point distribution

The impact of both GCP density and distribution on vertical accuracy were analyzed using data from a test site at Swan Island, Maryland. Increased GCP density was associated with decreasing model error (Figure 2). Regularly distributed ("spaced") GCPs minimized model error as compared to unevenly spaced ("clustered") GCPs (Figure 2). This trend held for both SfM softwares, though error was more pronounced at low GCP density using Agisoft Metashape.

Pix4D-generated products demonstrate sensitivity to GCP distributions, with substantially lower vertical RMSE using spaced distributions as compared to that of clustered distributions in all three density scenarios (0.25, 0.5, 1 GCPs/ha). Metashape-generated products appear sensitive to spacing at low GCP densities, with extreme vertical error (1.39 m RMSE) using clustered 0.25 GCP/ha, but low error (0.03–0.06 m RMSE) for clustered and spaced iterations at mid-range GCP densities (0.5 and 1 GCP/ha). Using both softwares, spaced distributions of GCPs resulted in low vertical error (<0.06 RMSE) for GCP densities of 0.5 GCPs/ha and greater. The result of the GCP spatial analysis was used to inform the distribution of GCPs at the two sampling sites (NC NERR and NIWB NERR).

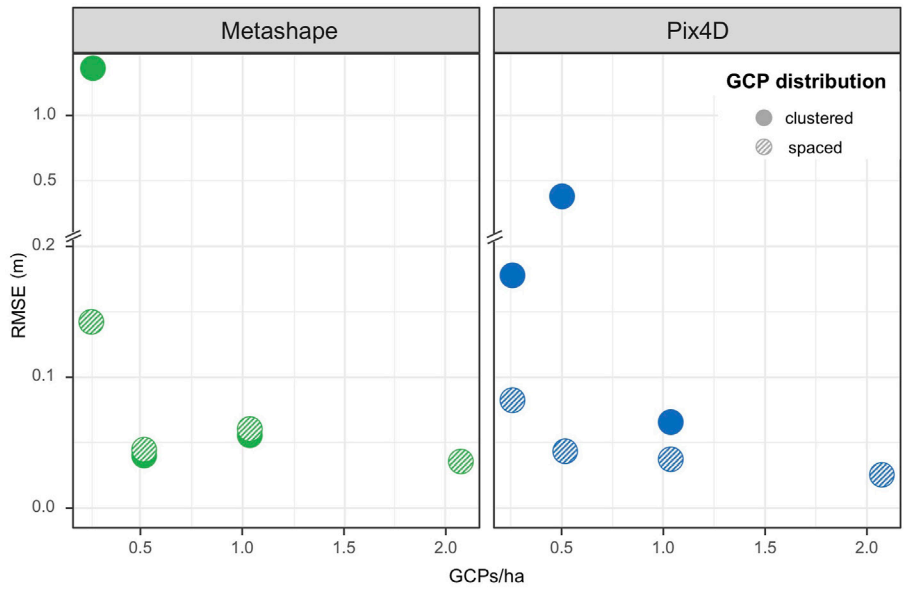

FIGURE 2
Vertical Root Mean Square Error (RMSE) is minimized at higher GCP densities with regularly spaced GCPs. Vertical RMSE is calculated from differences between SfM-computed DSM elevations and GNSS-recorded true elevations at checkpoints (n = 115) across the test site at Swan Island. *Y*-axes are segmented for visualization of extreme values.

TABLE 2 Ground Control Point (GCP) reprojection error in the XY plane is similar (<5 cm) across softwares, altitudes, and sites. RMSE error is calculated as the average of reported X and Y RMSE. Horizontal RMSE is computed in SfM softwares by comparing of GNSS-recorded GCP (n = 5–12) positions with SfM-computed GCP positions. GNSS recorded positions are recorded with less than 1 cm of horizontal error.

Site	Season	Flight altitude (m)	GSD (cm)	Horizontal RMSE (cm)
				Pix4d, Agisoft
NC	September	25	0.57	0.119, 2.01
NC	February	25	0.59	0.396, 3.66
NC	September	50	1.17	1.395, 3.28
NC	February	50	1.17	1.110, 4.06
NC	September	120	2.83	1.94, 2.595
NC	February	120	2.84	1.58, 2.835
NIWB	September	25	1.18	0.7195, 1.300
NIWB	February	25	1.08	0.996, 1.44
NIWB	September	50	2.35	1.11, 0.885
NIWB	February	50	2.16	2.345, 2.175
NIWB	September	120	5.72	0.9325, 0.575
NIWB	February	120	5.26	1.245, 0.995

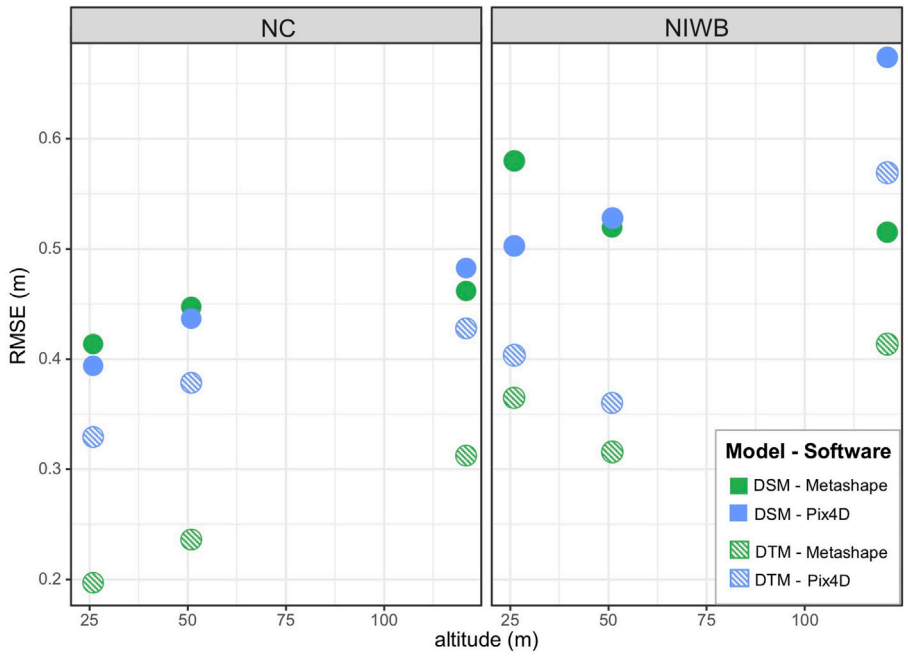

FIGURE 3
Vertical error appeared to differ across models and altitudes. Vertical error was calculated as the difference between GNSS-recorded elevations and SfM-computed model elevation at site checkpoints. Checkpoints recorded during both September (n = 46, NC, n = 64, NIWB) and February (n = 56, NC, n = 42, NIWB) were included in the RMSE.

With information from the Swan Island distributional analysis, well-spaced GCPs were distributed around NC NERR resulting in a density of approximately 3.5 GCPs/ha. Permanent GCP targets clustered along a boardwalk in the center of the site were used at NIWB NERR. While spacing could not be modified as much of the marsh area is inaccessible at NIWB NERR, the resultant GCP density was approximately 3 GCPs/ha.

3.1.2 Horizontal error

Horizontal error, calculated as the difference between GNSS-recorded GCP position and SfM-software computed GCP position, is reported for each site orthomosaic. Ground Sampling Distances (GSDs), or pixel sizes, differed across sites, sensors, and altitude (Table 2). Altum-derived GSDs were approximately twice as large as Mavic Pro-derived GSDs at the same altitude. GSD differences between softwares were negligible (<0.1 mm). Reprojection error in the XY direction was similar (<5 cm) for Pix4D and Agisoft across altitudes, seasons, and sites. There does not appear to be a trend in XY error across altitudes despite the increasing GSD.

3.1.3 Vertical error

Elevation root mean square error (RMSE) at checkpoints ranged from approximately 0.2–0.7 m. RMSE appeared to increase with altitude, with higher RMSEs reported at higher UAS flight altitudes. Within each altitude, DTMs were associated with lower RMSE as compared to DSMs. RMSE values were similar across softwares for the DSMs (mean RMSE difference = 5 cm) while DTM RMSE values showed greater spread (mean RMSE difference = 10 cm).

At NIWB, 50 m altitude DTMs appeared to minimize vertical error relative to 25 and 120 m altitude models (Figure 3). For the DSMs, 50 m altitude models showed a slight uptick in vertical error using Pix4D models (<5 cm), but a large jump in vertical error from 50 to 120 m altitude models (>10 cm RMSE). Metashape model error was minimized in both the DTMs and DSMs using 50 m altitude imagery. At NC, 50 m altitude models demonstrated slight increases in vertical error (<5 cm RMSE). Additionally, because less images are contained in higher altitude datasets, processing time decreases with altitude. From this analysis, models constructed from 50 m imagery were chosen for all further analyses to reduce vertical error and optimize processing time.

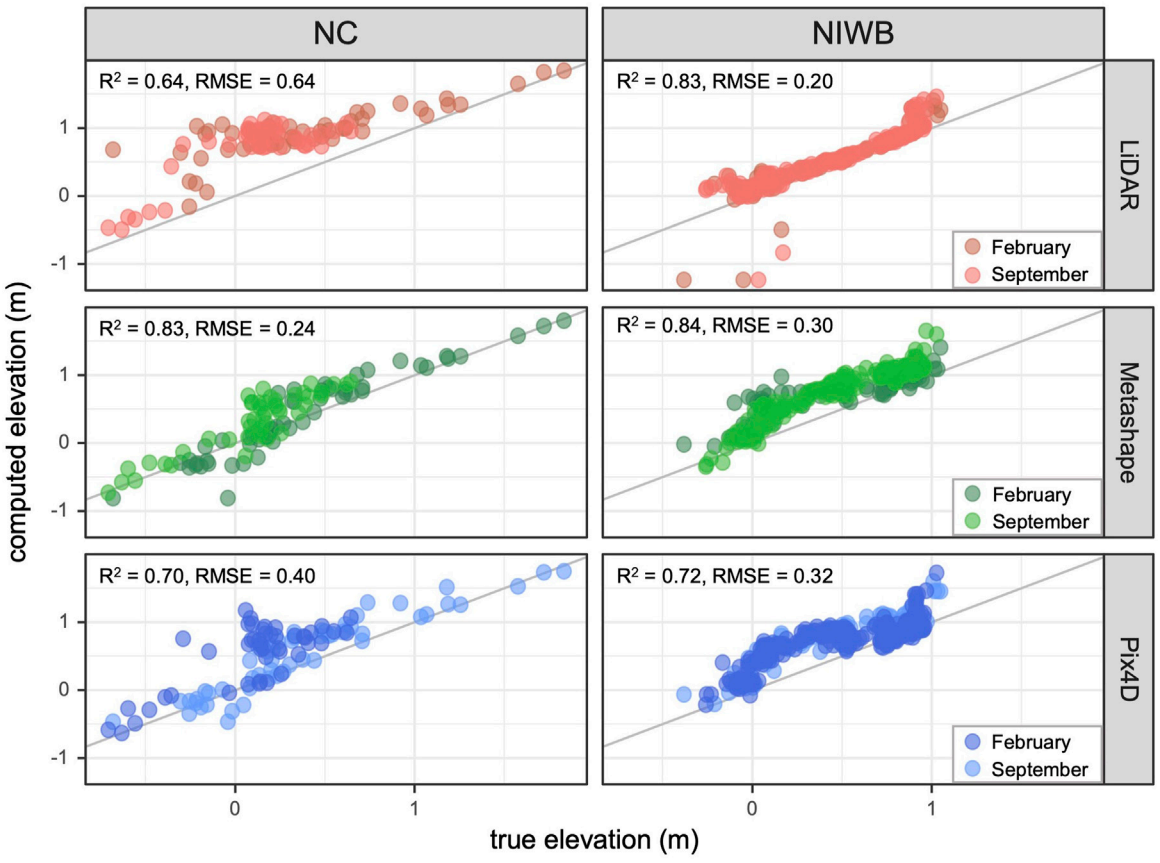

FIGURE 4
LiDAR datasets demonstrate higher vertical error than SfM-derived models at NC but lower error at NIWB. DTM vertical error is calculated as the difference between model elevation and GNSS-recorded elevations and represented for each site-method pair as the Root Mean Square Error (RMSE).

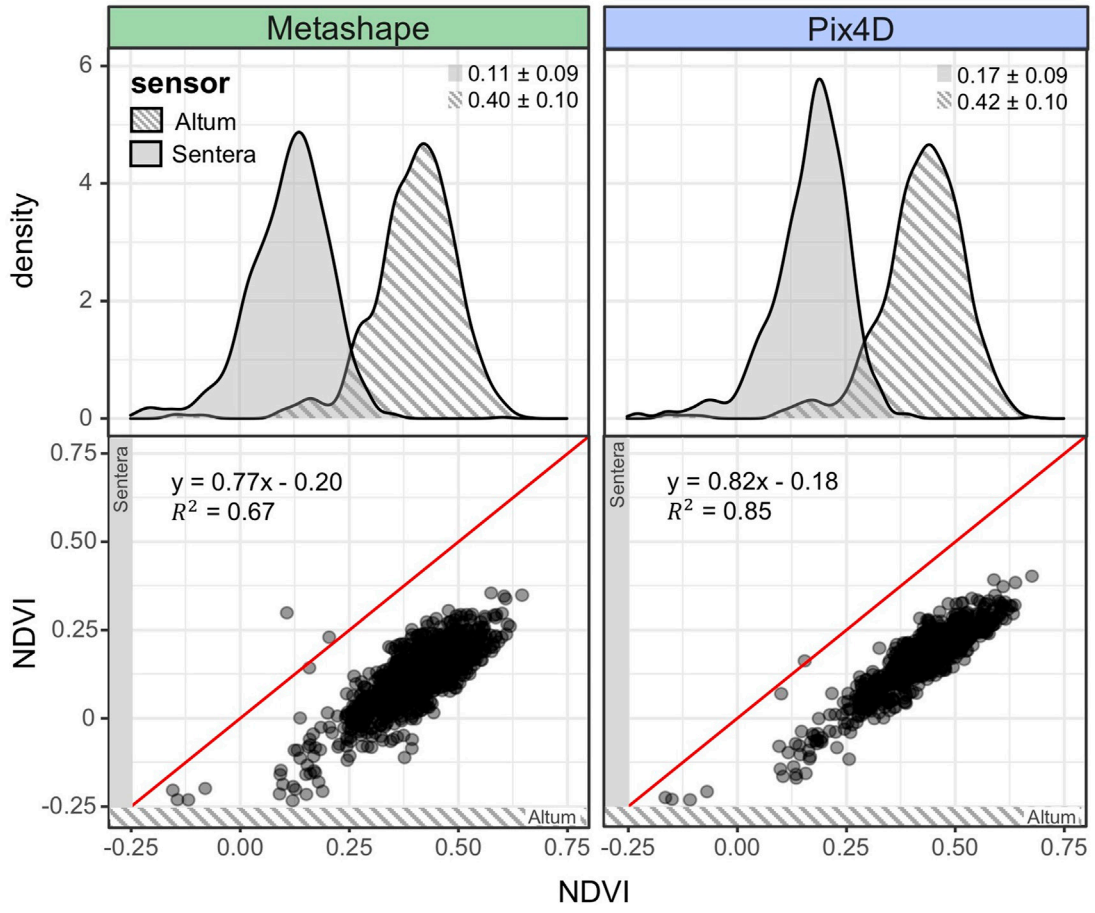

FIGURE 5
Multispectral sensors used in this analysis demonstrate different NDVI readings of the same area. Random 0.25 m^2 samples (n = 1,000) were generated across SfM-derived NDVI rasters and the mean NDVI value was compared across sensors and softwares.

Vertical error at checkpoints was compared across SfM-derived DTMs and available LiDAR datasets (Figure 4). Root mean square error (RMSE) are used to show agreement between computed and true data and indicate overshooting or undershooting of digitally-computed models. At NC and NIWB, computed and true elevations are well correlated using all three methods (R^2 = 0.64–0.84) with relatively low error (RMSE = 0.24–0.32 m). At NC, UAS-SfM processing workflows outperform LiDAR datasets in accuracy (UAS-SfM: RMSE = 0.24–0.40 m, LiDAR: RMSE = 0.64) (Figure 4). At NIWB, the LiDAR DTM yields a lower error (RMSE = 0.20 m) than either UAS-SfM software (RMSE = 0.30–0.32 m). Comparing across sites, DTM performance was similar within each UAS-SfM software, but noticeable differences in accuracy were observed using the LiDAR datasets (NC LiDAR: R^2 = 0.64, RMSE = 0.64 m, NIWB LiDAR: R^2 = 0.83, RMSE = 0.20 m).

3.2 Vegetative metrics

Preliminary analyses of 3D surface models indicated that the 50 m altitude imagery represented the optimal tradeoff between model accuracy and processing time (details in Section 3.1.3). All image based vegetation metrics were calculated using models generated from 50 m altitude imagery in Pix4D only. An initial appraisal of the models generated in the two softwares indicated good agreement, so only Pix4D was used to evaluate vegetation metrics to reduce the number of variables present.

3.2.1 NDVI

The two multispectral sensors used in this analysis (MicaSense Altum and Sentera Double 4K) demonstrated different NDVI readings when flown concurrently over the same test site (Figure 5). An analysis of mean NDVI at

TABLE 3 Vegetation indices demonstrate significant relationships with ground-derived biomass measurements. Data represented are Pix4D-processed data using 50 m altitude flights in both February and September. ***: $p < 0.001$, **: $p < 0.01$, *: $p < 0.05$

Vegetation index	Site	Season	Best fit line	R^2	p
NDVI	NC	September	*y = 5.08e-4 x + 0.022*	0.69	***
		February	*y = 7.77e-4 x + 0.0086*	0.65	**
NDVI	NIWB	September	*y = 4.50e-4 x + 0.32*	0.73	***
		February	*y = 8.19e-4 x + 0.35*	0.43	*
ExG	NC	September	*y = 1.46e-4x + 0.0050*	0.46	*
		February	*y = 2.73e-4 x + 0.017*	0.56	**
ExG	NIWB	September	*y = 2.16e-5 x + 0.017*	0.52	**
		February	*y = 3.98e-5 x + 0.016*	0.17	
VIg	NC	September	*y = 9.90e-6 x + 0.015*	0.01	
		February	*y = -2.22e-05 x - 0.00020*	0.008	
VIg	NIWB	September	*y = 1.63e-4 x + 0.069*	0.38	*
		February	*y = 2.46e-4 x - 0.0044*	t0.18	

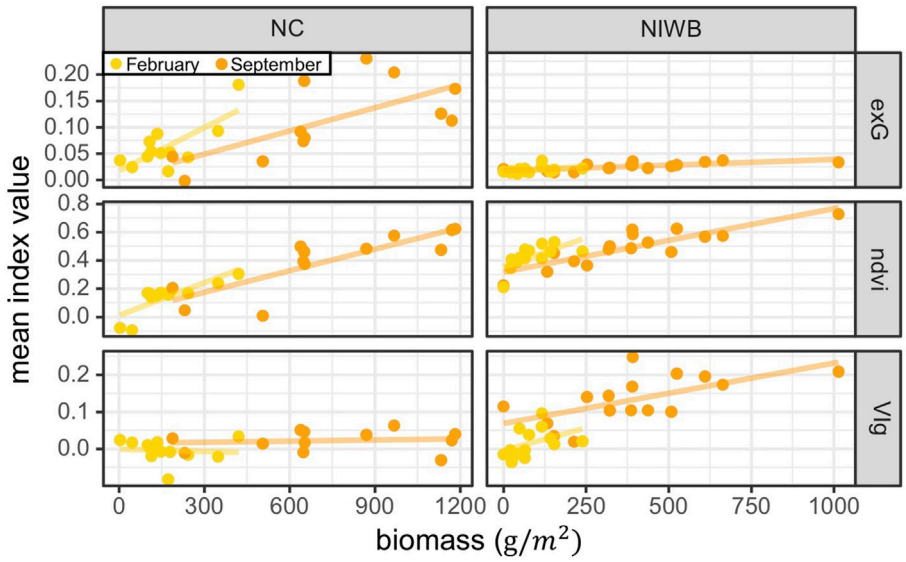

FIGURE 6
Mean vegetation index values within biomass sampling plots demonstrate varying relationships with ground-derived *S. alterniflora* above ground biomass (AGB). Excess Green (exG) and Normalized Difference Vegetation Index (NDVI) correlate well with AGB, but these relationships vary by season (denoted by color), and Vegetation Index Green (VIg) shows no clear relationship with AGB.

randomly generated test plots (n = 1,000) across the marsh platform showed that NDVI readings are highly correlated between sensors (Pix4D: R^2 = 0.85, Metashape: R^2 = 0.67). However, Altum NDVI readings were greater than Sentera readings by a mean of 0.29 in Pix4D and 0.25 in Metashape. Sensor resolution and specifications potentially driving these differences are detailed in Table 1. Within sensors, reading differences across softwares may be a result of unique software workflows and processing algorithms as described in Section 2.4.

3.2.2 Above-ground biomass

There was a strong positive correlation between SfM-computed NDVI and field-derived above ground biomass (Table 3). Imagery collected in September, when biomass was near its annual maximum, demonstrated higher computed

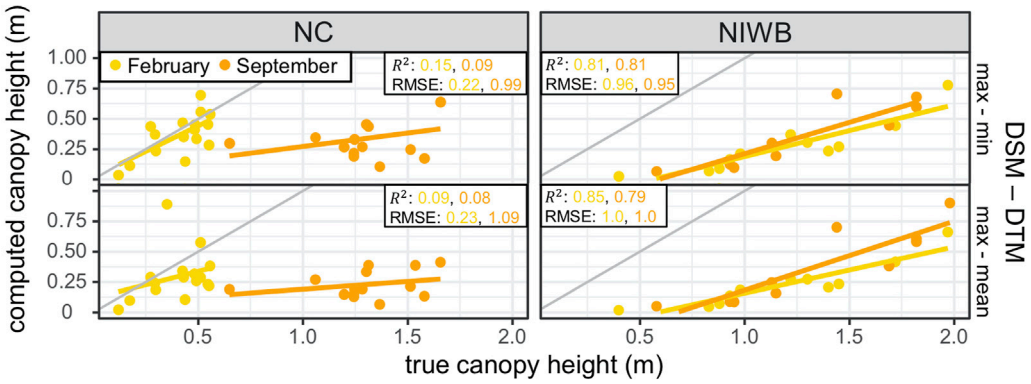

FIGURE 7
Computed canopy height underpredicts true canopy height. Data is visualized by season and NERRS site. Each point represents a canopy height sampling plot from which ground data (*x*-axis) and UAS-SfM computed data (*y*-axis) were extracted. Red line represents the identity line. R^2 is assessed for individual linear relationships. Error is computed as the Root Mean Square Error (RMSE) observed vs expected data (error as it relates to the 1:1 line) are computed to assess the goodness of fit. Subpanels represent differences between DSM and DTM values within a given digitized sampling plot (e.g. max - min: maximum DSM value - minimum DTM value).

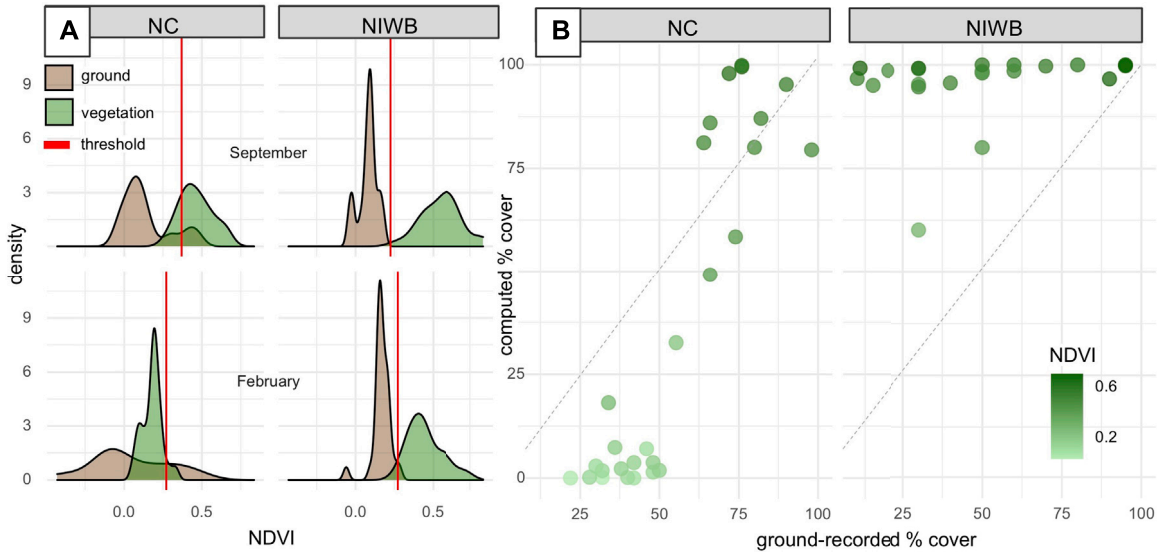

FIGURE 8
Percent cover estimates. **(A)** An NDVI threshold, denoted in red, is used to distinguish between ground and vegetation. **(B)** Computed percent cover estimates are compared to ground-recorded data, demonstrating weak alignment. Example sampling plots projected onto site orthomosaics are included. Points are colored by ground-recorded canopy height values within a sampling plot. Dashed lines represent the identity line.

NDVI values. February imagery, collected when standing dead vegetation was abundant, demonstrated lower computed NDVI values (Figure 6). Alternative indices derived from optical data demonstrated variable performance relative to that of NDVI. Excess Green (ExG) demonstrated a strong linear correlation with biomass at both sites (NC: R^2 = 0.50, NIWB: R^2 = 0.65) (Table 3). VIg demonstrated a weak relationship with biomass at both sites (NC: R^2 = 0.13, NC: R^2 = 0.15).

3.2.3 Canopy height

Canopy height, assessed using two different methods (Eqn. 4a, 4b), is substantially underpredicted by UAS-SfM computed methods (Figure 7). At higher true stem heights, canopy height is underpredicted by greater amounts as shown by the comparison of computed data to the 1:1 line (Figure 7). At NC, there were no significant relationships between ground and computed measurements ($p > 0.05$) with R^2 values ranging from 0.08 to

0.15. At NIWB, ground-derived and UAS-SfM computed measurements were significantly correlated ($p < 0.01$) using all methods, with R^2 ranging from 0.79 to 0.85.

3.2.4 Percent cover

Pixel-based percent cover estimates demonstrate difficulty assessing percent cover on the scale of ground-recorded measurements in 1 m^2 plots (Figure 8). Manual identification of ground and vegetated points revealed distinct NDVI signatures at NIWB in both September and February. However, NDVI signatures were mixed with overlapping ranges in both seasons at NC (Figure 8A). Thresholds developed according to Equation 5 were employed to produce computed percent cover estimates. Percent cover estimates demonstrated weak alignment with ground-recorded data at NC (Figure 8B) and no alignment with ground-recorded data at NIWB. Percent cover estimates were high at NIWB (mean = 95.05%, sd = 12.40%) despite ground estimates encompassing a wide range of values between 10 and 95%.

4 Discussion

The findings of this study reveal that the quality of UAS-based mapping products can be substantially impacted by survey design. In addressing aim 1), we demonstrate that optimal GCP density and distributions can improve product georectification and UAS survey altitude impacts product resolution and surface model error. Moreover, data collection and analysis methods, which often vary across studies, can introduce variability. SfM software packages and platform-sensor combinations can have variable outputs, limiting comparability and flexibility of this approach. To address aim 2), we show that UAS hold promise for monitoring wetlands, with particular success using indexed-based proxies of above-ground biomass. In detailing UAS-SfM methods and analyzing product alignment, the results of this study lay the groundwork for a standardized methodology for UAS-SfM based monitoring of coastal wetlands.

4.1 Spatial error analyses

4.1.1 Ground control point distribution

The observed relationship between GCP density and error reinforces that increased GCP density leads to an improved ability for UAS-SfM softwares to properly georectify the orthomosaic and provide accurate ground elevation estimates (Figure 2), which has been supported by other studies (Tonkin and Midgley, 2016; Seymour et al., 2018; Villanueva and Blanco, 2019). While increasing GCPs density improves the product accuracy via georeferencing, the return on effort appears minimal at densities greater than 1 GCP/Ha (Figure 2). Studies of unvegetated habitats also show this pattern of diminishing returns in vertical accuracy at GCP densities greater than 1-2 GCP/ha (Martínez-Carricondo et al., 2018; Brunetta et al., 2021). In addition to density, this study finds that the distribution of GCPs can substantially influence vertical accuracy. Large vertical errors and high variance using "clustered" spacing highlights the importance of regularly spaced GCPs (Figure 2). This is supported by other studies which note that GCPs should stretch to the site edges to avoid tilt in the resultant elevation models (James et al., 2017), and reinforce the relationship between well-spaced GCPs and reduced model error (Tonkin and Midgley, 2016). However, in this study, both GCP distribution and density are analyzed together to provide a comprehensive recommendation for study designs. Minimal vertical errors using regularly-spaced GCPs with density 0.5 GCPs/ha or greater were observed (Figure 2), revealing a threshold that optimizes product accuracy while minimizing GCP density since each GCP requires time and effort to deploy and survey. Thus, coastal wetlands potentially do not need to be overloaded with GCPs for SfM processing if GCPs are well spaced. However, this distributional analysis also indicates that increasing the density of GCPs can reduce error to offset the impact of clustered GCPs. At many protected coastal sites it may be infeasible to regularly distribute GCPs across the study area due to inaccessibility or habitat protections. In these cases, it would be recommended to increase the number of GCPs to 2 GCP/ha or greater. NIWB NERR represented one such site, where permanent GCPs were fairly clustered along a boardwalk. High GCP densities (~3 GCPs/ha) were used to offset errors introduced by spacing and maximize model accuracy.

4.1.2 Horizontal error

The horizontal reprojection error analysis demonstrates the tradeoff between flight altitude, with higher altitudes allowing for greater area coverage, and product resolution. Within a given UAS sensor, pixel size (GSD) increases proportionally with altitude. Across sensors, GSD differences were the result of differences in sensor resolutions (see Table 1), as GSD depends on inherent camera properties. The Mavic (NC) demonstrated higher resolution products indicated by a lower GSD as compared to the Altum (NIWB) likely due to sensor resolution differences (Table 1). The resultant GSD of Mavic flights at 50 m altitude approximately matches that of Altum flights at 25 m, indicating that users can decrease UAS flight altitude to offset reduced sensor resolutions and still achieve an optimal GSD for mapping purposes.

Horizontal error remained fairly constant across altitudes, even whilst product resolution (GSD) increased substantially (Table 2). For mapping projects, high UAS flight altitudes (>100 m) may be optimal as it allows the user to rapidly cover large areas without sacrificing much horizontal accuracy. However, the increase in GSD with altitude should be noted for projects intending to precisely map fine-scale

features or boundaries. Horizontal error was generally similar (<4 cm difference) across SfM software packages, but Pix4D-generated products tended to produce smaller errors (Table 2), potentially indicating a heightened ability to georectify orthomosaics to meet ground-surveyed points. Overall, low horizontal errors (<5 cm) demonstrated by this analysis provide promising information for precise mapping of coastal and estuarine habitats, improving abilities to perform spatial analyses like the delineation of ecological boundaries and assessment of marsh retreat and advancement.

4.1.3 Vertical error

The analysis of GCP distribution at Swan Island (Section 3.1) demonstrated that with well-spaced GCPs at a density of 1 per hectare, vertical accuracies on the order of 5 cm or less are achieved on unvegetated surfaces. When vegetation is present, SfM-derived surface models represent the top of the vegetative canopy rather than the ground surface. As a result, comparisons between modeled (SfM) and measured (GNSS) elevations are influenced by the presence of vegetation. With SfM, as with LiDAR, the ability to accurately sense marsh sediment elevation is dependent upon the density of vegetative cover as this determines the number of ground hits (ie. pixels that represent sediment surface) that are sampled.

DSMs are constructed to represent the marsh canopy (i.e. plant tips) while DTMs (created by filtering the 3D point cloud to remove all points above the ground surface) represent bare-earth models intended to exclude vegetation and other structures. Because these sites are vegetated ecosystems, it is expected that GNSS-recorded, "true" values represent bare-earth elevation and therefore should closely align with DTM-derived elevations. Anders et al. (2019) assessed Agisoft Metashape-generated (formerly Agisoft Photoscan) DTMs over shrubland habitat which yielded an RMSE of 0.5m, similar to the values observed in this study (Figure 3) (Anders et al., 2019). However, the range of RMSE values for both surface and terrain models demonstrate the challenges with accurately measuring vegetation height from imagery. With *S. alterniflora* stems ranging from approximately 0–2 m tall, high error in elevation models means that, proportionally, much of the plant stem may be missed in calculations.

Comparing error across softwares, the notable differences in DTM error is potentially a result of dissimilarity in DTM construction methods across softwares. Metashape allows for more user input in the DTM construction, permitting the user to define the maximum angle and distance between points to filter the DSM in the creation of a DTM (Agisoft Metashape User Manual - Professional Edition, Version 1.5). In contrast, Pix4D does not allow these parameters to be defined (Pix4D, 2022). Because of these differences, the DTMs do not appear to be comparable across softwares. The DSMs contain higher RMSE than DTMs but are more consistent when comparing across softwares (Figure 3) presumably due to software similarities in DSM construction methods.

Analyzing altitudinal trends, the increase in vertical error observed at higher altitudes speaks to the tradeoff between efficiency (higher altitude flights cover a larger area in fewer images) and precision (Figure 3, Supplementary Figure S1). For this study, 50 m was chosen as the optimal flight altitude based on Figure 3, as it minimizes DSM RMSE at NIWB, only shows a slight increase in error from 25 m altitude at NC, and is the most consistent across softwares. While there is a clear tradeoff in product resolution with flight altitude (see Table 2), vertical accuracy does not demonstrate a clear trend with altitude. A similar study using a consumer-grade UAS to survey a shrubland area revealed an increase in vertical error with altitude (altitude range: 126–235 m) at the first site and consistent vertical error across altitudes at the second site (Anders et al., 2020). The range of low altitudes (25–120 m) used in this study are those most commonly used by United States UAS pilots given that flight altitudes above 120 m are restricted by the Federal Aviation Administration (FAA). In analyzing product accuracy over this relevant altitudinal range, this study may inform flight planning for efficient mapping of coastal vegetated areas.

UAS-SfM-derived DTM errors are similar to that of other studies of similar habitats (Yanagi and Chikatsu, 2016; Goodbody et al., 2018). For example, Goodbody et al. (2018), using a fixed-wing UAS to construct DTMs of vegetated habitats, reported an average of 0–0.5 m error in shrubland habitats. UAS-SfM DTM error in similar short vegetation in this study is comparable (RMSE: 0.24–0.32 m; Figure 4). Comparing the two UAS-SfM methods to LiDAR data, it is clear that LiDAR datasets, though substantially lower in resolution and lacking real-time observations, yield comparable elevation estimates to UAS-SfM-constructed bare-earth models. This observation, which is supported by other studies, may be due to the high-accuracy positioning of aircraft hosting LiDAR sensors (Dayamit et al., 2015; DiGiacomo et al., 2020). Comparing all three methods, Metashape-generated DTMs align best with GNSS-recorded values with high R^2 values and low RMSE estimates (Figure 4). This may be explained by noting that Metashape DTM-generation, discussed in Section 2.4, allows for a high level of user input.

4.2 Vegetation metrics

4.2.1 NDVI

The observed differences in NDVI readings across sensors indicate that raw NDVI values cannot be compared across the two sites (Figure 5). With an observed difference in NDVI readings between sensors of approximately 0.3 across the biomass values observed in this study, it is clear that absolute NDVI values cannot be compared across sensors, even when flying the same site under the same conditions. For comparative

work (i.e. observing changes in marsh biomass over time), it is therefore recommended that the same sensor is used. However, this may become difficult as sensors improve and change over time. For this reason, test flights of the same area under the same conditions may be flown to develop a transformation between sensors and enable direct comparisons of NDVI values. Sensor-specific differences in NDVI values have been outlined across different satellite-derived datasets and between UAS and satellite data and attributed to differences in bandwidths, spatial resolutions, and data processing (Huang et al., 2021). One important distinction is that multispectral data from the Micansense Altum (NIWB) sensor is radiometrically calibrated using a calibration panel while that of the Sentera Double 4K (NC) is non-calibrated. Radiometric calibration, which converts the sensor radiance into reflectance values and accounts for changes in ambient light, works to provide standardized data that is more comparable across conditions (Lu, 2006). While this adds greater consistency and reliability to the Altum dataset, it has been noted that the factory-provided calibration of commercial-grade UAS with multispectral capabilities can be limited and fail to account for sensor changes and deterioration over time (Mamaghani and Salvaggio, 2019). Alternative calibration methods have been developed to improve accuracy across flights, but these methods may require additional time and specialized knowledge (Mamaghani and Salvaggio, 2019).

4.2.2 above-ground biomass

NDVI is recommended as the most reliable option as it has the strongest relationship with biomass (R^2 = 0.42–0.73, Table 3) and is significantly linearly correlated with biomass across sites and seasons. Moreover, these linear relationships (slopes, intercepts) are consistent across seasons at each site (Table 3). This indicates the potential to use a linear model to accurately predict biomass changes over time at a given site from UAS imagery. Previous studies of *S. alterniflora* biomass using SPOT6 satellite remote sensing images and airborne hyperspectral scanners report a similar relationship with NDVI (R^2 = 0.499, R^2 = 0.635, respectively) (Wang et al., 2017; Zhou et al., 2018). Several UAS-based studies have shown clear linear relationships between biomass and NDVI readings in coastal wetlands (Zhou et al., 2018; Doughty and Cavanaugh, 2019). This study supports the ability of UAS-based multispectral imagery to provide non-invasive estimates of wetland biomass across multiple sites and seasons.

Indices that rely on optical data alone, like ExG and VIg, provide a clear advantage in that these data are more accessible and generally less expensive. ExG also demonstrates a strong relationship with biomass (R^2 = 0.17–0.56, Table 3), although the strength of this relationship is variable across seasons (Figure 6). In the absence of multispectral data, ExG may provide reliable estimates during peak biomass that don't require advanced multispectral sensors or calibrations. While VIg largely fails to capture changes in biomass in this study, it is possible that VIg may perform well in other systems. This is supported by other work showing that VIg is tightly correlated to biomass in studies using commercial-grade UAS to survey maize fields (R^2 = 0.68) (Niu et al., 2019) and hyperspectral UAS to study changes in summer barley biomass (R^2 = 0.62) (Bendig et al., 2015). While these represent several common vegetation indices, future work may explore the potential of more complex indices, or combinations of indices, which have been shown in certain studies to improve predictions of AGB (Huete, 1988; Qi et al., 1994; Fuentes-Peailillo et al., 2018; Poley and McDermid, 2020).

Relationships with biomass should be further analyzed with an understanding that many current vegetation characteristics are designed for allometric-based estimates of above-ground biomass. Traditional approaches involve clipping plants, like the ground-based data in this study, to assess biomass. Even non-invasive approaches, like measuring density and stem height as a proxy for biomass, require substantial effort and result in sparse data points across a dynamic habitat. Furthermore, in many coastal marshes the sediments of the lower elevations are so unconsolidated as to make access for ground-based measurements impractical or simply too physically destructive to warrant repeat sampling. The ability to estimate AGB using image-based indices across landscapes transforms the scale at which we can monitor these ecosystems. Moreover, the consistency across seasonal endpoints (dormant season and peak-biomass) demonstrated by linear models (Table 3) indicates potential to accurately monitor biomass within a given site. In this way, UAS may be used to rapidly and efficiently collect vegetation data over time, allowing researchers and managers to estimate biomass across meaningful spatiotemporal scales.

4.2.3 Canopy height

All canopy height estimation methods employed here indicate that canopy height is substantially underestimated by UAS-derived heights and that UAS-SfM methods underestimate plant height more at higher stem heights (Figure 7). This trend, observed in previous studies of *S. alterniflora* structure, has been addressed in other studies by inflating UAS-SfM computed plant heights to improve the accuracy of canopy height estimates (DiGiacomo et al., 2020). Because the purpose of this study is to understand the feasibility of the SfM software user to produce canopy height estimates from UAS-SfM products, a transformation was not employed and only raw values were analyzed. The finding that canopy height underprediction increases with stem height is likely due to the fact that taller *S. alterniflora* plants tend to bend more under their own weight and the outer leaves of tall plants often drape outward from the main stem, whereas shorter plants tend be more compact and erect. The results of the current investigation indicate that canopy height estimate accuracy is variable across sites and seasons. Site-based differences may be explained by the fact that the two sites represent different ranges of canopy heights, with NIWB generally representing taller plants (mean ± sd: 1.26 ± 0.45 m) and NC representing shorter plants (0.81 ± 0.49 m). While short

plants (0–0.5 m) appear to fall close to the 1:1 line with low error (RMSE: 0.22–0.23 m), deviation from the 1:1 line becomes more pronounced with canopy height (Figure 7). Tall plants (height >0.5 m) observed at both sites and seasons have large errors (RMSE: 0.95–1.09 m). Seasonal differences in canopy height estimation accuracy may be explained by this height-driven error, as plant height tends to be reduced in the dormant season. Methodological differences for height measurements across seasons (see Section 2.5), however, may also impact this relationship as stem straight-line length was measured in the peak-biomass data, while sloped stem height was measured in the dormant season. While we might therefore expect to observe more underestimation in plant height by UAS in the September data, which is observed at NC (Figure 7), it is difficult to tease apart whether methodological differences or true seasonal differences in plant height (i.e. senescence) drive these observed differences. We believe that this highlights the need to re-evaluate and standardize field practices for canopy height measurements. While it is typical to use straight-line stem height as "true" canopy height in manual vegetation height field studies, remotely sensed measurements record natural, or sloped, canopy height (Currin et al., 2008; DiGiacomo et al., 2020). However, in the dormant season, when the same ground-based methods were employed across sites, a better fit was still observed at NC (Figure 7). This may be explained by lower vertical error in NC DSM and DTM products (Figure 3) or the previously mentioned difference in ranges of canopy heights across sites. Future studies might better resolve this trend by targeting field sites with a wider range of stem heights to reduce the number of variables potentially impacting metrics of canopy height error. Additionally, as canopy height may vary within a 1 m^2 area, we suggest that future work decrease the plot size within which ground-based measurements of stem height are recorded.

4.2.4 Percent cover

The NDVI signatures of ground and vegetation at NC show considerable overlap, indicating a difficulty to separate ground from vegetation using a fixed NDVI threshold at NC (Figure 8A). In contrast, the distinct NDVI signatures observed at NIWB (Figure 8A) may provide evidence for the possibility of NDVI-based thresholding to separate ground and vegetation pixels for percent cover estimates. However, as can be seen in Figure 8B, this thresholding approach does not produce percent cover values aligned with ground-recorded estimates. The failure of a pixel-based percent cover approach to align with field-recorded values may be a result of an oversaturation of NDVI. Spectral indices such as NDVI can present a saturation problem, where indices plateau at a threshold where the index is fully saturated, typically an issue in areas characterized by densely vegetated canopies (Asner et al., 2003; Lu, 2006; Zhao et al., 2016). As a result, changes in cover beyond these thresholds cannot be isolated. With taller plants at NIWB, and therefore greater leaf area, computed percent cover estimates appear to become saturated with all image-based estimates nearing 100% cover (Figure 8B). These tall plants (>1.0 m) are associated with high percent cover estimates (mean ± sd: 84.38 ± 24.26%), while short plants (defined as < 0.5 m), that characterize NC are associated with lower computed percent cover estimates (mean = 20.17%, sd = 35.78%). Therefore, beyond canopy density, as outlined in previous studies (Lu, 2006; Zhou et al., 2018), plant height may influence aerial multispectral estimates of percent cover given that there is greater leaf area. It is also possible that, given the resolution of the sensors, percent cover may not be feasible to extract on this scale. Classification of wetland imagery and the development of percent cover estimates has been executed using UAS-based approaches at larger scales, such as Chabot and Bird (2013), who used 25 m radius circular plots to successfully assess percent cover (Chabot and Bird, 2013).

Though, in this study, ground-based estimates of percent cover are considered to be "true" data, it should be noted that these manual estimates vary in methodology and may be inconsistent. Differences in percent cover ground data collection methods at NC and NIWB may be a source of variability in the data. The point-intercept method used at NC may be more objective, as it has rigorous quantitative metrics for computing cover (see Section 2.5), which may help to explain the increased alignment of UAS and ground data at NC (Figure 8A). Ground-based methods for assessing percent cover may be limited by the horizontal frame of reference and impacted by canopy height, density, and vegetation type. For these reasons, aerial estimates may be less subjective than ground-based estimates and provide more consistent, reliable estimations of vegetation cover.

5 Conclusion

Inexpensive, widely available UAS platforms provide a valuable tool for habitat monitoring and change detection in coastal ecosystems. We demonstrate that mapping product accuracy is impacted by GCP density and distribution as well as common UAS operational parameters. With adequate attention to flight planning and SfM processing routines, UAS can be used to estimate plant biomass and create marsh surface models that are comparable in accuracy to manually-derived products. The consistently low error in XY position associated with UAS-SfM models suggests that these products will also be of great value for measuring elevation change and structural metrics over time in the face of rapid change in coastal and estuarine habitats. In describing the variability and tradeoffs associated with UAS-based mapping operations and parameters, this study helps to increase transparency and comparability of UAS-SfM based monitoring and assessment of coastal wetlands. The results of this work will expand our ability to accurately and rapidly assess and monitor coastal wetlands on unprecedented scales, a critical step forward in light of recent coastal change and restoration efforts.

Data availability statement

The datasets presented in this study can be found in online repositories. The names of the repository/repositories and accession number(s) can be found below: https://doi.org/10.7924/r4sb46t2c.

Author contributions

Conceptualization, JD, JR, ES, and BP; methodology, AD, RG, JD, JR, BP, and ES; software, AD and RG; validation, AD and RG; formal analysis, AD and RG; investigation, BP and ES; resources, BP, ES, JD, and JR; data curation, AD and RG; writing—original draft preparation, AD; writing—review and editing, AD, JD, JR, BP, ES, and RG; visualization, AD; supervision, JD and JR; project administration, JD, JR, ES, and BP; funding acquisition, JD JR, ES, and BP. All authors have read and agreed to the published version of the manuscript.

Funding

This work was made possible by a grant from the NOAA Office of Oceanic and Atmospheric Research (Grant #W8KSCXR).

Acknowledgments

The authors would like to thank Bryan Costa and Leanne Poussard of NCCOS for preliminary reviews of this manuscript. Brittany Morse of NI-WB NERR and Charlie Deaton of NCNERR supported field sampling and image acquisition. Chris Kinkade of the National Estuarine Research Reserve program played a pivotal role in project administration and outreach.

Conflict of interest

RG was employed by Consolidated Safety Services Inc, for National Oceanic and Atmospheric Administration.

The remaining authors declare that the research was conducted in the absence of any commercial or financial relationships that could be construed as a potential conflict of interest.

Publisher's note

Supplementary material

The Supplementary Material for this article can be found online at: https://www.frontiersin.org/articles/10.3389/frsen.2022.924969/full#supplementary-material

References

Adam, E., Mutanga, O., and Rugege, D. (2010). Multispectral and hyperspectral remote sensing for identification and mapping of wetland vegetation: A review. *Wetl. Ecol. Manag.* 18, 281–296. doi:10.1007/s11273-009-9169-z

Agisoft LLC (2021). Agisoft metashape user manual—professional edition. Version 1.7 Available at: https://www.agisoft.com/metashape-pro_1_7_en (Accessed January 1, 2021).

Altum and MicaSense (2021). Altum | MicaSense. Available at: https://micasense.com/altum/(Accessed May 12, 2021).

Anders, N., Smith, M., Suomalainen, J., Cammeraat, E., Valente, J., and Keesstra, S. (2020). Impact of flight altitude and cover orientation on Digital Surface Model (DSM) accuracy for flood damage assessment in Murcia (Spain) using a fixed-wing UAV. *Earth Sci. Inf.* 13, 391–404. doi:10.1007/s12145-019-00427-7

Anders, N., Valente, J., Masselink, R., and Keesstra, S. (2019). Comparing filtering techniques for removing vegetation from UAV-based photogrammetric point clouds. *Drones* 3, 61. doi:10.3390/drones3030061

Asner, G. P., Scurlock, J. M. O., and Hicke, J. A. (2003). Global synthesis of leaf area index observations: Implications for ecological and remote sensing studies. *Glob. Ecol. Biogeogr.* 12, 191–205. doi:10.1046/j.1466-822X.2003.00026.x

Barbier, E. B., Hacker, S. D., Kennedy, C., Koch, E. W., Stier, A. C., and Silliman, B. R. (2011). The value of estuarine and coastal ecosystem services. *Ecol. Monogr.* 81, 169–193. doi:10.1890/10-1510.1

Barnas, A. F., Chabot, D., Hodgson, A. J., Johnston, D. W., Bird, D. M., and Ellis-Felege, S. N. (2020). A standardized protocol for reporting methods when using drones for wildlife research. *J. Unmanned Veh. Syst.* 8, 89–98. doi:10.1139/juvs-2019-0011

Bendig, J., Yu, K., Aasen, H., Bolten, A., Bennertz, S., Broscheit, J., et al. (2015). Combining UAV-based plant height from crop surface models, visible, and near infrared vegetation indices for biomass monitoring in barley. *Int. J. Appl. Earth Obs. Geoinf.* 39, 79–87. doi:10.1016/j.jag.2015.02.012

Brunetta, R., Duo, E., and Ciavola, P. (2021). Evaluating short-term tidal flat evolution through uav surveys: A case study in the Po delta (Italy). *Remote Sens. (Basel).* 13, 2322. doi:10.3390/rs13122322

Chabot, D., and Bird, D. M. (2013). Small unmanned aircraft: Precise and convenient new tools for surveying wetlands. *J. Unmanned Veh. Syst.* 01, 15–24. doi:10.1139/juvs-2013-0014

Chen, Y., Dong, J., Xiao, X., Zhang, M., Tian, B., Zhou, Y., et al. (2016). Land claim and loss of tidal flats in the Yangtze Estuary. *Sci. Rep.* 6, 24018. doi:10.1038/srep24018

Currin, C. A., Delano, P. C., and Valdes-Weaver, L. M. (2008). Utilization of a citizen monitoring protocol to assess the structure and function of natural and stabilized fringing salt marshes in North Carolina. *Wetl. Ecol. Manag.* 16, 97–118. doi:10.1007/s11273-007-9059-1

Dayamit, O. M., Pedro, M. F., Ernesto, R. R., and Fernando, B. L. (2015). "Digital elevation model from non-metric camera in UAS compared with lidar technology," in International Conference on Unmanned Aerial Vehicles in Geomatics, Toronto, Canada. The International Archives of the Photogrammetry, Remote Sensing and

Spatial Information Sciences XL-1/W4, 411–414. doi:10.5194/isprsarchives-XL-1-W4-411-2015

DiGiacomo, A. E., Bird, C. N., Pan, V. G., Dobroski, K., Atkins-Davis, C., Johnston, D. W., et al. (2020). Modeling salt marsh vegetation height using unoccupied aircraft systems and structure from motion. *Remote Sens. (Basel).* 12, 2333. doi:10.3390/rs12142333

Double 4K Sensor - Sentera (2021). Sentera Double 4K sensor | Sentera | red edge Sentera. Available at: https://sentera.com/product/double-4k-sensor/(Accessed May 12, 2021).

Doughty, C. L., and Cavanaugh, K. C. (2019). Mapping coastal wetland biomass from high resolution unmanned aerial vehicle (UAV) imagery. *Remote Sens. (Basel).* 11, 540. doi:10.3390/rs11050540

Farris, A. S., Defne, Z., and Ganju, N. K. (2019). Identifying salt marsh shorelines from remotely sensed elevation data and imagery. *Remote Sens. (Basel).* 11, 1795. doi:10.3390/rs11151795

Fennessy, M. S., Jacobs, A. D., and Kentula, M. E. (2007). An evaluation of rapid methods for assessing the ecological condition of wetlands. *Wetlands* 27, 543–560. doi:10.1672/0277-5212(2007)27[543:AEORMF]2.0.CO;2

Fraser, B. T., and Congalton, R. G. (2018). Issues in unmanned aerial systems (UAS) data collection of complex forest environments. *Remote Sens. (Basel).* 10, 908. doi:10.3390/rs10060908

Fuentes-Peailillo, F., Ortega-Farías, S., Rivera, M., Bardeen, M., and Moreno, M. (2018). "Comparison of vegetation indices acquired from RGB and Multispectral sensors placed on UAV," in Proceedings of the 2018 IEEE International Conference on Automation/XXIII Congress of the Chilean Association of Automatic Control (ICA-ACCA), Concepcion, Chile, October 17–19, 2018, 1–6. doi:10.1109/ICA-ACCA.2018.8609861

Goodbody, T. R. H., Coops, N. C., Hermosilla, T., Tompalski, P., and Pelletier, G. (2018). Vegetation phenology driving error variation in digital aerial photogrammetrically derived terrain models. *Remote Sens. (Basel).* 10, 1554. doi:10.3390/rs10101554

Green, E. P., Mumby, P. J., Edwards, A. J., and Clark, C. D. (1996). A review of remote sensing for the assessment and management of tropical coastal resources. *Coast. Manage.* 24, 1–40. doi:10.1080/08920759609362279

Haskins, J., Endris, C., Thomsen, A. S., Gerbl, F., Fountain, M. C., and Wasson, K. (2021). UAV to inform restoration: A case study from a California tidal marsh. *Front. Environ. Sci.* 9, 642906. doi:10.3389/fenvs.2021.642906

Huang, S., Tang, L., Hupy, J. P., Wang, Y., and Shao, G. (2021). A commentary review on the use of normalized difference vegetation index (NDVI) in the era of popular remote sensing. *J. For. Res.* 32, 1–6. doi:10.1007/s11676-020-01155-1

Huete, A. R. (1988). A soil-adjusted vegetation index (SAVI). *Remote Sens. Environ.* 25, 295–309. doi:10.1016/0034-4257(88)90106-X

Jackson, J. B. C., Kirby, M. X., Berger, W. H., Bjorndal, K. A., Botsford, L. W., Bourque, B. J., et al. (2001). Historical overfishing and the recent collapse of coastal ecosystems. *Science* 293, 629–637. doi:10.1126/science.1059199

James, M. R., Robson, S., d'Oleire-Oltmanns, S., and Niethammer, U. (2017). Optimising UAV topographic surveys processed with structure-from-motion: Ground control quality, quantity and bundle adjustment. *Geomorphology* 280, 51–66. doi:10.1016/j.geomorph.2016.11.021

James-Pirri, M.-J., Roman, C. T., and Erwin, R. M. (2002). *Field methods manual: US fish and wildlife service (region 5) salt marsh study* Narragansett, RI: University of Rhode Island.

Kameyama, S., and Sugiura, K. (2021). Effects of differences in structure from motion software on image processing of unmanned aerial vehicle photography and estimation of crown area and tree height in forests. *Remote Sens. (Basel).* 13, 626. doi:10.3390/rs13040626

Klemas, V. (2013). Remote sensing of coastal wetland biomass: An overview. *J. Coast. Res.* 29, 1016–1028. doi:10.2112/JCOASTRES-D-12-00237.1

Laengner, M. L., Siteur, K., and van der Wal, D. (2019). Trends in the seaward extent of saltmarshes across europe from long-term satellite data. *Remote Sens. (Basel).* 11, 1653. doi:10.3390/rs11141653

Lopes, C. L., Mendes, R., Caçador, I., and Dias, J. M. (2020). Assessing salt marsh extent and condition changes with 35 years of Landsat imagery: Tagus Estuary case study. *Remote Sens. Environ.* 247, 111939. doi:10.1016/j.rse.2020.111939

Lotze, H. K., Lenihan, H. S., Bourque, B. J., Bradbury, R. H., Cooke, R. G., Kay, M. C., et al. (2006). Depletion, degradation, and recovery potential of estuaries and coastal seas. *Science* 312, 1806–1809. doi:10.1126/science.1128035

Lu, D. (2006). The potential and challenge of remote sensing-based biomass estimation. *Int. J. Remote Sens.* 27, 1297–1328. doi:10.1080/01431160500486732

MacKay, H., Finlayson, C. M., Fernández-Prieto, D., Davidson, N., Pritchard, D., and Rebelo, L.-M. (2009). The role of earth observation (EO) technologies in supporting implementation of the ramsar convention on wetlands. *J. Environ. Manage.* 90, 2234–2242. doi:10.1016/j.jenvman.2008.01.019

Mamaghani, B., and Salvaggio, C. (2019). Multispectral sensor calibration and characterization for sUAS remote sensing. *Sensors* 19, 4453. doi:10.3390/s19204453

Martínez-Carricondo, P., Agüera-Vega, F., Carvajal-Ramírez, F., Mesas-Carrascosa, F.-J., García-Ferrer, A., and Pérez-Porras, F.-J. (2018). Assessment of UAV-photogrammetric mapping accuracy based on variation of ground control points. *Int. J. Appl. Earth Obs. Geoinf.* 72, 1–10. doi:10.1016/j.jag.2018.05.015

Mavic 2 (2021). Mavic 2 - product information - DJI DJI off. Available at: https://www.dji.com/mavic-2/info (Accessed May 12, 2021).

McCarthy, M. J., Colna, K. E., El-Mezayen, M. M., Laureano-Rosario, A. E., Méndez-Lázaro, P., Otis, D. B., et al. (2017). Satellite remote sensing for coastal management: A review of successful applications. *Environ. Manage.* 60, 323–339. doi:10.1007/s00267-017-0880-x

Meixler, M. S., Kennish, M. J., and Crowley, K. F. (2018). Assessment of plant community characteristics in natural and human-altered coastal marsh ecosystems. *Estuaries Coast.* 41, 52–64. doi:10.1007/s12237-017-0296-0

Meyer, G. E., and Neto, J. C. (2008). Verification of color vegetation indices for automated crop imaging applications. *Comput. Electron. Agric.* 63, 282–293. doi:10.1016/j.compag.2008.03.009

Minchinton, T. E., Shuttleworth, H. T., Lathlean, J. A., McWilliam, R. A., and Daly, T. J. (2019). Impacts of cattle on the vegetation structure of mangroves. *Wetlands* 39, 1119–1127. doi:10.1007/s13157-019-01143-0

Morris, J. T., Sundareshwar, P. V., Nietch, C. T., Kjerfve, B., and Cahoon, D. R. (2002). Responses of coastal wetlands to rising sea level. *Ecology* 83, 2869–2877. doi:10.1890/0012-9658(2002)083[2869:ROCWTR]2.0.CO;2

National Estuarine Research Reserve System (2021). National estuarine research Reserve system. Available at: https://coast.noaa.gov/nerrs/about/(Accessed May 3, 2021).

Niu, Y., Zhang, L., Zhang, H., Han, W., and Peng, X. (2019). Estimating above-ground biomass of maize using features derived from UAV-based RGB imagery. *Remote Sens. (Basel).* 11, 1261. doi:10.3390/rs11111261

NOAA (2021). NOAA: Data access viewer. Available at: https://coast.noaa.gov/dataviewer/(Accessed July 14, 2021).

Noss, R. F., Platt, W. J., Sorrie, B. A., Weakley, A. S., Means, D. B., Costanza, J., et al. (2015). How global biodiversity hotspots may go unrecognized: Lessons from the North American coastal plain. *Divers. Distrib.* 21, 236–244. doi:10.1111/ddi.12278

OCM Partners (2017). 2017 SC DNR lidar DEM: Georgetown county. Available at: https://www.fisheries.noaa.gov/inport/item/57134 (Accessed September 1, 2021).

OCM Partners (2018). 2018 USACE NCMP post-florence Topobathy lidar DEM: Southeast coast (VA, NC, SC). Available at: https://www.fisheries.noaa.gov/inport/item/57345 (Accessed September 1, 2021).

Peterson, P. M., Romaschenko, K., Arrieta, Y. H., and Saarela, J. M. (2014). A molecular phylogeny and new subgeneric classification of Sporobolus (Poaceae: Chloridoideae: Sporobolinae). *Taxon* 63, 1212–1243. doi:10.12705/636.19

Pettorelli, N., Bühne, H. S., Tulloch, A., Dubois, G., Macinnis-Ng, C., Queirós, A. M., et al. (2018). Satellite remote sensing of ecosystem functions: Opportunities, challenges and way forward. *Remote Sens. Ecol. Conserv.* 4, 71–93. doi:10.1002/rse2.59

Pham, T. D., Xia, J., Ha, N. T., Bui, D. T., Le, N. N., and Tekeuchi, W. (2019). A review of remote sensing approaches for monitoring Blue carbon ecosystems: Mangroves, seagrassesand salt marshes during 2010–2018. *Sensors* 19, 1933. doi:10.3390/s19081933

Pix4D (2022). Pix4D manual – support. Available at: https://support.pix4d.com/hc/en-us/sections/360003718992-Manual (Accessed April 7, 2022).

Poley, L. G., and McDermid, G. J. (2020). A systematic review of the factors influencing the estimation of vegetation aboveground biomass using unmanned aerial systems. *Remote Sens. (Basel).* 12, 1052. doi:10.3390/rs12071052

Psuty, N. P., Ames, K., Habeck, A., and Schmelz, W. (2018). Responding to coastal change: Creation of a regional approach to monitoring and management, northeastern region, U.S.A. *Ocean. Coast. Manag.* 156, 170–182. doi:10.1016/j.ocecoaman.2017.08.004

Qi, J., Chehbouni, A., Huete, A. R., Kerr, Y. H., and Sorooshian, S. (1994). A modified soil adjusted vegetation index. *Remote Sens. Environ.* 48, 119–126. doi:10.1016/0034-4257(94)90134-1

Roman, C. T., James-PirriMary-Jane, M.-J., and Heltshe, J. F. (2001). *Monitoring salt marsh vegetation: A protocol for the long-term coastal ecosystem monitoring program at cape cod national seashore*. Narragansett, RI: USGS Patuxent Wildl. Res. Cent. Coast. Res. Field Stn. Univ. R. I., 55.

Roughgarden, J., Running, S. W., and Matson, P. A. (1991). What Does Remote Sensing Do For Ecology? *Ecology* 72, 1918–1922. doi:10.2307/1941546

Seymour, A. C., Ridge, J. T., Rodriguez, A. B., Newton, E., Dale, J., and Johnston, D. W. (2018). Deploying Fixed Wing Unoccupied Aerial Systems (UAS) for Coastal Morphology Assessment and Management. *J. Coast. Res.* 34, 704. doi:10.2112/jcoastres-d-17-00088.1

Sona, G., Pinto, L., Pagliari, D., Passoni, D., and Gini, R. (2014). Experimental analysis of different software packages for orientation and digital surface modelling from UAV images. *Earth Sci. Inf.* 7, 97–107. doi:10.1007/s12145-013-0142-2

Spalding, M. D., Ruffo, S., Lacambra, C., Meliane, I., Hale, L. Z., Shepard, C. C., et al. (2014). The role of ecosystems in coastal protection: Adapting to climate change and coastal hazards. *Ocean. Coast. Manag.* 90, 50–57. doi:10.1016/j.ocecoaman.2013.09.007

Thomsen, A. S., Krause, J., Appiano, M., Tanner, K. E., Endris, C., Haskins, J., et al. (2021). Monitoring Vegetation Dynamics at a Tidal Marsh Restoration Site: Integrating Field Methods, Remote Sensing and Modeling. *Estuaries Coast.* 45, 523–538. doi:10.1007/s12237-021-00977-4

Tonkin, T. N., and Midgley, N. G. (2016). Ground-Control Networks for Image Based Surface Reconstruction: An Investigation of Optimum Survey Designs Using UAV Derived Imagery and Structure-from-Motion Photogrammetry. *Remote Sens. (Basel).* 8, 786. doi:10.3390/rs8090786

Trueblood, D., Almazán-Casali, S., Arnott, J., Brass, M., Lemos, M. C., Matso, K., et al. (2019). Advancing Knowledge for Use in Coastal and Estuarine Management: Competitive Research in the National Estuarine Research Reserve System. *Coast. Manage.* 47, 337–346. doi:10.1080/08920753.2019.1598221

Villanueva, J. K. S., and Blanco, A. C. (2019). Optimization Of Ground Control Point (GCP) Configuration For Unmanned Aerial Vehicle (UAV) Survey Using Structure From Motion (SFM). *Int. Arch. Photogramm. Remote Sens. Spat. Inf. Sci.* XLII-4/W12, 167–174. doi:10.5194/isprs-archives-XLII-4-W12-167-2019

Wang, J., Liu, Z., Yu, H., and Li, F. (2017). Mapping Spartina alterniflora Biomass Using LiDAR and Hyperspectral Data. *Remote Sens. (Basel).* 9, 589. doi:10.3390/rs9060589

Whitehead, K., and Hugenholtz, C. (2014). Remote sensing of the environment with small unmanned aircraft systems (UASs), part 1: a review of progress and challenges. *J. Unmanned Veh. Syst.* 02, 69–85. doi:10.1139/juvs-2014-0006

Yanagi, H., and Chikatsu, H. (2016). Performance Evaluation of 3d Modeling Software for Uav Photogrammetry. *Int. Arch. Photogramm. Remote Sens. Spat. Inf. Sci.* 41, 147–152. doi:10.5194/isprs-archives-XLI-B5-147-2016

Zhao, P., Lu, D., Wang, G., Wu, C., Huang, Y., and Yu, S. (2016). Examining Spectral Reflectance Saturation in Landsat Imagery and Corresponding Solutions to Improve Forest Aboveground Biomass Estimation. *Remote Sens. (Basel).* 8, 469. doi:10.3390/rs8060469

Zhou, Z., Yang, Y., and Chen, B. (2018). Estimating Spartina alterniflora fractional vegetation cover and aboveground biomass in a coastal wetland using SPOT6 satellite and UAV data. *Aquat. Bot.* 144, 38–45. doi:10.1016/j.aquabot.2017.10.004

frontiers | Frontiers in Remote Sensing

TYPE Original Research
PUBLISHED 21 October 2022
DOI 10.3389/frsen.2022.1021781

OPEN ACCESS

EDITED BY
Erin Bunting,
Michigan State University, United States

REVIEWED BY
Grant Gunn,
University of Waterloo, Canada
Samuel Tuttle,
Syracuse University, United States
John Walsh,
University of Alaska Fairbanks,
United States

*CORRESPONDENCE
Claire L. Parkinson,
claire.l.parkinson@nasa.gov

SPECIALTY SECTION
This article was submitted to a special issue on Women in Remote Sensing in the journal
Frontiers in Remote Sensing

RECEIVED 17 August 2022
ACCEPTED 20 September 2022
PUBLISHED 21 October 2022

CITATION
Parkinson CL (2022), Arctic sea ice coverage from 43 years of satellite passive-microwave observations. *Front. Remote Sens.* 3:1021781. doi: 10.3389/frsen.2022.1021781

Arctic sea ice coverage from 43 years of satellite passive-microwave observations

Claire L. Parkinson*

Cryospheric Sciences Laboratory, Goddard Space Flight Center, National Aeronautics and Space Administration (NASA), Greenbelt, MD, United States

Satellite passive-microwave instrumentation has allowed the monitoring of Arctic sea ice over the past 43 years, and this monitoring has revealed and quantified major changes occurring in Arctic sea ice coverage. The 43-year 1979–2021 record shows considerable interannual variability but also a long-term downward trend in Arctic sea ice that is clear from many vantage points: A linear-least-square trend of −54,300 ± 2,700 km^2/year for yearly average sea ice extents; statistically significant negative trends for each of the 12 calendar months; negative trends for each of nine regions into which the Arctic sea ice cover is divided; the fact that for all 12 calendar months the highest monthly average sea ice extent came in the first 8 years of the record and the lowest monthly average sea ice extent came in the last 10 years of the record; and a prominent shortening of the sea ice season throughout much of the marginal ice zone, with the length of the sea ice season in some locations decreasing by over 100 days and some locations previously experiencing months-long sea ice seasons now typically no longer having a sea ice season at all. The overall, Arctic-wide trend value of the yearly average sea ice extents since 1979 has consistently had a negative magnitude exceeding two standard deviations of the trend line slope since 1990 and has remained in the narrow range of −53,000 km^2/yr to −55,500 km^2/yr since 2011.

KEYWORDS

sea ice, Arctic sea ice, Arctic, climate change, polar climate change, satellite Earth observations

1 Introduction

Prior to the 1970s, sea ice was one of the lesser-known climate variables. With sea ice extending over vast areas and no permanent settlements on the sea ice, the records were generally limited to those obtained from explorers and from ships traversing the area for economic reasons, often whaling and sealing, plus some records from coastal communities and from the few scientific expeditions that had ventured into the Arctic sea ice territory. The most prominent coastal-community record is a centuries-long record from Iceland (Koch, 1945).

The situation today regarding records of the Arctic sea ice cover is remarkably different from what it had been prior to the 1970s, and in substantial part this is due to the records obtained from satellite data. Satellites go a long way toward "leveling the playing

field" when it comes to data collection. With satellites there is no advantage or disadvantage to being close to a human settlement. Passive-microwave instrumentation in particular has allowed a satellite record of Arctic sea ice coverage that extends back to the late 1970s.

This paper presents an array of results from a 43-year record of Arctic sea ice derived from a sequence of satellite passive-microwave instruments. These results quantify the decreasing Arctic sea ice coverage over the last 43 years, robustly illustrating the changes in one key component of the Earth's climate system. Sea ice coverage matters to the Earth system in many ways: It reflects solar radiation back to space, thereby keeping the polar regions colder than they otherwise would be; it is an insulator between the liquid ocean and the atmosphere, restricting exchanges of heat, mass, and momentum; it is a buffer helping to protect coasts from wind-driven waves; it transports cold, relatively fresh water equatorward; and it serves as a platform for such polar animals as polar bears and Arctic foxes, while hindering the movement of such marine animals as whales (e.g., Barry et al., 1993; Walsh, 2013; Meier et al., 2014; Vihma, 2014). Without sea ice, the Arctic climate and ecosystem would be quite different from what they are today.

2 Data and methods

The data used in this paper come from satellite passive-microwave instruments, specifically the Scanning Multichannel Microwave Radiometer (SMMR) on NASA's Nimbus 7 satellite, the Special Sensor Microwave Imager (SSMI) on the F8, F11, and F13 satellites of the United States (U.S.) Department of Defense's Defense Meteorological Satellite Program (DMSP), and the SSMI Sounder (SSMIS) on the DMSP F17 satellite. The Nimbus 7 satellite was launched on 24 October 1978; the F8 satellite, carrying the first SSMI instrument, was launched on 18 June 1987; and the F17 satellite was launched on 4 November 2006. For this study, SMMR data are used for January 1979–mid-August 1987, SSMI data for mid-August 1987–December 2007, and SSMIS data for January 2008–December 2021. The SMMR, SSMI, and SSMIS are not identical instruments orbiting in identical orbits: They fly at different altitudes, they take measurements at different combinations of frequencies, and they have different fields of view even for channels with the same frequencies. Still, they are similar enough that an extensive effort at intercalibration between successive instruments has yielded a consistent long-term record. Details of the instrument differences and the intercalibration process are provided in Cavalieri et al. (1999) for the SMMR/SSMI transition and in Cavalieri et al. (2012) for the SSMI/SSMIS transition. Advances in satellite instrumentation have been quite noticeable in the reduction of missing and flawed data when moving from the SMMR to the SSMI and from the SSMI to the SSMIS.

One of the primary reasons that the SMMR, SSMI, and SSMIS can each provide robust records of sea ice coverage is that they each measure at one or more frequencies where there is a sharp contrast between the microwave emissions of ice *versus* liquid water. For instance, for the SMMR 18 GHz horizontally polarized data, the brightness temperature of liquid water tends to be ~98.5 K, whereas the brightness temperature of first-year ice is ~225.2 K and the brightness temperature of older, multiyear ice is ~186.8 K (Cavalieri et al., 1999). The corresponding values for the SSMIS 19 GHz horizontally polarized data are 113.4 K for liquid water, 232.0 K for first-year ice, 196.0 K for multiyear ice (Cavalieri et al., 2012). With such large distinctions between ice and water, the ice edge tends to be readily distinguished on maps of the 18 and 19 GHz data. Furthermore, there are sharply different contrasts at other frequencies, with, for instance, liquid water having a brightness temperature (~199.4 K) between the brightness temperatures of first-year ice (~239.8 K) and multiyear ice (~180.8 K) for the SMMR 37 GHz vertically polarized data (Cavalieri et al., 1999). By incorporating these different contrasts, algorithms are able to distinguish first-year ice from multiyear ice as well as ice from liquid water.

Two other crucial factors enhancing the value of passive-microwave sensors for sea ice studies are: 1) microwave radiation (at selected microwave wavelengths) can pass through clouds, thereby enabling sea ice observations in the presence of clouds as well as under cloud-free conditions; and 2) the microwave radiation is emitted from within the Earth system rather than being reflected sunlight, thereby enabling sea ice observations in the dark winter months as well as during sunlit periods. These two factors provide major advantages for the use of microwave radiation rather than visible radiation in generating and analyzing climate-relevant sea ice data sets.

The passive-microwave data are gridded onto a polar stereographic projection with grid cell (or pixel) areas of approximately 625 km^2 (25 km × 25 km) at 70° latitude, ranging up to approximately 665 km^2 at the North Pole. The gridded radiative data are received at NASA Goddard Space Flight Center from the U.S. National Snow and Ice Data Center (NSIDC) and are then used to calculate sea ice concentrations, which are sent to NSIDC for archival and distribution. Sea ice concentrations are the percent areal coverages of sea ice in each grid cell. The algorithm used to calculate the sea ice concentrations is the NASA Team Algorithm described in Gloersen et al. (1992). This algorithm has been widely used in analyses of sea ice coverage from satellite passive-microwave data, for both the Arctic and the Antarctic (e.g., Parkinson et al., 1999; Zwally et al., 2002).

The sea ice concentrations provide the basis for the calculation of sea ice extents, with sea ice extent, at any given time, being the sum of the areas of each grid cell in the region of interest having a calculated or assumed sea ice concentration of at least 15%. [Calculations are done for each ocean pixel covered by the satellite data. The only assumed sea ice concentrations are for

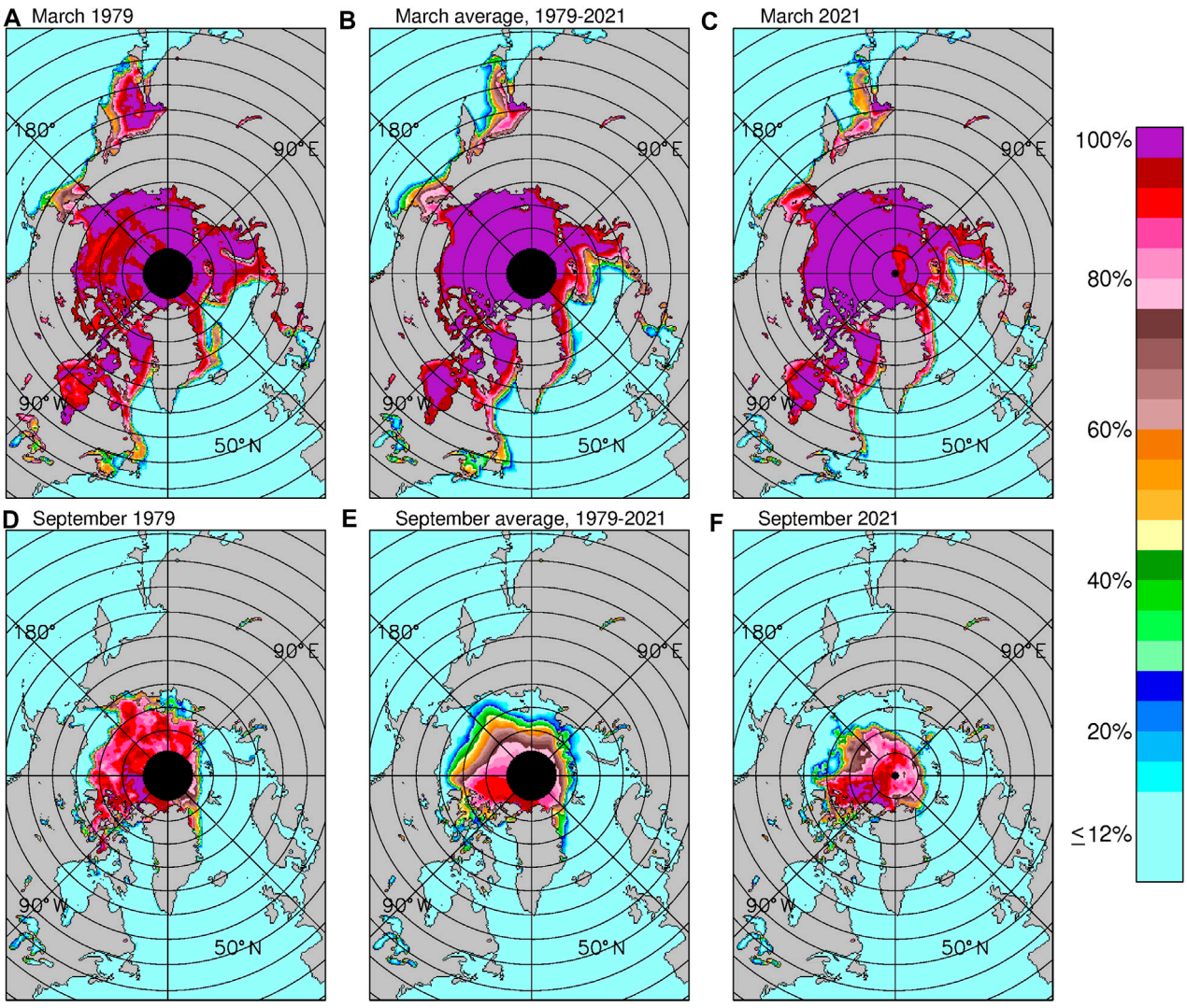

FIGURE 1
Average Arctic sea ice concentrations for: **(A)** March 1979, **(B)** the 43-year March average, 1979–2021, **(C)** March 2021, **(D)** September 1979, **(E)** the 43-year September average, 1979–2021, **(F)** September 2021. The prominent black circular region centered on the North Pole in the 1979 and 1979–2021 images represents missing data and reflects the fact that the orbit of the Nimbus 7 satellite, obtaining the data for the first 8.6 years of the 43-year record, did not bring the satellite close enough to the Pole to allow data collection poleward of 84.6°N.

pixels in the immediate vicinity of the North Pole, where there are no SMMR, SSMI, or SSMIS data due to the satellites not passing directly over the Pole. The satellite orbits and instrument scanning characteristics differ, with the result that the SMMR data extend poleward to 84.6°N, the SSMI data extend poleward to 87.6°N, and the SSMIS data extend poleward to 89.2°N. Fortunately, in each case the data surrounding the missing-data region suggest that it is extremely likely that each pixel within the Pole-centered missing-data region has an ice concentration of at least 15%, and consequently that is the assumption made in the calculation of ice extents.] Sea ice extents are calculated on a daily basis (every-other-day for the SMMR data) and are combined to monthly and yearly averages. Linear-least-square trends are calculated both for the yearly averages and for a variable called "monthly deviations," which eliminates the prominent annual cycle in the monthly average data by subtracting from each individual month (e.g., January 1979) the average of that calendar month's values through the entire record (e.g., the average January for 1979–2021). Standard deviations of the slopes of the linear-least-square trend lines are calculated following Draper and Smith (1981) and Taylor (1997).

The satellite passive-microwave datasets used in this study are archived at NSIDC in Boulder, Colorado, and are available on the NSIDC website, https://nsidc.org (Cavalieri et al., 1996, updated yearly).

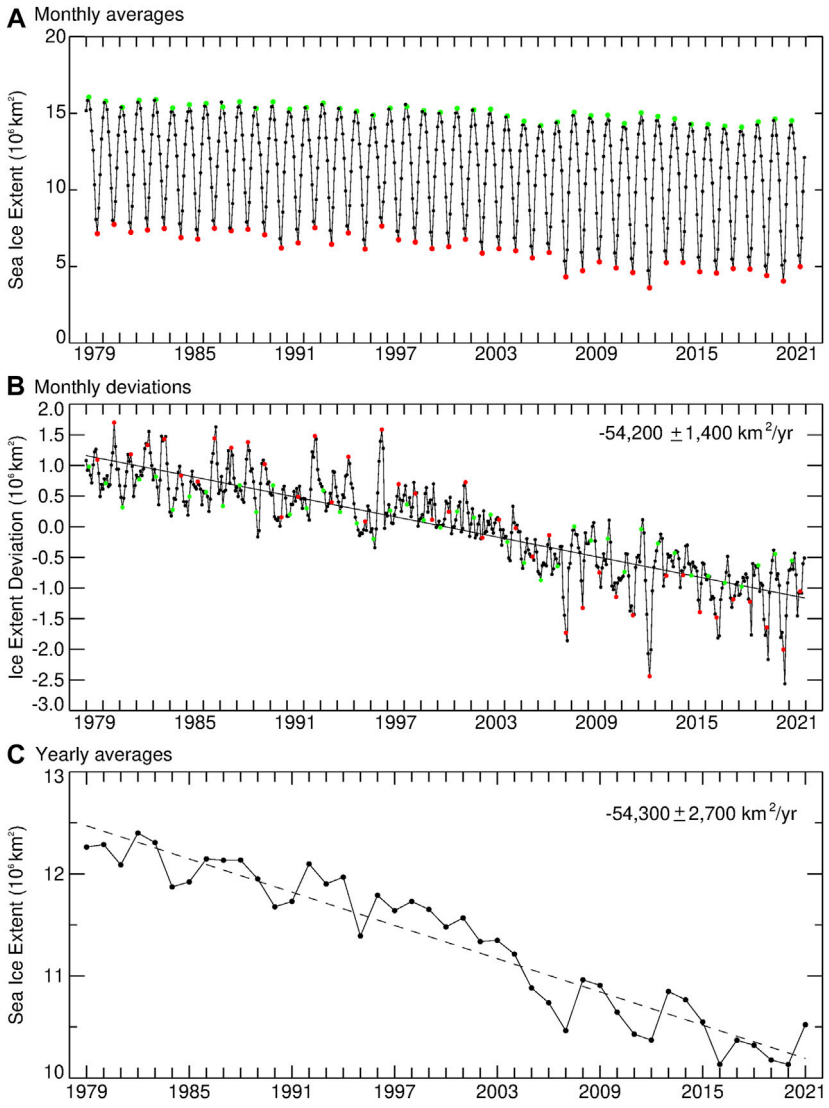

FIGURE 2
(A) Monthly average Arctic sea ice extents, January 1979–December 2021. March ice extents are depicted in green, September ice extents in red, and all others smaller and in black. **(B)** Monthly Arctic sea ice extent deviations, January 1979–December 2021, with March values in green, September values in red, and all others smaller and in black. **(C)** Yearly average Arctic sea ice extents, 1979–2021. The **(B)** and **(C)** plots both include the linear-least-square trend line through the data and the trend line slope and standard deviation. The *x*-axis tick marks for plots **(A)** and **(B)** come at the January values for each year.

3 Results

3.1 Sea ice concentrations and geographic expanse

Every year, Arctic sea ice coverage undergoes a substantial expansion in autumn and winter and a substantial decay in spring and summer, with sea ice in March extending over almost the entire Arctic Ocean and many of the surrounding seas and bays (Figures 1A–C) and sea ice coverage by the end of summer reducing to an area largely within the Arctic Ocean (Figures 1D–F). Ice concentrations tend to be greater than 90% for most of the region in late winter but much lower at the end of summer (Figure 1). The winter ice distributions reflect the importance of the Gulf Stream in bringing warm waters northeast across the North Atlantic, resulting in ice-free waters at quite high latitudes (70–75°N) immediately north of Norway (Figures 1A–C). In contrast, Hudson Bay remains covered with ice in late winter, despite its much lower latitudes (52–65°N), as a result of the continentality effect, wherein mid-continent locations tend to have colder winters and hotter summers than coastal locations affected by the moderating effect of the oceans (Figures 1A–C).

The lesser sea ice coverage in 2021 *versus* 1979 is apparent in both the March and September maps (Figure 1). For instance, in March the ice-free waters to the north of Norway extended noticeably further north in 2021 than in 1979, and much of the eastern half of the Sea of Okhotsk (the sea centered at about 54°N, 150°E) was ice-free in March 2021 but ice-covered in March 1979 (Figures 1A,C). Comparison of the 1979 and 2021 September images reveals notably less sea ice coverage in 2021 than in 1979 to the east of northern Greenland and in the Canadian Archipelago region and, even more strikingly, to the north of Russia. In September 2021, a ship could have traversed a northeast passage from the Atlantic to the Pacific in the waters north of Russia with little if any complications from sea ice, whereas that would not have been the case in September 1979 (Figures 1D,F).

3.2 Sea ice extents and trends

3.2.1 Arctic-wide sea ice extents and trends

Figure 2 presents the monthly average sea ice extents, monthly deviations, and yearly averages for the entire 43-year record. In every one of the years 1979–2021, the month with the lowest monthly average northern hemisphere sea ice extent was September, with the September average values ranging from 3.60×10^6 km^2 in 2012 to 7.75×10^6 km^2 in 1980 and averaging 6.05×10^6 km^2 overall (Figure 2A). The month with the highest monthly average sea ice extent was March for every year except 1987, 1989, 1998, and 2015, in which instances it was February by a narrow margin (Figure 2A). These monthly-high values ranged from 14.10×10^6 km^2 in March 2018 to 16.05×10^6 km^2 in March 1979, with the overall average March ice extent being 15.07×10^6 km^2 (Figure 2A).

The prominent annual cycle of Arctic sea ice extents, with far more sea ice coverage in winter than in summer, dominates plots of monthly averages (Figure 2A). In fact, in the early years of the record, it was not immediately obvious from the monthly average plots that there was a downward trend, although by the late 1990s this had become obvious through the removal of the annual cycle in the monthly deviation and yearly average calculations (Parkinson et al., 1999). By now, the downward trend is apparent even from the monthly average plots (Figure 2A), although it is still more strongly highlighted through the monthly deviations (Figure 2B) and yearly averages (Figure 2C), where the downward trend is quite prominent, with linear-least-square trend lines having slopes of −54,200 ± 1,400 km^2/yr for the monthly deviations and −54,300 ± 2,700 km^2/yr for the yearly averages. This equates, on average, to an areal loss of sea ice extent each year exceeding the area of Costa Rica (area of 51,100 km^2).

There had been vague hints of a downward trend in Arctic sea ice extents as early as the late 1980s (e.g., Parkinson and Cavalieri, 1989) and more solid indications by the late 1990s (e.g., Johannessen et al., 1995; Maslanik et al., 1996; Parkinson et al., 1999). Quantitatively, it is with the 1990 data that the negative trend in yearly average Arctic sea ice extents since 1979 first reaches a value low enough that two standard deviations above it is also negative (Figure 3). This has continued to be the case ever since, with a narrowing of the standard deviation bars as more years are added (Figure 3). The calculated trend value has been in the narrow range of −53,000 km^2/yr to −55,500 km^2/yr since 2011 (Figure 3).

Despite the downward trend being apparent for many years before 2007, the major plummeting of the ice cover in summer 2007 (Figure 2B) came as a shock to the sea ice research community. Not only did the 2007 decrease in ice extent establish a new record low for Arctic sea ice extent in the satellite era, at 4.1×10^6 km^2, on 14 September 2007, but it was 24% below the previous record low, 5.4 million km^2, reached 2 years earlier on 21 September 2005. The 2007 decrease was so stunning that speculations arose regarding the possibility of a sea-ice-free late-summer Arctic occurring within the next decade. This did not happen, as instead the ice extents rebounded somewhat in the subsequent few years, before falling to a new record low in 2012 (as reflected in Figures 2A,B).

Both the 2007 and 2012 cases generated studies examining why the ice retreat in those 2 years was anomalously large, with results in both cases attributing the unusually low ice extents to a combination of preconditioning of the ice cover [with thinner ice and more open water than was common at the start of the satellite record (e.g., Maksym, 2019)] and the specific weather conditions in those two summer seasons. In the 2007 case, weather conditions included higher than normal temperatures and winds blowing into the Beaufort and Chukchi seas from the south, pushing the ice to the north (e.g., Comiso et al., 2008), and the fact that conditions were unusually cloud-free over the Arctic Ocean, favoring increased melt through increased incident solar radiation (Kay et al., 2008). In the 2012 case, a major storm in the central Arctic in early August contributed to the ice decreases (Simmonds and Rudeva, 2012; Parkinson and Comiso, 2013), as likely did also the unusual amount of relatively warm water discharged into the sea ice region north of Alaska and northwestern Canada by the Mackenzie River by early July (Nghiem et al., 2014). Through use of a computer model, Zhang et al. (2013) were able to simulate the August 2012 storm and examine different variables and processes, concluding that the decrease in ice volume during the storm was in large part due to increased bottom melt caused by the increased upward ocean heat flux from the wind-induced enhanced ocean mixing.

Because September is almost always the month when Arctic sea ice coverage reaches its annual minimum ice extent, and because September has also experienced a strong downward trend in sea ice coverage, it tends to be the month when media attention to Arctic sea ice is greatest. However, all 12 calendar months have experienced decreasing ice coverage

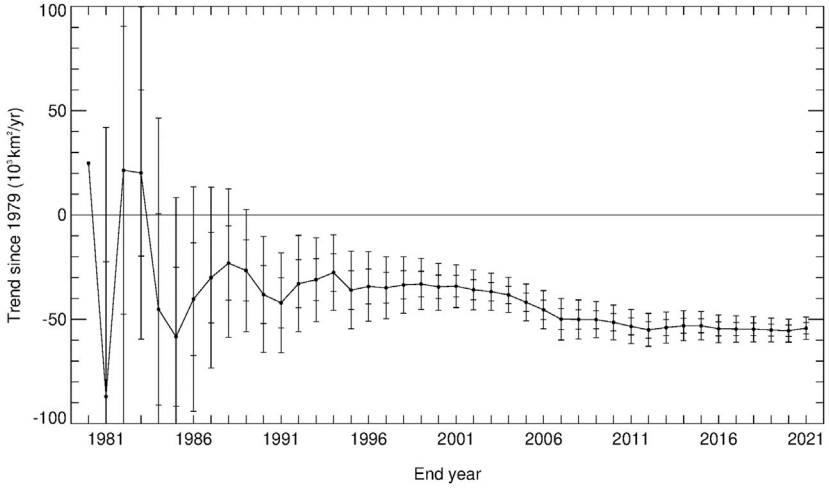

FIGURE 3
Linear-least-square slopes of the trend line in Arctic yearly average sea ice extents, from the 1979–1980 slope with only 2 years of data to the 1979–2021 slope with 43 years of data. The bars centered on each trend value after the first have ticks marking one and two standard deviations from the trend.

since 1979, and the 1979–2021 negative trend for October is comparable to (numerically even very slightly greater in magnitude than) that for September (Figure 4). In both the 2007 and 2012 cases of record low sea ice coverages, July was the month when the unusually low ice conditions became apparent, continuing in August, and lasting beyond September into October (Figure 4). For all 12 months, the sea ice extent trends since 1979 have been consistently below 0 by at least two standard deviations at least since 1998. The 2 months consistently clearing the two-standard-deviation threshold for the longest period are April and May, both of which first cleared the threshold with the 1979–1989 trend and have continued to do so ever since.

The 43-year time series of ice extents for the individual months (Figure 4) and for the yearly averages (Figure 2C) all illustrate the variability of the Arctic sea ice cover as well as the downward trend in sea ice coverage. For every calendar month and the yearly averages, there is at least one period of 6 years or longer when the trend in ice extents was positive rather than negative (Figure 2C, Figure 4). For instance, the rebounding from the still-record-low in 2012 results in positive August and September trends for the final 10 years of the record (2012–2021), despite August and September having quite substantial downward trends overall (Figure 4). Interannual variability is a common feature of climate records, and Figure 2C and Figure 4 are illustrative of that for the Arctic sea ice cover.

3.2.2 Sea ice extent record highs and lows

Another way to assess the changes in Arctic sea ice extents, complementary to the trend results, is to examine the occurrences and frequency of new record high and record low ice extent values. This was first done in a 2016 paper covering the SMMR/SSMI/SSMIS record for 1979–2015 (Parkinson and DiGirolamo, 2016) and was later updated through 2020 (Parkinson and DiGirolamo, 2021). These studies specify for each calendar month every time a new record high was reached for that month and every time a new record low was reached for that month. The results are striking, and since no new records were reached in 2021, the Parkinson and DiGirolamo (2021) results remain valid for the full 1979–2021 period. Specifically: 1) There has not been a single new record high monthly average Arctic sea ice extent for any of the 12 calendar months since 1986, when a record high was registered for October; 2) 93 new record low monthly average Arctic sea ice extents have occurred since 1986; 3) every one of the 12 calendar months has experienced at least one new record low since 2011; 4) on a yearly average basis, the last record high was in 1982, with 12 new record low yearly average sea ice extents since that time, the latest (and hence current record low for yearly averages) coming in 2020 (Parkinson and DiGirolamo, 2021). These results add compelling confirmation of the declining Arctic sea ice coverage.

Figure 5 presents the 43-year average annual cycle of monthly average Arctic sea ice extents along with the highest and lowest monthly average values reached for each month and the years in which those values occurred. For 3 months the record high came in 1979, the first year of the 43-year record, and for all 12 months the record high came in the first 8 years of the record, whereas all 12 record lows came in the last 10 years of the record (Figure 5). Still, for most months (December through June), the percent difference between the highest and lowest monthly average value over the 43 years is less than 18% (Figure 5).

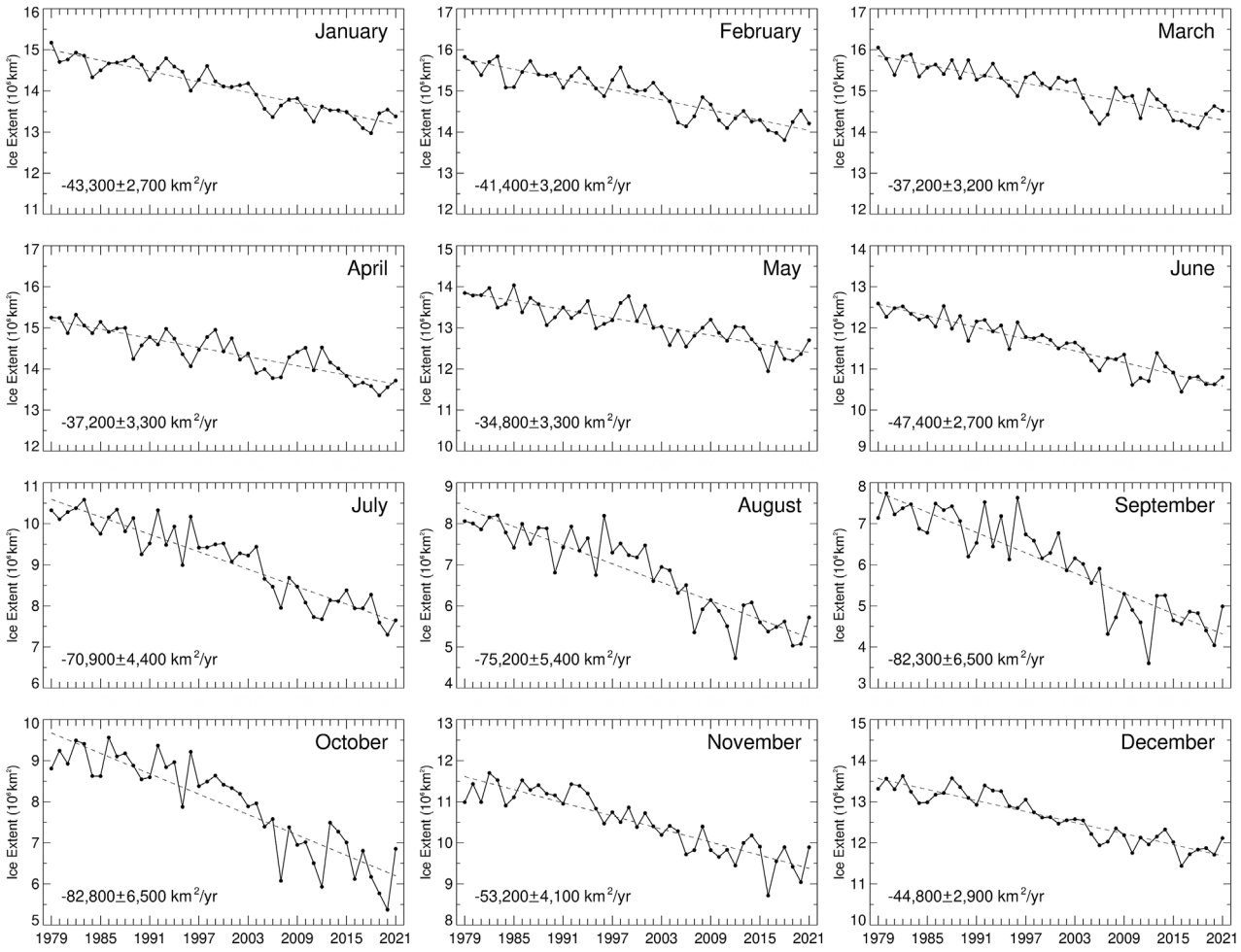

FIGURE 4
Arctic sea ice extents and trends, 1979–2021, for each of the 12 calendar months. The *y*-axis values vary for the different months, but in each case there is a range of 5 × 10^6 km^2, to allow ready visual comparison of the trend-line slopes.

3.2.3 Regional results

Examination of different regions within the Arctic sea ice cover reveals much greater variability in the regional results than in the results for the Arctic sea ice cover as a whole. Still, using nine regions identified in earlier studies (e.g., Parkinson et al., 1999), every one of the regions has a negative trend over the course of the 43-year 1979–2021 record (Figure 6). This is decidedly not the case for shorter time periods. For instance, the Gulf of St. Lawrence and Baffin Bay/Labrador Sea had visually prominent upward (positive) trends through 1994 and 1993, respectively, and the Bering Sea had a clearly positive trend even as late as 2013, for the 1979–2013 period (Figure 6). In fact, the trend values of the annual average Bering Sea ice extents since 1979 were consistently positive (although not statistically significant) from the start of the trend record, at 1979–1980, to the 1979–2002 period, then slightly negative from the 1979–2003 period to the 1979–2008 period, then positive again for 1979–2009 through 1979–2015, before turning negative at 1979–2016 and finally clearing a two-standard-deviation threshold with the 1979–2019 trend (Figure 7). Although the nine regions vary greatly in the sequence of their trend values, by the end of the record all nine have 1979–2021 negative trends that have magnitudes exceeding two standard deviations of the trend slope, some much more so than others (Figure 7). Furthermore, in a study covering the 42-year 1979–2020 period, Meier et al. (2022) subdivide the Arctic-wide sea ice cover into more regions and find negative trends for all 14 of them.

Many studies have examined sea ice conditions within individual regions and/or differences between regions. For instance, in the case of the Sea of Okhotsk, examinations have been done on the impacts on the sea ice cover of oceanic processes (e.g., Alfultis and Martin, 1987) and atmospheric conditions, including the Siberian High and Aleutian Low

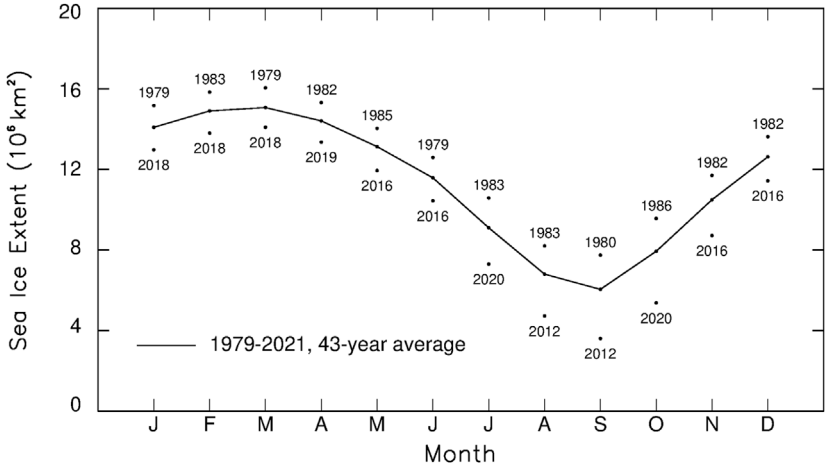

FIGURE 5
Average annual cycle of monthly-average Arctic sea ice extents over the 43-year period 1979–2021, along with the 43-year highest and lowest monthly-average values for each month and the years in which those highs and lows occurred.

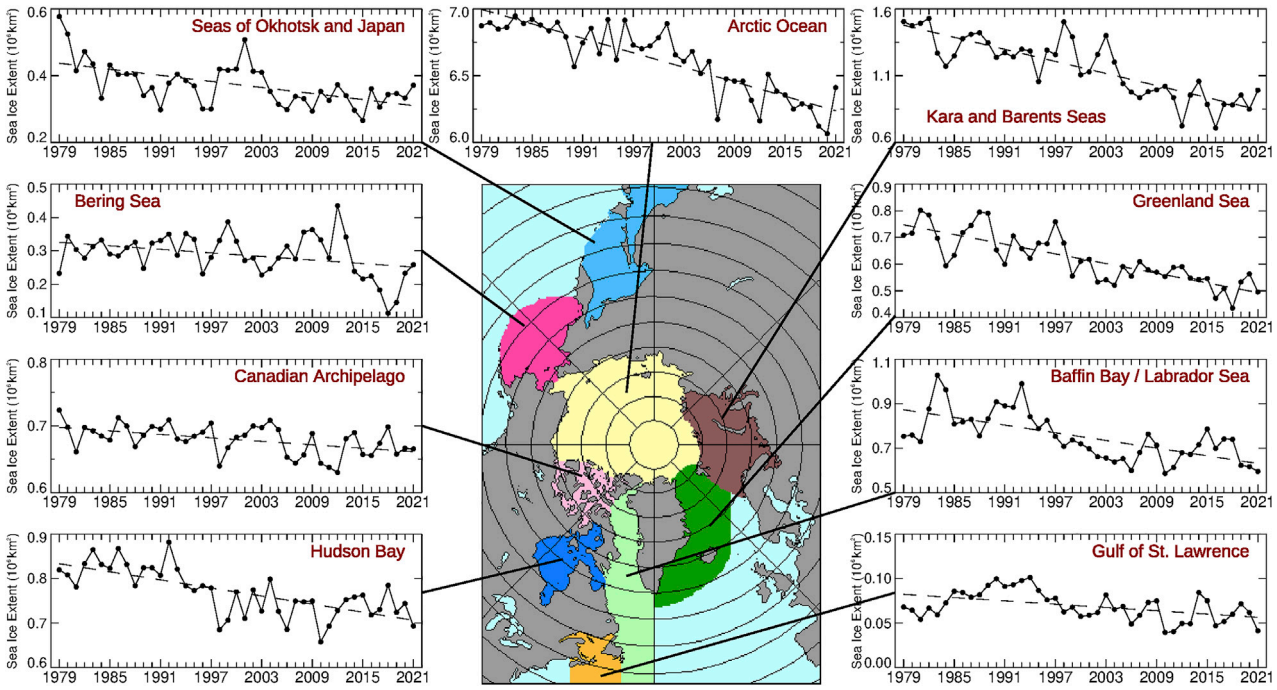

FIGURE 6
Yearly average sea ice extents and least-square trend lines, 1979–2021, for the following regions: Seas of Okhotsk and Japan; Bering Sea; Canadian Archipelago; Hudson Bay; Arctic Ocean; Kara and Barents Seas; Greenland Sea; Baffin Bay/Labrador Sea; and Gulf of St. Lawrence.

pressure systems (e.g., Parkinson, 1990; Rikiishi and Takatsuji, 2005), and the impact of sea ice formation, movement, and melting on the ocean (e.g., Nihashi et al., 2012). The contrast between generally rising sea ice extents in the Bering Sea and falling sea ice extents in the Seas of Okhostk and Japan in the early years of the record (Figure 6) have been examined in the

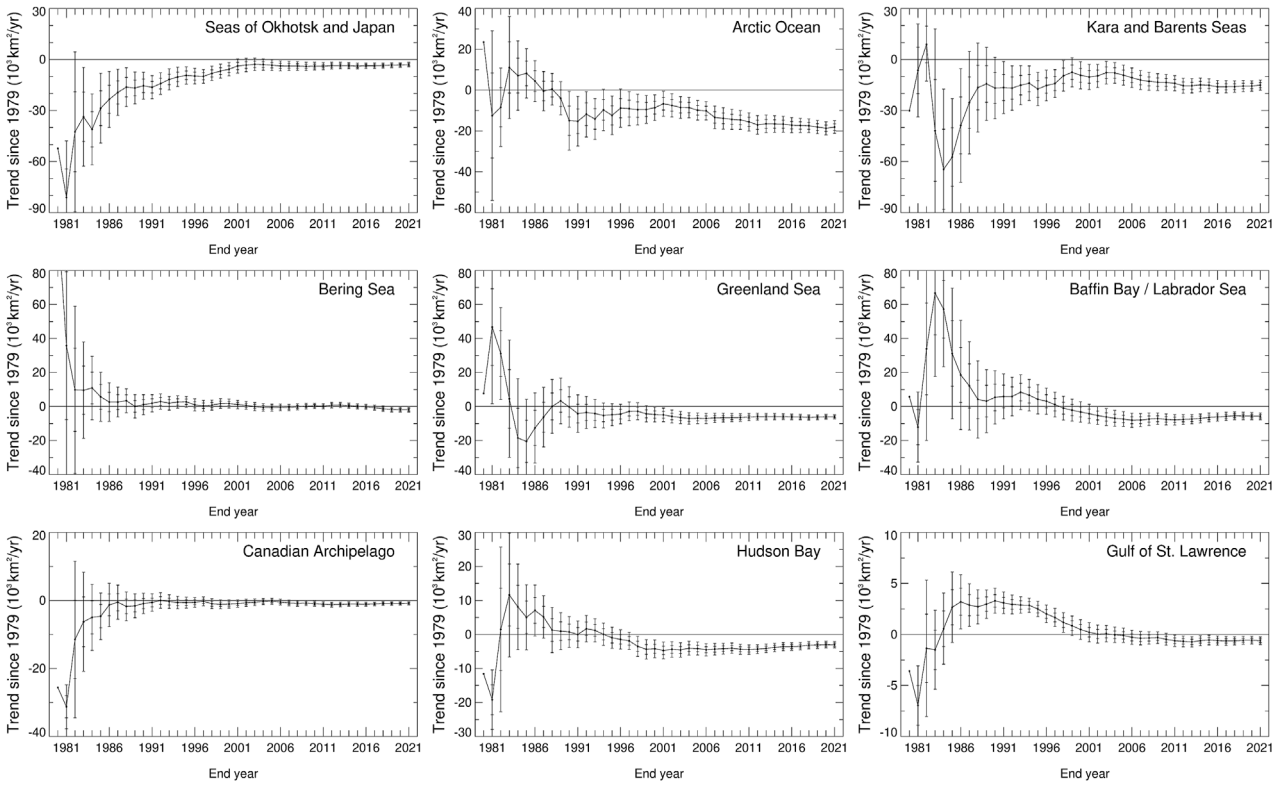

FIGURE 7
Linear-least-square slopes of the trend line in yearly average sea ice extents, from the 1979–1980 slope with only 2 years of data to the 1979–2021 slope with 43 years of data, for the following regions: Seas of Okhotsk and Japan; Arctic Ocean; Kara and Barents Seas; Bering Sea; Greenland Sea; Baffin Bay/Labrador Sea; Canadian Archipelago; Hudson Bay; and Gulf of St. Lawrence. The bars centered on each trend value after the first have ticks marking one and two standard deviations from the trend.

context of atmospheric circulation patterns (e.g., Cavalieri and Parkinson, 1987; Rikiishi and Takatsuji, 2005); the sea ice patterns in the Labrador Sea, Greenland Sea, and Barents Sea have been examined in connection with the atmospheric North Atlantic Oscillation (NAO) (Fang and Wallace, 1994); and the relationship between the late-autumn sea ice cover of the Kara and Barents Seas and the winter NAO have been further examined in a modeling study that reproduces the observed relationship through simulated atmospheric internal variability (Warner et al., 2020).

3.3 Length of the sea ice season

To examine trends at a pixel-by-pixel level rather than on a regional level, Parkinson (1992) introduced the concept of the length of the sea ice season, defined for each pixel as the number of days in the year when the pixel had a calculated sea ice concentration of at least 15%. This definition intentionally avoided the complications of having to determine a start and end date for the sea ice season, which can be highly controversial given the fluid nature of the sea ice cover and the fact that winds can lead to a pixel becoming free of ice briefly even in the midst of winter.

When initially introduced, the length of the sea ice season calculations were done for the 1979–1986 period of the SMMR record and were done with ice-concentration cutoffs of 30% and 50% as well as 15%. The 1979–1986 results found a coherent picture of trends that was extremely consistent irrespective of the choice of ice-concentration cutoff. Results showed that during 1979–1986 the sea ice season shortened in the marginal ice zones of the eastern hemisphere and the Greenland Sea but lengthened in much of the western hemisphere other than the Greenland Sea (Parkinson, 1992).

As the passive-microwave data set has lengthened with the addition of the SSMI and SSMIS data, the picture of the length of the sea ice season trends has become increasingly dominated by shortening sea ice seasons (e.g., see Parkinson, 2014 for the 1979–2013 results). By now, with a 43-year 1979–2021 record, comparison of the length of the sea ice season for the start and end years of the record shows substantial differences (Figure 8), and the 43-year trends show shortened sea ice seasons

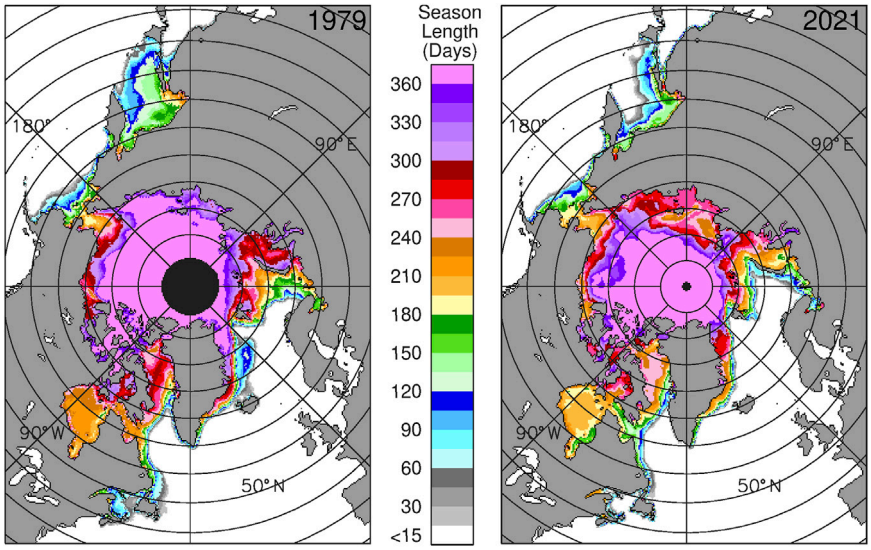

FIGURE 8
Length of the sea ice season in 1979 and 2021, as determined from satellite passive-microwave data by tallying, for each pixel, the number of days with calculated sea ice concentration at least 15%.

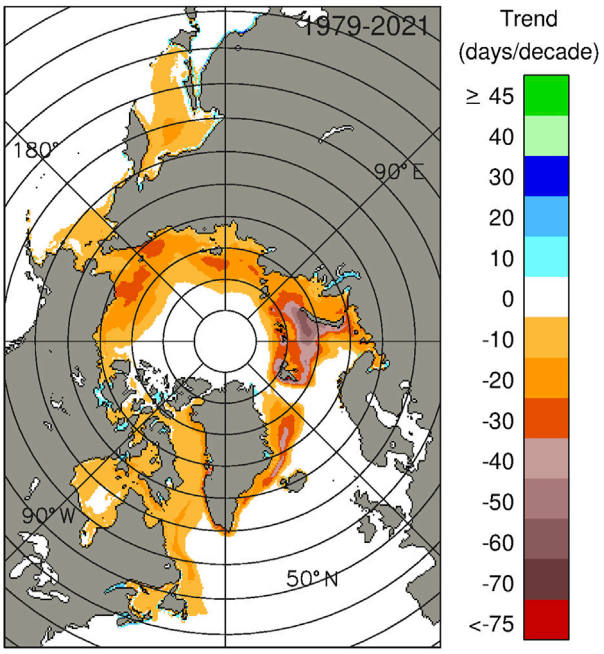

FIGURE 9
Trends in the length of the sea ice season, 1979–2021. For each pixel, the linear-least-square trend was calculated from the 43 yearly values of the length of the sea ice season at that pixel.

throughout almost the entire marginal sea ice zone, with very few locations having a lengthened sea ice season and those almost entirely along the coast and hence subject to contamination of the gridded pixels by land presence (Figure 9).

Visually, some particularly prominent contrasts between the 1979 and 2021 maps of sea ice season length are: 1) A sizeable portion of the eastern Sea of Okhotsk that had ice seasons lasting up to as much as 120 days in 1979 had no ice season at all in 2021; 2) in the northern Barents Sea to the north of Norway, there were locations with ice seasons exceeding 180 days in 1979 that had no ice season in 2021; 3) in the Arctic Ocean, the area with ice seasons exceeding 360 days is considerably smaller in 2021 than in 1979 (Figure 8). The highest magnitude trends for the 43-year period occur in the northern Barents Sea, where some pixels have negative trends with magnitudes exceeding 5 days/year (50 days/decade), equating to a shortening of the sea ice season by 210 days or more over the full 43 years (Figure 9).

4 Discussion

In significant part because of the convincing satellite-based record of Arctic sea ice decreases in the past several decades, sea ice has transitioned from being a relatively little-discussed climate variable to now often being a "poster child" for climate change discussions, frequently accompanied by pictures of forlorn polar bears seated uncomfortably on small remaining ice floes. This paper documents some important aspects of what the satellite record shows, including decreased sea ice concentrations, decreased sea ice extents, and decreased sea ice season lengths (Figures 1–9). However, these are far from the only important changes occurring in the Arctic sea ice cover.

Other satellite-based studies using passive-microwave data have documented substantial additional evidence of the declining Arctic sea ice cover, from decreases in multiyear ice coverage (Maslanik et al., 2011; Comiso, 2012; Bi et al., 2020) to earlier onset of melt of the

ice and/or its snow cover (Markus et al., 2009; Bliss and Anderson, 2014, 2018; Singh et al., 2021). Satellite radar altimetry has been used to document thinning of the Arctic ice in the 2002–2018 period (Mallett et al., 2021), and satellite laser and radar altimetry have been used to document thinning of the ice in the 2018–2021 period, with thinning found to be especially large for multiyear ice (Kacimi and Kwok, 2022). Submarine sonar records have documented Arctic sea ice thinning in the second half of the 20th century (Rothrock et al., 1999; Yu et al., 2004). While the submarine records extend much further back in time than the satellite records, they are far less comprehensive geographically and far less frequent and regular in their observations. Satellite altimetry provides likely the best hope for eventual long-term records of Arctic sea ice thickness, although obtaining ice thickness from the satellite data remains challenging, hindered by such complicating factors as snow cover on the ice and clouds above the ice (e.g., Kwok et al., 2021; Mallett et al., 2021).

Studies extending the sea ice record back to well before the start of the satellite era include the data-based study of Walsh et al. (2016), synthesizing the sparse pre-satellite records with the more complete modern records into a database extending back to 1850, and the model-based study of Schweiger et al. (2019), presenting a reconstruction of Arctic sea ice thickness and volume back to 1901. The Schweiger et al. (2019) reconstruction was produced by forcing the Pan-Arctic Ice Ocean Modeling and Assimilation System (PIOMAS) with atmospheric data.

In light of the expectation of warming and the very close tie between temperature and sea ice formation and decay, Arctic sea ice decreases had been expected, although, overall, the ice extent decreases have occurred at a noticeably faster rate than model simulations predicted (e.g., Stroeve et al., 2007; Stroeve et al., 2012). As the sea ice extent decreases, the resulting lessened reflection of solar radiation back to space contributes to further regional warming and hence to the much greater warming experienced in recent decades in the Arctic than over the globe as a whole (Rantanen et al., 2022).

The decreases in Arctic sea ice have consequences ranging far beyond contributing to Arctic warming, as the interconnectedness of the global climate system ensures that major changes in one region of the globe will influence other regions as well. A study done with the Goddard Institute for Space Studies (GISS) climate model even found that 37% of the global warming simulated for a doubling of atmospheric carbon dioxide was due explicitly to the inclusion of sea ice calculations in the model simulation (Rind et al., 1995). Furthermore, the sea ice calculations increased the simulated warming at all latitudes, not just in the polar regions (Rind et al., 1995). Both observational and modeling studies have suggested that Arctic sea ice changes could impact mid-latitude weather events (e.g., Francis et al., 2009; Francis and Vavrus, 2012; Mori et al., 2014; Nakamura et al., 2016; McCusker et al., 2017; Luo et al., 2019; Cohen et al., 2021; Sun et al., 2022) and even the Indian Ocean Dipole (Chen et al., 2021). Other studies have questioned how great the influence might be (e.g., Overland, 2016; Blackport et al., 2019; Blackport and Screen, 2021); but given the interconnectedness of the system, some influence is almost assured despite the fact that scientists have not yet sorted out exactly what and how great the influence is.

In addition to the climate and weather impacts, Arctic sea ice changes impact many polar species, including most prominently polar bears (e.g., Stirling and Parkinson 2006; Stirling and Derocher, 2012) but going well beyond polar bears to the entire polar ecosystem, both marine and terrestrial (e.g., Post et al., 2013). Impacts also extend to human economic activities, among them the increased viability of shipping routes through the Arctic (Smith and Stephenson, 2013; Stephenson and Smith, 2015).

The analyzed Antarctic changes over the past several decades are not nearly so well aligned with global warming and sea ice expectations (e.g., Parkinson, 2019; Meier et al., 2022), but the Arctic results quite compellingly show a warming Arctic (e.g., Rantanen et al., 2022) and lessened sea ice coverage (this paper), and the satellite data have been crucial in solidly establishing these results.

Data availability statement

The datasets analyzed in this study are publicly available. The ice concentration data are at doi:10.5067/8GQ8LZQVL0VL (Cavalieri et al., 1996), and the ice extent data are at doi: 10.5067/AE1XN2DQO5G4 (Parkinson and DiGirolamo, 2022).

Author contributions

CP conceived, wrote, revised, and edited the article.

Funding

This work was funded by the National Aeronautics and Space Administration (NASA) Earth Science Division.

Acknowledgments

The author greatly appreciates the help provided by Nick DiGirolamo of Science Systems and Applications, Inc. (SSAI) in generating the figures. Thanks also go to the organizers of this special issue on Women in Remote Sensing, highlighting the contributions that women have made to remote sensing science over the years.

Conflict of interest

The author declares that the research was conducted in the absence of any commercial or financial relationships that could be construed as a potential conflict of interest.

Publisher's note

References

Alfultis, M. A., and Martin, S. (1987). Satellite passive microwave studies of the Sea of Okhotsk ice cover and its relation to oceanic processes, 1978-1982. *J. Geophys. Res.* 92 (C12), 13013–13028. doi:10.1029/jc092ic12p13013

Barry, R. G., Serreze, M. C., Maslanik, J. A., and Preller, R. H. (1993). The Arctic sea ice-climate system: Observations and modeling. *Rev. Geophys.* 31 (4), 397–422. doi:10.1029/93rg01998

Bi, H., Liang, Y., Wang, Y., Liang, X., Zhang, Z., Du, T., et al. (2020). Arctic multiyear sea ice variability observed from satellites: A review. *J. Oceanol. Limnol.* 38, 962–984. doi:10.1007/s00343-020-0093-7

Blackport, R., and Screen, J. A. (2021). Observed statistical connections overestimate the causal effects of Arctic sea ice changes on midlatitude winter climate. *J. Clim.* 34, 3021–3038. doi:10.1175/jcli-d-20-0293.1

Blackport, R., Screen, J. A., van der Wiel, K., and Bintanja, R. (2019). Minimal influence of reduced Arctic sea ice on coincident cold winters in mid-latitudes. *Nat. Clim. Chang.* 9, 697–704. doi:10.1038/s41558-019-0551-4

Bliss, A. C., and Anderson, M. R. (2014). Snowmelt onset over Arctic sea ice from passive microwave satellite data: 1979-2012. *Cryosphere* 8, 2089–2100. doi:10.5194/tc-8-2089-2014

Bliss, A. C., and Anderson, M. R. (2018). Arctic sea ice melt onset timing from passive microwave-based and surface air temperature-based methods. *J. Geophys. Res. Atmos.* 123, 9063–9080. doi:10.1029/2018JD028676

Cavalieri, D. J., and Parkinson, C. L. (1987). On the relationship between atmospheric circulation and the fluctuations in the sea ice extents of the Bering and Okhotsk seas. *J. Geophys. Res.* 92 (C7), 7141–7162. doi:10.1029/jc092ic07p07141

Cavalieri, D. J., Parkinson, C. L., Gloersen, P., and Zwally, H. J. (1996). *Sea ice concentrations from Nimbus-7 SMMR and DMSP SSM/I-SSMIS passive microwave data, version 1. NASA National Snow and Ice Data Center Distributed Active Archive Center*. Boulder, Colorado, United States. updated yearly. doi:10.5067/8GQ8LZQVL0VL

Cavalieri, D. J., Parkinson, C. L., Gloersen, P., Comiso, J. C., and Zwally, H. J. (1999). Deriving long-term time series of sea ice cover from satellite passive-microwave multisensor data sets. *J. Geophys. Res.* 104 (C7), 15803–15814. doi:10.1029/1999JC900081

Cavalieri, D. J., Parkinson, C. L., DiGirolamo, N., and Ivanoff, A. (2012). Intersensor calibration between F13 SSMI and F17 SSMIS for global sea ice data records. *IEEE Geosci. Remote Sens. Lett.* 9 (2), 233–236. doi:10.1109/LGRS.2011.2166754

Chen, P., Sun, B., Wang, H., and Zhu, B. (2021). Possible impacts of December Laptev Sea ice on Indian Ocean Dipole conditions during spring. *J. Clim.* 34, 6927–6943. doi:10.1175/jcli-d-20-0980.1

Cohen, J., Agel, L., Barlow, M., Garfinkel, C. I., and White, I. (2021). Linking Arctic variability and change with extreme winter weather in the United States. *Science* 373 (6559), 1116–1121. doi:10.1126/science.abi9167

Comiso, J. C., Parkinson, C. L., Gersten, R., and Stock, L. (2008). Accelerated decline in the Arctic sea ice cover. *Geophys. Res. Lett.* 35, L01703. doi:10.1029/2007GL031972

Comiso, J. C. (2012). Large decadal decline of the Arctic multiyear ice cover. *J. Clim.* 25, 1176–1193. doi:10.1175/JCLI-D-11-00113.1

Draper, N. R., and Smith, H. (1981). *Applied regression analysis*. second edition. New York: John Wiley, 709 p.

Fang, Z., and Wallace, J. M. (1994). Arctic sea ice variability on a timescale of weeks and its relation to atmospheric forcing. *J. Clim.* 7, 1897–1914. doi:10.1175/1520-0442(1994)007<1897:asivoa>2.0.co;2

Francis, J. A., and Vavrus, S. J. (2012). Evidence linking Arctic amplification to extreme weather in mid-latitudes. *Geophys. Res. Lett.* 39, L06801. doi:10.1029/2012GL051000

Francis, J. A., Chan, W., Leathers, D., Miller, J. R., and Veron, D. E. (2009). Winter northern hemisphere weather patterns remember summer Arctic sea ice extent. *Geophys. Res. Lett.* 36, L07503. doi:10.1029/2009GL037274

Gloersen, P., Campbell, W. J., Cavalieri, D. J., Comiso, J. C., Parkinson, C. L., and Zwally, H. J. (1992). *Arctic and Antarctic sea ice, 1978-1987: Satellite passive-microwave observations and analysis*. Washington, D.C.: National Aeronautics and Space Administration, 290 p. NASA SP-511.

Johannessen, O. M., Miles, M., and Bjørgo, E. (1995). The Arctic's shrinking sea ice. *Nature* 376, 126–127. doi:10.1038/376126a0

Kacimi, S., and Kwok, R. (2022). Arctic snow depth, ice thickness, and volume from ICESat-2 and CryoSat-2: 2018-2021. *Geophys. Res. Lett.* 49, e2021GL097448. doi:10.1029/2021GL097448

Kay, J. E., L'Ecuyer, T., Gettelman, A., Stephens, G., and O'Dell, C. (2008). The contribution of cloud and radiation anomalies to the 2007 Arctic sea ice extent minimum. *Geophys. Res. Lett.* 35, L08503. doi:10.1029/2008GL033451

Koch, L. (1945). The East Greenland ice. *Medd. Groenl.* 130 (3), 1–374.

Kwok, R., Petty, A. A., Bagnardi, M., Kurtz, N. T., Cunningham, G. F., Ivanoff, A., et al. (2021). Refining the sea surface identification approach for determining freeboards in the ICESat-2 sea ice products. *Cryosphere* 15, 821–833. doi:10.5194/tc-15-821-2021

Luo, D., Chen, X., Overland, J., Simmonds, I., Wu, Y., and Zhang, P. (2019). Weakened potential vorticity barrier linked to recent winter Arctic sea ice loss and midlatitude cold extremes. *J. Clim.* 32, 4235–4261. doi:10.1175/jcli-d-18-0449.1

Maksym, T. (2019). Arctic and Antarctic sea ice change: Contrasts, commonalities, and causes. *Ann. Rev. Mar. Sci.* 11, 187–213. doi:10.1146/annurev-marine-010816-060610

Mallett, R. D. C., Stroeve, J. C., Tsamados, M., Landy, J. C., Willatt, R., Nandan, V., et al. (2021). Faster decline and higher variability in the sea ice thickness of the marginal Arctic seas when accounting for dynamic snow cover. *Cryosphere* 15 (5), 2429–2450. doi:10.5194/tc-15-2429-2021

Markus, T., Stroeve, J. C., and Miller, J. (2009). Recent changes in Arctic sea ice melt onset, freezeup, and melt season length. *J. Geophys. Res.* 114, C12024. doi:10.1029/2009JC005436

Maslanik, J. A., Serreze, M. C., and Barry, R. G. (1996). Recent decreases in Arctic summer ice cover and linkages to atmospheric circulation anomalies. *Geophys. Res. Lett.* 23 (13), 1677–1680. doi:10.1029/96GL01426

Maslanik, J., Stroeve, J., Fowler, C., and Emery, W. (2011). Distribution and trends in Arctic sea ice age through spring 2011. *Geophys. Res. Lett.* 38, L13502. doi:10.1029/2011GL047735

McCusker, K. E., Kushner, P. J., Fyfe, J. C., Sigmond, M., Kharin, V. V., and Bitz, C. M. (2017). Remarkable separability of circulation response to Arctic sea ice loss and greenhouse gas forcing. *Geophys. Res. Lett.* 44, 7955–7964. doi:10.1002/2017GL074327

Meier, W. N., Hovelsrud, G. K., van Oort, B. E. H., Key, J. R., Kovacs, K. M., Michel, C., et al. (2014). Arctic sea ice in transformation: A review of recent observed changes and impacts on biology and human activity. *Rev. Geophys.* 51, 185–217. doi:10.1002/2013RG000431

Meier, W. N., Stewart, J. S., Windnagel, A., and Fetterer, F. M. (2022). Comparison of hemispheric and regional sea ice extent and area trends from NOAA and NASA passive microwave-derived climate records. *Remote Sens.* 14, 619. doi:10.3390/rs14030619

Mori, M., Watanabe, M., Shiogama, H., Inoue, J., and Kimoto, M. (2014). Robust Arctic sea-ice influence on the frequent Eurasian cold winters in past decades. *Nat. Geosci.* 7, 869–873. doi:10.1038/NGEO2277

Nakamura, T., Yamazaki, K., Iwamoto, K., Honda, M., Miyoshi, Y., Ogawa, Y., et al. (2016). The stratospheric pathway for Arctic impacts on midlatitude climate. *Geophys. Res. Lett.* 43, 3494–3501. doi:10.1002/2016GL068330

Nghiem, S. V., Hall, D. K., Rigor, I. G., Li, P., and Neumann, G. (2014). Effects of Mackenzie River discharge and bathymetry on sea ice in the Beaufort Sea. *Geophys. Res. Lett.* 41, 873–879. doi:10.1002/2013GL058956

Nihashi, S., Ohshima, K. I., and Kimura, N. (2012). Creation of a heat and salt flux dataset associated with sea ice production and melting in the Sea of Okhotsk. *J. Clim.* 25, 2261–2278. doi:10.1175/jcli-d-11-00022.1

Overland, J. E. (2016). Is the melting Arctic changing midlatitude weather? *Phys. Today* 69 (3), 38–43. doi:10.1063/pt.3.3107

Parkinson, C. L., and Cavalieri, D. J. (1989). Arctic sea ice 1973-1987: Seasonal, regional, and interannual variability. *J. Geophys. Res.* 94 (C10), 14499–14523. doi:10.1029/jc094ic10p14499

Parkinson, C. L. (1990). The impact of the Siberian High and Aleutian Low on the sea-ice cover of the Sea of Okhotsk. *Ann. Glaciol.* 14, 226–229. doi:10.1017/s0260305500008636

Parkinson, C. L. (1992). Spatial patterns of increases and decreases in the length of the sea ice season in the north polar region, 1979-1986. *J. Geophys. Res.* 97 (C9), 14377–14388. doi:10.1029/92JC01367

Parkinson, C. L., Cavalieri, D. J., Gloersen, P., Zwally, H. J., and Comiso, J. C. (1999). Arctic sea ice extents, areas, and trends, 1978-1996. *J. Geophys. Res.* 104 (C9), 20837–20856. doi:10.1029/1999JC900082

Parkinson, C. L., and Comiso, J. C. (2013). On the 2012 record low Arctic sea ice cover: Combined impact of preconditioning and an August storm. *Geophys. Res. Lett.* 40, 1356–1361. doi:10.1002/grl.50349

Parkinson, C. L. (2014). Spatially mapped reductions in the length of the Arctic sea ice season. *Geophys. Res. Lett.* 41, 4316–4322. doi:10.1002/2014GL060434

Parkinson, C. L., and DiGirolamo, N. E. (2016). New visualizations highlight new information on the contrasting Arctic and Antarctic sea-ice trends since the late 1970s. *Remote Sens. Environ.* 183, 198–204. doi:10.1016/j.rse.2016.05.020

Parkinson, C. L. (2019). A 40-y record reveals gradual Antarctic sea ice increases followed by decreases at rates far exceeding the rates seen in the Arctic. *Proc. Natl. Acad. Sci. U. S. A.* 116 (29), 14414–14423. doi:10.1073/pnas.1906556116

Parkinson, C. L., and DiGirolamo, N. E. (2021). Sea ice extents continue to set new records: Arctic, Antarctic, and global results. *Remote Sens. Environ.* 267, 112753. doi:10.1016/j.rse.2021.112753

Parkinson, C. L., and DiGirolamo, N. E. (2022). *Arctic monthly sea ice extents. NASA National Snow and Ice Data Center Distributed Active Archive Center*. Boulder, Colorado, United States. doi:10.5067/AE1XN2DQO5G4 updated yearly

Post, E., Bhatt, U. S., Bitz, C. M., Brodie, J. F., Fulton, T. L., Hebblewhite, M., et al. (2013). Ecological consequences of sea-ice decline. *Science* 341 (6145), 519–524. doi:10.1126/science.1235225

Rantanen, M., Karpechko, A. Y., Lipponen, A., Nordling, K., Hyvarinen, O., Ruosteenoja, K., et al. (2022). The Arctic has warmed nearly four times faster than the globe since 1979. *Commun. Earth Environ.* 3, 168. doi:10.1038/s43247-022-00498-3

Rikiishi, K., and Takatsuji, S. (2005). On the growth of ice cover in the Sea of Okhotsk with special reference to its negative correlation with that in the Bering Sea. *Ann. Glaciol.* 42, 380–388. doi:10.3189/172756405781812619

Rind, D., Healy, R., Parkinson, C., and Martinson, D. (1995). The role of sea ice in 2 x CO_2 climate model sensitivity. Part 1: The total influence of sea ice thickness and extent. *J. Clim.* 8 (3), 449–463. doi:10.1175/1520-0442(1995)008<0449:trosii>2.0.co;2

Rothrock, D. A., Yu, Y., and Maykut, G. A. (1999). Thinning of the Arctic sea-ice cover. *Geophys. Res. Lett.* 26 (23), 3469–3472. doi:10.1029/1999gl010863

Schweiger, A. J., Wood, K. R., and Zhang, J. (2019). Arctic sea ice volume variability over 1901-2010: A model-based reconstruction. *J. Clim.* 32, 4731–4752. doi:10.1175/JCLI-D-19-0008.1

Simmonds, I., and Rudeva, I. (2012). The great Arctic cyclone of August 2012. *Geophys. Res. Lett.* 39, L23709. doi:10.1029/2012GL054259

Singh, R. K., Singh, T. V., and Singh, U. S. (2021). Long-term observation of the Arctic sea ice melt onset from microwave radiometry. *J. Indian Soc. Remote Sens.* 49, 357–364. doi:10.1007/s12524-020-01220-6

Smith, L. C., and Stephenson, S. R. (2013). New trans-Arctic shipping routes navigable by midcentury. *Proc. Natl. Acad. Sci. U. S. A.* 110 (13), E1191–E1195. doi:10.1073/pnas.1214212110

Stephenson, S. R., and Smith, L. C. (2015). Influence of climate model variability on projected Arctic shipping futures. *Earth's Future* 3, 331–343. doi:10.1002/2015ef000317

Stirling, I., and Derocher, A. E. (2012). Effects of climate warming on polar bears: A review of the evidence. *Glob. Chang. Biol.* 18, 2694–2706. doi:10.1111/j.1365-2486.2012.02753.x

Stirling, I., and Parkinson, C. L. (2006). Possible effects of climate warming on selected populations of polar bears (*Ursus maritimus*) in the Canadian Arctic. *Arctic* 59 (3), 261–275. doi:10.14430/arctic312

Stroeve, J., Holland, M. M., Meier, W., Scambos, T., and Serreze, M. (2007). Arctic sea ice decline: Faster than forecast. *Geophys. Res. Lett.* 34, L09501. doi:10.1029/2007GL029703

Stroeve, J. C., Kattsov, V., Barrett, A., Serreze, M., Pavlova, T., Holland, M., et al. (2012). Trends in Arctic sea ice extent from CMIP5, CMIP3 and observations. *Geophys. Res. Lett.* 39, L16502. doi:10.1029/2012GL052676

Sun, J., Liu, S., Cohen, J., and Yu, S. (2022). Influence and prediction value of Arctic sea ice for spring Eurasian extreme heat events. *Commun. Earth Environ.* 3, 172. doi:10.1038/s43247-022-00503-9

Taylor, J. R. (1997). *An introduction to error analysis: The study of uncertainties in physical measurements*. second edition. Sausalito, California: University Science Books, 327 p.

Vihma, T. (2014). Effects of Arctic sea ice decline on weather and climate: A review. *Surv. Geophys.* 35, 1175–1214. doi:10.1007/s10712-014-9284-0

Walsh, J. E. (2013). Melting ice: What is happening to Arctic sea ice, and what does it mean for us? *Oceanogr.* 26 (2), 171–181. doi:10.5670/oceanog.2013.19

Walsh, J. E., Fetterer, F., Stewart, J. S., and Chapman, W. L. (2016). A database for depicting Arctic sea ice variations back to 1850. *Geogr. Rev.* 107 (1), 89–107. doi:10.1111/j.1931-0846.2016.12195.x

Warner, J. L., Screen, J. A., and Scaife, A. A. (2020). Links between Barents-Kara sea ice and the extratropical atmospheric circulation explained by internal variability and tropical forcing. *Geophys. Res. Lett.* 47 (1), e2019GL085679. doi:10.1029/2019GL085679

Yu, Y., Maykut, G. A., and Rothrock, D. A. (2004). Changes in the thickness distribution of Arctic sea ice between 1958-1970 and 1993-1997. *J. Geophys. Res.* 109, C08004. doi:10.1029/2003JC001982

Zhang, J., Lindsay, R., Schweiger, A., and Steele, M. (2013). The impact of an intense summer cyclone on 2012 Arctic sea ice retreat. *Geophys. Res. Lett.* 40, 720–726. doi:10.1002/grl.50190

Zwally, H. J., Comiso, J. C., Parkinson, C. L., Cavalieri, D. J., and Gloersen, P. (2002). Variability of Antarctic sea ice 1979-1998. *J. Geophys. Res.* 107 (C5), 3041. doi:10.1029/2000JC000733

frontiers | Frontiers in Remote Sensing

TYPE Original Research
PUBLISHED 16 January 2023
DOI 10.3389/frsen.2022.1085808

OPEN ACCESS

EDITED BY
Steven Michael De Jong,
Utrecht University, Netherlands

REVIEWED BY
Ethan Theuerkauf,
Michigan State University, United States
Ranjeet John,
University of South Dakota, United States

*CORRESPONDENCE
Kelsey Huelsman,
ksh5s@virginia.edu

SPECIALTY SECTION
This article was submitted to Unoccupied Aerial Systems (UASs and UAVs), a section of the journal Frontiers in Remote Sensing

RECEIVED 31 October 2022
ACCEPTED 28 December 2022
PUBLISHED 16 January 2023

CITATION
Huelsman K, Epstein H, Yang X, Mullori L, Červená L and Walker R (2023), Spectral variability in fine-scale drone-based imaging spectroscopy does not impede detection of target invasive plant species. *Front. Remote Sens.* 3:1085808. doi: 10.3389/frsen.2022.1085808

Spectral variability in fine-scale drone-based imaging spectroscopy does not impede detection of target invasive plant species

Kelsey Huelsman[1]*, Howard Epstein[1], Xi Yang[1], Lydia Mullori[1], Lucie Červená[2] and Roderick Walker[3]

[1]Department of Environmental Science, Unversity of Virginia, Charlottesville, VA, United States, [2]Department of Applied Geoinformatics and Cartography, Charles University, Prague, Czechia, [3]Blue Ridge PRISM, Inc., Charlottesville, VA, United States

Land managers are making concerted efforts to control the spread of invasive plants, a task that demands extensive ecosystem monitoring, for which unoccupied aerial vehicles (UAVs or drones) are becoming increasingly popular. The high spatial resolution of unoccupied aerial vehicles imagery may positively or negatively affect plant species differentiation, as reflectance spectra of pixels may be highly variable when finely resolved. We assessed this impact on detection of invasive plant species *Ailanthus altissima* (tree of heaven) and *Elaeagnus umbellata* (autumn olive) using fine-resolution images collected in northwestern Virginia in June 2020 by a unoccupied aerial vehicles with a Headwall Hyperspec visible and near-infrared hyperspectral imager. Though *E. umbellata* had greater intraspecific variability relative to interspecific variability over more wavelengths than *A. altissima*, the classification accuracy was greater for *E. umbellata* (95%) than for *A. altissima* (66%). This suggests that spectral differences between species of interest and others are not necessarily obscured by intraspecific variability. Therefore, the use of unoccupied aerial vehicles-based spectroscopy for species identification may overcome reflectance variability in fine resolution imagery.

KEYWORDS

hyperspectral, spectral variability, invasive plants, drone, visible, near-infrared, discriminant analysis

1 Introduction

Globally, invasive plants pose significant threats to natural ecosystems (Gurevitch & Padilla, 2004) and biodiversity (Gaertner et al., 2009; Kimothi & Dasari, 2010; Peerbhay et al., 2016). Across the state of Virginia, invasive, non-native plants are radically altering natural environments by inhibiting the growth of native species upon which native wildlife and insects depend (Miller et al., 2013). These widespread changes in species composition also have broader impacts on soil chemistry and forest canopies, with effects on dynamics of carbon, nutrients, water, and energy (Liao et al., 2008; Lovett et al., 2016).

Ailanthus altissima (tree of heaven) is a notably widespread and harmful invasive tree not only in Virginia but across the U.S. (Burkholder, 2010). It tends to impact the soil chemistry and species composition of ecosystems in which it is present by: increasing nutrient cycling rates; increasing soil C, N, K, and Mg; and encouraging the encroachment of other plant species that thrive in high nutrient environments (Gómez-Aparicio & Canham, 2008). *Elaeagnus umbellata*

(autumn olive) is a common invasive shrub; as of 2017, it was found on 39,000 ha in the U.S. (Oliphant et al., 2017). It has a relationship with N-fixing endosymbionts and affects nitrifying (ammonium-oxidizing) microorganisms (Naumann et al., 2010; Malinich et al., 2017), and therefore is especially competitive in disturbed areas with N-poor soils (Malinich et al., 2017). In addition to its tolerance of nutrient-poor conditions, *E. umbellata* is also drought resistant and able to survive in a wide range of soil moisture conditions (Naumann et al., 2010; Malinich et al., 2017). Last, it can outcompete native plants after establishment due to its dense shading (Oliphant et al., 2017).

Land managers are making concerted efforts to control the spread of invasive plant species, a task that demands extensive ecosystem monitoring (Miller et al., 2013). Traditional approaches to ecosystem observation and monitoring are satellite-based and ground-based. Each approach, however, has caveats. Satellite imagery covers large areas but cannot provide fine-scale details, whereas ground surveying, despite its ability to provide fine-scale details, is labor intensive, and is challenging for surveying broad areas. Unoccupied aerial vehicles (UAVs) provide data on an intermediate scale, with much higher spatial resolution than satellite data and with more spatial coverage than ground surveys (Alvarez-Vanhard et al., 2021). As UAVs merge the benefits of more traditional satellite-based and ground-based monitoring, they are becoming an increasingly popular means to observe ecosystems, including invasive plant species monitoring (Sun & Scanlon, 2019).

Whereas UAVs are becoming increasingly popular as a vehicle for invasive plant species monitoring, spectroscopy has been and continues to be used for the remote sensing of plant and ecosystem observation. Spectroscopy, which includes a large number of narrow, contiguous bands, provides detailed spectral information (Kaufmann et al., 2008; Chance et al., 2016), which is influenced by differences in biophysical and biochemical characteristics of plants (Matongera et al., 2016; Yang et al., 2016; Wang et al., 2020), including: pigments (Mahlein et al., 2010; Xiao et al., 2014), such as chlorophyll (Asner & Martin, 2008; Thenkabail et al., 2014; Chance et al., 2016), anthocyanins, and carotenoids (Blackburn, 2007); plant water and vegetation stress (Thenkabail et al., 2014); and leaf N, P, and K (Mutanga et al., 2004; Asner & Martin, 2008; Thenkabail et al., 2014; Chance et al., 2016). Thus, spectroscopic data, which serve as an indication of plant chemical and structural properties, vary within and across ecosystems (Martin & Aber, 1997; Ustin et al., 2004).

Spectra are strongly related to certain biochemical and structural plant traits (Jacquemoud et al., 2009; Ollinger 2010; Kattenborn et al., 2019). Generally, greater spectral variation is associated with species or trait variation (Palmer et al., 2002). Certain wavelengths, such as those associated with upper-canopy pigments, water, and nitrogen, can be analyzed to differentiate among species. Intraspecific (within species) trait variability, however, is sometimes similar to or even greater than interspecific (among species) variation (Jung et al., 2010; Messier et al., 2010; Leps et al., 2011; Auger & Shipley 2013).

Though imaging spectroscopy has been previously used to identify individual plant species (Mishra et al., 2017), particularly invasive species (Chance et al., 2016; Aneece & Epstein, 2017; Kganyago et al., 2017; Skowronek et al., 2017), using spectroscopic sensors in concert with UAVs is a relatively new application for these technologies. Whereas a few UAV-based studies have been successful in identifying individual plant species, this has been accomplished in large monocultures where the target plant is easily distinguished from the surrounding vegetation (Huang & Asner, 2009).

Additionally, UAV imagery has much finer spatial resolution than satellites. It is not known, however, whether the very fine spatial resolution of data provided by UAVs is beneficial or detrimental to the process of differentiation. Smaller pixel size overcomes the challenge of averaged spectral properties of large pixel sizes over heterogeneous landscapes (Underwood et al., 2007). Peña et al. (2013), for example, found that increased resolution from 2.4 m to 1.2 m increased the differentiability of tree species by 25%. Similarly; Roberts et al. (2004) found that plant species were least distinct at the stand scale and most distinct at the branch scale, a scale similar to that of Peña et al. (2013). Detection of invasive plant species is likely improved by the fine spatial resolution that a UAV can achieve, as it does not require large and homogeneous infestation stands. With very fine spatial resolution, however, spectral variation among pixels will be greater than with coarser spatial resolution, which yields a smoothing effect of extreme values. It is expected, then, that spectral variation will be greater with decreasing spatial resolution. It is essential to understand the mechanisms that allow for the detection of target invasive plant species within these fine-resolution images.

To explore the fundamental questions of whether variability caused by fine-resolution spectroscopy enhances or impedes the ability to differentiate plant species, we collected images during the 2020 growing season from forest canopies in northwestern Virginia at the Blandy Experimental Farm (BEF), where invasive species are present and common. We address the following questions:

1) Over which wavelengths do intra-individual and intraspecific variability of target invasive plant species exceed interspecific variability?
2) Can the spectral signal from individual pixels within a tree crown be used to effectively detect target invasive plant species in an image?
3) How much does intra-individual and intraspecific variability of target invasive plant species impede the ability to differentiate among species?

2 Materials and methods

2.1 Study site

Blandy Experimental Farm (BEF), a biological field station owned by the University of Virginia, is located in the Shenandoah Valley in northwestern Virginia (39.06°N, 78.07°W). At 190 m elevation, BEF has a mean annual precipitation of 975 mm, a mean annual temperature of 12°C, and a mean July high temperature of 31.5°C. It contains 80 ha of old fields in various stages of succession (Bowers, 1997).

Aerial spectroscopic data collection took place over three 1-ha fields at BEF, based on their abundance of the invasive plant species of interest, *A. altissima* and *E. umbellata*, along with several other trees, shrubs, forbs, and grasses. The fields are in early-to mid-successional stages and are approximately 20, 25, and 30 years in age (Figure 1; green, blue, and purple polygons, respectively). Each field is located on low-relief topography. The early successional field (green polygon in Figure 1A; Figure 1B) contains abundant invasive shrubs, including *E. umbellata* within a heterogeneous matrix of forbs, graminoids, shrubs, and trees (including *A. altissima*). The 25-year-old early-to-mid-successional field (blue polygon in Figure 1A; Figure 1C) contains

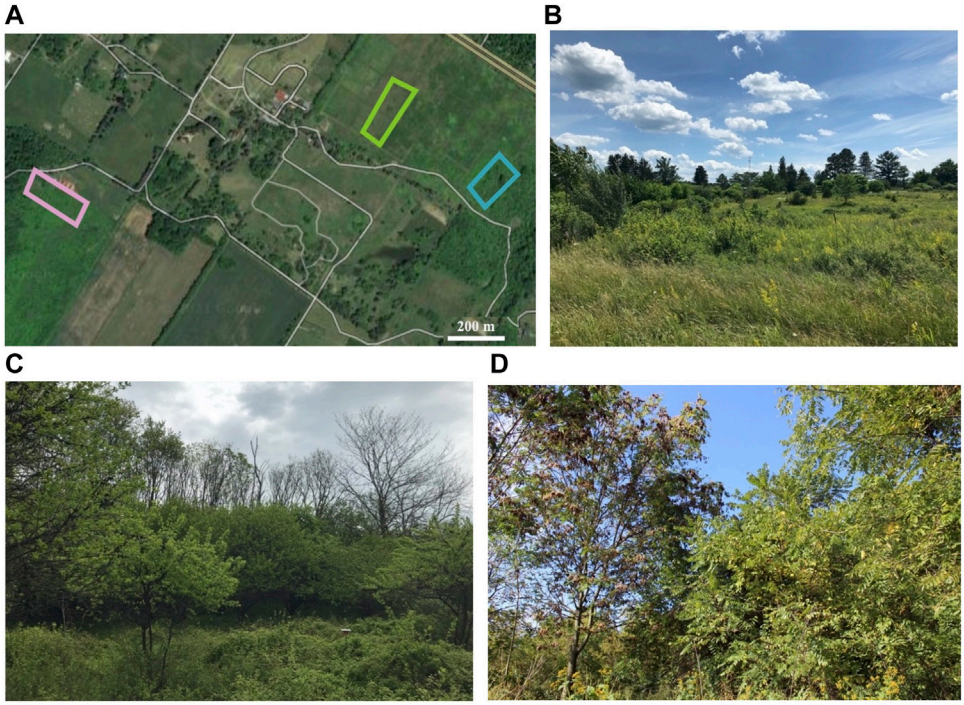

FIGURE 1
(A). Locations of fields in which spectroscopic data were collected during the 2020 growing season. A field in early secondary succession, an intermediate early-to-mid successional field, and a mid-successional field, shown in green, blue, and purple, respectively. **(B)**. Early successional field, which is about 20 years in age and contains abundant invasive shrubs, including *E. umbellata*. **(C)**. Mid-successional field, which is about 30 years in age and contains abundant invasive shrubs, along with *A. altissima*. **(D)**. Early-to-mid successional field, which is about 25 years in age and contains abundant invasive shrubs, including *E. umbellata*.

abundant invasive shrubs, including *E. umbellata*, within a heterogeneous matrix of forbs, graminoids, shrubs, and trees, but with more prevalent trees and shrubs than the early successional field. The mid successional field (purple polygon in Figure 1A; Figure 1D) contains abundant invasive shrubs, along with abundant *A. altissima*.

2.2 Data collection and image post-processing

Spectroscopic images were collected using a DJI Matrice 600 Pro drone equipped with a high-precision GPS system and an imaging spectrometer (Nano-Hyperspec, Headwall Photonics, Bolton, MA). The imaging spectrometer has a spectral range of 400–1,000 nm (in the visible and NIR portions of the electromagnetic spectrum), with a spectral resolution of 2–3 nm over 270 spectral bands. Flight plans over each field were created using universal Ground Control Software (UgCS), in which the UAV would fly in straight lines at a consistent height of 48 m above the ground to obtain images with 3 cm pixels. The imaging spectrometer was programmed to capture images along the flight plan using HyperSpec III software (Headwall Photonics, Bolton, MA).

Images were collected in the middle of the growing season in late June (DOY 178), midday between 10h and 15 h to reduce bidirectional reflectance distribution function (BRDF) effects and under consistent sky conditions. This date of collection was chosen for its proximity to when the National Ecological Observatory Network (NEON) collects spectroscopic images using a fixed-wing aircraft with coarser resolution (approximately 1 m resolution, compared to .03 m resolution). Collected spectroscopic images were adjusted for incoming and scattered solar radiation using a sampled dark reference at the time of flight and a grey scale reference tarp with known reflectance located in the flight scene, respectively. Using HyperSpec III software, terrain and perspective effects were removed with a 1-m digital elevation model provided by the US Geological Survey, and a mosaic of multiple images was created.

2.3 Image sampling

Individuals of 16 tree and shrub species and plant types (*A. altissima*, *Celastrus orbiculatus*, *E. umbellata*, *Gleditsia triacanthos*, *Galium verum*, *Maclura pomifera*, *Juglans nigra*, *Juniperus virginiana*, *Lonicera japonica*, *Lonicera maackii*, *Pinus virginiana*, *Rhamnus davurica*, *Rubus sp.*, *Solidago altissima*, *Symphoricarpos orbiculatus*, and graminoids) were identified in each of the three fields using a high-precision Trimble GPS with measurement accuracy of 0.5 m and used to catalogue individuals within imagery. If a given species was present in images of a field, up to eight individuals were selected for analysis. In cases where fewer than eight individuals were present, as many as were present were sampled.

Within the images, 15 well-lit and representative pixels were selected for spectral sampling from each individual. To remove outliers, a mean was taken across all wavelengths for each reflectance spectrum of a pixel, and a mean was calculated in a similar fashion for all 15 pixels from each individual. Any pixel within an individual that differed more than 25% from the mean

of the individual was removed from the dataset. This removed approximately 1% of pixels from observation.

2.4 Assessing variability due to fine-scale images

Both relative and absolute intraspecific (among individuals within a species) spectral variability were calculated. Relative variability was determined using the coefficient of variation (CV), which compares the variability among the means of each individual to the grand mean of the species. Absolute variability was determined using standard deviation (SD). CV and SD were calculated across all wavelengths for each species. Interspecific (among species) spectral variability was also quantified using CV and SD for comparison to intraspecific variability.

To differentiate *A. altissima* and *E. umbellata*, individuals from Fields E and M were used to train an algorithm with Partial Least Squares Discriminant Analysis (PLS-DA) using the pls R package (Liland et al., 2022). To create an algorithm to detect *A. altissima*, pixels known to be species other than *A. altissima* were recoded into "other" and were separated from *A. altissima*. The same process was followed for *E. umbellata*. Once an algorithm was established using reflectance at each wavelength to separate *A. altissima* and *E. umbellata* pixels in the component space from other species, it was applied to a testing dataset using Field EM, to test the effectiveness of each algorithm. The algorithms to detect *A. altissima* and *E. umbellata* with PLS-DA on the training data were applied to each pixel in the testing dataset. Because the pls R package applies the PLS-DA algorithm to each pixel in both components, only pixels categorized as the species of interest in both components were classified as the species of interest, while pixels categorized as the species of interest in only one component were not.

Then the percentage of pixels within each individual tree or shrub was calculated for each class, and if over half the pixels were classified as the species of interest, the individual was classified as the species of interest. If fewer than half the pixels were classified as the species of interest, the individual was classified as other species. This was done for all individuals using each algorithm to detect both *A. altissima* and *E. umbellata*. Following classification, omission error (false negatives), commission error (false positives), overall accuracy, and Matthew's Correlation Coefficient (MCC; Eq. 1) were calculated. MCC uses the balance of true positives (TP), true negatives (TN), false positives (FP), and false negatives (FN) and can range from −1 to 1, where -1 is entirely incorrect classification and 1 is entirely correct classification. An MCC value of 0 represents classification due to chance.

$$\frac{(TP*TN) - (FP*FN)}{\sqrt{(TP + FP)*(TP + FN)*(TN + FP)*(TN + FN)}} \quad (1)$$

3 Results

3.1 Intra-individual and intraspecific variability relative to interspecific variability

The CV of intra-individual variability exceeded the CV of interspecific variability at 454 nm, 514–663 nm and 694–714 nm in *A. altissima*, with the greatest ratio of relative intra-individual to interspecific variability of 1.42 occurring at 701 nm. The CV of intra-individual variability of *E. umbellata* did not exceed the CV of interspecific variability (Figure 2A). The SD of intra-individual variability exceeded the SD of interspecific variability in *A. altissima* at 530 nm, 570 nm, 574 nm, 583–645 nm, 696–714 nm, and 940 nm and in *E. umbellata* from 450 to 530 nm and 585–705 nm. The greatest ratio of absolute intra-individual to interspecific variability of 1.18 in *A. altissima* occurred at 703 nm and at 459 nm with a ratio of 1.35 in *E. umbellata* (Figure 2B).

The CV of intraspecific variability exceeded interspecific variability in *A. altissima* from 527 to 641 nm and 699–719 nm and in *E. umbellata* from 516 to 521 nm, 603–667 nm, and 690–703 nm. The greatest ratio of relative intraspecific to interspecific variability of 1.29 in *A. altissima* occurred at 703 nm and 1.29 in *E. umbellata* at 696 nm (Figure 3A). The SD of intraspecific variability in *A. altissima* exceeded the SD of interspecific variability at 603 nm, 607 nm, and from 701 to 719 nm and in *E. umbellata* from 450 to 530 nm and 585–705 nm. The greatest ratio of absolute intraspecific to interspecific variability of 1.16 in *A. altissima* occurred at 707 nm and 2.04 in *E. umbellata* at 690 nm (Figure 3B).

3.2 Detection using pixel spectra

The two components of the PLS-DA used to differentiate *A. altissima* pixels from all other species explained a total of 81% of variability in the training data (36% in component 1, and 45% in component 2). *A. altissima* separated most from other species in component 1 and overlapped considerably in the component space (Figure 4A). Wavelengths in the NIR region (763–935 nm) loaded heavily in component 1 (Figure 4B), and wavelengths in the green to yellow spectral region (525–590 nm) loaded heavily in component 2, with the greatest loading values occurring around 540–550 nm (Figure 4C). The two components of the PLS-DA to differentiate *E. umbellata* pixels from all other species explained a total of 72% of variability in the training data (46% in component 1, and 26% in component 2). Unlike *A. altissima*, which separated most in component 1, *E. umbellata* separated from other species in both components and overlapped much less in the component space (Figure 5A). Wavelengths in the blue to green spectral regions (450–510 nm) loaded heavily in component 1 in the negative direction, with a maximum magnitude occurring around 480 nm (Figure 5B). Wavelengths in the red edge region (705–725 nm) loaded most heavily in component 2 (Figure 5C).

Applying the algorithm to the test field to detect *A. altissima* provided an overall accuracy of 66%, with all 3 *A. altissima* individuals (5% of all individuals) falsely classified as not *A. altissima* and 17 individuals (29% of individuals) falsely classified as *A. altissima*. Of the 17 individuals incorrectly classified as *A. altissima*, 5 were *Lonicera maackii*, an invasive shrub, and 3 were *Maclura pomifera* and *Rhamnus davurica*. Overall accuracy to detect *E. umbellata* was 95%, with 7 out of 8 individuals correctly classified as *E. umbellata* and 2 individuals falsely classified as *E. umbellata* (Table 1).

3.3 Variability and differentiation

Wavelengths in the visible spectral region with a ratio of relative intra-individual to interspecific variability (CV) greater than 1 also loaded heavily in component 2 in the PLS-DA to separate *A. altissima* from other species in discriminant analysis (Figure 6A). Wavelengths in the visible and red edge

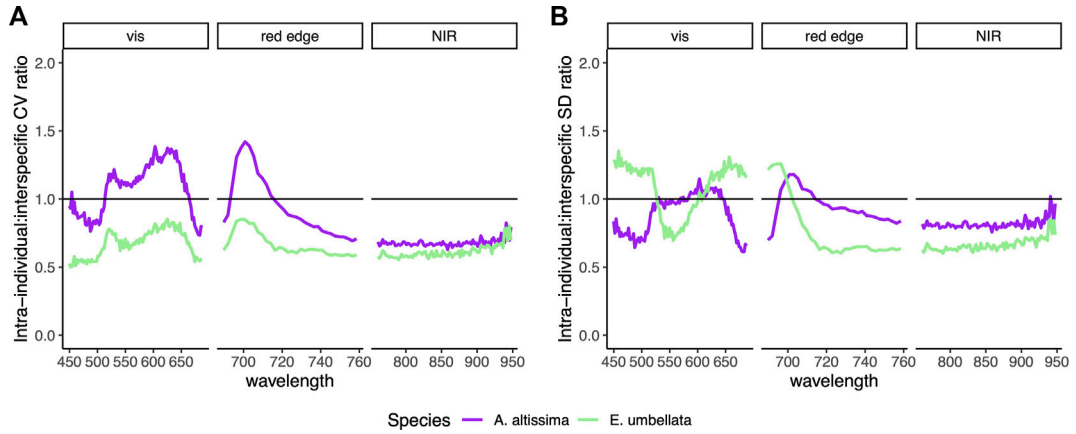

FIGURE 2
(A) Ratio of intra-individual (within individuals, averaged for a single species) to interspecific (among species) coefficient of variation (CV; the variation normalized by mean) across all wavelengths. **(B)** Ratio of intra-individual to interspecific standard deviation (SD) across all wavelengths. Spectra are split into visible, red edge, and near-infrared regions. Ratio values over 1 indicate variability that is greater on average within individuals of a species than among species.

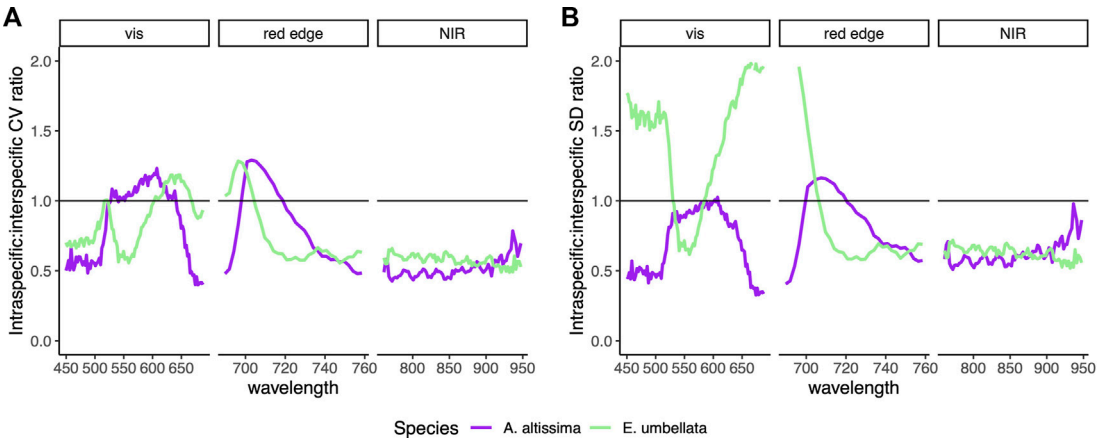

FIGURE 3
(A) Ratio of intraspecific (among individuals within a species) to interspecific (among species) coefficient of variation (CV; the variation normalized by mean) across all wavelengths. **(B)** Ratio of intraspecific to interspecific standard deviation (SD) across all wavelengths. Spectra are split into visible, red edge, and near-infrared regions. Ratio values over 1 indicate variability that is greater on average among individuals within a species than among species.

spectral regions with a ratio of absolute intra-individual to interspecific variability (SD) greater than 1 also loaded heavily in component 1 to separate *E. umbellata* from other species in discriminant analysis (Figure 6B).

Wavelengths in the visible spectral region with a ratio of relative intraspecific to interspecific variability (CV) greater than 1 also loaded heavily in component 2 to separate *A. altissima* from other species in discriminant analysis (Figure 7A). Wavelengths in the visible and red edge spectral regions with ratios of relative and absolute intraspecific to interspecific variability (CV and SD, respectively) greater than 1 also loaded heavily in component 1 to separate *E. umbellata* from other species in discriminant analysis (Figure 7B).

4 Discussion

We utilized both relative (CV) and absolute (SD) variability, as they provide complementary pieces of information; relative variability is calculated by normalizing differences by the mean absolute reflectance values. Normalizing using absolute reflectance values can inflate variability in wavelengths with generally low reflectance values (e.g., visible), compared to those wavelengths with typically higher reflectances (e.g., near infrared). Together however, these two indices provide a more holistic perspective of variability.

Spectral signals from individual pixels detect *E. umbellata* more accurately than *A. altissima*, even with some wavelengths exhibiting absolute intraspecific variability more than twice that of interspecific variability. Despite the overall degree of absolute intraspecific variability for *E. umbellata*, it exceeds interspecific variability over fewer wavelengths compared to *A. altissima*, and the relative variability within *E. umbellata* individuals (intra-individual variability) does not exceed interspecific variability for any wavelength. These patterns suggest that not only degree of variability but also frequency of high levels of variability, metric of variability, and scale at which variability occurs are all of importance.

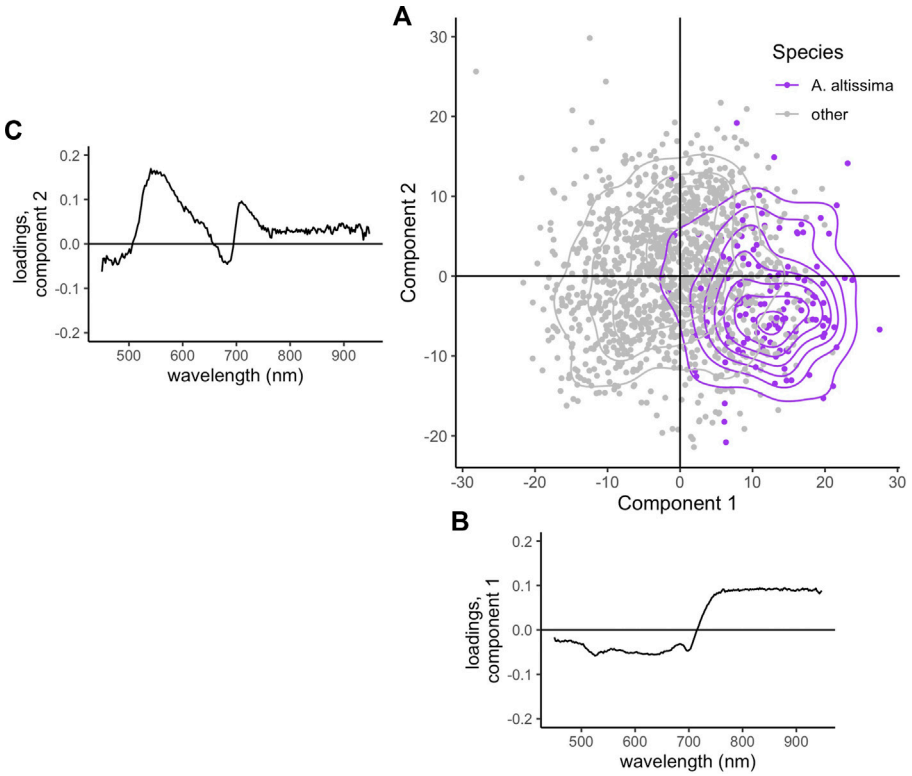

FIGURE 4
(A) Location of all *E. umbellata* training pixels (purple) and all other species (grey) in component space. **(B)** Shown below the *x*-axis is Component 1, and **(C)** beside the *y*-axis are the loadings for each wavelength in Component 2.

Spectral regions in which both relative and absolute intra-individual or intraspecific variability exceed interspecific variability are of interest, as they may hinder differentiation of species. Wavelengths at which both relative and absolute intra-individual variability exceed interspecific variability in *A. altissima* are 530 nm, 570 nm, 574 nm, 583–645 nm, and 696–714 nm. Wavelengths at which both relative and absolute intraspecific variability exceed interspecific variability in *A. altissima* are 603 nm, 607 nm, and 701–719 nm. Wavelengths at which both relative and absolute intraspecific variability exceed interspecific variability in *E. umbellata* are 516–521 nm, 603–667 nm, and 690–703 nm, whereas relative intra-individual variability in *E. umbellata* does not exceed interspecific variability for any wavelengths. Therefore overall variability likely does not impede classification of *E. umbellata* to the same extent as for *A. altissima*.

In addition to considering the degrees to which and frequencies with which intra-individual and intraspecific variability exceed interspecific variability, the specific wavelengths over which variability is high and how they relate to separation in PLS-DA are also important. Intra-individual variability exceeds interspecific variability over some wavelengths that are important for separation in PLS-DA for both species. For *A. altissima*, only relative intra-individual variability exceeds interspecific variability in wavelengths that are important for separation, while absolute intra-individual variability does not. For *E. umbellata*, only absolute intra-individual variability exceeds interspecific variability at wavelengths that are important for separation, while relative intra-individual variability does not. The lack of overlap between wavelengths important for separation and both high relative and absolute variability for each species suggests intra-individual variability likely does not influence classification.

Intraspecific variability also exceeds interspecific variability over some wavelengths that are important for separation in PLS-DA for both species. For *A. altissima*, only relative intraspecific variability exceeds interspecific variability in wavelengths that are important for separation, while absolute intra-individual variability does not. For *E. umbellata*, both absolute and relative intraspecific variability exceed interspecific variability for wavelengths that are important for separation. As both relative and absolute variability are high in wavelengths important for separation of *E. umbellata* from other species, intraspecific variability could potentially influence classification, but intra-individual variability likely does not.

The classification results suggest that differences between the species of interest and all other species are more important than the variability among all species, represented by interspecific variability. The amount of overlap in locations of pixels in the PLS-DA component space further supports that factors in addition to intra-individual and intraspecific variability may affect classification. Not only is classification of *E. umbellata* ultimately more accurate than that of *A. altissima*, but also *A. altissima* overlaps with other species more than *E. umbellata* does in the PLS-DA component space. The lower accuracy of *A. altissima* classification, as well as its location in the PLS-DA component space, suggests that similarities in spectra across

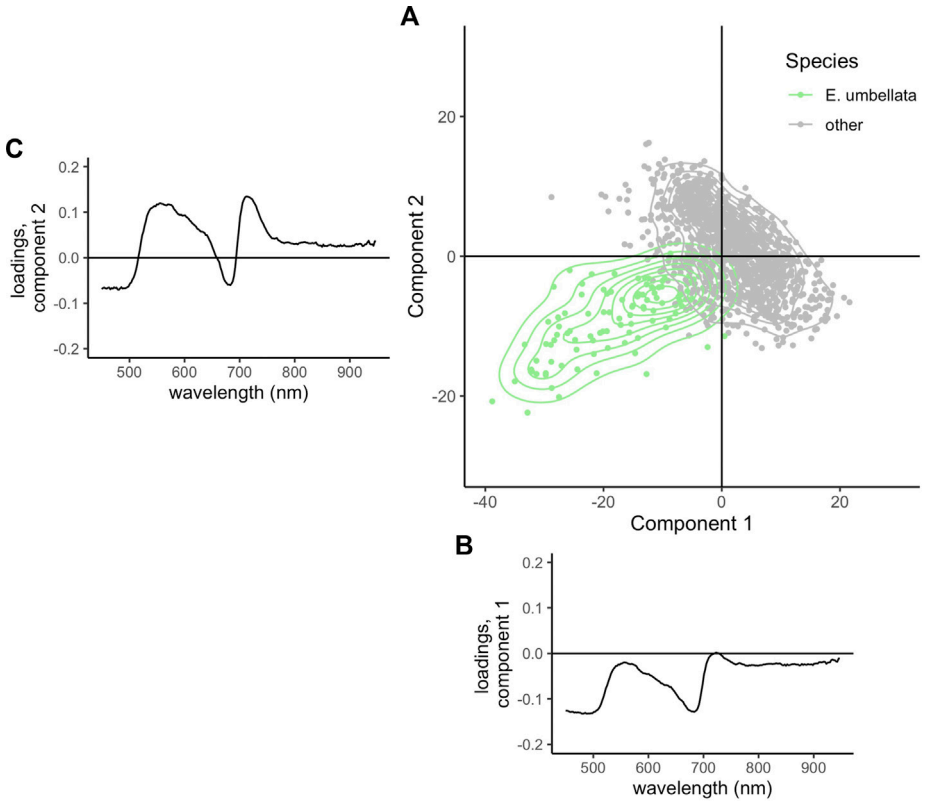

FIGURE 5
(A) Location of all *E. umbellata* training pixels (light green) and all other species (grey) in component space. **(B)** Shown below the *x*-axis is Component 1, and **(C)** beside the *y*-axis are the loadings for each wavelength in Component 2.

TABLE 1 Accuracy of the algorithm to detect A. altissima and E. umbellata in a test field. Individuals were classified based on the classification in each component. True positives and negatives and false positives and negatives are given as number of individuals out of 59 total individuals.

	True positive	True negative	Omission error (false negative)	Commission error (false positive)	Overall accuracy (%)	Matthew's correlation coefficient
A. altissima	0	39	3	17	66	−0.15
E. umbellata	7	49	1	2	95	.96

individuals of multiple species may have a greater impact on detection than intra-individual and intraspecific variability. This implies that *A. altissima* has more spectral features in common with other species, particularly *L. maackii, M. pomifera, and R. davurica*. The similarities of reflectance spectra among a subset of all species are not necessarily captured in the values of interspecific variability, which is why examining pixels in the PLS-DA component space is an additional useful tool.

Traditional hyperspectral data collection efforts are inadequate on the basis of either time or space. For example, satellite data, though temporally robust and therefore providing phenological data, are often too coarse in resolution to detect individual tree and shrub canopies. Collection by fixed-wing aircraft has a finer spatial resolution but is typically collected at much lower frequency, often on an annual basis. Fixed-wing aircraft data collection also requires an open field, which can be a challenge in some forest studies. UAV-based data collection combines the spatial and temporal benefits of each data collection method to provide data with high temporal and spatial resolution. Our results suggest the very fine, leaf-scale resolution of hyperspectral data collected by UAV does not impede differentiation, but rather, the differences among the species of interest and all other species are most important. As these data were collected mid-growing season when phenological differences are least noticeable, utilizing additional dates for differentiation will likely improve detection of invasive plant species.

According to a 2021 literature review (Dainelli et al., 2021), utilizing UAVs to identify invasive plants is not only novel but also tends to be used in concert with RGB, thermal, or multispectral sensors rather than hyperspectral sensors. Researchers who have used hyperspectral imagery to accomplish species recognition and detection have done so in Brazilian tropical forests (Miyoshi et al., 2020a; Miyoshi et al., 2020b), boreal forest (Nezami et al., 2020), and subtropical forest fragments (Sothe et al., 2019) to detect vines, conifers, and broadleaf trees. To our knowledge, this is the first effort to

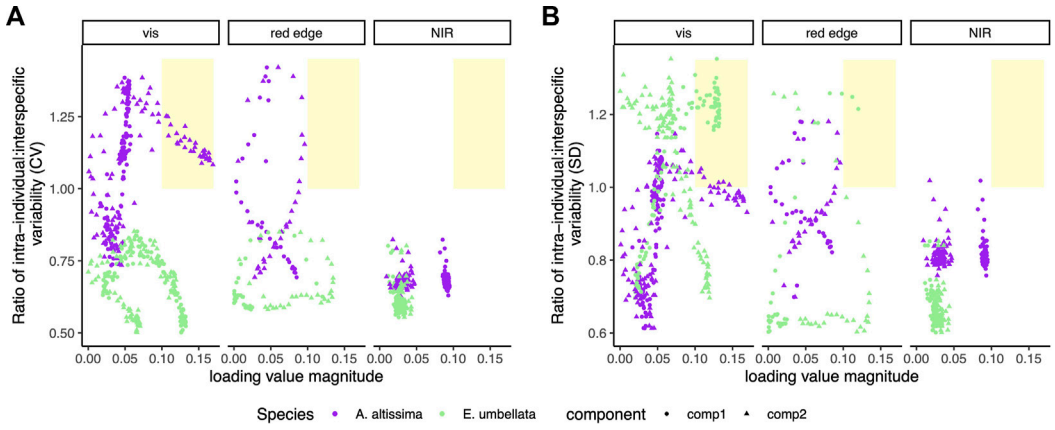

FIGURE 6
Magnitude of loading values for a given wavelength plotted against the ratio of relative and absolute intra-individual to interspecific variability, given as CV **(A)** and SD **(B)**, respectively, for that wavelength. Component 1 and component 2 are shown as circles and triangles, respectively, and *A. altissima* and *E. umbellata* are purple and green, respectively. Wavelengths that both load heavily and have high intra-individual variability relative to interspecific variability are shaded in yellow.

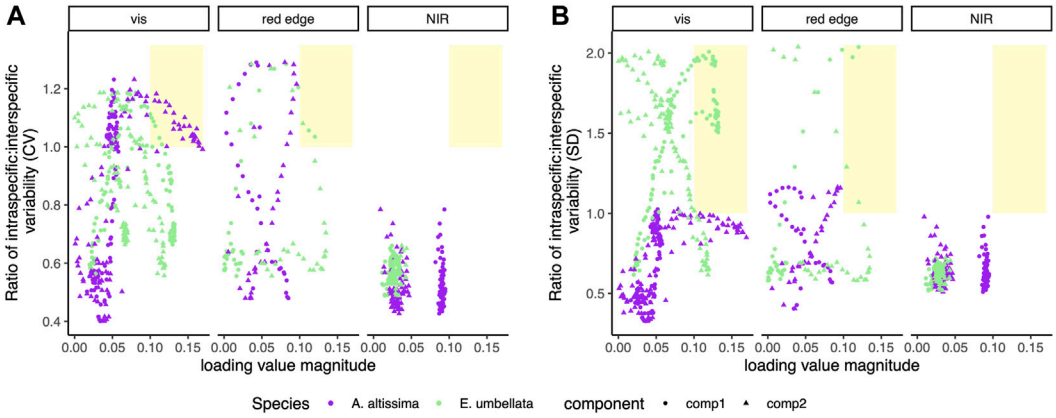

FIGURE 7
Magnitude of loading values for a given wavelength plotted against the ratio of relative and absolute intra-individual to interspecific variability, given as CV **(A)** and SD **(B)**, respectively, for that wavelength. Component 1 and component 2 are shown as circles and triangles, respectively, and *A. altissima* and *E. umbellata* are purple and green, respectively. Wavelengths that both load heavily and have high intra-individual variability relative to interspecific variability are shaded in yellow.

identify and map invasive plant species within heterogeneous vegetation communities using UAV-based hyperspectral data in plant communities typical of the eastern U.S.

We expect to produce an effective general methodology in utilizing spectroscopy to identify and locate targeted invasive plants, although we focused here on the invasive tree *A. altissima* and shrub *E. umbellata* from aerial images. These two invasive plants are commonly occurring across the U.S. and are particularly relevant to the understanding of the ecological impact of invasive species. The conclusion that differences between the species of interest and all other species is more important than intra-individual and intraspecific variability indicates that the temporal flexibility of sampling *via* UAV will aid in the effort of individual species detection. The ability to detect invasive plants allows for the potential to map and monitor their spread. Future work may build on this foundation to generalize detection of these plants in additional plant communities. The addition of spectroscopy in these efforts also provides the opportunity to incorporate an understanding of the variability in plant chemical and structural traits, from canopy to landscape scales.

Data availability statement

The raw data supporting the conclusion of this article will be made available by the authors, without undue reservation.

Author contributions

KH, HE, XY, and RW contributed to conception and design of the study. LČ contributed to field methods. KH and LM organized the

database. KH performed the statistical analysis. KH wrote the first draft of the manuscript. All authors contributed to manuscript revision, read, and approved the submitted version.

Funding

This research was funded by a grant from the USDA (NR 1833A7XXXXG001), the Virginia Space Grant Consortium, and the University of Virginia's Blandy Experimental Farm. LČ was supported by Ministry of Education of the Czech Republic, project LTAUSA18154: Assessment of ecosystem function based on Earth observation of vegetation quantitative parameters retrieved from data with high spatial, spectral and temporal resolution.

Conflict of interest

The authors declare that the research was conducted in the absence of any commercial or financial relationships that could be construed as a potential conflict of interest.

Publisher's note

References

Alvarez-Vanhard, E., Corpetti, T., and Houet, T. (2021). UAV & satellite synergies for optical remote sensing applications: A literature review. *Sci. Remote Sens.* 3, 100019. doi:10.1016/j.srs.2021.100019

Aneece, I., and Epstein, H. (2017). Identifying invasive plant species using field spectroscopy in the VNIR region in successional systems of north-central Virginia. *Int. J. Remote Sens.* 38, 100–122. doi:10.1080/01431161.2016.1259682

Asner, G. P., and Martin, R. E. (2008). Spectral and chemical analysis of tropical forests: Scaling from leaf to canopy levels. *Remote Sens. Environ.* 112, 3958–3970. doi:10.1016/j.rse.2008.07.003

Auger, S., and Shipley, B. (2013). Inter-specific and intra-specific trait variation along short environmental gradients in an old-growth temperate forest. *J. Veg. Sci.* 24, 419–428. doi:10.1111/j.1654-1103.2012.01473.x

Blackburn, G. A. (2007). Hyperspectral remote sensing of plant pigments. *J. Exp. Bot.* 58, 855–867. doi:10.1093/jxb/erl123

Bowers, M. A. (1997). University of Virginia's blandy experimental farm. *Bull. Ecol. Soc. Am.* 78, 220–225.

Burkholder, A. (2010). Seasonal trends in separability of leaf reflectance spectra for Ailanthus altissima and four other tree species. *Graduate Theses, Diss. Prob. Rep.* 77, 793–804. doi:10.14358/PERS.77.8.793

Chance, C. M., Coops, N. C., Plowright, A. A., Tooke, T. R., Christen, A., and Aven, N. (2016). Invasive shrub apping in an urban nvironment from yperspectral and LiDAR-derived attributes. *Front. Plant Sci.* 7, 1528. doi:10.3389/fpls.2016.01528

Dainelli, R., Toscano, P., Di Gennaro, S. F., and Matese, A. (2021). Recent advances in unmanned aerial vehicles orest emote ensing— systematic eview. Part II: Research pplications. *Forests* 12, 397. doi:10.3390/f12040397

Gaertner, M., Den Breeyen, A., Hui, C., and Richardson, D. (2009). Impacts of alien plant invasions on species richness in mediterranean-type ecosystems: meta-analysis. *Prog. Phys. Geogr.* 33, 319–338. doi:10.1177/0309133309341607

Gómez-Aparicio, L., and Canham, C. (2008). Neighborhood models of the effects of invasive tree species on ecosystem processes. *Ecol. Monogr.* 78, 69–86. doi:10.1890/06-2036.1

Gurevitch, J., and Padilla, D. K. (2004). Are invasive species a major cause of extinctions?. *Trends Ecol. Evol.* 19, 470–474. doi:10.1016/j.tree.2004.07.005

Huang, C.-Y., and Asner, G. P. (2009). Applications of remote sensing to alien invasive plant studies. *Sensors (Basel)* 9, 4869–4889. doi:10.3390/s90604869

Jacquemoud, S., Verhoef, W., Baret, F., Bacour, C., Zarco-Tejada, P. J., Asner, G. P., et al. (2009). PROSPECT+SAIL models: A review of use for vegetation characterization. *Remote Sens. Environ.* 113, S56–S66. doi:10.1016/j.rse.2008.01.026

Jung, V., Violle, C., Mondy, C., Hoffmann, L., and Muller, S. (2010). Intraspecific variability and trait-based community assembly. *J. Ecol.* 98, 1134–1140. doi:10.1111/j.1365-2745.2010.01687.x

Kattenborn, T., Fassnacht, F. E., and Schmidtlein, S. (2019). Differentiating plant functional types using reflectance: hich traits make the difference?. *Remote Sens. Ecol. Conservation* 5, 5–19. doi:10.1002/rse2.86

Kaufmann, H., Segl, K., Guanter, L., Hofer, S., Förster, K.-P., Stuffler, T., et al. (2008). "Environmental apping and nalysis program (EnMAP)–recent advances and status," in IGARSS 2008–2008 IEEE International Geoscience and Remote Sensing Symposium, Boston, MA, USA, 07–11 July, 2008.

Kganyago, M., Odindi, J., Adjorlolo, C., and Mhangara, P. (2017). Selecting a subset of spectral bands for mapping invasive alien plants: Case of discriminating parthenium hysterophorus using field spectroscopy data. *Int. J. Remote Sens.* 38, 5608–5625. doi:10.1080/01431161.2017.1343510

Kimothi, M. M., and Dasari, A. (2010). Methodology to map the spread of an invasive plant (*Lantana camara* L.) in forest ecosystems using Indian remote sensing satellite data. *Int. J. Remote Sens.* 31, 3273–3289. doi:10.1080/01431160903121126

Leps, J., Bello, F., Šmilauer, P., and Doležal, J. (2011). Community trait response to environment: Disentangling species turnover vs intraspecific trait variability effects. *Ecography* 34, 856–863. doi:10.1111/j.1600-0587.2010.06904.x

Liao, C., Peng, R., Luo, Y., Zhou, X., Wu, X., Fang, C., et al. (2008). Altered ecosystem carbon and nitrogen cycles by plant invasion: Meta-analysis. *New Phytol.* 177, 706–714. doi:10.1111/j.1469-8137.2007.02290.x

Liland, K. H., Mevik, B.-H., Wehrens, R., and Hiemstra, P. (2022). pls: Partial least squares and principal component regression. Available at: https://CRAN.R-project.org/package=pls (Accessed October 14, 2022).

Lovett, G., Weiss, M., Liebhold, A., Holmes, T., Leung, B., Lambert, K., et al. (2016). Nonnative forest insects and pathogens in the United States: Impacts and policy options. *Ecol. Appl.* 26, 1437–1455. doi:10.1890/15-1176

Mahlein, A.-K., Steiner, U., Dehne, H.-W., and Oerke, E.-C. (2010). Spectral signatures of sugar beet leaves for the detection and differentiation of diseases. *Precis. Agric.* 11, 413–431. doi:10.1007/s11119-010-9180-7

Malinich, E., Lynn-Bell, N., and Kourtev, P. S. (2017). The effect of the invasive Elaeagnus umbellata on soil microbial communities depends on proximity of soils to plants. *Ecosphere* 8, e01827. doi:10.1002/ecs2.1827

Martin, M. E., and Aber, J. D. (1997). High pectral resolution emote ensing of orest anopy lignin, itrogen, and cosystem rocesses. *Ecol. Appl.* 7, 431–443. doi:10.1890/1051-0761(1997)007

Matongera, T., Mutanga, O., and Lottering, R. (2016). Detection and mapping of bracken fern weeds using multispectral remotely sensed data: A review of progress and challenges. *Geocarto Int.* 33, 209–224. doi:10.1080/10106049.2016.1240719

Messier, J., McGill, B. J., and Lechowicz, M. J. (2010). How do traits vary across ecological scales? A case for trait-based ecology. *Ecol. Lett.* 13, 838–848. doi:10.1111/j.1461-0248.2010.01476.x

Miller, J. H., Manning, S. T., and Enloe, S. F. (2013). *A management guide for invasive plants in southern forests*. Asheville, NC: U.S. Department of Agriculture Forest Service, Southern Research Station.

Mishra, P., asaari, M., shahrimie, M., Herrero-Langreo, A., Lohumi, S., Diezma, B., et al. (2017). Close range hyperspectral imaging of plants: A review. *Biosyst. Eng.* 164, 49–67. doi:10.1016/j.biosystemseng.2017.09.009

Miyoshi, G., Imai, N. N., Garcia Tommaselli, A. M., Antunes de Moraes, M. V., and Honkavaara, E. (2020a). Evaluation of yperspectral multitemporal information to improve ree pecies identification in the highly diverse atlantic orest. Available at: https://10.3390/rs12020244 (Remote sensingAccessed November 21, 2022).

Miyoshi, G. T., Arruda, M., dos, S., Osco, L. P., Marcato Junior, J., Gonçalves, D. N., et al. (2020b). A novel deep earning ethod to identify single ree pecies in UAV-ased yperspectral images. *Remote Sens.* 12, 1294. doi:10.3390/rs12081294

Mutanga, O., Skidmore, A. K., and Prins, H. H. T. (2004). Predicting *in situ* pasture quality in the Kruger national Park, South Africa, using continuum removed absorption features. *Remote Sens. Environ.* 89, 393–408. doi:10.1016/j.rse.2003.11.001

Naumann, J. C., Bissett, S. N., Young, D. R., Edwards, J., and Anderson, J. E. (2010). Diurnal patterns of photosynthesis, chlorophyll fluorescence, and PRI to evaluate water stress in the invasive species, Elaeagnus umbellata Thunb. *Elaeagnus umbellata Thunb. Trees* 24, 237–245. doi:10.1007/s00468-009-0394-0

Nezami, S., Khoramshahi, E., Nevalainen, O., Pölönen, I., and Honkavaara, E. (2020). Tree pecies lassification of drone yperspectral and RGB magery with deep earning convolutional neural networks. *Remote Sens.* 12, 1070. doi:10.3390/rs12071070

Oliphant, A. J., Wynne, R. H., Zipper, C. E., Ford, W. M., Donovan, P. F., and Li, J. (2017). Autumn olive (*Elaeagnus umbellata*) presence and proliferation on former surface coal mines in Eastern USA. *Biol. Invasions* 19, 179–195. doi:10.1007/s10530-016-1271-6

Ollinger, S. V. (2011). Sources of variability in canopy reflectance and the convergent properties of plants. *New Phytol.* 189, 375–394. doi:10.1111/j.1469-8137.2010.03536.x

Palmer, M. W., Earls, P. G., Hoagland, B. W., White, P. S., and Wohlgemuth, T. (2002). Quantitative tools for perfecting species lists. *Environmetrics* 13, 121–137. doi:10.1002/env.516

Peerbhay, K., Mutanga, O., Lottering, R., Bangamwabo, V., and Ismail, R. (2016). Detecting bugweed (*Solanum mauritianum*) abundance in plantation forestry using multisource remote sensing. *ISPRS J. Photogramm. Remote Sens. C* 121, 167–176. doi:10.1016/j.isprsjprs.2016.09.014

Peña, M. A., Cruz, P., and Roig, M. (2013). The effect of spectral and spatial degradation of hyperspectral imagery for the Sclerophyll tree species classification. *Int. J. Remote Sens.* 34, 7113–7130. doi:10.1080/01431161.2013.817712

Roberts, D., Ustin, S., Ogunjemiyo, S., Greenberg, J., Dobrowski, S., Chen, J., et al. (2004). Spectral and structural measures of northwest orest egetation at eaf to landscape cales. *Ecosystems* 7, 545–562. doi:10.1007/s10021-004-0144-5

Skowronek, S., Ewald, M., Isermann, M., Van De Kerchove, R., Lenoir, J., Aerts, R., et al. (2017). Mapping an invasive bryophyte species using hyperspectral remote sensing data. *Biol. Invasions* 19, 239–254. doi:10.1007/s10530-016-1276-1

Sothe, C., Dalponte, M., Almeida, C. M., Schimalski, M. B., Lima, C. L., Liesenberg, V., et al. (2019). Tree pecies lassification in a highly diverse subtropical orest integrating UAV-ased photogrammetric point cloud and yperspectral ata. *Remote Sens.* 11, 1338. doi:10.3390/rs11111338

Sun, A. Y., and Scanlon, B. R. (2019). How can big ata and machine learning benefit environment and water management: Survey of methods, applications, and future directions. *Environ. Res. Lett.* 14, 073001. doi:10.1088/1748-9326/ab1b7d

Thenkabail, P. S., Gumma, M. K., Teluguntla, P., and Mohammed, I. A. (2014). Hyperspectral emote ensing of egetation and agricultural crops. *Photogramm. Eng. Remote Sens. (PE&RS)* 80, 697–723.

Underwood, E., Ustin, S., and Ramirez, C. (2007). A comparison of patial and pectral image resolution for apping nvasive lants in coastal California. *Environ.* 39, 63–83. doi:10.1007/s00267-005-0228-9

Ustin, S. L., Roberts, D. A., Gamon, J. A., Asner, G. P., and Green, R. O. (2004). Using maging pectroscopy to study cosystem rocesses and roperties. *BioScience* 54, 523–534. doi:10.1641/0006-3568(2004)054[0523:UISTSE]2.0.CO;2

Wang, Z., Chlus, A., Geygan, R., Ye, Z., Zheng, T., Singh, A., et al. (2020). Foliar functional traits from imaging spectroscopy across biomes in eastern North America. *New Phytol.* 228, 494–511. doi:10.1111/nph.16711

Xiao, Y., Zhao, W., Zhou, D., and Gong, H. (2014). Sensitivity nalysis of egetation eflectance to biochemical and biophysical variables at eaf, anopy, and regional cales. *IEEE Trans.* 52, 4014–4024. doi:10.1109/TGRS.2013.2278838

Yang, X., Tang, J., Mustard, J. F., Wu, J., Zhao, K., Serbin, S., et al. (2016). Seasonal variability of multiple leaf traits captured by leaf spectroscopy at two temperate deciduous forests. *Remote Sens. Environ.* 179, 1–12. doi:10.1016/j.rse.2016.03.026

frontiers | Frontiers in Remote Sensing

TYPE Original Research
PUBLISHED 18 January 2023
DOI 10.3389/frsen.2023.1063188

OPEN ACCESS

EDITED BY
Taifeng Dong,
Agriculture and Agri-Food Canada (AAFC), Canada

REVIEWED BY
Xiuzhi Chen,
Sun Yat-sen University, China
Miao Zhang,
Aerospace Information Research Institute (CAS), China

*CORRESPONDENCE
Jane Southworth,
jsouthwo@ufl.edu

SPECIALTY SECTION
This article was submitted to Remote Sensing Time Series Analysis, a section of the journal Frontiers in Remote Sensing

RECEIVED 06 October 2022
ACCEPTED 09 January 2023
PUBLISHED 18 January 2023

CITATION
Southworth J, Ryan SJ, Herrero HV, Khatami R, Bunting EL, Hassan M, Muir CS and Waylen P (2023), Latitudes and land use: Global biome shifts in vegetation persistence across three decades. *Front. Remote Sens.* 4:1063188. doi: 10.3389/frsen.2023.1063188

Latitudes and land use: Global biome shifts in vegetation persistence across three decades

Jane Southworth[1]*, Sadie J. Ryan[1], Hannah V. Herrero[2], Reza Khatami[1], Erin L. Bunting[3], Mehedy Hassan[1], Carly S. Muir[1] and Peter Waylen[1]

[1]Department of Geography, University of Florida, Gainesville, FL, United States, [2]Department of Geography, The University of Tennessee, Knoxville, TN, United States, [3]Department of Geography, Environment, and Spatial Sciences, Michigan State University, East Lansing, MI, United States

Introduction: The dynamics of terrestrial vegetation are shifting globally due to environmental changes, with potential repercussions for the proper functioning of the Earth system. However, the response of global vegetation, and the variability of the responses to their changing environment, is highly variable. In addition, the study of such changes and the methods used to monitor them, have in of themselves, been found to significantly impact the findings.

Methods: This research builds on a recently developed vegetation persistence metric, which is simple to use, is user-controlled to assess levels of statistical significance, and is readily reproducible, all designed to avoid these potential pitfalls. This study uses this vegetation persistence metric to present a global exploration of vegetation responses to climatic, latitudinal, and land-use changes at a biomes level across three decades (1982–2010) of seasonal vegetation activity via the Normalized Difference Vegetation Index (NDVI).

Results: Results demonstrated that positive vegetation persistence was found to be greater in June, July, August (JJA), and September, October, November (SON), with an increasing vegetation persistence found in the Northern Hemisphere (NH) over the Southern Hemisphere (SH). While vegetation showed positive persistence overall, this was not constant across all studied biomes. Overall forested biomes along with mangroves showed positive responses towards enhanced vegetation persistence in both the northern hemisphere and southern hemisphere. Contrastingly, desert, xeric shrubs, and savannas exhibited no significant persistence patterns, but the grassland biomes showed more negative persistence patterns and much higher variability over seasons, compared to the other biomes. The main drivers of changes appear to relate to climate, with tropical biomes linking to the availability of seasonal moisture, whereas the northern hemisphere forested biomes are driven more by temperature. Grasslands respond to moisture also, with high precipitation seasonality driving the persistence patterns. Land-use change also affected biomes and their responses, with many biomes having been significantly impacted by humans such that the vegetation response matched land use and not biome type.

Discussion: The use here of a novel statistical time series analysis of NDVI at a pixel level, and looking historically back in time, highlights the utility and power of such techniques within global change studies. Overall, the findings match greening trends of other research but within a finer scale both temporally and spatially which is a critical new development in understanding global vegetation shifts.

KEYWORDS
vegetation persistence, NDVI, land use, biome, AVHRR, greening, seasonality

Introduction

The dynamics of terrestrial vegetation are shifting globally due to environmental changes, with potential repercussions for the proper functioning of the Earth system and provision of ecosystem services. These changes are most apparent in the vegetation composition and/or structure, with shifts in species dominance and/or abundance, and changes in phenology. In some cases, there may be a complete loss of vegetation cover. Such changes can alter the local climate, hydrology, and soil properties, affecting a range of other ecosystem processes. The consequences of these vegetation changes can be far-reaching, impacting human societies through alterations in the provision of food, water, fuel, and timber resources, as well as affecting carbon storage and greenhouse gas emissions. Therefore, it is essential to monitor and quantify landscape level vegetation change to anticipate and adapt to the consequences of environmental change (Winkler et al., 2021; Potapov et al., 2022).

The vegetation of the Earth is constantly changing in response to a variety of biotic and abiotic factors. The study of vegetation change, and the methods used to monitor it, have in themselves been found to significantly impact the findings. Vegetation variability is a function of many factors, including climate, land use, and disturbance regime. Climate variability, for example, can cause changes in vegetation type, composition, and distribution. Land use can also impact vegetation, through activities such as deforestation, agriculture, and urbanization (Winkler et al., 2021; Friedl et al., 2022; Potapov et al., 2022). Disturbance regimes (such as fire or grazing) can also affect vegetation changes. Monitoring vegetation change is essential to understanding the health of our ecosystems. Vegetation provides critical ecosystem services such as carbon sequestration, water and soil conservation, and habitat for wildlife. Changes in vegetation can therefore have profound impacts on the environment and human wellbeing (Winkler et al., 2021).

There is large variability in the way vegetation responds to changes in the environment. This variability is due to a range of factors, including the species composition of vegetation, the growth form of plants (e.g., trees vs. shrubs), the level of disturbance, climatic conditions, and the soil type. For example, forests are more likely to respond slowly to environmental change than grasslands or savannas, due to the longer life span of trees. In addition, deciduous species are generally more responsive than evergreen species, as annual leaf drop means a quicker response to short-term changes in conditions. The magnitude and direction of vegetation change also varies regionally. In general, vegetation changes are more pronounced in the northern hemisphere than in the southern hemisphere, due to the greater land area and more diverse range of vegetation types. Finally, vegetation changes are typically more rapid in the tropics than in other regions, due to the higher levels of radiation and precipitation.

The study of vegetation change is essential to understanding the health of our ecosystems and the potential impacts of environmental change on human wellbeing. A variety of monitoring techniques are available to researchers, each with its own advantages and disadvantages. The selection of the most appropriate method(s) depends on the vegetation type of interest, the scale of analysis, and the desired level of detail. There are a variety of methods used to monitor vegetation change. Remote sensing techniques, such as satellite imagery, are commonly used to detect changes in vegetation cover. Ground-based monitoring, such as vegetation surveys, can provide detailed information on vegetation type and composition. Finally, model-based approaches can be used to simulate vegetation change under different scenarios. It is important to monitor vegetation change in order to anticipate and adapt to the consequences of environmental change.

Remote sensing is a powerful tool for monitoring vegetation change, as it allows for repeated measurements over large areas. Satellite-based remote sensing provides global coverage and can be used to track changes in vegetation cover and structure. By measuring the reflectance of vegetation in different spectral bands, we can produce an index known as the Normalized Difference Vegetation Index (NDVI). This index can be used to track changes in vegetation health and density over time. The Advanced Very High Resolution Radiometer (AVHRR) is a satellite sensor that is often used for this purpose. AVHRR data has been used to monitor trends in global vegetation cover since the early 1980s (de Jong et al., 2012; Cortes et al., 2021). More recently, satellite based NDVI products have become available from other sensors, such as the Moderate Resolution Imaging Spectroradiometer (MODIS). These products provide higher spatial resolution and more frequent coverage, making them ideal for tracking short-term changes in vegetation cover. Vegetation monitoring is important for a variety of reasons. Changes in vegetation cover can be used to track the progress of land degradation and deforestation. Additionally, NDVI data can be used to monitor the effects of drought and other environmental stresses on vegetation health. Ultimately, satellite remote sensing provides a cost-effective means of monitoring large areas of vegetation over time, which is essential for understanding and managing the world's natural resources (Southworth and Muir, 2021).

Vegetation is viewed as one of the more significant elements in the land-atmosphere system (Liu et al., 2020), involved in maintaining the water cycle, GPP (Gross Primary Productivity), and the fluxes of carbon between the atmosphere and land (Yao et al., 2019). In addition, vegetative biomass (above-ground) is also one of the chief sources of carbon sink, hence modulating ecosystem services *via* carbon sequestration (Tian et al., 2021). With the increase in the concentration of carbon dioxide (CO_2) in the atmosphere owing to anthropogenic stresses, the global vegetation cover and amount, often referred to as "greenness," is also increasing, and this greening is most often attributed to CO_2 fertilization (it speeds up photosynthesis and limits leaf transpiration of plants) and afforestation (Lenka and Lal, 2012). Studies have suggested an increase in greenness is expected to continue until 2,100, which will alter the dynamics of vegetation globally (Zhu et al., 2016; Liu et al., 2022). Thus, monitoring such change is indispensable given their susceptibility to anthropogenic pressures (land-use change and release of CO_2), including those associated with climatic variability (atmospheric temperature, humidity, and precipitation) and the importance of monitoring change and understanding the drivers is of critical importance (de Jong et al., 2012; 2013).

Global greening is a phenomenon that has been studied over the last few decades, and most evidence details such global greening signals from the beginning of the satellite record in the early 1980s

(Nemani and Running 1997; Nemani et al., 2003; de Jong et al., 2012; 2013; Zhu et al., 2016; Piao et al., 2020; Jiang et al., 2022). It was only the development of satellite technologies that led us to be able to monitor such changes globally and then link these greening signals to potential drivers of change. Globally, the dominant driver of greening which has been identified relates to CO_2 fertilization (Zhu et al., 2016; Piao et al., 2020) with additional drivers becoming important only at more regional scales. Most global greening studies have focused on satellite data as the variable under study, and most often have utilized vegetation metrics, such as NDVI, a measure which links to the amount and health of green vegetation biomass, often used as a proxy for net primary production (NPP) globally (Piao et al., 2020). Such greenness measures are thus used to identify trends of NDVI as measured over space and time, which may relate to vegetation type; fertilization of plant growth (in the form of more leaves, bigger leaves or even different species); the start, length and duration of the growing season; and thus the signal of greening measured, and also potential changes in crop production and multiple crop cycles. As such, the observed signal is an index representing a wide range of possible ground level changes, and while some studies do integrate limited ground-based data, given that many such studies are globally focused, real ground truthing is not always feasible. Modelling is frequently utilized to link the greening measures to possible drivers of change. Such modelling exercises clearly highlight the role of increased CO_2 concentration as the main driver of the observed greening, with matches over seasons and years.

Regional scale drivers have been identified as land cover change and changing management, such as reforestation, afforestation and improved agricultural practices (irrigation, improved crop types, intensification, etc.), nitrogen deposition and changing climate (especially changes in temperature and precipitation patterns and ranges) (Nemani and Running 1997; Xiao and Moody 2005; Zhu et al., 2016; Piao et al., 2020). Climatic drivers have also been identified, with different regions globally responding to different drivers. More climate focused drivers were identified by Xiao and Moody (2005), whereas Chen et al. (2019) focused on human land-use management, specifically related to agricultural lands and system improvements in China and India as the leading cause of greening. Across many drylands regions precipitation change is linked most directly to the greening signal (Herrmann et al., 2005) and concomitantly, linked to decreases in NPP related to large-scale droughts and a drying trend seen in the Southern Hemisphere (Zhao and Running, 2010).

One limitation of most of these studies of greening, as highlighted by de Jong et al. (2012) is related to the type of data used within such studies. Specifically, all of the greening studies have utilized remotely sensed time-series of vegetation indices, most of which have seasonality and serial auto-correlation, and while the studies attempted to correct for these trends using such techniques as harmonic regression, linear models with non-parametric components for seasonality, time series development from calendar days, and similar techniques, de Jong et al. (2012) found the results in terms of greening or browning, varied significantly, depending on the methods used. In addition, no single ideal method was identified and the difficulty of comparisons across different methods and outcomes was highlighted. In response to such difficulties, as identified by multiple researchers, the creation of a simple, statistically valid, and repeatable method has become increasingly warranted. NDVI time series can be used to study global vegetation change in several ways. For example, NDVI data can be used to map the areal extent of vegetation changes, as well as to quantify the magnitude and direction of those changes. NDVI data can also be used to assess the temporal patterns of vegetation change, allowing scientists to identify possible drivers of those changes. Finally, NDVI data can be used to estimate net primary productivity, which is an important measure of ecosystem health. NDVI time series also provides a way to assess the statistical significance of changes in vegetation greenness at a pixel level (Southworth and Muir, 2021). This is important for understanding whether the observed changes are due to natural variability or to anthropogenic activity.

Waylen et al. (2014) developed an NDVI-derived time-series of remotely sensed data products within which the user could define the appropriate statistical significance for their given research question. The directional persistence (D) metric allowed for the analysis of change in NDVI relative to a fixed benchmark value—which could be defined as a period, e.g., the beginning of a time series such as in analysis of greening, or an event, e.g., a drought, thereby facilitating a much more detailed and nuanced understanding of a given landscape. The D statistic borrows heavily from the theory associated with random walk processes (Wilson and Kirkby, 1980), in which each positive departure from the previous value in the time series cumulates the statistic by +1, and each negative departure by −1. The null hypothesis against which the statistic can be tested is that the statistics for a time series is not significantly different from zero. Critical values of the test statistic at various significance levels and for varying length of time series are derived from Monte Carlo simulations. The statistic has the benefits of being easy to calculate, readily interpreted in terms of the natural processes, comparable spatially, and the capability of being tested for significance by a method based in statistical theory. This metric has been tested at a smaller scale to understand vegetation persistence across Florida (Tsai et al., 2014) and within specific ecosystems types more broadly (Southworth et al., 2016; Bunting et al., 2018). Results have been very promising in terms of their innovation and in making the continuous vegetation metrics approach both more useful and more rigorous for use in global change studies.

Utilizing the length of the satellite data record and such measures as the D metric, such systematic quantification of vegetation change globally can be derived, and then interpreted with a view to better understand the spatial patterns and trends and how these relate to different global biomes and their land use diversity. Given the recent focus on greening papers to attempt to better determine the more regional-scale drivers of change, often completed at a more regional focus, e.g., China, India (Chen et al., 2019) or review papers which highlight the need for this regional level view at this time (Piao et al., 2020), our research will utilize this new metric, D, to evaluate global trends in vegetation persistence since the more reliable records of remotely sensed data began in the early 1980s. Specifically though, we will focus on the differences in patterns of vegetation persistence as a function of their biomes, and also the actual land use diversity at the pixel level, as determined by FAO data (FAO 2010 data available at FAO.org). Biomes are selected as the broad unit of analysis, as these represent similar ecosystems which, by definition, share comparable processes and major vegetation types wherever they are found. Studying at the level of biomes is important because they may display substantial variation in the extent of change, face different drivers of change, and there may be differences in the options for mitigating or managing these drivers. Biomes are important, but so is

land cover and related land use diversity. As such, even within our biomes, we will also account for the land use diversity, as stated by FAO in their 2010 global product (FAO.org), which will reflect the final use or end point of the time series in terms of land use with a reputable data source such as FAO which is readily available and downloadable for analysis. In addition, FAO products are considered comparable globally. As such, this research will cover over 30 years of vegetation persistence analysis at the biomes level, accounting for land use diversity and evaluating at a seasonal scale. Seasons are something that show different patterns and as such, it is important to both explain and account for these possible phenological signals.

This research addresses the following questions: 1) Globally, does the pattern of Vegetation Persistence, or D, match the findings demonstrated in previous global greening papers, and do the observable patterns and trends match up spatially? 2) Do these trends, most of which were analyzed at an annual time step, hold constant across seasons or do trends vary within the growing season? 3) How do the trends and patterns vary across the different biomes and are there obvious winners or losers to the greening trend? Lastly, 4) how does land use diversity impact these biomes-based trends and findings? Given the focus on the metric D as opposed to continuous indices measures of NDVI, this research bypasses many of the concerns of methods utilized potentially influencing the trend of the findings (de Jong et al., 2012), while also providing a very simple and easily understandable and replicable final product.

Materials and methods

Remote sensing of vegetation cover

The NDVI 3rd generation time-series product from the Global Inventory Monitoring and Modeling System (GIMMS) was used to study vegetation dynamics globally in this research. The NDVI product is constructed based on AVHRR observations and has a temporal resolution of 15 days. Spatial resolution of the NDVI product is five arc minutes which translates to about 8 km at the equator. In this research, data from 1982 to 2010 was used. While MODIS or other products could be used to extend the time series into more current time periods the importance of consistency of data source and the known variability between MODIS and AVHRR data make this problematic. As such, the goal of determining global environmental change signals with NDVI persistence metrics from 1982 to 2010 was considered ideal and a better data source to provide accuracy to this approach and to test the validity and robustness of this new persistence metric. The use of a benchmark value is required in this analysis as all pixel values are compared to this initial value. The AVHRR data series, beginning in 1982 and running through 2010 was used for this analysis, resulted in the first 5 years being utilized to create this benchmark. A five-year series removes the likelihood of selecting an anomalous year climatically and in creating a five-year average benchmark value from 1982 to 1986 data, a more reliable and robust measure of change can be obtained. It is worth noting that the selection of an anomalous or otherwise unrepresentative benchmark could invalidate the results and so care must be taken in this selection process.

First, the NDVI product's quality band was used to mask poor quality pixels. Then, any pixel with more than 20% masked observations of the whole time-series was excluded from the analysis. The missing values of the included pixels, due to quality masking, were gap-filled using a temporal interpolation. The biweekly NDVI values were aggregated to monthly composites based on per-pixel maximum NDVI value. To account for seasonality, the monthly NDVI composites were aggregated into four boreal seasons and the analysis was conducted independently for each season. The seasons included 1) December, January, February = DJF (boreal winter); 2) March, April, May = MAM (boreal spring); 3) June, July, August = JJA (boreal summer); and 4) September, October, November = SON (boreal autumn). Finally, seasonal NDVI composites were calculated based on maximum monthly values from the corresponding months.

Vegetation change analysis was conducted based on the time-series analyses of NDVI seasonal composites, as a proxy of vegetation abundance and health. Previous research has utilized the actual NDVI time-series information in studies of global vegetation change (Nemani and Running 1997; Xiao and Moody 2005; Zhu et al., 2016; Piao et al., 2020). One limitation of most of these studies of greening, as highlighted by de Jong et al. (2012) is related to the type of data used within such studies. Specifically, all of the greening studies have utilized remotely sensed time-series of vegetation indices, most of which have seasonality and serial auto-correlation (Herrmann et al., 2005; Zhao and Running, 2010). While the studies attempted to correct for these trends using such techniques as harmonic regression, linear models with non-parametric components for seasonality, time series development from calendar days, and similar techniques, de Jong et al. (2012) found the results in terms of greening or browning, varied significantly, depending on the methods used and so consistency in results and a global trend was impossible to ascertain from these studies. In addition, no single ideal method was identified and the difficulty of comparisons across different methods and outcomes was highlighted. In response to such difficulties, as identified by multiple researchers, the creation of a simple, statistically valid, and repeatable method has become increasingly warranted. As such, our research group has developed such a metric (see Waylen et al., 2014 for in depth discussion of metric development), which is central to this analysis, and which is known as directional persistence "D" (Tsai et al., 2014; Waylen et al., 2014; Southworth et al., 2016; Bunting et al., 2018). This metric is used to detect vegetation gain, loss, or no change at the pixel level using its time-series NDVI observations. To calculate directional persistence for a pixel, first, its initial or benchmark NDVI value was established based on its average NDVI value for 1982 to 1986. The five-year averaging was used to obtain robust benchmark values. Then, the pixel's NDVI values for the subsequent 23 years were compared to the benchmark value to identify the numbers of years with observed NDVI larger and smaller than the benchmark value. The persistence metric value, D, simply counts the difference between the number of years with NDVI observations larger and smaller than the benchmark. Thus, the persistence value of a pixel was calculated using the following equation:

$$D = \sum_{i=1}^{n} t_i;\ where\ t_i = \begin{cases} -1\ if\ NDVI_{BM} > NDVI_i \\ +1\ if\ NDVI_{BM} < NDVI_i \end{cases}$$

where n was equal to 23, i.e., the number of years after the benchmark period, $NDVI_{BM}$ and $NDVI_i$ were the benchmark and ith year NDVI values, respectively, and t_i indicates if NDVI of the ith year was larger or smaller than the benchmark NDVI. The persistence values were calculated independently per-pixel/per-season. This resulted in four

TABLE 1 Global biomes used for analysis and their descriptions, from the WWF (2020).

Biome	Description
Deserts and xeric shrublands	Less than 10 inches precipitation annually, evaporation exceeds rainfall. Extreme temperature variability due to lack of plants and global distribution. Woody plants characterize these regions to minimize water loss. Unusually adapted plants, like the giant cacti in North America.
Tropical and subtropical moist broadleaf forests	Large discontinuous patches around the equatorial belt. High rainfall and low temperature variability. Dominated by semi-evergreen and evergreen deciduous trees. Highest species diversity of any terrestrial biome. 5 layers: overstory with emergent crowns, medium layer of canopy, lower canopy, shrub level, and understory.
Tropical and subtropical dry broadleaf forests	Warm year-round with several hundred centimeters of rain. Long dry season. Deciduous trees dominate.
Tropical and subtropical coniferous forests	Low precipitation and moderate temperature variability. Diverse species of conifers. Thick, closed canopy with little underbrush. Fungi and ferns thrive instead.
Temperate Broadleaf and Mixed Forests	Temperate forests experience a wide variability in temperature and precipitation, which is why they are mixed species and types. 4 layers: canopy, lower layer of mature trees, shrub, understory of herbaceous plants.
Temperate Coniferous Forest	Evergreen forests in areas with warm summers and cool winters. Common in coastal areas with mild winters with heavy rainfall or inland with drier climate and montane areas. Understory (herbaceous and shrub) and overstory (trees). Highest biomass of the terrestrial biomes.
Boreal forests/Taiga	Low annual temperatures, high northern latitudes, most precipitation falls as snow. Nutrient poor soils and permafrost favor coniferous trees. Low species richness.
Tropical and subtropical grasslands, savannas and shrublands	Large expanses where rainfall limits extensive tree cover. Grassland dominated with scattered trees. Large mammal fauna.
Temperate grasslands, savannas and shrublands	Prairies and steppes. Differ from tropical grassland by being mostly devoid of trees except riparian forests. Large vertebrates.
Flooded grasslands and savannas	Large expanses of flood grasslands. Large congregation of waterbirds. Sensitive to hydrologic uses in these areas.
Montane grasslands and shrublands	High elevation grasses and shrubs. Can be tropical, subtropical, and temperate. High endemism.
Tundra	Treeless polar desert found at high latitudes. Sedges, health, and dwarf shrubs are supported, though vegetation is patchy. Most precipitation falls as snow in winter.
Mediterranean Forests, woodlands, and scrubs	Fire dependent plants. Occur in regions with hot, dry summers and cool, moist winters.
Mangroves	Short trees with prop-like roots that thrive in saline waterlogged areas along coasts.

global persistence products, corresponding to the four boreal seasons. Given the focus on the metric D as opposed to continuous indices measures of NDVI, this research bypasses many of the concerns of methods utilized potentially influencing the trend of the findings (de Jong et al., 2012), while also providing a very simple and easily understandable and replicable final product.

Statistical tests were conducted to investigate if the observed persistence value of a given pixel was statistically significant. Under the null hypothesis of no change, i.e., no vegetation gain or loss over the period of 1987–2010 with respect to the benchmark period of 1982–1986, t_i is expected to have a Bernoulli distribution with success and failure outcomes corresponding to $NDVI_i$ being larger or smaller than $NDVI_{BM}$, respectively. The t_i sequence represents a Bernoulli process with $p = 0.5$ and the total number of successes or failures would follow a binomial distribution (with $n = 23$ and $p = 0.5$). Therefore, the persistence value, D, would follow a random walk process with the distribution of values represented by Pascal's triangle, which can be used to identify the critical values of statistical tests (Waylen et al., 2014). Based on Pascal's triangle, for $n = 23$, D values larger than 10 or smaller than −10 are statistically significant at a significance level of 0.05. Accordingly, the D values in the persistence product outputs were categorized to positive significance ($n = \geq 10$), negative significance ($n = \leq -10$), and not significant ($n = -9$ to $+9$). This resulted in four global persistence significance products, corresponding to the four boreal seasons. This analysis uses a high threshold to indicate significance of the D statistic for the Persistence metric. Utilizing a rigorous threshold enables detection of pixels in which there has been significant change in vegetation dynamics over the study period, as compared to the baseline. This approach emphasizes identification of long-term shifts in vegetation greenness and is less concerned with small-scale individual events that impact local areas. To better capture pixels with significant change in NDVI for individual events, it is possible to adjust the baseline values and temporal scale, though given the global extent of this study it is not possible to account for all local level change in NDVI.

Biomes

This study used the World Wildlife Fund (WWF) terrestrial ecoregions (biomes) data (Olson et al., 2001). This data is archived as a part of the Millennium Ecosystem Assessment (MEA) project, which seeks to assess the consequences of ecosystem change in the context of human wellbeing ("Millennium Ecosystem Assessment," 2005). The MEA project details conditions and trends of the world's various ecosystems and their resultant ecosystem services. It also supports a scientific basis for conservation and sustainable use of ecosystems. The ecoregions data comes from a

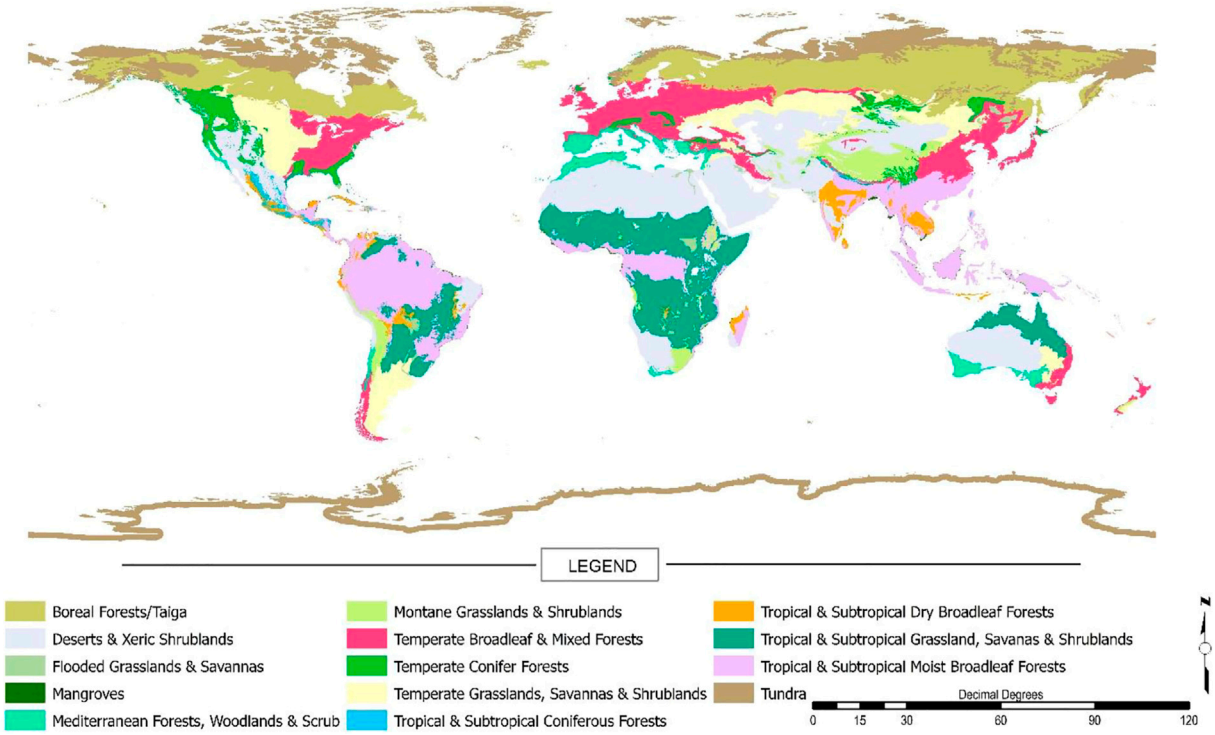

FIGURE 1
Map of the global distribution of the fourteen WWF designated biomes WWF (2020).

shapefile of WWF designated biomes globally (Olson et al., 2001). There are fourteen defined global biomes (Table 1), and their global distribution is highlighted in Figure 1. Biomes were selected as the unit of analysis given that these ecosystems share dominant vegetation types wherever they are found, most often based on similar biophysical processes and climatic regimes. In addition, studying at the level of biomes is important because they display substantial variation in the extent of change, they face different drivers of change, and there may be differences in the options for mitigating or managing such changes.

Utilizing the length of the satellite data record and the D metric, systematic quantification of vegetation change globally can be derived, and then interpreted with a view to better understand the spatial patterns and trends and how these relate to different global biomes as defined here from the WWF product. Specifically, we will focus on the differences in patterns of vegetation persistence as a function of biome type. Biomes are selected as the broad unit of analysis, as these represent similar ecosystems which, by definition, share comparable processes and major vegetation types wherever they are found. Studying at the level of biomes is important because they may display substantial variation in the extent of change, face different drivers of change, and there may be differences in the options for mitigating or managing these drivers. As such, this research will cover over 30 years of vegetation persistence analysis at the biomes level which is calculated from the global persistence product we created, extracted for each of the 14 biome types. In addition, these biomes are each evaluated at a seasonal scale (DJF, MAM, JJA, and SON) as seasons are something that show different patterns and as such, it is important to both explain and account for these possible phenological signals. Therefore, the created products for analysis and statistical comparison are the persistence patterns for each of the 14 WWF biomes (Table 1; Figure 1) for each of our four seasons, with statistical significance further summarized at a pixel scale and presented for both negative and positive vegetation persistence.

FAO land use diversity data

Information on global land use is of paramount importance within this analysis. Determining biome type does not mean that the land use or land cover matches this type as in many locations land cover change because of changes in land use has already occurred (Winkler et al., 2021; Friedl et al., 2022; Potapov et al., 2022). Therefore, in order to account for the differences as predicted by biomes based on climate and biophysical factors, versus the actual land use, an additional data set was needed. Global data on land use is collected by the Food and Agriculture Organization (FAO) of the United Nations and provides a standardized methodology for land use classification and mapping globally. Given this study was undertaken at a global scale a reputable and readily available global land use data set was needed. The data used for this study was the global land use data product for 2010 which was selected as it related to the end point of the time series used (fao.org website for data download, last accessed September 2022) and so could be used to indicate the actual land use diversity within each biome type. The land use classes available were at a very broad scale and were agriculture, grazing, wetlands, urban, forest, natural non-forest, and open water. The use of the FAO data, allowed us to

10.3389/frsen.2023.1063188

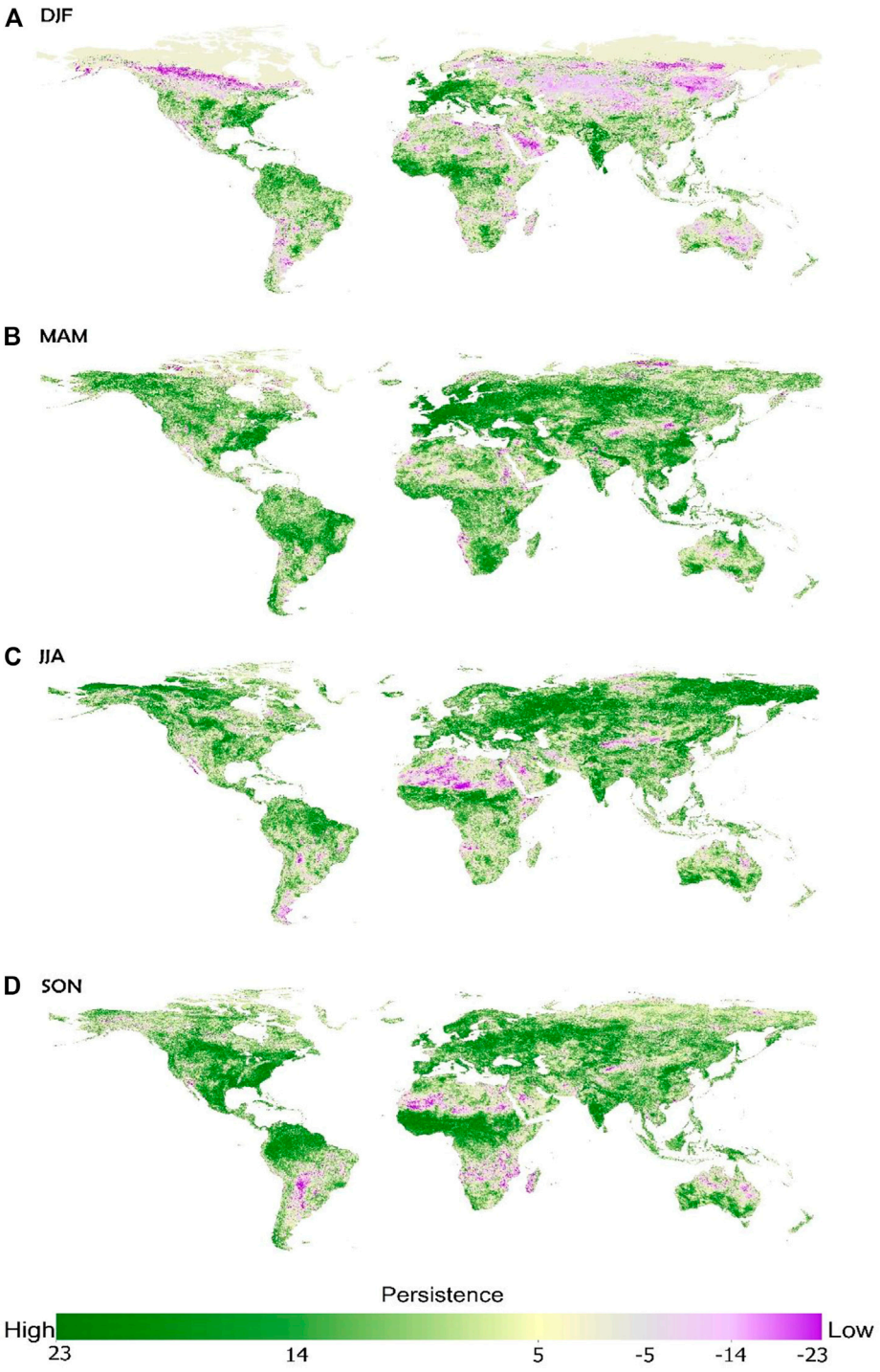

FIGURE 2
Global persistence by season for 1987–2010, compared to the baseline of 1982–1986 for **(A)** December, January, February (DJF); **(B)** March, April, May (MAM); **(C)** June, July, August (JJA); and **(D)** September, October, November (SON). Positive versus negative trends are shown in green versus purple respectively.

understand land use diversity within each biome class, where land area within the biome was previously converted, for example, to agricultural or development-based uses, by providing a land use diversity product for 2010. While this data is not ideal, and the time period used was only 2010 it was still useful in interpreting the persistence metrics by biome and by latitude, through a land use diversity analysis, to link to the vegetation dynamics highlighted by the persistence analysis. This allowed us to identify and highlight regions of significant land use diversity, which resulted in the changes in persistence. The data on land use was obtained for the entire globe and then subdivided by biomes, and within each biome was broken down into latitudinal bands, in 10-degree blocks. This was also useful to

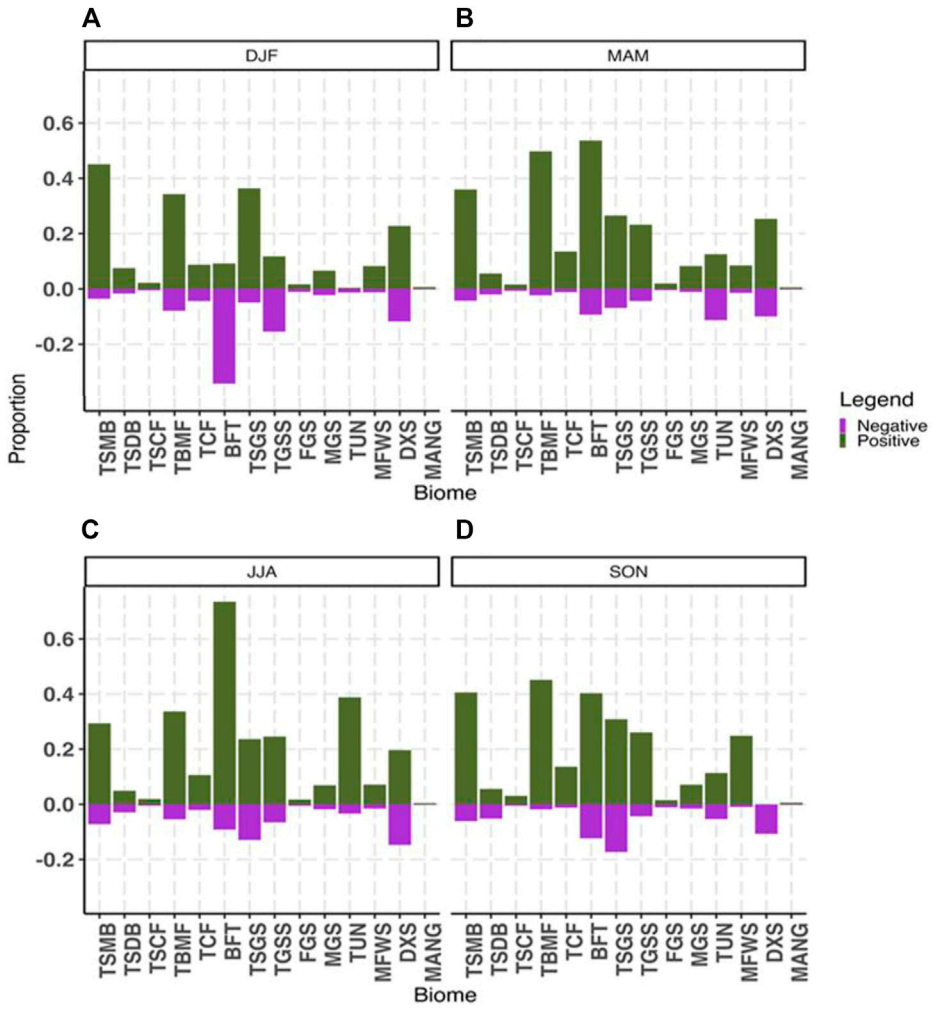

FIGURE 3
Proportion of each biome type globally representing either significant positive vegetation persistence (green) or significant negative vegetation persistence (purple) as a function of total pixels in that biome, and shown for all four seasons for **(A)** December, January, February (DJF); **(B)** March, April, May (MAM); **(C)** June, July, August (JJA); and **(D)** September, October, November (SON). Where acronyms are: TSMB, Tropical Subtropical Moist Broadleaf Forest; TSDB, Tropical Subtropical Dry Broadleaf Forest; TSCF, Tropical Subtropical Coniferous Forest; TBMF, Temperate Broadleaf and Mixed Forest; TCF, Temperate Coniferous Forest; BFT, Boreal Forests-Taiga; TSGS, Tropical Subtropical Grasslands, Savannas, and Shrublands; TGSS, Temperate Grasslands, Savanna, Shrubland; FGS, Flooded Grassland and Savanna; MGS, Montane Grassland and Shrubland; TUN, Tundra; MFWS, Mediterranean Forest, Woodlands, and Scrub; DXS, Deserts and Xeric Shrublands; and MANG, Mangroves.

highlight land use diversity across the northern and southern hemispheres when interpreting the results.

Utilizing the length of the satellite data record and the D metric, systematic quantification of vegetation change globally can be derived, and then interpreted with a view to better understand the spatial patterns and trends and how these relate to land use diversity as calculated here from the FAO product. Specifically, we will focus on the differences in patterns of vegetation persistence as a function of the actual land use diversity at the pixel level, as determined by FAO data (FAO 2010 data available at FAO.org). Biomes are important, but so is land cover and related land use diversity. Therefore, we will calculate the diversity of land uses occurring within each Biomes, and in order to assist interpretation we will calculate this land use diversity for every 10° north and south. This will allow us to add land use diversity into the already complex analysis incorporating biome and season. While this is an added level of complexity, it is essential to highlight the land use diversity within the global biomes data, and how variable this is over the different hemispheres of analysis.

Results

Global patterns of vegetation persistence

We calculated vegetation persistence at a pixel level for each season, for each year, and compared every season/year from 1987 to 2010 to the baseline period of 1982–1986. Initial analysis found AVHRR and MODIS to differ enough that they were not compatible for use within this type of analysis and may impact the findings due to different products and so bias results. Due to these differences across satellite products we chose to utilize the dataset with the longest timeframe and hence selected the AVHRR data product. The results can be evaluated spatially (Figure 2) and an initial review would highlight the overwhelmingly positive pattern of vegetation persistence globally. Despite these overall patterns it is also evident that some regions differ, and negative patterns of vegetation

persistence do exist, especially in Africa, and over time, the DFJ or boreal winter experiences more negative persistence patterns. MAM, boreal spring has the most positive patterns of persistence. Such global analysis, while useful, simply provides an overview within which we can start to breakdown findings by biomes and seasons and begin to evaluate potential drivers of these changes.

Vegetation persistence patterns by season and biome

Evaluating changes in vegetation persistence by season and biomes provides much more useful data and starts to highlight differences over time and place (Figure 3). For the months DJF there were higher positive trends overall, especially for Tropical Subtropical Moist Broadleaf Forests, Temperate Broadleaf and Mixed Forests, and Tropical Subtropical Grasslands, Savannas and Shrubs (Figure 3A). Two biomes had higher negative persistence patterns over positive patterns, and these were Boreal Forests-Taiga and Temperate Grasslands, Savanna, and Shrublands. The behaviour of these biomes were significantly different for the DJF period, and given their locations may relate in part to data issues related to snow cover at the more northern latitudes recording as low NDVI. As the recorded value is the maximum NDVI in the period this variability with snow cover and snowmelt could result in some erroneous results in terms of vegetation. This also links to the higher areas of negative persistence in the map for DJF (Figure 2A) which helps support this theory.

For MAM, the results were overwhelmingly positive, with the lowest number of negative pixels for any period. The biomes with the highest numbers of positive persistence values were Boreal Forests/-Taiga, the Temperate Broadleaf and Mixed Forest, and the Tropical Subtropical Moist Broadleaf Forests. The Tundra had equal proportions in negative and positive persistence, all other classes the persistence was dominated by the positive patterns (Figures 2B, 3B). Such an overwhelmingly positive pattern of vegetation persistence in the boreal spring most likely relates to the dominance of the NH in terms of land mass, and the spring season equating to plant growth. Over the time period of study, this indicates that at a pixel level the dominant patterns one of higher NDVI values every year compared to the baseline period, for all biomes except Tundra. This is a real dominance of positive vegetation persistence globally.

During the JJA periods there were overwhelmingly higher positive persistence patterns in every single biome. Again, this likely relates to the growing cycle and the dominance of the NH land mass in the signal. The result of no biomes experiencing more negative persistence versus positive persistence trends though is clearly a major finding. The most significant positive persistence proportions were found in Boreal Forests (with the highest recorded proportion of pixels in the positive persistence class at almost 80%), and then Tundra, Temperate Broadleaf and Mixed Forests, Tundra, Tropical Subtropical Moist Broadleaf Forests, (Figures 2C, 3C).

Finally, for SON there were higher positive persistence patterns again for most classes, although with lower proportions of pixels than for the MAM and JJA periods. The largest proportion of positive persistence was in Temperate Broadleaf and Mixed Forests, followed by Tropical Subtropical Moist Broadleaf Forests and Boreal Forests—Taiga (Figures 2D, 3D). The Deserts and Xeric Shrublands class only record negative persistence patterns and Tropical Subtropical Dry Broadleaf Forests has equal amounts of negative and positive persistence values. As the boreal autumn season occurs then, some of the water-limited or drier environments do appear to have more negative persistence patterns, and the overall greening or vegetative persistence patterns are lower than in the boreal spring and summer periods.

Looking overall at these results, we can view across seasons, and state that positive vegetation persistence is greater in the MAM and JJA seasons (Figures 2, 3) and this likely relates to growing season and more positive vegetation persistence is found in the NH over the SH (Figure 2). Biomes which always have a strong pattern of positive vegetation persistence are the Tropical Subtropical Moist Broadleaf Forests, Temperate Broadleaf and Mixed Forests, and to a lesser degree Tropical Subtropical Grasslands, Savannas and Shrublands. Boreal Forests-Taiga, has very strong patterns of positive vegetation persistence, except for the DJF period, which we believe relates more to snow cover variations than actual land cover. Reviewing these biomes (Figure 1), except for the Argentina pampas grasslands and the tropical subtropical grasslands, savannas and shrublands, these are dominated by the northern hemisphere locations. Overall, it can be seen from the analysis by biomes that forests tend to exhibit more positive patterns of vegetation persistence. Savannas, grasslands and desert regions seem to exhibit much more mixed trends, with more variability intra-annually, or across seasons and hemispheres. From these overview results more information is available and can be extracted to discern any possible drivers of change. As such, the biome data is further broken down, to better understand and explain these trends.

Vegetation persistence patterns accounting for land use diversity within biomes and variation with latitude

Persistence patterns for each biome by latitudinal bands and land use diversity to aid in the analysis and interpretation of the persistence patterns, are illustrated in Figures 4–7. Only those latitudes that represent greater than 5% of the global land surface area of that biome are now included and a vertical grid has been inserted at 33.3% and 66.7% on the significant change bars to provide a rough quantitative estimate of percentages of pixels showing significant positive or negative changes. In addition, each graph also has a right-hand bar chart extended horizontally to accommodate and display the breakdown of land use diversity data in the biome, within each latitudinal band. As such we can interpret the changes in persistence by latitude and discuss each in terms of the actual land use diversity observed within each biome type. This is to account for the land cover changes which have occurred globally, such that a biome has often been converted from its natural vegetation type to more human-dominated uses. This is important to clarify. The biome data represents the vegetation type which would result naturally, but in many cases human driven changes have occurred and the resulting land use is different from the original biome. Therefore, it is essential to highlight that within the biome type the land use diversity is highly variable, emphasizing the alteration that has already occurred within each biome. Clustering of biome types with similar patterns and outcomes can thus be determined and possible reasons for these patterns of change discussed. The patterns of biome responses can be grouped

10.3389/frsen.2023.1063188

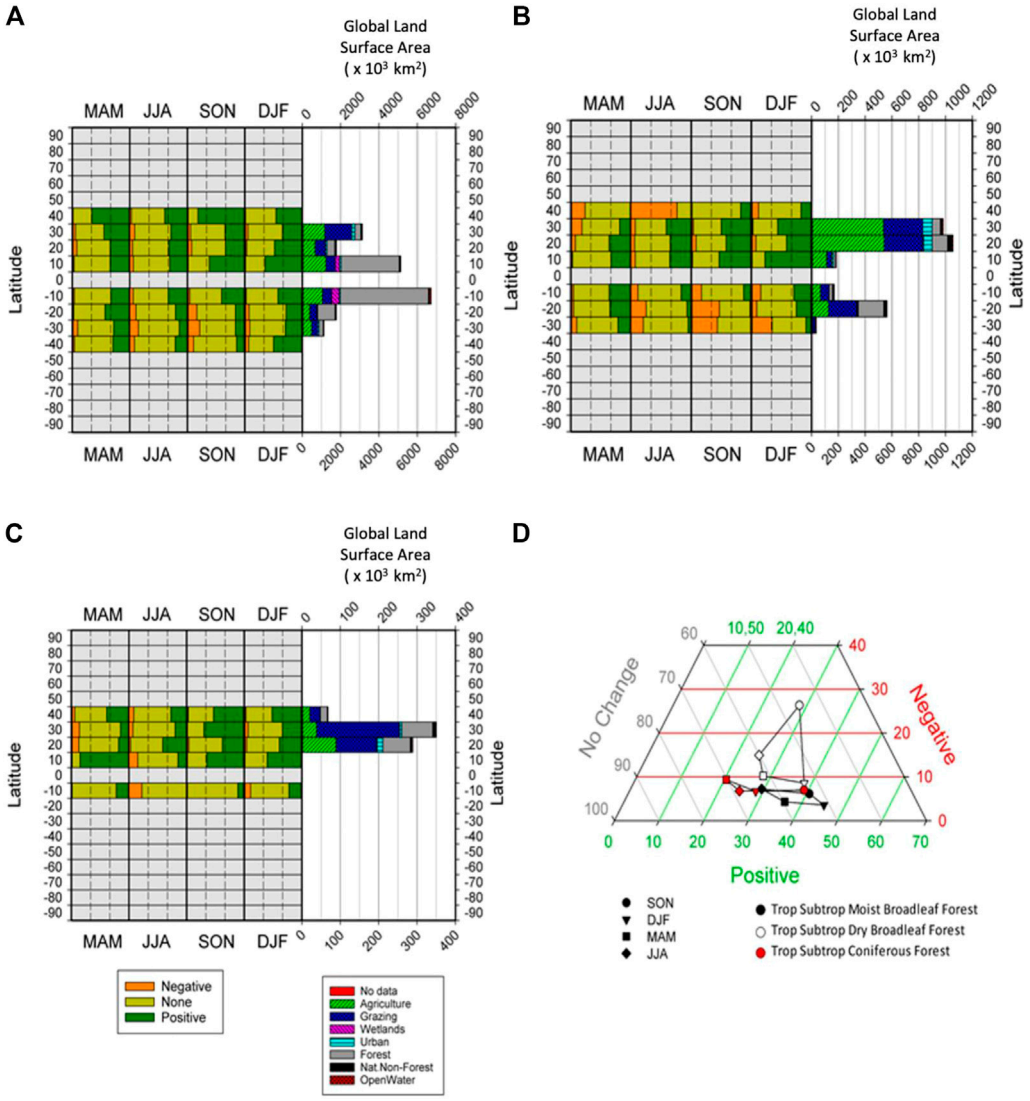

FIGURE 4
Composition of significant persistence values (Negative, None, Positive) in each biome, broken down by latitudinal band, with land use diversity of each bank also shown, for **(A)** Tropical Subtropical Moist Broadleaf Forest, **(B)** Tropical Subtropical Dry Broadleaf Forest, **(C)** Tropical Subtropical Coniferous Forest, and **(D)** Ternary plot of the seasonal changes in percentages of global areas returning significant percentages of positive and negative persistence, and those reporting to significant persistence, for three tropical forest biomes.

into some similar types where the resulting patterns do appear to follow some similar trends and patterns. To highlight these similar trends in persistence patterns, across seasons, for these biome clusters we have plotted them together (Figures 4D, 5D, 6E, 7E). These graphs show the proportion of pixels in each persistence category (so each biome and season = 100%, similar to soil type triangular charts or "textural triangles") and plotting by biome across seasons allows us to highlight shifts by season and so link to climatic drivers more effectively.

Tropical Subtropical Moist Broadleaf Forest reveals a significant amount of forest cover is remaining in this biome (Figure 4A) and that the dominant trend is that of positive vegetation persistence. In addition, this trend is clearly stronger in the NH than in the SH. Tropical Subtropical Dry Broadleaf Forest (Figure 4B) has been significantly converted to agriculture and pasture land-uses. The NH shows more positive persistence patterns and for the seasons SON and DJF there is a strong negative trend in the SH. Also, of note, there is more forest cover left in the SH, thus representing more of this original biome cover. Tropical Subtropical Coniferous Forest (Figure 4C) is dominated more by grazing lands, than forest cover along with some agriculture classes.

Positive persistence dominates and this trend is stronger in the NH than the SH, although there is very little SH area in this biome. Figure 4D shows the Tropical and Subtropical Forest types and we can see that Moist Broadleaf and Coniferous Forest types basically run horizontally with very low percentages (5%–10%) of pixels reporting significant negative persistence. By contrast the Tropical and Subtropical Dry Broadleaf Forests show higher percentages of negative persistence in JJA and SON than the other two tropical forest biomes. Given the limiting factors on growth for these biomes, it looks like seasonal availability of moisture may be causing the differences in these three forest types.

10.3389/frsen.2023.1063188

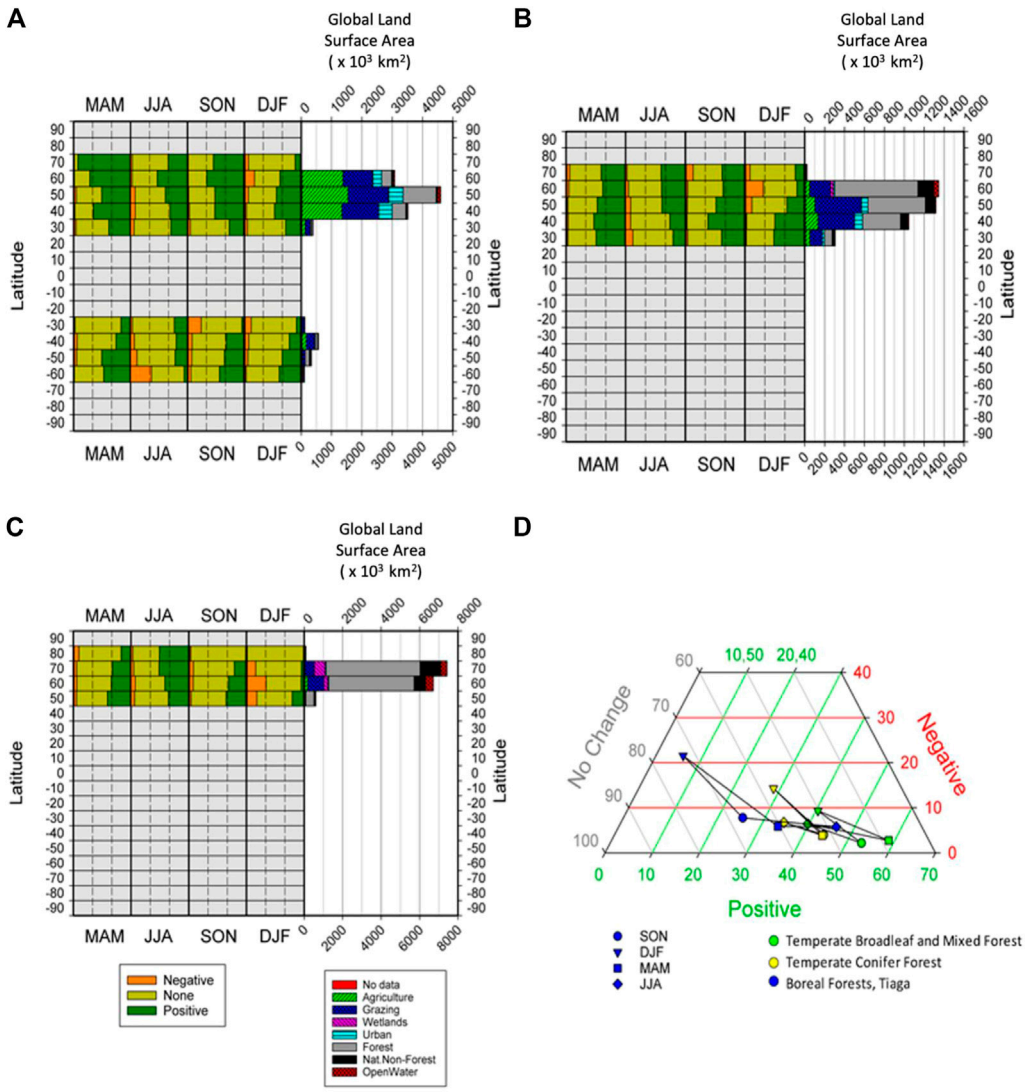

FIGURE 5
Composition of significant persistence values (Negative, None, Positive) in each biome, broken down by latitudinal band, with land use diversity of each bank also shown, for **(A)** Temperate Broadleaf Mixed Forest, **(B)** Temperate Coniferous Forest, **(C)** Boreal Forest -Taiga, and **(D)** Ternary plot of the seasonal changes in percentages of global areas returning significant percentages of positive and negative persistence, and those reporting to significant persistence, for three non-tropical forest biomes.

Temperate Broadleaf and Mixed Forest (Figure 5A) is now mainly agriculture and grazing lands, with only some limited areas of forest cover left. As with other forest biomes, we find that positive persistence dominates, and this trend is stronger in the NH than the SH. Temperate Coniferous Forest (Figure 5B) has lots of forest cover left, and some limited grazing areas. Again, positive persistence dominates. This biome is only found in the NH and so there is no NH versus SH variability. Boreal Forest-Taiga (Figure 5C) is still predominantly forest cover with much lower rates of conversion and is also found only in the NH. Once again, as with all the forested biome types, positive persistence dominates, especially in the growing season. All non-tropical forest biomes are almost exclusively limited to the NH and display roughly similar shapes, with three triads showing little change in percentages of negative persistence (3%–8%) and DJF (winter) showing the greatest propensity towards negative persistence (Figure 5D). Boreal Forests-Taiga indicate lower percentages (5%–35%) of positive changes, and Temperate Broadleaf and Mixed Forests higher ones (40%–60%). Given limiting factors on growth in these biomes, temperatures seem to have a big role here. In general, cooler temps lead to, a) fewer positive values, b) slightly more negatives (especially DJF), c) more "no significant" and d) a greater amplitude in these observations between the various seasons.

Tropical Subtropical Grasslands, Savannas, Shrublands (Figure 6A) have experienced significant conversion, and are now mainly areas of grazing, with some agriculture. Positive persistence dominates in the NH but the SH is much more variable, with more negative persistence in their winter and spring seasons (JJA and SON respectively). Temperate Grasslands, Savannas, and Shrublands (Figure 6B) have again been mainly transformed to areas of agriculture and grazing. Positive persistence dominates in the NH with the SH again

10.3389/frsen.2023.1063188

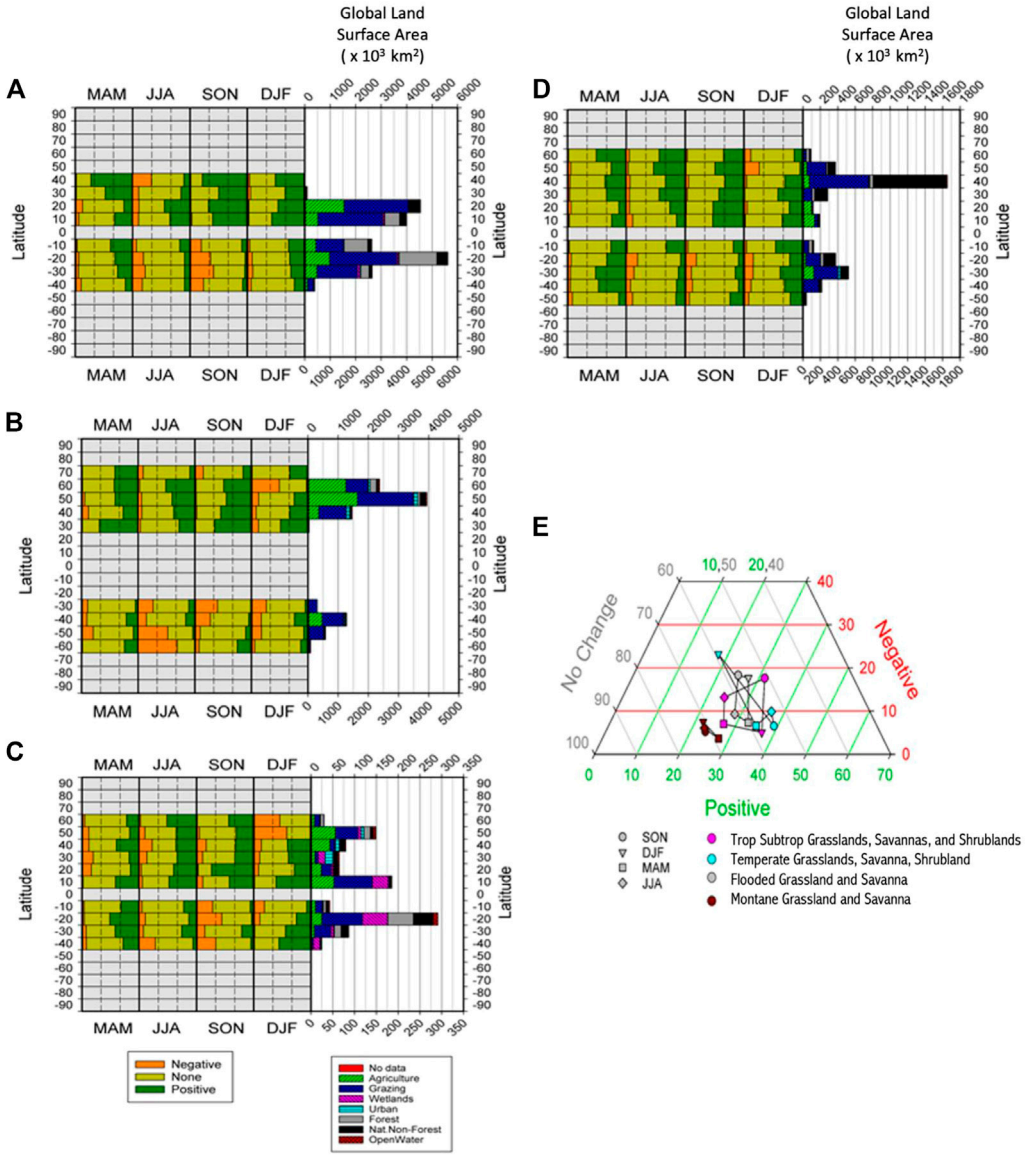

FIGURE 6
Composition of significant persistence values (Negative, None, Positive) in each biome, broken down by latitudinal band, with land use diversity of each bank also shown, for **(A)** Tropical and Subtropical grasslands, savannas and shrublands, **(B)** Temperate grasslands, savannas and shrublands, **(C)** Flooded grasslands and savanna, **(D)** Montane grassland and shrubland and **(E)** Ternary plot of the seasonal changes in percentages of global areas returning significant percentages of positive and negative persistence, and those reporting to significant persistence, for four grassland biomes.

reflecting a more mixed response, with more negative persistence in their winter and spring. Also of note is that these areas are very spatially limited in the SH. Flooded Grassland, and Savanna (Figure 6C) has very mixed actual land uses but despite this, positive persistence dominates in the NH although in the SH results are much more mixed, with more negative persistence in their spring (SON). Montane Grassland and Shrubland (Figure 6D) is composed of mainly grazing and natural vegetation and follows the same trend of positive persistence dominating in the NH, with the SH being a little more mixed, but generally positive overall. Seasonal patterns of persistence for grasslands are very distinct from those of the forest biomes (Figure 6E). The dominant orientation of forest biomes (except tropical dry forest) is horizontal, whereas diagonal (temperate and montane grasslands) and box-like (subtropical and flooded grasslands) shapes dominate here. Flooded grasslands evince greater variability in the vertical position on the graph than tropical grasslands which tend towards a more equilateral shape. From these patterns it seems most likely that they are responding to high seasonality in their rainfall regimes within these grassland biomes.

Tundra (Figure 7A) has mainly natural vegetation cover. Positive persistence dominates in the NH during their growing season. The SH is again much more mixed across seasons although also of note, the SH has very limited area spatially. Mediterranean Forest, Woodlands, and Scrub (Figure 7B) have been heavily converted and so are now mainly agriculture and grazing lands. Positive persistence dominates and this trend is much stronger in the NH than for the SH. Deserts and Xeric Shrublands

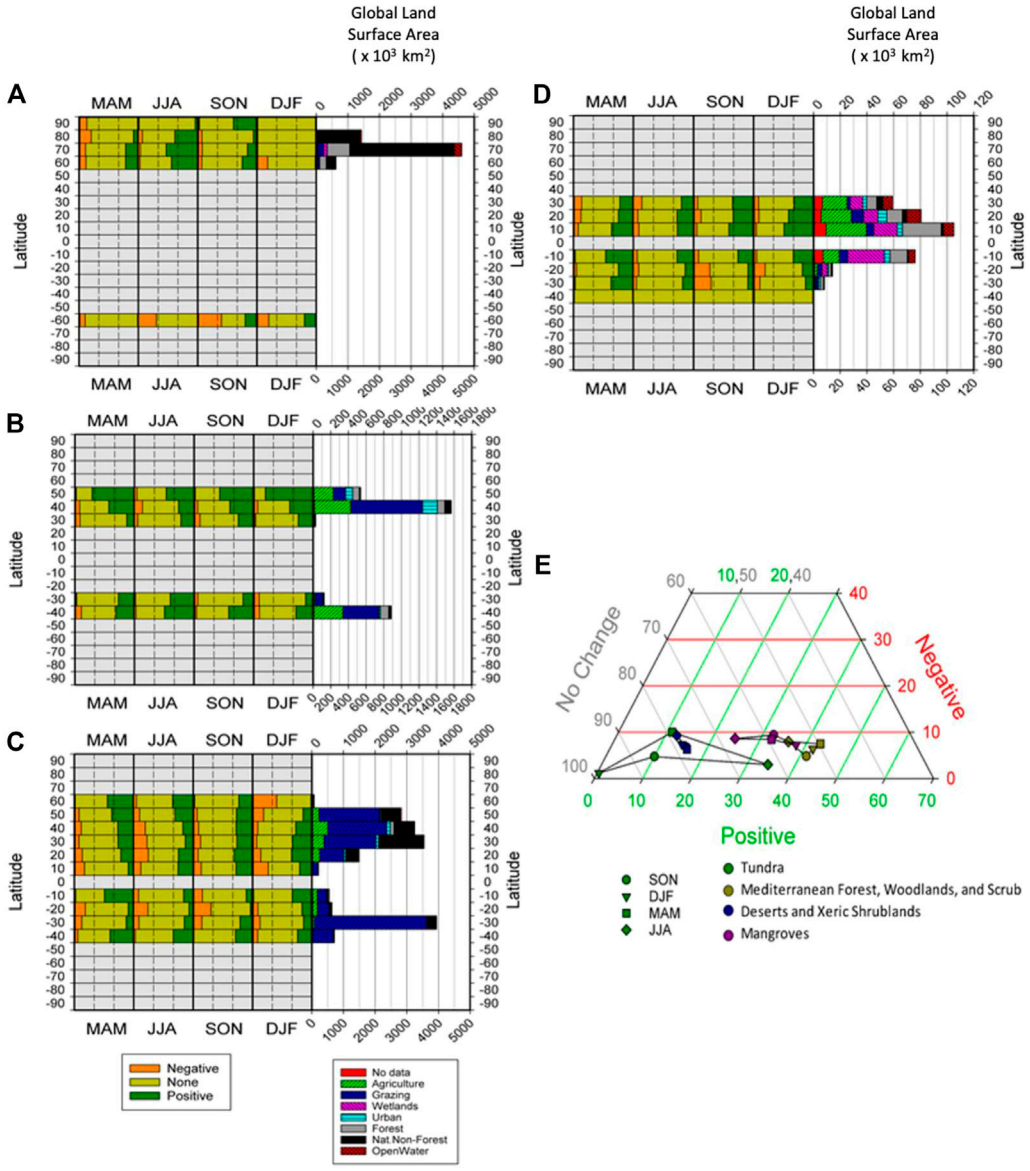

FIGURE 7
Composition of significant persistence values (Negative, None, Positive) in each biome, broken down by latitudinal band, with land use diversity of each bank also shown, for **(A)** Tundra, **(B)** Mediterranean Forest, Woodlands and Scrub, **(C)** Deserts and Xeric Shrublands, **(D)** Mangroves and **(E)** Ternary plot of the seasonal changes in percentages of global areas returning significant percentages of positive and negative persistence, and those reporting to significant persistence, for four other biomes.

(Figure 7C) are made up of mainly grazing and natural vegetation. Positive persistence dominates in the NH and following the patterns of many of the grassland and shrub regions, the patterns in the SH are much more variable. Finally, Mangroves (Figure 7D) are greatly transformed and so actually represent very mixed land covers and very small areas. Positive persistence dominates in the NH with the SH more mixed, but with positive persistence overall. Tundra exists almost exclusively in the northern hemisphere, during JJA a high percentage (35%) now exhibit positive persistence, and with very few (<5%) examples of negative persistence (Figure 7D). Between 30% and 40% of the three remaining biomes lie within the southern hemisphere, so what little seasonal variability they exhibit should be interpreted with caution. Regardless of season, just under 80% of the pixels in the desert and xeric shrub biome report no significant persistence and so a discussion of possible drivers of change is not possible.

One important issue here, and a cautionary note on the interpretation of these graphs is related to the fact that any expression and physical interpretation of these changes is partially dependent upon the hemispheric distribution of each biome. As such, it is important to review this percentage of biomes by latitude and hemisphere (Figures 4–8) when reviewing and assigning importance to these results, as we have attempted here.

Discussion

This study utilizes a novel approach to analysing NDVI timeseries to better understand global distributions of changes in vegetation greenness. The importance of seasons, biomes, and land use in shaping

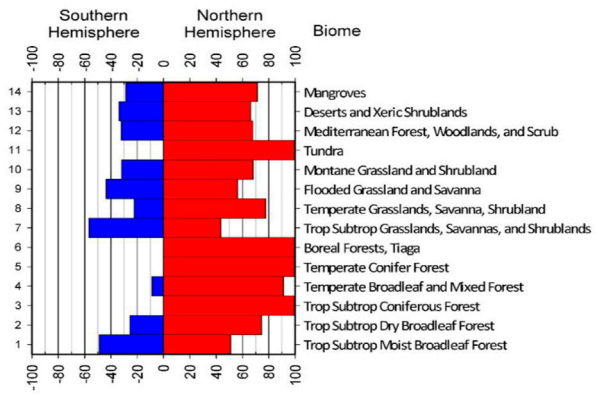

FIGURE 8
Percentage of global biomes by their hemispheric and latitudinal distribution for the 14 biomes under study.

greenness trajectories was also investigated. This highlighted several advantages and strengths of the directional persistence metric, which utilizes a time series analysis of vegetation persistence, with initial benchmark conditions (1982–1986), and implementing statistical significance at a pixel level for the globe. NDVI time series was shown to be a powerful tool for understanding vegetation change at the global scale. This approach emphasizes identification of long-term shifts in vegetation greenness and is less concerned with small-scale individual events that impact local areas, even though these may be of interest at these more local and regional scales, e.g., forest mortality, disaster related clearing activities, etc. To better capture pixels with significant change in NDVI for individual events, it is possible to adjust the baseline values and temporal scale, though given the global extent of this study it is not possible to account for all local level change in NDVI in the analysis presented here. Future research could look more closely at some areas of interesting change, that do not hit the required significance levels for this research (±9). By using NDVI data to assess the areal extent, magnitude, direction, and temporal patterns of vegetation change, scientists can gain important insights into how vegetation is responding to changes in climate and other environmental conditions, as well as understand the health of ecosystems globally (Southworth et al., 2016; Southworth and Muir 2021).

We calculated vegetation persistence at a pixel level for each season, for each year, and compared every season/year from 1987 to 2010 to the baseline period of 1982–1986. The results highlight the overwhelmingly positive pattern of vegetation persistence globally, although there were also clear regional patterns and variations with season (Figure 2). Looking overall at these results, positive vegetation persistence is greater in the MAM and JJA seasons (Figures 2, 3) and this likely relates to growing season and more positive vegetation persistence as found in the NH over the SH (Figure 2). Overall, forests tend to exhibit more positive patterns of vegetation persistence. Savannas, Grasslands and Desert regions seem to exhibit much more mixed trends, with more variability intra-annually, or across seasons and hemispheres. When broken down further to include land use diversity and latitudinal variation, clearer patterns emerge related to biome types. Tropical Subtropical Moist Broadleaf Forest, Tropical Subtropical Dry Broadleaf and Tropical Subtropical Coniferous Forest have all been heavily converted to agricultural land uses, and the seasonal availability of moisture may be causing the differences in these three forest types (Figure 4). Temperate Broadleaf and Mixed Forest has also been heavily converted to agricultural uses, unlike the Temperate Coniferous Forest Boreal Forest, or Taiga, which are still predominantly intact forest cover. As with all the forested biome types, positive persistence again dominates, especially in the growing season. Given limiting factors on growth in these biomes, temperatures seem to have a big role here in terms of increased patterns of positive vegetation persistence with warmer temperatures (Figure 5). Tropical Subtropical Grasslands, Savannas, Shrublands and Temperate Grasslands, Savannas, and Shrublands have again been largely transformed to areas of agriculture and grazing, whereas Flooded Grassland, and Savanna has very mixed actual land uses. Montane Grassland and Shrubland is composed of mainly grazing and natural vegetation. All follow the same trend of positive persistence dominating in the NH, with the SH being a little more mixed, but generally positive overall. Seasonal patterns of persistence for grasslands are very distinct from those of the forest biomes. From the seasonal patterns and amplitudes (Figure 6) it seems most likely that these grassland biomes are responding to high seasonality in their rainfall regimes. Tundra has mainly natural vegetation cover. Mediterranean Forest, Woodlands, and Scrub and Mangroves have both been heavily converted and so are now mainly agriculture/grazing and mixed covers, and Deserts and Xeric Shrublands are made up of mainly grazing and natural vegetation. Positive persistence dominates in the NH with the SH more mixed, but with positive persistence overall. Variability across these final biome types is high and areal extent often quite small, and no clear patterns or drivers were discernable from the results.

Vegetation persistence (D) is a metric that can be used to understand dynamics and highlight areas of vulnerability based on the patterns of positive and negative vegetation persistence over time. NDVI is a key measure of vegetation health, and by tracking changes in NDVI over time, D can be used to identify areas where vegetation is greening or browning. Positive persistence indicates greening, while negative persistence indicates browning. Areas with high levels of positive persistence are more likely to be resilient to disturbance, while areas with high levels of negative persistence are more vulnerable. By understanding the patterns of vegetation persistence, we can better understand the dynamics of ecosystems and identify areas of possible current or future vulnerability. Over and above that, traditional approaches only highlight the conversion of systems, but "directional persistence," D, can be used to understand dynamics and highlight areas of vulnerability based on the patterns of positive and negative vegetation persistence over time, as presented here.

This research finds that vegetation persistence exhibited a positive trend overall which matches many of the reports of global greening over the same period (de Jong et al., 2012; 2013; Cortés et al., 2021). Notably, in seasons, positive vegetation persistence is greater in the growing season in the NH. More positive vegetation persistence was found in the NH over the SH, which also corroborates the seasonal and the NH trends exhibited here, and similarly found by other researchers (de Jong et al., 2012; 2013; Cortés et al., 2021). Cortez emphasizes the need for reliable statistically valid tests to detect vegetation change, specifically significant trends related to vegetation greening and browning globally. The research presented here helps validate research finding global greening with much more significant

statistical patterns in the NH regions and during the NH growing season, as well as trends of browning, which are much more limited, but found most in the SH. In addition, the importance of land use change and land cover conversions are highlighted and the importance of such land use changes, which are documented as impacting approximately one-third of the global land area since 1960, is critical to incorporate within such studies of global greening or browning (Winkler et al., 2021). The research presented here combines all of these requirements utilizing a well-regarded NDVI vegetation index within a novel and innovative statistical approach, which incorporates mathematical theory to apply statistical significance in a rigorous and repeatable manner, while incorporating season, latitude, and land use diversity. One limitation of this research lies with the use of a single date to develop the land use diversity variable, rather than using multiple dates to determine land use changes. However, the purpose of this research was to focus on the vegetation dynamics represented by the NDVI time-series analysis creating the vegetation persistence metric. Therefore, the use of the single date land use product to create the land use diversity analysis for 2010, to highlight that within each biome type the land use diversity is highly variable, emphasizing the alteration that has already occurred within each biome, is an ideal compromise, within this global focus.

This analysis builds on these previous greening studies of Lu et al. (2016), Piao et al. (2020), Cortés et al. (2021), and Zhu et al. (2016), with the important additions of changes by season, biome, and land use diversity. More regionally and spatially variable, changes in temperature and precipitation, CO_2 fertilization, changes in land cover, and the important role of seasons are all highlighted in these former research studies, as crucial drivers of global greening (vegetation persistence), as can also be observed in the present research. Drivers of global greening from earlier studies, with the key driver being CO_2 fertilization (Lu et al., 2016; Zhu et al., 2016). In the boreal region, temperature change was regarded as the major driver behind vegetation greening as summer facilitated the growth of plants (Lucht et al., 2002), which is in line with findings presented here. But Piao et al. (2005) and Nemani et al. (2002) discovered precipitation as a cause behind enhanced vegetation productivity overall, which again showed congruity with this research, and also highlights the importance of looking within biomes and latitudinal zones, and not just at global trends.

The higher greenness trend in the NH over the SH, is explained by Kaufmann et al. (2002), as rising temperature in the NH as the key factor behind improved vegetation growth. Zhou et al. (2001) and Nemani et al. (2003) also documented enhanced terrestrial greenness in high and middle latitudes of the NH from 1980 to 2000. Box (2002) suggested that because of increased rates of temperate increase in the NH greenness rates are increasing at a higher rate there as compared to the SH. Complimentarily, Piao et al. (2020) suggested that the SH has experienced a wide-ranging trend of greening since 1980, but this rate is lower than compared to higher latitude NH locations. Chen et al. (2019) also regarded the NH as a vegetation greening hotspot because of its faster rates of greening. Winkler et al. (2021) studied sub-Saharan grasslands and savanna systems and showed that the greening pattern is consistent with an increase in rainfall. Zhu et al. (2016) further gave justifications that like climate change, land-use change (deforestation, afforestation, and agricultural intensification) also put forth a highly spatially variable influence on vegetation changes. Deforestation in tropical forests reduced vegetative persistence, described by Brandt et al. (2017), while afforestation increased greenness in the temperate region (Curtis et al., 2018). Additionally, agricultural intensification in terms of irrigation, fertilizer and pesticide use, multiple cropping, etc. contribute significantly (25%–50%) in leaf area enhancement in Mediterranean forest, temperate broadleaf forest, mangroves, and temperate grasslands, as depicted by Feng et al. (2016); Chen et al. (2019), and Winkler et al. (2021). Our research not only supports these same findings but also helps to highlight the latitudinal, seasonal and land use related variations causing these trends.

Conclusion

Vegetation greening is one of the most distinguished characteristics of biosphere change, since 1980, as indicated from long-term satellite records (Lu et al., 2016; Zhu et al., 2016; Piao et al., 2020; Cortés et al., 2021). This study presented an approach to analyzing vegetation persistence for three decades (1982–2010), thus highlighting significant spatial and temporal variations at biome, season and land use diversity levels. By setting 1982–1986 as a benchmark period, the subsequent 23 years of data revealed that forests overall have positive vegetation persistence, but this trend is not consistent across all biomes. Savannas, desert, and grasslands seem to be the most vulnerable although results are highly variable. In contrast, tundra, moist broadleaf forests, boreal forests, and coniferous forests exhibited the highest positive vegetation persistence proportions.

This method in time series remote sensing analysis is pivotal in importance to assist in the user designed, easily replicated, analysis of patterns of vegetation change, which—once identified—can lead to more in-depth and regional scale studies of drivers (Southworth et al., 2016; Southworth and Muir 2021). Vegetation persistence methods, such as the approach in this study, using the vegetation persistence or "D" metric, are much more reproducible and innovative than traditional approaches to vegetation analysis. They take into account patterns of longer-term vegetation persistence, at a pixel level, over extended time periods, rather than just an absolute value. This enables identification of patterns of vegetation change over time, which can then be used to study the drivers of those changes.

This study found similar results to other global studies (de Jong et al., 2012; 2013; Cortés et al., 2021; Jiang et al., 2022), which found an increase in global vegetation persistence since the early 1980s, frequently referred to as the "global greening" trend. However, this study also highlights the importance of exploring these trends across seasons, biomes, and land use diversity, revealing that this trend is not consistent across all locations. Savannas, desert and grasslands seem to be the most vulnerable and highly variable, and forest biomes have the highest patterns of positive vegetation persistence, especially within the growing season. There is a lot of interest in the global greening trend, as it has potential implications for food security, the water cycle and carbon sequestration. However, there is still much work to be done to fully understand the drivers of these trends and their implications. This study provides a valuable contribution to this debate by

highlighting the importance of using time series approaches, such as the one presented here, to understand vegetation dynamics and identify areas of vulnerability.

The pixel-level perspective of the vegetation persistence method is useful for understanding dynamics of change and identifying areas of vulnerability. The ability to assign statistical significance to pixel level trajectories helps to further understand the patterns of change. This time series based remote sensing approach has many potential applications for monitoring environmental change. Vegetation persistence, D, can be used to understand dynamics and highlight areas of vulnerability based on the patterns of positive and negative vegetation persistence over time. This can help identify which areas are most likely to experience change and where management action may be necessary to protect against further change. As such, this is a simple and valuable tool for resource managers and policymakers as it provides insight into the long-term impacts of human activities on landscapes.

Data availability statement

The raw data supporting the conclusion of this article will be made available by the authors, without undue reservation.

Author contributions

JS, HH, SR, and EB conceptualized the research, JS, PW, HH, RK, and EB completed analysis, JS, SR, PW, EB, and HH wrote the initial draft, JS, MH, SR, and CM, edited and refined document.

Conflict of interest

The authors declare that the research was conducted in the absence of any commercial or financial relationships that could be construed as a potential conflict of interest.

Publisher's note

All claims expressed in this article are solely those of the authors and do not necessarily represent those of their affiliated organizations, or those of the publisher, the editors and the reviewers. Any product that may be evaluated in this article, or claim that may be made by its manufacturer, is not guaranteed or endorsed by the publisher.

References

Ahlbeck, J. R. (2002). Comment on "Variations in northern vegetation activity inferred from satellite data of vegetation index during 1981–1999" by L. Zhou et al. *J. Geophys. Res. Atmos.* 107 (D11), ACH 9-1–ACH 9-2. doi:10.1029/2001jd001389

Box, E. O. (2002). Vegetation analogs and differences in the northern and southern hemispheres: A global comparison. *Plant Ecol.* 163 (2), 139–154. doi:10.1023/A:1020901722992

Brandt, M., Rasmussen, K., Peñuelas, J., Tian, F., Schurgers, G., Verger, A., et al. (2017). Human population growth offsets climate-driven increase in woody vegetation in sub-Saharan Africa. *Nat. Ecol. Evol.* 1 (4), 0081–0086. doi:10.1038/s41559-017-0081

Bubenik, P., De Silva, V., and Scott, J. (2015). Metrics for generalized persistence modules. *Found. Comput. Math.* 15 (6), 1501–1531. doi:10.1007/s10208-014-9229-5

Bunting, E. L., Southworth, J., Herrero, H., Ryan, S. J., and Waylen, P. (2018). Understanding long-term savanna vegetation persistence across three drainage basins in Southern Africa. *Remote Sens.* 10 (7), 1013. doi:10.3390/rs10071013

Chen, C., Park, T., Wang, X., Piao, S., Xu, B., Chaturvedi, R. K., et al. (2019). China and India lead in greening of the world through land-use management. *Nat. Sustain.* 2 (2), 122–129. doi:10.1038/s41893-019-0220-7

Corlett, R. T. (2011). Impacts of warming on tropical lowland rainforests. *Trends Ecol. Evol.* 26 (11), 606–613. doi:10.1016/j.tree.2011.06.015

Cortés, J., Mahecha, M. D., Reichstein, M., Myneni, R. B., Chen, C., and Brenning, A. (2021). Where are global vegetation greening and browning trends significant? *Geophys. Res. Lett.* 48, e2020GL091496. doi:10.1029/2020GL091496

Curtis, P. G., Slay, C. M., Harris, N. L., Tyukavina, A., and Hansen, M. C. (2018). Classifying drivers of global forest loss. *Science* 361 (6407), 1108–1111. doi:10.1126/science.aau3445

de Jong, R., Verbesselt, J., Schaepman, M. E., and de Bruin, S. (2012). Trend changes in global greening and browning: Contribution of short-term trends to longer-term change. *Glob. Change Biol.* 18, 642–655. doi:10.1111/j.1365-2486.2011.02578.x

de Jong, R., Verbesselt, J., Zeileis, A., and Schaepman, M. E. (2013). Shifts in global vegetation activity trends. *Remote Sens.* 5, 1117–1133. doi:10.3390/rs5031117

Feng, X., Fu, B., Piao, S., Wang, S., Ciais, P., Zeng, Z., et al. (2016). Revegetation in China's Loess Plateau is approaching sustainable water resource limits. *Nat. Clim. Change* 6 (11), 1019–1022. doi:10.1038/nclimate3092

Fensholt, R., and Proud, S. R. (2012). Evaluation of Earth observation based global long term vegetation trends—comparing GIMMS and MODIS global NDVI time series. *Remote Sens. Environ.* 119, 131–147. doi:10.1016/j.rse.2011.12.015

Food and Agricultural Organization of the United Nations (2010). Data available via https://www.fao.org/faostat/en/#data/RL. Last accessed September 1 2022.

Friedl, M. A., Woodcock, C. E., Olofsson, P., Zhu, Z., Loveland, T., Stanimirova, R., et al. (2022). Medium spatial resolution mapping of global land cover and land cover change across multiple decades from landsat. *Front. Remote Sens.* 3, 894571. doi:10.3389/frsen.2022.894571

Gómez, C., White, J. C., and Wulder, M. A. (2016). Optical remotely sensed time series data for land cover classification: A review. *ISPRS J. Photogrammetry Remote Sens.* 116, 55–72. doi:10.1016/j.isprsjprs.2016.03.008

Herrmann, S. M., Anyamba, A., and Tucker, C. J. (2005). Recent trends in vegetation dynamics in the African Sahel and their relationship to climate. *Glob. Environ. Change* 15 (4), 394–404. doi:10.1016/j.gloenvcha.2005.08.004

Jiang, F., Deng, M., Long, Y., and Sun, H. (2022). Spatial pattern and dynamic change of vegetation greenness from 2001 to 2020 in tibet, China. *Front. Plant Sci.* 13, 892625. doi:10.3389/fpls.2022.892625

Kaufmann, R. K., Zhou, L., Tucker, C. J., Slayback, D., Shabanov, N. V., and Myneni, R. B. (2002). Reply to Comment on 'Variations in northern vegetation activity inferred from satellite data of vegetation index during 1981–1999 by JR Ahlbeck. *J. Geophys. Res.* 107 (4127), ACL 7-1–ACL 7-3. doi:10.1029/2001jd001516

Keenan, T. F., and Riley, W. J. (2018). Greening of the land surface in the world's cold regions consistent with recent warming. *Nat. Clim. change* 8 (9), 825–828. doi:10.1038/s41558-018-0258-y

Lanfredi, M., Simoniello, T., and Macchiato, M. (2004). Temporal persistence in vegetation cover changes observed from satellite: Development of an estimation procedure in the test site of the Mediterranean Italy. *Remote Sens. Environ.* 93 (4), 565–576. doi:10.1016/j.rse.2004.08.012

Lenka, N. K., and Lal, R. (2012). Soil-related constraints to the carbon dioxide fertilization effect. *Crit. Rev. Plant Sci.* 31 (4), 342–357. doi:10.1080/07352689.2012.674461

Liu, H., Jiao, F., Yin, J., Li, T., Gong, H., Wang, Z., et al. (2020). Nonlinear relationship of vegetation greening with nature and human factors and its forecast–a case study of Southwest China. *Ecol. Indic.* 111, 106009. doi:10.1016/j.ecolind.2019.106009

Liu, Y., Chai, Y., Yue, Y., Huang, Y., Yang, Y., Zhu, B., et al. (2022). Effects of global greening phenomenon on water sustainability. *CATENA* 208, 105732. doi:10.1016/j.catena.2021.105732

Lu, X., Wang, L., and McCabe, M. F. (2016). Elevated CO2 as a driver of global dryland greening. *Sci. Rep.* 6 (1), 20716–20717. doi:10.1038/srep20716

Lucht, W., Prentice, I. C., Myneni, R. B., Sitch, S., Friedlingstein, P., Cramer, W., et al. (2002). Climatic control of the high-latitude vegetation greening trend and Pinatubo effect. *Science* 296 (5573), 1687–1689. doi:10.1126/science.1071828

Lunetta, R. S., Knight, J. F., Ediriwickrema, J., Lyon, J. G., and Worthy, L. D. (2006). Land-cover change detection using multi-temporal MODIS NDVI data. *Remote Sens. Environ.* 105 (2), 142–154. doi:10.1016/j.rse.2006.06.018

Marshall, E., Valavi, R., Connor, L. O., Cadenhead, N., Southwell, D., Wintle, B. A., et al. (2021). Quantifying the impact of vegetation-based metrics on species persistence when choosing offsets for habitat destruction. *Conserv. Biol.* 35 (2), 567–577. doi:10.1111/cobi.13600

Nemani, R., and Running, S. (1997). Land cover characterization using multitemporal red, near-IR, and thermal-IR data from NOAA/AVHRR. *Ecological applications* 7 (1), 79–90.

Nemani, R. R., Keeling, C. D., Hashimoto, H., Jolly, W. M., Piper, S. C., Tucker, C. J., et al. (2003). Climate-driven increases in global terrestrial net primary production from 1982 to 1999. *Science* 300 (5625), 1560–1563. doi:10.1126/science.1082750

Nemani, R., White, M., Thornton, P., Nishida, K., Reddy, S., Jenkins, J., et al. (2002). Recent trends in hydrologic balance have enhanced the terrestrial carbon sink in the United States. *Geophys. Res. Lett.* 29 (10), 106-1–106-4. doi:10.1029/2002gl014867

Olson, D. M., Dinerstein, E., Wikramanayake, E. D., Burgess, N. D., Powell, G. V. N., and Underwood, E. C. (2001). Terrestrial ecoregions of the world: A new map of life on Earth. *Bioscience* 51 (11), 933–938.

Piao, S., Fang, J., Zhou, L., Zhu, B., Tan, K., and Tao, S. (2005). Changes in vegetation net primary productivity from 1982 to 1999 in China. *Glob. Biogeochem. Cycles* 19 (2). doi:10.1029/2004gb002274

Piao, S., Friedlingstein, P., Ciais, P., Zhou, L., and Chen, A. (2006). Effect of climate and CO2 changes on the greening of the Northern Hemisphere over the past two decades. *Geophys. Res. Lett.* 33 (23), L23402. doi:10.1029/2006gl028205

Piao, S., Wang, X., Park, T., Chen, C., Lian, X. U., He, Y., et al. (2020). Characteristics, drivers and feedbacks of global greening. *Nat. Rev. Earth Environ.* 1 (1), 14–27. doi:10.1038/s43017-019-0001-x

Potapov, P., Hansen, M. C., Pickens, A., Hernandez-Serna, A., Tyukavina, A., Turubanova, S., et al. (2022). The global 2000-2020 land cover and land use change dataset derived from the landsat archive: First results. *Front. Remote Sens.* 3, 856903. doi:10.3389/frsen.2022.856903

Samanta, A., Ganguly, S., Hashimoto, H., Devadiga, S., Vermote, E., Knyazikhin, Y., et al. (2010). Amazon forests did not green-up during the 2005 drought. *Geophys. Res. Lett.* 37 (5). doi:10.1029/2009gl042154

Southworth, J., and Muir, C. (2021). Specialty grand challenge: Remote sensing time series analysis. *Front. Remote Sens.* 2, 770431. doi:10.3389/frsen.2021.770431

Southworth, J., Zhu, L., Bunting, E., Ryan, S. J., Herrero, H., Waylen, P. R., et al. (2016). Changes in vegetation persistence across global savanna landscapes, 1982–2010. *J. Land Use Sci.* 11 (1), 7–32. doi:10.1080/1747423X.2015.1071439

Tian, F., Liu, L. Z., Yang, J. H., and Wu, J. J. (2021). Vegetation greening in more than 94% of the Yellow River Basin (YRB) region in China during the 21st century caused jointly by warming and anthropogenic activities. *Ecol. Indic.* 125, 107479. doi:10.1016/j.ecolind.2021.107479

Tsai, H., Southworth, J., and Waylen, P. (2014). Spatial persistence and temporal patterns in vegetation cover across Florida, 1982–2006. *Phys. Geogr.* 35 (2), 151–180. doi:10.1080/02723646.2014.898126

Wang, X., Dannenberg, M. P., Yan, D., Jones, M. O., Kimball, J. S., Moore, D. J., et al. (2020). Globally consistent patterns of asynchrony in vegetation phenology derived from optical, microwave, and fluorescence satellite data. *J. Geophys. Res. Biogeosciences* 125 (7), e2020JG005732. doi:10.1029/2020jg005732

Washington-Allen, R. A., West, N. E., Ramsey, R. D., and Efroymson, R. A. (2006). A protocol for retrospective remote sensing–based ecological monitoring of rangelands. *Rangel. Ecol. Manag.* 59 (1), 19–29. doi:10.2458/azu_jrm_v59i1_allen

Waylen, P., Southworth, J., Gibbes, C., and Tsai, H. (2014). Time series analysis of land cover change: Developing statistical tools to determine significance of land cover changes in persistence analyses. *Remote Sens.* 6 (5), 4473–4497. doi:10.3390/rs6054473

Wilson, A. G., and Kirkby, M. J. (1980). *Mathematics for Geographers and Planners*. 2nd Edn. Oxford, United Kingdom: Oxford University Press.

Winkler, A. J., Myneni, R. B., Hannart, A., Sitch, S., Haverd, V., Lombardozzi, D., et al. (2021). Slowdown of the greening trend in natural vegetation with further rise in atmospheric CO_2 *Biogeosciences* 18 (17), 4985–5010. doi:10.5194/bg-18-4985-2021

Winkler, K., Fuchs, R., Rounsevell, M., and Herold, M. (2021). Global land use changes are four times greater than previously estimated. *Nat. Commun.* 12, 2501. doi:10.1038/s41467-021-22702-2

Xiao, J., and Moody, A. (2005). A comparison of methods for estimating fractional green vegetation cover within a desert-to-upland transition zone in central New Mexico, USA. *Remote Sens. Environ.* 98 (2–3), 237–250. doi:10.1016/j.rse.2005.07.011

Yao, R., Wang, L., Huang, X., Chen, X., and Liu, Z. (2019). Increased spatial heterogeneity in vegetation greenness due to vegetation greening in mainland China. *Ecol. Indic.* 99, 240–250. doi:10.1016/j.ecolind.2018.12.039

Zhao, M., and Running, S. (2010). Drought-induced reduction in global terrestrial net primary production from 2000 through 2009. *Science* 329 (5995), 940–943. doi:10.1126/science.1192666

Zhou, L., Tucker, C. J., Kaufmann, R. K., Slayback, D., Shabanov, N. V., and Myneni, R. B. (2001). Variations in northern vegetation activity inferred from satellite data of vegetation index during 1981 to 1999. *J. Geophys. Res. Atmos.* 106 (D17), 20069–20083. doi:10.1029/2000jd000115

Zhu, Z., Piao, S., Myneni, R. B., Huang, M., Zeng, Z., Canadell, J. G., et al. (2016). Greening of the earth and its drivers. *Nat. Clim. change* 6 (8), 791–795. doi:10.1038/nclimate3004

frontiers | Frontiers in Remote Sensing

TYPE Original Research
PUBLISHED 18 January 2023
DOI 10.3389/frsen.2023.1086085

OPEN ACCESS

EDITED BY
Jane Southworth,
University of Florida, United States

REVIEWED BY
Yu-Hsuan Tu,
King Abdullah University of Science and Technology, Saudi Arabia
Alireza Sharifi,
Shahid Rajaee Teacher Training University, Iran

*CORRESPONDENCE
Chloe M. Mattilio,
cmattili@uwyo.edu
chloe.mattilio@gmail.com

SPECIALTY SECTION
This article was submitted to Satellite Missions, a section of the journal Frontiers in Remote Sensing

RECEIVED 01 November 2022
ACCEPTED 04 January 2023
PUBLISHED 18 January 2023

CITATION
Mattilio CM, Tekiela DR and Norton U (2023), Remote mapping of leafy spurge (*Euphorbia esula,* L.) in Northwestern Colorado.
Front. Remote Sens. 4:1086085.
doi: 10.3389/frsen.2023.1086085

Remote mapping of leafy spurge (*Euphorbia esula,* L.) in Northwestern Colorado

Chloe M. Mattilio[1]*, Daniel R. Tekiela[2] and Urszula Norton[1]

[1]Department of Plant Sciences, University of Wyoming, Laramie, WY, United States, [2]United States Department of Agriculture, Invasive Plant and Pesticide Use Program, United States Forest Service, Lakewood, CO, United States

Leafy spurge (*Euphorbia esula L.*) has been introduced to the Yampa River in Northwestern Colorado for over 40 years and flood and runoff events transport leafy spurge propagules onto adjacent landscapes. The spread of leafy spurge beyond the river channels has yet to be mapped and recorded, and this research was conducted to map leafy spurge occurrence in the Yampa River Valley. Significant stakeholder mapping efforts took place in the summer of 2019–2021, leading to excellent spatial data on leafy spurge presence and absence along the main channel. In summer 2019, multispectral SPOT seven satellite imagery, stakeholder ground mapping efforts, and bright yellow-green leafy spurge bracts were used to interpret imagery, identify dense, unobscured patches of leafy spurge, and digitize them. Spectral signatures from training samples for leafy spurge and other land cover classes (generalized as "not leafy spurge") were then used to train a Random Forest machine learning classification. In the summer of 2021, generated classification maps were compared to multispectral satellite imagery and stakeholder ground mapped leafy spurge presence. Mismatches were identified, and 271 validation locations were identified, navigated to, and evaluated for leafy spurge presence. Leafy spurge training samples were classified with 96% accuracy. Correctly classified leafy spurge locations had higher leafy spurge coverage and lower overstory canopy than missed leafy spurge locations. Leafy spurge growing beneath shrub canopy or growing as individual plants along the riverbanks were more likely to be missed. A frequency analysis for other plant species found at validation locations determined that smooth brome (*Bromus inermis* Leyss.), dandelion (*Taraxacum officinale* L.), and willow (*Salix* sp.) were most frequently misclassified as leafy spurge. In conclusion, multispectral satellite imagery was useful at remote detection of leafy spurge in open areas with dense leafy spurge coverage, but more work must be done for identification of sparse and diffuse leafy spurge infestations.

KEYWORDS

invasive plant mapping, leafy spurge (*Euphorbia* esula L.), satellite remote sensing, validation mapping, rangeland management

1 Introduction

Leafy spurge (*Euphorbia esula* L.) is a perennial invasive weedy species that has successfully established across a wide range of ecosystems and has a noxious weed designation in 22 US states (Goodwin et al., 2001). Leafy spurge is difficult to eradicate, despite heavy use of herbicides, targeted grazing, and various biocontrol agents (Goodwin et al., 2001). Leafy spurge is adapted to a wide range of growing conditions, including disturbed areas, rangelands, pastures, and river bottoms (Hyder et al., 2008).

With blue-green stems, linear leaves, small green flowers, and bright yellow bracts, mature leafy spurge is easily identifiable. Individual stems can produce over 200 seeds annually, which when mature, can be expelled up to 15 feet from the plant (St. John and Tilley, 2014). Seeds are small and buoyant, easily transported by water to areas downstream. Tissues contain a milky white sap that contains ingenol, which is released when plants are injured (Larry Leistritz, 2004). Once ingested, leafy spurge can be toxic to livestock, horses and wildlife, and result in significant economic losses to producers and other land users (Goodwin et al., 2001).

Remote sensing for leafy spurge mapping has been conducted since 1995, when leafy spurge was mapped with real color aerial imagery at Theodore Roosevelt National Park and found to be associated with high proximity to waterways (r^2 = .98) (Anderson et al., 1996). Multispectral sensors, which record reflectance beyond the visible spectrum in 3–10 spectral bands, have been used in a mixed-grass prairie in North Dakota (Casady et al., 2006) Leafy spurge was mapped with 67% accuracy, with decreasing classification accuracy when grown with herbaceous vegetation (Casady et al., 2006).

Successful remote detection of leafy spurge depends on capturing spectral differences between leafy spurge and other land cover, and imagery with limited spectral bands can make identifying leafy spurge challenging (Hunt andParker Williams, 2006). In a heterogeneous landscape near Devil's Tower National Monument Crook County, Wyoming, hyperspectral (remote sensing imagery consisting of hundreds to thousands of spectral wavelengths) classifications performed best in prairie vegetation, and better in bottomlands than uplands, which was caused by dense leafy spurge cover in riparian areas and longer periods of blooming in moist habitats (Williams and Raymond, 2002). In a study by Parker and Hunt. (2004), leafy spurge was well correlated with higher near infrared (NIR) reflectance, which is also known to be well correlated with dense vegetation cover. Leafy spurge was detected with 95% accuracy, and classification performed well in mixed-prairie and riparian vegetation than in forested areas (Williams and Raymond, 2002). In the sagebrush (*Artemisia tridentata subsp. tridentata*) steppe of Swan Valley, Idaho with 84%–94% accuracy (Glenn et al., 2005) and with 96%–99.5% accuracy at the mixed-grass prairie at Theodore Roosevelt National Park (O'Neill et al., 2000).

Leafy spurge has been spreading along the Yampa River main channel and constructed irrigation ditches for over 40 years (Yampa River Leafy Spurge Association, 2018; Turnage, 2021). The Yampa River flows for 250 river miles in Moffat and Routt Counties, Colorado, United States. Increased presence of leafy spurge in this area can be indicative of disturbance and large flooding events (Yampa River Leafy Spurge Project, 2018; Goodwin et al., 2001). The Yampa is one of the last free-flowing rivers in the Western United States, with seasonal flooding temporarily inundating sandbars and terraces away from the active river channel (Merritt and Cooper, 2000). Understanding the current extent of leafy spurge invasion with high spatial resolution is critical as its presence has already been observed beyond the riverbanks and floodplains, such as upland meadows, hillslopes and mountain ridges. High spatial resolution is a priority, as small satellite clusters of leafy spurge away from the main invasion are more likely to be effectively managed and to spread to new areas (Westbrooks, 2004). This project aimed to: 1) produce detailed maps of the current leafy spurge infestation along the Yampa River corridor with SPOT seven satellite remote sensing and 2), visit locations and validate leafy spurge presence or absence to describe classification performance.

2 Materials and methods

2.1 Study area

The Yampa River flows from the Flattops Wilderness to a confluence with the Green River deep inside of Dinosaur National Monument. The stretch of the Yampa River under investigation flows through the Moffat and the Routt Counties, between Hayden, Colorado, and Dinosaur National Monument (Figure 1). There, leafy spurge has already invaded riparian areas such as riverbanks and islands and is now advancing to uplands covered by juniper forests, sagebrush shrublands, grasslands, and agricultural fields. Figure 2.

2.2 Data collection

2.2.1 Ground mapping of leafy spurge

Ground mapping of leafy spurge took place during over three summers between 2019 and 2021, as water levels allowed each year. Mapping was conducted by stakeholder volunteers from the Yampa River Leafy Spurge Project (YRLSP) *via* water to map the extent of infestation along the Yampa's main channel and beyond riverbanks. Coverage was extensive, with one or more observers scanning the riverbanks of the main channel for leafy spurge rafts to map the perimeter of the invasion to full extent or property lines where owners rejected mapping requests. During each stop, the location and presence of leafy spurge (density, abundance, and patch size), land characteristics, vegetation type and overstory canopy cover were recorded on location service enabled tablets equipped with Map It Fast (Agterra, 2017) (Table 1.a). All information was imported into a Geographic Information System (GIS) (ArcMap 10.5 (ESRI, 2018) and used for identification of leafy spurge presence visible in the imagery. These mapped polygons were not used directly as classification training samples, as the imagery represented one sample in time, leafy spurge growing beneath shrubs and trees, and leafy spurge infestations that were too small to be represented by tablet spatial accuracy and imagery spatial resolution.

2.2.2 Satellite imagery acquisition

YRLSP funds were acquired and budgeted to purchase one set of SPOT seven satellite imagery from early July of 2019 from L3Harris Geospatial (L3Harris Geospatial, 2019). The beginning of summer in 2019 was cool and wet, so this sampling represents the late peak bloom of 2019. The spatial extent of this satellite imagery and resulting classification covers the area from Hayden, Colorado to Cross Mountain within 1.5 miles of the Yampa River channel (Figure 1). The imagery consists of five spectral bands, one panchromatic (1.5 m × 1.5 m pixels, 450–745 nm) and four multispectral: red (625–695 nm), green (530–590 nm), blue (450–520 nm), and near infrared (NIR, 760–890 nm) (6 m × 6 m pixels). Multispectral imagery was resampled to approximately 4 m × 4 m pixels using the finer resolution panchromatic band in ArcMap to increase the spatial resolution and identify the smallest clusters of leafy spurge plants possible with this imagery set. Despite this resampling of pixels of the spectral imagery, pan-sharpened imagery showed spectral patterns that delineated land cover classes that were difficult to distinguish, like riparian hay meadows, sparse rangeland vegetation, and wetlands. Once pan-sharpened, band combinations and representation were experimented with to highlight contrasts between ground mapped leafy spurge polygons and other recognizable land cover classes.

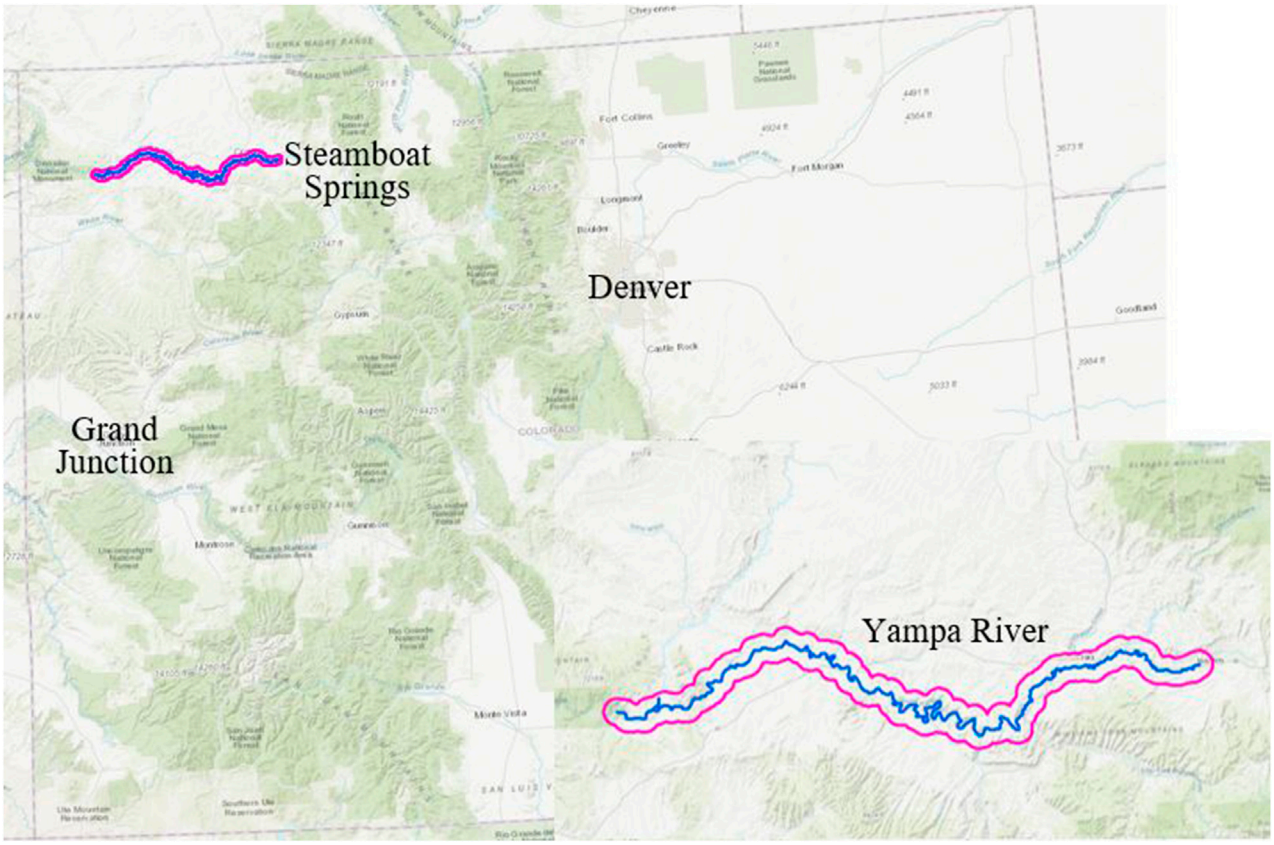

FIGURE 1
Map of the Yampa River study area, with location in Colorado (upper panel) and closer view of study area (lower panel) with satellite imagery extent buffered to 1.5 miles from river's edge (pink).

2.3 Data analysis

2.3.1 Training and classification

One hundred and eight training polygons of unobscured leafy spurge were digitized based on interpretation of the YRLSP ground mapped leafy spurge presence in the imagery in ArcMap. Volunteer ground mapping work was essential for development of these training samples, as they covered the main channel comprehensively with locations and detailed descriptions of leafy spurge presence. In addition, 96 polygons were developed for other land cover classes within the study area (water, forage fields, other vegetation, roads, structures, bare ground, etc.) and combined to create a "not leafy spurge" dataset. These training polygons represent the leafy spurge invasion as of imagery collection in July of 2019, and were imported into Program R, where SPOT seven imagery spectral reflectance values (red, green, blue, and NIR) were extracted to train the classification algorithm for leafy spurge and not leafy spurge. The method used a machine learning technique known as Random Forest (Breiman and Cutler, 2001), from the random Forest package in Program R (Liaw and Wiener, 2002). For this classification, 101 trees were grown, and 20% of the training samples were reserved for an internal validation. Two classification maps were developed with both, binary classification of "leafy spurge" and "not leafy spurge" classes using a probabilistic scale from 0 (most likely to be not leafy spurge) to 1 (most likely to be leafy spurge).

An accuracy assessment of the binary leafy spurge classification was conducted using a confusion matrix of classified and digitized training data, and users' accuracy, producer's accuracy, and overall accuracy. The kappa coefficient for the classification accuracy was calculated. To investigate differences in reflectance for red, green, blue, and NIR bands, correctly and incorrectly classified ground mapped leafy spurge presence polygons were selected from the classification map, and reflectance values were extracted for all four spectral bands for each class. To test differences in reflectance for detected and missed leafy spurge polygons for each spectral band, a two-way analysis of variance (ANOVA) was conducted in Program R.

2.3.2 Validation

To better understand classification performance, ground validation was conducted by identifying 271 points of interest, especially suspected classification mismatches within the study area. These areas were identified and discussed in 2020 during multiple remote open table discussions with Yampa River stakeholders in who know the area well and conducted ground mapping efforts for the YRLSP. These locations were selected to cover a broad range of habitat types and areas with known leafy spurge infestations. Within these locations, four or more pixels of the same class were generalized to make polygons of the same class. To avoid GPS inaccuracies, validation points were placed within these polygon centroids. In June of 2021, these validation points were visited by floating the

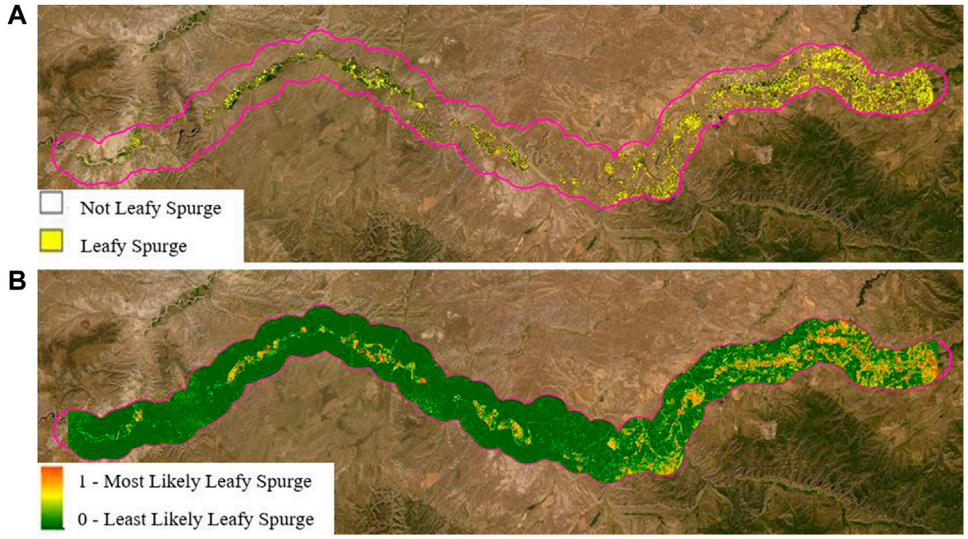

FIGURE 2
a and b. Random Forest classification predictions for imagery study area (magenta outline) for a binary classifier **(A)** and a probabilistic classifier **(B)**. The binary map shows pixels not classified as leafy spurge as colorless (negatives) and pixels classified as leafy spurge in yellow (positives). The probabilistic model represents values from 0 to 1, for least likely to be leafy spurge in dark green and most likely to be leafy spurge in red.

TABLE 1 a and b (top to bottom). Categorical infestation characteristics recorded and levels of each infestation characteristic from a. Ground mapped leafy spurge polygons and b. Validation leafy spurge locations.

Infestation Characteristic	Level 1	Level 2	Level 3	Level 4
Leafy Spurge Abundance	Single	Scattered	Scattered Dense	Dense Monoculture
Bare Ground Coverage	Trace	Low	Moderate	High
Overstory Canopy Coverage	Trace	Low	Moderate	High
Geomorphologic Type	Active Channel	Bank	Seasonally Inundated	Upland
Vegetation Type	Riparian Herbaceous	Riparian Shrub	Riparian Forest	Sparsely Vegetated

Infestation Characteristic	Level 1	Level 2	Level 3	Level 4	Level 5	Level 6	Level 7	Level 8
Discrete Patch	No	Yes						
Inundation Type	Never	100 years	20 years	Annual				
Geomorphologic Type	Active Channel	Bank	Seasonal Creek	Seasonal Floodplain	Agricultural			
Vegetation Type	Riparian Herbaceous	Riparian Shrub	Riparian Forest	Herbaceous	Irrigated Pasture	Upland		
Count of Other Plant Species	0	1	2	3	4	5	6	7

river and on foot with a handheld preprogrammed GPS unit. Selected locations were scattered at the Yampa River State Wildlife Area, through Craig, Colorado, in the Little Yampa Canyon, and through Axial Basin. In addition to confirming leafy spurge presence and absence, binary classification performance (correct or incorrect), geomorphologic type, vegetation type, count and identification of other species present, inundation frequency, leafy spurge cover, canopy cover, and bare ground were recorded (Table 1 b).

Binary and continuous classification maps were exported back to ArcMap where classification values were extracted from both, classification methods for leafy spurge presence polygons from Yampa River Leafy Spurge Project ground mapping and from 2021 validation points. Proportion of correctly identified leafy spurge polygons from the binary classification were calculated for each level of infestation characteristic (i.e. trace, low, moderate, and high for the overstory canopy cover infestation characteristic). Characteristics recorded were geomorphological features, vegetation type, leafy spurge cover and density; overstory canopy cover and the presence of bare ground (Table 1.a). Binary classification (leafy spurge vs. not leafy spurge) was fit to a logistic regression to determine the effect of infestation on classification accuracy from ground mapped data. The same approach was applied to the 2021 validation points, with proportional correct classification recorded for each level of infestation characteristic and binary classification. Results were fitted to a logistic regression model to determine which infestation characteristics (geomorphologic type, vegetation type, count of other

TABLE 2 Confusion matrix for Random Forest classification of imagery pixels as leafy spurge (positive) and not leafy spurge (negative) with training and validation samples correctly classified contributing to class and overall classification accuracy and misclassified other ground cover (false positives) and missed leafy spurge training samples (false negatives) and reducing class and overall classification accuracy.

		Training class				
		Positive	Negative	Producer's accuracy (%)	Kappa	Overall accuracy (%)
Classification Class	**Positive**	103 True positive	5 False positive	95.4	.902	90.7
	Negative	14 False negative	83 True negative	86.5		
		88.0%	94.3%			
		User's Accuracy				

TABLE 3 Results table from t-test for differences between reflectance in each spectral band (red, green, blue, and NIR) for true positives (Leafy Spurge) and false negative (Missed Leafy Spurge) leafy spurge polygons. Values shown are mean reflectance (Mean) and *p*-values (*p*-value) testing the differences between the class means for each spectral band. *p*-values marked with * are significantly different.

	Spectral band of multispectral imagery							
	Red		Green		Blue		Near infrared	
Assigned Class	Mean	*p*-value	Mean	*p*-value	Mean	*p*-value	Mean	*p*-value
Leafy Spurge	308	0.8	434	0.1	368	0.6	1359	.03*
Missed Leafy Spurge	309		433		367		1323	

species present, inundation frequency, proportional leafy spurge cover, proportional canopy cover, and proportional bare ground) affect classification accuracy within the validation dataset (Table 1 b).

3 Results

3.1 Imagery classification

Leafy spurge training samples were identified in the Random Forest classification of multispectral satellite imagery with an overall accuracy rate of 90.7%. The same classification resulted in a 95.4% class producer's accuracy and 88% class user's accuracy for leafy spurge (positive) (Table 2). The final accuracy metric calculated for the remote sensing classification was a coefficient of agreement, kappa (ranges from −1–1, with values close to 0 showing that the classification performed no better than random and one describing the data perfectly). Kappa was equal to 0.902, indicating that our remote sensing classification described our leafy spurge population samples well. Correctly classified leafy spurge spectral reflectance was not significantly different from missed leafy spurge reflectance for the red, green, and blue spectral bands, but was significantly higher for the NIR spectral band (*p*-value = 0.031) (Table 3).

Across a range of environmental and infestation conditions, the number of correctly mapped presence locations varied in the ground mapped dataset. Predictors that decreased correct classification likelihood of ground mapped leafy spurge polygons were single leafy spurge plant infestations (*p*-value = 0.011), leafy spurge located on riverbanks (*p*-value = 0.036), leafy spurge growing with shrubs (*p*-value = 0.021) and leafy spurge growing with trace amounts of bare ground (Table 4).

3.2 Classification validation

Much like the ground mapped leafy spurge dataset, the 271 ground validation points selected and visited represented a wide range of environmental and infestation conditions. Of these validation points that were classified as leafy spurge, 102 out of 190 were correctly classified (54% classification accuracy for leafy spurge). 190 out of 271 points were classified as leafy spurge (70%), 81 were classified as not leafy spurge (30%), and 159 out of the 271 total validation points were correctly classified (59% overall classification accuracy rate in the field). Successful classification of validation locations varied and predictors that increased likelihood of validation areas being correctly classified as leafy spurge are infestations that have higher leafy spurge percent cover (*p*-value = 5.8e-08) and infestations that have distinct boundaries, or discrete patches (*p*-value = 0.0480) (Table 5). Plant species that were misclassified as leafy spurge and growing alongside missed leafy spurge were smooth brome (*Bromus inermis* Leyss.), willows (*Salix sp.*), and dandelions (*Taraxacum officinale* L.) (Figure 3), while Sandberg bluegrass (*Poa secunda* J. Presl), western wheatgrass (*Pascopyrum smithii* Rydb.), poverty weed (*Iva axillaris* Pursh), dandelions, curlycup gumweed (*Grindelia squarrosa* Pursh.), tamarisk (*Tamarix ramosissima* L.), and whitetop (*Lepidium draba* L.) were misclassified as leafy spurge (Figure 4).

4 Discussion

The classification method identified mapped leafy spurge training samples with 95.4% accuracy training and an overall classification accuracy of 90.7%. If mapping was to take place again however, satellite imagery with additional wavelengths of near infrared spectra may be useful, as SPOT seven imagery NIR only covers the 760–890 nm

TABLE 4 Logistic regression output for statistically significant predictors of leafy spurge classification of ground mapped leafy spurge polygons with odds ratio (values < 1, decrease odds of correctly classifying leafy spurge, values > 1, increase odds of correctly classifying leafy spurge), impact on leafy spurge prediction rates, and *p*-values of logistic regression.

	Odds ratio	Leafy spurge classification likelihood	*p*-value
Geomorphology - Bank	.180	–	.036
Bare Ground - Low	23.515	+	.010
Bare Ground -Moderate	38.318	+	.003
Bare Ground - High	89.334	+	.000
Vegetation – Shrub	.106	–	.021
Leafy Spurge – Single Plant	.136	–	.011
Polygon Area	1.000	+	.018

TABLE 5 Logistic regression output for statistically significant predictors of leafy spurge classification of validation locations of leafy spurge with odds ratio (values < 1, decrease odds of correctly classifying leafy spurge, values > 1, increase odds of correctly classifying leafy spurge), impact on leafy spurge prediction rates, and *p*-values of logistic regression.

	Odds ratio	Odds of spurge	*p*-value
Discrete Patch	8.129	+	.0480
Leafy Spurge Percent Cover	1.556	+	5.8e-08

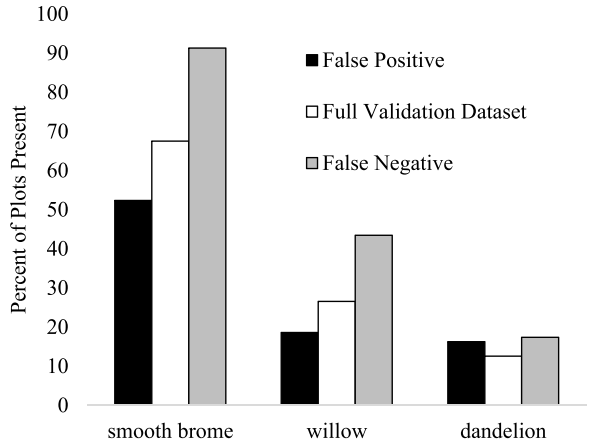

FIGURE 3
Results of frequency analysis of the three most mistaken species, smooth brome, willow, and dandelions, with their proportional presence in the full validation dataset (white), false positives (black, mistakenly classified as leafy spurge), and false negatives (grey, present with missed leafy spurge infestations).

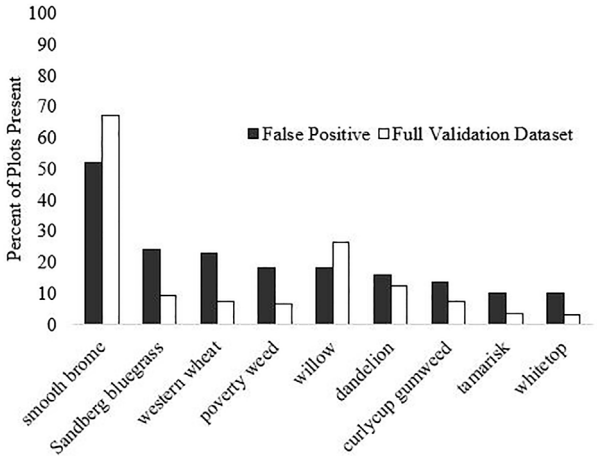

FIGURE 4
Results of frequency analysis of false positive plant species with their proportional presence in the full validation dataset (white) and false positives (black, mistakenly classified as leafy spurge).

of the spectrum. Near infrared reflectance was the only spectral band that was significantly different between correctly identified and missed leafy spurge polygons, so more bands of varying wavelengths of near infrared may be useful in distinguishing leafy spurge's unique spectral signature. Leafy spurge does seem to be spectrally identifiable within the narrow portion of the electromagnetic spectrum captured by multispectral satellite imagery products (Mitchell and Glenn, 2009). Our detection rates of leafy spurge varied, as infestations that consist of a single leafy spurge plant, leafy spurge growing with trace amounts of bare ground, leafy spurge growing on banks, and leafy spurge growing with riparian shrub vegetation cover types were more likely to be missed by our Random Forest imagery classification. This may be because the presence of a single leafy spurge population is much harder to detect with 1) somewhat limited spatial resolution (4 m × 4 m pixels), 2) changes to bank geomorphology caused by seasonal flooding during the period between satellite imagery collection and validation mapping, and 3), dense shrub cover obscuring leafy spurge invasions beneath their canopy. Overstory canopy coverage alone, however, was not a significant predictor of leafy spurge classification accuracy.

In other research projects where remote sensing was used to map leafy spurge, leafy spurge growing below overstory canopy coverage, leafy

spurge on steep slopes, sparse leafy spurge populations, and small infestations of leafy spurge were missed (Anderson et al., 1996; Parker and Hunt, 2004; Glenn et al., 2005), aligning with our decreased detection accuracy of singly leafy spurge plants and leafy spurge growing below shrub and tree canopy. In contrast to our challenges of mapping leafy spurge in riparian areas of the Yampa River, detection accuracy of leafy spurge mapping in Crook County, Wyoming was improved when growing in riparian areas (Williams and Raymond, 2002; Parker and Hunt, 2004). Adding ancillary spatial data, like vegetation cover maps and distance to waterways may improve remote sensing classification results (Hunt et al., 2010; Dubovik et al., 2021). Additionally, the incorporation of citizen science data of dense, unobscured leafy spurge presence collected and submitted from within the study area could be incorporated, to increase training samples and obtain samples away from the Yampa River riparian zone (Vaz et al., 2019) but increasing the temporal resolution of the imagery with a times series of multiple imagery scenes through the leafy spurge bloom could.

One major limitation of this project is the difference between June 2021 validation mapping and satellite imagery data collection in July of 2019. Imagery procurement was limited by YRLSP budget, and 2021 SPOT seven satellite imagery purchase and classification would have been beneficial, as leafy spurge invasions may have advanced. If further remote sensing was to be conducted for mapping general leafy spurge invasion in the area, free coarser resolution multispectral imagery like Sentinel-2 (10 m × 10 m pixels) could be used. As leafy spurge is a deep-rooted perennial and a prolific seed producer (St. John and Tilley, 2014) and largely uncontrolled in the Yampa River Valley, leafy spurge populations away from the dynamic riverbanks are unlikely to decrease, excepting extreme environmental conditions, like drought. In experimental plots where herbicide was applied in the fall of 2019, treatments that controlled leafy spurge reproduction left woody stems which were recognizable during validation mapping in the summer of 2021, so some signs of past leafy spurge may be recognizable even if plants do not regrow from established roots. Additionally, our training samples were biased toward dense, large, and unobscured leafy spurge recognizable in multispectral imagery sets and may not represent the full range of leafy spurge infestation abundance, size, and habitat type.

Though the success rates of the validation mapping efforts were generally low (59% of validation locations were correctly classified), the validation locations were chosen based on anomalies in YRLSP members expert knowledge of the area or features and areas of interest from the classification prediction. For example, a series of validation points were set in a seasonal Yampa River tributary, to see if positively classified pixels as leafy spurge were true leafy spurge locations. Leafy spurge detection accuracy varies within the 190 leafy spurge positive presence locations within the dataset, as the Random Forest classification was more accurate at identifying leafy spurge populations growing as discrete patches rather than scattered populations. Discrete patches of leafy spurge and infestations with higher leafy spurge percent cover were more likely to be correctly classified by the Random Forest imagery classification. Casady et al. (2006) found that detected leafy spurge patches had higher average leafy spurge percent cover and higher average patch size, with infestations smaller than 200 m^2 and 30% leafy spurge cover less likely to be identified (Casady et al., 2006). Dense populations with high leafy spurge cover may have more recognizable spectral signatures than sparse populations. Discrete boundaries of leafy spurge patches may be more identifiable, as scattered populations might share pixel space with other land cover types, though the number of additional species present at validation locations did not significantly influence classification accuracy of leafy spurge.

5 Conclusion

Satellite remote sensing appears to be a viable option for leafy spurge mapping on the Yampa River, but classification accuracy varies with leafy spurge infestation characteristics and environment. Small and/or sparse infestations of leafy spurge may go undetected, and detection rates decreased in areas with shrubs and overstory canopy coverage. Identification was most accurate when leafy spurge coverage was dense. Validation mapping suggests that leafy spurge is best identified when growing in discrete patches and when leafy spurge densities are higher.

If leafy spurge mapping was to be conducted again in the Yampa, a time series of imagery that represents early season and mid-season would be employed to try to differentiate leafy spurge from other vegetation, as suggested by Lake et al. in a heterogeneous Minnesota landscape (Lake et al., 2022). If left unmanaged, leafy spurge may become a much more prevalent invader in Moffat and Routt Counties, producing more propagules to spread through the Yampa, Green, and Colorado Rivers.

Data availability statement

The raw data supporting the conclusion of this article will be made available by the authors, without undue reservation.

Author contributions

All authors listed have made a substantial, direct, and intellectual contribution to the work and approved it for publication.

Funding

Funding for this work came from the Colorado Water Conservation Board Water Supply Reserve Fund through the Friends of the Yampa and the Y Cross Ranch Endowment. Publication costs were covered by the University of Wyoming Agricultural Experiment Station Hatch Fund.

Conflict of interest

The authors declare that the research was conducted in the absence of any commercial or financial relationships that could be construed as a potential conflict of interest.

Publisher's note

References

Anderson, G. L., Everitt, J. H., Escobar, D. E., Spencer, N. R., and Andrascik, R. J. (1996). Mapping leafy spurge (euphorbia esula) infestations using aerial photography and geographic information systems. *Geocarto Int.* 11 (1), 81–89. doi:10.1080/10106049609354526

Breiman, L. (2001). Random Forests. *Machine Learning* 45, 5–32. doi:10.1023/A:1010933404324

Casady, G. M., Hanley, R. S., and Seelan, S. K. (2006). Detection of leafy spurge (Euphorbia esula) using multidate high-resolution satellite imagery. *Weed Technol.* 19 (02), 462–467. doi:10.1614/wt-03-182r1

Dubovik, O., Schuster, G. L., Xu, F., Hu, Y., Bösch, H., Landgraf, J., et al. (2021). Grand challenges in satellite remote sensing. *Front. Remote Sens.* 2, 1–10. doi:10.3389/frsen.2021.619818

ESRI (2018). ArcGIS Desktop: Release 10.6. Redlands, CA: Environmental Systems Research Institute.

Glenn, N. F., Mundt, J. T., Weber, K. T., Prather, T. S., Lass, L. W., and Pettingill, J. (2005). Hyperspectral data processing for repeat detection of small infestations of leafy spurge. *Remote Sens. Environ.* 95 (3), 399–412. doi:10.1016/j.rse.2005.01.003

Goodwin, K., Sheley, R., Nowierski, R., and Lym, R. (2001). Leafy spurge: Biology, ecology and management. AvaliableAt: http://store.msuextension.org/publications/AgandNaturalResources/EB0134.pdf.

Hunt, E. R., Gillham, J. H., and Daughtry, C. S. T. (2010). Improving potential geographic distribution models for invasive plants by remote sensing. *Rangel. Ecol. Manag.* 63 (5), 505–513. doi:10.2111/REM-D-09-00137.1

Hunt, E. R., and Parker Williams, A. E. (2006). Detection of flowering leafy spurge with satellite multispectral imagery published by: Society for range management detection of flowering leafy spurge with satellite multispectral imagery. *Rangel. Ecol. Manag.* 59 (5), 494–499. doi:10.2111/05-216R.1

Hyder, A., Leung, B., and Miao, Z. (2008). Integrating data, biology, and decision models for invasive species management: Application to leafy spurge (Euphorbia esula). *Ecol. Soc.* 13 (2), art12. doi:10.5751/ES-02485-130212

Lake, T. A., Runquist, R. D. B., and Moeller, D. A. (2022). Deep learning detects invasive plant species across complex landscapes using Worldview-2 and Planetscope satellite imagery. *Remote Sens. Ecol. Conservation* 8, 875–889. doi:10.1002/rse2.288

Larry Leistritz, F., Dean, A., and Hodur, N. M. (2004). Assessing the economic impact of invasive weeds: The case of leafy spurge (Euphorbia esula). *Weed Technol.* 18, 1392–1395. doi:10.1614/0890-037x(2004)018[1392:ateioi]2.0.co;2

Liaw, A., and Wiener, M. (2022). Classification and Regression by randomForest. *R News* 2 (3), 18–22. https://CRAN.R-project.org/doc/Rnews/.

Merritt, D. M., and Cooper, D. J. (2000). Riparian vegetation and channel change in response to river regulation: A comparative study of regulated and unregulated streams in the Green River basin, USA. *River Res. Appl.*, 16, 543–564. doi:10.1002/1099-1646(200011/12)16:6<543::aid-rrr590>3.0.co;2-n

Mitchell, J. J., and Glenn, N. F. (2009). Leafy spurge (Euphorbia esula) classification performance using hyperspectral and multispectral sensors. *Rangel. Ecol. Manag.* 62 (1), 16–27. doi:10.2111/08-100

O'Neill, M., Ustin, S. L., Hager, S., and Root, R. (2000). "Mapping the distribution of leafy spurge at Theodore Roosevelt national Park using AVIRIS," in *Proceedings of the 9th JPL airborne earth sciences workshop* (pp. 00-18) (Pasadena, California: NASA Jet Propulsion Laboratory).

Parker, A. E., and Hunt, E. R. (2004). Accuracy assessment for detection of leafy spurge with hyperspectral imagery. *J. Range Manag.* 57 (1), 106–112. doi:10.2111/1551-5028(2004)057[0106:aafdol]2.0.co;2

St. John, L., and Tilley, D. (2014). *Plant Guide for Leafy spurge (Euphorbia esula)*. Aberdeen, Idaho: Natural Resources Conservation Service, Plant Materials Center 83210.

Turnage, M. B. (2021). An invasion problem: Leafy spurge and its management efforts in Dinosaur National Monument and the Greater Yampa River Area. Avaliable At: https://storymaps.arcgis.com/stories/998e931b97024734bf988db86e1fde61. Google Play https://play.google.com/store/apps/details?id=com.agterra.MapItFastandhl=en_USandgl=US.

Vaz, A. S., Alcaraz-Segura, D., Vicente, J. R., and Honrado, J. P. (2019). The many roles of remote sensing in invasion science. *Front. Ecol. Evol.* 7, 1–5. doi:10.3389/fevo.2019.00370

Westbrooks, R. G. (2004). New approaches for early detection and rapid response to invasive plants in the United States[1]. *Weed Technol. Invasive Weed Symp. Weed Technol.* 18, 1468–1471. doi:10.1614/0890-037x(2004)018[1468:nafeda]2.0.co;2

Williams, A. P., and Raymond, E. (2002). Estimation of leafy spurge cover from hyperspectral imagery using mixture tuned matched filtering. Avaliable At: www.elsevier.com/locate/rse.

Yampa River Leafy Spurge Project (2018). Who we are. Yampa River Leafy Spurge Project. Available at: https://www.yampariverleafyspurgeproject.com/who-we-are.

frontiers | Frontiers in Remote Sensing

TYPE Original Research
PUBLISHED 13 February 2023
DOI 10.3389/frsen.2023.1041466

OPEN ACCESS

EDITED BY
Hannah Victoria Herrero,
The University of Tennessee, United States

REVIEWED BY
Joseph P. Messina,
University of Alabama, United States
Erin Bunting,
Michigan State University, United States

*CORRESPONDENCE
Yogita Karale,
karale.1@osu.edu

SPECIALTY SECTION
This article was submitted to Remote Sensing Time Series Analysis, a section of the journal Frontiers in Remote Sensing

RECEIVED 10 September 2022
ACCEPTED 23 January 2023
PUBLISHED 13 February 2023

CITATION
Karale Y and Yuan M (2023), Spatially lagged predictors from a wider area improve PM2.5 estimation at a finer temporal interval—A case study of Dallas-Fort Worth, United States.
Front. Remote Sens. 4:1041466.
doi: 10.3389/frsen.2023.1041466

Spatially lagged predictors from a wider area improve PM2.5 estimation at a finer temporal interval—A case study of Dallas-Fort Worth, United States

Yogita Karale* and May Yuan

Geospatial Information Sciences, the University of Texas at Dallas, Richardson, TX, United States

Fine particulate matter, also known as PM2.5, has many adverse impacts on human health. However, there are few ground monitoring stations measuring PM2.5. Satellite data help fill the gaps in ground measurements, but most studies focus on estimating daily PM2.5 levels. Studies examining the effects of environmental exposome need accurate PM2.5 estimates at fine temporal intervals. This work developed a Convolutional Neural Network (CNN) to estimate the PM2.5 concentration at an hourly average using high-resolution Aerosol Optical Depth (AOD) from the MODIS MAIAC algorithm and meteorological data. Satellite-acquired AOD data are instantaneous measurements, whereas stations on the ground provide an hourly average of PM2.5 concentration. The current work aimed to refine PM2.5 estimates at temporal intervals from 24-h to 1-h averages. Our premise posited the enabling effects of spatial convolution on temporal refinements in PM2.5 estimates. We trained a CNN to estimate PM2.5 corresponding to the hour of AOD acquisition in the Dallas-Fort Worth and surrounding area using 10 years of data from 2006–2015. The CNN accepts images as input. For each PM2.5 station, we strategically subset temporal MODIS images centering at the PM2.5 station. Hence, the resulting image-patch size represented the size of the area around the PM2.5 station. It thus was analogous to spatial lag in spatial statistics. We systematically increased the image-patch size from 3×3, 5×5, . . . , to $19 \times 19\ km^2$ and observed how increasing the spatial lag impacted PM2.5 estimation. Model performance improved with a larger spatial lag; the model with a $19 \times 19\ km^2$ image-patch as input performed best, with a correlation coefficient of 0.87 and a RMSE of $2.57\ g/m^3$ to estimate PM2.5 at *in situ* stations corresponding to the hour of satellite acquisition time. To overcome the problem of a reduced number of image-patches available for training due to missing AOD, the study employed a data augmentation technique to increase the number of samples available to train the model. In addition to avoiding overfitting, data augmentation also improved model performance.

KEYWORDS

PM2.5, MODIS MAIAC, aerosol optic depth, convolational neural netwwork, spatial lag effect

1 Introduction

The Global Burden Disease study reported that air pollution caused 4.2 million deaths in 2015 due to particulate matter (Cohen et al., 2017). In addition, recent studies found a link between PM2.5 and several neurological disorders like dementia, Alzheimer's, and Parkinson's diseases (Kioumourtzoglou et al., 2016; Chen et al., 2017). Despite the harmful effects of PM2.5 on health, ground monitoring stations providing information about PM2.5 concentration are considerably sparse and unsuitable for spatial interpolation at a local scale. As a result, interpolations of PM2.5 from the nearest available monitoring stations to estimate the exposure in epidemiological studies are likely unreliable due to the underestimation of spatial variability in PM2.5 (Özkaynak et al., 2013). In an effort to overcome sparse measurements from ground stations, satellite-derived PM2.5 is widely used. These efforts focus on estimating daily PM2.5 levels. However, PM2.5 data over finer temporal intervals are necessary for accurate environmental exposure estimation. This study explores the use of satellite data to estimate PM2.5 over a temporal interval of 1 h in contrast to daily PM2.5 levels.

A common approach to characterize the spatial distribution of PM2.5 utilizes satellite-based Aerosol Optical Depth (AOD) as one of the predictor variables (Chudnovsky et al., 2014; Lary et al., 2014; Xie et al., 2015; Guo et al., 2017). AOD measures the amount of aerosols present in the atmosphere according to the optical properties of aerosols in an atmospheric column. However, the relationship between PM2.5 and AOD is complicated. AOD is affected by the size of the particles, the type of the particles, and meteorological factors. Depending on the source, the composition of the particles may vary in space and time (Bell et al., 2007). Meteorological factors (such as cloud fraction, relative humidity, temperature, boundary layer height, wind speed, and others) also affect this relationship (Lary et al., 2014; Guo et al., 2017). Several studies report PM2.5-AOD relationship varies with geography (Engel-Cox et al., 2004), time (Guo et al., 2017), the scale of regional or local studies (Chudnovsky et al., 2014), and AOD data resolution (Chudnovsky et al., 2014; Xie et al., 2015; Guo et al., 2017). Therefore, empirical models using AOD to estimate PM2.5 developed for one geographical area cannot be used for others.

The limited number of air quality stations in a geographical area may not meet the sample size requirements of parametric statistical frameworks, such as multiple linear regression. As a general rule of thumb, a multiple linear regression requires a minimum of 30 observations. Thus, these approaches are unsuitable in areas with sparse monitoring stations. Low-cost sensors such as PurpleAir (https://www2.purpleair.com/) have been deployed in large numbers across the United States. While these low-cost sensors help reduce the gap in spatial coverage of PM2.5 measurements, the accuracy of these sensors remains a cause of concern. A field evaluation of three PurpleAir sensors carried out at Rubidoux Air Monitoring Station in California for 2 months indicates that, in general, PurpleAir sensors can show an overall trend of PM2.5 within a day and across days but tend to overestimate PM2.5 concentration most of the times (Gupta et al., 2018). Specifically, the California study highlights that the bias of PurpleAir sensors increases with rising PM2.5 concentration. Moreover, PurpleAir sensors' observations deviate from 0% to 90% of their hourly mean values.

A specification error due to the incorrect functional form between dependent and independent variables leads to biases in estimation (Ramsey, 1969), and proper relationship specifications are challenging for PM2.5 models using AOD (Lary et al., 2014). *In-situ* stations measure PM2.5 as the ground-level concentration of particles with an aerodynamic diameter less than 2.5 micrometers. In contrast, AOD measures the extinction of light due to aerosols in the atmospheric column (Nam et al., 2018). AOD and PM2.5 are independently affected by meteorological parameters (Guo et al., 2017), further complicating their relationship. Furthermore, AOD is an instantaneous measurement from space, and PM2.5 is an hourly average measured *in situ* at respective ground monitoring stations. Researchers proposed diverse modeling approaches to overcome the complicated relationship but lacked sufficient attention to the differences in temporal representations of AOD and PM2.5.

Literature reported several approaches to model the PM2.5-AOD relationship, like land-use regression (Lee, 2019), geographically weighted regression (Hu et al., 2013; van Donkelaar et al., 2015), back propagation artificial neural network (Gupta and Christopher, 2009a), mixed effect models (Xie et al., 2015), linear regression models (Gupta and Christopher, 2009b), and chemical transport models (Geng et al., 2015). The mixed effect modeling approach appeared popular among these approaches to 24-h average PM2.5 estimation. Some studies used AOD as the only predictor (Chudnovsky et al., 2014; Xie et al., 2015); others included additional parameters to improve model performance (Hu et al., 2014; Stafoggia et al., 2017). Xie et al. (2015) used a mixed effect model to account for spatiotemporal variations in PM2.5-AOD relationship with day-specific and site-specific parameters for AOD. Moreover, several other studies implemented similar mixed effect models by including AOD and additional spatiotemporal parameters (Hu et al., 2014; Stafoggia et al., 2017). In addition to day-specific random parameters, Stafoggia et al. (2017) introduced region-specific random parameters to account for variation in PM10-AOD relations across different regions in Italy. In the Southeastern United States, Hu et al. (2014) used a mixed effect model to capture temporal variability in the PM2.5-AOD relationship and followed with Geographically Weighted Regression on the residuals to account for spatial variability. Spatial and temporal parameters considered in these studies include population density, emission data, elevation, land cover, road density, Normalized Difference Vegetation Index (NDVI), meteorological data, etc. Zheng et al. (2013) applied a deep learning framework to predict the hourly Air Quality Index (AQI) for Beijing at 1 km resolution with region-specific parameters representative of traffic features (e.g., mean, standard deviation, and distribution of speeds on the road) and human mobility features (e.g., number of people arriving and departing a location). Such region-specific parameters may not be available or appropriate for areas outside Beijing.

Machine learning recently gained traction in modeling PM2.5 (Lary et al., 2014; Di et al., 2016; Hu et al., 2017; Li et al., 2017; Park et al., 2020). Several of these studies incorporated spatial dependence in the machine learning methods. Di et al. (2016) used an artificial neural network (ANN) for the northeastern United States to calibrate PM2.5 obtained from a chemical transport model, and Li et al. (2017) used the deep belief network approach to estimate PM2.5 in China. They considered spatial and temporal autocorrelation using lagged spatial and temporal terms. Spatial lag was incorporated by using PM2.5 measurements from nearby stations weighted by the inverse of

their distance from the monitor under consideration, hence, essentially the classic spatial interpolation based on inverse distance weighting. An alternative way of applying weights in PM2.5 estimation was the boosting technique in machine learning. Boosting gave more weight to observations with high errors to improve model performance. Zhan et al. (2017) used geographically weighted gradient boosting to account for spatial non-stationarity in PM2.5 and AOD as well as meteorological factors. These methods refine the spatial resolution of PM2.5 estimation but retain temporal resolution at daily averages.

Advances in deep learning opened opportunities to convolute *in situ* and satellite observations for PM2.5 estimation. Park et al. (2020) used a convolutional neural network (CNN) to estimate the 24-h averaged PM2.5 across the conterminous United States using the 1-year data from 2011. Hu et al. (2017) incorporated inverse distance weighted PM2.5 from nearby stations as input to the random forest model. Clouds or high surface brightness might obscure AOD data from MODIS. Due to the high missing rate of AOD, both studies applied the GEOS-Chem model to simulate AOD data; Hu et al. (2017) used GEOS-Chem AOD when MODIS AOD was missing, whereas Park et al. (2020) used both MODIS AOD and GEOS-Chem AOD. Along with the AOD data, both studies used meteorological data, land-use variables, and National Emission Inventory (NEI) data as predictors. Several data issues were prominent in both studies. NEI database provided information about pollutant-wise emissions at annual scales. However, methods used to estimate these emissions might vary from year to year (U.S. Environmental Protection Agency, 2020). Therefore, the data from these emission inventories were unsuitable for multi-year studies. Land-use data were static and could contribute very little in explaining hourly PM2.5 variation. Li et al. (2017) reported that the inclusion of road networks as one of the predictors showed a minimal impact on model performance, whereas population worsened the model performance. Furthermore, in areas with sparsely distributed monitoring stations, a model developed with land-use and population density around very few monitoring stations might not be representative enough to allow model generalizability for the entire study area. Xu et al. (2014) observed an increase in AOD values in areas with increased human activities and decreased AOD in areas with increasing forested land. They concluded that changes in land-use led to changes in AOD patterns. Therefore, our study assumes that AOD data embed the spatial effects of land-use and surrounding activities on PM2.5 in a given hour.

Several studies assessed model performance in estimating PM2.5 through cross-validation in three different approaches for setting cross-validation data: spatially separated cross-validation (SS-CV), temporally separated cross-validation (TS-CV), and overall cross-validation (O-CV) approach (Di et al., 2016; Hu et al., 2017; Park et al., 2020). As the names suggest, SS-CV shares no common locations between the training dataset and the cross-validation dataset; TS-CV uses observations for the training dataset from different days than the observations in the cross-validation dataset. In contrast, the O-CV approach imposed no restrictions in days or locations on training and cross-validation datasets. Results from studies by Di et al. (2016), Hu et al. (2017), and Park et al. (2020) showed that models using O-CV and TS-CV outperformed the ones using the SS-CV approach. It suggested that models developed for a set of locations did not perform well at unseen locations; the models were spatially untransferable. The performance of models using either the O-CV or T-CV approach for cross-validation was comparable. Therefore, this our study took the O-CV approach for cross-validation.

Incorporating geographical correlations can improve model performance in PM2.5 estimation (Li et al., 2017), but four main challenges remain. First, many studies incorporate spatial dependence and include spatially lagged predictors and spatially lagged PM2.5 in the model (Hu et al., 2017; Li et al., 2017; Zhan et al., 2017; Park et al., 2020). For the models developed by Hu et al. (2017) and Park et al. (2020), spatially lagged PM2.5 measurements rise to the most important variable in estimating PM2.5. However, obtaining spatially lagged PM2.5 for areas with sparse distribution of monitoring stations is challenging. Covariates from nearby stations depend on the spacings between stations and the spatial distribution of the target phenomenon PM2.5. Therefore, the density of the PM2.5 stations can affect the accuracy of the PM2.5 estimates. A covariate-based estimator would perform poorly in areas with sparse monitoring networks. In contrast, an objective of this study is to develop a model suitable even in areas with very few monitoring stations. Moreover, the use of spatially lagged PM2.5 conceals the role of explanatory variables in the spatial variation of PM2.5. The second challenge relates to the hindrance of real-time PM2.5 estimation without data from nearby monitoring stations. The third challenge speaks for the mismatch between PM2.5 estimates and satellite observations. For example, AOD data are instantaneous observations around 10:30 a.m. and 1:30 p.m. by Terra and Aqua satellites, respectively. Although few studies, such as Tian and Chen (2010) and Xie et al. (2015), used PM2.5 obtained near MODIS AOD acquisition time, most studies in the literature estimated the PM2.5 concentration averaged over 24 h using instantaneous AODs. Finally, the fourth challenge relates to previous studies incorporating spatial dependence. These studies used predictors from a fixed spatial extent around the PM2.5 station. Therefore, how the model might perform over different spatial extents is not known.

Our study fills the research gaps considering these challenges by developing a model to estimate PM2.5 in the hour corresponding to satellite data acquisition time. The model considers only spatially lagged predictors from MODIS and meteorological data but does not include PM2.5 from nearby stations. Finally, the study investigates the model performance using CNN, where the input image-patch size varies from 3×3, 5×5,. . to 19×19, with a PM2.5 station located in the central pixel or cell of the image. Thus, the input image-patch size represents the size of the spatial lag. Varying the input image-patch size allows for examining the effect of spatial lag size on PM2.5 estimation. While the research focused on PM2.5, the proposed approach is applicable to other spatially continuous variables, such as temperature or greenness indices, with observations at *in situ* stations, remote sensing acquisitions, and relevant auxiliary data. In particular, data from *in situ* observations are commonly available as averaged values over time, such as PM2.5 hourly, daily, or monthly averages at a specific site. In contrast, remote sensing acquisitions are instant measures across multiple locations. The proposed approach explores the spatial measures captured in consecutive remote sensing images that can aid down-scaled temporal estimates at sites. Specifically in our study, consecutive MODIS images were taken ~3 or ~21 h apart. If we can accurately estimate time-averaged PM2.5 values in-between MODIS acquisitions at sites, we will be able to derive a space-time cube of PM2.5 (or other spatial variables). Our proposed approach used

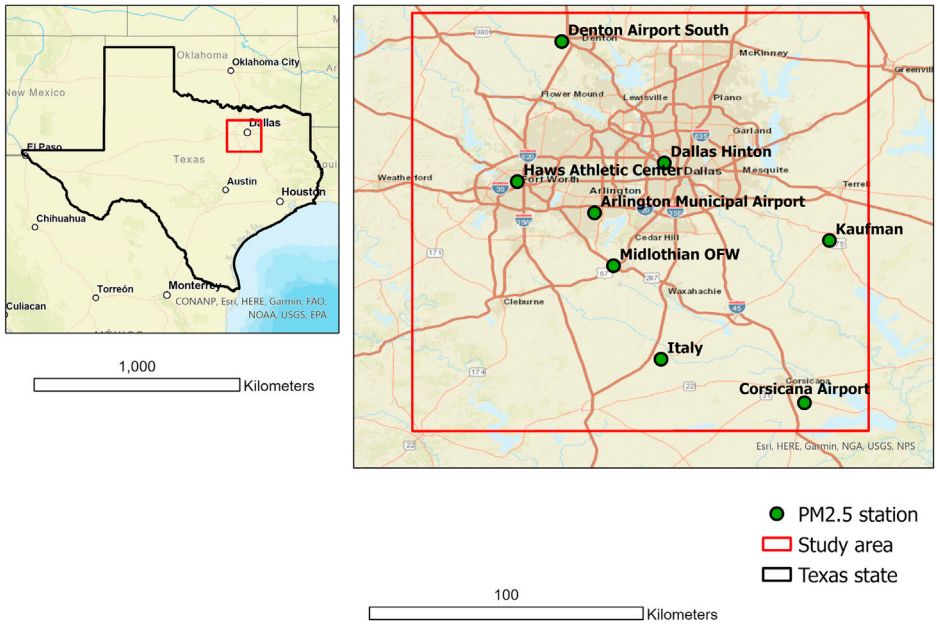

FIGURE 1
Locations of PM2.5 stations in the study area.

hourly observations from *in situ* stations to train a model and validate the model that estimates the PM2.5 hourly values corresponding to two MODIS images using both AOD data and meteorological data. Our findings showed the spatial-lag effects on the downscaled temporal estimates. Effective spatial lags shall vary with spatial variables. In our study, the effective spatial lag for PM2.5 expands to 10 km.

2 Data and methods

2.1 Study area

The study area is the Dallas-Fort Worth (DFW) metroplex with more than 7.5 million people. The DFW metroplex and its surrounding area have only eight air-quality monitoring stations measuring hourly PM2.5 from 2006–2015, leaving most of the metroplex unmonitored (Figure 1). Out of the eight monitoring stations, three are located in urban areas, whereas five are at the periphery of the urban areas. Information on the spatiotemporal distribution of PM2.5 at the appropriate level of detail is important because of the harmful effects of PM2.5 on health, especially for those already suffering from respiratory and cardiovascular diseases. Informed of the spatiotemporal distribution of PM2.5 at a fine interval, people can avoid areas with high concentration and reduce the geographic context uncertainty for epidemiological studies of PM2.5 exposure. Nevertheless, a step towards estimating the spatiotemporal distribution of PM2.5 is to test how well an O-CV approach can use AOD to estimate PM2.5 at these stations corresponding to the hour of satellite overpass time. If the estimation is acceptable at these sites, the proposed model can provide the foundation for building a spatial interpolation method with AOD to estimate PM2.5 at unmonitored locations with AOD data.

2.2 Data

The study used two sets of input data: 1) aerosol optical depth (AOD) and AOD-related variables from MODIS 2) meteorological data to estimate PM2.5 corresponding to the hour of MODIS overpass time.

2.2.1 PM2.5

Terra and Aqua satellites, with an equatorial crossing time of ~10: 30 a.m. and 1:30 p.m. (local time) respectively, overpass the study area twice a day. Nevertheless, due to the broader swath of 2,330 km, MODIS AOD is sometimes available at times other than overpass times. PM2.5 data from ground monitoring stations are available at an hourly interval. The study used PM2.5 for the hour MODIS overpasses the study area. For example, if MODIS overpasses at 10:30 a.m., the PM2.5 measured between 10 a.m. and 11 a.m. was used. The data was downloaded from the Environmental Protection Agency's website (https://aqs.epa.gov/aqsweb/airdata/download_files.html#Raw) with the parameter code of the PM2.5 data 88502. A total of 10-year PM2.5 observations from 2006–2015 were downloaded for the study area.

2.2.2 AOD data

MODIS AOD data have been available only at 10 km resolution. A recently developed algorithm, Multi-Angle Implementation of Atmospheric Correction (MAIAC) downscales AOD to 1 km

TABLE 1 List of predictors.

Sr No.	Predictor	Measurement unit	Spatial resolution
1	AOD	—	1 km
2	AOD QA Flag	—	1 km
3	Column Water Vapor	cm	1 km
4	Cosine of Solar Zenith Angle	—	5 km
5	2-m Temperature	K	~13 km
6	2-m Dew Point Temperature	K	~13 km
7	Clear Sky Surface Photosynthetically Active Radiations	J m^{-2}	~13 km
8	Photosynthetically Active Radiations at the Surface	J m^{-2}	~13 km
9	Total Column Water Vapor	kg m^{-2}	~13 km
10	Boundary Layer Dissipation	J m^{-2}	~13 km
11	Boundary Layer Height	m	~13 km
12	Total Cloud Cover	Expressed as a fraction between 0–1	~13 km
13	Medium Cloud Cover	Expressed as a fraction between 0–1	~13 km
14	High Cloud Cover	Expressed as a fraction between 0–1	~13 km
15	Convective Precipitation	m	~13 km
16	Convective Available Potential Energy	J kg^{-2}	~13 km
17	10-m U Wind Component (Eastward)	m s^{-1}	~13 km
18	10-m V Wind Component (Northward)	m s^{-1}	~13 km
19	10-m Wind Gust	m s^{-1}	~13 km
20	Evaporation	m of water equivalent	~13 km
21	Total Precipitation	m	~13 km

resolution (Lyapustin and Wang, 2018). At 10-km resolution, two separate algorithms, Dark Target (DT) and Deep Blue (DB) retrieve aerosols from MODIS data. DT retrieves AOD data for dark/vegetated land surfaces, whereas DB works wells for bright land surfaces. In contrast, MAIAC retrieves aerosols over both dark and bright land surfaces. Besides providing AOD data at a finer spatial resolution, AOD data from MAIAC has better spatial coverage, higher retrieval frequency, low bias, and high correlation with AOD from the Aerosol Robotic Network (AERONET) stations (Superczynski et al., 2017; Jethva et al., 2019; Mhawish et al., 2019).

Because of the superiority of AOD data from MAIAC over other AOD algorithms and its availability at a higher resolution, this study selected the MCD19A2 version-6 data product for AOD estimated with MAIAC algorithm (hereafter, MAIAC AOD data). AOD is available at two wavelengths: 470 nm and 550 nm. This study used AOD at 470 nm because AOD provided at 550 nm is derived from AOD at 470 nm, and AOD at 550 nm is marginally inferior in quality compared to AOD at 470 nm (Lyapustin and Wang, 2018). MAIAC AOD data was transformed to WGS 1984 coordinate system using MODIS Reprojection Tool (MRT), and then space and time references of the MAIAC AOD were used to extract matching PM2.5 observations from the air quality monitoring stations. MAIAC AOD data also provided quality flags for AOD and data on satellite retrieved water vapor content and viewing zenith angle. This study used these variables along with MAIAC AOD. Data about the zenith angle were available at 5 km resolution. Zenith angle data were resampled using nearest neighbor resampling to match the resolution of AOD data.

2.2.3 Meteorological data

Meteorological data came from European Centre for Medium-range Weather Forecast (ECMWF). ECMWF provides reanalysis data worldwide, at 3, 6, 9, and 12 h from 0:00 and 12:00 UTC (Berrisford et al., 2011). Thus, the ECMWF reanalysis data were available for the Dallas-Fort Worth metroplex four times a day, at 9 a.m., 12 p.m., 3 p.m., and 6 p.m. local standard time, and at a spatial resolution of 0.125° (~13 km). The reanalysis data combine weather observations with the most up-to-date weather models and provide information on different weather variables as a continuous grid at each of the 4 hours (Parker, 2016). The various weather parameters obtained from ECMWF included horizontal and vertical components of the wind, wind gust, temperature, dew point temperature, clear sky surface photosynthetically active radiations, total precipitation, boundary layer height, boundary layer dissipation, total cloud cover, medium cloud cover, high cloud cover, convective precipitation, convective available potential energy, and evaporation. The study retrieved meteorological data closer (in time) to satellite acquisition time.

In total, the study used 21 predictor variables (see Table 1) to model PM2.5 from 8 air quality monitoring stations around the Dallas-Fort Worth area. The first four predictors came from

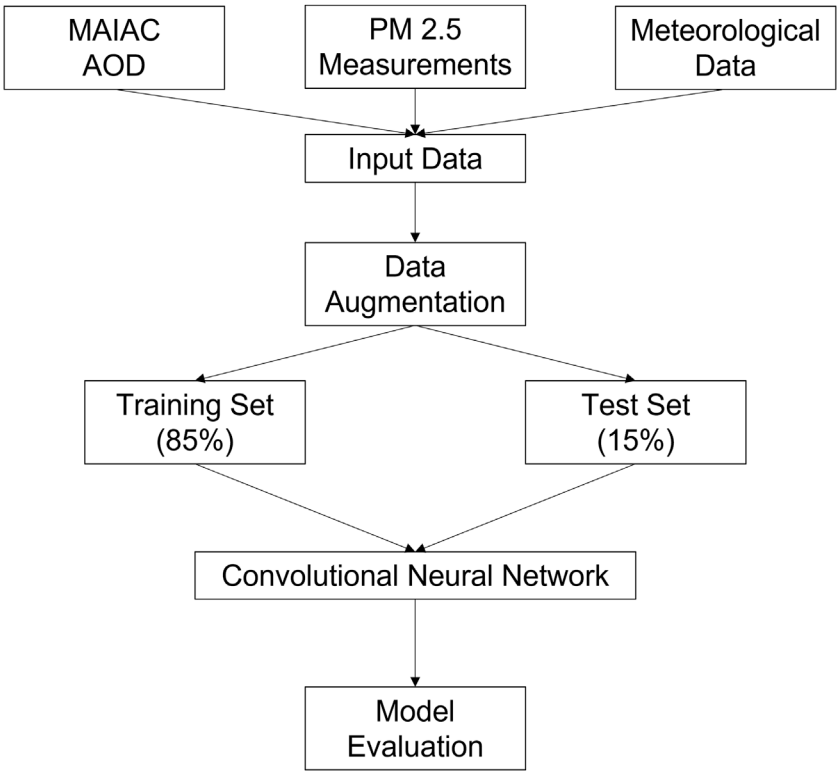

FIGURE 2
Flowchart of data and methodology.

MODIS MAIAC AOD products, and the remaining variables were from ECMWF reanalysis data. Predictors obtained from MODIS data presented instantaneous observations at the time of satellite passing, whereas ECMWF reanalysis data provided four estimates per day.

2.3 Methodology

Figure 2 shows the flowchart of the data and method used in the study. The study resampled meteorological data to match the resolution of the MAIAC AOD data using the nearest neighbor resampling method. This section discusses data processing, model architecture, and evaluation.

Through convolution operations, the Convolutional Neural Network (CNN) algorithm takes into account the very spatial nature of the images. It applies two-dimensional filters, also known as kernels, on the input. The filter moves over the input image and extracts features. Two-dimensional filters applied to compute convolutional layers use values of spatially adjacent pixels for feature extractions. This process, also known as convolution, exploits the spatial patterns and relationships (Dumoulin and Visin, 2016). An optimization algorithm with backward propagation minimizing a loss function determines weights in these filters (Indolia et al., 2018). These weights define the nature of the spatial relationship among spatially adjacent grid-cells yielding the output (LeCun et al., 1998). For the phenomenon affected by explanatory variables in the surrounding areas, it is essential to account for the influence of spatially adjacent locations. As discussed in the introduction, many studies have improved the performance of models estimating PM2.5 after considering a correlation among variables in space. Specifically, many studies incorporated a weighted average of PM2.5 from nearby stations. Their approach captured existing spatial autocorrelation in the PM2.5 values across *in situ* stations for PM2.5 estimation even though these stations might be too sparse to acquire PM2.5 spatial variances among them. On the contrary, our study intended to develop a model that relies on variables other than spatially lagged PM2.5 and thus may help explore the effects of other explanatory variables on PM2.5. Therefore, we did not use measurements from nearby PM2.5 monitoring stations but aimed to develop a model that uses AOD and meteorological data to estimate PM2.5 corresponding to an hour of AOD acquisition at specific sites.

Park et al. (2020) investigated spatially lagged variables over a fixed distance using an image size of 5 × 5 but due to the coarser resolution of the AOD data (10 km) they used, it corresponded to an area of 50 km × 50 km. Instead, this study examined the influence of spatial lag size to evaluate the spatial scale effects of meteorological variables with AOD on PM2.5 estimates. The underlying grid resolution of AOD data was 1 km × 1 km. CNN accepts images as input. We located the grid cell in which the particular PM2.5 station is located and expanded upon that grid cell to extract a 3 km × 3 km image. We followed a similar process for all predictor variables- AOD quality flag data, column water vapor, resampled zenith angle, and meteorological data. Since there are 21 predictors, the input image-patch size for one PM2.5 observation from a particular PM2.5 station is 3 × 3 × 21. The process was repeated for all PM2.5 observations from eight

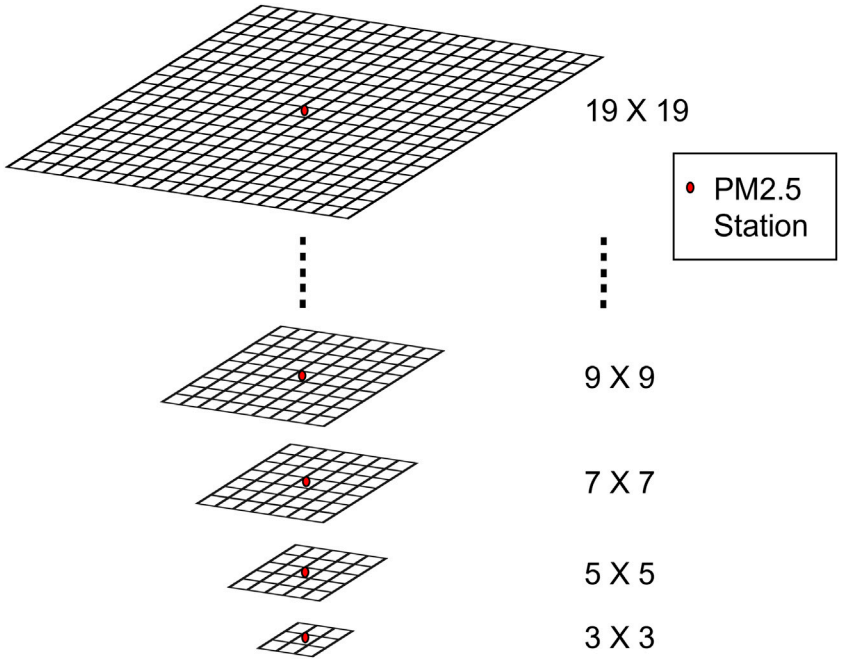

FIGURE 3
Different sized image-patches centered on a cell with a PM2.5 station.

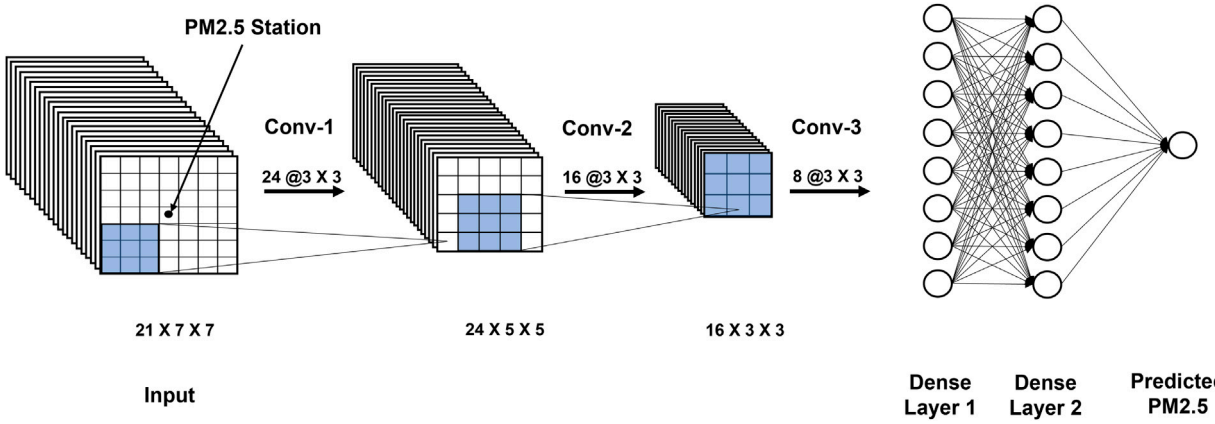

FIGURE 4
The study's CNN architecture.

monitoring stations in the study area during 2006–2015 to form an input dataset to build a model in an O-CV approach. Similarly, we extracted image-patches of sizes $5 \times 5, 7 \times 7, 9 \times 9, \ldots 19 \times 19$ to form a total of nine different input datasets (Figure 3). We stopped at 19×19 because of the gaps in AOD data due to cloud cover (more discussion in Section 2.3.2). With a PM2.5 station in a central cell, the input image-patch size represented the size of the area around the PM2.5 station. Thus, it was analogous to the concept of spatial lag in spatial statistics. A total of nine CNN models, one for each image-patch size, were developed and compared to evaluate the effect of input image-patch size on PM2.5 estimation.

2.3.1 CNN models of PM2.5 predictions

A larger image contains more information. With larger sizes, spatial relations become more intricate. A neural network learns to recognize more complex features with more convolution layers (Lopez Pinaya et al., 2020). Therefore, depending on the size, the study used variable convolutional layers to account for varying complexity in spatial relations. This led to nine separate CNN models, one for each image-patch size. The larger the image-patch, the more convolutional layers are. Predictors were convoluted using filters of size 3×3 until the input image-patch reduces to 1×1. The first and the second convolutions consisted of 24 and 16 filters, respectively, whereas each of the remaining

TABLE 2 AOD data availability.

Image-patch size	Number of samples
3x3	14570
5x5	12674
7x7	10686
9x9	8407
11x11	7488
13x13	6660
15x15	5703
17x17	5165
19x19	4205

FIGURE 5
Sample image-patch of size 5 × 5.

convolutions consisted of eight. Each of the dense or fully connected layers had eight neurons. Input image-patches of sizes 3 × 3 and 5 × 5 required only one and two convolutions, respectively, whereas the remaining input image-patch sizes required more than two convolutions. A 7 × 7 image-patch required three convolutions, whereas a 19 × 19 image-patch required seven convolutions. Figure 4 shows the architecture of the CNN used in the study for a 7 × 7 image-patch. A blue square represents 3 × 3 filters used in all convolutions. The study used a sigmoid activation function for all layers except for the last year, which outputs the model predictions with a linear activation function, since the sigmoid limits the output range from 0 to 1 and the linear activation regressed the predictions. The study used the Adam optimization algorithm, an extension to the stochastic gradient decent and appropriate for non-stationary objectives, problems with noisy or sparse gradients, and computationally efficient, and typically low demand on tuning parameters (Kingma and Ba, 2014). The study set a learning rate of 0.01 and 200 epochs for training. The learning rate of 0.01 was found to balance learning time and accuracy. To minimize parameters for training, the study used stride one and no padding across all convolutions. Also, batch normalization followed each convolution and dense layer prior to the ensuing activation function.

2.3.2 Data augmentation

AOD data can be missing due to clouds, snow or brighter surface conditions. The problem of missing data in AOD was well documented in the literature (Goldberg et al., 2019; Hu et al., 2017; Park et al., 2020). The study included only those data points for which AOD data was available for cells in an image-patch of considered size. This problem of missing AOD led to decreasing number of samples for larger image-patch sizes in our study (Table 2). A larger image-patch comprised of more cells than a smaller image-patch, and the chances of having at least 1 cell with missing AOD were greater for larger image-patch sizes. Due to the limited number of samples available for larger image-patch sizes, we restricted our largest input image-patch size to 19 × 19.

Machine learning approaches, such as CNN, require a large number of samples or data points. The relatively small study area and only 10 years of the study period resulted in small samples in the context of machine learning. Data augmentation, a common practice used in machine learning to increase the sample size, provided a way to generate additional samples. We used the geometric transformations method to augment available data because it was computationally simple and did not introduce new information to original data. Geometric transformation generates additional samples by flipping, scaling, rotating, and cropping original images (Taylor and Nitschke, 2019). The study flipped and rotated an original image-patch (Figure 5) to generate additional image-patches (Figure 6). Flipping generated mirror copies along an axis, whereas rotation arranged original image-patches in different orientations (Figure 6). Image-patches of all the input variables in a particular sample or data point were flipped or rotated in the same way to form a new sample or data point. As a result, the process of data augmentation only repositioned the original sample or data point without making any change to original data values or their inter-relation in spatial configuration. As the study used six different ways to augment the data (Figure 6), each sample was reconfigured in six different ways, resulting in a 6-fold increase in the number of samples available for training and cross-validation.

2.3.3 Cross-validation

As previously noted in the introduction, out of three commonly used cross-validation approaches for AOD-based PM2.5 models, the overall (O-CV) and temporally separated (TS-CV) approaches outperformed the spatially separated approach (SS-CV). The TS-CV approach can result in the training of a model for a specified period. Therefore, this study used the O-CV approach to evaluate model performance. Specifically, the study adopted the five-fold O-CV approach. The data was split into five groups; each group was iteratively used to test the model performance, and the remaining four trained the model. The average correlation coefficient R) and root mean squared error (RMSE) across all five groups were used to compare model performance.

2.3.4 Reliability assessment

The data augmentation technique helped increase the size of the data available for training by generating additional artificial samples from the existing data. However, it raised concerns about the model's ability to accurately estimate the PM2.5 concentration level of a specific data point regardless of whether it was augmented or not in the training process. In other words, though the same data point was present in the dataset multiple times in different forms, the model's PM2.5 estimates across these multiple forms may vary. To evaluate the model's reliability, it was necessary to consider the precision of these estimates or how closely they match each other. We trained a model using an entire dataset (consisting of original data points and augmented data points) and repeated the process for each image-patch size to evaluate the model's ability to provide precise estimates. The use of the entire dataset for model development enabled the assessment of the variability in PM2.5 estimates of each data point,

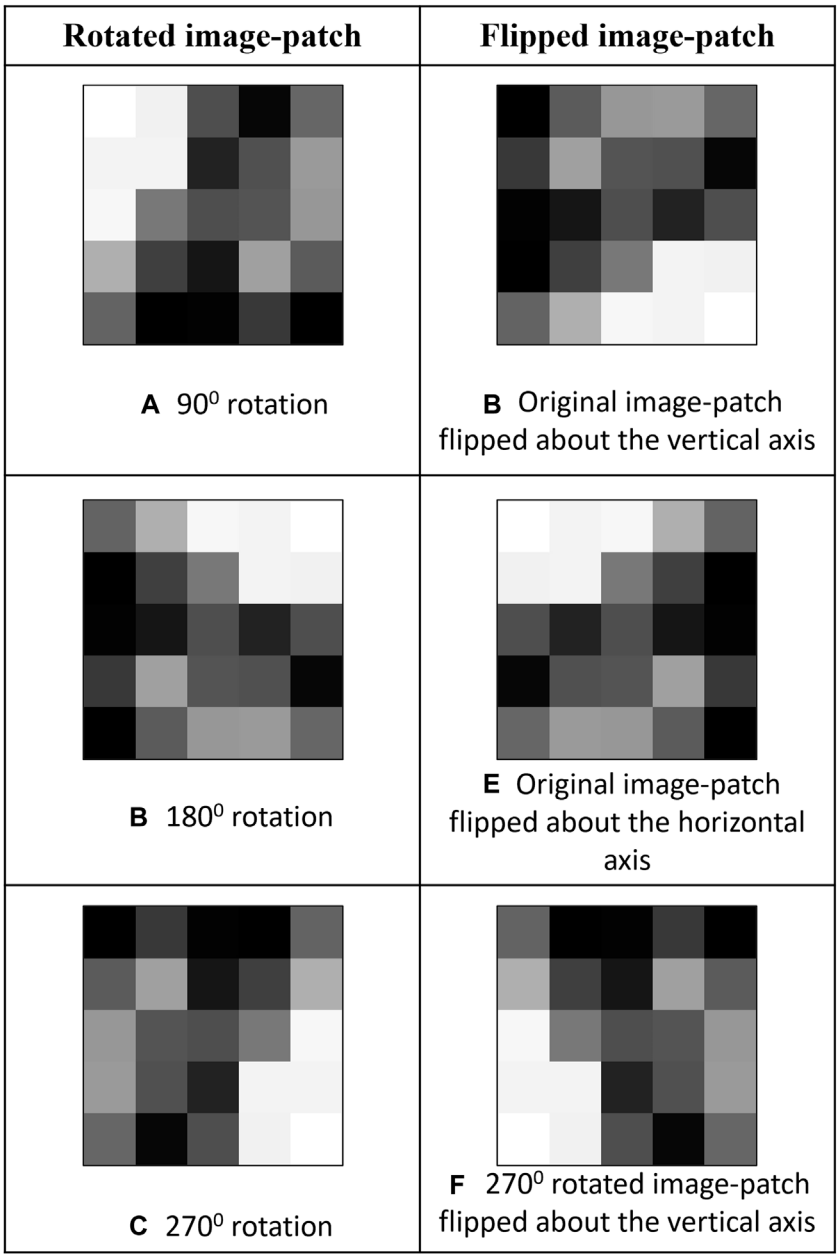

FIGURE 6
Augmented image-patch derived from a sample image-patch in Figure 5.

which we repeated six more times in the augmented dataset. We then calculated the difference between the maximum and minimum estimates (also referred as the range of the PM2.5 estimates) for each data point and calculated the statistics of these values for nine models, each using an input image-patch of a different size.

3 Results

3.1 Description of PM2.5 data

Figure 1 showed the locations of eight monitoring stations in the Dallas-Fort Worth metroplex and its surrounding area. During 2006–2015, the average hourly PM2.5 was 9.29 μg/m^3 and 77216 valid hourly PM2.5 measurements were available at satellite image acquisition times across these eight stations (Table 3). The median values at all stations are less than the respective means indicating the positively skewed distribution of PM2.5 concentration at each station. On an average 50% of the values are below 8.29 μg/m^3. The average interquartile range of PM2.5 values across all stations is 6.88 μg/m^3 with middle 50% values ranging between 5.27 μg/m^3 to 12.15 μg/m^3. There were several zero and negative values in the data, which were removed based on the assumption that those were the result of potential measurement errors. The table also presents the average hourly PM2.5 level at each station at all available satellite acquisition times during the study period. MODIS acquired data around 10:30 a.m. and 1:30 p.m. The mean PM2.5 value during the satellite acquisition times is lower than the average PM2.5 value at each station because of

TABLE 3 PM2.5 concentration and data availability during 2006–2015.

Station name	Hourly PM2.5 during 2006–2015 (μg/m^3)						Hourly PM2.5 during satellite acquisition times	
	Mean	Median	Min	Q1	Q3	Max	Mean	Number of PM2.5 measurements available
Arlington Municipal Airport	9.30	8.3	0.1	5.2	12.2	266.3	7.94	10354
Corsicana Airport	9.07	8.1	0.1	5.2	11.8	106.6	7.47	7790
Dallas Hinton	9.50	8.6	0.1	5.3	12.6	172.7	9.67	10711
Denton Airport South	9.05	8.0	0.1	4.9	12.1	137.7	7.76	9942
Haws Athletic Center	10.19	9.1	0.1	5.9	13.3	362.2	7.97	10404
Italy	8.97	8.0	0.1	5.3	11.5	222.6	7.59	8240
Kaufman	9.17	8.2	0.1	5.3	11.9	153.3	7.72	10358
Midlothian OFW	9.11	8.0	0.1	5.1	11.8	176.0	7.68	9417
Average	9.29	8.29	0.1	5.27	12.15	199.65	7.97	Total 77216

TABLE 4 Descriptive statistics of PM2.5 values across all image sizes.

Image-patch size	Number of samples	Hourly PM2.5	
		Mean	Standard deviation
3x3	14570	7.07	5.54
5x5	12674	6.79	5.34
7x7	10686	6.56	5.24
9x9	8407	6.46	5.18
11x11	7488	6.38	5.18
13x13	6660	6.27	5.12
15x15	5703	6.30	5.17
17x17	5165	6.17	5.14
19x19	4205	5.90	4.96

the improved circulation around noon. PM2.5 values were generally higher in the early morning and late evening.

AOD data are often susceptible to data gaps due to cloud cover or bright surfaces. The study incurred a high missing rate in AOD data for the same reasons. Image-patches of 3 × 3 km^2 with complete AOD data constituted only 18.87% of the total AOD data; those of 19 × 19 km^2, merely 5.44%. Table 4 presents the mean and standard deviation of hourly PM2.5 for the different-sized input patches considered in the study. The number of samples (e.g., complete patches) decreased as the patch size increased; the reduced sample size (e.g., number of patches) reduced the mean and standard deviation of PM2.5 available for training the model. PM2.5 decreased from 7.07 μg/m^3 to 5.90 μg/m^3, and the standard deviation from 5.54 to 4.96 from the smallest to the largest patch size.

3.2 Model evaluation

Machine learning methods require a large amount of data to train the model. To overcome the challenge of a limited number of samples to train the model, we used a data augmentation technique to artificially increase the number of samples by introducing relational variance of input data patches to PM2.5 data at the same site and time of MODIS observations. Below are the results of CNN models with augmented data.

Figure 7 shows the results for CNN across different-sized image-patches. Out of all sizes, the model with patch size 19 × 19 km^2 performed best with the correlation coefficient R) of 0.87 (or R^2 of 0.76) and root mean squared error (RMSE) of 2.57 μg/m^3 for PM2.5 estimation at station locations. Unlike other studies in the literature, this study achieved comparably good performance without including PM2.5 covariates from nearby stations. For example, modeling PM2.5 over the contiguous United States, Di et al. (2016) achieved R^2 of 0.84, whereas Park et al. (2020) reported R^2 of 0.84 and RMSE of 2.55 μg/m^3 for 24-h averages of PM2.5. Similarly, a study performed in China for daily PM2.5 estimation reported R^2 and RMSE of 0.76 and 13 μg/m^3 respectively (Zhan et al., 2017). Because of the differences in the geographic locations and regional extents and levels of air pollution, results from the studies in the literature cannot be directly compared to our results. Noteworthily, our study estimated PM2.5 corresponding to the hour of MODIS data acquisition time in contrast to a 24-h average of PM2.5 in the above-mentioned studies.

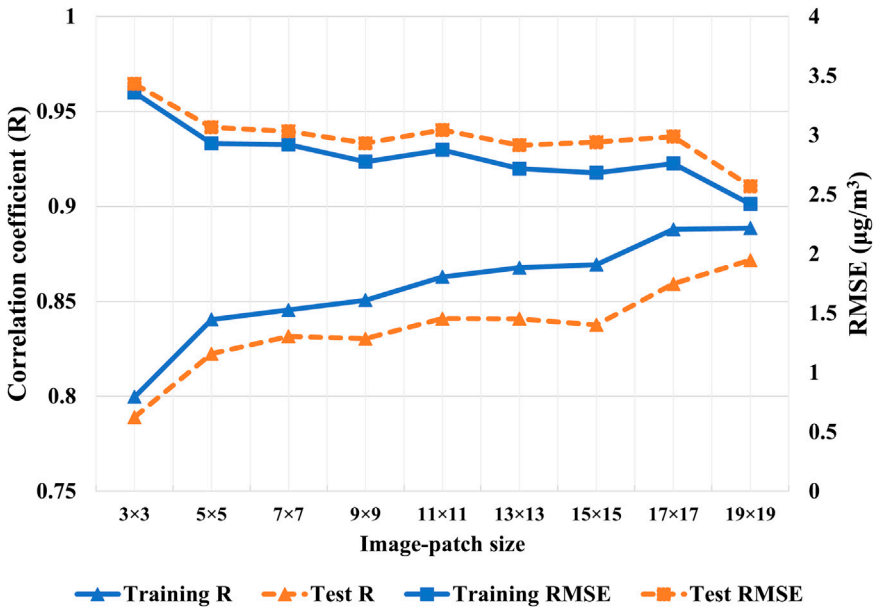

FIGURE 7
Correlation coefficient and RMSE for CNN with varying image-patch sizes with data augmentation.

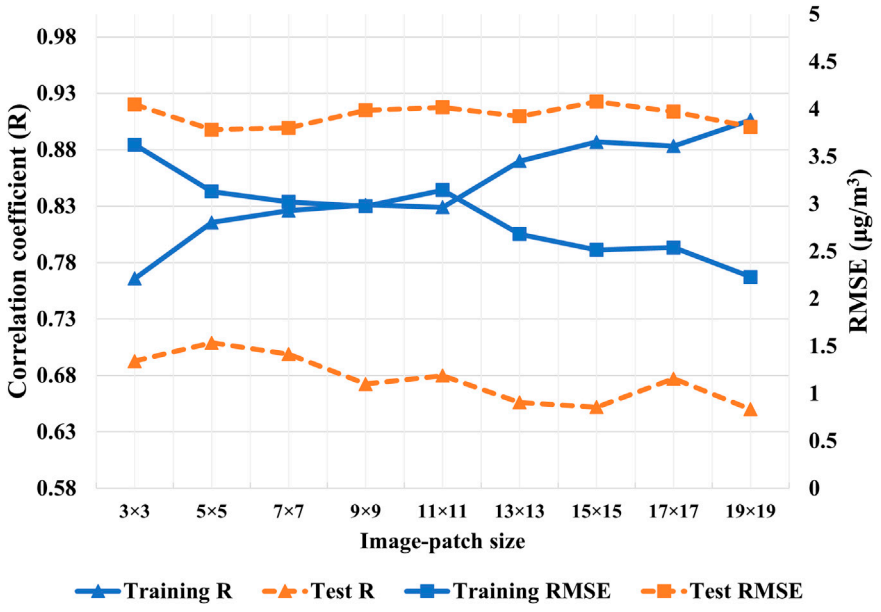

FIGURE 8
Correlation coefficient and RMSE for CNN with varying image-patch size without data augmentation.

3.3 Comparison with models not using data augmentation

Without data augmentation, a correlation between estimated PM2.5 from MAIAC AOD and observed PM2.5 at monitoring stations for the training dataset increased with the input image-patch size. However, the correlation degraded for the test dataset (Figure 8). Similarly, the models did not perform as well on the test dataset as the training dataset in terms of RMSE. This suggested that the models performed well on the training dataset with a smaller number of data points but failed to perform equally well over unseen data, a case of overfitting. Finally, we compared the performance of models with and without data augmentation on the test dataset. Data augmentation improved R and decreased RMSE for all image-patch sizes (Figure 9). Moreover, models with larger image-patch sizes, despite relatively small sample size even with data augmentation, outperformed models with smaller-sized image-patches. It suggested that a wider area around the PM2.5 station improved PM2.5 estimation.

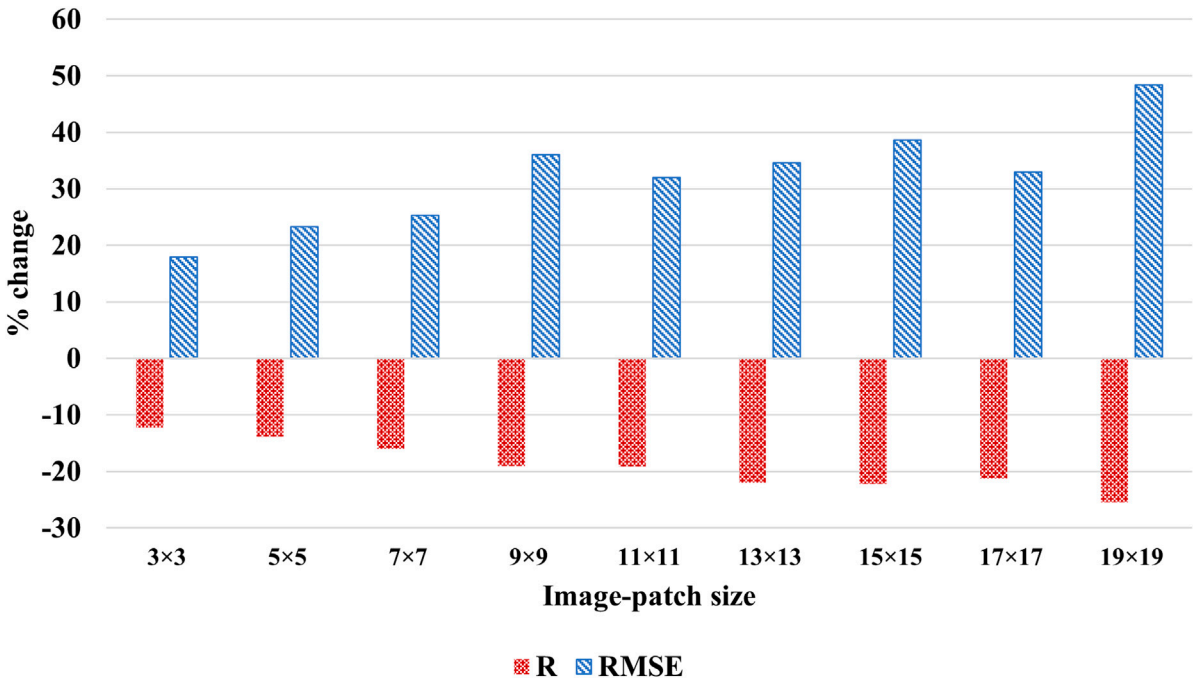

FIGURE 9
Percent change in R and RMSE in models without data augmentation across image-patch sizes.

The implemented data augmentation process retained spatial variance among cells in an input data image-patch (MAIAC AOD and weather data) and the patch's spatial pattern across all augmented data items but altered the orientation and facing of the patch. No augmentation was applied to *in situ* observations. Therefore, the data augmentation changed only spatial orientation of the input data associated with a particular observation and, as such, introduced variance to how the interaction between MAIAC-AOD and weather data may relate to *in situ* PM2.5 observations. The increased relational variance in training data made the model more difficult to converge during the training process (i.e., reaching the set of parameters that minimize the model's loss function). Meanwhile, the increased variance also lowered the risk of model overfitting. In machine learning, a model is considered overfitting if it performs well on training data but poorly on test data. Figures 7, 8 show the results of CNN models over augmented and non-augmented data, respectively. The R and RMSE values over augmented training and test data are comparable (Figure 7), whereas their apparent discrepancies with non-augmented training and test data suggest poor model performance (Figure 8). As such, the data augmentation helps overcome the data sparsity due to missing AOD without overfitting for PM2.5 estimation in this study.

3.4 Precision evaluation on PM2.5 estimates

The data augmentation technique proved helpful to increase the training data size and improved the model performance. However, due to the repeated data points used in this technique, it was essential to assess the robustness of PM2.5 estimates across these repeated data points. For each image-patch size, a model was developed using the entire dataset to assess the variability in the PM2.5 estimates across the repeated measurements. Table 5 provides descriptive statistics of the difference between maximum and minimum estimates obtained for the same observation across different image-patch sizes. Overall, quartile 1 (Q1), median, and quartile 3 (Q3) values increased as image-patch size increased, while minimum values remained consistently low. However, the magnitude of this increase was relatively small, with the variability only rising from 0.05 for a 3 × 3 image-patch size, 0.58 for 17 × 17, and 0.39 for a 19 × 19 image-patch size. The results suggested that while the precision of the PM2.5 estimates varied across the image-patch sizes, with a smaller patch size producing more precise estimates. Yet, the difference in precision was relatively small. Although the maximum estimated PM2.5 range varied quite a lot across different image-patch sizes, % of values with the range of PM2.5 estimates greater than 2.5 were less than 6.5% across all image-patch sizes, with the lowest percentage of 0.01 for 3 × 3 and the highest percentage of 6.44 for 15 × 15 image-patch size.

4 Discussion

In this study, PM2.5 concentration corresponding to the hour of satellite data acquisition time was estimated using the Convolutional Neural Network (CNN) approach for Dallas-Fort Worth metroplex and its surrounding area. A simple CNN model achieved a correlation coefficient of 0.87 and RMSE of 2.57 μg/m^3 without using PM2.5 data from nearby monitoring stations (also called spatially lagged PM2.5). In spatial statistics, the spatially lagged dependent variables are used in the model structure to account for the existing spatial dependence in

TABLE 5 Descriptive statistics of the range of PM2.5 estimates across image-patch sizes.

Image-patch size	Min	Q1	Median	Q3	Max	% Below 2.5 μg/m^3
3x3	0.00	0.02	0.05	0.14	2.63	0.01
5x5	0.00	0.07	0.16	0.41	8.52	0.87
7x7	0.00	0.12	0.28	0.61	8.78	1.88
9x9	0.00	0.22	0.48	0.97	10.89	4.63
11x11	0.00	0.16	0.32	0.63	10.46	1.86
13x13	0.00	0.25	0.51	1.02	11.98	5.42
15x15	0.01	0.29	0.60	1.20	12.70	6.44
17x17	0.01	0.29	0.58	1.11	13.40	5.58
19x19	0.00	0.19	0.39	0.80	7.66	3.88

the dependent variable (Anselin, 2003). While these models aim to derive unbiased estimators by accounting for existing spatial autocorrelation in the dependent variable (Anselin and Bera, 1998), for PM2.5 studies, obtaining spatially lagged PM2.5 is challenging because the sparse distribution of air quality monitoring stations may be distant beyond the spatial dependence. Furthermore, PM2.5 come from point (e.g., industry and burns) and non-point (e.g., traffic, diffusion from nearby regions) sources. As such, co-variates from nearby stations may not be useful since a constant spatial gradient between two stations is unlikely. Yet, the convolutional process in our CNN models embedded spatial covariates among MAIAC-AOD cells, which were closer than the distance between nearby stations. In addition, the CNN models also considered spatially lagged independent variables. Without covariates from nearby stations, our best model estimated PM2.5 corresponding to the hour of MODIS data acquisition time, at a finer temporal interval than the 24-h averaged PM2.5 concentration estimated by previous studies.

The MODIS satellite overpasses any area twice a day; however, the recent launch of the geostationary satellite GOES-R has made it possible to acquire AOD data with an increasing frequency of every 5 and 15 min (Schmit et al., 2017). Extending the CNN architecture from this study to these frequently available AOD data will help explore the diurnal trend in PM2.5 and increase the data available for studies investigating the effects of the environmental exposome. In addition, the independent variables used in our model are also readily available everywhere. Therefore, this model can be easily trained for other regions.

This study systematically investigated the effects of the input image-patch size on model performance. The missing AOD problem resulted in a smaller sample size for the larger spatial extents or image-patch sizes considered in the study. The mean and variance of the PM2.5 decreased slightly as the image-patch size increased (Table 4). While it may appear that the improved model performance with larger patch sizes is due to the reduced variance, it is important to note that with a larger spatial extent or patch-size, the model complexity also increased. With larger spatial extents, the model must account for spatial dependence over a larger area around a PM2.5 station. Even with the added complexity and smaller sample size, models with larger image patch-size demonstrated consistently better performance with data augmentation that introduced relational variance in training data. The improved model performance with increased input image-patch size suggests that including spatially lagged independent variables from a wider area around the PM2.5 station improves model performance. Among considered image-patch sizes, image-patch of size 19 km by 19 km performed best with R^2 of 0.76 and RMSE of 2.57 μg/m^3. With a PM2.5 station at the center, image-patch of size 19 km × 19 km, considers spatially lagged explanatory variables within 10 km of the PM2.5 station. It suggests that adjacent locations as far as 10 km also affect the PM2.5 concentration in addition to local factors, indicating the broader scale at which spatial processes driving PM2.5 are operating. Harrison et al. (2015) collected street-level PM2.5 data in our study region's 10 km by 10 km area. Their study found that depending on weather conditions, the spatial scale of PM2.5 variation in the area varied between 0.8 and 5.2 km. Thus, depending on the synoptic weather conditions, a smaller image-patch may be sufficient to estimate PM2.5. However, further investigation is required to confirm the same. One way to investigate this is to classify the training dataset into several groups, each group representing homogeneous weather conditions, and investigate if better performance is achieved with a smaller image-patch size in certain conditions.

Although CNN incorporated information from adjacent areas to model PM2.5, this study did not investigate how spatially adjacent locations influence PM2.5 at the estimation location. An explainable AI technique may help uncover this information. Park et al. (2020) used Layerwise Relevance Propagation (LRP) to identify important variables in the model. Their analysis also visualized the spatial pattern of the importance of each predictor. These patterns help investigate how adjacent areas are contributing to PM2.5 concentration. Future studies can use a similar approach to examine the role of adjacent locations, especially in scenarios leading to elevated PM2.5 concentrations. Park et al. (2020) found the weighted average of spatially lagged PM2.5 to be the most important variable. Unlike their study, this study did not use spatially lagged PM2.5. Further analysis of the model using explainable AI techniques may help gain insights into how variables other than spatially lagged PM2.5 contribute to PM2.5 concentration and what information about the factors contributing to PM2.5 this model provides compared to models

using nearby PM2.5 measurements. Moreover, the use of spatially lagged PM2.5 assumes that the spatial gradient of PM2.5 between two stations is smooth. However, this cannot always hold true as the different point and non-point sources of PM2.5 between stations may vary. In our study area, the average distance between two PM2.5 stations was 36.26 km with a range from 20.17 km to 58.19 km. The convolution process in the CNN allows embedding MAIAC AOD values from grid cells that are closer than the nearby PM2.5 stations. Additionally, our study aimed to develop a MAIAC AOD-based model to estimate hourly PM2.5 corresponding to the satellite data acquisition times.

The study demonstrated that the data augmentation technique, commonly used in computer vision tasks to increase the sample size, can be used to overcome the problem of limited samples due to missing AOD data. Several studies addressed this problem through a data-filling approach (Hu et al., 2014; Goldberg et al., 2019; Meng et al., 2021). However, depending on the factors responsible for incomplete AOD, missing AOD data can be systematic or non-random. As a result, this introduces bias in the model due to reliance on selective data. The data augmentation technique used in the study does not help address this limitation. In contrast, gap-filling methods can help alleviate this problem to some extent by increasing the AOD availability. Nevertheless, the data augmentation method by increasing sample size helps the model learn complex patterns and relationships. Therefore, even when sufficient data is available for model training, it would be interesting to compare models using augmented data with those that do not and how it affects model performance.

Our study is subject to the following limitations, which also present opportunities for future research. Li and Tartarini (2020) showed the impact of human activities on PM2.5 pollution. Our study assumed that AOD embedded the effect of human activities on PM2.5. However, the AOD is available at 1 km resolution, and human activities can vary widely in 1 km^2. Additionally, grid-cells of 1 km spatial resolution are used to obtain point-level PM2.5 measurements from ground monitoring stations. This spatial mismatch can be remedied to some extent by including fine-grained information on human activities associated with PM2.5 pollution such as traffic and other emission sources, especially when human-activity patterns are highly variable over short distances. Another spatial mismatch issue arises because of the position of a PM2.5 station in the assigned grid cell of the input data. Because of the coarser resolution of the input datasets (1 km, 5 km and 13 km), some PM2.5 stations may fall near the center of the cell while others may fall near the edge. One solution to this problem is to resample the data to ensure the PM2.5 station is centrally located in a grid cell. However, resampling is subjected to additional errors and uncertainty in the data. Weather-related variables used in the study had the coarsest resolution of 13 km among all the input variables. However, as weather variables vary at a mesoscale, values between adjacent cells do not vary much. That the model at 19 km × 19 km performed the best also supports that the position of the PM2.5 station with respect to the cell center will not affect the results. Due to insufficient MAIAC-AOD data, the study could not test spatial extents around PM2.5 stations or sensitivity tests beyond 19 × 19 km^2. MODIS acquisitions are vulnerable to cloudy conditions that result in data gaps. While statistical methods can interpolate the missing data gaps (Yang and Hu, 2018), our study used only available AOD data to avoid additional uncertainty from interpolated errors. Moreover, PM2.5 estimates showed variability when repeated data points were taken after data augmentation. While this variability was relatively small across different input image-patch sizes, future studies may explore its causes.

Data availability statement

The raw data supporting the conclusions of this article will be made available by the corresponding author, without undue reservation.

Author contributions

MY and YK- conception; YK-design, data collection, analysis, interpretation of results, and original draft preparation, review, and editing; MY-supervision, review, and editing.

Funding

The research was partially supported by funds from the University of Texas System STAR program, the School of Economic, Political, and Policy Sciences at the University of Texas at Dallas, and a scholarship from Pioneer Natural Resources, Inc. The authors declare that this study received funding from Pioneer Natural Resources, Inc. The funder was not involved in the study design, collection, analysis, interpretation of data, the writing of this article, or the decision to submit it for publication.

Conflict of interest

The authors declare that the research was conducted in the absence of any commercial or financial relationships that could be construed as a potential conflict of interest.

Publisher's note

References

Anselin, L., and Bera, A. (1998). "Spatial dependence in linear regression models with an introduction to spatial econometrics," in *Handbook of applied economic statistics*. Editor A. Ullah (New York: CRC Press), 237–290.

Anselin, L. (2003). "Spatial econometrics," in *A companion to theoretical econometrics* (Malden, MA, USA: Blackwell Publishing Ltd), 310–330. doi:10.1002/9780470996249.ch15

Bell, M. L., Dominici, F., Ebisu, K., Zeger, S. L., and Samet, J. M. (2007). Spatial and temporal variation in PM2.5 chemical composition in the United States for health effects studies. *Environ. Health Perspect.* 115, 989–995. doi:10.1289/ehp.9621

Berrisford, P., Dee, D. P., Poli, P., Brugge, R., Fielding, M., Fuentes, M., et al. (2011). The ERA-Interim archive Version 2.0. 23. Available at: https://www.ecmwf.int/node/8174.

Chen, H., Kwong, J. C., Copes, R., Hystad, P., van Donkelaar, A., Tu, K., et al. (2017). Exposure to ambient air pollution and the incidence of dementia: A population-based cohort study. *Environ. Int.* 108, 271–277. doi:10.1016/j.envint.2017.08.020

Chudnovsky, A., Lyapustin, A., Wang, Y., Tang, C., Schwartz, J., and Koutrakis, P. (2014). High resolution aerosol data from MODIS satellite for urban air quality studies. *Central Eur. J. Geosciences* 6, 17–26. doi:10.2478/s13533-012-0145-4

Cohen, A. J., Brauer, M., Burnett, R., Anderson, H. R., Frostad, J., Estep, K., et al. (2017). Estimates and 25-year trends of the global burden of disease attributable to ambient air pollution: An analysis of data from the global burden of diseases study 2015. *Lancet* 389, 1907–1918. doi:10.1016/S0140-6736(17)30505-6

Di, Q., Kloog, I., Koutrakis, P., Lyapustin, A., Wang, Y., and Schwartz, J. (2016). Assessing PM2.5 exposures with high spatiotemporal resolution across the continental United States. *Environ. Sci. Technol.* 50, 4712–4721. doi:10.1021/acs.est.5b06121

Dumoulin, V., and Visin, F. (2016). *A guide to convolution arithmetic for deep learning*. Montreal, Quebec. doi:10.48550/arxiv.1603.07285

Engel-Cox, J. A., Holloman, C. H., Coutant, B. W., and Hoff, R. M. (2004). Qualitative and quantitative evaluation of MODIS satellite sensor data for regional and urban scale air quality. *Atmos. Environ.* 38, 2495–2509. doi:10.1016/j.atmosenv.2004.01.039

Geng, G., Zhang, Q., Martin, R. v., van Donkelaar, A., Huo, H., Che, H., et al. (2015). Estimating long-term PM2.5 concentrations in China using satellite-based aerosol optical depth and a chemical transport model. *Remote Sens. Environ.* 166, 262–270. doi:10.1016/J.RSE.2015.05.016

Goldberg, D. L., Gupta, P., Wang, K., Jena, C., Zhang, Y., Lu, Z., et al. (2019). Using gap-filled MAIAC AOD and WRF-Chem to estimate daily PM2.5 concentrations at 1 km resolution in the Eastern United States. *Atmos. Environ.* 199, 443–452. doi:10.1016/J.ATMOSENV.2018.11.049

Guo, J., Xia, F., Zhang, Y., Liu, H., Li, J., Lou, M., et al. (2017). Impact of diurnal variability and meteorological factors on the PM2.5 - AOD relationship: Implications for PM2.5 remote sensing. *Environ. Pollut.* 221, 94–104. doi:10.1016/j.envpol.2016.11.043

Gupta, P., and Christopher, S. A. (2009a). Particulate matter air quality assessment using integrated surface, satellite, and meteorological products: 2. A neural network approach. *J. Geophys. Res. Atmos.* 114, D20205. doi:10.1029/2008JD011497

Gupta, P., and Christopher, S. A. (2009b). Particulate matter air quality assessment using integrated surface, satellite, and meteorological products: Multiple regression approach. *J. Geophys. Res. Atmos.* 114, 14205. doi:10.1029/2008JD011496

Gupta, P., Doraiswamy, P., Levy, R., Pikelnaya, O., Maibach, J., Feenstra, B., et al. (2018). Impact of California fires on local and regional air quality: The role of a low-cost sensor network and satellite observations. *Geohealth* 2, 172–181. doi:10.1029/2018gh000136

Harrison, W. A., Lary, D., Nathan, B., and Moore, A. G. (2015). The neighborhood scale variability of airborne particulates. *J. Environ. Prot. (Irvine, Calif.* 06, 464–476. doi:10.4236/jep.2015.65045

Hu, X., Belle, J. H., Meng, X., Wildani, A., Waller, L. A., Strickland, M. J., et al. (2017). Estimating PM2.5 concentrations in the conterminous United States using the random forest approach. *Environ. Sci. Technol.* 51, 6936–6944. doi:10.1021/acs.est.7b01210

Hu, X., Waller, L. A., Al-Hamdan, M. Z., Crosson, W. L., Estes, M. G., Estes, S. M., et al. (2013). Estimating ground-level PM2.5 concentrations in the southeastern U.S. using geographically weighted regression. *Environ. Res.* 121, 1–10. doi:10.1016/J.ENVRES.2012.11.003

Hu, X., Waller, L. A., Lyapustin, A., Wang, Y., Al-Hamdan, M. Z., Crosson, W. L., et al. (2014). Estimating ground-level PM2.5 concentrations in the Southeastern United States using MAIAC AOD retrievals and a two-stage model. *Remote Sens. Environ.* 140, 220–232. doi:10.1016/j.rse.2013.08.032

Indolia, S., Goswami, A. K., Mishra, S. P., and Asopa, P. (2018). Conceptual understanding of convolutional neural network- A deep learning approach. *Procedia Comput. Sci.* 132, 679–688. doi:10.1016/J.PROCS.2018.05.069

Jethva, H., Torres, O., and Yoshida, Y. (2019). Accuracy assessment of MODIS land aerosol optical thickness algorithms using AERONET measurements over North America. *Atmos. Meas. Tech.* 12, 4291–4307. doi:10.5194/AMT-12-4291-2019

Kingma, D. P., and Ba, J. L. (2014). "Adam: A method for stochastic optimization," in 3rd International Conference on Learning Representations, ICLR 2015 - Conference Track Proceedings, San Diego, California, May 7–9, 2014. doi:10.48550/arxiv.1412.6980

Kioumourtzoglou, M. A., Schwartz, J. D., Weisskopf, M. G., Melly, S. J., Wang, Y., Dominici, F., et al. (2016). Long-term PM2.5 exposure and neurological hospital admissions in the northeastern United States. *Environ. Health Perspect.* 124, 23–29. doi:10.1289/ehp.1408973

Lary, D. J., Faruque, F. S., Malakar, N., Moore, A., Roscoe, B., Adams, Z. L., et al. (2014). Estimating the global abundance of ground level presence of particulate matter (PM2.5). *Geospat Health* 8, 611. doi:10.4081/gh.2014.292

LeCun, Y., Bottou, L., Bengio, Y., and Haffner, P. (1998). Gradient-based learning applied to document recognition. *Proc. IEEE* 86, 2278–2324. doi:10.1109/5.726791

Lee, H. J. (2019). Benefits of high resolution PM 2.5 prediction using satellite MAIAC AOD and land use regression for exposure assessment: California examples. *Environ. Sci. Technol.* 53, 12774–12783. doi:10.1021/acs.est.9b03799

Li, J., and Tartarini, F. (2020). Changes in air quality during the COVID-19 lockdown in Singapore and associations with human mobility trends. *Aerosol Air Qual. Res.* 20, 1748–1758. doi:10.4209/AAQR.2020.06.0303

Li, T., Shen, H., Yuan, Q., Zhang, X., and Zhang, L. (2017). Estimating ground-level PM2.5 by fusing satellite and station observations: A geo-intelligent deep learning approach. *Geophys Res. Lett.* 44 (11), 11,985–11,993. doi:10.1002/2017GL075710

Lopez Pinaya, W. H., Vieira, S., Garcia-Dias, R., and Mechelli, A. (2020). Convolutional neural networks. *Mach. Learn. Methods Appl. Brain Disord.*, 173–191. doi:10.1016/B978-0-12-815739-8.00010-9

Lyapustin, A., and Wang, Y. (2018). *MODIS multi-angle implementation of atmospheric correction (MAIAC) data user's guide collection 6 (ver. Of june 2018) version 2.0*. Greenbelt, Maryland.

Meng, X., Liu, C., Zhang, L., Wang, W., Stowell, J., Kan, H., et al. (2021). Estimating PM2.5 concentrations in Northeastern China with full spatiotemporal coverage, 2005–2016. *Remote Sens. Environ.* 253, 112203. doi:10.1016/J.RSE.2020.112203

Mhawish, A., Banerjee, T., Sorek-Hamer, M., Lyapustin, A., Broday, D. M., and Chatfield, R. (2019). Comparison and evaluation of MODIS multi-angle implementation of atmospheric correction (MAIAC) aerosol product over south asia. *Remote Sens. Environ.* 224, 12–28. doi:10.1016/J.RSE.2019.01.033

Nam, J., Kim, S. W., Park, R. J., Park, J. S., and Park, S. S. (2018). Changes in column aerosol optical depth and ground-level particulate matter concentration over East Asia. *Air Qual. Atmos. Health* 11, 49–60. doi:10.1007/s11869-017-0517-5

Özkaynak, H., Baxter, L. K., Dionisio, K. L., and Burke, J. (2013). Air pollution exposure prediction approaches used in air pollution epidemiology studies. *J. Expo. Sci. Environ. Epidemiol.* 23, 566–572. doi:10.1038/jes.2013.15

Park, Y., Kwon, B., Heo, J., Hu, X., Liu, Y., and Moon, T. (2020). Estimating PM2.5 concentration of the conterminous United States via interpretable convolutional neural networks. *Environ. Pollut.* 256, 113395. doi:10.1016/j.envpol.2019.113395

Parker, W. S. (2016). Reanalyses and observations: What's the Difference? *Bull. Am. Meteorol. Soc.* 97, 1565–1572. doi:10.1175/BAMS-D-14-00226.1

Ramsey, J. B. (1969). Tests for specification errors in classical linear least-squares regression analysis. *J. R. Stat. Soc. Ser. B Methodol.* 31, 350–371. doi:10.1111/J.2517-6161.1969.TB00796.X

Schmit, T. J., Griffith, P., Gunshor, M. M., Daniels, J. M., Goodman, S. J., and Lebair, W. J. (2017). A closer look at the ABI on the GOES-R Series. *Bull. Am. Meteorol. Soc.* 98, 681–698. doi:10.1175/BAMS-D-15-00230.1

Stafoggia, M., Schwartz, J., Badaloni, C., Bellander, T., Alessandrini, E., Cattani, G., et al. (2017). Estimation of daily PM10 concentrations in Italy (2006–2012) using finely resolved satellite data, land use variables and meteorology. *Environ. Int.* 99, 234–244. doi:10.1016/j.envint.2016.11.024

Superczynski, S. D., Kondragunta, S., and Lyapustin, A. I. (2017). Evaluation of the multi-angle implementation of atmospheric correction (MAIAC) aerosol algorithm through intercomparison with VIIRS aerosol products and AERONET. *J. Geophys Res.* 122, 3005–3022. doi:10.1002/2016JD025720

Taylor, L., and Nitschke, G. (2019). "Improving deep learning with generic data augmentation," in Proceedings of the 2018 IEEE Symposium Series on Computational Intelligence (SSCI), 1542–1547. doi:10.1109/SSCI.2018.8628742

Tian, J., and Chen, D. (2010). A semi-empirical model for predicting hourly ground-level fine particulate matter (PM2.5) concentration in southern Ontario from satellite remote sensing and ground-based meteorological measurements. *Remote Sens. Environ.* 114, 221–229. doi:10.1016/j.rse.2009.09.011

U.S. Environmental Protection Agency (2017). National emissions inventory: January 2021 updated release, technical support document. Available at: https://www.epa.gov/sites/default/files/2021-02/documents/nei2017_tsd_full_jan2021.pdf (Accessed March 31, 2022).

van Donkelaar, A., Martin, R. v., Spurr, R. J. D., and Burnett, R. T. (2015). High-resolution satellite-derived PM2.5 from optimal estimation and geographically weighted regression over north America. *Environ. Sci. Technol.* 49, 10482–10491. doi:10.1021/ACS.EST.5B02076/ASSET/IMAGES/MEDIUM/ES-2015-02076K_0008.GIF

Xie, Y., Wang, Y., Zhang, K., Dong, W., Lv, B., and Bai, Y. (2015). Daily estimation of ground-level PM2.5 concentrations over beijing using 3 km resolution MODIS AOD. *Environ. Sci. Technol.* 49, 12280–12288. doi:10.1021/acs.est.5b01413

Xu, J., Jiang, H., Zhang, X., Lu, X., and Peng, W. (2014). Study on spatial-temporal variation of aerosol optical depth over the Yangtze Delta and the impact of land-use/cover. *Int. J. Remote Sens.* 35, 1741–1755. doi:10.1080/01431161.2014.882033

Yang, J., and Hu, M. (2018). Filling the missing data gaps of daily MODIS AOD using spatiotemporal interpolation. *Sci. Total Environ.* 633, 677–683. doi:10.1016/J.SCITOTENV.2018.03.202

Zhan, Y., Luo, Y., Deng, X., Chen, H., Grieneisen, M. L., Shen, X., et al. (2017). Spatiotemporal prediction of continuous daily PM2.5 concentrations across China using a spatially explicit machine learning algorithm. *Atmos. Environ.* 155, 129–139. doi:10.1016/j.atmosenv.2017.02.023

Zheng, Y., Liu, F., and Hsieh, H. P. (2013). "U-Air: When urban air quality inference meets big data," in Proceedings of the ACM SIGKDD International Conference on Knowledge Discovery and Data Mining, Chicago, Illinois, August 11–14, 2013. doi:10.1145/2487575.2488188

frontiers | Frontiers in Remote Sensing

TYPE Brief Research Report
PUBLISHED 12 April 2023
DOI 10.3389/frsen.2023.1111696

OPEN ACCESS

EDITED BY
Hannah Victoria Herrero,
The University of Tennessee,
United States

REVIEWED BY
Chen Wang,
Ministry of Ecology and Environment,
China
Mayra Roman-Rivera,
The University of Tennessee,
United States

*CORRESPONDENCE
Breylla Campos Carvalho,
b.carvalho@alumni.usp.br

†PRESENT ADDRESS
Breylla Campos Carvalho, Center of Marine Biology, University of São Paulo, São Sebastião, Brazil

SPECIALTY SECTION
This article was submitted to Remote Sensing Time Series Analysis, a section of the journal Frontiers in Remote Sensing

RECEIVED 30 November 2022
ACCEPTED 27 March 2023
PUBLISHED 12 April 2023

CITATION
Carvalho BC, Gomes CLS and Guerra JV (2023), Spatio-temporal morphological variability of a tropical barrier island derived from the Landsat collection. *Front. Remote Sens.* 4:1111696. doi: 10.3389/frsen.2023.1111696

Spatio-temporal morphological variability of a tropical barrier island derived from the Landsat collection

Breylla Campos Carvalho*†, Carolina Lyra da Silva Gomes and Josefa Varela Guerra

Department of Geological Oceanography, School of Oceanography, Rio de Janeiro State University, Rio de Janeiro, Brazil

Barrier islands are low-lying elongated, narrow sandy deposits, usually parallel to the coastline, separated from the continent by a lagoon. Due to their low elevation above sea level, barrier islands are environments susceptible to drastic morphological changes depending on the meteo-oceanographic conditions to which they are subjected. This work presents the morphological changes between 1985 and 2021 in "Restinga da Marambaia"—a 40 km long barrier island on Brazil's Southeastern coast. One hundred thirty-four scenes from the Landsat collection were processed, enabling the quantification of the barrier island area. Additionally, the rates of change in the position of the shorelines facing the Atlantic Ocean, Sepetiba Bay, and Marambaia Bay were computed. The barrier island's total area and the central sector's width present significant seasonal variability, which is maximum during the austral fall and winter seasons. On the shores facing the Atlantic Ocean and Sepetiba Bay, it is noted that the central and far eastern sectors show an erosional trend. In contrast, the coastline is more stable on the shore facing Marambaia Bay. The seasonal variations of the barrier island area occur during a period of low rainfall and more energetic waves associated with local winds, which produce coastal currents, transporting the available sediments.

KEYWORDS

coastal dynamics, interannual changes, intra-annual variability, coastal geomorphology, remote sensing, shoreline variability, Marambaia barrier island

1 Introduction

Barrier islands are low-lying elongated, narrow sandy deposits, usually parallel to the coastline, separated from the continent by a lagoon (Kusky, 2005). Their formation and maintenance are related to the geological environment, sediment supply, sediment transport mechanism, wave and tidal regimes, and sea level behavior (Pilkey et al., 2009; Stutz and Pilkey, 2011; Otvos, 2012). Due to their low elevation above sea level, barrier islands are environments susceptible to drastic morphological changes depending on the meteo-oceanographic conditions to which they are subjected.

It is a central issue for coastal studies to comprehend and predict the morphological changes and the shoreline variability, as different temporal scales are involved (Turki et al., 2013; Hapke et al., 2016). Also, some uncertainties result from the short-scale natural

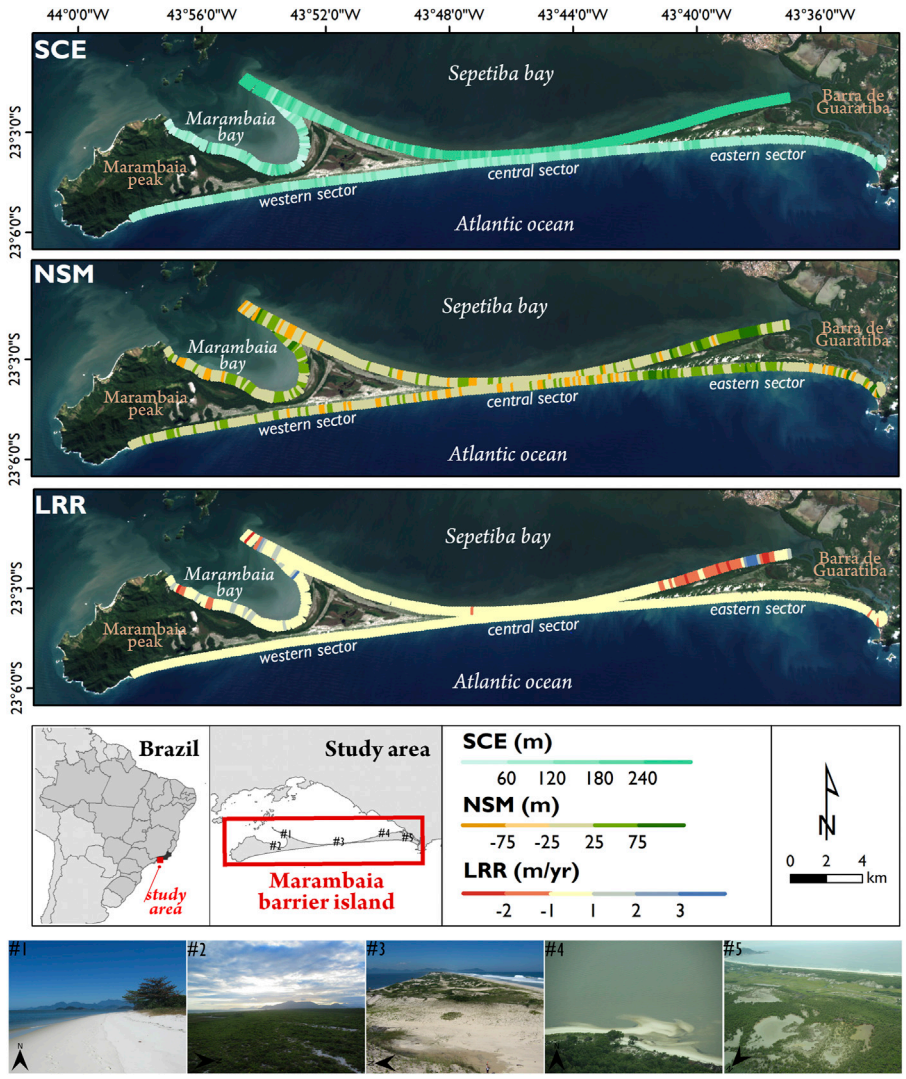

FIGURE 1
Marambaia barrier island location. SCE, shoreline change envelope; NSM, net shoreline movement; LRR, linear regression rate. Landsat 8 satellite imagery from 05/Jun/2021, 4R3G2B composition.

variability and the mean sea level that are not easy to identify (Ruggiero et al., 2003; Lazarus et al., 2011).

Several tools are used in coastal studies, and remote sensing has been one of the most applied in the last decades (Zakaria et al., 2006; Batista et al., 2009; Garcia-Rubio et al., 2012; Sud et al., 2012; Cenci et al., 2015; Sánchez-García et al., 2015; Azevedo et al., 2016; Behling et al., 2018; Pardo-Pascual et al., 2018; Xu, 2018; Mitri et al., 2020). Landsat's freely available images, spanning a few decades, make it possible to analyze the changing morphology and position of the coastline (Young et al., 2017). Additionally, satellite image processing tools have evolved considerably, especially in handling large volumes of images, improving performance, accuracy, and applicability (Gorelick et al., 2017; Obi Reddy and Singh, 2018).

Throughout the last decade, the 40 km long Marambaia barrier island has been investigated for its sedimentary dynamics and geological evolution (e.g., Borges and Nittrouer, 2016; Gomes et al., 2019; Carvalho and Guerra, 2020; Reis et al., 2020; Dadalto et al., 2022), with fewer studies quantifying the shoreline dynamics (Oliveira et al., 2008; Bahiense et al., 2014; Santos et al., 2019; Carvalho et al., 2020). Given the geomorphological importance of this barrier island and the emergency to understand the morphological behavior of coastal features due to scenarios of sea level rise (IPCC, 2022) and increased storminess (Young and Ribal, 2019; Rey et al., 2021), this work presents a contribution to the diagnostic of its morphological trends over 36 years (1985–2021), supported by Landsat imagery analysis. In contrast to the previous works, this study expands the time scale of the observation, and more images were processed. While Oliveira et al. (2008) and Bahiense et al. (2014) used, respectively, nine and five images, we used more than a hundred. Therefore, our results are robust and allow the

detailed observation of the seasonal changes in shoreline position and their consequences in the barrier island area over time.

2 Methods

2.1 Study area

The 40 km long Marambaia barrier island is located on the southern coastline of Rio de Janeiro (SE Brazil), with an east-west orientation and width varying from 120 to 1800 m. In the westernmost limit, the barrier island is anchored at a pre-Cambrian massif, the Marambaia Peak. In the easternmost limit lie the tidal channels of Barra de Guaratiba (Figure 1). This barrier island may be divided into three sectors: 1) Western, including beach ridges, marshlands, inter-ridge paleo lagoons, and overland flow features; 2) Central, where the barrier island becomes strikingly narrow; and 3) Eastern, characterized by a dune field, tidal wetlands and beach ridges (Dadalto et al., 2022).

Based on the Köppen classification, Alvares et al. (2013) state that there are two types of climate in this region: tropical without dry season (Af) and tropical monsoon (Am), characterized by annual mean temperature between 22°C and 24°C and annual rainfall between 1,300 and 1,600 mm. The South Atlantic Subtropical Anticyclone (SASA) affects the area, which, in the face of frontal systems, causes increased cloud cover and strong winds (Dereczynski and Menezes, 2015).

The wave climate in the Rio de Janeiro littoral is characterized by fair-weather short-period waves from northeast and eastern directions and storm waves from S and SSW, with higher amplitudes and longer periods (Parente et al., 2015; Carvalho et al., 2021).

Marambaia barrier island partially isolates Sepetiba bay from the Atlantic Ocean, strongly influencing its circulation, which is affected by river discharge in its northern and eastern sectors (Fragoso, 1999). The coastal region is under a microtidal regime, with tide heights varying between 0.3 and 1.2 m (Criado-Sudau et al., 2019) and with tidal propagation from east to west (Harari and Camargo, 1994).

2.2 Landsat imagery

Landsat satellite imagery has been globally applied for environmental studies, including shoreline monitoring (Zakaria et al., 2006; Misra and Balaji, 2015; Ozturk et al., 2015; Konlechner et al., 2020; Sánchez-García et al., 2020; McAllister et al., 2022). These images are extensively used since they have global coverage and are freely distributed (Young et al., 2017). For this work, using the Google Earth Engine (GEE) platform (Gorelick et al., 2017), the TM, ETM+, and OLI sensors images were imported from the Landsat Tier 1 collection (Supplementary Figure S1) calibrated top-of-atmosphere (TOA) reflectance, encompassing the period between 1985 and 2021, with a cloud coverage of less than 10% of the scene. One hundred thirty-four scenes, with orbit/point 217/76, were used to map the Marambaia barrier island. The atmospheric correction was done using the Dark Object Subtraction (DOS) model (Chavez, 1988) to obtain surface reflectance. This model is widely used for mapping change detection, enabling reliable surface reflectance values (Kawakubo et al., 2011; Cui et al., 2014; Nazeer et al., 2014; Pacheco et al., 2015; Phan and Stive, 2022).

2.3 Shoreline detection and analysis

Shoreline delineation was performed on the GEE platform by applying the Normalized Difference Water Index (NDWI) (McFeeters, 1996) (Eq. 1), and the output rasters were converted to vector polygons.

$$NDWI = (GREEN - NIR)/(GREEN + NIR) \quad (1)$$

In the Landsat 5 and 7 series, the green and near-infrared (NIR) bands correspond to bands 2 and 4, respectively, while in the Landsat 8 series, they represent bands 3 and 5, respectively.

Afterward, the quantification of the barrier island area and its central sector's width were conducted in the QGIS 3.16 program. Marambaia peak was excluded from the computation of the barrier area. The width of the central sector was computed at a location close to photography #3, shown in Figure 1 (between coordinates 43° 44′31.43″ W, 23° 3′30.04″ S and 43° 44′30.66″ W, 23° 3′34.30″ S). With the computed values, it was possible to estimate the annual average and median barrier island area and central sector width, as well as their seasonality.

The rates of change in the position of the shorelines facing the Atlantic Ocean, Sepetiba Bay, and Marambaia Bay were calculated in the Digital Shoreline Analysis System (DSAS) program (Himmelstoss et al., 2021) for ArcMap™ 10.8. For that, the polygons were converted into polylines, representing the shorelines for each image. Five hundred and seventy-four transversal transects, equispaced 150 m, were used to compute the Shoreline Change Envelope (SCE), the Net Shoreline Movement (NSM), and the Linear Regression Rate (LRR) (Himmelstoss et al., 2021).

The SCE is obtained by calculating the largest distance among all shorelines on each transect, representing the total variation in shoreline position, and is not related to the dates of the images (Himmelstoss et al., 2021). Conversely, the NSM is the difference between the oldest and the most recent shoreline position in each transect. The LRR is obtained from a line of best fit, calculated using the least squares method, with all shoreline positions in each transect (Dolan et al., 1991), reflecting rates that indicate erosion, accretion, or stability of the coastline.

DSAS considers information on the uncertainty and horizontal accuracy of the shoreline mapping in the calculations of standard errors and confidence intervals (Ruggiero et al., 2013). In the case of using satellite imagery for determining shoreline position, these uncertainties consider data quality (pixel error, E_p), georeferencing error (E_g), high tide level uncertainty (E_v), and shoreline digitization error (E_d), compiled as a total error (E_t) (Hapke et al., 2016; Nassar et al., 2019). For the mapping presented in this manuscript, the annualized E_t was ±3.2 m/year, and the estimated uncertainty (U_R) of the shoreline change rate was 0.2 m/year,

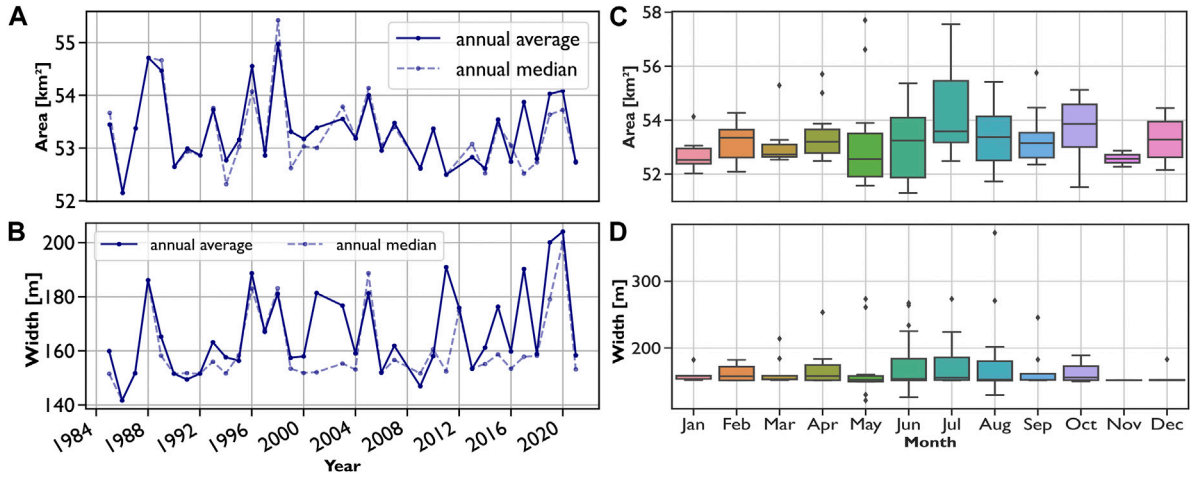

FIGURE 2
Marambaia barrier island variability (1985–2021): annual averages and medians of **(A)** total area and **(B)** central section width; and monthly variation of **(C)** total area and **(D)** central section width.

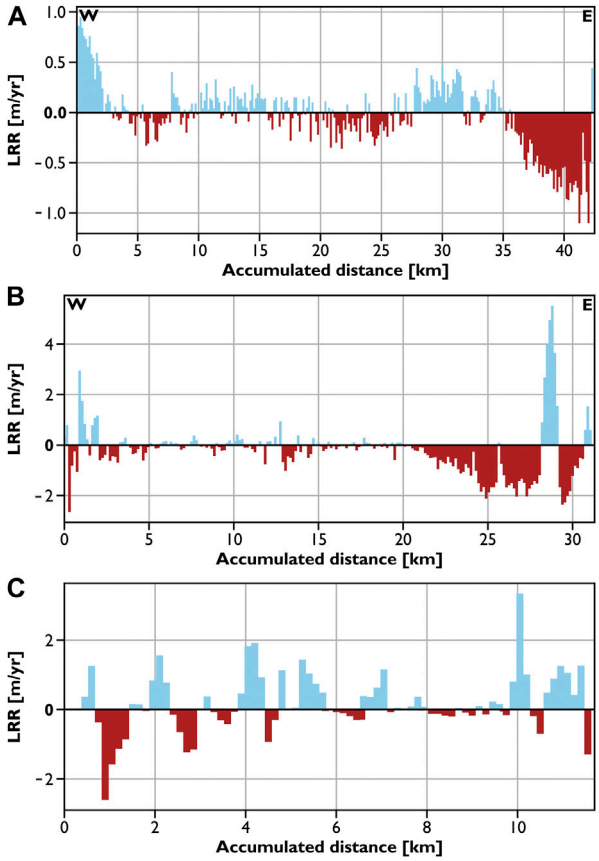

FIGURE 3
Shoreline change rates (1985–2021): **(A)** facing the open ocean; **(B)** back-barrier; **(C)** facing marambaia bay.

with values similar to those reported by Carvalho et al. (2020), where the authors analyzed the Marambaia barrier island shoreline facing the Atlantic Ocean. So, when analyzing the values expressed as LRR, rates above 0.2 m/year indicate accretion, between −0.2 and 0.2 m/year indicate stability, and below −0.2 m/year indicate erosion.

3 Results

3.1 Barrier island area and central sector width variability

From 1985 to 2021, the barrier island area varied between 51.3 and 57.7 km^2, averaging 53.3 ± 1.2 km^2 (Figure 2A). The lowest average area was recorded in 1986 (52.1 ± 0.6 km^2), while the largest was recorded in 1998 (55.0 ± 2.1 km^2). The central sector width, one of the lowest regions of the barrier island, varied between 121.7 and 372.3 m, with an average of 168.4 ± 34.9 m (Figure 2B). The smallest average width was determined for 1986 (141.6 ± 16.7 m), while the largest was observed in 2020 (204.0 ± 60.2 m).

The barrier island's total area and the central sector's width presented significant seasonal variability, maximum between May and August, that corresponds to the austral fall and winter seasons (Figures 2C, D). November is the month when the barrier island presents the smallest average area (52.6 ± 0.4 km^2), while the largest value occurred in July (54.3 ± 1.6 km^2). About the width of the central area, the lowest monthly average was found in November (151.8 ± 0.2 m), whereas the highest monthly average was observed in August (178.4 ± 57.4 m).

3.2 Shoreline change metrics and rates (SCE, NSM, and LRR)

In Figure 1 are spatialized the shoreline change envelope (SCE), net shoreline movement (NSM), and the linear regression rate (LRR). Regarding the shoreline facing the open ocean, the

TABLE 1 Statistical parameters of the metrics and rates of barrier island each sector.

Shoreline metrics		Open ocean shore				Back-barrier shore				Marambaia bay shore
		Western	Central	Eastern	Total length	Western	Central	Eastern	Total length	
Lenght (km)		18 (43%)	11 (26%)	13 (31%)	42 (100%)	12 (38%)	11 (36%)	8 (26%)	31 (100%)	12
SCE (m)	Min	60.24	30.06	60.00	30.06	94.95	150.01	242.09	94.95	−67.62
	max	182.57	151.09	276.83	276.83	589.19	470.00	893.58	893.58	87.57
	avg	106.01	98.64	108.35	104.98	238.65	296.02	469.38	317.58	15.62
	std	25.70	21.21	29.79	25.79	201.25	300.02	447.25	107.70	23.91
	md	93.28	90.54	92.06	91.66	201.25	300.02	447.25	303.10	5.09
NSM (m)	max_r	−31.26	−30.26	−61.52	−61.52	−60.86	−60.91	−31.94	−60.91	−2.06
	max_a	60.15	115.35	94.15	115.35	101.91	31.38	184.87	184.87	2.76
	avg	2.84	0.69	21.35	8.64	−0.32	2.70	42.22	11.58	0.05
	std	10.84	19.40	28.77	20.61	0.00	0.00	31.37	24.17	0.23
	md	0.00	0.00	8.68	0.00	0.00	0.00	31.37	0.00	0.00
LRR (m/yr)	max_r	−0.33	−0.36	−1.10	−1.10	−2.65	−1.02	−2.36	−2.65	0.00
	max_a	0.95	0.44	0.47	0.95	2.95	0.95	5.52	5.52	0.77
	avg	0.09	−0.04	−0.21	−0.03	0.00	−0.16	−0.63	−0.22	0.16
	std	0.17	0.14	0.36	0.23	−0.02	−0.08	−1.22	0.63	0.17
	md	0.05	−0.06	−0.16	−0.01	−0.02	−0.08	−1.22	−0.11	0.04
%	Erosion	5	16	45	20	25	36	79	43	19
	Stability	79	77	37	65	59	57	2	44	43
	Accretion	16	7	18	14	16	7	19	13	38

Legend: SCE, shoreline change envelope; NSM, net shoreline movement; LRR, linear regression rate; yr, year; %, pecentage; min, minimum; max, maximum; avg, average; std, standard deviation; md, median; max_r, maximum retreat; max_a, maximum advance.

beach envelope varied between 30 and 277 m (SCE), ranging from −62 m to +115 m (NSM), resulting in a rate of change between −1.1 and +1.0 m/year (LRR) (Figure 3A; Table 1). The eastern sector shows higher variability (maximum SCE of 277 m) and erosive tendency (maximum NSM retreat of −61.5 m and maximum LRR retreat of −1.1 m/year), representing 10% of the whole shoreline under erosion, especially near Barra de Guaratiba. The central area shows some stability (~20% of the whole shoreline), since areas under erosion (26%) and under accretion (53%) alternate along this sector (panel NSM on Figure 1), culminating in average rates of −0.04 m/year. The western sector is the most stable, making up 34% of the shoreline with an average LRR of 0.09 m/year (Table 1).

On the back-barrier shoreline, the beach envelope (SCE) varied between 95 and 894 m, ranging between −61 m and +185 m (NSM), showing a rate of change between −2.7 and +5.5 m/year (LRR) (Figure 3B; Table 1). Similarly to the coastline facing the open ocean, the eastern sector of the shoreline facing Sepetiba Bay exhibits the highest erosion rate (mean LRR of −0.6 m/year), comprising 31% of the backbarrier shoreline that is eroding. The central sector also shows erosional trends (mean LRR of −0.2 m/year), although most of this sector is stable (~10% of the entire back-barrier coastline). The western sector is the most stable (mean LRR of 0 m/year), where almost 60% of this sector (~6% of this shoreline) is stable (Table 1).

Finally, on the coastline facing Marambaia Bay, the beach envelope (SCE) oscillated between 0 and 320 m, ranging from −68 m to +88 m (NSM), with a rate of change between −2.6 and +3.3 m/year (LRR) (Figure 3C; Table 1). This shoreline is more stable (average NSM of 0.05 m) and exhibits the highest accretion rates on the barrier island (38%), with an average LRR of 0.2 m/year (Table 1).

4 Discussion

The Marambaia barrier island morphometric and shoreline behavior suggest that the intrannual variability is the primary driver of barrier island remodeling, intensified by interannual changes and geological control. As for the seasonal variations of

the barrier island area, they occur during a period of low rainfall (Supplementary Figure S2), more energetic waves (Parente et al., 2015; Carvalho et al., 2020), and most significant mean sea level variation (Carvalho et al., 2023). This combination is conducive to sediment transport conditions that favor the maintenance of overwash zones observed in the barrier island (Photo #3 in Figure 1).

In general, the back-barrier shore presented a broader envelope of shoreline change compared to the shores facing Marambaia Bay and the open ocean. In this region are observed striking rhythmic features, classified as elongated transverse finger bars (Gomes et al., 2019). The highest average number of NE-SW oriented bars, determined by satellite imagery, occurs in August, reaching 11 bars/km (Gomes et al., 2019). Thus, it is suggested that these features influence shoreline variability. Ashton and Murray (2006); Murray et al. (2014) associated these rhythmic patterns with sediment erosion and accretion on the coastline.

The eastern sector of the back-barrier shore presents the highest shoreline change envelope (SCE >240 m) determined in the present study. This might be a consequence of its proximity to the mouth of rivers debouching into the bay and intermittent channels that drain wetlands (Photo #5 in Figure 1) present in the barrier (Dadalto et al., 2022). For example, the Piraquê river, near the eastern sector, is one of the main tributaries of Sepetiba bay, with an average discharge of 2.5 m^3/s (Cunha et al., 2006). Furthermore, in the satellite images and aerial photographs is possible to observe the presence of intermittent channels that induce the formation of spur-like features (Photo #4 in Figure 1) of variable sizes.

Although the coastline is more stable along the Marambaia Bay shore, there is an erosional trend in its southwestern sector and a prograding trend in the northeastern sector (Photo #1 in Figure 1). These sediment transport trends are evidenced by morphological features and grain size trend analysis (Carvalho and Guerra, 2020). On the open-ocean shore, the Barra de Guaratiba tidal channels influence the erosional trend observed in the far eastern sector, which had been previously noted (Carvalho et al., 2020).

Regarding the width of the central sector of the barrier island, Oliveira et al. (2008), using Landsat and CBERS satellite images from 1975 to 2004, documented a variation from 158 m (in 1975) to 100 m (in 2004). In our study, which encompasses a larger temporal scale, the width increased from 151 m to 180 m. Also, between 1984 and 2004, Oliveira et al. (2008) documented a reduction of 58 m in the central sector width, while we observed a slight increase (+29 m). Using aerial photographs and GeoEye satellite images, Bahiense et al. (2014) verified that between 1975 and 2011, there was an alternation of areas of accretion and erosion on both sides of the barrier island's central sector, with rates ranging between −0.30 and 0.15 m/yr.

The seasonality of shoreline change is a common trend observed in other sandy shorelines studied in other parts of the world. Still, the reasons for this seasonality differ regionally. For example, Bishop-Taylor et al. (2021) found that 16% of Australia's shoreline retreated or progressed at rates greater than 0.5 m/year, indicating that these may be extreme coastal change hot spots. On the Calabrian coast (southern Italy), Foti et al. (2022) studied the evolution of the coastline at different time scales. They noted that eroding areas prevailed over accreting ones when analyzed over long and medium-term time scales, while accretion prevailed over short-term time scales. Therefore, the authors emphasize the importance of jointly analyzing human pressures and natural processes to understand shoreline dynamics. In this regard, Bamunawala et al. (2021), in assessing projections of worldwide shoreline changes near tidal inlets, emphasized that several impacts of climate change can severely modify the morphological dynamics of the shoreline. They mention, for instance, changes in mean sea level and suppression of sediment supply in coastal areas. Thus, it is apparent the importance of understanding the processes subjacent to the changes in the position of the coastline in its different temporal and spatial scales, taking into account the natural and anthropic influences.

Despite the geomorphological complexity observed on the Marambaia barrier island, using Landsat satellite images enabled us to quantify the morphological changes over the last 35 years. Remote sensing is a powerful tool in places of difficult access, such as the study area, associated with the scarcity of financial and human resources to monitor the coastline. The observed trends demonstrated the importance of the seasonality of coastal processes, reinforcing the need to fully understand these systems to cope with the changes they will undergo in scenarios of sea level rise and an increased number of storm events.

Data availability statement

The raw data supporting the conclusion of this article will be made available by the authors, without undue reservation.

Author contributions

BC designed the study, prepared and processed the satellite images and made the statistical analysis. BC and CG analyzed and interpreted the data. All authors were involved in writing or revising the manuscript.

Funding

Fundação de Amparo à Pesquisa do Estado do Rio de Janeiro (FAPERJ) financial support [E-26/010.002642/2014 and E-26/010.002208/2019].

Acknowledgments

The authors thank Fundação de Amparo à Pesquisa do Estado do Rio de Janeiro (FAPERJ) for the financial support for this research and the colleagues and institutions that supported the authors' efforts over the last decade. They also thank the reviewers for their comments and suggestions, which helped improve this manuscript. To the editors of Women in Remote Sensing: 2022 and Rebecca Thompson, journal

specialist, our thanks for their administrative efforts on this manuscript.

Conflict of interest

The authors declare that the research was conducted in the absence of any commercial or financial relationships that could be construed as a potential conflict of interest.

Publisher's note

All claims expressed in this article are solely those of the authors and do not necessarily represent those of their affiliated organizations, or those of the publisher, the editors and the reviewers. Any product that may be evaluated in this article, or claim that may be made by its manufacturer, is not guaranteed or endorsed by the publisher.

Supplementary material

The Supplementary Material for this article can be found online at: https://www.frontiersin.org/articles/10.3389/frsen.2023.1111696/full#supplementary-material

SUPPLEMENTARY FIGURE S1
Temporal distribution of landsat imagery (DOY: Day Of Year).

SUPPLEMENTARY FIGURE S2
Monthly averaged air temperature and accumulated precipitation from Marambaia metereological station (2002 to 2021), located at 43° 36′ W and 23° 03′ S. Data provided by the National Institute of Meteorology (INMET).

References

Alvares, C. A., Stape, J. L., Sentelhas, P. C., Gonçalves, J. L., de, M., and Sparovek, G. (2013). Köppen's climate classification map for Brazil. *Zeitschrift* 22, 711–728. doi:10.1127/0941-2948/2013/0507

Ashton, A. D., and Murray, A. B. (2006). High-angle wave instability and emergent shoreline shapes: 2. Wave climate analysis and comparisons to nature. *J. Geophys. Res. Earth Surf.* 111, F04012–F04017. doi:10.1029/2005jf000423

Azevedo, I. F. D., Carvalho, B. C., and Guerra, J. V. (2016). Utilização de imagens de satélite LANDSAT para análise da variabilidade morfológica de pontais arenosos na planície costeira de Caravelas (NE do Brasil). *Rev. Bras. Geomorfol.* 17, 695–709. doi:10.20502/rbg.v17i4.843

Bahiense, F., Pereira, S. D., Geraldes, M. C., and Menezes, G. (2014). "Emprego de análise multitemporal de fotografias aéreas na evolução geomorfológica da restinga da Marambaia, Rio de Janeiro – brasil," in *Formação e Ocupação de Litorais nas Margens do Atlântico - brasil/Portugal* Rio de Janeiro: Corbã, 33–52.

Bamunawala, J., Ranasinghe, R., Dastgheib, A., Nicholls, R. J., Murray, A. B., Barnard, P. L., et al. (2021). Twenty-first-century projections of shoreline change along inlet-interrupted coastlines. *Sci. Rep.* 11, 14038. doi:10.1038/s41598-021-93221-9

Batista, E. D. M., Souza Filho, P. W. M., and da Silveira, O. F. M. (2009). Avaliação de áreas deposicionais e erosivas em cabos lamosos da zona costeira Amazônica através da análise multitemporal de imagens de sensores remotos. *Rev. Bras. Geofis.* 27, 83–96.

Behling, R., Milewski, R., and Chabrillat, S. (2018). Spatiotemporal shoreline dynamics of Namibian coastal lagoons derived by a dense remote sensing time series approach. *Int. J. Appl. Earth Obs. Geoinf.* 68, 262–271. doi:10.1016/j.jag.2018.01.009

Bishop-Taylor, R., Nanson, R., Sagar, S., and Lymburner, L. (2021). Mapping Australia's dynamic coastline at mean sea level using three decades of Landsat imagery. *Remote Sens. Environ.* 267, 112734. doi:10.1016/j.rse.2021.112734

Borges, H. V., and Nittrouer, C. A. (2016). Sediment accumulation in Sepetiba bay (Brazil) during the holocene: A reflex of the human influence. *J. Sediment. Environ.* 1, 90–106. doi:10.12957/jse.2016.21868

Carvalho, B. C., Araujo, T. A. A., Guerra, J. V., and Reis, A. T. D. (2023). "Mean sea level trends based on tide gauge records and their possible morphological effects on the coastline of southern Rio de Janeiro (SE Brazil)," in *Appl. Geogr. Submitted*.

Carvalho, B. C., Dalbosco, A. L. P., and Guerra, J. V. (2020). Shoreline position change and the relationship to annual and interannual meteo-oceanographic conditions in Southeastern Brazil. *Estuar. Coast. Shelf Sci.* 235, 106582. doi:10.1016/j.ecss.2020.106582

Carvalho, B. C., and Guerra, J. V. (2020). Aplicação de Modelo de Tendência Direcional de Transporte ao Longo de uma Ilha-Barreira: Restinga da Marambaia (RJ, SE Brasil). *Anuário do Inst. Geociências - UFRJ* 43, 101–118. doi:10.11137/2020_2_101_118

Carvalho, B. C., Lins-de-Barros, F. M., Silva, P., Pena, J. D. N., and Guerra, J. V. (2021). Morphological variability of sandy beaches due to variable oceanographic conditions: A study case of oceanic beaches of Rio de Janeiro city (Brazil). *J. Coast. Conserv.* 25, 28. doi:10.1007/s11852-021-00821-8

Cenci, L., Persichillo, M. G., Disperati, L., Oliveira, E. R., Alves, F. L., Pulvirenti, L., et al. (2015). "Remote sensing for coastal risk reduction purposes: Optical and microwave data fusion for shoreline evolution monitoring and modelling," in *2015 IEEE international geoscience and remote sensing symposium (IGARSS)*, 1417–1420. doi:10.1109/IGARSS.2015.7326043

Chavez, P. S. (1988). An improved dark-object subtraction technique for atmospheric scattering correction of multispectral data. *Remote Sens. Environ.* 24, 459–479. doi:10.1016/0034-4257(88)90019-3

Criado-Sudau, F. F., Nemes, D. D., and Gallo, M. N. (2019). Rip currents dynamic of a swell dominated microtidal beach. *J. Coast. Res.*, 121–127. doi:10.2112/SI92-014.1

Cui, L., Li, G., Ren, H., He, L., Liao, H., Ouyang, N., et al. (2014). Assessment of atmospheric correction methods for historical landsat TM images in the coastal zone: A case study in jiangsu, China. *China. Eur. J. Remote Sens.* 47, 701–716. doi:10.5721/eujrs20144740

Cunha, C. D. L. D. N., Rosman, P. C. C., Ferreira, A. P., and Carlos do Nascimento Monteiro, T. (2006). Hydrodynamics and water quality models applied to Sepetiba Bay. *Cont. Shelf Res.* 26, 1940–1953. doi:10.1016/j.csr.2006.06.010

Dadalto, T. P., Carvalho, B. C., Guerra, J. V., Reis, A. T. D., and Silva, C. G. (2022). Holocene morpho-sedimentary evolution of Marambaia barrier island (SE Brazil). *Quat. Res.* 105, 182–200. doi:10.1017/qua.2021.43

Dereczynski, C. P., and Menezes, W. F. (2015). "Meteorologia da Bacia de Campos," in *Meteorologia e Oceanografia*. Editors R. P. Martins and G. S. Grossmann-Matheson (Rio de Janeiro: Elsevier Editora Ltda), 1–54. doi:10.1016/B978-85-352-6208-7.50008-8

Dolan, R., Fenster, M. S., and Holme, S. J. (1991). Temporal analysis of shoreline recession and accretion. *J. Coast. Res.* 7, 723–744. doi:10.2307/4297888

Foti, G., Barbaro, G., Barillà, G. C., Mancuso, P., and Puntorieri, P. (2022). Shoreline evolutionary trends along calabrian coasts: Causes and classification. *Front. Mar. Sci.* 9. doi:10.3389/fmars.2022.846914

Fragoso, M. R. (1999). *Estudo numérico da circulação marinha da região das baías de Sepetiba e Ilha Grande (RJ)*.

Garcia-Rubio, G., Huntley, D., and Russell, P. (2012). "Assessing shoreline change using satellite-derived shorelines in Progreso, Yucatán, México," in *Coastal engineering proceedings (santander)*, 1–13.

Gomes, C. L., da, S., Guerra, J. V., and Gallo, M. N. (2019). "Mapeamento de bancos transversais (tipo "finger bars") na margem norte da restinga da Marambaia (Baía de Sepetiba, RJ)," in *Anais do XIX simpósio brasileiro de Sensoriamento remoto*, 96716. Available at: https://proceedings.science/sbsr-2019/papers/mapeamento-de-bancos-transversais–tipo––finger-bars–––na-margem-norte-da-restinga-da-marambaia–baia-de-sepetiba–r.

Gorelick, N., Hancher, M., Dixon, M., Ilyushchenko, S., Thau, D., and Moore, R. (2017). Google Earth engine: Planetary-scale geospatial analysis for everyone. *Remote Sens. Environ.* 202, 18–27. doi:10.1016/j.rse.2017.06.031

Hapke, C. J., Plant, N. G., Henderson, R. E., Schwab, W. C., and Nelson, T. R. (2016). Decoupling processes and scales of shoreline morphodynamics. *Mar. Geol.* 381, 42–53. doi:10.1016/j.margeo.2016.08.008

Harari, J., and Camargo, R. D. (1994). Simulação da propagação das nove principais componentes de maré na plataforma sudeste brasileira através de modelo numérico hidrodinâmico. *Braz. J. Oceanogr.* 42, 35–54. doi:10.1590/s1679-87591994000100003

Himmelstoss, E., Henderson, R., Kratzmann, M., and Farris, A. (2021). Digital shoreline analysis system (DSAS) version 5.1 user guide. doi:10.3133/ofr20211091

Intergovernmental Panel on Climate Change (IPCC) (2022). "sea level rise and implications for low-lying islands, coasts and communities," in *The Ocean and cryosphere in a changing climate* (Cambridge University Press), 321–446. doi:10.1017/9781009157964.006

Kawakubo, F. S., Morato, R. G., Nader, R. S., and Luchiari, A. (2011). Mapping changes in coastline geomorphic features using landsat TM and ETM+ imagery: Examples in southeastern Brazil. *Int. J. Remote Sens.* 32, 2547–2562. doi:10.1080/01431161003698419

Konlechner, T. M., Kennedy, D. M., O'Grady, J. J., Leach, C., Ranasinghe, R., Carvalho, R. C., et al. (2020). Mapping spatial variability in shoreline change hotspots from satellite data; a case study in southeast Australia. *Estuar. Coast. Shelf Sci.* 246, 107018. doi:10.1016/j.ecss.2020.107018

Kusky, T. (2005). *Encyclopedia of Earth science*. New York: Facts On File.

Lazarus, E., Ashton, A., Tebbens, S., Murray, A. B., Tebbens, S., Burroughs, S., et al. (2011). Cumulative versus transient shoreline change: Dependencies on temporal and spatial scale. *J. Geophys. Res. Earth Surf.* 116, 1–10. doi:10.1029/2010jf001835

McAllister, E., Payo, A., Novellino, A., Dolphin, T., and Medina-Lopez, E. (2022). Multispectral satellite imagery and machine learning for the extraction of shoreline indicators. *Coast. Eng.* 174, 104102. doi:10.1016/j.coastaleng.2022.104102

McFeeters, S. K. (1996). The use of the Normalized Difference Water Index (NDWI) in the delineation of open water features. *Int. J. Remote Sens.* 17, 1425–1432.

Misra, A., and Balaji, R. (2015). A study on the shoreline changes and Land-use/land-cover along the south Gujarat coastline. *Procedia Eng.* 116, 381–389. doi:10.1016/j.proeng.2015.08.311

Mitri, G., Nader, M., Abou Dagher, M., and Gebrael, K. (2020). Investigating the performance of sentinel-2A and Landsat 8 imagery in mapping shoreline changes. *J. Coast. Conserv.* 24, 40. doi:10.1007/s11852-020-00758-4

Murray, A. B., Coco, G., and Goldstein, E. B. (2014). Cause and effect in geomorphic systems: Complex systems perspectives. *Geomorphology* 214, 1–9. doi:10.1016/j.geomorph.2014.03.001

Nassar, K., Mahmod, W. E., Fath, H., Masria, A., Nadaoka, K., and Negm, A. (2019). Shoreline change detection using DSAS technique: Case of North Sinai coast, Egypt. *Mar. Georesources Geotechnol.* 37, 81–95. doi:10.1080/1064119x.2018.1448912

Nazeer, M., Nichol, J. E., and Yung, Y.-K. (2014). Evaluation of atmospheric correction models and Landsat surface reflectance product in an urban coastal environment. *Int. J. Remote Sens.* 35, 6271–6291. doi:10.1080/01431161.2014.951742

Obi Reddy, G. P., and Singh, S. K. (2018). *Geospatial technologies in land resources mapping, monitoring and management*. 1st ed. New York: Springer International Publishing.

Oliveira, F. S. C., Kampel, M., and Amaral, S. (2008). Multitemporal assessment of the geomorphologic evolution of the restinga of Marambaia, Rio de Janeiro, Brazil. *Int. J. Remote Sens.* 29, 5585–5594. doi:10.1080/01431160802061696

Otvos, E. G. (2012). Coastal barriers - Nomenclature, processes, and classification issues. *Geomorphology* 139–140, 39–52. doi:10.1016/j.geomorph.2011.10.037

Ozturk, D., Beyazit, I., and Kilic, F. (2015). Spatiotemporal analysis of shoreline changes of the kizilirmak delta. *J. Coast. Res.* 31, 1389–1402. doi:10.2112/jcoastres-d-14-00159.1

Pacheco, A., Horta, J., Loureiro, C., and Ferreira (2015). Retrieval of nearshore bathymetry from landsat 8 images: A tool for coastal monitoring in shallow waters. *Remote Sens. Environ.* 159, 102–116. doi:10.1016/j.rse.2014.12.004

Pardo-Pascual, J., Sánchez-García, E., Almonacid-Caballer, J., Palomar-Vázquez, J., Priego de los Santos, E., Fernández-Sarría, A., et al. (2018). Assessing the accuracy of automatically extracted shorelines on microtidal beaches from landsat 7, landsat 8 and sentinel-2 imagery. *Remote Sens.* 10, 326. doi:10.3390/rs10020326

Parente, C. E., Nogueira, I. C. M., and Ribeiro, E. O. (2015). "Climatologia de ondas," in *Meteorologia e Oceanografia*. Editors R. P. Martins and G. S. Grossmann-Matheson (Rio de Janeiro: Elsevier Editora Ltda.), 55–96. doi:10.1016/B978-85-352-6208-7.50009-X:

Phan, M. H., and Stive, M. J. F. (2022). Managing mangroves and coastal land cover in the Mekong Delta. *Ocean. Coast. Manag.* 219, 106013. doi:10.1016/j.ocecoaman.2021.106013

Pilkey, O. H., Cooper, J. A. G., and Lewisa, D. (2009). Global distribution and geomorphology of fetch-limited barrier islands. *J. Coast. Res.* 254, 819–837. doi:10.2112/08-1023.1

Reis, A. T. D., Amendola, G., Dadalto, T. P., Silva, C. G., Tardin Poço, R., Guerra, J. V., et al. (2020). Arquitetura e evolução deposicional da sucessão sedimentar pleistoceno tardio-holoceno (Últimos ~20 Ka) da baía de sepetiba (RJ). *Geosci. Geociências* 39, 695–708. doi:10.5016/geociencias.v39i03.14366

Rey, W., Ruiz-Salcines, P., Salles, P., Urbano-Latorre, C. P., Escobar-Olaya, G., Osorio, A. F., et al. (2021). Hurricane flood hazard assessment for the archipelago of san andres, providencia and santa catalina, Colombia. *Front. Mar. Sci.* 8. doi:10.3389/fmars.2021.766258

Ruggiero, P., Kaminsky, G. M., Gelfenbaum, G., Ruggierof, P., Kaminskyt, G. M., and Gelfenbaumf, G. (2003). Linking proxy-based and datum-based shorelines on a high-energy coastline: Implications for shoreline change analyses. *J. Coast. Res.*, 57–82.

Ruggiero, P., Kratzmann, M. G., Himmelstoss, E. A., Reid, D., Allan, J., and Kaminsky, G. (2013). *National assessment of shoreline change — historical shoreline change along the pacific northwest coast: U.S. Geological survey open-file report 2012–1007*. Available at: https://pubs.usgs.gov/of/2012/1007/.

Sánchez-García, E., Palomar-Vázquez, J. M., Pardo-Pascual, J. E., Almonacid-Caballer, J., Cabezas-Rabadán, C., and Gómez-Pujol, L. (2020). An efficient protocol for accurate and massive shoreline definition from mid-resolution satellite imagery. *Coast. Eng.* 160, 103732. doi:10.1016/j.coastaleng.2020.103732

Sánchez-García, E., Pardo-Pascual, J. E., Balaguer-Beser, A., and Almonacid-Caballer, J. (2015). "Analysis of the shoreline position extracted from landsat TM and ETM+ imagery," in *International archives of the photogrammetry, remote sensing and spatial information sciences - ISPRS archives* (Berlin: International Society of Photogrammetry and Remote Sensing), 991–998. doi:10.5194/isprsarchives-XL-7-W3-991-2015

Santos, C., da, C. S., Dias, F. F., Franz, B., Alves dos Santos, P. R., Rodrigues, F., et al. (2019). Relative sea level rise effects at the Marambaia barrier island and Guaratiba mangrove: Sepetiba bay (SE Brazil). *J. Sediment. Environ.* 4, 249–262. doi:10.12957/jse.2019.44397

Stutz, M. L., and Pilkey, O. H. (2011). Open-Ocean barrier islands: Global influence of climatic, oceanographic, and depositional settings. *J. Coast. Res.* 27, 207–222. doi:10.2112/09-1190.1

Sud, B., Tohannic, C. D., Ensibs, B., and Cedex, V. (2012). "Automated mapping of coastline from high resolution satellite images using supervised segmentation," in *4th GEOBIA*, 515–517.

Turki, I., Medina, R., Gonzalez, M., and Coco, G. (2013). Natural variability of shoreline position: Observations at three pocket beaches. *Mar. Geol.* 338, 76–89. doi:10.1016/j.margeo.2012.10.007

Xu, N. (2018). Detecting coastline change with all available landsat data over 1986-2015: A case study for the state of Texas, USA. *Atmos. (Basel)* 9. doi:10.3390/atmos9030107

Young, I. R., and Ribal, A. (2019). Multiplatform evaluation of global trends in wind speed and wave height. *Science* 364, eaav9527. doi:10.1126/science.aav9527

Young, N. E., Anderson, R. S., Chignell, S. M., Vorster, A. G., Lawrence, R., and Evangelista, P. H. (2017). A survival guide to Landsat preprocessing. *Ecology* 98, 920–932. doi:10.1002/ecy.1730

Zakaria, R., Rosnan, Y., Saidin, S. A., Yahaya, M. H., and Kasawani, I. (2006). "Shoreline detection and changes for Terengganu river mouth from satellite imagery (Landsat 5 and Landsat 7)," in *Universiti Malaysia terengganu (UMT)*.

frontiers | Frontiers in Remote Sensing

TYPE Original Research
PUBLISHED 10 May 2023
DOI 10.3389/frsen.2023.1132208

OPEN ACCESS

EDITED BY
Erin Bunting,
Michigan State University, United States

REVIEWED BY
Kyla Dahlin,
Michigan State University, United States
Tianyu Hu,
Institute of Botany (CAS), China

*CORRESPONDENCE
Lisa Patrick Bentley,
lisa.bentley@sonoma.edu

†PRESENT ADDRESS
Alexander Barajas-Ritchie,
Department of Computer Science,
Oregon State University, Corvallis, OR,
United States

RECEIVED 27 December 2022
ACCEPTED 13 April 2023
PUBLISHED 10 May 2023

CITATION
Krause P, Forbes B, Barajas-Ritchie A, Clark M, Disney M, Wilkes P and Bentley LP (2023), Using terrestrial laser scanning to evaluate non-destructive aboveground biomass allometries in diverse Northern California forests. *Front. Remote Sens.* 4:1132208. doi: 10.3389/frsen.2023.1132208

Using terrestrial laser scanning to evaluate non-destructive aboveground biomass allometries in diverse Northern California forests

Paris Krause[1], Brieanne Forbes[1], Alexander Barajas-Ritchie[1†], Matthew Clark[2,3], Mathias Disney[4,5], Phil Wilkes[4,5] and Lisa Patrick Bentley[1*]

[1]Department of Biology, Sonoma State University, Rohnert Park, CA, United States, [2]Department of Geography, Environment and Planning, Sonoma State University, Rohnert Park, CA, United States, [3]Center for Interdisciplinary Geospatial Research, Sonoma State University, Rohnert Park, CA, United States, [4]Department of Geography, University College London, London, United Kingdom, [5]NERC National Centre for Earth Observation, University College London, London, United Kingdom

A crucial part of carbon accounting is quantifying a tree's aboveground biomass (AGB) using allometric equations, but species-specific equations are limited because data to inform these equations requires destructive harvesting of many trees which is difficult and time-consuming. Here, we used terrestrial laser scanning (TLS) to non-destructively estimate AGB for 282 trees from 5 species at 3 locations in Northern California using stem and branch volume estimates from quantitative structure models (QSMs) and wood density from the literature. We then compared TLS QSM estimates of AGB with published allometric equations and used TLS-based AGB, diameter at breast height (DBH), and height to derive new species-specific allometric AGB equations for our study species. To validate the use of TLS, we used traditional forestry approaches to collect DBH (n = 550) and height (n = 291) data on individual trees. TLS-based DBH and height were not significantly different from field inventory data (R^2 = 0.98 for DBH, R^2 = 0.95 for height). Across all species, AGB calculated from TLS QSM volumes were approximately 30% greater than AGB estimates using published Forest Service's Forest Inventory and Analysis Program equations, and TLS QSM AGB estimates were 10% greater than AGB calculated with existing equations, although this variation was species-dependent. In particular, TLS AGB estimates for *Quercus agrifolia* and *Sequoia sempervirens* differed the most from AGB estimates calculated using published equations. New allometric equations created using TLS data with DBH and height performed better than equations that only included DBH and matched most closely with AGB estimates generated from QSMs. Our results support the use of TLS as a method to rapidly estimate height, DBH, and AGB of multiple trees at a plot-level when species are identified and wood density is known. In addition, the creation of new TLS-based non-destructive allometric equations for our 5 study species may have important applications and implications for carbon quantification over larger spatial scales, especially since our equations estimated greater AGB than previous approaches.

KEYWORDS

terrestrial laser scanning (TLS), tree aboveground biomass, allometric equations, *Quercus agrifolia*, *Quercus garryana*, *Sequoia sempervirens*, *Pinus ponderosa*, *Abies concolor*

1 Introduction

Globally, forested ecosystems store more carbon both above- and below-ground than any other terrestrial sink, making climate-smart forest management an important strategy to mitigate excess anthropogenic carbon production (Canadell and Schulze, 2014). Unfortunately, the specific drivers that promote long-term carbon storage and improve forest health are often challenging and complicated to identify without accurate data related to the size of trees (Pugh et al., 2018). In addition, traditional forestry-based survey approaches (i.e., hand-measured data or non-remote sensing data) to estimate aboveground size of trees (aboveground biomass, or AGB) may be inaccurate for a large percentage of species due to a lack of availability of destructive harvest data (Burt et al., 2020). In Northern California, an area of high regional species diversity, it is unknown how much error is introduced into AGB estimates when using general equations based on diameter at breast height (DBH) and height data that originate from outside the study area and are not locally calibrated. Due to the increased prevalence of drought and wildfire in Northern California and the need to accurately estimate carbon in trees, there is a need to focus on: 1) improving the quantification of AGB for tree species in this region, and 2) determining if there is a more efficient and accurate method to estimate AGB than traditional approaches based on destructive sampling.

Terrestrial Laser Scanning (TLS), which can measure three-dimensional (3D) structure to millimeter accuracy and precision at plot (e.g., 100–1,000 m^2) scales (Disney et al., 2018), can be a solution to these needs. In forests, TLS has been shown to be more accurate than traditional field methods for sampling forest structure (Hudak et al., 2009; Calders et al., 2015a; Kelly and Di Tommaso, 2015; Liang et al., 2016; de Tanago et al., 2018; Stovall et al., 2018). Although there are relatively few papers related to the use of TLS to estimate AGB (reviewed in Liang et al., 2016), AGB estimates from TLS have been found to strongly correlate with estimates from destructive sampling. Calders et al. (2015a) found that TLS AGB estimates highly correlated with AGB from destructive sampling (R^2 = 0.98), with an overestimation of 9.7%; in contrast, AGB derived from allometric equations had a lower correlation with reference biomass samples (R^2 = 0.68–0.78) and underestimation of 36.6%–29.9%. The study also found AGB error with allometric equations to increase exponentially with increasing DBH, whereas TLS error was DBH independent. Since the detailed 3D data generated from TLS can be rapid, non-destructive, and automated with high precision, TLS data can be used to update general allometric equations or establish specific equations for a geographic region (Liang et al., 2016; Lau et al., 2018; Demol et al., 2022).

To estimate AGB from TLS data, automated algorithms and Quantitative Structure Models (QSMs) are often used (Calders et al., 2015a; Lau et al., 2018; Stovall et al., 2018; Lau et al., 2019; Momo Takoudjou et al., 2018; de Tanago et al., 2018; Malhi et al., 2018; Disney et al., 2020). QSMs are a set of hierarchically structured cylinders that can be fitted to TLS point clouds to estimate the volume of trunk (stem) and branches of the tree, and calculate a total (Raumonen et al., 2013; Calders et al., 2015a; Calders et al., 2015b). Stovall et al. (2018) found that TLS stem volume modeling via QSMs was an appropriate method of non-destructive allometric equation development and reducing uncertainty in tree-level AGB estimates. Similarly, Disney et al. (2020) found QSMs of *Sequoia sempervirens* (redwood) to agree with AGB estimates derived from detailed manual measurements within 2% AGB from values from allometric equations, with no change in regression slope.

In light of the need for non-destructive, accurate estimates of carbon for species specific to Northern California regions, we used TLS to non-destructively estimate AGB for 282 trees from 5 species at 3 locations using stem and branch volume estimates from quantitative structure models (QSMs) and wood density from the literature. We aimed to determine if estimates of AGB calculated using TLS QSM volume or TLS DBH and height would differ from AGB calculated from multiple published allometric equations. We also used TLS measurements to derive new allometric equations for our study species using both DBH and height. We hypothesized that both TLS-based volume AGB estimates and AGB calculated via an individual tree's TLS DBH and height would be greater than AGB calculated from published equations, as TLS is species-specific and directly measures the volume of each individual tree whereas published allometries are often based on a small destructive sample from a singular genus or forest type. Additionally, we predicted that there would be less differences between TLS-based AGB and AGB calculated from existing allometric equations for coniferous species compared to broadleaf species (*Quercus* sp.), as tree shape and biomass distribution is similar across conifers of the size classes in our study areas, and allometric equations often assume tapered, cylindrical growth of a single stem (e.g., conifer growth pattern).

2 Methods

2.1 Study sites

Data were collected from three study sites in northern California, United States: (Figure 1): Pepperwood Preserve (38° 34′ 57.5″ N, 122° 42′ 37.3″ W; Sonoma County), Saddle Mountain Open Space Preserve (38° 30′ 3.3″ N, 122° 37′ 44.6″ W; Sonoma County) and Latour Demonstration State Forest, 40° 38′ 21.5″ N, 121° 43' 26.0" W; Shasta County). At Pepperwood Preserve, the most prominent forest community is oak woodlands. Trees at Pepperwood were selected from multiple plots (20 × 20 m) stratified across topographic gradients along a narrow elevational range (120–460 m) where DBH and height data had already been manually collected in the past year (Evett et al., 2013; Ackerly et al., 2020). Saddle Mountain primarily consists of mixed hardwood and conifer forest, oak woodland, grassland, and chaparral shrublands. Trees at Saddle Mountain were selected from multiple plots (11.3-m radius) along a narrow elevational range (233–549 m) where a suite of forest structure variables were collected simultaneously (Forbes et al., 2020). Latour Demonstration State Forest (LDSF) is located at the southern tip of the Cascade Mountain Range (1,158 m to 2,550 m) and is comprised of many conifer species. Trees at Latour were selected from Continuous Forest Inventory (CFI) plots (11.3-m radius)

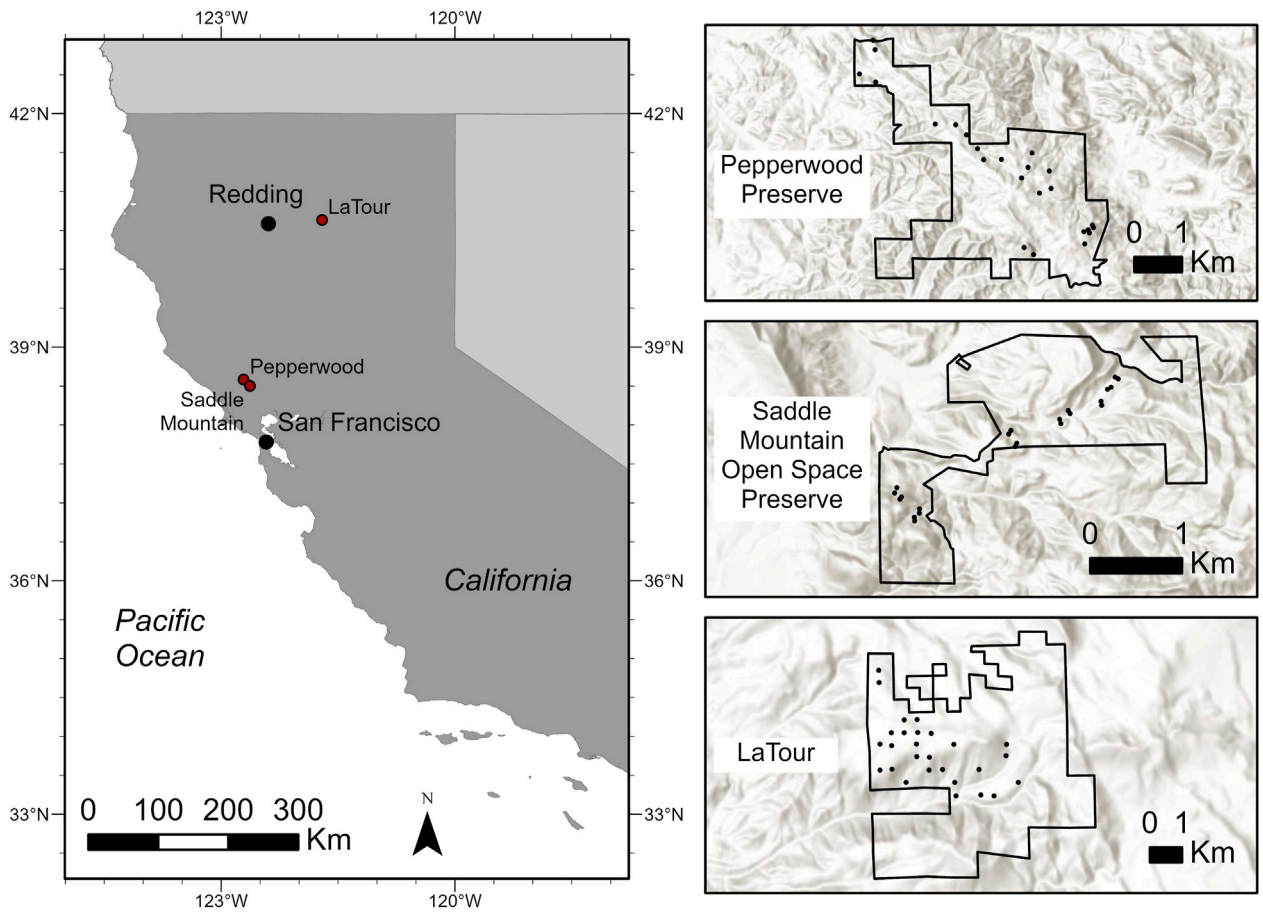

FIGURE 1
Map of the 3 study locations in Northern California (Latour Demonstration State Forest, Pepperwood Preserve, and Saddle Mountain Open Space Preserve) with expanded detail showing the plots (black circles) where trees were selected.

where DBH and height data had already been manually collected in the past year.

2.2 Species selection

Five species (*Quercus agrifolia*, *Q. garryana*, *S. sempervirens*, *Pinus ponderosa*, and *Abies concolor*) were chosen based on both their distribution in the study areas and availability of existing allometric equations. Specifically, each species had to have a minimum of 60 individuals within the surveyed plots across all three study sites to ensure a large enough sample size for allometric equation determination (Stovall et al., 2018). Additionally, *Q. agrifolia* and *Q. garryana* were chosen because there is only one known published species-specific allometric equation for either species (Pillsbury et al., 1984). Redwoods, *S. sempervirens*, were selected because local species-specific allometric equations do exist, based on detailed partial-destructive sampling and crown mapping (Sillett et al., 2019). *S. sempervirens*, *P. ponderosa*, and *A. concolor* were also chosen because they are important timber species, making accurate AGB estimates crucial for foresters. No species was present at all three study sites.

2.3 Field measurements of DBH and height

Data collection included DBH, total tree height, and tree species. For each tree included in this study, DBH was collected at 1.37 m from the base of the uphill side on the trunk to the 10th of a centimeter using a DBH tape for all selected species. To measure the height of each tree, a Laser Technology Impulse 200 LR Rangefinder was used by aiming the laser at eye level on the trunk of the tree, then at the base of the uphill side of the trunk, and at the top of the tallest piece of living or dead tree material. Height was collected for all trees at Pepperwood Preserve and Saddle Mountain, but at LDSF, height was only collected on select trees of interest due to time constraints.

2.4 TLS field measurements and plot-level post-processing

A RIEGL VZ-400i (Horn, Austria) laser scanner was used for all TLS measurements. One 360° vertical and one 360° horizontal scan were collected per scan position by rotating the TLS on a tilt-mount on the scanner surveying tripod to rotate 90° while remaining in its fixed scan position. This scanner has a 1550-

nm wavelength and a 0.35-mrad beam divergence (Wilkes et al., 2017; de Tanago et al., 2018). At all plots, nine scan positions were used on a 10 × 10-m grid to ensure full scan visibility in densely forested plots (Wilkes et al., 2017). Additional details related to TLS field scanning is included in the Supplemental Material and in Forbes et al. (2022).

Co-registration of TLS data was completed in RiSCAN PRO (Riegl, www.riegl.com) where each scan was aligned to a common local coordinate system. First, a coarse registration used voxelized point clouds and an on-board Global Navigation Satellite System (GNSS) to align the scans relative to the first scan position. Then a Multi-Station Adjustment (MSA) (RIEGL Laser Measurement Systems GmbH) performed a fine adjustment where planes fit to the point data were aligned using a least squares approach. Using GNSS, data were transformed to NAD83 (2011)/UTM Zone 10N and geoid 12B for accurate height data. Once registered, the TLS pointcloud of the entire plot was aligned to 2013 airborne LiDAR scanner (ALS) data within RiSCAN PRO to create an accurate digital elevation model (DEM), to better align with ALS and unoccupied aerial system (UAS) data used in other studies at the same field sites (see Forbes et al., 2022; Reilly et al., 2021 for more details). The program Lidar360 (GreenValley International, greenvalleyintl.com) was then used to create a DEM by triangular irregular network (TIN) for each plot and height normalize plot-level TLS data.

2.5 Data analyses

2.5.1 Allometric equations

To estimate AGB, allometric equations were used that have been developed from destructive sampling of relatively small numbers of trees in the same region (≥2.5 cm stem diameter) for a subset of common species. These species-specific equations relate main stem cubic volume via DBH or other diameter type (e.g., above buttress), wood density and height, as well as biomass of additional leaf and branch components (Jenkins et al., 2003; California Air Resources Board, 2014; Chojnacky et al., 2014; Sillett et al., 2019).

Multiple tree allometry protocols were used to calculate AGB for each tree species: 1) U.S. Forest Service's Forest Inventory and Analysis Program (FIA) protocol; 2) Jenkins et al.'s (2003) protocol; 3) Chojnacky et al.'s (2014) protocol; and 4) a local species-specific allometry (if available). For the FIA protocol, volume and AGB of live trees were determined with allometric equations approved by California's Air Resource Board (CARB) for cubic volume and wood density (density of tree bole/stem, bark, and branches) (CARB, 2014). Each species was assigned a specific equation for live volume estimation, using each stem's DBH and height as inputs. The AGB of the tree stems (in kilograms) was calculated as:

$$AGB_{stem} = \left(volume\ ft^3 \times wood\ density\ lb/ft^3\right) \times 0.453592\ kg/lb \quad (1)$$

The CARB FIA protocol species-specific wood densities and specific gravities were used in Eq. 1. Some genera with largely varying wood specific gravities were divided into two different taxa groups. Supplementary Table S1 shows each species within the equation taxa group for Jenkins et al., 2003 and Chojnacky et al., 2014. Additional details related to the specific allometric equations used are included in the Supplemental Material.

2.5.2 TLS data

Using plot-level data, semi-automated segmentation of individual trees from a respective seed point was performed in Lidar360. The profile view of an individual tree was used to manually measure the DBH and height of a single stem, where height was determined by the tallest visual points of the tree. After each tree was segmented and measured, it was manually edited in CloudCompare (www.danielgm.net/cc) to remove extraneous points (Supplemental Figure S1) and processed *via* TLSeparation (v1.3.2; tlseparation.github.io/documentation) to remove the foliage so only wood was remaining.

Tree volume was estimated directly from the segmented and cleaned point cloud of wood-only data using Quantitative Structure Models (QSM) (Raumonen et al., 2013; Calders et al., 2015b; Disney et al., 2018; Lau et al., 2018; Raumonen, 2020). A range of TreeQSM input parameters were tested to optimize QSM outputs. All QSMs were visually compared to the segmented point cloud and any that did not produce visually similar structured models (i.e., large branches missing) were discarded and not used in subsequent analyses. Additional details related to tree segmentation, tree measurements and QSM functions and optimization are included in the Supplemental Materials.

2.5.3 Data comparisons

As general indicators of model accuracy, root mean square error (RMSE) (kg), coefficient of variation root mean square error (CV RMSE) (%), bias (kg), and percent bias (%) were calculated via Eqs 2–5:

$$RMSE = \sqrt{\frac{\sum_{i=1}^{n}\left(\hat{y}_i - y\right)^2}{n}} \quad (2)$$

$$CV\ RMSE = \frac{RMSE}{mean\left(\hat{y}\right)} \times 100 \quad (3)$$

$$Bias = \frac{\sum_{i=1}^{n}\left(\hat{y}_i - y\right)^2}{n} \quad (4)$$

$$\%\ Bias = mean\left(\frac{\hat{y}_i - y}{\hat{y}}\right) \times 100 \quad (5)$$

where, $\hat{y}_i$ is *i*th TLS-derived volume or AGB estimate for an individual tree, y is the allometry-derived value, and n is the sample size (Calders et al., 2015a; Stovall et al., 2018). Bias and RMSE were both represented in the units of their inputs and divided by mean volume or AGB to calculate CV RMSE and percent bias (unitless measures that represent a ratio). This normalized the data to allow for more accurate comparisons due to differences amongst the species, such as sample size and overall tree size. Slope and intercept values of orthogonal regression models between TLS-derived volume or AGB and field-measured values were used to identify departure from the 1:1 line, and the R-squared value was used to evaluate the regression fit (de Tanago et al., 2018; Stovall et al., 2018).

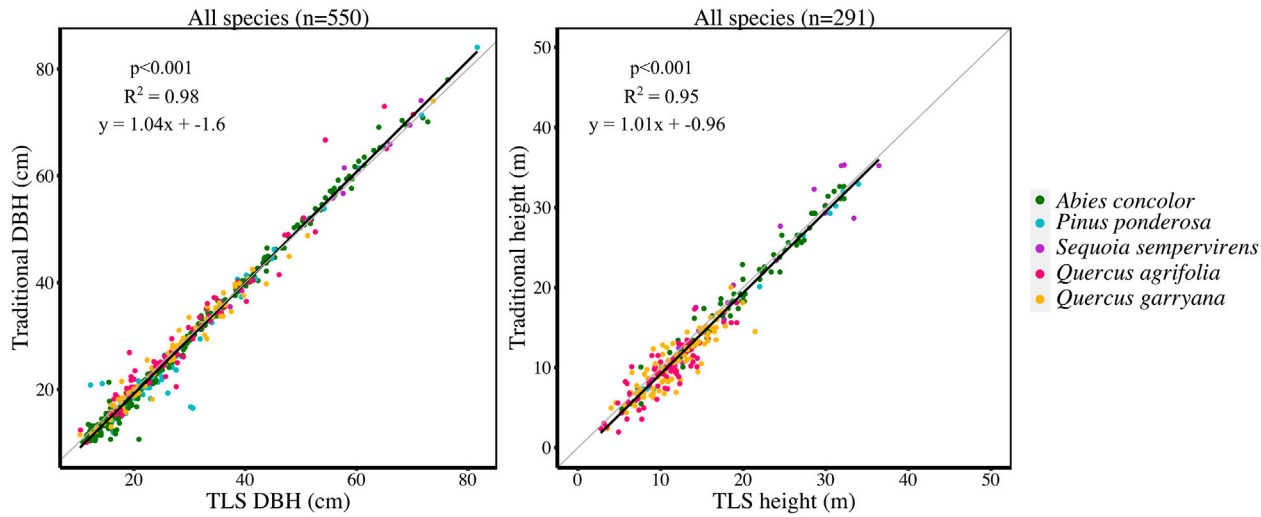

FIGURE 2
(LEFT) Linear regression of traditional DBH (cm) compared to TLS DBH (cm) and (RIGHT) linear regression of traditional height (m) compared to TLS height (m) for each tree measured in the study plots (550 trees for DBH and 291 trees for height; sample sizes are different because traditional height was not measured on all trees).

2.5.4 Updated allometric equations

DBH, height, volume, and AGB were used to derive a DBH and height and a DBH only allometric equations per species (10 equations total). TLS derived allometric equations were computed using a linear regression model, with TLS QSM AGB as the response and TLS DBH and height per species as predictors. The log-transformed ordinary least squares regression method detailed in Stovall et al. (2018) was used to determine the slope coefficient, β_1, and intercept, β_0, with DBH and height H). Specifically, two equation forms were used:

AGB Eq. 1:

$$ln(Biomass) = \beta_0 + \beta_1 ln\ (DBH) \text{ or}$$
$$Biomass = Exp\ (\beta_0 + \beta_1 ln\ (DBH)) \quad (6)$$

AGB Eq. 2:

$$Biomass = \beta_0 + \beta_1 (DBH^2 \times H) \quad (7)$$

All analyses were performed using R Statistical Software (v3.6.2; R Core Team, 2021).

3 Results

3.1 TLS vs inventory data for height and DBH estimation

For 550 trees, DBH ranged from 10.9–76.4 cm. For 291 trees, height ranged from 3.16–38.74 m. Across all species, TLS derived metrics accurately estimated DBH and height when compared to field measured DBH and height (R^2 = 0.98 for DBH, R^2 = 0.95 for height) (Figure 2).

3.2 QSM volume estimates compared to national FIA equations

Successful QSMs were created for 282 trees across 5 species. Across all species, except *P. ponderosa*, AGB calculated from TLS QSM volumes were approximately 30% greater than AGB estimates using published Forest Service's Forest Inventory and Analysis Program (FIA) equations (Figure 3, Supplemental Table S3, Supplemental Table S8). Conifer species (*A. concolor, P. ponderosa, S. sempervirens*) had QSM volumes closer to FIA volumes compared to hardwood species (*Q. agrifolia, Q. garryana*) (Figure 3, Supplemental Table S3, Supplemental Table S8).

3.3 TLS QSM AGB estimates compared to AGB calculated from national allometric equations

TLS derived AGB estimates were compared to AGB calculated using published allometric equations from FIA, Jenkins et al. (2003), Chojnacky et al. (2014), and Sillett et al. (2019; for *S. sempervirens* only) (Figure 4, Supplemental Table S4). In general, comparisons between TLS AGB and AGB calculated from Jenkins et al. (2003) equations had the lowest CV RMSE (36.10%) and bias (1%). Comparisons between TLS AGB and AGB calculated using Chojnacky et al. (2014) and FIA equations had 39.09% and 40.34% CV RMSE and 20% and 11% bias, respectively. For *A. concolor,* when comparing AGB from species-specific published allometries to TLS AGB, FIA equations had the lowest CV RMSE of 31.78%, a bias of 59.41 kg, and percent bias of 12%. For *P. ponderosa*, AGB comparisons between the three equations only differ by 1.23 kg with FIA producing the lowest CV RMSE of

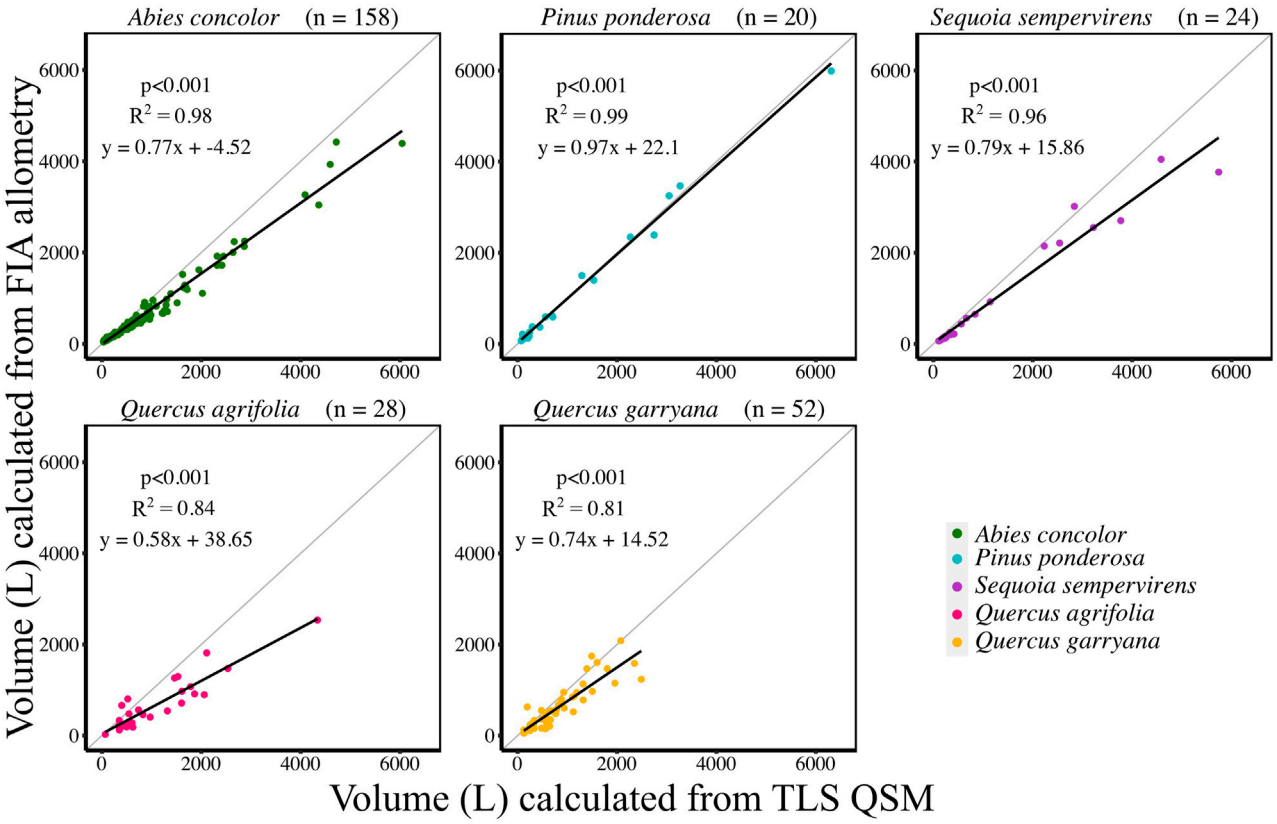

FIGURE 3
Individual tree volume comparison between TLS QSM volumes (L) and FIA volumes (L) by species. Individual tree sample sizes are listed next to species names in parentheses. Grey line indicates 1:1 line.

25.35%. However; Chojnacky et al. (2014) equations had an CV RMSE of 25.62% with a lower bias of 23.49 kg and percent bias of 5% than either FIA or Jenkins et al. (2003); Jenkins et al. (2003) equations comparisons for AGB had the lowest CV RMSE, bias, and percent bias for the other three species, *S. sempervirens*, *Q. agrifolia*, and *Q. garryana* (Supplemental Table S4). Despite Sillett et al. (2019) having updated equations from detailed measurements, comparisons of TLS AGB with AGB calculated using these equations did not produce the lowest CV RMSE for *S. sempervirens*. RMSE only differed between Jenkins et al. (2003) and Sillett et al. (2019) by 2.78 kg, and Sillett et al. (2019) had a much lower bias of 16.53 kg compared to 93.85 kg for Jenkins et al. (2003) for *S. sempervirens*. Both hardwood species, *Q. agrifolia* and *Q. garryana*, had TLS AGB estimates that were most similar to Jenkins et al. (2003) AGB estimates when evaluated with CV RMSE and bias.

3.4 New species-specific allometric equations created from TLS QSM AGB data

New allometric equations were developed for each species using either DBH (Eq. 6), or both DBH and height (Eq. 7) as covariates with TLS QSM AGB. The species-specific equation coefficients, β_0 and β_1, for each equation are reported in Table 1 and visualized in Supplemental Figures S2, 3 The R^2 and CV RMSE values for each species-specific equation demonstrated that the height-DBH equations were a better fit than the DBH only, for all species except *Q. garryana*, where there was no difference in R^2.

3.5 AGB calculated from new TLS species-specific allometries compared to AGB calculated from published allometries and TLS QSMs

AGB calculated from new allometric equations derived from TLS data were compared to FIA, Jenkins et al. (2003), Chojnacky et al. (2014), and Sillett et al. (2019) (*S. sempervirens* only) AGB estimates. AGB estimates created from TLS QSM AGB and DBH (Eq. 6) were more closely correlated (CV RMSE and bias) to AGB estimates using Jenkins et al. (2003) equations for all species (Figure 5, Supplemental Table S5). When comparing equations created with TLS QSM AGB and height and DBH (Eq. 7), Jenkins et al. (2003) AGB estimates were the closest to TLS data for all species except for *A. concolor* and *P. ponderosa*, which had the lowest CV RMSE for AGB calculated using the FIA equations (Figure 6, Supplemental Table S6). TLS AGB (kg) estimated from QSMs compared to TLS AGB estimated from the new allometric equations had slightly greater R^2 for Eq. 6 (DBH^2H) compared to Eq. 7 (DBH) across all species (Figure 7, Supplemental Table S7).

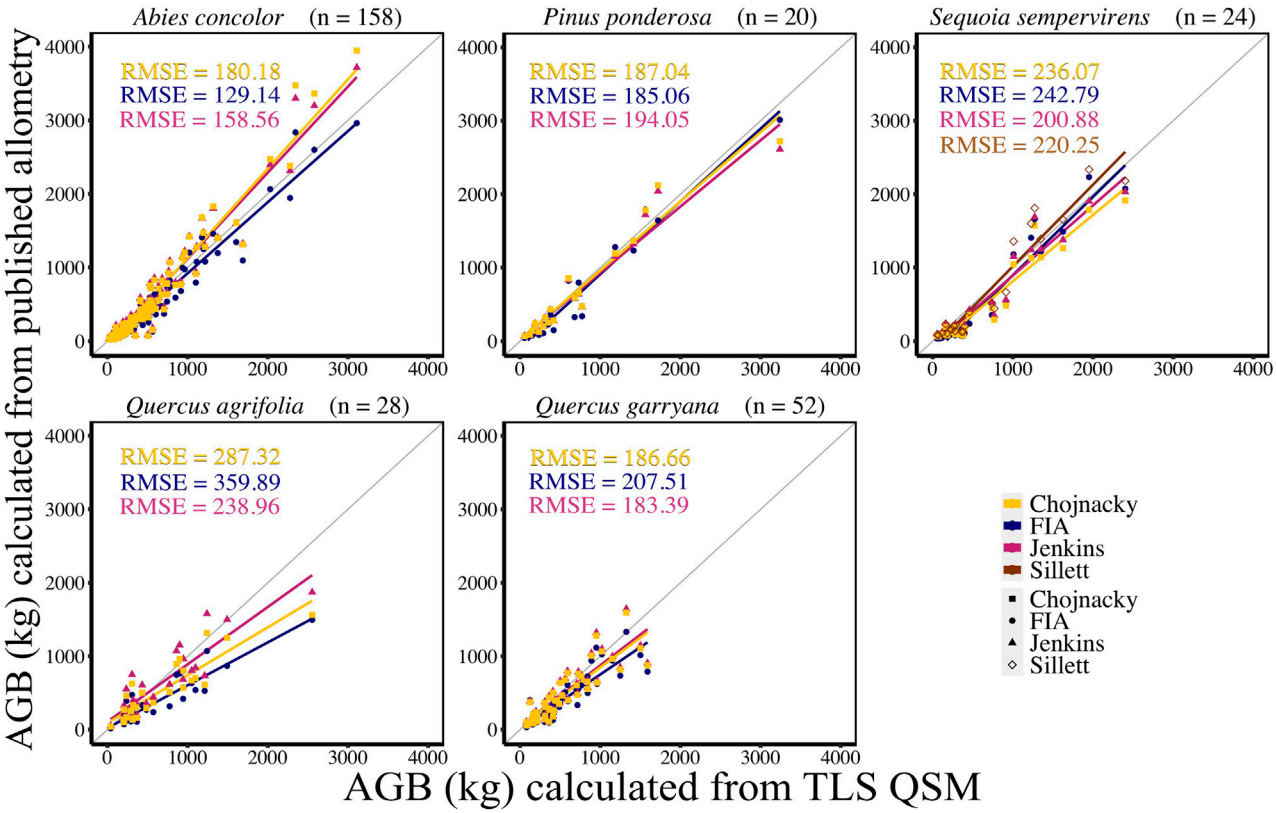

FIGURE 4
Linear regression of FIA, Jenkins et al. (2003), and Chojnacky et al. (2014) and Sillett et al. (2019) individual tree AGB (kg) compared to TLS QSM AGB (kg) for each species. Sillett et al. (2019) is used for *Sequoia sempervirens* only.

TABLE 1 New species-specific allometric equations created from TLS QSM AGB data.

Species by Equation Variable	β_0	β_0 SE	β_1	β_1 SE	R^2	RMSE (kg)	CV RMSE (%)
AGB Equation 1 using DBH: $ln\ (Biomass) = \beta_0 + \beta_1\ ln\ (DBH)$ or $Biomass = Exp\ (\beta_0 + \beta_1\ ln\ (DBH))$							
Abies concolor	−2.09	0.1889	2.35	0.0588	0.91	119.28	29.35
Pinus ponderosa	−1.93	0.4937	2.29	0.1395	0.94	196.95	26.98
Sequoia sempervirens	−0.69	0.6568	1.95	0.1868	0.83	179.22	25.73
Quercus agrifolia	−1.06	0.7638	2.17	0.2283	0.78	270.06	41.43
Quercus garryana	−0.87	0.4700	2.12	0.1459	0.81	177.76	35.43
AGB Equation 2 using DBH^2H: $Biomass = \beta_0 + \beta_1\ (DBH^2 \times H)$							
Abies concolor	85.51	11.0220	168.48	3.1680	0.95	115.21	28.35
Pinus ponderosa	126.08	47.0250	145.78	7.1820	0.96	154.50	21.16
Sequoia sempervirens	209.21	50.1864	108.57	7.0237	0.92	183.13	26.29
Quercus agrifolia	85.12	69.9093	451.56	42.5176	0.81	232.18	35.62
Quercus garryana	96.33	37.7261	383.34	27.2875	0.80	171.93	34.27

4 Discussion

Due to a lack of comprehensive destructive sampling, allometric equations developed for a few species are often applied to many species across large spatial areas (i.e., often outside their domain) which may introduce error into AGB estimates. Further, in order to apply these equations to any forest stand, multiple measurements from individual trees must still be measured in the field via

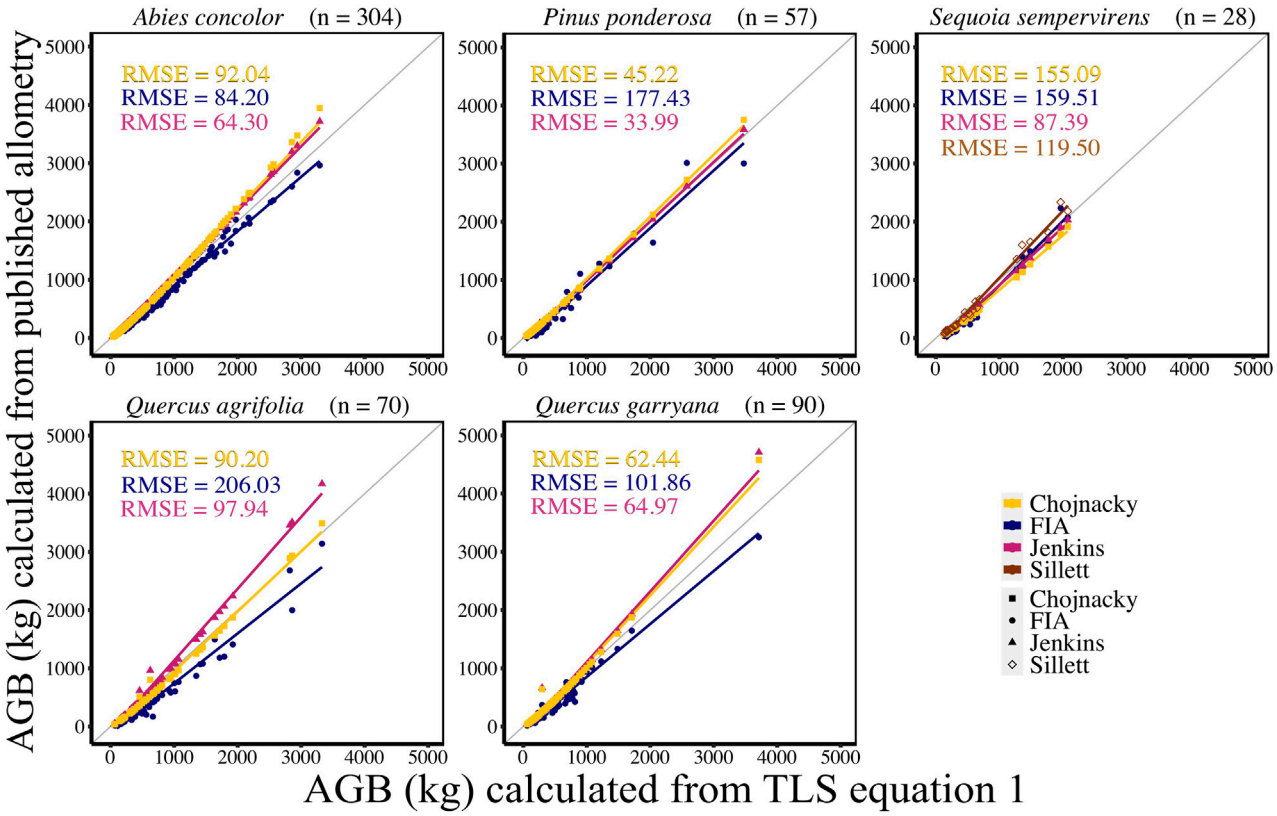

FIGURE 5
New species-specific TLS DBH-based AGB estimates (kg) (AGB Eq. 1) compared to AGB estimated using FIA, Jenkins et al. (2003), Chojnacky et al. (2014) and Sillett et al. (2019) equations for all trees using TLS DBH. Sillett et al. (2019) equations are used for *Sequoia sempervirens* only.

expensive, time-consuming on-the-ground surveys. This study used a relatively rapid, remote sensing approach (TLS) to estimate AGB of 5 tree species in Northern California by calculating and then comparing TLS QSM estimates of AGB with AGB estimated from published allometric equations (FIA, Jenkins et al., 2003; Chojnacky et al., 2014; Sillett et al., 2019). Data from TLS were then used to measure AGB, DBH, and height to create new allometric equations for these species and to compare these new equations, and their resulting AGB, to AGB of published allometric equations and AGB estimated directly from QSMs.

Before estimating AGB, we validated the use of TLS to accurately capture tree dimensions by comparing TLS data to field DBH from a tape measure and height from a laser rangefinder. Similar to other TLS studies which also extracted these measurements and compared them to field measurements (Olofsson et al., 2014; Calders et al., 2015a; Liang et al., 2016; Stovall et al., 2018; Lau et al., 2019), we determined that DBH and height could be accurately measured for the trees sampled here. Importantly, the TLS data processing approach developed for these measurements occurred at the plot-level, indicating that one can easily and semi-automatically extract DBH and height for multiple trees within a plot without individual tree segmentation or QSM processing.

When volume estimates from TLS QSMs were compared to volume estimated with FIA equations (the only allometries that estimate volume directly), all TLS volumes were greater than FIA estimated volumes (20%–86% greater), except for *P. ponderosa* (only 1.6% greater). Also, larger AGB discrepancies between TLS and published FIA volume-based allometries were observed for hardwoods (51%–86%) compared to softwoods (2%–46%). It is possible that these volumes showed large differences because FIA volumes allometries are developed from field-measured DBH and height, whereas the TLS volume measurements are based on TLS measured cylinders that measure the main stem and branches. Since allometric equations often assume tapered cylindrical trunk growth of a single stem and do not incorporate coppice growth with multiple tapering stems and interlocking limbs (e.g., redwood/tanoak forests or oak-woodlands regenerating after fire), species that do not grow strictly following a typical fractal growth pattern are expected to show the greatest deviations (Bentley et al., 2013). In Sonoma County, California, allometric equations to estimate height from DBH were found to overestimate heights for large trees, requiring corrections *via* airborne light detection and ranging (LiDAR) data (Duncanson et al., 2017). These results imply that volume estimates using FIA equations where height is modeled might significantly underestimate actual tree volume, especially for hardwood species.

TLS based estimates of AGB were also greater than AGB estimated from published allometric equations, but on average only 10% greater, with much less variation by species than volume-based FIA estimates. Jenkins et al. (2003) estimated

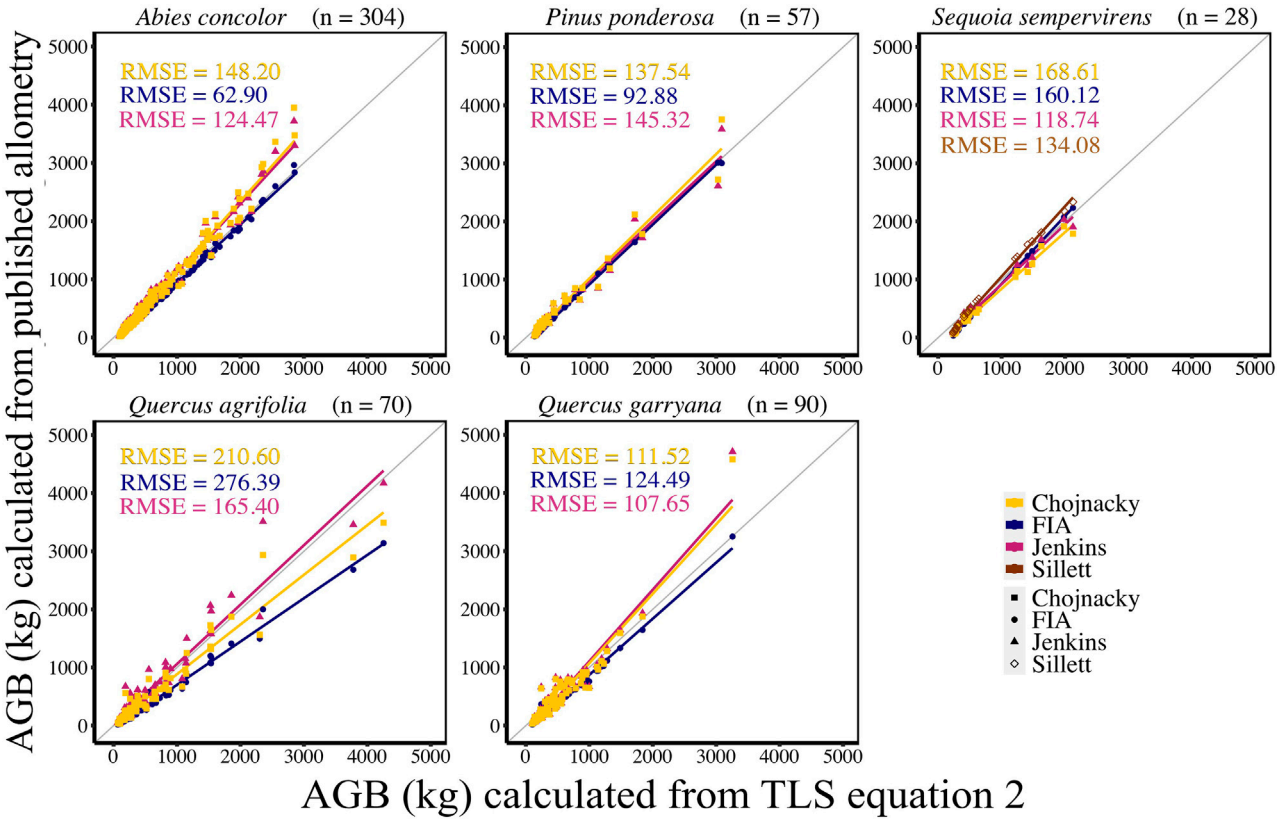

FIGURE 6
New species-specific TLS DBH^2 * height-based AGB estimates (kg) (AGB Eq. 2) compared to AGB estimated using FIA, Jenkins et al. (2003), and Chojnacky et al. (2014) and Sillett et al. (2019) equations with TLS DBH and TLS height. Sillett et al. (2019) equations are used for *Sequoia sempervirens* only.

hardwood AGB were very similar to TLS AGB estimates, perhaps because stem AGB is captured by both estimates and might be the main component of total AGB. Duncanson et al. (2017) also found that Jenkins et al. (2003) and Chojnacky et al. (2014) equations produced AGB estimates that were statistically similar to each other, on a plot- and forest-scale, while FIA equation AGB estimates were 20% less than Jenkins et al. (2003) and Chojnacky et al. (2014) overall. Importantly, the greatest deviations we observed were for *S. sempervirens* (23.5% greater) and *Q. agrifolia* (15.3% greater). Disney et al. (2020) found that AGB for *S. sempervirens* in Sonoma County calculated using TLS was 30% higher than AGB calculated using Jenkins et al. (2003); Chojnacky et al. (2014) equations for large redwoods. Further research (including validation through destructive sampling) should be done to determine if the allometric equations generated for these species differ due to site-specific variation. Local conditions are often ignored when creating allometric equations via destructive sampling, but can greatly influence the morphology and biomass of the tree as trees respond to abiotic and biotic stresses experienced throughout their lifetime (Anderson-Teixeira et al., 2015).

New allometric equations created using TLS data validated the use of TLS to generate new allometric equations, as these equations produce AGB values similar to QSM volume measurements and values using already accepted and published equations. New allometric equations created using TLS data for AGB, DBH and height, performed better than equations that only included TLS AGB and DBH, perhaps because accurate TLS heights were used in these equations. In addition, allometric equations created using TLS data agreed most closely with general Jenkins et al. (2003) equations, rather than FIA equations. This was surprising since FIA equations are the only of the three biomass equation protocols that incorporate height and use California species-specific Q. *agrifolia* and *Q. garryana* equations (Pillsbury et al., 1984). Possibly, the close agreement of our data with Jenkins et al. (2003) equations and not FIA equations is due to the variety in tree form due to regional biotic and abiotic factors that can be better quantified by more general equations. Can general allometries in a region be used across species without species-specific information? Equation development for Jenkins et al. (2003) and Chojnacky et al. (2014) compiles thousands of equations for over 100 species. While the varying levels of agreement among TLS AGB and published allometric AGB is most likely due to differences in species form, forest density, or destructive sampling/published equations inaccuracies, it is possible that these differences may not matter as much as previously believed. Nevertheless, there is an assumption that wood densities are consistent within a species, and even within an individual. This might not be entirely realistic due to wood density differences between heartwood and sapwood, or branches vs bole (Sillett

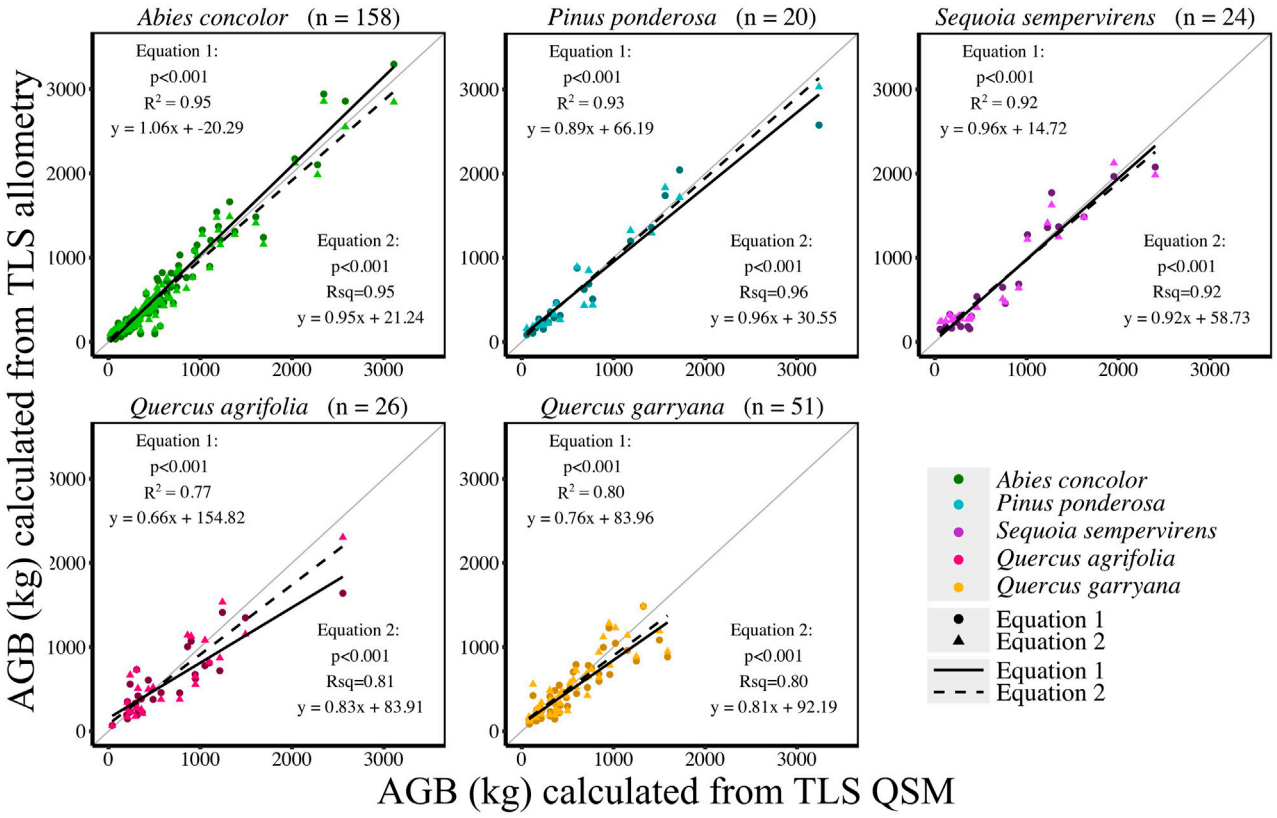

FIGURE 7
TLS AGB (kg) compared to TLS allometric equation derived AGB (kg) using AGB Eq. 1 (DBH only) and AGB Eq. 2 (DBH and Height).

et al., 2019) and should be verified with field measurements for future model development and testing.

It is also possible that closer agreement between TLS AGB and AGB estimates from Jenkins et al. (2003) equations are due to the fact that our analysis did not include tree size as an interaction term. Other studies comparing TLS derived AGB to AGB calculated from published allometries often examine the effect of tree size (DBH, height) on the success of the QSM and may even generate distinct allometric equations from TLS data based on size (Lau et al., 2018; Stovall et al., 2018; Lau et al., 2019). While we did not have a large enough range of tree sizes to perform this analysis, larger individual trees in this study did tend to deviate farther from the 1:1 line than smaller individuals as in Disney et al. (2020). It is possible that larger (older) trees have more complex branching architecture and bigger contribution of branches to biomass, not captured as easily by a regression allometry based on DBH and height. It is important that future work should focus on comparing the effect of tree size, such as height or DBH, on TLS based allometric equations using these data.

In addition, future work related to estimation of AGB using TLS data should focus on QSM optimization improvement. While optimizing QSMs for tree size, QSMs failed consistently for individual trees without clear point clouds due to close proximity to the TLS instrument in the field or dense foliage in the understory. These study sites were in predominantly evergreen forests during leaf-on conditions for deciduous species, which most likely increased occlusion compared to less dense forests. These issues with QSM generation suggest that future work should experiment with different algorithms for fitting volume to TLS point clouds rather than TreeQSM. Other methods such as convex hull (Stovall et al., 2017) and complex primitives (Åkerblom et al., 2015) are currently being explored with promising results as an alternative to TreeQSM (Calders et al., 2020). Lastly, development of improved automation of tree extraction and leaf-separation techniques would greatly improve the feasibility of TLS over broader spatial scales (Vicari et al., 2019; Moorthy et al., 2020).

We recognize that TLS may not be necessary at a local spatial scale or in regions with low stand density (i.e., few trees) to measure AGB due to the time needed to process TLS data being greater than the time to complete field measurements. Nevertheless, this work supports the use of TLS for non-destructive AGB estimation and allometric equation derivation, which is incredibly useful for species that do not yet have species-specific or local equations, because destructive sampling is challenging or impossible due to protection from local or federal law. While Duncanson et al. (2017) and Disney et al. (2020) both evaluated LiDAR derived AGB in Sonoma County, in similar regions where *S. sempervirens*, *Q. agrifolia*, and *Q. garryana* data were collected for this study, there are no known studies which specifically evaluate allometric equations for AGB of *Q. agrifolia, Q. garryana*, or other hardwood species in California, with or without TLS (Pillsbury et al., 1984), until now.

Lastly, TLS may offer a uniform, cost effective, and precise method to collect DBH and height or estimate AGB on broader

spatial scales or in regions with high stand density, where traditional methods and access are laborious, but species are identified and appropriate wood density values are known. Importantly, since we found that current traditional approaches for estimating AGB for well-studied species produce values that are up to 85% less than TLS AGB estimates, the implications for calculating AGB for regional carbon budgets using TLS are large. Once height-based and/or regional allometric equations can be evaluated, validated or improved for a larger number of species across California, TLS has the potential to supplement airborne or spaceborne LiDAR biomass estimates for rapid, regional-scale, or global applications (Silva et al., 2021).

Data availability statement

The datasets presented in this study can be found in online repositories. The names of the repository/repositories and accession number(s) can be found below: https://doi.org/10.5061/dryad.b5mkkwhhware.

Author contributions

PK—Conceptualization, Data curation, Formal Analysis, Funding Acquisition, Investigation, Methodology, Resources, Software, Visualization, Writing—original draft. BF—Data curation, Formal Analysis, Funding Acquisition, Investigation, Methodology, Resources, Software, Visualization, Writing—review and editing. AB-R—Data curation, Funding Acquisition, Investigation, Methodology, Software. MC—Funding acquisition, Investigation, Software, Writing—review and editing. MD—Funding acquisition, Investigation, Writing—review and editing. PW—Investigation, Writing—review and editing. LB—Conceptualization, Data curation, Funding Acquisition, Investigation, Methodology, Project administration, Resources, Supervision, Validation, Visualization, Writing—original draft.

Funding

This research was funded by CAL FIRE Forest Health and Forest Legacy Program (8GG18806) and California State University Agricultural Research Institute (20-01-106) grants to LB and MC, a Joint Fire Science Program Graduate Research Innovation Grant (20-1-01-20) to BF and LB, a Save the Redwoods League grant to AB-R and LB, and SSU RSCA funding to LB. MD and PW received capital funding from NERC via UCL Geography and NCEO.

Acknowledgments

This project would not have been possible without the hard work and dedication of the undergraduate and graduate students in the Bentley Lab at Sonoma State University who assisted with data processing including: Sarah Arroyo-Chavez, Jolene Markarian, Lauren Webster, Lauryn Calderon, Kristi Faro, Renzo Grimaldi, Karishma Patel, Zane Cooper, and Alanna Post. We are grateful to Sean Place and Nicole Molinari for their conceptual guidance and thoughtful comments on the manuscript and to Sean Reilly for his assistance with programming allometric equations and their interpretation. We additionally thank the Sonoma County Agricultural Preservation and Open Space District, Pepperwood Preserve, Latour DSF and David Ackerly for granting us access to their sites and facilitating our research data collection. We especially appreciate Jason Poburko at CALFIRE for arranging site access and data sharing.

Conflict of interest

The authors declare that the research was conducted in the absence of any commercial or financial relationships that could be construed as a potential conflict of interest.

Publisher's note

All claims expressed in this article are solely those of the authors and do not necessarily represent those of their affiliated organizations, or those of the publisher, the editors and the reviewers. Any product that may be evaluated in this article, or claim that may be made by its manufacturer, is not guaranteed or endorsed by the publisher.

Supplementary material

The Supplementary Material for this article can be found online at: https://www.frontiersin.org/articles/10.3389/frsen.2023.1132208/full#supplementary-material

References

Ackerly, D. D., Kling, M. M., Clark, M. L., Papper, P., Oldfather, M. F., Flint, A. L., et al. (2020). Topoclimates, refugia, and biotic responses to climate change. *Front Ecol Environ.* 18 (5), 288–297.

Åkerblom, M., Raumonen, P., Kaasalainen, M., and Casella, E. (2015). Analysis of geometric primitives in quantitative structure models of tree stems. *Remote Sens.* 7 (4), 4581–4603. doi:10.3390/rs70404581

Anderson-Teixeira, K. J., Mcgarvey, J. C., Muller-Landau, H. C., Park, J. Y., Gonzalez-Akre, E. B., Herrmann, V., et al. (2015). Size-related scaling of tree form and function in a mixed-age forest. *Funct. Ecol.* 29 (12), 1587–1602. doi:10.1111/1365-2435.12470

Bentley, L. P., Stegen, J. C., Savage, V. M., Smith, D. D., von Allmen, E. I., Sperry, J. S., et al. (2013). An empirical assessment of tree branching networks and implications for plant allometric scaling models. *Ecol. Lett.* 16 (8), 1069–1078. doi:10.1111/ele.12127

Burt, A., Calders, K., Cuni-Sanchez, A., Gómez-Dans, J., Lewis, P., Lewis, S. L., et al. (2020). Assessment of bias in pan-tropical biomass predictions. *Front. For. Glob. Change* 3. doi:10.3389/ffgc.2020.00012

Calders, K., Newnham, G., Burt, A., Murphy, S., Raumonen, P., Herold, M., et al. (2015a). Nondestructive estimates of above-ground biomass using terrestrial laser scanning. *Methods Ecol. Evol.* 6 (2), 198–208. doi:10.1111/2041-210X.12301

Calders, K., Newnham, G. J., Armston, J. D., Disney, M. I., Schaaf, C. B., and Paynter, I. (2015b). "Terrestrial LIDAR for forest monitoring. A sourcebook of methods and procedures for monitoring and reporting anthropogenic greenhouse gas emissions and removals associated with deforestation, gains and losses of carbon stocks in forests remaining forests, and forestation," in *GOFC-GOLD land cover project office* (Netherlands: Wageningen University). (Gofc-gold ed.).

Calders, K., Adams, J., Armston, J., Bartholomeus, H., Bauwens, S., Bentley, L. P., et al. (2020). Terrestrial laser scanning in forest ecology: expanding the horizon. *Remote Sens Environ.* 251, 112102.

California Air Resources Board (CARB) (2014). *Compliance offset protocol*. U.S. Forest Offset Protocol.

Canadell, J. G., and Schulze, E. D. (2014). Global potential of biospheric carbon management for climate mitigation. *Nat. Commun.* 5, 5282. doi:10.1038/ncomms6282

Chojnacky, D. C., Heath, L. S., and Jenkins, J. C. (2014). Updated generalized biomass equations for North American tree species. *Forestry* 87 (1), 129–151. doi:10.1093/forestry/cpt053

de Tanago, J. G., Lau, A., Bartholomeus, H., Herold, M., Avitabile, V., Raumonen, P., et al. (2018). Estimation of above-ground biomass of large tropical trees with terrestrial LiDAR. *Methods Ecol. Evol.* 9 (2), 223–234. doi:10.1111/2041-210X.12904

Demol, M., Verbeeck, H., Gielen, B., Armston, J., Burt, A., Disney, M. I., et al. (2022). *Estimating forest aboveground biomass with terrestrial laser scanning: Current status and future directions*. Methods in Ecology and Evolution, 13 (8), 1628–1639. Available at: https://besjournals.onlinelibrary.wiley.com/doi/full/10.1111/2041-210X.13906.

Disney, M., Burt, A., Wilkes, P., Armston, J., and Duncanson, L. (2020). New 3D measurements of large redwood trees for biomass and structure. *Sci. Rep.* 10 (1), 16721. doi:10.1038/s41598-020-73733-6

Disney, M. I., Vicari, M. B., Burt, A., Calders, K., Lewis, S. L., Raumonen, P., et al. (2018). Weighing trees with lasers: Advances, challenges and opportunities. *Interface Focus* 8 (2), 20170048. doi:10.1098/rsfs.2017.0048

Duncanson, L., Huang, W., Johnson, K., Swatantran, A., McRoberts, R. E., and Dubayah, R. (2017). Implications of allometric model selection for county-level biomass mapping. *Carbon Balance Manag.* 12 (1), 18. doi:10.1186/s13021-017-0086-9

Evett, R. R., Arthur Dawson, and James, W. B. (2013). Estimating vegetation reference conditions by combining historical source analysis and soil phytolith analysis at Pepperwood Preserve, northern California Coast Ranges, United States. *Restor. Ecol.* 21 (4), 464–473.

Forbes, B., Reilly, S., Clark, M., Ferrell, R., Kelly, A., Krause, P., et al. (2022). Comparing Remote Sensing and Field-Based Approaches to Estimate Ladder Fuels and Predict Wildfire Burn Severity. *Front. for. glob. change.* 5.

Hudak, A. T., Evans, J. S., and Stuart Smith, A. M. (2009). LiDAR utility for natural Resource managers. *Remote Sens.* 1 (4), 934–951. doi:10.3390/rs1040934

Jenkins, J. C., Chojnacky, D. C., Heath, L. S., and Birdsey, R. A. (2003). National scale biomass estimators for United States tree species. *For. Sci.* (49), 12–35.

Kelly, M., and Di Tommaso, S. (2015). Mapping forests with Lidar provides flexible, accurate data with many uses. *Calif. Agric.* 69 (1), 14–20. doi:10.3733/ca.v069n01p14

Lau, A., Bentley, L. P., Martius, C., Shenkin, A., Bartholomeus, H., Raumonen, P., et al. (2018). Quantifying branch architecture of tropical trees using terrestrial LiDAR and 3D modelling. *Trees - Struct. Funct.* 32 (5), 1219–1231. doi:10.1007/s00468-018-1704-1

Lau, A., Calders, K., Bartholomeus, H., Martius, C., Raumonen, P., Herold, M., et al. (2019). Tree biomass equations from terrestrial LiDAR: A case study in Guyana. *Forests* 10 (6), 527. doi:10.3390/f10060527

Liang, X., Kankare, V., Hyyppä, J., Wang, Y., Kukko, A., Haggrén, H., et al. (2016). Terrestrial laser scanning in forest inventories. *ISPRS J. Photogrammetry Remote Sens.* 115, 63–77. doi:10.1016/j.isprsjprs.2016.01.006

Malhi, Y., Jackson, T., Patrick Bentley, L., Lau, A., Shenkin, A., Herold, M., et al. (2018). New perspectives on the ecology of tree structure and tree communities through terrestrial laser scanning. *Interface Focus.* 8 (2), 20170052.

Momo Takoudjou, S., Ploton, P., Sonk é, B., Hackenberg, J., Griffon, S., De Coligny, F., et al. (2018). Using terrestrial laser scanning data to estimate large tropical trees biomass and calibrate allometric models: a comparison with traditional destructive approach. *Methods Ecol. Evol.* 9 (4), 905–916.

Moorthy, S. M. K., Calders, K., Vicari, M. B., and Verbeeck, H. (2020). Improved supervised learning-based approach for leaf and wood classification from LiDAR point clouds of forests. *IEEE Trans. Geoscience Remote Sens.* 58 (5), 3057–3070. doi:10.1109/TGRS.2019.2947198

Olofsson, K., Holmgren, J., and Olsson, H. (2014). Tree stem and height measurements using terrestrial laser scanning and the RANSAC algorithm. *Remote Sens.* 6 (5), 4323–4344. doi:10.3390/rs6054323

Reilly, S., Clark, M. L., Bentley, L. P., Matley, C., Piazza, E., and Oliveras Menor, I. (2021). The potential of multispectral imagery and 3D point clouds from unoccupied aerial systems (UAS) for monitoring forest structure and the impacts of wildfire in mediterranean-climate forests. *Remote Sens.* 13 (19), 3810.

Pillsbury, N. H., and Kirkley, M. L. (1984). *Equations for total, wood, and saw-log volume for thirteen California hardwoods*. U.S. Department of Agriculture, Forest Service, PNW-RN-414. Pacific Northwest Forest and Range Experiment Station. doi:10.2737/PNW-RN-414

Pugh, T. A. M., Jones, C. D., Huntingford, C., Burton, C., Arneth, A., Brovkin, V., et al. (2018). A large committed long-term sink of carbon due to vegetation dynamics. *Earth's futur.* 6 (10), 1413–1432.

R Core Team (2021). *R: A language and environment for statistical computing*. Vienna, Austria: R Foundation for Statistical Computing. Available at: https://www.R-project.org/.

Raumonen, P., Kaasalainen, M., Markku, Å., Kaasalainen, S., Kaartinen, H., Vastaranta, M., et al. (2013). Fast automatic precision tree models from terrestrial laser scanner data. *Remote Sens.* 5 (2), 491–520. doi:10.3390/rs5020491

Raumonen, P. (2020). *TreeQSM quantitative structure models of single trees from laser scanner data instructions for MATLAB-software TreeQSM*. version 2.4.0.

Sillett, S. C., Pelt, R. V., Carroll, A. L., Campbell-Spickler, J., Coonen, E. J., and Iberle, B. (2019). Allometric equations for Sequoia sempervirens in forests of different ages. *For. Ecol. Manag.* 433, 349–363. doi:10.1016/j.foreco.2018.11.016

Silva, C. A., Duncanson, L., Hancock, S., Neuenschwander, A., Thomas, N., Hofton, M., et al. (2021). Fusing simulated GEDI, ICESat-2 and NISAR data for regional aboveground biomass mapping. *Remote Sens. Environ.* 253, 112234. doi:10.1016/j.rse.2020.112234

Stovall, A. E. L., Shugart, H. H., Stovall, A. E. L., Anderson-Teixeira, K. J., and Anderson-Teixeira, K. J. (2018). Assessing terrestrial laser scanning for developing non-destructive biomass allometry. *For. Ecol. Manag.* 427, 217–229. doi:10.1016/j.foreco.2018.06.004

Stovall, A. E. L., Vorster, A. G., Anderson, R. S., Evangelista, P. H., and Shugart, H. H. (2017). Non-destructive aboveground biomass estimation of coniferous trees using terrestrial LiDAR. *Remote Sens. Environ.* 200, 31–42. doi:10.1016/j.rse.2017.08.013

Vicari, M. B., Disney, M., Wilkes, P., Burt, A., Calders, K., and Woodgate, W. (2019). Leaf and wood classification framework for terrestrial LiDAR point clouds. *Methods Ecol. Evol.* 10 (5), 680–694. doi:10.1111/2041-210X.13144

Wilkes, P., Lau, A., Disney, M., Calders, K., Burt, A., de Tanago, J. G., et al. (2017). Data acquisition considerations for Terrestrial Laser Scanning of forest plots. *Remote Sens. Environ.* 196, 140–153. doi:10.1016/j.rse.2017.04.030

frontiers | Frontiers in Remote Sensing

TYPE Original Research
PUBLISHED 16 May 2023
DOI 10.3389/frsen.2023.1099430

OPEN ACCESS

EDITED BY
Jane Southworth,
University of Florida, United States

REVIEWED BY
André Lima,
University of Maryland, College Park, United States
Rogério Negri,
São Paulo State University, Brazil

*CORRESPONDENCE
Pamela Boelter Herrmann,
pamela.herrmann@ufrgs.br

RECEIVED 15 November 2022
ACCEPTED 02 May 2023
PUBLISHED 16 May 2023

CITATION
Herrmann PB, Nascimento VF, Freitas MWDd and Ometto JP (2023), Fire in highland grasslands in the Atlantic Forest Biome, a burned areas time series analysis and its correlation with the legislation.
Front. Remote Sens. 4:1099430.
doi: 10.3389/frsen.2023.1099430

Fire in highland grasslands in the Atlantic Forest Biome, a burned areas time series analysis and its correlation with the legislation

Pamela Boelter Herrmann[1]*, Victor Fernandez Nascimento[2], Marcos Wellausen Dias de Freitas[1] and Jean Pierre Ometto[3]

[1]Remote Sensing Graduate Program, Federal University of Rio Grande do Sul, Porto Alegre, Brazil, [2]Engineering, Modelling, and Applied Social Sciences Center, Federal University of ABC, Santo André, Brazil, [3]Earth System Science Center, National Institute for Space Research, São Jose dos Campos, Brazil

Fire has been an intrinsic ecological component of the ecosystems, affecting the public, economic, and socio-cultural policies of human-nature interactions. Using fire over grassland vegetation is a traditional practice for livestock in the highland grasslands and has economic and environmental consequences that have not yet been understood. A better description of the spatio-temporal biomass burning patterns is needed to analyze the effects of creation and application in these areas. This study used remote sensing techniques based on Sentinel-2 data and machine learning algorithms to identify burning scars and compare them with a national fire collection database for the highland grasslands in the Atlantic Forest Biome in Brazil. The aim is to evaluate public management tools and legislation evolution during the 35 years of the time series analyzed. The results indicated that 12,285 ha of grasslands were converted to other uses, losing about 24% of their original formation, with 10% occurring after banned this practice in 2008. The burned areas classification using the Random Forest algorithm obtained an AUC = 0.9983. Divergences in the burned area's extent and frequency were found between the municipality's authorized license and those classified as burned. On average, only 43% of the burned area in the Parque Estadual do Tainhas and its buffer zone had an environmental permit in the last 5 years. This research's results provide subsidies for revising and creating public policies and consequently help territorial management.

KEYWORDS

fire, grasslands, ΔNBR, GEE, MapBiomas, time series

1 Introduction

Fire activity in Brazil is influenced by several factors, the result of complex and dynamic processes generated by interactions between climatic conditions, vegetation attributes, land use and land cover, dynamics between regeneration, productivity and ignition patterns (Fidelis et al., 2021; Pivello et al., 2021). Brazilian biomes have a long history of fire conflicts, as in the Atlantic Forest Biome (AFB), one of the most critical biodiversity hotspots in the world (Myers et al., 2000).

Currently, the AFB remnants are highly fragmented and restricted to highland grassland areas in southern Brazil, where there are mosaics of Araucaria (Brazilian pine) forests and grasslands linked to a fire events history (Pillar et al., 2009; Meireles and Shepherd, 2015).

In these areas, fire has been an intrinsic ecological component of the ecosystems, affecting the public, economic, social, and even cultural policies of human interactions with nature (Andrade et al., 2015).

In recent years, conflicts related to fire use have presented economic and environmental consequences that have not yet been clearly understood. The fire use on grassland vegetation in the northeastern Rio Grande do Sul (RS) state is a traditional practice for livestock (Carvalho and Andrades-Filho, 2019). However, it was prohibited by Law 9,519/1992 (Rio Grande do Sul, 1992). This has led to natural grassland area changes to simplified land uses, such as agriculture and forestry, leading to biodiversity loss and difficulties in recuperating degraded areas (Buisson et al., 2019). Subsequently, Law 13,931/2012, which amended Law 9,519/1992 (Rio Grande do Sul, 2012), attributes to the municipal government the power to authorize and supervise the use of fire as a grasslands management practice in areas that cannot be mechanized or as a form of phytosanitary treatment.

Therefore, a better description of biomass burning spatio-temporal pattern is needed to analyze the effects of fire legislation. So, the use of remote sensing derived products such as 1) the Modis product MCD64A1—Collection 6, with 500 m resolution at a global scale (Giglio et al., 2018); 2) the MapBiomas Fire—Collection 1, based on Landsat time series, with 30 m resolution for the Brazil territory (Alencar et al., 2022), and 3) the global forest loss by fire product, also at a spatial resolution of 30 m (Tyukavina et al., 2022) are consolidated as an essential data source by covering vast areas with a multitemporal and multispectral information.

In this study, to minimize these products limitations, such as the spatial resolution, we used Sentinel-2 data developed by the European Space Agency (ESA), which has four bands with 10 m, six with 20 m, and three bands with 60 m (ESA, 2022). Therefore, this study's objective is to improve the spatial resolution of burned areas and compare them with the national MapBiomas Fire product to evaluate the fire use legislation over time in the highland grasslands in Atlantic Forest Biome in Brazil.

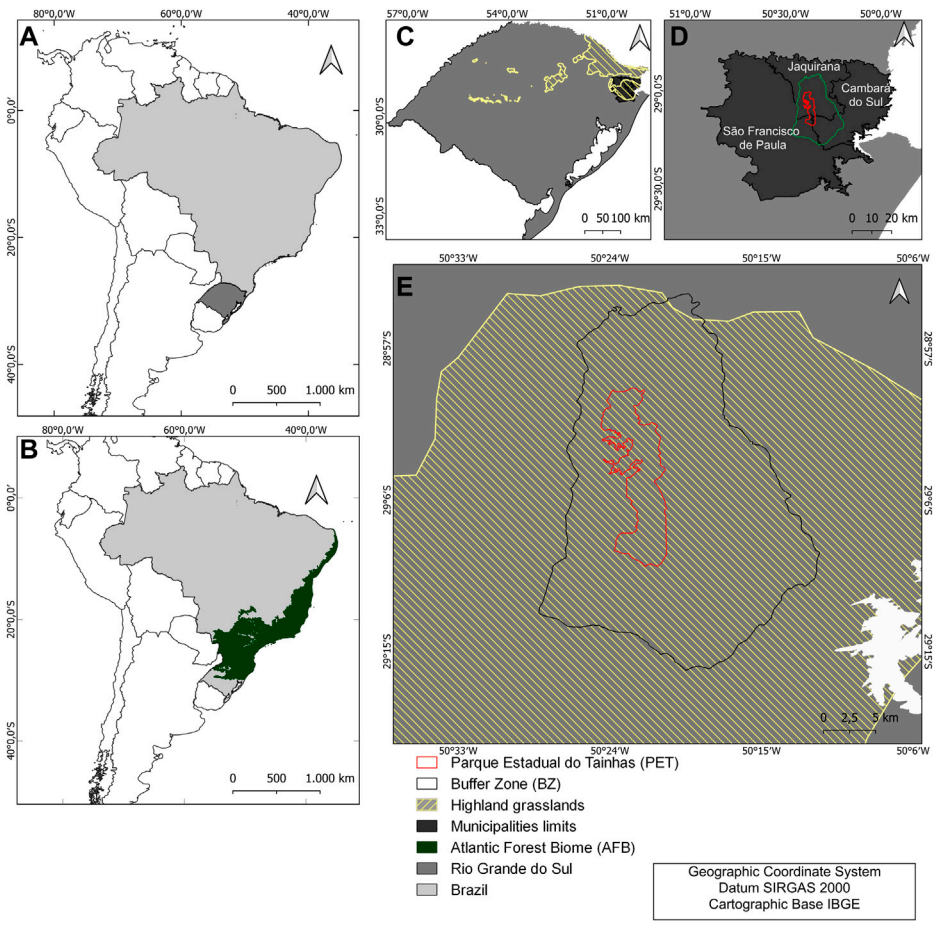

FIGURE 1
(A) Rio Grande do Sul location, **(B)** AFB location, **(C)** Highland grasslands distribution, **(D)** Location of the municipalities that make up PET, **(E)** Location of the PET and its BZ in relation to the highland grasslands.

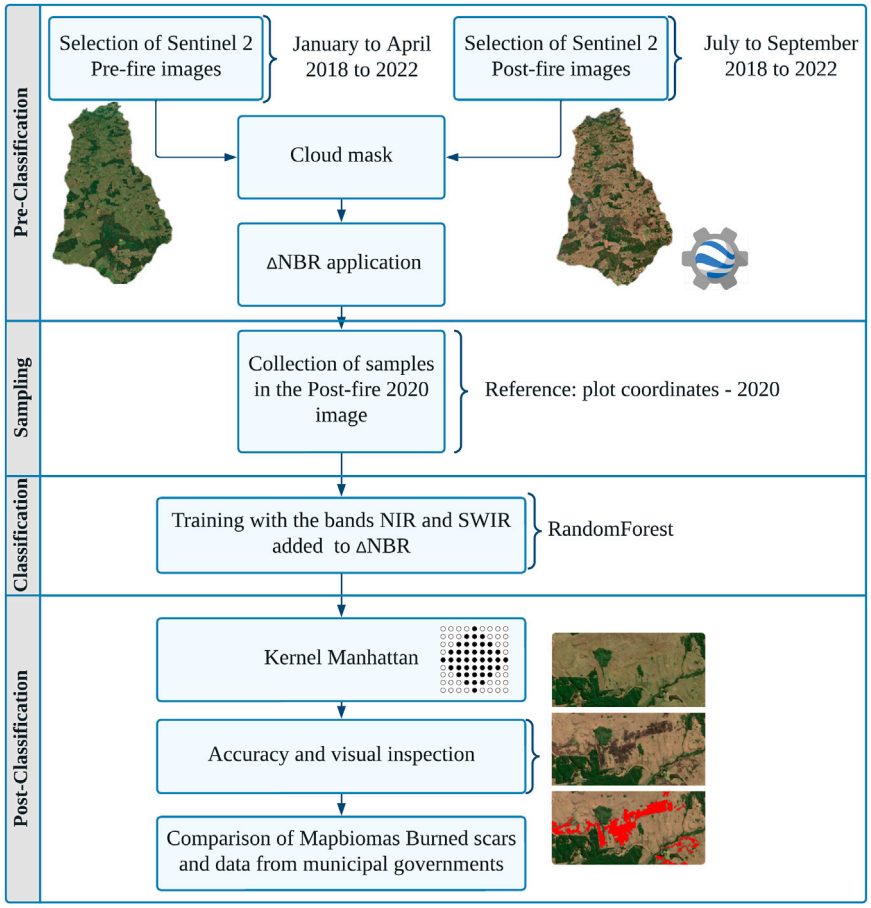

FIGURE 2
Overview of the burned area classification method.

2 Materials and methods

2.1 Study area

This study was conducted in the conservation area denominate Parque Estadual do Tainhas (PET) and its buffer zone (BZ) located at latitude 29°5′15″S and longitude 50°22′4″W (Figure 1). The PET was established in 1975 to protect the grasslands and forests in the Tainhas river valley, inserted in the AFB.

The Park is formed by mosaics of forests with Araucaria pine, grasslands, and flooded areas (wetlands) with flatter terrain in the southern portion to valleys in the northern part (SEMA, 2008). It has an area of 6,654 ha with a BZ of approximately 60,000 ha, covering the municipalities of Jaquirana (69.8%), São Francisco de Paula (20.6%), and Cambará do Sul (9.6%) of the Park's area. Around the PET, communities in its BZ depend on agriculture, forestry, and livestock and regularly use fire as a management tool (Bond-Buckup, 2008).

The PET is close to other protected areas, which favors the emergence of the biogeographic conditions that can contribute to the interconnection of these units through ecological corridors, helping preserve fauna and flora populations and maintain the ecosystem services balance in the region.

2.2 Burned areas classification in highland grasslands (BACHG)

The methodological approach for burned area detection used in this study is shown in the flowchart (Figure 2). We use Sentinel-2 MSI Multispectral Instrument, Level-2A data. The Level-2A product provides Bottom Of Atmosphere (BOA) imagery derived from the associated Level-1C products. The imagery used is available from the Google Earth Engine (GEE). This platform combines three tools (code editor, explorer, and client libraries) for users to perform geospatial analysis in the cloud (Adagbasa, Adelabu, and Okello, 2020). We select images from 2018 to 2022, before the start of the fire season, from January 1 to April 1, denominating as "pre-fire" images, while the post-fire images were selected from July 15 to September 15 of each year, when the "burning window" allowed by municipal legislation was established. A cloud mask was applied. First, the function defines two bitmask values for clouds and cirrus (bit 10 and bit 11, respectively) and selects the image's pixel quality band (QA). Then, the function creates a mask that filters out all the pixels where the cloud and cirrus bits are equal to zero, indicating clear conditions.

We used the GEE to collect spectral signatures of the burned and unburned areas, which served as samples for the model

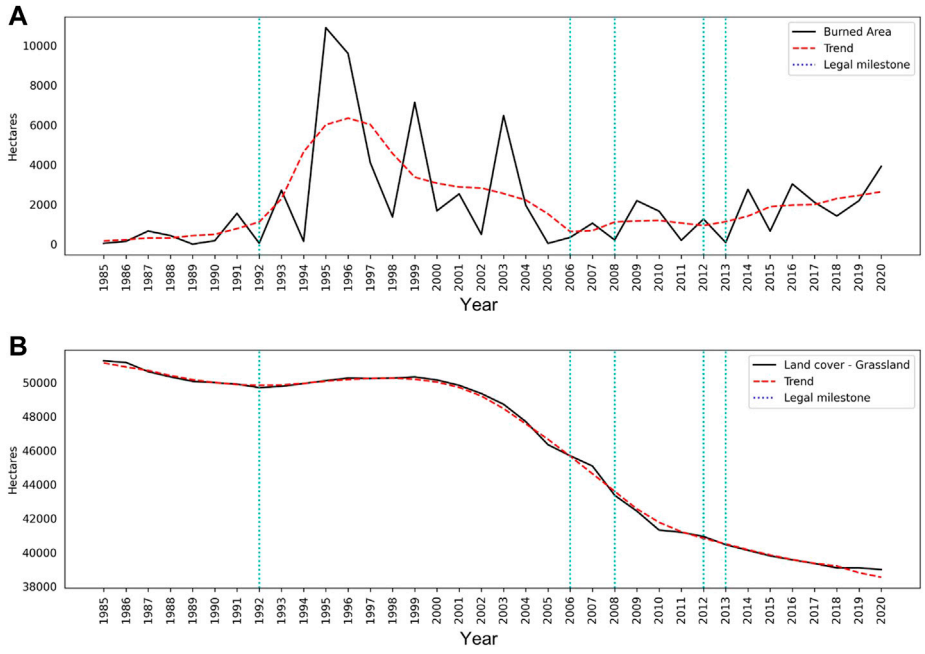

FIGURE 3
(A) Burned area accordingly MapBiomas Fire—Collection 1.0, and **(B)** Grassland accordingly MapBiomas—Collection 7.0, both in the PET and its BZ from 1985–2020.

TABLE 1 Relationship of burnt areas (hectares per year) mapped and permissions of environmental permits.

Legislation	Event	Burned area (ha)	Grasslands (ha)
Law n°9.519/92	Fire use prohibition in the Rio Grande do Sul state	44	49,709
Law n°11.428/2006	Atlantic Forest Biome Law—Prohibits the conversion of grassland to other land uses	339	45,689
Decree n° 6.660/2008	Regulates the provisions of the Atlantic Forest law and defines the legal framework for the conversion of areas	210	43,378
Law n° 13.931/2012	Conditional fire use permission	1,262	40,943
Municipal Law n° 2.954/2013 (Cambará do Sul)	Regulation of fire use licensing by municipal agencies	80	40,464
Municipal Law n° 1.083/2013 (Jaquirana)			
Municipal Law n° 2.924/2013 (São Francisco de Paula)			

classification. In addition, we used data collected from the field in the year 2020 as a reference for sampling in this year's post-fire images. This effort resulted in 7,133 sampled pixels, manually collected as small polygons from burned areas (2,295 sampled pixels) and the unburned regions (4,838 sampled pixels).

For training, we used the shortwave infrared (SWIR) and near-infrared (NIR) bands and the result of the Normalized Burn Ratio spectral index (ΔNBR) calculation.

The NBR is a ratio of the NIR to the SWIR region, developed to identify post-fire burned areas and provide a quantitative measure of burn severity (Key and Benson, 2006). The NBR is calculated by the pre- and post-fire difference (denoted as ΔNBR) using Eqs. 1, 2.

$$NBR = \frac{NIR - SWIR}{NIR + SWIR} \quad (1)$$

$$\Delta NBR = NBR_{pre-fire} - NBR_{pos-fire} \quad (2)$$

The algorithm used for our classification was the Random Forest (RF) (Breiman, 2001; Goehry et al., 2021), which is an ensemble algorithm operated by building multiple decision trees in a training session and assigning the target class by majority vote (PAL, 2005). In this study, we used the RandomForest function in the GEE library. The parameters used were: number0fTrees (20), variablesPerSplit (null), minLeafPopulation (1), bagFraction (0.5), maxNodes (null), and seed (0). After classification, we applied a spatial filter to remove noise and fill

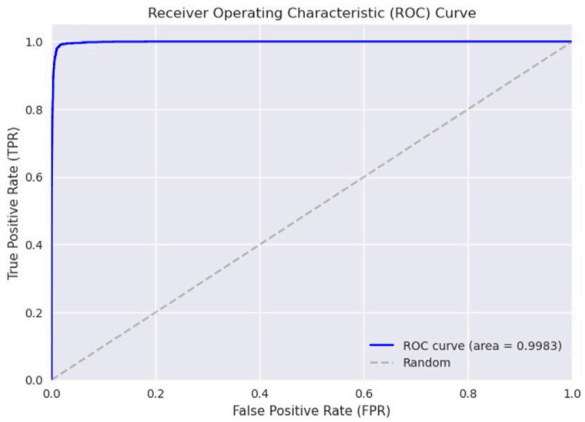

FIGURE 4
ROC curve.

in gaps, where burned areas smaller than or equal to 1 ha (5 × 5 pixels) were removed, and, in the same way, internal spaces were filled as burned. The spatial filter selected was the Manhattan Kernel, which generates a distance kernel based on rectilinear distance (city-block). Reduction is performed by calculating the mode (most common value) of the pixel values in a neighborhood defined by the specified kernel (or window). The filter size was determined considering the difference in the spatial resolution of the Landsat 8 satellite, which was used for the MAPBIOMAS product methodology proposed for exclusion. Finally, the Receiver Operating Characteristic (ROC curve) was calculated to measure and compare the binary classification model's performance.

2.3 Temporal analysis of burned areas

To evaluate the management tools available in conjunction with the classification data generated, we used data on the annual area

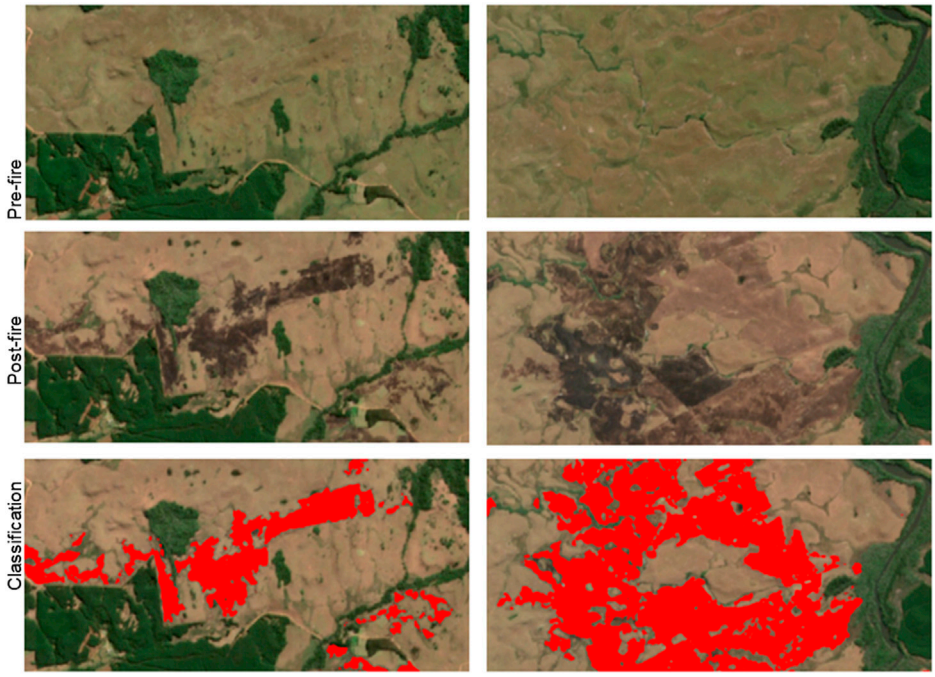

FIGURE 5
Examples of burned area classification using RF.

TABLE 2 Comparison of burned areas (ha) authorized by the municipality between mapped by mapbiomas and BACHG.

	2018	2019	2020	2021	2022
Mapbiomas	1,417	2,189	3,909	-	-
BACHG	5,380	7,373	7,859	2,813	4,681
Match pixels BACHG and Mapbiomas	772	1,132	2,616	-	-
Municipalities	2,587	2,479	1,851	1,953	2,038

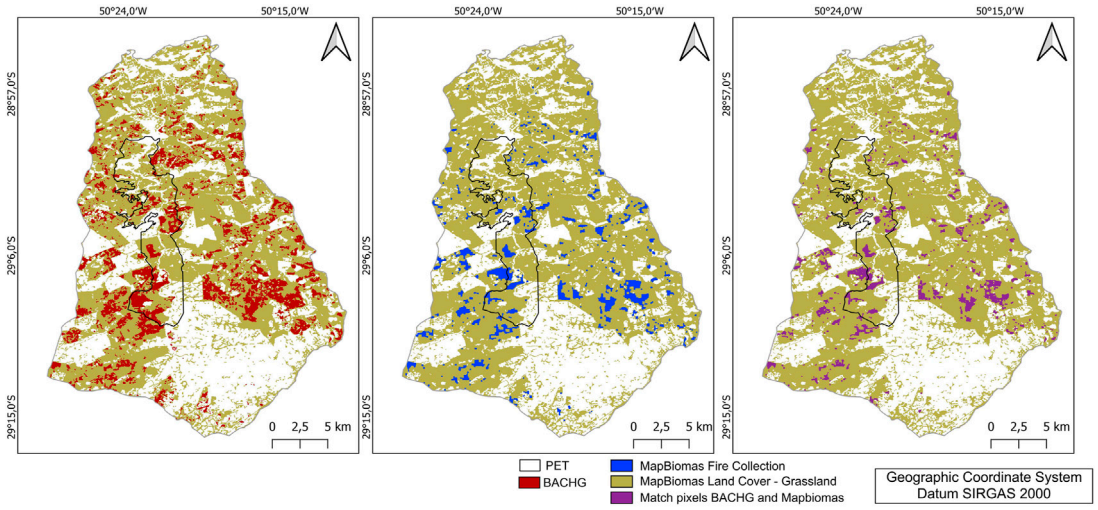

FIGURE 6
Representation of the comparison of classified areas in both methods for 2020.

burned by MapBiomas Fire—Collection 1.0 (Alencar et al., 2022) and the land use and land cover areas classified as grassland from 1985 to 2020 available in MapBiomas Collection 7.0 (Souza et al., 2020). In addition, we also used the extent area authorized for burning by Jaquirana, São Francisco de Paula, and Cambará do Sul municipalities located within PET and its BZ.

The annual burned areas stationarity trend covered by grassland was checked using the Augmented Dickey-Fuller (ADF) test. The ADF test is an "augmented" version of the Dicker-Fuller test. The ADF test expands the test equation to include high-order regression processes in the model.

Afterward, the trend was verified through time series decomposition to verify the seasonality and the residuals. Results are obtained by first estimating the trend by applying a convolution filter to the data. Therefore, the trend is removed from the series, and the average of this unbiased series for each period is the seasonal component returned (McKinney, Perktold and Seabold, 2011).

3 Results

3.1 Reconstructing the history of fire use

The burnt areas and the grasslands from 1985 to 2020 in the PET and its BZ are shown in (Figure 3). In this figure is highlighted in vertical dotted lines, the primary legislation, which is also presented in (Table 1) together with the grasslands and the total burned area values. This analysis reveals an increasing trend for the burned area, while there is a decreasing trend for grassland in the PET.

We can observe that the burnt areas remained low after the fire use prohibition in 1992. However, this pattern was not established for a long time, and the highest values for the time series analyzed occurred in 1995 and 1996, with about ten thousand hectares burnt each year.

The most significant burned areas reduction occurred in 2002, reaching the lowest value in 2005, with only 35 ha. By observing the trend curves of burnt area and area occupied by grassland formation, the curve's decline in the same years is noticed.

In 2002, the area corresponding to grassland was 49,359 ha, while in 2005, it was 46,345 ha. Therefore, the PET and its BZ lost more than 3,000 ha in only 3 years. These years precede the AFB Law creation (Brasil, 2006) and its regulation decree (Brasil, 2008), prohibiting new conversions of areas with native vegetation in the biome.

During the 35 years of the analyzed time series, 12.285 ha of grassland areas were converted to other uses, losing about 24% of their original formation, with 10% occurring after the AFB decree banned this practice in 2008 (Brasil, 2008).

Finally, concerning the burned areas only when municipalities begin to legislate about the use of fire, in 2013, a trend definition and a biannual frequency can be observed, as provided by several municipal legislation (Municipio de Cambará do Sul, 2013; Municipio de Jaquirana, 2013; Municipio de São Francisco de Paula, 2013).

3.2 Burned area and frequency of occurrence

The burned areas classification with the RF algorithm obtained an AUC = 0.9983 (Figure 4). With a visual inspection, the scar's demarcation can be identified when comparing the pre-fire and post-fire images (Figure 5).

The results show that larger areas were burned for all years than those allowed by the municipalities' environmental permits. In addition, larger burned areas were found in our classification than those presented by the MapBiomas Fire collection, as can be seen in (Table 2).

The licenses issued correspond to only 48.09% (2018), 33.62% (2019), 23.55% (2020), 69.43% (2021), and 43.54% (2022) of the area identified as burned in our classification. For the three available years of the analyzed period from the MapBiomas collection, they represent only 26.34% (2018), 29.69% (2019), and 49.74% (2020) of the burned areas.

The Mapbiomas burned areas that coincide with our classification represent only 21% of the total classified area on average (Figure 6). The MapBiomas burned omission areas are

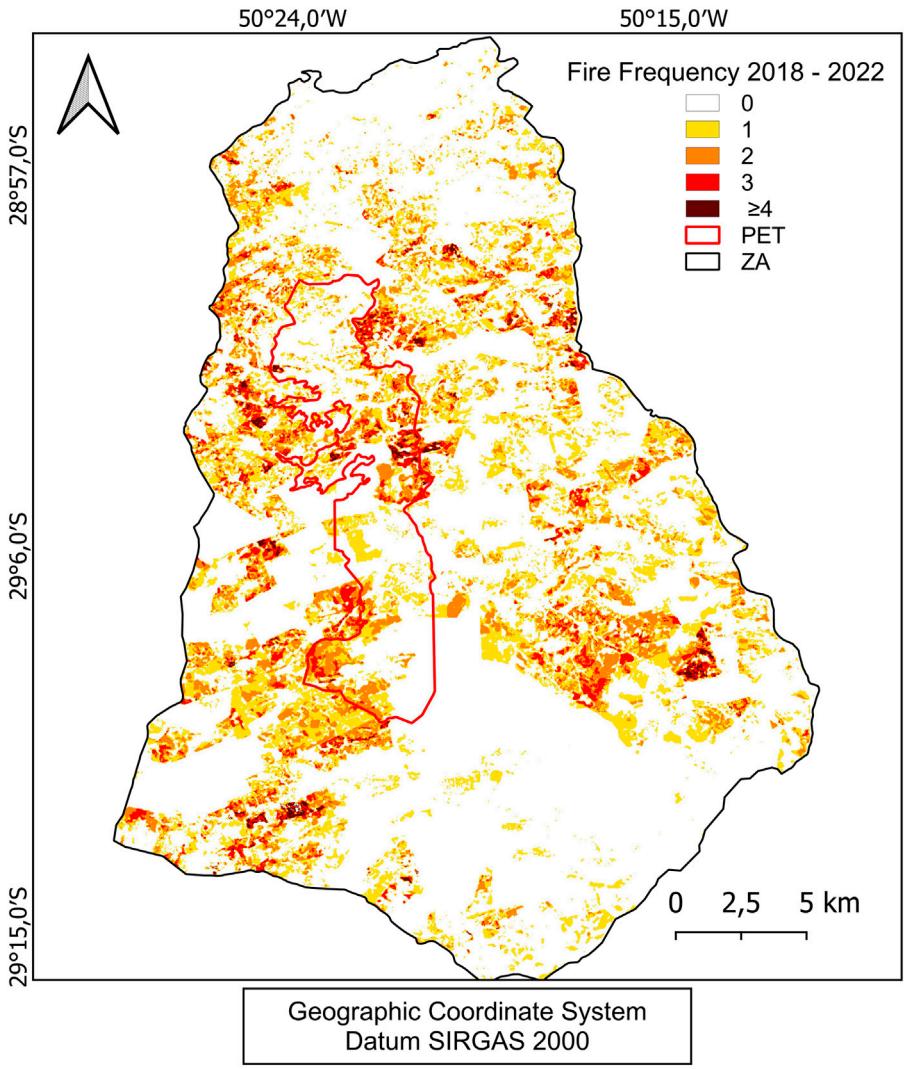

FIGURE 7
Fire frequency in the PET and its BZ.

formed by scars smaller than 10 ha or with sites that present a non-continuous formation with gaps of 1 ha.

In addition to the burning extent, the frequency of areas affected by the fire was verified, and about 28% of the PET and its BZ were burned at least once, as shown in (Figure 7). Notably, according to the legislation, the areas could present a burning frequency of 2–3 times for 5 years. However, the results showed that 353 ha were burned 4 to 5 times, exceeding the legal requirements for this period. These areas are within the Jaquirana municipality territory inside the PET or near its boundaries.

4 Discussion

4.1 Legislation analysis and remote sensing

No stationary trends were found in the time series, even though there is a long history of legislation to regulate fire use and vegetation protection practices.

During the 20 years (1992–2012) of fire use practice prohibition, producers changed their economic profile, and extensive native grassland areas conversion to monocultures in the region occurred (Boziki, Beroldt, Printes, 2011; Buffon, Printes, Andrades-Filho, 2018). Grasslands are important for livestock, especially where other agricultural practices are not viable. In this study, we noticed that legislation changes over the time series are related to changes in land use.

Conservation areas (CAs) in Brazil are managed under the National System of Conservation Units (SNUC), which is designed to protect the country's diverse ecosystems (BRASIL, 2000). The SNUC comprises 12 categories of CAs, each with specific objectives regarding protection and use. The PET falls under the Park category, which provides full protection and allows only non-consumptive uses of natural resources. This means that handling fire is not permitted inside the PET. Conservation areas like the PET are essential for preserving Brazil's rich biodiversity and ensuring the long-term sustainability of the country's natural resources.

The fire management practice in the winter period is expected in the region, and it is used to remove dry biomass to provide the vegetation regrowth that will be used to feed the cattle herd in spring and summer (Pillar et al., 2009).

Once forbidden, it can be replaced by other activities much more environmentally damaging than the old fire management grasslands practice, such as forestry and monocultures, which have been advancing into the grasslands (Buffon, Printes and Andrades-Filho, 2018).

It was observed during the study that municipalities lack data and tools to manage and enforce current environmental legislation. So it is necessary to evaluate the effectiveness of existing environmental management tools regulated by municipal laws related to the use of fire (Santos and Andrades-Filho, 2021).

In addition to the environmental laws presented, it was verified the irregularity in the data availability by the municipalities, which do not meet the legal provisions of free access to information in Brazil, especially regarding publicity, accessibility, and transparency, making technological advancement impossible (Brasil, 2011).

4.2 New burned area classification approach

The brief characteristics of the fire marks left on satellite imagery complicate the burned area's detection. There are few fire products available globally, and only one at the national level (Alencar et al., 2022). So, evaluating its applicability to different regions and vegetation formations in Brazil is extremely important.

Our study found significant differences in areas mapped as burned, increasing by more than 50% in our study using a better spatial resolution. The improvement of available products is substantial and progresses with the recent technologies emergence. In previous studies of Russian grassland, the difference in the area mapped between satellites with lower spatial resolutions also increased dramatically from no burning to as much as 19% of the total study area (Dubinin et al., 2010). The strategy of using ΔNBR in conjunction with the NIR and SWIR bands for burned areas classification reduced noise and class confusion, especially with wetlands. The areas with the highest commission error were exposed soil from recently cleared forestry areas.

Due to the rugged relief and mosaics of forest and mountainous grassland vegetation that form the area's landscape, remote sensing data with higher spatial resolution can be explored as they become available. Therefore, Earth observation can significantly support public fire prescription policies and add to other factors that consider CO^2 emissions (Herrmann, Nascimento and Freitas, 2022).

5 Conclusion

This study uses remote sensing techniques to evaluate legislation related to fire use in highland grasslands in Brazil. Long-term time series and exploring new enhancement methodologies are essential to identify the main impacts of human-induced changes.

Divergences in extent and frequency were found between the burned areas authorized by the municipalities and those classified as burned. On average, only 43% of the burned area in the PET and its BZ was licensed in the last 5 years. The municipal databases had recorded only from the year 2018, and it is possible to improve the time series from the continuity of data collection.

Our newly burned area methodological classification developed in this article presented results that provide subsidies for reviewing and creating public policies and territorial management.

Data availability statement

The original contributions presented in the study are included in the article/supplementary material, further inquiries can be directed to the corresponding author.

Author contributions

PH designed the study, collected the data, performed the analysis, wrote the paper, discussed the results, and contributed to the final manuscript. VN provided critical feedback, supervised the project, verified the analytical methods, discussed the results, and contributed to the final manuscript. MF and JO verified the analytical methods, discussed the results, and contributed to the final manuscript. All authors contributed to the article and approved the submitted version.

Funding

This research was funded by Fundação de Amparo á Pesquisa do Estado de São Paulo (FAPESP) project number (2017/22269-2).

Acknowledgments

The authors thank the Graduate Program in Remote Sensing at the Federal University of Rio Grande do Sul and the Federal University of ABC in Brazil.

Conflict of interest

The authors declare that the research was conducted in the absence of any commercial or financial relationships that could be construed as a potential conflict of interest.

Publisher's note

References

Adagbasa, E. G., Adelabu, S. A., and Okello, T. W. (2020). Development of post-fire vegetation response-ability model in grassland mountainous ecosystem using GIS and remote sensing. *ISPRS J. Photogrammetry Remote Sens.* 164, 173–183. doi:10.1016/j.isprsjprs.2020.04.006

Alencar, A. A. C., Arruda, V. L. S., Silva, W. V. D., Conciani, D. E., Costa, D. P., Crusco, N., et al. (2022). Long-term landsat-based monthly burned area dataset for the Brazilian biomes using deep learning. *Remote Sens.* 14 (11), 2510. doi:10.3390/rs14112510

Andrade, B. O., Koch, C., Boldrini, I. I., Vélez-Martin, E., Hasenack, H., Hermann, J. M., et al. (2015). Grassland degradation and restoration: A conceptual framework of stages and thresholds illustrated by southern Brazilian grasslands. *Nat. Conserv.* 13 (2), 95–104. doi:10.1016/j.ncon.2015.08.002

Boldrini, I. (1997). *Campos do Rio Grande do Sul: Caracterização fisionômica e problemática ocupacional*. Porto Alegre, Brazil: Boletim do Instituto de Biociências, 1–39.

Bond-Buckup, G. (2008). *Biodiversidade dos Campos de Cima da Serra*. New York, NY, USA: Livro de Atividades, 96.

Boziki, D., Beroldt S, L., and Printes, C., R. (2011). Situação atual da utilização de agrotóxicos e destinação de embalagens na área de Proteção Ambiental Estadual Rota Sol, Rio Grande De Sul Brasil. *Rev. Vitas – Visões* 1 (31), 1–35.

Brasil (2008). *Decreto nº 6.660, de 21 de novembro de 2008. Regulamenta dispositivos da Lei no 11.428, de 22 de dezembro de 2006, que dispõe sobre a utilização e proteção da vegetação nativa do Bioma Mata Atlântica*. Planalto, Brazil: Planalto Gov.

Brasil (2006). *Lei nº 11.428, de 22 de dezembro de 2006. Dispõe sobre a utilização e proteção da vegetação nativa do Bioma Mata Atlântica, e dá outras providências*. Planalto, Brazil: Planalto Gov.

BRASIL (2000). *Sistema Nacional de Unidades de Conservação LEI No 9.985 DE 18 DE JULHO DE 2000*. Planalto, Brazil: Planalto Gov.

Brasil (2011). *Lei nº 12.527 de 18 de novembro de 2011. Regula o acesso a informações previsto no inciso XXXIII do art 5° no inciso II do § 3° do art 37 e no § 2° do art 216 da Constituição Federal*. Planalto, Brazil: Planalto Gov.

Breiman, L. (2001). Random forests. *Mach. Learn.* 45, 5–32. doi:10.1023/A:1010933404324

Buffon, I., Printes, R. C., and Andrades-Filho, C. D O. (2018). Licenciamento ambiental do uso do fogo nos Campos de Cima da Serra, Rio Grande do Sul, Brasil: Determinação do período de pousio e sugestões para uma rotina de monitoramento. *Rev. Eletrônica Científica UERGS* 4, 447–469. doi:10.21674/2448-0479.43.447-469

Buisson, E., Le Stradic, S., Silveira, F. A. O., Durigan, G., Overbeck, G. E., Fidelis, A., et al. (2019). Resilience and restoration of tropical and subtropical grasslands, savannas, and grassy woodlands. *Biol. Rev.* 94 (2), 590–609. doi:10.1111/brv.12470

Carvalho, E. D., and Andrades-Filho, C. D O. (2019). *Análise Espaço-Temporal do uso e cobertura do solo em São Francisco De Paula, RS/Brasil, Mudanças nos sistemas agrícolas e territórios no Brasil*. Porto Alegre, Brasil: Planalto Gov. doi:10.21674/9788560231.118-145

Dubinin, M., Potapov, P., Lushchekina, A., and Radeloff, V. C. (2010). Reconstructing long time series of burned areas in arid grasslands of southern Russia by satellite remote sensing. *Remote Sens. Environ.* 114 (8), 1638–1648. doi:10.1016/j.rse.2010.02.010

ESA (2022). Sentinel 2. https://sentinel.esa.int/web/sentinel/missions/sentinel-2 (Accessed August 15, 2022).

Fidelis, A., Roy, D. P., Humber, M. L., and Justice, C. O. (2021). What matters for vegetation regeneration in Brazilian subtropical grasslands: Seeders or resprouters? *Flora Morphol. Distribution, Funct. Ecol. Plants* 279, 151817. doi:10.1016/j.flora.2021.151817

Giglio, L. (2018). The Collection 6 MODIS burned area mapping algorithm and product. *Remote Sens. Environ.* 217, 72–85. doi:10.1016/j.rse.2018.08.005

Goehry, B. (2021). Random forests for time series.HAL archives-ouvertes. Available at: https://hal.archives-ouvertes.fr/hal-03129751.

Herrmann, P. B., Nascimento, V. F., and Freitas, M. W. D. d. (2022). Fire analysis in grasslands using remote sensing: A systematic review. *Rev. Bras. Cartogr.* 74 (2), 437–458. doi:10.14393/rbcv74n2-63739

Key, C. H., and Benson, N. C. (2006). *Landscape Assessment (LA) sampling and analysis methods*. 164 RMRS-GTR. Washington, D.C., United States: USDA Forest Service - General Technical Report RMRS-GTR.

McKinney, W., Perktold, J., and Seabold, S. "Time series analysis in Python with statsmodels," in Proceedings of the 10th Python in Science Conference, (Scipy), Austin, Texas, United States, July 2011, 107–113. doi:10.25080/majora-ebaa42b7-012

Meireles, L. D., and Shepherd, G. J. (2015). Structure and floristic similarities of upper montane forests in Serra Fina mountain range, southeastern Brazil. *Acta Bot. Bras.* 29 (1), 58–72. doi:10.1590/0102-33062014abb3509

Municipio de Cambará do Sul (2013). *Lei municipal nº 2.954, de 26 de julho de 2013*. Brazil: Lei de Queima Controlada.

Municipio de Jaquirana (2013). *Lei ordinária nº 1083, de 16 de julho de 2013*. Brazil: Lei de Queima Controlada.

Municipio de São Francisco de Paula (2013). *Lei nº 2924, de 12 de junho 2013*. Brazil: Lei de Queima Controlada.

Myers, N., Mittermeier, R. A., Mittermeier, C. G., da Fonseca, G. A. B., and Kent, J. (2000). Biodiversity hotspots for conservation priorities. *Nature* 403 (6772), 853–858. doi:10.1038/35002501

Overbeck, G. E., Muller, S., Fidelis, A., Pfadenhauer, J., Pillar, V., Blanco, C., et al. (2007). Brazil's neglected biome: The South Brazilian Campos. *Perspect. Plant Ecol. Evol. Syst.* 9 (2), 101–116. doi:10.1016/j.ppees.2007.07.005

Pal, M. (2005). Random forest classifier for remote sensing classification. *Int. J. Remote Sens.* 26, 217–222. doi:10.1080/01431160412331269698

Pillar, V. D. P. (2009). *Campos Sulinos - conservação e uso sustentável da biodiversidade*. Brasília: Ministério do Meio Ambiente, 403.

Pivello, V. R., Vieira, I., Christianini, A. V., Ribeiro, D. B., da Silva Menezes, L., Berlinck, C. N., et al. (2021). Understanding Brazil's catastrophic fires: Causes, consequences and policy needed to prevent future tragedies. *Perspect. Ecol. Conservation* 19 (3), 233–255. doi:10.1016/j.pecon.2021.06.005

Rio Grandedo Sul (2012). *Lei nº 13.931, de 30 de janeiro de 2012*. Brasil: Código Florestal Estadual.

Rio Grandedo Sul (1992). *Lei nº 9.519, de 21 de janeiro de 1992*. Brasil: Código Florestal Estadual.

Rio Grandedo Sul (2008). *Plano de manejo do Parque Estadual do Tainhas*. Porto Alegre, Brasil: Planalto Gov.

Santos, D., and Andrades-Filho, C. D. O. (2021). Uso do fogo nos campos de altitude do sul do brasil: Análise do licenciamento ambiental a partir de geotecnologias. *Rev. Bras. Meio Ambiente* 164, 146–164.

Souza, C. M., Z. Shimbo, J., Rosa, M. R., Parente, L. L., A. Alencar, A., Rudorff, B. F. T., et al. (2020). Reconstructing three decades of land use and land cover changes in Brazilian biomes with Landsat archive and Earth engine. *Remote Sens.* 12 (17), 2735. doi:10.3390/rs12172735

Tyukavina, A., Potapov, P., Hansen, M. C., Pickens, A. H., Stehman, S. V., Turubanova, S., et al. (2022). Global trends of forest loss due to fire from 2001 to 2019. *Front. Remote Sens.* 3, 1–20. doi:10.3389/frsen.2022.825190

frontiers | Frontiers in Remote Sensing

TYPE Original Research
PUBLISHED 20 June 2023
DOI 10.3389/frsen.2023.1196554

OPEN ACCESS

EDITED BY
Hannah Victoria Herrero,
The University of Tennessee,
United States

REVIEWED BY
Mahlatse Kganyago,
University of Johannesburg, South Africa
Ross Hill,
Bournemouth University,
United Kingdom

*CORRESPONDENCE
Jody C. Vogeler,
jody.vogeler@colostate.edu

RECEIVED 30 March 2023
ACCEPTED 06 June 2023
PUBLISHED 20 June 2023

CITATION
Vogeler JC, Fekety PA, Elliott L, Swayze NC, Filippelli SK, Barry B, Holbrook JD and Vierling KT (2023), Evaluating GEDI data fusions for continuous characterizations of forest wildlife habitat.
Front. Remote Sens. 4:1196554.
doi: 10.3389/frsen.2023.1196554

Evaluating GEDI data fusions for continuous characterizations of forest wildlife habitat

Jody C. Vogeler[1]*, Patrick A. Fekety[1], Lisa Elliott[2], Neal C. Swayze[1], Steven K. Filippelli[1], Brent Barry[2], Joseph D. Holbrook[3] and Kerri T. Vierling[2]

[1]Natural Resources Ecology Laboratory, Colorado State University, Fort Collins, CO, United States, [2]Department of Fish and Wildlife Resources, University of Idaho, Moscow, ID, United States, [3]Department of Zoology and Physiology, University of Wyoming, Laramie, WY, United States

Continuous characterizations of forest structure are critical for modeling wildlife habitat as well as for assessing trade-offs with additional ecosystem services. To overcome the spatial and temporal limitations of airborne lidar data for studying wide-ranging animals and for monitoring wildlife habitat through time, novel sampling data sources, including the space-borne Global Ecosystem Dynamics Investigation (GEDI) lidar instrument, may be incorporated within data fusion frameworks to scale up satellite-based estimates of forest structure across continuous spatial extents. The objectives of this study were to: 1) investigate the value and limitations of satellite data sources for generating GEDI-fusion models and 30 m resolution predictive maps of eight forest structure measures across six western U.S. states (Colorado, Wyoming, Idaho, Oregon, Washington, and Montana); 2) evaluate the suitability of GEDI as a reference data source and assess any spatiotemporal biases of GEDI-fusion maps using samples of airborne lidar data; and 3) examine differences in GEDI-fusion products for inclusion within wildlife habitat models for three keystone woodpecker species with varying forest structure needs. We focused on two fusion models, one that combined Landsat, Sentinel-1 Synthetic Aperture Radar, disturbance, topographic, and bioclimatic predictor information (combined model), and one that was restricted to Landsat, topographic, and bioclimatic predictors (Landsat/topo/bio model). Model performance varied across the eight GEDI structure measures although all representing moderate to high predictive performance (model testing R^2 values ranging from 0.36 to 0.76). Results were similar between fusion models, as well as for map validations for years of model creation (2019–2020) and hindcasted years (2016–2018). Within our wildlife case studies, modeling encounter rates of the three woodpecker species using GEDI-fusion inputs yielded AUC values ranging from 0.76–0.87 with observed relationships that followed our ecological understanding of the species. While our results show promise for the use of remote sensing data fusions for scaling up GEDI structure metrics of value for habitat modeling and other applications across broad continuous extents, further assessments are needed to test their performance within habitat modeling for additional species of conservation interest as well as biodiversity assessments.

KEYWORDS

GEDI, forest structure, wildlife habitat, mapping, Landsat, Sentinel-1

1 Introduction

The current generation of spatiotemporal representations of ecological patterns provide a critical component for conservation and management of ecosystem services. Spatial information of vegetation structure is incorporated in the identification and management of biodiversity hotspots (Roll et al., 2017; Thom et al., 2017; Donald et al., 2019), distribution maps of endangered species (Dunk et al., 2019; Colyn et al., 2020), and relationships between carbon sequestration and patterns of biodiversity (Buotte et al., 2020; Soto-Navarro et al., 2020). Forest planning, in particular, often requires assessing the trade-offs and synergies associated with maintaining biodiversity compared to meeting single species habitat needs (Wilson et al., 2019), while also considering additional, often conflicting, ecosystem services such as carbon sequestration and the supply of timber resources (Kline et al., 2016). With ever increasing human populations, habitat loss, invasive species, climate change, and a myriad of other threats to the loss of species and ecosystem function (Ceballos et al., 2017; Ceballos et al., 2020), the need for spatiotemporal data to describe a wide variety of ecological patterns and processes becomes increasingly salient.

Complex multi-use forest planning draws great benefit from spatial and temporal mapping products at resolutions and extents that reflect the patterns and processes important for balancing silvicultural activities with environmental characteristics that are critical for maintenance of quality animal habitat and biodiversity. Vertical forest structure is among the more important remotely sensed characteristics that can provide relevant information for studies of carbon sequestration, species habitat modeling, and biodiversity patterns at local scales, and airborne lidar is frequently the source of those vertical structure data (Vierling et al., 2008; Davies and Asner, 2014; Vogeler and Cohen, 2016). At local scales, the use of airborne lidar data, also referred to as airborne laser scanning (ALS), has improved our understanding of species distributions for organisms that range in size from beetles and spiders (Müller and Brandl, 2009; Vierling et al., 2011) to elephants (Davies et al., 2018), and ALS has been incorporated in studies of biodiversity that address patterns of alpha, beta, and functional diversity perspectives (Asner et al., 2017; Bae et al., 2018).

As central as ALS has been for multiple ecological studies, it is limited in spatial extent, and acquisitions across areas often vary in point densities and other collection parameters, raising concerns about comparing spatial products derived from different acquisitions (Hudak et al., 2012; Eitel et al., 2016). Additionally, the cost of ALS data often precludes multiple acquisitions across short time frames, and the time lags between ALS acquisition and wildlife data collection are important considerations of studies relating ALS structure variables to patterns of animal habitat and/or diversity (Vierling et al., 2014; Hill and Hinsley, 2015). Recent spaceborne lidar missions, such as the Global Ecosystems Dynamics Investigation (GEDI), may provide an opportunity for characterizing forest structure across broad extents, although the moderate resolution footprints along orbital tracks of the International Space Station on which the sensor is mounted, do not constitute continuous coverage across landscapes and are temporally restricted through the limited mission lifespan (Dubayah et al., 2020). What GEDI footprints do provide are a consistent sample of forest architectures across near global extents (Dubayah et al., 2020), including countries and forested regions which are often lacking in reliable forest sampling efforts. GEDI data also represent a free publicly available, easily accessible, and consistently collected forest plot data base for regional to near-global summaries of forest patterns (Dubayah et al., 2020), or for use in scaling up forest structure information to continuous extents using additional earth observation imagery sources (Healey et al., 2020; Sothe et al., 2022).

Data fusion frameworks that expand high resolution depictions of forest structure to greater spatiotemporal extents using moderate resolution spectral data sources, such as Landsat, have been widely applied across different forest types and regions with varying success (Matasci et al., 2018; Filippelli et al., 2020). Single date or annual composites of Landsat-derived spectral indices may be able to predict some vertical structure components, such as canopy cover (Coulston et al., 2012; Vogeler et al., 2018), but the 2-D nature of spectral data may fall short for characterizing more complex aspects of the canopy profile and variability in heights (Zald et al., 2016; Matasci et al., 2018), which are often important for identifying habitat (Burns et al., 2020) or biodiversity patterns (Vogeler et al., 2014). While single date Landsat-derived information may have some limitations for predicting forest structure, studies are finding improvements in such efforts by incorporating the value of the long-running Landsat archive for characterizing disturbance histories which often drive current forest structure (Pflugmacher et al., 2012; Vogeler et al., 2016). In addition, Synthetic Aperture Radar (SAR) systems like Sentinel-1 are often more limited in temporal extents than the Landsat archive but may capture some aspects of 3-D structure that optical data are less sensitive to, providing more accurate forest structure mapping.

Data fusion frameworks that are based on freely available public data, such as those from the GEDI, Landsat, and Sentinel-1 programs, support the implementation of methodologies for a wide variety of conservation and management applications across regions where financial resources for acquiring imagery may be limited. If such data sources are available through time, there may also be opportunities to hindcast spatial prediction models of forest variables (Matasci et al., 2018; Vogeler et al., 2018) to monitor sources of change in habitat as well as better match the timing of wildlife data collections. Testing data fusions for scaling up GEDI information within the diverse forest systems of the western U.S. provides the opportunity to evaluate GEDI as a reference data source. This western U.S. region is also rich in ALS collections which can serve as a validation baseline to inform future efforts across international regions which may not have similar validation data availabilities.

Lidar data have been incorporated within wildlife or biodiversity applications across a wide variety of species, spatial scales, and with a diverse set of lidar technologies (Davies and Asner, 2014; Müller and Vierling, 2014; Olsoy et al., 2015; Stitt et al., 2019; Acebes et al., 2021; Smith et al., 2022; Shokirov et al., 2023). The potential benefit of GEDI data for wildlife applications is therefore exciting, and as with other remotely sensed products used for wildlife and biodiversity applications, it is important to understand how different accuracies and biases in spatial vegetation data could possibly affect wildlife model outcomes. For example, the use of a forest height metric is

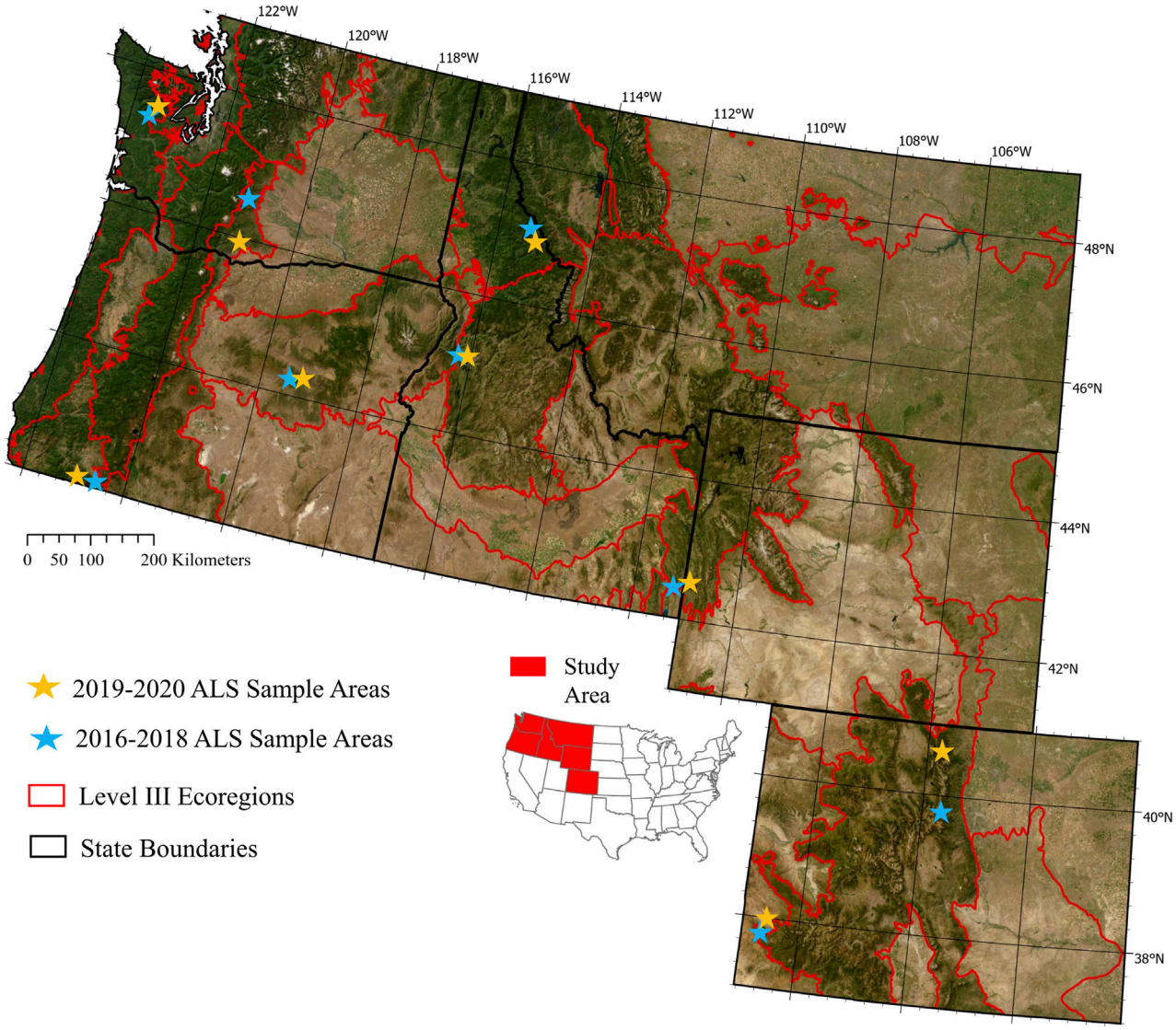

FIGURE 1
Western U.S. study region divided by EPA Level III Ecoregions with locations of validation ALS units designated by stars: orange stars depict validation collections for the years of model creation, and blue stars represent validation collections for years of model hindcasting.

common in wildlife studies because tall trees (and associated diameters) are a critical habitat component for many species of management concern (Acebes et al., 2021); understanding the biases and accuracies of the spatial layers that depict forest height (or other GEDI structure metrics) can have implications for models developed for the management of sensitive species if those metrics are over- or underestimated within certain environmental conditions.

Within our study, we tested the value and trade-offs of free publicly available continuous remote sensing data products for producing wall-to-wall predictions of GEDI-derived forest structure metrics (referred to as "GEDI-fusion" maps here forward) relevant for wildlife and biodiversity applications. The objectives of this study were to: 1) investigate the value and limitations of satellite data sources for generating GEDI-fusion models and 30 m resolution predictive maps of eight forest structure measures (representing height and vegetation profile information) across six western U.S. states (Colorado, Wyoming, Idaho, Oregon, Washington, and Montana); 2) evaluate the suitability of GEDI footprint data as a reference data source and assess any spatiotemporal biases of GEDI-fusion maps using samples of airborne lidar data; and 3) examine differences in GEDI-fusion products for inclusion within wildlife habitat models for three keystone wildlife species. We selected three cavity excavating case study species with varying forest structure needs that operate at three different spatial scales. Tree cavity excavators (e.g., woodpeckers) facilitate habitat for a diversity of species within communities of forest-dwelling animals, so understanding woodpecker-habitat relationships can have implications for other species (Martin et al., 2004).

2 Materials and methods

2.1 Study area

We focused on six western U.S. states that represent a range of forest types and ecoregions (Figure 1). Tree species composition ranged from subalpine forests dominated by subalpine fir (*Abies lasiocarpa*), Englemann spruce (*Picea englemannii*) and lodgepole pine (*Pinus contorta*) to more xeric forests dominated by ponderosa pine (*Pinus ponderosa*). The study area transitions from wetter climate forests in the Pacific Northwest to the drier southern Rocky Mountain range, and thus captures a wide variety of climatic conditions, forest disturbance dynamics, and compositional gradients. Disturbance regimes within the study area range in their patterns of severities and frequencies, but dominant change agents across the area include timber harvest, fire (natural and prescribed), insect mortality or defoliation, and weather-driven events (e.g., drought, wind blow-down).

2.2 Remote sensing model data

2.2.1 GEDI data

Forest wildlife habitat modeling efforts often include measures of forest height, canopy cover, foliage height diversity, and/or the availability of vegetation within specific strata of the forest (e.g., understory or upper canopy); these measures often correlate with important structure components necessary to meet life history needs for species, or to promote overall diversity of habitat niches (Bergen et al., 2009). After preliminary evaluations of available GEDI metrics in the context of frequently identified forest structure measures of value for habitat modeling purposes, we chose to focus our modeling efforts on several GEDI-derived height, cover, foliage height diversity, and summarized plant area density profile metrics corresponding to important habitat structure components for a variety of wildlife species. GEDI level 2A relative height (RH) metrics represent the height at which a defined percentage of GEDI waveform energy is contained. For instance, RH98 corresponds to the height at which 98% of the waveform energy is captured - comparable to a canopy height measure. We also included RH50 and RH75 within our modeling efforts to test their utility for wildlife modeling in future applied research efforts. Among the GEDI level 2B metrics, we selected two commonly used forest measures in wildlife habitat modeling, fractional canopy cover (COVER) and foliage height diversity (FHD). Among the Level 2B plant area vegetation density (PAVD) profile metrics, we choose the lowest single profile available through the GEDI waveform metrics that represents the 5–10 m strata (PAVD5-10 m), as well as summarizing plant area densities above 20 m (PAVD>20 m) and 40 m (PAVD>40 m) to represent the presence of a mature upper canopy within different forest types.

We leveraged the rGEDI package (Silva et al., 2020) implemented in the R Statistical Software (R Core Team, 2021) to download and filter GEDI version 2 footprint data across our study area. We restricted our target GEDI footprints within a summer season date range of June 6th - September 30th for both 2019 and 2020 to limit any bias in canopy cover and vegetation density profiles in mixed or deciduous forests outside of the primary growing season. We further filtered the summer season GEDI shots with a series of conditional arguments to retain only the highest quality observations to serve as model reference and testing data, including a solar elevation below 0°, a degrade flag of 0, a quality flag of 1, a beam sensitivity of greater than or equal to 0.95, and only employing full power beams. After filtering, the remaining GEDI footprints were intersected with the study area and each footprint observation was reprojected into an Albers Equal Area Projection (EPSG 5070).

While the rich spatial density of GEDI footprints provides value for a wide suite of applications including direct quantification and monitoring of forest patterns across broad extents, for our purposes in leveraging GEDI footprints as a model reference source, we chose to spatially thin our GEDI footprints to balance computational efficiency while maximizing model performance. We developed a set of spatial thinning steps to reduce the density of GEDI footprints while ensuring a spatially balanced sample across our study area. We first took a random subsample of 150,000 observations for each year. Constructing a set of polygon tiles with a 60 × 60-km resolution over the desired study region, we generated a Euclidean distance matrix for the subsetted footprints within each tile. Based on the distance between each footprint, 225 maximally distanced footprints were retained per 3,600 square kilometers. The resulting spatially subsetted dataset consisted of 99,766 observations for 2019 and 100,003 observations for 2020.

2.2.2 Continuous remote sensing predictors

We leveraged the computational efficiency of Google Earth Engine (GEE) to generate a suite of 31 active and passive remote sensing predictor layers for upscaling GEDI forest structure metrics to a continuous 30 m resolution grid and to apply models at annual time steps from 2016–2020. We wanted to test the utility of GEDI-fusion models for hindcasting structure metrics to years outside model creation, but were restricted to the 2016 forward time period due to the temporal availability of Sentinel-1 data included within our data fusion assessments. All dynamic predictors (e.g., Sentinel-1 and Landsat) were summarized for the summer growing season to match the temporal window of our GEDI data. From median summer composites of the Sentinel-1 C-band Synthetic Aperture Radar (SAR) dataset, we compiled the vertical-vertical (VV) and vertical-horizontal (VH) polarizations along with several ratios derived from the median VV and VH data including:

$$VHVVratio = VH/VV$$

$$normalized\ difference\ radar\ index = \frac{[VV - VV]}{[VH + VV]}$$

$$radar\ vegetation\ index = \frac{[4^{*}VH]}{[VV + VH]}$$

For our Landsat spectral predictors, we created Medoid image composites for the annual summer seasons for the full Landsat archive (1984–2021), from which annual spectral indices were then calculated. Studies have found that when forest attribute models are created for a particular time period and then applied across a longer time period, using a temporal segmentation fitting algorithm can aid in producing more stabilized temporal representations of the modeled attribute within predicted maps (Moisen et al., 2016; Kennedy et al., 2018a). We used one such trend fitting algorithm,

TABLE 1 Continuous predictor variables grouped by data source incorporated within GEDI-fusion modeling frameworks. Those predictors retained in final models after removing highly correlated variables within individual models sets are marked with an X.

Predictor set	Predictor abbreviation	Description	Retained in modeling
Landsat 8 (median summer composites)	blue	Landsat 8 band 2	
	green	Landsat 8 band 3	
	red	Landsat 8 band 4	
	nir	Landsat 8 band 5	
	swir1	Landsat 8 band 6 - shortwave infrared 1	
	swir2	Landsat 8 band 7 - shortwave infrared 2	
	NDVI	Normalized difference vegetation index	X
	NBR	Normalized burn ratio	X
	EVI	Enhanced vegetation index	
	TCB	Tasseled cap brightness	X
	TCG	Tasseled cap greenness	X
	TCW	Tasseled cap wetness	X
Landsat time series disturbance	TSD	Time since most recent fast disturbance derived from LCMS	X
Sentinel-1 (median summer composites)	VV median	Median composite of vertical polarizations	X
	VH median	Median composite of vertical horizontal polarizations	X
	VHVV ratio	VH/VV	
	nDiff	Normalized difference radar index	
	rvi	Radar vegetation index	X
Topography	elevation	SRTM elevation (m)	X
	slope	SRTM derived slope (degrees)	X
	aspect	SRTM derived aspect (degrees)	X
	eastness	Aspect transformation	X
	northness	Aspect transformation	X
	TOPODIV	Topographic diversity index	X
	CHILI	Continuous heat-insolation load index	X
	mTPI	Multi-scale topographic position index	X
	LANDFORM	Landform classification	X
Bioclimatic	CMD	climatic moisture deficit	X
	GDD	growing degree days	X
	MAP	mean annual precipitation	X
	MAT	mean annual temperature	X
	MWT	mean winter temperature	X

LandTrendr in GEE (Kennedy et al., 2018b), to calculate vertices within each spectral index and the original bands to produce annual "fitted" values for all Landsat predictors (Table 1). In additional to the original Landsat bands, we incorporated several Landsat spectral indices in our "fitted" Landsat predictor set that are commonly used within forest attribute modeling and change detection: tasseled cap brightness, greenness, and wetness (Crist and Cicone, 1984); the normalized difference vegetation index (Rouse et al., 1974); the enhanced vegetation index (Liu and Huete, 1995); and the normalized burn ratio (Key and Benson, 2006).

While annual Landsat information may be correlated with some forest measures such as canopy cover (Coulston et al., 2012), previous research has highlighted the additional value of Landsat time series derived information of disturbance histories for improving structure predictions (Pflugmacher et al., 2012; Vogeler et al., 2016). To test for similar improvements, we

generated a model predictor related to disturbance histories derived from the United States Forest Service Landscape Change Monitoring System (LCMS) dataset (Housman et al., 2022). We filtered the annual dataset to derive an image collection representing the most recent year of abrupt, or "fast", forest change. We subtracted this most recent disturbance year from the year of interest (depending on the year of GEDI data or mapping year) to derive an annual raster layer indicating the number of years since the last fast disturbance (here forward referred to as time since disturbance, TSD).

To complement the dynamic spectral and SAR predictors and to represent the gradients that exist across our study area, we also extracted topographic and bioclimatic information (Table 1). Utilizing the Satellite Radar Topography Mission (SRTM) dataset, we calculated elevation, slope, aspect and aspect transformations (eastness and northness). We also incorporated additional topographic predictors based on SRTM including the Topographic Diversity Index (TOPODIV), Continuous Heat-Insolation Load Index (CHILI), Multi-Scale Topographic Position Index (mTPI), and landform classes created by combining CHILI and mTPI (LANDFORM) (Theobald et al., 2015). ClimateNA (version 7.2.1; Wang et al., 2016) was used to generate a set of bioclimatic variables derived from PRISM 4 km × 4 km gridded monthly climate for the 1961–1990 "normal" period (Daly et al., 2008), which were downscaled using the global 1-arcsecond v3 SRTM digital elevation model. We chose this "normal" period as it likely corresponds to the time when many of our mature forests were developing across our study area. More recent normals may provide an updated version of this data for the period impacting younger forest development, but we believe that the older versions are still appropriate for our purpose of representing relative differences in climatic gradients across our study region. The resulting bioclimatic variables included climatic moisture deficit, growing degree days, mean annual precipitation, mean annual temperature, and mean winter temperature (Table 1).

The spatial resolution of the processed predictor datasets varied from 10 m (SAR) to 270 m (some of the topographic position and diversity indices). All predictors were either aggregated or resampled to a common 30 m grid and exported from GEE for local modeling and predictive mapping using the EPSG 5070 projection within analysis ready dataset tiles. The spatially filtered GEDI locations for each year were buffered by 12.5 m to generate polygons representative of the 25 m diameter of the GEDI footprints. All above predictors were extracted using an area weighted mean pixel value from all pixels intersecting a footprint's polygon, and for temporally dynamic predictors the year used for extraction corresponded to that of the GEDI footprint's acquisition year.

2.3 GEDI-fusion modeling and mapping

A primary goal of our study was to test the utility of GEDI data as a reference source combined with various continuous predictor layers for scaling up structure information relevant to habitat modeling across continuous regional extents at 30 m spatial resolutions from 2016–2020. Different predictor data sources (e.g., Landsat, Sentinel-1) may have various tradeoffs as to model performance, spatial biases, and potential hind-casting capabilities. Thus, comparing different predictor sets can help inform the potential value and trade-offs of data fusion frameworks. All model accuracies and errors were assessed using a withheld set of testing GEDI footprints. Further spatial bias and temporal transferability were evaluated using our sample of ALS collections across two-time mapping windows representing years of model creation and model hindcasting (Figure 1; *section 2.4.2*). We completed an initial evaluation of random forest regression (Breiman, 2001) with progressively larger training samples to identify the number of training samples at which model performance began to stabilize for a sample set of GEDI metrics (i.e., a learning curve), and we used this number of training and testing samples for subsequent model development and evaluation.

We defined an *a priori* set of data fusion model combinations (Table 2) to compare model performances and spatiotemporal biases. Within each single-source predictor set (e.g., Landsat, topography), we first tested for highly correlated variables using a correlation threshold of 0.95. Only those not highly correlated were retained within the model comparisons (Table 1). The reduced variable sets were also combined to determine the best overall model for each GEDI metric in terms of model performance and errors as assessed using the withheld testing set of footprints. The fusion models representing the full set of predictors (combined model) and the model incorporating Landsat, topography, and bioclimatic predictors (Landsat/topo/bio model) were applied to the predictor layers to produce 30 m resolution maps of the GEDI metrics across the study area and on annual time steps from 2016–2020. As a final post-processing step, we developed an open-water mask using the Global Surface Water Layer v1.4 within GEE (Pekel et al., 2016), which we applied to all final maps to minimize false vegetation structure measures as a result of our GEDI filtering approaches that removed all water GEDI points; therefore, water bodies were outside the scope of our model reference data.

2.4 Validation assessments

2.4.1 GEDI Footprint-ALS comparisons

GEDI-fusion frameworks are based on the assumption that the information provided by the GEDI footprints are accurate representations of forest structure for serving as modeling reference data. To test this assumption and to inform sources of error in the GEDI-fusion maps, such as the potential for up to 10 m geolocation errors within the GEDI data, we compared footprint estimates of focal metrics to those from ALS samples. ALS data may be limited in spatial extents and temporal coverage, but the sources of errors and vertical/horizontal accuracies are well established and can serve as a baseline for comparisons with GEDI-derived forest measures and for comparing patterns in spatiotemporal biases between GEDI-fusion maps. We identified a set of ALS collections for the years of our GEDI footprint samples (2019 and 2020) that represent the forest-dominated ecoregions of the study area based on the EPA Level III Ecoregions (US EPA, 2015; Figure 1). The sample ALS collections also captured a wide range of forest structure variability and disturbance patterns. While our models and predicted maps encompass the extent of our six study states, the focal area for our habitat case studies were the forested regions of those states. As such, our ALS validation samples

TABLE 2 GEDI-fusion model comparisons using *a priori* model predictor sets. All accuracy and error statistics calculated using a withheld testing set of ~140,000 GEDI footprints. The combined model includes metrics from all predictor sets.

GEDI metrics	*A Priori* model sets											
	Combined			Landsat/Topo/Bio			Landsat			Sentinel-1		
	R^2	RMSE	Bias	R^2	RMSE	Bias	R^2	RMSE	Bias	R^2	RMSE	Bias
RH98	0.757	5.445	0.130	0.750	5.526	0.128	0.651	6.525	0.113	0.492	7.888	0.032
RH75	0.707	4.238	0.098	0.698	4.298	0.096	0.603	4.930	0.071	0.388	6.142	0.042
RH50	0.651	3.369	0.078	0.639	3.426	0.079	0.553	3.815	0.051	0.292	4.831	0.041
FHD	0.739	0.392	−0.005	0.730	0.399	−0.004	0.643	0.458	0.004	0.564	0.507	−0.001
COVER	0.684	0.146	0.004	0.674	0.148	0.003	0.599	0.164	0.003	0.459	0.191	0.001
PAVD 5–10 m	0.363	0.051	0.002	0.359	0.052	0.002	0.288	0.054	0.001	0.224	0.057	<0.001
PAVD >20 m	0.580	0.058	0.001	0.562	0.059	0.001	0.481	0.065	0.001	0.200	0.081	0.001
PAVD >40 m	0.447	0.034	0.001	0.442	0.034	0.001	0.335	0.038	<0.001	0.079	0.045	<0.001

represent forest and shrubland cover types and our validations are only representative of forested lands in the region.

The majority of ALS data are collected using discrete lidar sensors, while GEDI is a full-waveform system. To convert the ALS measures to those comparable to waveform derived structure metrics, we employed the GEDI waveform simulator, gediSimulator (Hancock et al., 2019), frequently used within GEDI-ALS comparisons. That said, by simulating waveforms with discrete ALS, we acknowledge that we may be introducing some level of error within our validation data set although allowing for more direct comparisons of metrics than possible between waveform and discrete lidar. Within the selected ALS comparison units (Supplemental Table S1), we clipped the ALS point clouds at our filtered GEDI footprint locations corresponding to the year of ALS. Preprocessing the ALS clips involved identifying lidar returns within 60 cm of the ground surface and reclassifying those lidar returns as ground returns to account for topographic variations within a simulated footprint (Hancock, 2023). The gediSimulator tool, gediRat, was used to convert the ALS point clouds into a simulated waveform, which were passed to gediMetric to calculate waveform metrics. Simulated cover outputs are reported to be particularly sensitive to variations in topography within a footprint (Hancock, 2023), which can be significant within our study area. Implementing the suggested pre-processing steps for minimizing the impacts of topographic variations on ALS simulated metrics did not appear to improve the simulated cover metric for our sample ALS areas. Therefore, we chose to directly compare discrete ALS cover to our GEDI footprint and map cover estimates, although we acknowledge that slightly different measures of canopy cover may be represented by these two measures. We calculated the discrete ALS cover metric as the proportion of first returns above 2 m within the FUSION lidar processing software (McGaughey, 2022). We then compared the simulated or direct ALS-based metrics to the GEDI-based metrics for matching years (e.g., 2019 GEDI footprints compared to simulated 2019 ALS metrics) by calculating the coefficient of determination (R^2), mean bias (*bias*), and root mean squared error (*RMSE*). We were unable to include our PAVD metrics within the footprint and map level validations as these are not direct outputs available from gediSimulator (Hancock, 2023), nor are there readily comparable metrics from discrete ALS. Evaluations for the PAVD metrics were restricted to the prediction assessments from the large set of withheld testing GEDI footprints (described in *section 2.3*).

Many studies comparing simulated ALS waveforms to GEDI footprints conduct an additional step to better georeference the GEDI footprints based on the ALS information as GEDI version 2 footprints may have up to 10 m geolocation error. For our purposes, we wanted to directly compare GEDI footprints to ALS information without additional georeferencing steps to directly test the utility of footprints as reference data in areas where we do not have corresponding ALS data sets for location corrections. Therefore, some of the variability observed within our footprint level comparisons may be due to geospatial mismatches between the ALS data and the recorded footprint locations. As such, the comparisons are not intended as direct validations of the GEDI instrument measurements in the absence of geolocation errors, but instead validations of the footprint level information in their original form as a reference data source for scaling up structure information which may aid in understanding the errors observed within our resulting study-area wide GEDI-fusion predicted maps.

2.4.2 Structure map validations

In addition to comparing model performance through the withheld set of independent GEDI footprints, we also evaluated biases within the predicted maps and temporal transferability of models. We leveraged our sample set of ALS units for years of model creation (2019–2020) and a set of ALS collections from 2016–2018 to represent years of model hindcasting to evaluate differences in map accuracies when models were applied to years outside of the model training data (Supplemental Table S1). We ensured that the sampled collections within both time windows were representative of the range of forested ecoregions within our study area (Figure 1).

Maps of simulated gridded waveform metrics within the ALS sample units were created using a similar approach as outlined for

footprint level comparisons above (*section 2.4.1*). PDAL (PDAL, 2022) was used to filter ALS lidar in the sample units to include only ground and vegetation returns, as well as reclassifying all returns within 60 cm of the ground surface as ground returns. The preprocessed ALS files were then converted to simulated waveforms and waveform metrics (Hancock, 2023). Following our same comparison approach for cover measures as used in our footprint-level comparisons, we utilized a gridded ALS cover measure created within FUSION representing the proportion of first returns above 2 m (McGaughey, 2022). The size of the ALS collections used in the comparisons ranged between 150 and 450 km^2 (Supplemental Table S1), therefore a random sample of 1,100 cells were drawn from each ALS unit for a total of 9,900 pixels selected during the years of creation (2019–2020) and 9,900 pixels from hindcasted years (2016–2018). We created scatterplots of the map validation sample points for each time period, as well as calculating R^2, bias, and RMSE for each temporal validation dataset.

2.5 Case study: wildlife habitat modeling

Primary cavity excavators are considered a keystone wildlife guild because they excavate tree cavities that provide nesting and roosting habitat for multiple other species who cannot excavate those cavities themselves (Martin et al., 2004; Gentry and Vierling, 2008; Tarbill et al., 2015). For instance, Bunnell et al. (1999) noted that 25%–30% of vertebrates within Pacific Northwest forests are reliant on woodpecker cavities for either nesting or roosting, and many of these secondary cavity users are themselves species of management interest (e.g., fishers (*Pekania pennanti*) and marten (*Martes* spp.); Bissonette and Broekhuizen, 1995; Matthews et al., 2019). We chose three cavity excavator avian species which occur within our study region and are associated with different forest structural elements. These include the downy woodpecker (*Dryobates pubescens*), the Northern flicker (*Colaptes auratus*), and the pileated woodpecker (*Dryocopus pileatus*). Downy woodpeckers are small woodpeckers that prefer deciduous forest elements, small trees, and low canopy cover (Jackson et al., 2020). Conversely, pileated woodpeckers are associated with more mature forest elements, particularly tall trees (Bull and Jackson, 2020). Northern flickers are intermediately sized between the other two woodpecker species, and are associated with forest edges (Wiebe et al., 2017).

We followed best practices (Johnston et al., 2019; Strimas-Mackey et al., 2020) to obtain pileated woodpecker, Northern flicker, and downy woodpecker observations from eBird records (eBird, 2021). As a general workflow, we obtained stationary eBird checklists conducted in the study area between June 1 and July 31 of 2016–2020. For pileated woodpeckers, we restricted checklists to those taking place at longitudes west of −108.723868°, to account for the limited range of this species in the study area. Northern flicker and downy woodpecker occur throughout the study area and therefore checklists for these species were not restricted by longitude. After spatiotemporal subsampling (following Strimas-Mackey et al., 2020), we obtained the effective sample size for positive observations for each species and retained 20% of the data for model evaluation. We selected modeling scales based on estimated home range sizes for each species. We used a 250 m radius buffer size for downy woodpeckers (Jackson et al., 2020), 500 m radius buffers for Northern flickers (Wiebe et al., 2017), and a 1 km radius buffer size for pileated woodpeckers (Bull and Jackson, 2020). In random forest regression models, we used the observations for each species as our response variables and the following predictor variables: survey particulars (survey duration and time of day); forest type (confer, deciduous, or mixed) from MODIS data (Friedl and Sulla-Menashe, 2015); elevation, slope, eastness and northness from SRTM; and our set of GEDI-fusion maps produced as explained above. We first generated models for each woodpecker species using the GEDI-fusion layers created from the combined model and then repeated the process for each species using only the restricted Landsat/topo/bio model outputs. This direct comparison allows us to ascertain how models with different accuracies and biases affect wildlife model outputs.

3 Results

Overall, our data fusion approaches leveraging GEDI footprint forest structure information and continuous remote sensing data sources proved valuable for producing regional extent gridded maps of forest architecture with moderate to high model performances which were of value to wildlife habitat assessments for three cavity nester species representing different forest structure associations. Specific data, modeling, and mapping validations are presented below.

3.1 GEDI-fusion model assessments

Model performance stabilized at approximately 60,000 training footprints in our initial model testing, which was the sample size used for subsequent model development along with a withheld set of approximately 140,000 footprints for model testing. All reported model accuracies and errors were quantified using the independent testing set of footprints.

Our random forest combined models predicting GEDI structure metrics from continuous satellite remote sensing data sources had high model performance for the majority of the GEDI metrics. Within the combined models incorporating all predictor data sources, the highest performance was observed for RH98 (R^2 = 0.76, RMSE = 5.46 m) and FHD (R^2 = 0.74, RMSE = 0.39). Lower model performances were observed for the PAVD metrics, with R^2 values ranging from 0.36 (PAVD5-10 m) to 0.58 (PAVD>20 m), and RMSE values ranging from 0.03 (PAVD>40 m) to 0.06 (PAVD>20m; Table 2). The performance of the Landsat/topo/bio models were only slightly lower than that of the combined model for all GEDI metrics (Table 2). When comparing the single source Landsat model to the Sentinel-1 model, the Landsat model exhibited higher model performance for all metrics (Table 2). These differences in performance for the single source predictive models were the lowest for FHD, COVER, and RH98, in that order.

When comparing relative importance of predictor variables within the combined random forest models, Landsat variables were common among the top five most important predictors for all GEDI metrics (Table 3). Sentinel-1 metrics were also within

TABLE 3 Random forest variable importance rankings for the top 10 predictor metrics within the combined models for GEDI-fusion metrics.

Predictor set (abbrev.)		Combined model top 10 variable importance ranking							
		RH98	RH75	RH50	FHD	COVER	PAVD 5–10 m	PAVD >20 m	PAVD >40 m
Landsat 8 (L8)	NDVI	4	4	3	4	5	5	3	3
	NBR	5	3	2	7	4	6	1	1
	TCB	1	2	4	1	2	3	4	4
	TCG	2			9			7	6
	TCW		1	1	2	1	2	2	2
Disturbance (Dist)	TSD							9	
Sentinel-1 (S1)	VV median	8	8	8		8	9		
	VH median	3	5	5		3	1	8	
	RVI								9
Topography (Topo)	elevation				10		10	10	10
	slope	7	7	7	5	6	4		8
	aspect								
	eastness								
	northness								
	TOPODIV	9			6	9	8		
	CHILI								
	mTPI								
	LANDFORM								
Bioclimatic (Bio)	CMD	10	9		8	10			
	GDD				10				
	MAP	6	6	6	3	7	7	5	7
	MAT				9			6	5
	MWT		10						

TABLE 4 Comparison statistics for GEDI Level 2A and 2B footprint metrics and ALS metrics for a sample of ALS units across our study area. Simulated waveform metrics from ALS were used for all comparisons with the exception of COVER, which was produced directly from discrete ALS data (proportion of first returns above 2 m). Validation results are not included for PAVD metrics as those are not available as outputs from the GEDI simulator or directly from discrete ALS. RMSE units are in meters for relative height (RH) metrics and proportions for COVER. FHD is unitless.

GEDI footprint metric	R^2	RMSE	Bias
RH98	0.735	6.831	0.782
RH75	0.698	5.629	−0.119
RH50	0.664	4.551	−0.256
FHD	0.608	2.143	−2.107
COVER	0.436	0.271	−0.142

the top five predictors for most GEDI metrics, and within the top ten predictors for all GEDI metrics apart from FHD (Table 3). Disturbance information (TSD) was only among the top ten predictors for PAVD>20 m. Topography and bioclimatic variables were among the top ten predictors for all GEDI metrics, and among the top five for FHD and the PAVD metrics (Table 4), representing the importance of macro (bioclimatic) and micro (driven by topographic patterns) climatic gradients on driving vegetation within particular forest strata as well as for promoting overall diversity of the vertical vegetation profile.

3.2 Validation assessments

3.2.1 GEDI footprint- ALS comparisons

Comparisons between ALS simulated (RH and FHD metrics) or direct discrete ALS measures (COVER) to those from GEDI footprints showed variability in accuracies across the GEDI metrics (Table 4). We observed the highest comparison accuracies for RH98 (R^2 = 0.74, RMSE = 6.83 m) and the lowest accuracies for COVER (R^2 = 0.44, RMSE = 0.27). The

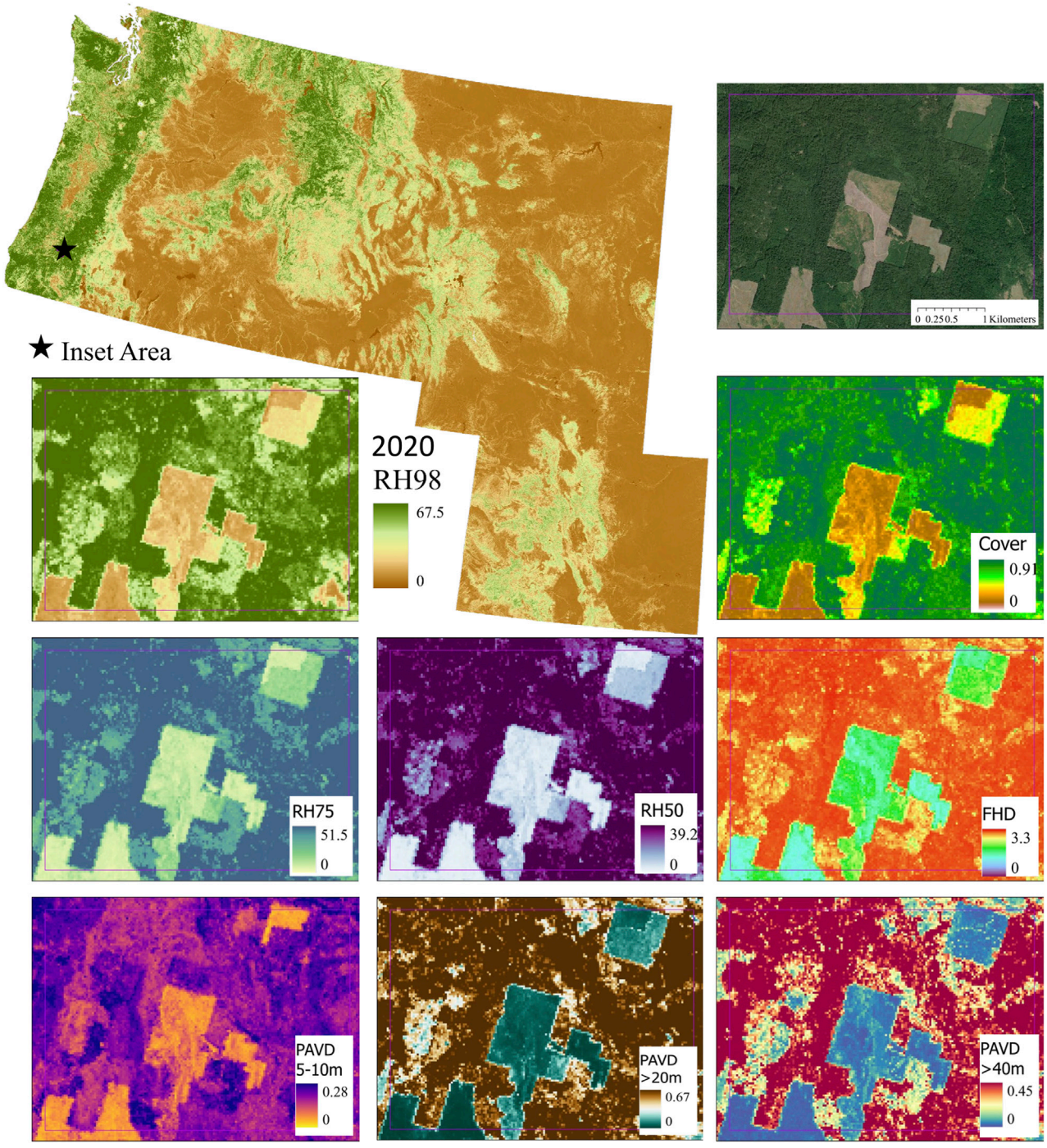

FIGURE 2
GEDI-fusion RH98 2020 map across our 6-state study area with an example inset area showing 2020 maps of the full set of GEDI-fusion maps created using the combined model (RH98, RH75, RH50, FHD, COVER, PAVD 5–10m, PAVD >20m, and PAVD >40 m). All height metrics are in meters, COVER and PAVD metrics are proportions, and FHD is unitless.

remaining height metrics of RH75 and RH50 along with the FHD metric had comparable accuracies, with R^2 values of 0.70, 0.66, and 0.61, respectively. The majority of the metrics had a negative bias with the exception of RH98, which means that the GEDI footprints tended to underestimate values compared to ALS measures. The simulated FHD values exhibited a systematic bias in that they had a higher range of values to those from the GEDI footprints (bias = −2.107), but still exhibited a good validation comparison with the actual GEDI footprint values (Table 4). The lower model performances observed between the GEDI and direct ALS cover measures may be influenced by a multitude of factors; these include the different

TABLE 5 GEDI-fusion gridded predicted map validation with GEDI-simulator ALS (or direct discrete ALS for COVER) sample units for maps created with the combined predictor model and the Landsat/topo/bio model. Validation results are not included for PAVD metrics as those are not available as outputs from the GEDI simulator used to simulate comparable waveform metrics from the ALS sample units, or through direct discrete ALS measures.

	GEDI fusion map metric	Combined model			Landsat/Topo/Bio model		
		R^2	RMSE	Bias	R^2	RMSE	Bias
Modeling Years Maps (2019–2020)	RH98	0.673	6.996	1.109	0.664	7.079	0.961
	RH75	0.633	5.675	0.710	0.625	5.730	0.616
	RH50	0.591	4.589	0.384	0.584	4.612	0.307
	FHD	0.745	2.197	−2.173	0.726	2.207	−2.182
	COVER	0.681	0.235	−0.144	0.674	0.238	−0.148
Hindcasting Map Years (2016–2018)	RH98	0.690	6.296	0.618	0.684	6.344	0.439
	RH75	0.650	5.171	0.563	0.643	5.213	0.325
	RH50	0.599	4.329	0.384	0.596	4.325	0.137
	FHD	0.719	2.198	−2.176	0.717	2.196	−2.174
	COVER	0.653	0.206	−0.126	0.647	0.213	−0.135

representations of cover within waveform vs discrete lidar measures of cover, geolocation errors within the GEDI footprints, or issues with the ground finding algorithm within the GEDI footprint influencing the resulting cover estimate.

3.2.2 Structure map validations

Through our GEDI-fusion frameworks, we were able to successfully scale up GEDI structure information to continuous extents, capturing horizontal and vertical structural patterns across our six-state western U.S. study area (Figure 2). Our results show variability in map performance across the GEDI-fusion metrics although all had moderate to high predictive performance (R^2 = 0.59–0.75; Table 5). Map accuracies and errors were comparable between maps within years of model creation to those representing hindcasted years for both the combined and Landsat/topo/bio models (Table 5). Map accuracy was only slightly higher from the combined model than from the Landsat/topo/bio model for all GEDI-fusion metrics (Table 5). The comparable accuracies and errors between the model-map versions and the consistency between years of model creation to hindcasted years, show promise for the potential of further map hindcasting using the Landsat/topo/bio model prior to years of Sentinel-1 data. From here forward we focus on map validation results for the combined model-based maps for the years of model creation.

Among the GEDI-fusion metrics, FHD had the best map accuracy (R^2 = 0.745), although it still exhibited the systematic bias observed within the footprint level comparisons (Figure 3). RH50 had the lowest map accuracy with an R^2 of 0.59 and RMSE of 4.59 m (Table 5) and map predictions underestimated RH50 compared to simulated values, particularly among higher RH50 simulated heights (Figure 3). The order of validation performance rankings of the GEDI-fusion metrics was different between the footprint- and map-level validations, but the general range of accuracies and errors and moderate-high performance was consistent between scales of analyses (Tables 4, 5).

3.3 Case study: wildlife habitat modeling

Our GEDI-fusion maps show promise for supporting large extent forest wildlife habitat modeling efforts according to the results of our case study, which focused on three species representing different forest structure associations and home range scales. We were able to successfully model habitat for our three cavity-nesting avian species with "good" performance according to AUC values (Swets, 1988) by incorporating structure information provided by the GEDI-fusion maps (Table 6). Habitat models for the pileated woodpecker exhibited the highest AUC values, closely followed by the downy woodpecker, and then the Northern flicker (Table 6). In general, the habitat models had very high specificity with lower sensitivity (Table 6), meaning that the maps were better at predicting areas where the species were not encountered than areas where they were present.

When comparing habitat models incorporating the two different GEDI-fusion mapping versions, we observed minimal differences for all species, with only slightly higher (or directly comparable) AUC values for the habitat models incorporating the GEDI-fusion metrics from the combined models compared to those from the Landsat/topo/bio fusion maps (Table 6). The two versions of the random forest habitat models for each species also had similar ranking for relative importance of predictors (Table 7), so here forward we will only discuss the habitat models incorporating the GEDI-fusion metrics from the combined fusion maps. Following eBird habitat modeling best practices, we incorporated variables within our models related to survey timing and durations. Not surprisingly, both metrics were among the top five predictors for all three species (Table 7). There was a greater probability of detecting an individual of the species earlier in the day when birds are known to be more active and vocal, and as survey durations covered longer periods of time (Figures 4–6). Likewise, measures of topography were included in the top 9 predictors for all three species. Elevation was particularly important for downy woodpecker, for which it was the single most important variable (Table 7). Slope was in the top

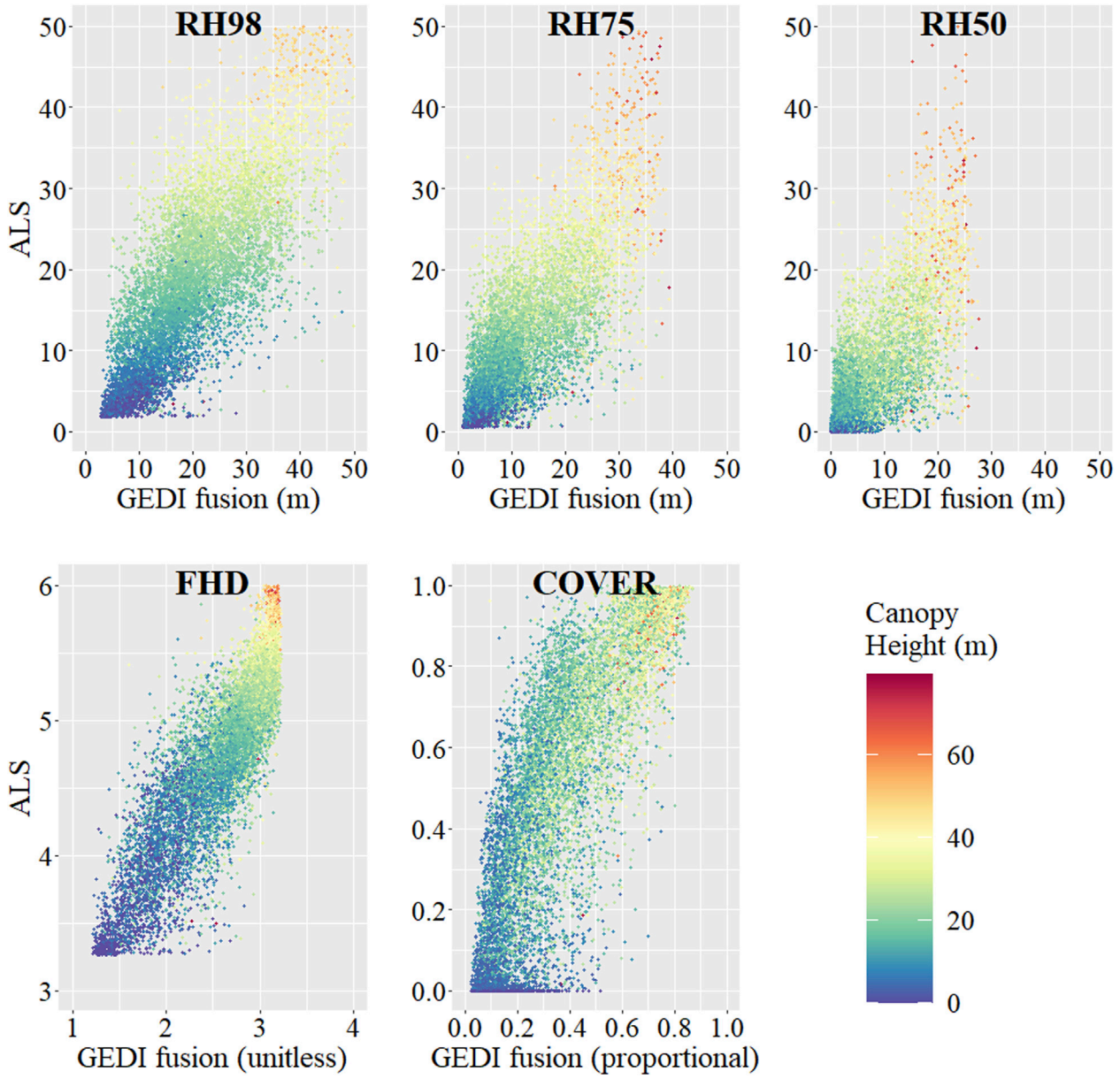

FIGURE 3
Scatterplots of the predicted GEDI-fusion metrics maps (GEDI-fusion) compared to simulated waveform grids (or direct discrete ALS grids in the case of COVER) for our validation ALS units (ALS) for a random sample of validation pixels. Relationships shown are those for the combined model GEDI-fusion maps and for map years and ALS units representing years of model creation (2019–2020). Scatterplot color scale depicts discrete ALS-derived maximum canopy height.

TABLE 6 Comparison of habitat models for three case study wildlife species that incorporate the GEDI-fusion metrics from either the combined model or the Landsat/topo/bio model. Model assessment statistics include the mean square error (MSE), sensitivity, specificity, and area under the curve (AUC).

	Combined GEDI-Fusion metrics				Landsat/Topo/Bio GEDI-Fusion metrics			
Species	MSE	Sensitivity	Specificity	AUC	MSE	Sensitivity	Specificity	AUC
Downy woodpecker	0.056	0.501	0.945	0.862	0.059	0.463	0.945	0.855
Northern flicker	0.135	0.538	0.814	0.762	0.135	0.526	0.826	0.762
Pileated woodpecker	0.039	0.313	0.965	0.865	0.039	0.306	0.968	0.864

TABLE 7 Random forest variable importance rankings for the top 10 predictor metrics within the wildlife case study habitat models using the GEDI-fusion metrics from the combined models. Survey detectability related predictors are italicized as they are not related to environmental occurrence drivers.

Importance ranking	Downy woodpecker (250 m habitat buffers)	Northern flicker (500 m habitat buffers)	Pileated woodpecker (1000 m habitat buffers)
1	elevation	*survey duration*	RH98
2	*survey duration*	*time survey started*	RH75
3	*time survey started*	FHD	*time survey started*
4	slope	RH98	*survey duration*
5	FHD	elevation	COVER
6	COVER	PAVD 5–10 m	Evergreen
7	PAVD >40 m	slope	PAVD >20 m
8	RH98	COVER	elevation
9	PAVD >20 m	RH75	RH50
10	RH75	northness	FHD

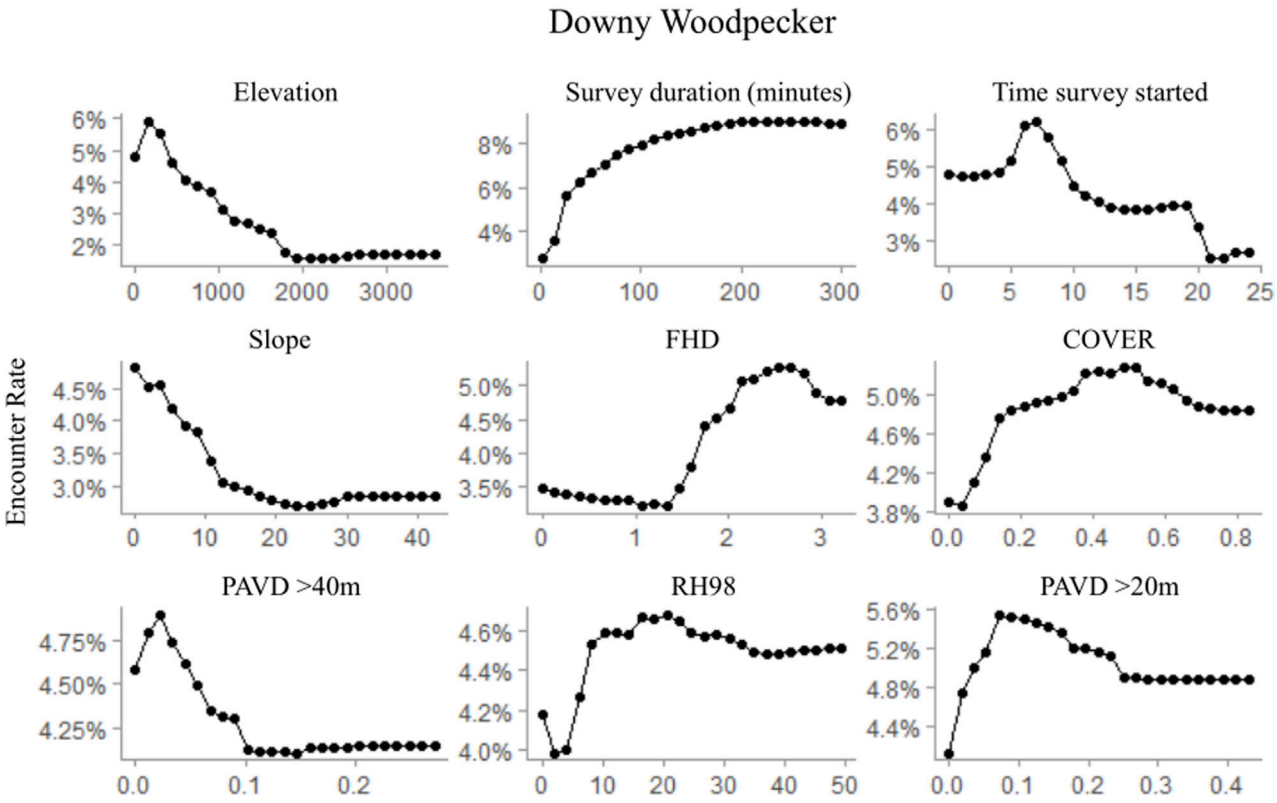

FIGURE 4
Partial dependence plots for the top nine ranked variables within the random forest downy woodpecker occurrence model depicting observed habitat relationships for GEDI-fusion, topographic, and survey timing metrics. Occurrence was modeled at a 250 m radius scale, comparable to the species average home range size.

7 predictors for downy woodpecker and Northern flicker, but not for pileated woodpecker (Table 7).

Regardless of the importance of topography and survey characteristics on detecting an occurrence for the species, GEDI-fusion metrics were also included among the top five most important variables for all species (Table 7). FHD was the most important GEDI-fusion metric for both downy woodpecker and Northern flicker, but was not ranked in the

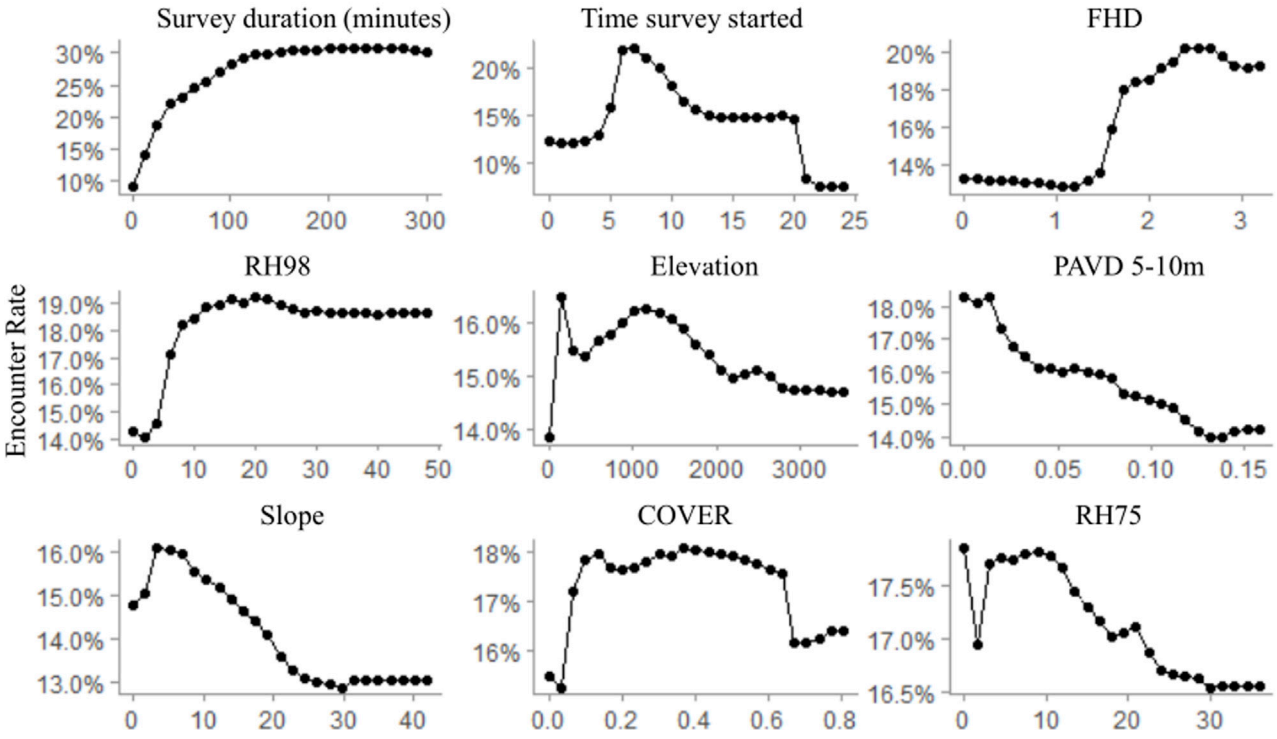

FIGURE 5
Partial dependence plots for the top nine ranked variables within the random forest Northern flicker occurrence model depicting observed habitat relationships for GEDI-fusion, topographic, and survey timing metrics. Occurrence was modeled at a 500 m radius scale, comparable to the species average home range size.

top ten variables for pileated woodpecker (Table 7). Both species showed higher encounter rates at higher FHD (Figures 5, 6). RH measures were particularly important for pileated woodpecker, with RH98 and RH75 ranked as the two most important variables overall and RH50 as the ninth most important variable (Table 7). All three species had highest encounter rates at high RH98 (Figures 4–6). Pileated woodpecker had the highest encounter rate at RH75 > 10 m (Figure 6), while Northern flicker encounter rate was negatively correlated with RH75 (Figure 5). COVER was ranked in the top eight variables for all three species (Table 7). For pileated woodpecker, encounter rate was highest at high COVER (Figure 6), while downy woodpecker and Northern flicker encounter rates peaked at moderate COVER (0.4–0.6; Figures 4, 5). PAVD metrics were included in the top 6–9 predictors for each species, but the strata of greatest importance were different across the species (Table 7). Downy woodpecker encounter rates peaked at low values (<0.05) of PAVD> 40 m and at PAVD>20 m values of approximately 0.1 (Figure 4). Northern flicker encounter rates were negatively related to PAVD5-10 m (Figure 5). Pileated woodpecker encounter rates were positively related to PAVD>20m, but reached an asymptote at PAVD>20 m values of approximately 0.1 (Figure 6).

4 Discussion

With the novel source of three-dimensional data provided by GEDI, it is critical to determine the advantages and drawbacks for use in modeling forest structure across a variety of forest types and architectures. Our study calibrated and tested predictive models across six western U.S. states with a variety of forest types across a bioclimatic gradient from the wetter coastal forests in western Washington and Oregon to the dryer southwest forests and woodlands of Colorado. Within our model assessments, we found moderate to high predictive performance for a set of eight GEDI structure metrics across our diverse study region. Much of the existing GEDI literature has focused on accuracy assessments of the GEDI waveform geolocations and structure measures (Adam et al., 2020; Li et al., 2023), developing footprint level biomass models (Duncanson et al., 2022), or leveraged simulated GEDI data *in lieu* of actual footprint samples (Burns et al., 2020; Silva et al., 2021). Studies have begun to investigate GEDI footprint samples as the basis for scaling up forest structure measures by leveraging fusions of passive and active satellite earth observations, although the majority of those studies have been focused on elevation, canopy height, or biomass (Healey et al., 2020; Potapov et al., 2021; Shendryk, 2022). Our comparison of additional GEDI metrics to ALS and our evaluation of the trade-offs between different data fusion

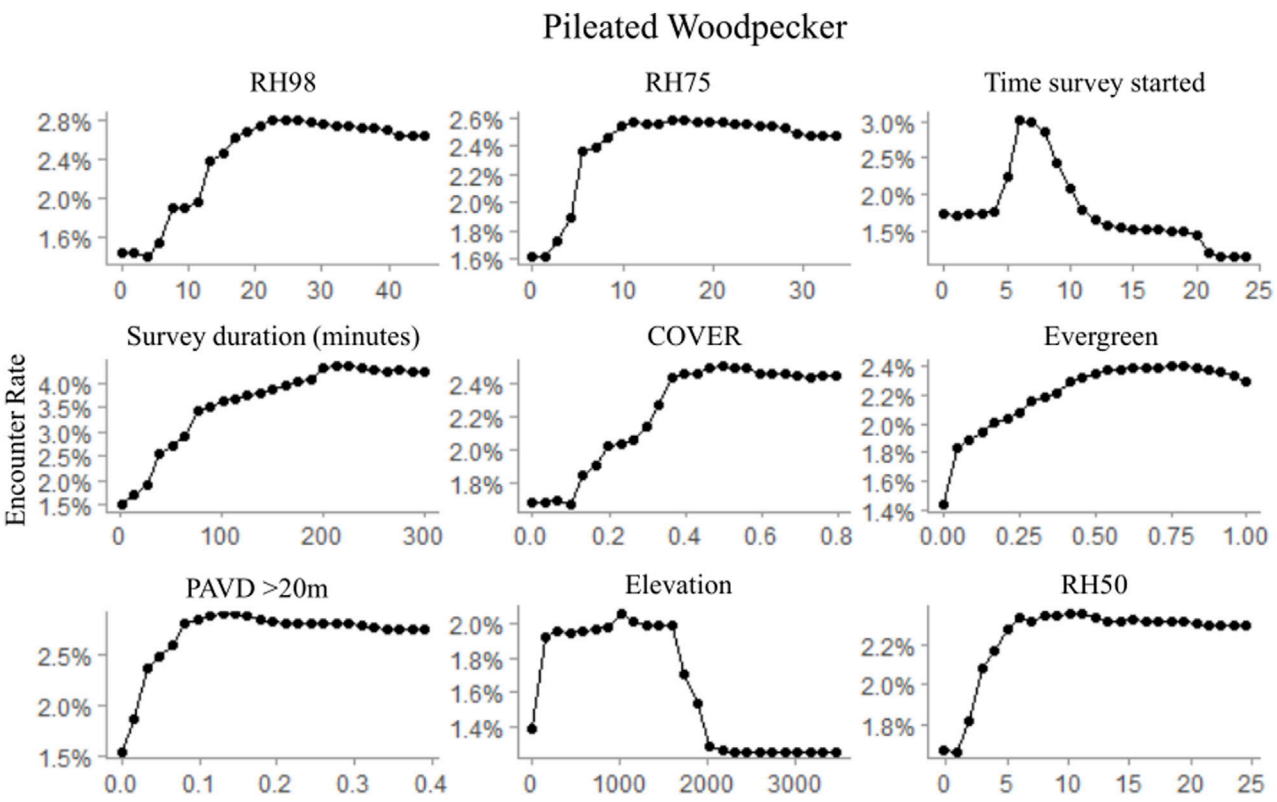

FIGURE 6
Partial dependence plots for the top nine ranked variables within the random forest pileated woodpecker occurrence model depicting observed habitat relationships for GEDI-fusion, topographic, and survey timing metrics. Occurrence was modeled at a 1,000 m radius scale, comparable to the species average home range size.

frameworks provides valuable information on the potential of using GEDI data fusions to provide wall-to-wall structure information across different forest types for metrics useful in wildlife applications. While ALS-validation results within this study varied slightly between the footprint- and map-level assessments, moderate to high performances were observed for all metrics and the general range of accuracies and errors were consistent between scales of analyses. The consistency between footprint- and map-level assessments further supports the promise of data fusion approaches for scaling up GEDI structure information to continuous extents, even with geolocation errors from both GEDI footprints (e.g., up to 10 m error within version 2 GEDI data) and satellite predictors (e.g., potential of 15 m error for Landsat pixels).

Among the studies focused on scaling up GEDI structure metrics through data fusion approaches, the majority have largely focused upon GEDI canopy heights (Healey et al., 2020; Sothe et al., 2022; Ngo et al., 2023). Similar to these previous studies, we found high accuracies within our maps scaling up RH98 samples to continuous extents through optical and radar-based data fusions with an R^2 of 0.673 and RMSE of 6.996 m when compared against simulated ALS validation samples, and an R^2 of 0.757 and RMSE of 5.445 m when assessed using withheld GEDI footprint testing data. Healey et al. (2020) found progressively improved predictions of RH98 when global-extent models were calibrated within blocks of decreasing sizes, with optimization at 3 km. At this 3 km local calibration scale, they were able to achieve an RMSE of 7.08 m for RH98 predictions using only Landsat predictors across global-extents (Healey et al., 2020), which shows promise for the potential of expanding GEDI structure measures to larger extents than included in our regional study. Within sample tropical forest sites in South America and Africa, Ngo et al. (2023) found the greatest modeling success with RH98 among the possible upper canopy height GEDI metrics, supporting our inclusion of this variable. Similar to our results, Ngo et al. (2023) also found optical data the most important predictors of RH98 even when radar was included, with a validation R^2 of 0.62 and RMSE of 5 m when compared to an ALS canopy height. All previous studies of scaled-up GEDI RH98 predictions reviewed here had similar biases to those from our study, with under predictions at taller heights and over predictions at lower RH98 values (Healey et al., 2020; Sothe et al., 2022; Ngo et al., 2023).

To our knowledge, our study represents one of the first studies to extend GEDI data fusion evaluations to additional structure metrics beyond canopy height and biomass across regional extents, such as FHD and PAVD metrics. The novelty of these additional metrics at moderate resolutions across broad extents are likely to be extremely informative for wildlife focused studies. FHD has long been noted to be an important driver of local bird diversity patterns (e.g., MacArthur and MacArthur, 1961). Furthermore, wildlife species are sensitive to the density of vegetation within different height

strata. For instance, a dense upper canopy is important for Pacific marten (*Martes caurina*), which are one of many forest mustelids of management interest (Buskirk and Ruggiero, 1994). Scaling up these metrics and producing continuous data layers is an important first step to explore structural characteristics that are likely to influence wildlife-habitat relationships.

Our results showed promise for applying GEDI-fusion models further back in time than our study period starting in 2016, where we found comparable map validation results for hindcasted years *versus* years of model creation for all structure metrics. We also found comparable performance for models based on Landsat, topographic, and bioclimatic predictors compared to the model that also incorporated Sentinel-1 and disturbance metrics, which supports the findings of Ngo et al. (2023) for the importance of optical data for scaling up GEDI information to continuous extents. The reliance on Landsat data for driving our GEDI-fusion models provides the opportunity to hindcast models further back across the Landsat archive prior to the availability of Sentinel-1 data. In addition, we compared the performance of the two GEDI-fusion map sets (one incorporating all predictors and the second only leveraging Landsat, topography, and bioclimatic predictors) within our wildlife habitat models for three case study species representing different forest structure associations. For all species, we found comparable habitat model performance between the two GEDI-fusion map sets. While Sentinel-1 data are likely to be helpful for wildlife modeling in multiple contexts (e.g., Koma et al., 2022), its exclusion from our GEDI-fusion models did not have downstream effects on wildlife modeling applications. Future studies expanding the time series of hindcasted GEDI-fusion models will require additional validation for the expanded temporal scope outside that of our study, as well as for implications within ecological applications.

The description of vegetation characteristics across broad extents, including vertical and horizontal structure patterns, is critical for managing and conserving wildlife species, since vegetation characteristics provide food, cover, and thermal resources for these organisms. While previous remote sensing-based wildlife habitat modeling efforts have shown value in the use of direct spectral indices from Landsat (Oeser et al., 2020), Sentinel-2 (Valerio et al., 2020), and MODIS (Viña et al., 2008), there is added applicability for habitat characterizations based on structure measures to meet the needs of forest managers who often manage their land in terms of across, or within, stand structure goals. When realized habitat relationships based on structural components can be mapped across the landscape as well as through time (Davies and Asner, 2014; Eitel et al., 2016), there are also opportunities for monitoring changes in habitat availabilities and connectivity through time, or to better match the timing of habitat variables with the timing of wildlife surveys. The annual maps of structure components for 2016–2020 which we produced here were successful in characterizing habitat for our three case study species. We were able to do so leveraging citizen science wildlife survey data sets (i.e., eBird data), where the multiple years of GEDI-fusion maps facilitated the matching of survey years to habitat predictors across multiple years, increasing our records. eBird data are now widely used in studies addressing bird distributions, movements, and diversity hotspots (e.g., Sullivan et al., 2014), and while a limited number of studies to date have included eBird data with GEDI data (Burns et al., 2020, this study), we anticipate that investigations of bird populations and communities that use scaled up, continuous GEDI-fusion data are likely to be of great benefit to the conservation and management of birds given their sensitivity to forest structure.

Important to the mapping of animal habitat are considerations of scale. Animals select their habitat at hierarchical scales from the species' geographic range down to the foraging and cover resources an individual utilizes within their territory (Johnson, 1980), and different species operate at different spatial scales. Spatially continuous representations of fine-moderate resolution vertical and horizontal forest structure and patch characteristics facilitate the simultaneous evaluation of multiple scales of habitat selection for different species (Holbrook et al., 2017), as well as the mapping of realized wildlife habitat relationships across the landscape (Lesmeister et al., 2019), providing valuable forest planning tools. Our study included three species with home ranges that ranged from 2 ha (downy woodpecker; Jackson et al., 2020) to approximately 400 ha (pileated woodpecker in Oregon; Bull and Jackson, 2020), and our analyses resulted in AUCs of 0.76–0.87, suggesting that the GEDI-derived structure data were successfully reflecting habitat elements. This finding is consistent with Smith et al. (2022), who found that GEDI-derived metrics were important for modeling a suite of mammal species that operated at different spatial scales (e.g., snowshoe hares (*Lepus americanus*) and coyotes (*Canis latrans*)). In general, our habitat models had very high specificity with lower sensitivity, meaning that the maps were better at predicting areas where the species were not encountered than areas where they were present; this is common within modeling of wildlife occurrence as a number of non-environmental factors may influence the occupancy of a suitable patch by an individual of a species, including inter- and intra-species competition, predator-prey dynamics, and population densities.

The GEDI metrics used in this study were hypothesized to reflect important forest structural elements for our selected species, and our findings suggest that the GEDI-fusion data were successful in representing those elements. For instance, pileated woodpeckers require large trees for nesting and roosting (Bull and Jackson, 2020), and our results that RH98 were positively associated with the species encounter rates are consistent with pileated woodpecker ecology. Northern flickers often forage at the edge of stands while nesting in large trees (Wiebe et al., 2017), and the positive relationship of this species with increasing levels of RH98 and FHD are again consistent with their nesting and foraging ecology. Burns et al. (2020) found that simulated GEDI data captured structural elements important for multiple bird species, and Smith et al. (2022) similarly found that GEDI-derived structural elements were important in improving distribution models of several mammal species. These studies, in addition to our findings, suggest that GEDI data represent structural elements at spatial scales that are important to a wide variety of wildlife species.

Beyond characterizing wildlife habitat, the remote sensing data fusion frameworks which we developed and tested for scaling up GEDI-based structure information to continuous regional extents may additionally provide value for other forest assessments. For instance, maps of forest structure components, such as height, canopy cover, and vegetation profiles, are also valuable for estimating biomass (Hudak et al., 2012) and forest management planning. In turn, this forest information may also serve as the basis

for studies assessing the tradeoffs between managing for carbon sequestration, timber production, species specific habitat, and overall biodiversity (Kline et al., 2016). Understanding spatial forest structure patterns can also aid in calibrating forest projection models for predicting impacts of land use and management practices, as well as climate change scenarios, on future forested systems (Fekety et al., 2020) and habitat availability. Our focus on the use of only publicly available remote sensing products within our data fusions also ensures the applicability of our developed methods across other regions around the globe and within projects or programs with limited financial resources.

While some countries, such as the United States, benefit from federally funded periodic and systematic forest sampling efforts, including the U.S. Forest Inventory and Analysis (FIA) program, many developing countries do not have comparable forest monitoring programs. These countries contain some of the forests and biodiversity hotspots experiencing the greatest rates of anthropogenic driven land conversions and other threats to forest health and function (Jetz et al., 2007). Such areas could greatly benefit from a consistent forest structure sampling data set, such as GEDI, for regional assessments and monitoring, or to serve as reference data in modeling approaches such as those presented in this study to predict forest structures across continuous extents at resolutions relevant for a diversity of ecological applications. Even within valuable field sampling programs such as FIA, there are drawbacks for serving as reference datasets for some spatial modeling applications because of the need for meeting data security protocols which can restrict their use within cloud computing workflows and through their view of the forest from the ground up with variable georeferencing accuracies (e.g., inconsistent GPS sampling errors across regions and plots). GEDI shows promise for filling this data gap for consistent, 3-dimensional characterizations of the forest strata as measured from above, and publicly available at near global extents (Dubayah et al., 2020). While these data may provide a novel data source in many regions of the world, the rich density and availability of ALS collections along with the diverse gradients of forest types and climatic gradients still make the U.S. a valuable location to test the utility of GEDI for driving such modeling efforts and for validating spatiotemporal biases of the resulting products.

5 Conclusion

The purpose of our study was to test the suitability of the rich reference source of structural information that GEDI footprints provide within various data fusion modeling frameworks for scaling up metrics of value to wildlife habitat modeling applications. We conducted this assessment across broad extents at 30 m resolutions that are of value to a variety of forest assessments. We chose to conduct our analyses within the diverse western U.S. where there were corresponding samples of ALS data for validation purposes. This evaluation was intended to provide insights into the strengths and limitations of the resulting predicted structure maps across a variety of forest types and structures, to better inform similar mapping efforts within regions which do not have ALS samples or forest inventory programs. Since our goal was to use computationally approachable workflows, we filtered and spatially thinned our GEDI footprints to a sample size that balanced model accuracy with computational needs. However, with the greater density of GEDI footprints now available and the hope of an extended mission, exciting opportunities arise for more of a census of forest structure at varying resolutions. Such a census should be tested for greater precision than those found in our study. Increased temporal extents of GEDI data from the originally planned mission period may also help in model stabilities for increased temporal transferability or for directly monitoring change in forest structure or habitat availabilities. Future studies should continue to expand the evaluations of the values and limitations of GEDI structure information and fusion products within assessments of a wider variety of wildlife species and for characterizing biodiversity patterns.

Data availability statement

The datasets presented in this study can be found in online repositories. The names of the repository/repositories and accession number(s) can be found below: ORNL DAAC, https://doi.org/10.3334/ORNLDAAC/2236; Associated code available at https://github.com/VogelerLab/GEDI_fusion_Vogeler_2023.

Author contributions

JV, JH, and KV designed the original study and funding proposal; PF, NS, SF, and JV all contributed at different stages of the study to the processing of remote sensing predictor grids and the filtering/sample design for the GEDI footprint data; JV conducted the statistical modeling and creation of final GEDI-fusion maps; PF processed the ALS validation data sets and worked with JV on validation design and analyses; LE led the case study habitat modeling including compiling of the ebird data sets, with contributions on study design by JV and KV; BB and JH provided input on study designs and interpretations throughout the study; JV led the writing of the article with contributed sections from PF, LE, and KV. All authors contributed to the article and approved the submitted version.

Funding

This work was supported as a funded GEDI Competed Science Team project, funded by NASA through award number 80NSSC21K0192.

Acknowledgments

We would like to thank the GEDI Science Team for advice on guidelines for GEDI data filtering and use during project development and Steven Hancock for assistance in troubleshooting with the gediSimulator. We would also like to acknowledge Sophie Gilbert for discussions early in project development.

Conflict of interest

The authors declare that the research was conducted in the absence of any commercial or financial relationships that could be construed as a potential conflict of interest.

Publisher's note

All claims expressed in this article are solely those of the authors and do not necessarily represent those of their affiliated organizations, or those of the publisher, the editors and the reviewers. Any product that may be evaluated in this article, or claim that may be made by its manufacturer, is not guaranteed or endorsed by the publisher.

Supplementary material

The Supplementary Material for this article can be found online at: https://www.frontiersin.org/articles/10.3389/frsen.2023.1196554/full#supplementary-material

SUPPLEMENTARY TABLE S1
Summary airborne laser scanning (ALS) collection information for sample validation units used within GEDI footprint level comparisons (2019–2020) and map level validations for years of model creation (2019–2020) and years of model hindcasting (2016–2018).

References

Acebes, P., Lillo, P., and Jaime-González, C. (2021). Disentangling LiDAR contribution in modelling species–habitat structure relationships in terrestrial ecosystems worldwide. A systematic review and future directions. *Remote Sens.* 13 (17), 3447. doi:10.3390/rs13173447

Adam, M., Urbazaev, M., Dubois, C., and Schmullius, C. (2020). Accuracy assessment of GEDI terrain elevation and canopy height estimates in European temperate forests: Influence of environmental and acquisition parameters. *Remote Sens.* 12 (23), 3948. doi:10.3390/rs12233948

Asner, G. P., Martin, R. E., Knapp, D. E., Tupayachi, R., Anderson, C. B., Sinca, F., et al. (2017). Airborne laser-guided imaging spectroscopy to map forest trait diversity and guide conservation. *Science* 355 (6323), 385–389. doi:10.1126/science.aaj1987

Bae, S., Müller, J., Lee, D., Vierling, K. T., Vogeler, J. C., Vierling, L. A., et al. (2018). Taxonomic, functional, and phylogenetic diversity of bird assemblages are oppositely associated to productivity and heterogeneity in temperate forests. *Remote Sens. Environ.* 215, 145–156. doi:10.1016/j.rse.2018.05.031

Bergen, K. M., Goetz, S. J., Dubayah, R. O., Henebry, G. M., Hunsaker, C. T., Imhoff, M. L., et al. (2009). Remote sensing of vegetation 3-D structure for biodiversity and habitat: Review and implications for lidar and radar spaceborne missions. *J. Geophys. Res. Biogeosci.* 114 (G2). doi:10.1029/2008JG000883

Bissonette, J. A., and Broekhuizen, S. (1995). *Martes populations as indicators of habitat spatial patterns: The need for a multiscale approach*. Wageningen, Netherlands: Wageningen University & Research.

Breiman, L. (2001). Random forests. *Mach. Learn.* 45 (1), 5–32. doi:10.1023/A:1010933404324

Bull, E. L., and Jackson, J. A. (2020). *Pileated woodpecker (*Dryocopus pileatus*), version 1.0*. Birds of the World. doi:10.2173/bow.pilwoo.01

Bunnell, F., Kremsater, L., and Wind, E. (1999). Managing to sustain vertebrate richness in forests of the Pacific Northwest: Relationships within stands. *Environ. Rev.* 7 (3), 97–146. doi:10.1139/a99-010

Buotte, P. C., Law, B. E., Ripple, W. J., and Berner, L. T. (2020). Carbon sequestration and biodiversity co-benefits of preserving forests in the Western United States. *Ecol. Appl.* 30 (2), e02039. doi:10.1002/eap.2039

Burns, P., Clark, M., Salas, L., Hancock, S., Leland, D., Jantz, P., et al. (2020). Incorporating canopy structure from simulated GEDI lidar into bird species distribution models. *Environ. Res. Lett.* 15 (9), 095002. doi:10.1088/1748-9326/ab80ee

Buskirk, S. W., and Ruggiero, L. F. (1994). "American marten,". Gen. Tech. Rep. RM-254 in *The scientific basis for conserving forest carnivores: American marten, Fisher, lynx, and wolverine in the western United States*. Editors L. F. Ruggiero, K. B. Aubry, S. W. Buskirk, L. J. Lyon, and W. J. Zielinski (Fort Collins: U.S. Department of Agriculture Forest Service, Rocky Mountain Forest and Range Experiment Station), 7–37.

Ceballos, G., Ehrlich, P. R., and Dirzo, R. (2017). Biological annihilation via the ongoing sixth mass extinction signaled by vertebrate population losses and declines. *Proc. Natl. Acad. Sci.* 114 (30), E6089–E6096. doi:10.1073/pnas.1704949114

Ceballos, G., Ehrlich, P. R., and Raven, P. H. (2020). Vertebrates on the brink as indicators of biological annihilation and the sixth mass extinction. *Proc. Natl. Acad. Sci.* 117 (24), 13596–13602. doi:10.1073/pnas.1922686117

Colyn, R. B., Ehlers Smith, D. A., Ehlers Smith, Y. C., Smit-Robinson, H., and Downs, C. T. (2020). Predicted distributions of avian specialists: A framework for conservation of endangered forests under future climates. *Divers. Distrib.* 26 (6), 652–667. doi:10.1111/ddi.13048

Coulston, J. W., Moisen, G. G., Wilson, B. T., Finco, M. V., Cohen, W. B., and Brewer, C. K. (2012). Modeling percent tree canopy cover: A pilot study. *Photogramm. Eng. Remote Sens.* 78 (7), 715–727. doi:10.14358/PERS.78.7.715

Crist, E. P., and Cicone, R. C. (1984). A physically-based transformation of thematic mapper data—The TM tasseled cap. *IEEE Trans. Geosci. Remote Sens.* 22 (3), 256–263. doi:10.1109/TGRS.1984.350619

Daly, C., Halbleib, M., Smith, J. I., Gibson, W. P., Doggett, M. K., Taylor, G. H., et al. (2008). Physiographically sensitive mapping of climatological temperature and precipitation across the conterminous United States. *Int. J. Climatol.* 28 (15), 2031–2064. doi:10.1002/joc.1688

Davies, A. B., and Asner, G. P. (2014). Advances in animal ecology from 3D-LiDAR ecosystem mapping. *Trends Ecol. Evol.* 29 (12), 681–691. doi:10.1016/j.tree.2014.10.005

Davies, A. B., Gaylard, A., and Asner, G. P. (2018). Megafaunal effects on vegetation structure throughout a densely wooded African landscape. *Ecol. Appl.* 28 (2), 398–408. doi:10.1002/eap.1655

Donald, P. F., Fishpool, L. D. C., Ajagbe, A., Bennun, L. A., Bunting, G., Burfield, I. J., et al. (2019). Important Bird and Biodiversity Areas (IBAs): The development and characteristics of a global inventory of key sites for biodiversity. *Bird. Conserv. Int.* 29 (2), 177–198. doi:10.1017/S0959270918000102

Dubayah, R., Blair, J. B., Goetz, S., Fatoyinbo, L., Hansen, M., Healey, S., et al. (2020). The global ecosystem dynamics investigation: High-resolution laser ranging of the earth's forests and topography. *Sci. Remote Sens.* 1, 100002. doi:10.1016/j.srs.2020.100002

Duncanson, L., Kellner, J. R., Armston, J., Dubayah, R., Minor, D. M., Hancock, S., et al. (2022). Aboveground biomass density models for NASA's Global Ecosystem Dynamics Investigation (GEDI) lidar mission. *Remote Sens. Environ.* 270, 112845. doi:10.1016/j.rse.2021.112845

Dunk, J. R., Woodbridge, B., Schumaker, N., Glenn, E. M., White, B., LaPlante, D. W., et al. (2019). Conservation planning for species recovery under the endangered species act: A case study with the northern spotted owl. *PLOS ONE* 14 (1), e0210643. doi:10.1371/journal.pone.0210643

eBird (2021). *eBird: An online database of bird distribution and abundance [web application]*. Ithaca, New York: eBird, Cornell Lab of Ornithology.

Eitel, J. U. H., Höfle, B., Vierling, L. A., Abellán, A., Asner, G. P., Deems, J. S., et al. (2016). Beyond 3-D: The new spectrum of lidar applications for Earth and ecological sciences. *Remote Sens. Environ.* 186, 372–392. doi:10.1016/j.rse.2016.08.018

Fekety, P. A., Crookston, N. L., Hudak, A. T., Filippelli, S. K., Vogeler, J. C., and Falkowski, M. J. (2020). Hundred year projected carbon loads and species compositions for four National Forests in the northwestern USA. *Carbon Balance Manag.* 15 (1), 5. doi:10.1186/s13021-020-00140-9

Filippelli, S. K., Falkowski, M. J., Hudak, A. T., Fekety, P. A., Vogeler, J. C., Khalyani, A. H., et al. (2020). Monitoring pinyon-juniper cover and aboveground biomass across the Great Basin. *Environ. Res. Lett.* 15 (2), 025004. doi:10.1088/1748-9326/ab6785

Friedl, M., and Sulla-Menashe, D. (2015). *MCD12C1 MODIS/Terra+ Aqua land cover type yearly L3 global 0.05 Deg CMG V006*. NASA EOSDIS Land Processes DAAC. Available at: https://lpdaac.usgs.gov/products/mcd12q1v006/ (Accessed December 15, 2022).

Gentry, D. J., and Vierling, K. T. (2008). Reuse of woodpecker cavities in the breeding and non-breeding seasons in old burn habitats in the black hills, South Dakota. *Am. Midl. Nat.* 160 (2), 413–429. doi:10.1674/0003-0031(2008)160[413:ROWCIT]2.0.CO;2

Hancock, S., Armston, J., Hofton, M., Sun, X., Tang, H., Duncanson, L. I., et al. (2019). The GEDI simulator: A large-footprint waveform lidar simulator for calibration and validation of spaceborne missions. *Earth Space Sci.* 6 (2), 294–310. doi:10.1029/2018EA000506

Hancock, S. (2023). *gediSimulator software and documentation*. Available at: https://bitbucket.org/StevenHancock/gedisimulator/src/master/(Last Accessed February 7, 2023).

Healey, S. P., Yang, Z., Gorelick, N., and Ilyushchenko, S. (2020). Highly local model calibration with a new GEDI LiDAR asset on Google earth engine reduces Landsat forest height signal saturation. *Remote Sens.* 12 (17), 2840. doi:10.3390/rs12172840

Hill, R. A., and Hinsley, S. A. (2015). Airborne lidar for woodland habitat quality monitoring: Exploring the significance of lidar data characteristics when modelling organism-habitat relationships. *Remote Sens.* 7 (4), 3446–3466. doi:10.3390/rs70403446

Holbrook, J. D., Squires, J. R., Olson, L. E., Lawrence, R. L., and Savage, S. L. (2017). Multiscale habitat relationships of snowshoe hares (Lepus americanus) in the mixed conifer landscape of the Northern Rockies, USA: Cross-scale effects of horizontal cover with implications for forest management. *Ecol. Evol.* 7 (1), 125–144. doi:10.1002/ece3.2651

Housman, I. W., Campbell, L. S., Heyer, J. P., Goetz, W. E., Finco, M. V., Pugh, N., et al. (2022). *US forest service landscape change monitoring system methods*. Version: 2021.7. Mapping Areas: Conterminous United States and Southeastern Alaska.

Hudak, A. T., Strand, E. K., Vierling, L. A., Byrne, J. C., Eitel, J. U. H., Martinuzzi, S., et al. (2012). Quantifying aboveground forest carbon pools and fluxes from repeat LiDAR surveys. *Remote Sens. Environ.* 123, 25–40. doi:10.1016/j.rse.2012.02.023

Jackson, J. A., Ouellet, H. R., and Rodewald, P. G. (2020). "Downy woodpecker (Dryobates pubescens), version 1.1," in *Birds of the world*. Editor P. G. Rodewald (Ithaca, NY, USA: Cornell Lab of Ornithology).

Jetz, W., Wilcove, D. S., and Dobson, A. P. (2007). Projected impacts of climate and land-use change on the global diversity of birds. *PLOS Biol.* 5 (6), e157. doi:10.1371/journal.pbio.0050157

Johnson, D. H. (1980). The comparison of usage and availability measurements for evaluating resource preference. *Ecology* 61 (1), 65–71. doi:10.2307/1937156

Johnston, A., Hochachka, W., Strimas-Mackey, M., Ruiz Gutierrez, V., Robinson, O., Miller, E., et al. (2019). Analytical guidelines to increase the value of citizen science data: Using eBird data to estimate species occurrence [preprint]. *Ecology*. doi:10.1101/574392

Kennedy, R. E., Ohmann, J., Gregory, M., Roberts, H., Yang, Z., Bell, D. M., et al. (2018a). An empirical, integrated forest biomass monitoring system. *Environ. Res. Lett.* 13 (2), 025004. doi:10.1088/1748-9326/aa9d9e

Kennedy, R. E., Yang, Z., Gorelick, N., Braaten, J., Cavalcante, L., Cohen, W. B., et al. (2018b). Implementation of the LandTrendr algorithm on Google earth engine. *Remote Sens.* 10 (5), 691. doi:10.3390/rs10050691

Key, C. H., and Benson, N. C. (2006). "Landscape assessment (LA)," in *FIREMON: Fire effects monitoring and inventory system*, 164, LA-1.

Kline, J. D., Harmon, M. E., Spies, T. A., Morzillo, A. T., Pabst, R. J., McComb, B. C., et al. (2016). Evaluating carbon storage, timber harvest, and habitat possibilities for a Western Cascades (USA) forest landscape. *Ecol. Appl.* 26 (7), 2044–2059. doi:10.1002/eap.1358

Koma, Z., Seijmonsbergen, A. C., Grootes, M. W., Nattino, F., Groot, J., Sierdsema, H., et al. (2022). Better together? Assessing different remote sensing products for predicting habitat suitability of wetland birds. *Divers. Distrib.* 28 (4), 685–699. doi:10.1111/ddi.13468

Lesmeister, D. B., Sovern, S. G., Davis, R. J., Bell, D. M., Gregory, M. J., and Vogeler, J. C. (2019). Mixed-severity wildfire and habitat of an old-forest obligate. *Ecosphere* 10 (4), e02696. doi:10.1002/ecs2.2696

Li, X., Wessels, K., Armston, J., Hancock, S., Mathieu, R., Main, R., et al. (2023). First validation of GEDI canopy heights in African savannas. *Remote Sens. Environ.* 285, 113402. doi:10.1016/j.rse.2022.113402

Liu, H. Q., and Huete, A. (1995). A feedback based modification of the NDVI to minimize canopy background and atmospheric noise. *IEEE Trans. Geosci. remote Sens.* 33 (2), 457–465. doi:10.1109/TGRS.1995.8746027

MacArthur, R. H., and MacArthur, J. W. (1961). On bird species diversity. *Ecology* 42 (3), 594–598. doi:10.2307/1932254

Martin, K., Aitken, K. E. H., and Wiebe, K. L. (2004). Nest sites and nest webs for cavity-nesting communities in interior British columbia, Canada: Nest characteristics and niche partitioning. *Condor* 106 (1), 5–19. doi:10.1093/condor/106.1.5

Matasci, G., Hermosilla, T., Wulder, M. A., White, J. C., Coops, N. C., Hobart, G. W., et al. (2018). Three decades of forest structural dynamics over Canada's forested ecosystems using Landsat time-series and lidar plots. *Remote Sens. Environ.* 216, 697–714. doi:10.1016/j.rse.2018.07.024

Matthews, S. M., Green, D. S., Higley, J. M., Rennie, K. M., Kelsey, C. M., and Green, R. E. (2019). Reproductive den selection and its consequences for Fisher neonates, a cavity-obligate mustelid. *J. Mammal.* 100 (4), 1305–1316. doi:10.1093/jmammal/gyz069

McGaughey, R. J. (2022). *FUSION/LDV: Software for LIDAR data analysis and visualization*, 4.30. Washington: USDA/Forest Service.

Moisen, G. G., Meyer, M. C., Schroeder, T. A., Liao, X., Schleeweis, K. G., Freeman, E. A., et al. (2016). Shape selection in Landsat time series: A tool for monitoring forest dynamics. *Glob. Change Biol.* 22 (10), 3518–3528. doi:10.1111/gcb.13358

Müller, J., and Brandl, R. (2009). Assessing biodiversity by remote sensing in mountainous terrain: The potential of LiDAR to predict forest beetle assemblages. *J. Appl. Ecol.* 46 (4), 897–905. doi:10.1111/j.1365-2664.2009.01677.x

Müller, J., and Vierling, K. (2014). "Assessing biodiversity by airborne laser scanning," in *Forestry applications of airborne laser scanning: Concepts and case studies*. Editors M. Maltamo, E. Næsset, and J. Vauhkonen (Springer Netherlands), 357–374. doi:10.1007/978-94-017-8663-8_18

Ngo, Y.-N., Ho Tong Minh, D., Baghdadi, N., and Fayad, I. (2023). Tropical forest top height by GEDI: From sparse coverage to continuous data. *Remote Sens.* 15 (4), 975. doi:10.3390/rs15040975

Oeser, J., Heurich, M., Senf, C., Pflugmacher, D., Belotti, E., and Kuemmerle, T. (2020). Habitat metrics based on multi-temporal Landsat imagery for mapping large mammal habitat. *Remote Sens. Ecol. Conserv.* 6 (1), 52–69. doi:10.1002/rse2.122

Olsoy, P. J., Forbey, J. S., Rachlow, J. L., Nobler, J. D., Glenn, N. F., and Shipley, L. A. (2015). Fearscapes: Mapping functional properties of cover for prey with terrestrial LiDAR. *BioScience* 65 (1), 74–80. doi:10.1093/biosci/biu189

PDAL (2022). *Point data abstraction library—pdal.io*. Available at: https://pdal.io/en/2.5.2/(Last Accessed December 5, 2022).

Pekel, J.-F., Cottam, A., Gorelick, N., and Belward, A. S. (2016). High-resolution mapping of global surface water and its long-term changes. *Nature* 540 (7633), 418–422. doi:10.1038/nature20584

Pflugmacher, D., Cohen, W. B., and Kennedy, E. R. (2012). Using Landsat-derived disturbance history (1972–2010) to predict current forest structure. *Remote Sens. Environ.* 122, 146–165. doi:10.1016/j.rse.2011.09.025

Potapov, P., Li, X., Hernandez-Serna, A., Tyukavina, A., Hansen, M. C., Kommareddy, A., et al. (2021). Mapping global forest canopy height through integration of GEDI and Landsat data. *Remote Sens. Environ.* 253, 112165. doi:10.1016/j.rse.2020.112165

R Core Team (2021). *R: A language and environment for statistical computing*. Vienna, Austria: R Foundation for Statistical Computing. from: https://www.r-project.org/(Retrieved May 26, 2021).

Roll, U., Feldman, A., Novosolov, M., Allison, A., Bauer, A. M., Bernard, R., et al. (2017). The global distribution of tetrapods reveals a need for targeted reptile conservation. *Nat. Ecol. Evol.* 1 (11), 1677–1682. doi:10.1038/s41559-017-0332-2

Rouse, J. W., Haas, R. H., Schell, J. A., and Deering, D. W. (1974). Monitoring vegetation systems in the great plains with ERTS. *NASA Spec. Publ.* 351 (1), 309.

Shendryk, Y. (2022). Fusing GEDI with Earth observation data for large area aboveground biomass mapping. *Int. J. Appl. Earth Observ. Geoinf.* 115, 103108. doi:10.1016/j.jag.2022.103108

Shokirov, S., Jucker, T., Levick, S. R., Manning, A. D., Bonnet, T., Yebra, M., et al. (2023). Habitat highs and lows: Using terrestrial and UAV LiDAR for modelling avian species richness and abundance in a restored woodland. *Remote Sens. Environ.* 285, 113326. doi:10.1016/j.rse.2022.113326

Silva, C., Hamamura, C., Valbuena, R., Hancock, S., Cardil, A., Broadbent, E., et al. (2020). *rGEDI: An R package for NASA's global ecosystem dynamics investigation (GEDI) data visualizing and processing*.

Silva, C. A., Duncanson, L., Hancock, S., Neuenschwander, A., Thomas, N., Hofton, M., et al. (2021). Fusing simulated GEDI, ICESat-2 and NISAR data for regional aboveground biomass mapping. *Remote Sens. Environ.* 253, 112234. doi:10.1016/j.rse.2020.112234

Smith, A. B., Vogeler, J. C., Bjornlie, N. L., Squires, J. R., Swayze, N. C., and Holbrook, J. D. (2022). Spaceborne LiDAR and animal-environment relationships: An assessment for forest carnivores and their prey in the Greater Yellowstone Ecosystem. *For. Ecol. Manag.* 520, 120343. doi:10.1016/j.foreco.2022.120343

Sothe, C., Gonsamo, A., Lourenço, R. B., Kurz, W. A., and Snider, J. (2022). Spatially continuous mapping of forest canopy height in Canada by combining GEDI and ICESat-2 with PALSAR and Sentinel. *Remote Sens.* 14 (20), 5158. doi:10.3390/rs14205158

Soto-Navarro, C., Ravilious, C., Arnell, A., de Lamo, X., Harfoot, M., Hill, S. L. L., et al. (2020). Mapping co-benefits for carbon storage and biodiversity to inform conservation policy and action. *Philos. Trans. R. Soc. B Biol. Sci.* 375 (1794), 20190128. doi:10.1098/rstb.2019.0128

Stitt, J. M., Svancara, L. K., Vierling, L. A., and Vierling, K. T. (2019). Smartphone LIDAR can measure tree cavity dimensions for wildlife studies. *Wildl. Soc. Bull.* 43 (1), 159–166. doi:10.1002/wsb.949

Strimas-Mackey, M., Hochachka, W. M., Ruiz-Gutierrez, V., Robinson, O. J., Miller, E. T., Auer, T., et al. (2020). *Best practices for using eBird data. Version 1.0.* Ithaca, NY: Cornell Lab of Ornithology. doi:10.5281/zenodo.3620739

Sullivan, B. L., Aycrigg, J. L., Barry, J. H., Bonney, R. E., Bruns, N., Cooper, C. B., et al. (2014). The eBird enterprise: An integrated approach to development and application of citizen science. *Biol. Conserv.* 169, 31–40. doi:10.1016/j.biocon.2013.11.003

Swets, J. A. (1988). Measuring the accuracy of diagnostic systems. *Science* 240 (4857), 1285–1293. doi:10.1126/science.3287615

Tarbill, G. L., Manley, P. N., and White, A. M. (2015). Drill, baby, drill: The influence of woodpeckers on post-fire vertebrate communities through cavity excavation. *J. Zool.* 296 (2), 95–103. doi:10.1111/jzo.12220

Theobald, D. M., Harrison-Atlas, D., Monahan, W. B., and Albano, C. M. (2015). Ecologically-relevant maps of landforms and physiographic diversity for climate adaptation planning. *PLoS One* 10 (12), e0143619. doi:10.1371/journal.pone.0143619

Thom, D., Rammer, W., Dirnböck, T., Müller, J., Kobler, J., Katzensteiner, K., et al. (2017). The impacts of climate change and disturbance on spatio-temporal trajectories

of biodiversity in a temperate forest landscape. *J. Appl. Ecol.* 54 (1), 28–38. doi:10.1111/1365-2664.12644

US EPA (2015). *Level III and IV Ecoregions of the continental United States [data and tools]*. Available at: https://www.epa.gov/eco-research/level-iii-and-iv-ecoregions-continental-united-states.

Valerio, F., Ferreira, E., Godinho, S., Pita, R., Mira, A., Fernandes, N., et al. (2020). Predicting microhabitat suitability for an endangered small mammal using sentinel-2 data. *Remote Sens.* 12 (3), 562. doi:10.3390/rs12030562

Vierling, K. T., Vierling, L. A., Gould, W. A., Martinuzzi, S., and Clawges, R. M. (2008). Lidar: Shedding new light on habitat characterization and modeling. *Front. Ecol. Environ.* 6 (2), 90–98. doi:10.1890/070001

Vierling, K. T., Bässler, C., Brandl, R., Vierling, L. A., Weiß, I., and Müller, J. (2011). Spinning a laser web: Predicting spider distributions using LiDAR. *Ecol. Appl.* 21 (2), 577–588. doi:10.1890/09-2155.1

Vierling, K. T., Swift, C. E., Hudak, A. T., Vogeler, J. C., and Vierling, L. A. (2014). How much does the time lag between wildlife field-data collection and LiDAR-data acquisition matter for studies of animal distributions? A case study using bird communities. *Remote Sens. Lett.* 5 (2), 185–193. doi:10.1080/2150704X.2014.891773

Viña, A., Bearer, S., Zhang, H., Ouyang, Z., and Liu, J. (2008). Evaluating MODIS data for mapping wildlife habitat distribution. *Remote Sens. Environ.* 112 (5), 2160–2169. doi:10.1016/j.rse.2007.09.012

Vogeler, J. C., and Cohen, W. B. (2016). A review of the role of active remote sensing and data fusion for characterizing forest in wildlife habitat models. *Rev. Teledetección.* 45 (45), 1–14. doi:10.4995/raet.2016.3981

Vogeler, J. C., Hudak, A. T., Vierling, L. A., Evans, J., Green, P., and Vierling, K. T. (2014). Terrain and vegetation structural influences on local avian species richness in two mixed-conifer forests. *Remote Sens. Environ.* 147, 13–22. doi:10.1016/j.rse.2014.02.006

Vogeler, J. C., Yang, Z., and Cohen, W. B. (2016). Mapping post-fire habitat characteristics through the fusion of remote sensing tools. *Remote Sens. Environ.* 173, 294–303. doi:10.1016/j.rse.2015.08.011

Vogeler, J. C., Braaten, J. D., Slesak, R. A., and Falkowski, M. J. (2018). Extracting the full value of the Landsat archive: Inter-sensor harmonization for the mapping of Minnesota forest canopy cover (1973–2015). *Remote Sens. Environ.* 209, 363–374. doi:10.1016/j.rse.2018.02.046

Wang, T., Hamann, A., Spittlehouse, D., and Carroll, C. (2016). Locally downscaled and spatially customizable climate data for historical and future periods for north America. *PLOS ONE* 11 (6), e0156720. doi:10.1371/journal.pone.0156720

Wiebe, K. L., Moore, W. S., and Rodewald, P. G. (2017). "Northern flicker (Colaptes auratus), version 2.1," in *The birds of north America*. Editor P. G. Rodewald (Ithaca, NY, USA: Cornell Lab of Ornithology), 2. Available at: Https://Doi.Org/10.2173/Bna. Norfli.

Wilson, S., Schuster, R., Rodewald, A. D., Bennett, J. R., Smith, A. C., La Sorte, F. A., et al. (2019). Prioritize diversity or declining species? Trade-Offs and synergies in spatial planning for the conservation of migratory birds in the face of land cover change. *Biol. Conserv.* 239, 108285. doi:10.1016/j.biocon.2019.108285

Zald, H. S. J., Wulder, M. A., White, J. C., Hilker, T., Hermosilla, T., Hobart, G. W., et al. (2016). Integrating Landsat pixel composites and change metrics with lidar plots to predictively map forest structure and aboveground biomass in Saskatchewan, Canada. *Remote Sens. Environ.* 176, 188–201. doi:10.1016/j.rse.2016.01.015

frontiers | Frontiers in Remote Sensing

TYPE Original Research
PUBLISHED 13 July 2023
DOI 10.3389/frsen.2023.1197523

OPEN ACCESS

EDITED BY
Rajesh Bahadur Thapa,
International Centre for Integrated Mountain Development, Nepal

REVIEWED BY
Chengcheng Gang,
Chinese Academy of Sciences (CAS), China
Likai Zhu,
East China Normal University, China

*CORRESPONDENCE
Di Yang,
dyang1@uwyo.edu

RECEIVED 31 March 2023
ACCEPTED 04 July 2023
PUBLISHED 13 July 2023

CITATION
Yang D, Fu C-S, Herrero HV, Southworth J and Binford M (2023), Linking forest management to surrounding lands: a citizen-based approach towards the regional understanding of land-use transitions. *Front. Remote Sens.* 4:1197523. doi: 10.3389/frsen.2023.1197523

Linking forest management to surrounding lands: a citizen-based approach towards the regional understanding of land-use transitions

Di Yang[1]*, Chiung-Shiuan Fu[2], Hannah Victoria Herrero[3], Jane Southworth[2] and Michael Binford[2]

[1]Wyoming Geographic Information Science Center, University of Wyoming, Laramie, WY, United States, [2]Department of Geography, University of Florida, Gainesville, FL, United States, [3]Department of Geography, University of Tennessee, Knoxville, TN, United States

The Southeastern United States has high landscape heterogeneity, with heavily managed forestlands, developed agriculture, and multiple metropolitan areas. The spatial pattern of land use is dynamic. Expansion of urban areas convert forested and agricultural land, scrub forests are converted to citrus groves, and some croplands transition to pine plantations. Previous studies have recognized that forest management is the predominant factor in structural and functional changes forests, but little is known about how forest management practices interact with surrounding land uses at the regional scale. The first step in studying the spatial relationships of forest management with surrounding landscapes is to be able to map management practices and describe their proximity to various land uses. There are two major difficulties in generating land use and land management maps at the regional scale by any method: the necessity of large training data sets and expensive computation. The combination of crowdsourced, citizen-science mapping and cloud-based computing may help overcome those difficulties. In this study, OpenStreetMap is incorporated into mapping land use and shows great potential for justifying and monitoring land use at a regional scale. Google Earth Engine enables large-scale spatial analysis and imagery processing by providing a variety of Earth observation datasets and computational resources. By incorporating the OpenStreetMap dataset into Earth observation images to map forest land management practices and determine the distribution of other nearby land uses, we develop a robust regional land-use mapping approach and describe the patterns of how different land uses may affect forest management and *vice versa*. We find that cropland is more likely to be near ecological forest management patches; few close spatial relationships exist between land uses and preservation forest management, which fulfills the preservation management strategy of sustaining the forests, and production forests have the strongest spatial relationships with croplands. This approach leads to increased understanding of land-use patterns and management practices at local to regional scales.

KEYWORDS

citizen science, machine learning, land use, land cover change, google earth engine (GEE), VGI (volunteered geographic information), forest management, landscape ecology

1 Introduction

Land-use change is greatly altering terrestrial ecosystems (Lambin and Meyfroidt, 2011; Forman, 2014). In the Southeastern United States (SEUS), land-use changes are responses to a wide array of socio-economic, environmental, and climate drivers. Not only land conversions but also land management changes alter large proportions of land over time (Wear and Greis, 2013). Land-use change, which is a local-scale land practice, has regional, continental, and global ecosystem consequences. Forest ecosystems are strongly affected by anthropogenic factors both inside and outside the forest, such as timber extraction and suburban growth and cultivation (Radeloff et al., 2010; Wear and Greis, 2012). Forest management practices, which are forest land uses, are one of the major drivers of changes in forest structure and function (Becknell et al., 2015; Marsik et al., 2018).

Forests play an important role in the ecological and social conditions of the SEUS. They provide critical habitat for a wide variety of plant and animal species, including many that are threatened or endangered. Forests also regulate local and regional water cycles, help control flooding and soil erosion, and contribute to the overall health of the landscape (Riitters et al., 2002). In addition to their ecological importance, forests are also an important part of the region's social and economic fabric (Marsik et al., 2018). They provide recreation opportunities for residents and tourists alike, support a thriving timber industry, and offer a host of other economic benefits. With all these benefits, it is clear that forests are a vital part of the SEUS. However, they are also under threat from a variety of sources, including development, pollution, and climate change (Becknell et al., 2015). It is important to work to protect and restore forests in the region so that they can continue to provide these important benefits for generations to come.

The interactions among different land-use types may be forces of landscape-wide and even global importance. Land-use transitions from one type to another are more likely in areas already close to the second land uses (Fischlin et al., 2007). For example, in the SEUS significant expansions of urban areas often convert forested land to urban uses, especially as urban land spreads outwards from the already urbanized areas, and cropland has been converted to pine plantations in areas where plantations are nearby (Wear and Greis, 2002; 2013). These kinds of landscape transitions may represent macrosystem changes depending on their scale and extent and can have immediate local social and ecological implications for landowners and their management practices (Schulte et al., 2007; Wassenaar et al., 2007). As such, understanding the relationships between various land-use patterns and forest management at a macrosystem level is of utmost importance. The current body of knowledge regarding the influence of different land-use patterns' proximity on forest management practices, and *vice versa*, remains limited. To address this gap, we undertake an investigation that will contribute to the study of effective forest management strategies and to understanding of the influence of the proximity of various land-use types on land-use and land-cover transitions.

One way to protect and restore forests is to understand better the land-use patterns around them. In many cases, human activities such as cultivation, housing developments, and industrial development, can influence forest ecosystems (Kramer and Doran, 2010; Wear and Greis, 2012; Wear and Greis, 2013). However, if we study these land uses and their effects on forest ecosystems, we can develop practices for mitigating the impacts. This will help to ensure that forests in the SEUS are healthy and thriving. Also, differently managed forests can spur developments and land-use changes in different ways (Kramer and Doran, 2010; Wear and Greis, 2012; Wear and Greis, 2013). For example, landscapes in proximity to preserved forested regions have more potential to be converted to residential areas (Kramer and Doran, 2010) and residential property close to protected areas is usually more valuable.

As implied by the material and energy flows and organism and gene exchanges that occur between them, forest ecosystems and the land use that surround them have an intricate relationship. While the interactions between protected forests and adjacent land uses have been extensively studied, our understanding of the effects of non-protected forest land conversion on adjacent land uses remains limited. Despite the fact that a number of theoretical interactions have been proposed (Groenveld et al., 2017; Briassoulis, 2020), the lack of generalizability in case studies has contributed to a paucity of knowledge regarding the mechanisms underlying these interactions. Effective land management strategies require a comprehensive and nuanced understanding of the relationship between non-protected forest land conversion and nearby land uses. Hansen and Ruth (2007) review on the ecological mechanisms linking protected areas to surrounding lands provides a valuable starting point for such investigations.

Changes in land use over time are also of critical importance. Land-use changes are associated with social and biophysical system changes (Turner et al., 1996). For example, land-use change can lead to the fragmentation of forests which can then impact ecosystem function (Riitters et al., 2002). Additionally, land-use change can also alter hydrological regimes and water quality. As such, it is important to consider land-use change when planning for the future of forest ecosystems in the SEUS. Changes in land-use intensity and land-use types influence nearby and even distant forest ecosystems (Dunford and Freemark, 2005; Fahrig, 2013). Most land change studies focus only on the transitions among the land covers at the class level across the landscape (e.g., the conversion between forest and cropland) (Verburg et al., 2002; Sohl and Sayler, 2008; Verburg et al., 2009), rather than the within-class transitions. e.g., an area stays forested but may change use from a natural forest area to silviculture or an agricultural cropping system, i.e., agroforestry. Researchers also focus on projecting land-use changes and trajectories based on past patterns (Lawler et al., 2014). In addition, ground-reference data related to land-use temporal changes are often omitted, most often due to lack of availability (Hurskainen et al., 2019).

The principles of mapping land use do not share the same assumptions as those of mapping land cover. Land cover refers to the physical land cover on the Earth's surface, including both natural and man-made features (Comber, 2008). Land cover is the physical land cover type, such as buildings, roads, forests, grassland, or wetland. It can be monitored using satellite remote-sensing techniques. Forest cover is one type of land cover that is of particular interest for many reasons, including the support it provides for biodiversity, ecohydrological processes, other environmental services, and combating climate change. By

monitoring forest cover, we can better understand the health of these ecosystems and take action to protect them (Becknell et al., 2015).

Land use is the human adoption of land cover to meet specific needs. Land use refers to the way humans use land cover, such as for agriculture, housing, or recreation (Comber, 2008). Land-use features are decided and driven by people's land-management behaviors. We can monitor land-use change by looking at both land-cover and land-use information. There are many ways to monitor land-use changes. One common method is remote sensing, which uses satellites or aircraft to collect images of the Earth's surface. This can be used to track changes in land cover over time (DeFries et al., 2007). Another common method is ground-reference data collection, which involves physically visiting sites on the ground to observe and document changes. Ground-reference data are often used in combination with remote sensing to verify and interpret satellite data (Sanchez-Azofeifa, 1996; Marsik et al., 2018). It can be difficult to distinguish land use from land cover using remote sensing alone, so ground-reference data are an important part of land-use monitoring.

There are many challenges to monitoring land-use change. One challenge is that land use can be hidden by land cover. For example, a forest may still be a forest even if it will soon be logged or is part of a protected area. Another challenge is that land use can vary greatly over short distances. For example, a field may be used for agriculture on one side and housing on large parcels on the other. This can make it difficult to create accurate maps of land use. Despite these challenges, it is important to monitor land-use change. Land use has a major impact on the environment and understanding how it is changing is essential for effective environmental management (Turner, 1994; Schulte et al., 2007).

In the phrase "social-ecological Earth observation dataset", the term "social" relates to information about human social systems and includes citizen-contributed data, satellite-collected Lights at Night data (Sutton et al., 2009; Li et al., 2017) and land ownership data. To map regional land management practices, we utilized ground data such as ownership information, long-term phenological patterns and their changes, and the structure of the surrounding landscape to infer forest management classes (Marsik et al., 2018). We use the Earth observation datasets, which have close relationships with human activities, such as the night light (VIIRS Stray Light Corrected Nighttime Day/Night) and land ownership (Marsik et al., 2018) databases. Citizen science is a term used for scientific research that is conducted by members of the public, rather than professional scientists (Goodchild, 2007). Citizen science projects can be used to collect data on a wide variety of topics, from environmental conditions to astronomical events (Goodchild and Glennon, 2010; Haklay, 2010). Citizen science has been used in land-use mapping for many years (Goodchild, 2007; Antoniou et al., 2016). These maps are important tools for conservation planning, as they can help decision-makers understand where different types of ecosystems are located. Citizen science projects can contribute to the creation of these maps by collecting data on the location and extent of different types of land cover (Yang et al., 2017). Recent advances in technology have made it possible for citizen science projects to collect data more efficiently and accurately than ever before (Haklay and Weber, 2008; Neis and Zielstra, 2014; Yang et al., 2017). For example, the use of GPS devices and smartphones can allow citizen scientists to quickly and easily record the location of different types of land cover and use. In addition, online mapping tools can be used to share data with other project participants and mapmakers. Citizen science projects like these are important and useful for creating accurate and up-to-date land-use maps. Citizen science can increase our understanding of land-use patterns and management practices while engaging the public at local, regional, and global scales to study their environment (Goodchild, 2007; Haklay and Weber, 2008; Goodchild and Glennon, 2010; Theobald et al., 2015). For example, citizen-contributed data from New York Breeding Bird Atlas detected the potential for colonization, extinction, and the absence of bird species due to forest fragmentation (Zuckerberg and Porter, 2010). Involving citizen science to inform land-use management and conservation practices can usually lead to a more effective outcome of research success and land management practices, because it raises awareness and garners support for the project among the public (Dickinson et al., 2012; Yang et al., 2017).

Open Street Map® (OSM) (www.OpenStreetMap.org) is a collaborative project to create a free, editable map of the world. The maps are created by volunteer contributors using GPS devices, aerial photography, and other sources. OSM is used by individuals and organizations for a variety of purposes, including land-use planning, disaster response, and route planning (Haklay and Weber, 2008; Neis and Zielstra, 2014; Yang et al., 2017). OSM is one example of a citizen science project that relies on the voluntary contributions of its participants to create a useful resource for the community. Organizations such as the Red Cross and the United Nations Office for Coordination of Humanitarian Affairs use OSM data to plan relief efforts and respond to natural disasters. Businesses such as Foursquare and Craigslist use OSM data to provide location-based services. Non-profit groups such as Mapbox and OpenStreetMap US use OSM data to create maps and apps that are available to the public. The success of OSM depends on the continued participation of its contributors.

In this research, we collect historical crowdsourced data from OSM to map regional land use and then generate a land-use change map over a 5-year period to determine how land use and thus land management have changed. We then examine the proximity of different land uses to areas with four different forest management approaches to determine the spatial relationships of forest management with land uses. We focus on the SEUS region, which has high landscape heterogeneity, heavily managed forestlands, developed agriculture, and multiple metropolitan areas.

There are two main types of forest ownership in the southeastern United States: public and private. Public forests are owned by governments and are managed for the benefit of the public. Private forests are owned by individuals or companies and are managed for their own benefit. In SEUS, we define forest management types in four categories: production forestry, ecological forestry, wilderness or preservation, and passive forestry (Becknell et al., 2015; Marsik et al., 2018). Ecological management involves managing the forest in such a way as to not only realize gains from timber harvest but also maintain or improve the forest's ecological health (Franklin et al., 2018). This may include activities such as planting native species, maintaining an uneven age structure so that forest structure will be more diverse, thinning non-native or invasive species, and reducing pollution. Passive management is a hands-off approach that generally involves

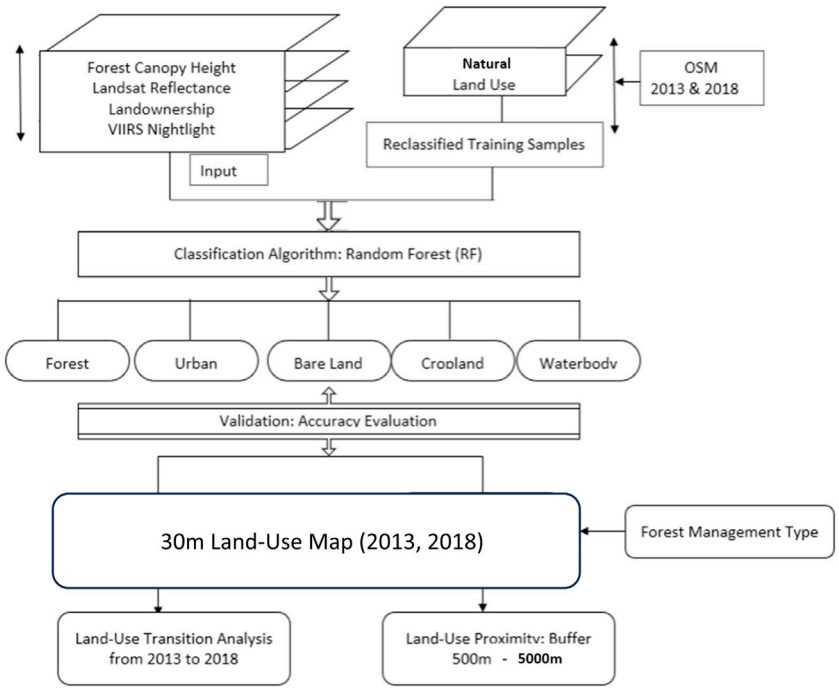

FIGURE 1
Flowchart detailing analysis steps for the study.

leaving the forest to its own devices. This approach is often used in areas where the forest is not actively threatened by human activity or natural disasters, is in soils too wet, such as riparian areas, to support harvesting machinery, or belongs to owners who simply want to have an intact forest. Wilderness or preservation management, in contrast, seeks to protect the forest in its natural state and may be used in certain public forests where conservation is the primary goal. Each of these management approaches comes with its unique set of consequences and complexities on the landscape, affecting not only the biodiversity within the forests but also the patterns of land use in surrounding regions. Recent developments in cloud computing, collaborative mapping, and user-generated content platforms, such as volunteered geographic information (VGI), have spawned a new era in geographic visualization (geo-visualization or mapping and visualizing the world), such that the combination of crowdsourced mapping and cloud-based computing may overcome these difficulties (Southworth and Muir, 2021).

In this study, OSM is incorporated into mapping land use to identify and monitor land use at a regional scale. We use Google Earth Engine (GEE) to enable large-scale spatial analysis and image processing by providing a variety of Earth observation datasets and powerful computational resources (Haklay and Weber, 2008; Southworth and Muir., 2021). By focusing our prime objective on the mapping of land management practices, a robust, automated regional land-use mapping approach is developed by incorporating the OSM dataset with GEE's available Earth observation imagery. Since the SEUS is heavily forested, the diverse land-use characteristics are often hidden under the canopy, which results in the land-use patterns of the SEUS not being visible with routine remote sensing methods. In this analysis, we incorporate anthropogenic Earth observation datasets (such as nightlight and ownership) with the crowdsourced OSM database to first create land-use maps for two dates: 2013 and 2018, across our study area, and to then create a land-use change analysis or transition image from these products. We then use these individual land-use maps for 2013 and 2018 to identify all forest patches, indicating forest management type as part of the patch type record, and highlight the fragmented nature of forest cover across this region as a function of extensive road networks (Reed et al., 1996; Heilman et al., 2002; Riitters et al., 2002). Finally, we then study the spatial relationships among these managed forest patches and the land use surrounding these patches as we increase in distance from the forest patch edge. By proposing a land-use change mapping framework, we aim to increase the accuracy of mapping land use and expand the ability to map land use at the regional scale. This analysis examines how the four dominant forest management types interact with the surrounding land use in the SEUS. In the heavily forested SEUS, we examine the spatial patterns of land uses surrounding forest ecosystem patches by asking the research question: "What are the land-use patterns extending outwards from differently managed forestlands and how do these change over time?"

2 Data sources and methods

The methods used within this study are highlighted in the flowchart (Figure 1) indicating the multiple input data and steps taken as part of this research. The specific data and details on the analysis are outlined below.

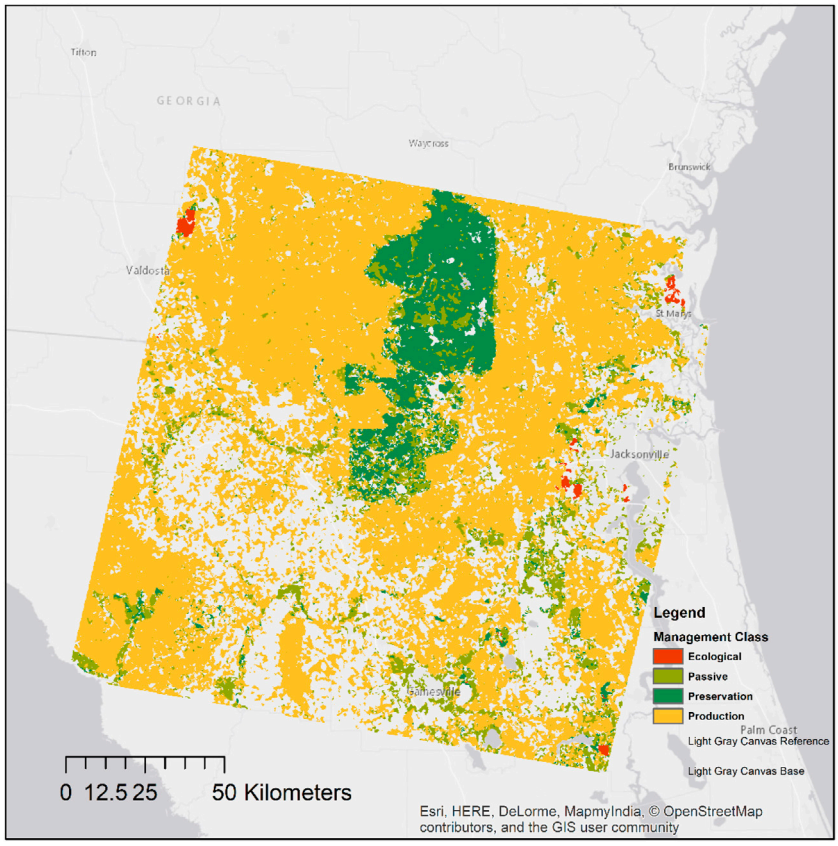

FIGURE 2
The map outlining the study region and the spatial distribution of forest-management types within the study region. The light gray part represents non-forest regions. Forest management classes were mapped by Marsik et al. (2018).

2.1 Study area

As a case for classifying land use and monitoring land-use change around public and private forests, we chose an area of the Southeastern U.S. Coastal Plain corresponding approximately with the Worldwide Reference Systems II (WRS-2) path 17 row 39 (P17 R39), with bounding latitude and longitude coordinates of approximately 31°13′N, 83°10′W (northwest corner), and 29°20′N, 81°41′W (southeast corner) (Figure 2). The study area covers an area of about 34,000 km^2. The study area has a good representation of all types of land uses and forest management practices in the SEUS. This heterogeneous landscape consists of a mixture of natural and plantation forests, large and small wetlands, several rivers with extensive riparian areas, urban centers, urban and rural residential areas, and commercial and small-scale agricultural operations. This diversity of land-cover types is spatially heterogeneous, and patch sizes within the vegetation classes vary across a wide range of scales.

2.2 Land-use change mapping strategy design

The integration of remote sensing and GIS presents a robust tool to monitor, quantify, and characterize landscape features in both time and space (Reed et al., 1996; Heilman et al., 2002; Riitters et al., 2002; Hawbaker and Radeloff, 2004; Espirito-Santo et al., 2014), making it a promising approach to land-use change mapping strategy design. The advent of Volunteered Geographic Information (VGI) platforms has ushered in a new era of mapping and visualizing land systems (Neis et al., 2011; Neils and Zielstra, 2014; Hakley, 2010). Notably, OpenStreetMap (OSM) is an excellent example of a VGI platform that facilitates the rapid expansion of big data and cloud-based computing while providing a more extensive range of applications than official geographic road databases (Zielstra and Hochmair, 2013). The use of OSM allows for the creation of more current and comprehensive maps that reflect temporal changes (Girres and Touya, 2010; Estima and Painho, 2013). Our land-use change mapping strategy design focuses on creating multi-functional management units, with urban areas being excluded from the study using urban boundaries from the TIGER database (TIGER, 2015).

2.3 Historical OSM

There are several definitions made by OSM ODbL that need to be clarified, namely,: objects, tags, and keys. The attributes of OSM

TABLE 1 Crosswalk dictionary between natural and land-use classes and OSM labels.

This paper land-use type	OSM labels		
	Key: Natural	Key: Landuse	Key: Amenities and places
Cropland/ Rangeland	Grassland, agricultural, or USER_DEFINED	Farmland, farmyard, grass, greenfield, greenhouse_horticulture, meadow, orchard, pasture, plant_nursery, recreation_ground, vineyard, or USER_DEFINED	
Commercial/ Industrial		Commercial, retail, cemetery, depot, garages, religious, Industrial, quarry, port, salt_pond, or USER_DEFINED	Bar, bbq, café, fast_food, food_court, restrurant, college, kindergarten, archive, school, university, boat_rental, car_rental, bus_station, parking, bank, clinic, dentist, casino, cinema, nightclub, studio, post_office, prison, or USER_DEFINED
Managed forests	Wood, tree_row, scrub, or USER_DEFINED	Forest, conservation, reservoir, or USER_DEFINED	
Residential		Residential, allotments, or USER_DEFINED	House, apartment
Water body	Water, wetland, bay, lake, springs, or USER_DEFINED	Basin, pond, or USER_DEFINED	

User-defined: Many land-use features are already on Map Features, but users are flexible in defining the features. https://taginfo.OpenStreetMap.org/.

are called "tags", and the major features stored in OSM are called "keys". An OSM "object", e.g., a building, a road, or a parcel, is composed of geographic location information and a set of "tags". Each object in the OSM must have at least one tag, but there is no limit to the number of tags a specified object can have. The official list of OSM tags is available on the map features wiki page: https://wiki.OpenStreetMap.org/wiki/Map_Features. The tag taxonomy has been agreed upon over years of experience and is still being updated, which reflects a folksonomy approach based on a negotiation process among OSM contributors (Ballatore and Mooney, 2015). The "tags" can be reorganized, combined, and grouped in various semantic ways to highlight the geospatial distribution of different topics, and as such, they can be utilized in different research projects.

The full historical OSM database is available at https://planet.osm.org. In this study, historical OSM was accessed through the OSM API (https://wiki.OpenStreetMap.org/wiki/API), which allows us to fetch, save, and analyze the raw data from OSM over time. In our study area in 2013, there were 1,199 objects representing buildings on the OSM in our study area, the number changed to 66,488 by October 2018. By 2018, there were more than 486 contributors who updated and edited the roads feature in the study area, 230 contributors fixed the building features OSM and 262 contributors to amenities features.

2.4 OSM land-use classification semantics

In OSM the land-use tags are often marked with different understandings of the land, e.g., for rangeland, it was marked as "yellow field" or "farm" and even "grass". The relationship between OSM tags and labels was built based on the land-use classification strategy with a framed dictionary (Table 1). To achieve this, we converted OSM tags to five land-use classes: cropland/rangeland, commercial/industrial, managed forest, residential areas and water body. We then regrouped the OSM tags into those targeted classes based on the framed dictionary (Table 1).

The OSM condensed land use definitions in this study are:

1) Cropland/rangeland—A land-use category, which is used to produce crops or has the potential for sustainable grazing (native grasses, grass-like vegetation, shrubs).
2) Commercial/Industrial—A land-use category consisting of industrial, commercial, and institutional land, construction sites, public administrative sites, railroad yards, cemeteries, airports, golf courses, quarries, water control structures (Wear and Greis, 2013).
3) Managed Forests—A land-use category that is covered with forest. The categories of forest management are generally consistent with the forest management type map produced by the MANDIFORE group (Marsik et al., 2018). We also included the areas that showed evidence of the natural regeneration of trees and not currently developed for non-forest use.
4) Residential—A land-use category consisting of single- or multi-family residential, apartment buildings, and small parks within the urban and built-up areas.
5) Waterbody—Open water

2.5 Earth observation data

Several different Earth observation datasets were used in the analysis, including.

1. We used Landsat data for 1/1/2013 and 8/1/2018, available on the GEE API (Google Earth engine ID: LANDSAT/LC8_L1T_ANNUAL_GREENEST_TOA). These Collection 2 Landsat 8 Operational Land Imager (OLI) data have a spatial resolution of 30-m and are Top-of-atmosphere (TOA) and Landsat 5 TOA reflectances (Chander et al., 2009).
2. We used global forest canopy height, version 2005 (Simard et al., 2011): This dataset represents the canopy height at a global level by incorporating the Geoscience Laser Altimeter System (GLAS)

and ancillary data (Google Earth engine ID: NASA/JPL/global_forest_canopy_height_2005)

3. Nighttime satellite imagery was used as proxies of mapping human wellbeing and urban development (Sutton et al., 2009; Li et al., 2017) (Google Earth engine ID: NOAA/VIIRS/DNB/MONTHLY_V1/VCMSLCFG). VIIRS Stray Light Corrected Nighttime Day/Night Band Composites Version 1 (Miller et al., 2013): The dataset of nighttime has the global monthly aggregated nightlight time data.
4. Land ownership is one of the key factors delineating land use and forest management, especially under the currently ongoing rapid urbanization and increasing rural development, which may affect and alter the forest management patterns. Landowners are classified as public and private. There are six sub-types of public ownership, which are federally protected, federal, state protected, state, military, and local. Also, there are four sub-types of private ownership: non-government organization, private, family, and corporate. The ownership classification strategy is made based on different management objectives, as well as landowner skills, budgets, and interests. The Protected Area Database for the United States (PAD-US) is the primary data source to identify public ownership (USGS-PADUS-2.0).

2.6 Random Forest classification

We built a Random Forest (RF) classifier by incorporating multiple remote sensing datasets as covariates, using GEE as the mapping platform, and crowdsourcing-derived geotags as training sample databases. We used OSM derived data as training points to extract spectral statistics for use in the RF classifier (Breiman, 2001). The efficiency and accuracy of the RF classifier have been widely tested and recorded throughout regional landscape mapping. The principle of RF is to apply a bootstrapping aggregated sampling technique to build a series of individual decision trees for the classifier. The major advantages of the RF classifier are the capability of handling a large number of training samples, its efficiency in dealing with the large regional database, and its robustness to outliers and noise. To remove the noise from the classification outputs, we used a 3 × 3 cell majority filter for all land-use classes, except for waterbodies for both the 2013 and 2018 images. All images were resampled to 30 m spatial resolution using the nearest-neighbor filter algorithm.

The total number of OSM-derived training samples are 3,150 and 3,870 for 2013 and 2018, respectively. We specified two sets of 10-fold cross internal validations for the RF classifier and assessed the individual contribution from each land-use type to the overall accuracy of the land-use pattern maps. To optimize the RF algorithm, we utilized 500 trees, a 70/30 split for training/validation, and modified other parameters. These parameters were carefully selected to balance model complexity and accuracy and to avoid overfitting. Our results demonstrate the effectiveness of the RF algorithm in accurately classifying land use from remote sensing data. Furthermore, we present a novel approach for generating training data using existing land use features, which enhances the accuracy and efficiency of the classification process. Overall, it highlights the potential of the RF algorithm for land use classification in complex and diverse landscapes.

TABLE 2 Management Patch size statistics of characteristics within the study area.

Unit (ha)	Min	Max	Mean	Std
Total area	5.37	194,137.30	26.60	718.08
Ecological	5.37	2,683.23	19.37	92.03
Passive	5.37	7,700.88	22.48	95.95
Preservation	5.37	194,137.30	40.73	2,208.42
Production	5.37	12,992.22	41.54	275.10

2.7 Forest patch analysis

First the forest patches, defined as groups of contiguous pixels of the same management type separated from other groups by other management types or non-forest pixels, were identified spatially, and the size characteristics of each patch were determined for both 2013 and 2018, as follows: For each forest patch the forest management type (ecological, passive, preservation or production) was recorded. To test the land-use variations around each type of managed forest, a series of spatial analyses were conducted. We created nine buffers at increasing distances from the edge of the forest patches, from 500 m to 5,000 m at an interval of 500 m. The reason to pick a buffer size ranging from 500 m to 5,000 m is based on the average patch size from the management map (Figure 2; Table 2). In the study area, the overall average management patch size is 26.6 ha, which leads to the appropriate minimum buffer rings starting at around 360 m, according to the methods in Defries et al. (2007). However, from Table 2, as the size range of management patches is variable, we set nine other increasing buffers to allow for an improved analysis of the landscape. The land-use combinations of 2013 and 2018 of cropland, residential areas, and commercial/industrial areas were compared by plotting the proportion of each land-use type in the different buffer distances. At larger scales of analysis, buffer overlap could influence the independence of samples; however, after calculating the maximum buffer overlap with other forested patches, which was 6.8% of the total study areas, we assume a minimal impact of buffer overlap regionally.

3 Results

3.1 Land-use compositions and dynamics

Land use maps for 2013 (Figure 3) and 2018 (Figure 4) are given here. Since the urban areas were masked, residential areas represent the exurban and rural residential areas. There are significant differences between the two study dates, despite their only being 5 years apart. The proportion of the landscape in the residential area increased from 4.93% to 8.87%. For the commercial/industrial class, an increase from 0.59% to 2.97% was found, and a similar trend was found with the cropland/rangeland class with an increase of 6.22%–10.32% (Table 3).

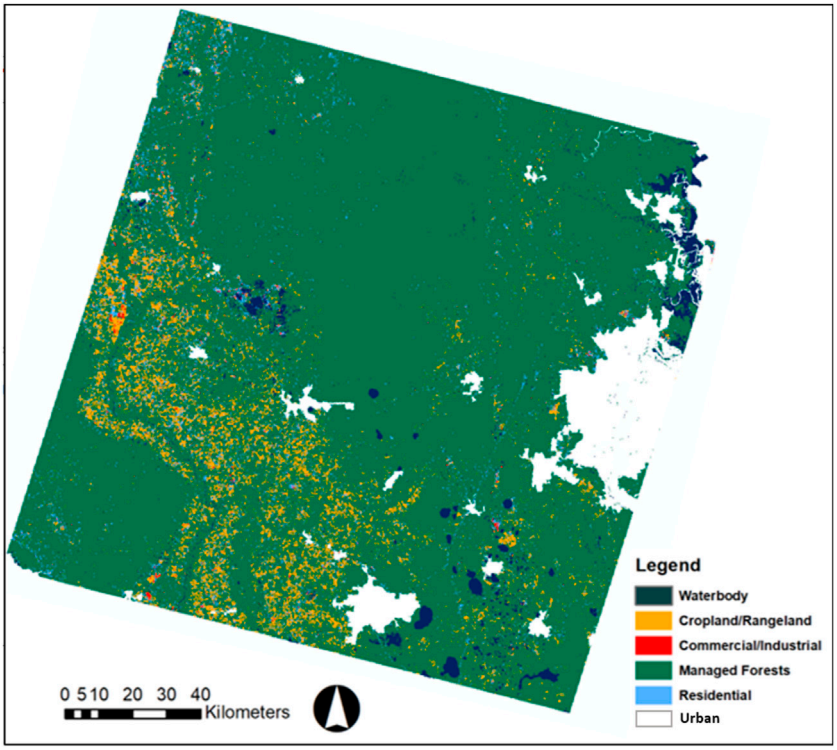

FIGURE 3
Land-Use Composition of the study area in 2013. Because the urban areas were subtracted, the residential and commercial/industrial areas are those located in the suburban and rural residential areas.

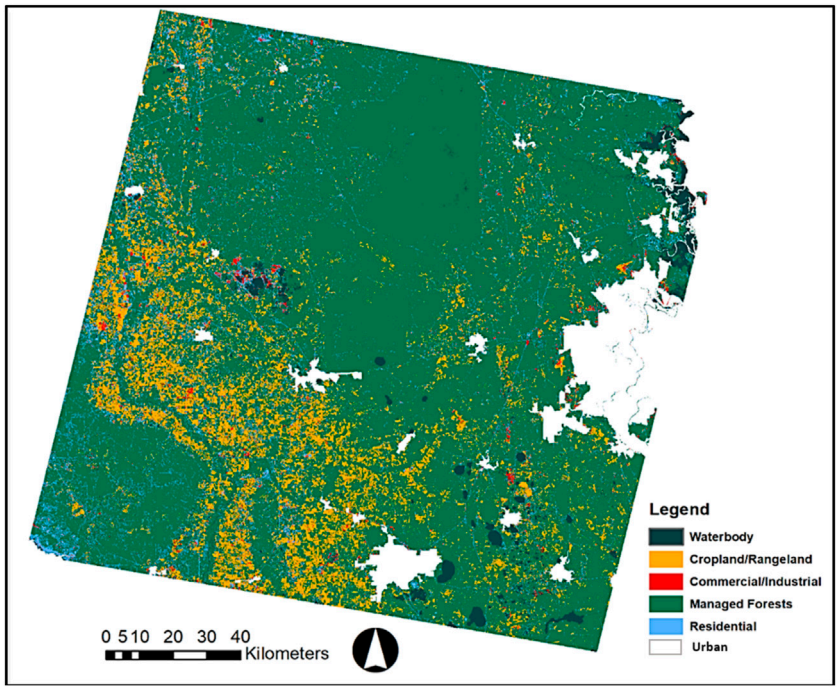

FIGURE 4
Land-Use Composition of the study area in 2018. Because the urban areas were subtracted, the residential and commercial/industrial areas are those located in the suburban and rural residential areas.

TABLE 3 Land-Use Change of Residential, commercial/industrial, and cropland/rangeland from 2013 to 2018.

Land-use type	2013		2018	
	Area (Ha)	Area percentage (%)	Area (Ha)	Area percentage (%)
Cropland/rangeland	184,519.17	6.22	306,119.70	10.32
Commercial/Industrial	17,367.66	0.59	88,159.05	2.97
Residential	146,158.2	4.93	263,094.12	8.87

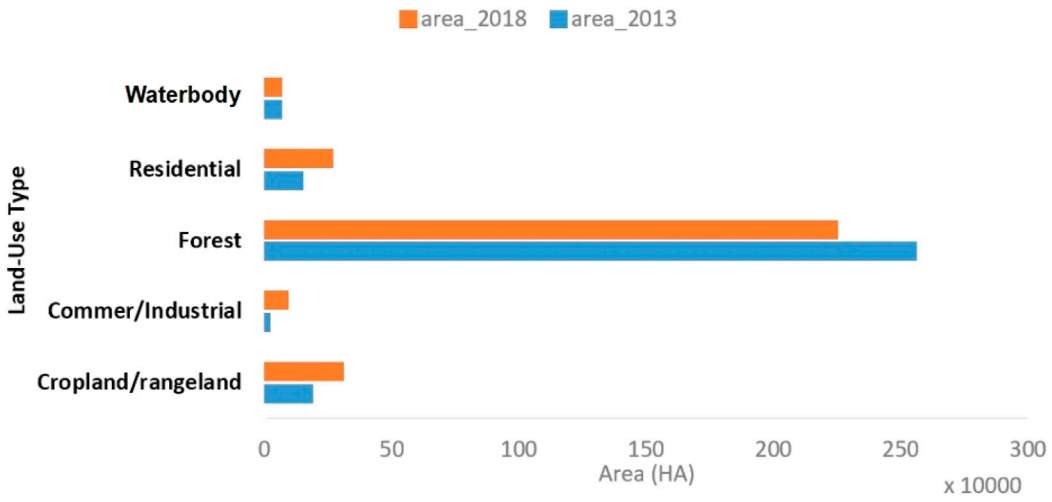

FIGURE 5
Land-Use Change of Residential, commercial/industrial, and cropland/rangeland from 2013 to 2018.

From Figure 5 and Table 3, we found a strong trend of deforestation and rural residential/suburban development, which increased by 80%. There was also a 66%increase in cropland area and a 407% increase in commercial/industrial area in the study area from 2013 to 2018.

3.2 Accuracy assessment

Building the RF classifier is the starting point of our landscape analysis; the results of the accuracy of land-use classification for both 2013 and 2018 are shown in Table 4. The land-use classification out-of-bag (OOB) overall accuracy was close to 97%, with corresponding Kappa values of 0.97 for both 2013 and 2018. Considering that land-use patterns of 2013 and 2018 were extracted using the same classification method and original image collections, we assumed that the classification accuracies of this land-use change dataset are comparable.

At the class level, the precision, or comparison of the true and false classifications, ranges from 94% to 99%. Overall, the RF classification rules, when coupled with crowd-sourced land-use training samples show a strong potential to classify land-use type well. In land-use mosaics from 2013, it was shown that the most complex land-use changes occur at cropland/rangeland and residential areas. This reflects the existence of rural residential areas as well as their continued development. The residential regions and the commercial/industrial areas are the classes in the 2018 land-use mosaics that have the most confusion. This indicates that it is difficult to differentiate between those two classes due to the high similarity of spectral signals in remote sensing imagery.

3.3 Adjacent land-use development

The percentage coverage of the five land uses adjacent to and within different buffers for each type of forest management approach from 2013 to 2018 is individually shown in Figures 3, 4 and is compared across the buffered region. We set the distance zones surrounding patches of each management from 500 m to 5,000 m with a 500 m interval, as those distances will cover enough spatial information to show the subtle land-use change at a landscape level (Sanchez Azofeifa, 1996; Carey et al., 2011). Adjacent land-uses surrounding each forest management type were analyzed. The results gave us an indication of the distribution of each land-use class immediately around different managed forest patches.

For the landscapes in proximity to ecological forests, there is not a strong spatial relationship between the ecologically managed forest and the surrounding lands, although there is more residential land

TABLE 4 Out-Of-Bag (OOB) error matrices for five land-uses classes in 2013 and 2018 in the study area.

2013		Classified data					
Class		Cropland	Commercial/ Industrial	Forests	Residential	Water	Producer's accuracy (%)
References Data	Cropland	373	1	6	7	2	95.89
	Commercial/ Industrial	2	447	0	2	1	98.89
	Forests	12	3	1,377	5	0	98.57
	Residential	7	5	17	657	0	95.77
	Waterbody	0	0	2	9	215	95.13
	User's Accuracy (%)	94.67	98.03	98.22	96.62	98.62	Overall Accuracy: 97.43%
2018		Classified data					
Class		Cropland	Commercial/ Industrial	Forests	Residential	Water	Producer's accuracy (%)
References Data	Cropland	468	1	12	7	2	95.51
	Commercial/ Industrial	2	539	1	25	2	94.73
	Forests	18	2	1,377	9	2	97.80
	Residential	0	4	1	792	3	99.00
	Waterbody	0	2	3	6	592	98.18
	User's Accuracy (%)	95.90	98.36	98.78	94.40	98.50	Overall Accuracy: 97.36%

Kappa coefficients k) of 2013 and 2018 are K_{2013} = 0.97 and K_{2018} = 0.97, respectively.

near ecological forests and that cropland is more likely to be near ecological forest management patches (Figure 6). The proportions of cropland, commercial/industrial and residential land uses decrease within 1,500 m and then are stable out to 5,000 m. For landscapes in proximity to passively managed forests, the surrounding land uses are quite stable surrounding the passive management forests, except for the croplands.

In Figure 6, few spatial relationships between land uses and management are found within 500 m of preservation forestry, which fulfills the preservation management strategy of sustaining the forests. From 2013 to 2018, cropland and residential area proportions increased with increasing distance from the preservation forests. Among all four types of management approaches, production forests have the strongest spatial relationships with croplands (Figure 6). The proportion of the croplands surrounding production forests reached a peak of 20% at a distance of 1,000 m, and then decreased rapidly. When the distance from production forests is about 3,500 m, the residential proportion did not change from 2013 to 2018.

As evident in Figure 6, there tends to be a sharp increase in land-use proportion among different types of land use adjacent to each management forest patch (except for cropland in 4,000–5,000 m proximity of production forests). In 2013, cropland land uses showed the strongest spatial relationships with production forest, followed by passively managed forest, ecological forest, and finally, preservation forest. However, in 2018, the order changed significantly with the strongest spatial relationships with production forests, followed by ecological forest, and then passively managed forest and preservation forests. In 2013, the proportion of cropland surrounding production forest patches increased from 3.3% to 8.6%. However, the trend in 2018 shows an exponential decrease with increasing distance, particularly from 1,000 m to 3,500 m.

3.4 Land-use change in SEUS from 2013 to 2018

Land use transitions are important to map and understand (Figure 7). Table 5 shows the different transitions possible across the study area with the associated land change. Notably, the dominant land transitions were identified into seven major categories: stability (no change (stability), commercialization, afforestation, cultivation, and rural residential and suburban growth. Table 5 also shows the land-use conversion matrix used by the spatial allocation procedure by determining the possible land-use transition sequences. Just four types from the land-use patterns map were used in this analysis: cropland, commercial/industrial, managed forest, and residential.

We created a land transition analysis by combining the OSM derived land-use maps for 2013 and 2018 to produce the land-use transition patterns over the study area with a 30 m resolution. This regional land-use pattern analysis seeks to identify the dominant

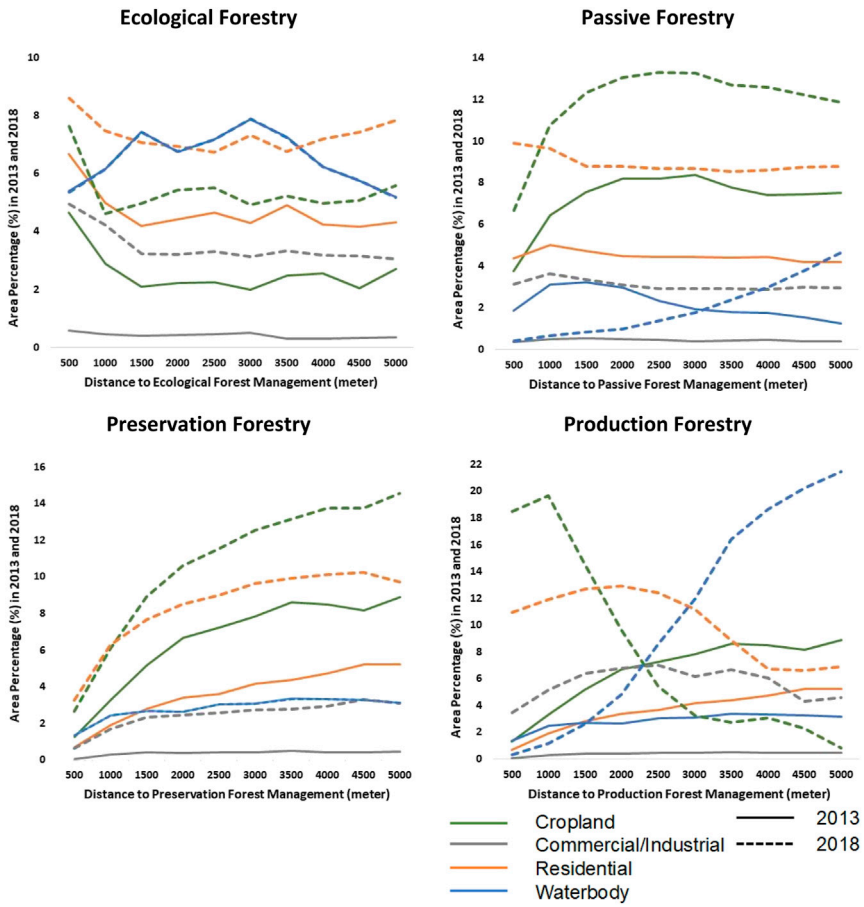

FIGURE 6
The percentage of different land use based on the distances from the nearest forest patches under different management types (ecological, passive, preservation, and production forest).

patterns of land use change. Across the study area, several major change patterns are recognized, together comprising a majority of suburban growth, commercialization, and cultivation.

4 Discussion

4.1 Land-use mapping with OSM as training samples

OSM was incorporated into mapping land use and showed great potential for justifying and monitoring land use at a regional scale. The results identified the spatial land-use patterns and the variations around each type of managed forest with buffers ranging from 500 m to 5,000 m for 2013 and 2018 (Figures 3, 4). Over the 34,000 km^2 study area, there has been a large amount of land-use conversion from 2013 to 2018 (Figure 7). Deforestation is a clear trend in the study area, despite economically valuable managed forests.

The nightlight remotely sensed images do a relatively better job representing and mapping human footprints (Li et al., 2017) when compared to using only the spectral imagery alone. The results of this study support the use of nightlight imagery when mapping land use. For example, Yang et al., 2017 used a variety of physical features from Earth observation datasets (i.e., forest canopy height, DEM, and EVI) to map regional land use in the same study area with an accuracy of 95% (internal validation) and 74% (external validation).

In this study, land-use classifiers' training sample sets were extracted from historical OSM and resulted in high internal validation accuracy (97% for 2013 and 97% for 2018). OSM provides different data collection mechanisms than the traditional authoritative geographic information obtained from official or governmental institutions, agencies, or Earth observations. The results demonstrate that OSM and citizen science data have potential for mapping regional human footprints (represented as land use in this study). In this study, the training samples extracted from OSM were randomly selected. The error matrices are based on internal validation. Based on our results, the classification methods presented in this study are recommended mainly for mapping broad land-use classes. Further accuracy testing through external validation requires a large amount of historical land-use documentary data, which can be a project for further study.

The data quality of OSM and its public participatory geospatial database has always been recognized as a major concern by researchers (Antoniou and Skopeliti., 2015; Mobasheri et al., 2018). The contribution of OSM mappers is often based on perceptions rather than scientific measurements, which makes it complex to measure the

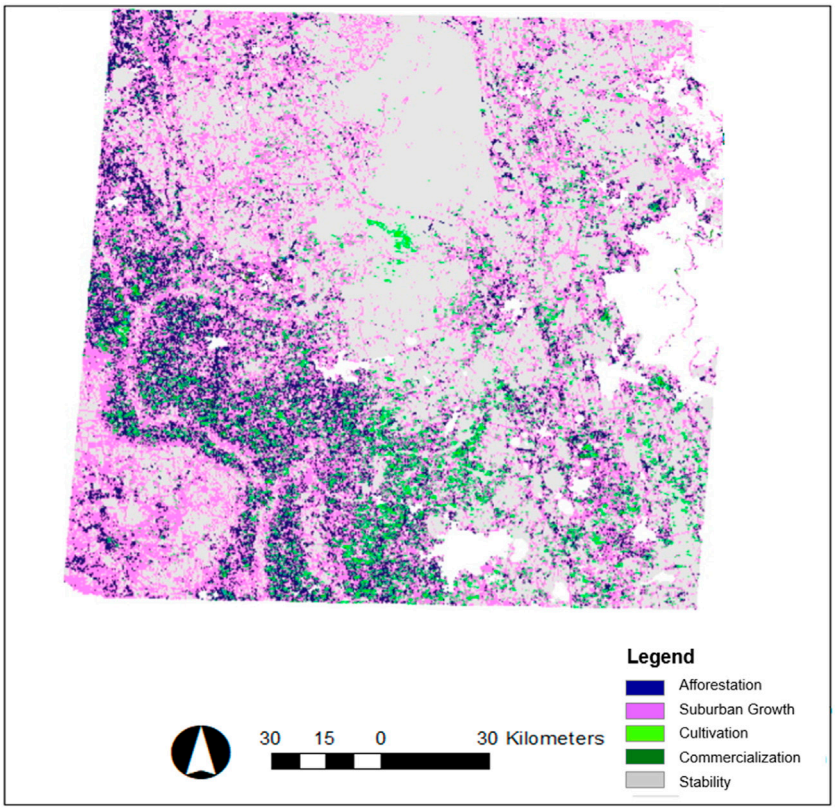

FIGURE 7
Land-use change derived from OSM from 2013 to 2018.

TABLE 5 Land-use changes in the study area and the associated land change are delineated. These categories include changes that may rarely or never occur (e.g., residential to managed forest or commercial/industrial or residential to croplands).

Land use in 2013	Land use in 2018			
	Cropland	Commercial/Industrial	Managed forest	Residential
Cropland	Stability	Commercialization	Afforestation	Rural/Suburban Growth
Commercial/Industrial	Cultivation	Stability	Afforestation	Rural/Suburban Growth
Managed Forest	Cultivation	Commercialization	Stability	Rural/Suburban Growth
Residential	Cultivation	Commercialization	Afforestation	Stability

mapping quality and positional accuracy. However, there are some strategies to overcome the credibility challenges of those participatory mapping databases. Firstly, there are always "superusers" in VGI mapping projects. Those "superusers" make tremendous contributions by providing a large amount of near-real time accurate information. In addition, the quality control of OSM itself is also a multi-user environmental validation process. Based on its "wiki" principle, the community of OSM mappers can act as quality filters, which means the dataset is self-validated by the other contributors' numerous times. In this analysis, we applied this strategy to the point of self-validation. Finally, because of the vast amount of OSM data, mapping effects are mostly aggregated based on the ground truth data provided by OSM mappers.

4.2 Proximity analysis

Due to the lack of precision in delineating boundaries that surround various ecosystems, there is much that cannot be clearly understood from the perspective of land management or the management of natural resources (Duncker et al., 2012). Our results show that there are similar trends in management for lands around ecological forests and passively managed forest, i.e., no significant increase or decrease of different land-use types in surrounding landscapes. We also found that for passively and ecologically managed forests, as the distances of specific land-use types from the nearest forest patches increase, the variance of the proportion of that specific land use to the total land becomes smaller, and finally levels off. Preservation forestry covers over

thirty percent of the total forest in the study area (Marsik et al., 2018). For surrounding land uses of production forests, we found patterns that imply interactions between production forests and cropland in the 1,500 m buffer. Land policy may contribute to this phenomenon as production forests, pasture, cropland, and citrus all belong to the same tax code (i.e., Commercial Agriculture Uses) in Florida, which lowers the property tax rate. There are several hypotheses to explain this phenomenon: 1) the landscapes are built out over a distance greater than 3,500 m; and 2) those areas belong to urban areas and are thus not included in the analysis. Moreover, the State of Florida does not have a minimum land area requirement for agricultural and timberland classification, which increases the potential for cropland—timberland two-way flows.

Residential developments also show a strong effect of land-use transitions on the surrounding lands, such as forests transformed into croplands or rangeland areas. As we found the increasing trend on both residential and commercial/industrial lands, nearly 45.9% of new residential lands in the study area were created from forests, with most of the rest resulting from the conversion of agricultural land. From 2013 to 2018, one of the most influential drivers of forest area change was the expansion and contraction of agricultural land. These patterns also point out how fast the rural residential areas are being developed in the heavily forested study area, especially near passive and production management forest patches (Figure 6).

The study area also experienced rapid population growth, based on the gridded population of the world v4/population count, there was a 170,130 increase from 2010 to 2020 (GPWv4). Most of the time this led to deforestation (the transfer of forest lands to developed lands). As the population increased, the potential need for residential areas, roads, commercial and industrial sites increased. The development of rural residential developments significantly contributed to land-use dynamics. The increasing rural residential areas show a strong signal of urbanization and deforestation, as most newly developed residential areas are developed on forested land. For the rural/suburban residential areas surrounding ecological forests, preservation forests, and passively managed forests, the trends of rural/suburban coverage all increased from 2013 to 2018.

5 Conclusion

The land uses in SEUS have been heavily transformed according to a variety of factors, such as population growth and economic growth. The forest ecosystems in the SEUS have been largely influenced by these land-use changes. The results of this study show that land-use patterns in the vicinity of forest under different management strategies vary substantially with the occurrences of forest patch isolation due to the proximity of agricultural development, rural residential development, and commercialization. Such land-use transitions alter the SEUS landscapes and may affect ecosystem functions. We infer the land-use information at the regional scales by using VGI from a diverse array of stand-level studies and other ancillary information.

By developing a crowdsourcing-based land-use change mapping framework over the SEUS we measured and calculated the proportion of land area that was located within nine increasing distance buffers from the nearest managed forest patches of any type of forest management, and mapped the results reclassified by land-use transitions. For lands surrounding preservation forests, we found the effectiveness of preservation in maintaining the forest cover in the first 500–1,000 m boundary buffers. However, rural residential developments are changing the lands surrounding the preservation areas. The lands surrounding production forestry, comprising important spatial relationships with croplands, show the strongest potential for land conversion between forests and croplands. For the passively managed forest surrounding landscapes, the land-use patterns represent a relatively neutral status because of the low management intensity with little interaction with croplands, which is the opposite for the production forest surroundings. For the lands surrounding ecologically managed forests, there are the least variances of land-use composition based on distances. This also supports the idea that the major principle of ecological forestry is to maintain the social-ecological functions.

Citizen science is contributing to land-change science, in ways that increase the magnitude of observations far beyond those that can be done by individual scientific projects. From a mapping land-use perspective, citizen science can be used to extend the training sample database, which is considered a huge challenge for large scale landscape classification processes. The proposed strategies seek contributions that demonstrate the application of citizen science projects supporting human-environment related research by complementing satellite observations and discussing novel methods for the collection of land management data.

The challenge of the work is that the rapid growth of OSM only started in 2013, and as such, the database has improved from both user numbers and quality perspectives, across the study period. From 2013 to 2018 is a relatively short time, only 5 years, to make a significant conclusion or assessment about any types of longer-term changes or drivers. Despite this limitation due to the short time-duration of this data source, however, this study shows a strong potential for mapping land change and human footprints at the regional scale by using VGI derived datasets as land-use indicators and proxies.

Data availability statement

The datasets presented in this study can be found in online repositories. The names of the repository/repositories and accession number(s) can be found below: https://doi.org/10.6084/m9.figshare.11406612.v1.

Author contributions

Conceptualization: DY and C-SF Methodology and software: DY Validation: C-SF Formal analysis: DY and C-SF Materials: DY Writing—original draft preparation: DY Writing—review and editing: DY, C-SF, HH, JS, MB Visualization: DY, C-SF, and MB Supervision: JS, and MB Funding acquisition: DY led the conceptualization of the research study and was primarily responsible for developing the methodology and software used in the study. DY wrote the initial draft of the manuscript and was heavily involved in the writing and editing process throughout. DY was also involved in visualization of the data. C-SF contributed to the conceptualization of the study, led the validation of the results, and provided overall supervision and guidance throughout the

research process. They were involved in writing and editing the manuscript and securing funding for the research. HH and JS contributed to the writing and editing of the manuscript. MB contributed to the supervision of the research study, provided overall guidance and leadership throughout the research process. He also involved in writing and editing of the manuscript. All authors contributed to the article and approved the submitted version.

Funding

The National Science Foundation (NSF #EF-1231860, and #EF-1702835, NSF-2305683) for the generous support of this project.

Acknowledgments

We extend our deepest gratitude to the contributors of OpenStreetMap, whose tireless efforts have provided invaluable data for our geographical analyses. We also wish to express our appreciation to Google Earth Engine for their innovative platform that has significantly enhanced our research capabilities. Special thanks are due to Peter Waylen and Greg Glass for their insightful reviews and constructive feedback.

Conflict of interest

The authors declare that the research was conducted in the absence of any commercial or financial relationships that could be construed as a potential conflict of interest.

Publisher's note

All claims expressed in this article are solely those of the authors and do not necessarily represent those of their affiliated organizations, or those of the publisher, the editors and the reviewers. Any product that may be evaluated in this article, or claim that may be made by its manufacturer, is not guaranteed or endorsed by the publisher.

References

Antoniou, V., Costa Fonte, C., See, L., Estima, J., Arsanjani, J., Lupia, F., et al. (2016). Investigating the feasibility of geo-tagged photographs as sources of land cover input data. *ISPRS Int. J. Geo-Information* 5 (5), 64. doi:10.3390/ijgi5050064

Antoniou, V., and Skopeliti, A. (2015). Measures and indicators of vgi quality: An overview. *ISPRS Ann. Photogrammetry, Remote Sens. Spatial Inf. Sci.* 2, 345–351. doi:10.5194/isprsannals-ii-3-w5-345-2015

Ballatore, A., and Mooney, P. (2015). Conceptualising the geographic world: The dimensions of negotiation in crowdsourced cartography. *Int. J. Geogr. Inf. Sci.* 29 (12), 2310–2327.

Becknell, J. M., Desai, A. R., Dietze, M. C., Schultz, C. A., Starr, G., Duffy, P. A., et al. (2015). Assessing interactions among changing climate, management, and disturbance in forests: A macrosystems approach. *BioScience* 65 (3), 263–274. doi:10.1093/biosci/biu234

Breiman, L. (2001). Random forests. *Mach. Learn.* 45 (1), 5–32. doi:10.1023/a:1010933404324

Briassoulis, H. (2020). *Analysis of land use change: Theoretical and modeling approaches*. 2nd edn. Edited by Scott Loveridge and Randall Jackson. WVU Research Repository.

Carey, R. O., Migliaccio, K. W., Li, Y., Schaffer, B., Kiker, G. A., and Brown, M. T. (2011). Land use disturbance indicators and water quality variability in the Biscayne Bay Watershed, Florida. *Ecol. Indic.* 11 (5), 1093–1104. doi:10.1016/j.ecolind.2010.12.009

Chander, G., Markham, B. L., and Helder, D. L. (2009). Summary of current radiometric calibration coefficients for Landsat MSS, TM, ETM+, and EO-1 ALI sensors. *Remote Sens. Environ.* 113 (5), 893–903. doi:10.1016/j.rse.2009.01.007

Comber, A. J. (2008). The separation of land cover from land use using data primitives. *J. Land Use Sci.* 3 (4), 215–229.

DeFries, R., Hansen, A., Turner, B. L., Reid, R., and Liu, J. (2007). Land use change around protected areas: Management to balance human needs and ecological function. *Ecol. Appl.* 17 (4), 1031–1038. doi:10.1890/05-1111

Dickinson, J. L., Shirk, J., Bonter, D., Bonney, R., Crain, R. L., Martin, J., et al. (2012). The current state of citizen science as a tool for ecological research and public engagement. *Front. Ecol. Environ.* 10 (6), 291–297.

Duncker, P. S., Barreiro, S. M., Hengeveld, G. M., Lind, T., Mason, W. L., Ambrozy, S., et al. (2012). Classification of forest management approaches: A new conceptual framework and its applicability to European forestry. *Ecol. Soc.* 17 (4).

Dunford, W., and Freemark, K. (2005). Matrix matters: Effects of surrounding land uses on forest birds near ottawa, Canada. *Landsc. Ecol.* 20 (5), 497–511. doi:10.1007/s10980-004-5650-5

Espírito-Santo, F. D., Gloor, M., Keller, M., Malhi, Y., Saatchi, S., Nelson, B., et al. (2014). Size and frequency of natural forest disturbances and the Amazon forest carbon balance. *Nat. Commun.* 5, 3434. doi:10.1038/ncomms4434

Estima, J., and Painho, M. (2013). "Exploratory analysis of openStreetMap for land use classification," in Paper presented at The Second ACM SIGSPATIAL International Workshop on Crowdsourced and Volunteered Geographic Information, GEOCROWD'13, Orlando, FL, United States, November 5–8, 39–46.

Fahrig, L. (2013). Rethinking patch size and isolation effects: The habitat amount hypothesis. *J. Biogeogr.* 40 (9), 1649–1663. doi:10.1111/jbi.12130

Fischlin, A., Midgley, G. F., Price, J. T., Leemans, R., Gopal, B., Turley, C., et al. (2007). *Ecosystems, their properties, goods and services*.

Forman, R. T. T. (2014). *Land mosaics: The ecology of landscapes and regions 1995*. Island Press, 217.

Franklin, J. F., Norman Johnson, K., and Johnson, D. L. (2018). *Ecological forest management*. Waveland Press.

Girres, J. F., and Touya, G. (2010). Quality assessment of the French OpenStreetMap Dataset. *Trans. GIS.* 14 (4), 435–459.

Goodchild, M. F. (2007). Citizens as sensors: The world of volunteered geography. *GeoJournal* 69 (4), 211–221. doi:10.1007/s10708-007-9111-y

Goodchild, M. F., and Glennon, J. A. (2010). Crowdsourcing geographic information for disaster response: A research frontier. *Int. J. Digital Earth* 3 (3), 231–241. doi:10.1080/17538941003759255

Groeneveld, J., Müller, B., Buchmann, C. M., Dressler, G., Guo, C., Hase, N., et al. (2017). Theoretical foundations of human decision-making in agent-based land use models – a review. *Environ. Model. Softw.* 87, 39–48. doi:10.1016/j.envsoft.2016.10.008

Haklay, M. (2010). How good is volunteered geographical information? A comparative study of OpenStreetMap and ordnance survey datasets. *Environ. Plan. B Plan. Des.* 37 (4), 682–703. doi:10.1068/b35097

Haklay, M., and Weber, P. (2008). Openstreetmap: User-generated street maps. *Ieee Pervas Comput.* 7 (4), 12–18. doi:10.1109/mprv.2008.80

Hansen, A. J., and Ruth, D. F. (2007). Ecological mechanisms linking protected areas to surrounding lands. *Ecol. Appl.* 17 (4), 974–988. doi:10.1890/05-1098

Hawbaker, T. J., and Radeloff, V. C. (2004). Roads and landscape pattern in northern Wisconsin based on a comparison of four road data sources. *Conserv. Biol.* 18 (5), 1233–1244. doi:10.1111/j.1523-1739.2004.00231.x

Heilman, G. E., Strittholt, J. R., Slosser, N. C., and Dellasala, D. A. (2002). Forest fragmentation of the conterminous United States: Assessing forest intactness through road density and spatial characteristics. *AIBS Bull.* 52 (5), 411–422. doi:10.1641/0006-3568(2002)052[0411:ffotcu]2.0.co;2

Hurskainen, P., Adhikari, H., Siljander, M., Pellikka, P. K. E., and Hemp, A. (2019). Auxiliary datasets improve accuracy of object-based land use/land cover classification in heterogeneous savanna landscapes. *Remote Sens. Environ.* 233, 111354. doi:10.1016/j.rse.2019.111354

Kramer, D. B., and Doran, P. J. (2010). Land conversion at the protected area's edge. *Conserv. Lett.* 3 (5), 349–358. doi:10.1111/j.1755-263x.2010.00122.x

Lambin, E. F., and Meyfroidt, P. (2011). Global land use change, economic globalization, and the looming land scarcity. *Proc. Natl. Acad. Sci.* 108 (9), 3465–3472. doi:10.1073/pnas.1100480108

Lawler, J. J., Lewis, D. J., Nelson, E., Plantinga, A. J., Polasky, S., Withey, J. C., et al. (2014). Projected land-use change impacts on ecosystem services in the United States. *Proc. Natl. Acad. Sci.* 111 (20), 7492–7497. doi:10.1073/pnas.1405557111

Li, X., Elvidge, C., Zhou, Y., Cao, C., and Warner, T. (2017). Remote sensing of night-time light. *Int. J. Remote Sens.* 38 (21), 5855–5859. doi:10.1080/01431161.2017.1351784

Marsik, M., Staub, C. G., Kleindl, W. J., Hall, J. M., Fu, C. S., Yang, D., et al. (2018). Regional-scale management maps for forested areas of the Southeastern United States and the US Pacific Northwest. *Sci. data* 5, 180165. doi:10.1038/sdata.2018.165

Miller, S. D., Straka, W., Mills, S. P., Elvidge, C. D., Lee, T. F., Solbrig, J., et al. (2013). Illuminating the capabilities of the suomi national polar-orbiting partnership (NPP) visible infrared imaging radiometer suite (VIIRS) day/night band. *Remote Sens.* 5 (12), 6717–6766. doi:10.3390/rs5126717

Mobasheri, A., Zipf, A., and Francis, L. (2018). OpenStreetMap data quality enrichment through awareness raising and collective action tools—Experiences from a European project. *Geo-spatial Inf. Sci.* 21 (3), 234–246. doi:10.1080/10095020.2018.1493817

Neis, P., and Zielstra, D. (2014). Recent developments and future trends in volunteered geographic information research: The case of OpenStreetMap. *Future Internet* 6 (1), 76–106. doi:10.3390/fi6010076

Neis, P., Zielstra, D., and Zipf, A. (2011). The street network evolution of crowdsourced maps: OpenStreetMap in Germany 2007–2011. *Future Internet* 4 (1), 1–21.

Radeloff, V. C., Stewart, S. I., Hawbaker, T. J., Gimmi, U., Pidgeon, A. M., Flather, C. H., et al. (2010). Housing growth in and near United States protected areas limits their conservation value. *Proc. Natl. Acad. Sci.* 107 (2), 940–945. doi:10.1073/pnas.0911131107

Reed, R. A., Johnson Barnard, J., and Baker, W. L. (1996). Contribution of roads to forest fragmentation in the Rocky Mountains. *Conserv. Biol.* 10 (4), 1098–1106. doi:10.1046/j.1523-1739.1996.10041098.x

Riitters, K. H., Wickham, J. D., O'neill, R. V., Jones, K. B., Smith, E. R., Coulston, J. W., et al. (2002). Fragmentation of continental United States forests. *Ecosystems* 5 (8), 0815–0822.

Sanchez-Azofeifa, G. A. (1996). *Assessing land use/cover change in Costa Rica*. University of New Hampshire.

Schulte, L. A., Mladenoff, D. J., Crow, T. R., Merrick, L. C., and Cleland, D. T. (2007). Homogenization of northern US Great Lakes forests due to land use. *Landsc. Ecol.* 22 (7), 1089–1103. doi:10.1007/s10980-007-9095-5

Simard, M., Pinto, N., Fisher, J. B., and Baccini, A. (2011). Mapping forest canopy height globally with spaceborne lidar. *J. Geophys. Res. Biogeosciences* 116 (G4), G04021. doi:10.1029/2011jg001708

Sohl, T., and Sayler, K. (2008). Using the FORE-SCE model to project land-cover change in the southeastern United States. *Ecol. Model.* 219 (1-2), 49–65. doi:10.1016/j.ecolmodel.2008.08.003

Southworth, J., and Muir, C. (2021). Specialty grand challenge: Remote sensing time series analysis. *Front. Remote Sens.* 2. doi:10.3389/frsen.2021.770431

Sutton, P. C., Anderson, S. J., Elvidge, C. D., Tuttle, B. T., and Ghosh, T. (2009). Paving the planet: Impervious surface as proxy measure of the human ecological footprint. *Prog. Phys. Geogr.* 33 (4), 510–527.

Theobald, E. J., Ettinger, A. K., Burgess, H. K., DeBey, L. B., Schmidt, N. R., Froehlich, H. E., et al. (2015). Global change and local solutions: Tapping the unrealized potential of citizen science for biodiversity research. *Biol. Conserv.* 181, 236–244. doi:10.1016/j.biocon.2014.10.021

TIGER (2015). *Cartographic boundary – urban areas*. prepared by the U.S. Census Bureau. Available from https://www.census.gov/geo/maps-data/data/kml/kml_ua.html.

Turner, B. L. (1994). Local faces, global flows: The role of land use and land cover in global environmental change. *Land Degrad. Dev.* 5 (2), 71–78. doi:10.1002/ldr.3400050204

Turner, M. G., Wear, D. N., and Flamm, R. O. (1996). Land ownership and land-cover change in the southern Appalachian highlands and the Olympic Peninsula. *Ecol. Appl.* 6 (4), 1150–1172. doi:10.2307/2269599

Verburg, P. H., Soepboer, W., Veldkamp, A., Limpiada, R., Espaldon, V., and Mastura, S. S. (2002). Modeling the spatial dynamics of regional land use: The CLUE-S model. *Environ. Manag.* 30 (3), 391–405. doi:10.1007/s00267-002-2630-x

Verburg, P. H., Van De Steeg, J., Veldkamp, A., and Willemen, L. (2009). From land cover change to land function dynamics: A major challenge to improve land characterization. *J. Environ. Manag.* 90 (3), 1327–1335. doi:10.1016/j.jenvman.2008.08.005

Wassenaar, T., Gerber, P., Verburg, P. H., Rosales, M., Ibrahim, M., and Steinfeld, H. (2007). Projecting land use changes in the Neotropics: The geography of pasture expansion into forest. *Glob. Environ. Change* 17 (1), 86–104. doi:10.1016/j.gloenvcha.2006.03.007

Wear, D. N., and Greis, J. G. (2002). Southern forest resource assessment: Summary of findings. *J. For.* 100 (7), 6–14.

Wear, D. N., and Greis, J. G. (2012). "The southern forest futures project: Summary report," in *Gen. Tech. Rep. SRS-GTR-168* (Asheville, NC: USDA-Forest Service, Southern Research Station), 168, 1–54.

Wear, D. N., and Greis, J. G. (2013). "The southern forest futures project: Technical report," in *Gen. Tech. Rep. SRS-GTR-178* (Asheville, NC: USDA-Forest Service, Southern Research Station), 178, 1–542.

Yang, D., Fu, C. S., Smith, A. C., and Yu, Q. (2017). Open land-use map: A regional land-use mapping strategy for incorporating OpenStreetMap with Earth observations. *Geo-spatial Inf. Sci.* 20 (3), 269–281. doi:10.1080/10095020.2017.1371385

Zielstra, D., and Hochmair, H. H. (2011). Digital street data: Free versus proprietary. *GIM Int.* 25, 29–33.

Zuckerberg, B., and Porter, W. F. (2010). Thresholds in the long-term responses of breeding birds to forest cover and fragmentation. *Biol. Conserv.* 143 (4), 952–962. doi:10.1016/j.biocon.2010.01.004

frontiers | Frontiers in Remote Sensing

TYPE Original Research
PUBLISHED 01 September 2023
DOI 10.3389/frsen.2023.1123254

OPEN ACCESS

EDITED BY
Erin Bunting,
Michigan State University, United States

REVIEWED BY
Rodrigo Rafael Souza De Oliveira,
Universidade do Estado do Pará, Brazil
Daniel Sombra,
Federal University of Pará, Brazil

*CORRESPONDENCE
Andressa Garcia Fontana,
andressagfontana94@gmail.com

RECEIVED 13 December 2022
ACCEPTED 17 August 2023
PUBLISHED 01 September 2023

CITATION
Fontana AG, Nascimento VF, Ometto JP and do Amaral FHF (2023), Analysis of past and future urban growth on a regional scale using remote sensing and machine learning.
Front. Remote Sens. 4:1123254.
doi: 10.3389/frsen.2023.1123254

Analysis of past and future urban growth on a regional scale using remote sensing and machine learning

Andressa Garcia Fontana[1]*, Victor Fernandez Nascimento[2], Jean Pierre Ometto[3] and Francisco Hélter Fernandes do Amaral[4]

[1]Graduate Program in Remote Sensing, Federal University of Rio Grande Do Sul, Porto Alegre, Brazil, [2]Engineering, Modelling, and Applied Social Sciences Center, Federal University of ABC (UFABC), Santo André, Brazil, [3]National Institute for Space Research, São José dos Campos, Brazil, [4]Department of Graduate Studies in Geography, Paulista State University Júlio de Mesquita Filho, Presidente Prudente, Brazil

This research investigates Land Use and Land Cover (LULC) changes in the Porto Alegre Metropolitan Region (RMPA). A 30-year historical analysis using Landsat satellite imagery was made and used to develop LULC scenarios for the next 20 years using a Multilayer Perceptrons (MLP) model through an Artificial Neural Network (ANN). These maps analyze the urban area's expansion over the years and project their potential development in the future. This research considered several critical factors influencing urban growth, including shaded relief, slope, distances from main roadways, railway stations, urban centers, and the state capital, Porto Alegre. These spatial variables were incorporated into the model's learning processes to generate future urbanization scenarios. The LULC historical maps precision showed excellent performance with a Kappa index greater than 88% for the studied years. The results indicate that the urbanization class witnessed an increase of 236.78 km^2 between 1990 and 2020. Additionally, it was observed that the primary concentration of urbanized areas since 1990 has predominantly occurred around Porto Alegre and Canoas. Lastly, the future forecasts for LULC changes in 2030 and 2040 indicate that the urban area of the RMPA is projected to reach 1,137.48 km^2 and 1,283.62 km^2, respectively. In conclusion, based on the observed urban perimeter in 2020, future projections indicate that urban areas are expected to increase by more than 443.29 km^2 by 2040. The combination of remote sensing data and Geographic Information System (GIS) enables the monitoring and modeling the metropolitan area expansion. The findings provide valuable insights for policymakers to develop more informed and conscientious urban plans, as well as enhance management techniques for urban development.

KEYWORDS

predicted LULC, ANN-CA, GEE, MOLUSCE, scenarios

1 Introduction

Changes in land use and land cover (LULC) are related to human activity, which tends to reside in cities in search of jobs, educational opportunities and access to better health services. Thus, due to economic growth, urbanization increases rapidly. Loss of natural areas and global climate change are just a few examples of environmental problems caused by LULC changes (Meraj et al., 2022). The transitions in built-up areas expansion could significantly impact the

population's quality of life (Ashaolu et al., 2019). Therefore, it is crucial to conduct urban expansion simulations.

There are various models available to simulate future scenarios, including regression models (Hu and Lo, 2007), cellular automata (Chen et al., 2016), and Markov chain models (Arsanjani et al., 2011), among others. The advancement of computational technology has enabled the integration of machine learning algorithms into studies involving cellular automata (CA) models. Algorithms such as Artificial Neural Network (ANN) (Li and Yeh, 2002), Support Vector Machine (SVM) (Yang et al., 2008), and Genetic Algorithm (GA) (Li et al., 2013) have been utilized to tackle challenges associated with parameter optimization in CA models. These methods optimize the model parameters to achieve the best possible results, effectively addressing simulation challenges related to multiple spatial variables.

However, there are different CA Models variants created to simulate urban sprawl change, such as SLEUTH (Clarke et al., 1997), the dynamic urban evolution model (Batty, 1997), the multicriteria decision analysis with cellular automato (MCDA-CA) (Wu and Webster, 2000), the multi-agent simulation model (MAS-CA) (Ligtenberg et al., 2001), the Voronoi-CA model (Shi and Pang, 2000), and the Markov-CA model (Vaz et al., 2014). This study conducted the urban sprawl simulation and the future LULC scenarios for the Porto Alegre Metropolitan Region (RMPA) using CA through the Modules of Land Use Change Evaluation (MOLUSCE) plugin within the QGIS software.

With a user-friendly and intuitive interface, MOLUSCE incorporates the Markovian-based probability matrix potential transition logic and a dynamic simulation framework based on Artificial Neural Networks (ANNs), Logistic Regression (LR), Multi-Criteria Evaluation (MCE), Weights of Evidence (WoE) models, and Multilayer Perceptrons (MLP) (Abbas et al., 2021). This study utilized the MLP model, an ANN type with supervised learning. They are commonly employed in pattern classification and tackling complex problems using the error backpropagation algorithm due to their training rules (Haykin, 2001).

Remote sensing combined with the Geographic Information System (GIS) has tools well-suited to assess LULC change. Therefore, understanding regional and temporal LULC changes benefits scientists, environmentalists, lawmakers, and urban planners (Guidigan et al., 2019). LULC transition models aim to predict when and how often such changes will occur. These future prediction models are widely used by researchers globally and are highly valuable in understanding past and future LULC change patterns (Perović et al., 2018). In recent years, spatial-temporal forecasting models utilizing CA have been developed to predict LULC change detection. The CA-ANN model, in particular, has emerged as a reliable tool used by researchers to analyze LULC changes (Alam et al., 2021). The CA model has been employed in urban planning studies due to its ability to integrate spatial and temporal elements of processes seamlessly. It is also utilized to examine temporal land-use changes and predict future land use (Saputra and Lee, 2019).

The RMPA is one of the largest urban concentrations in Brazil, housing approximately 4.4 million inhabitants. It is considered a significant area to understand the LULC's historical changes, as it has experienced substantial urban expansion in recent decades (IBGE, 2020). Therefore, recognizing and assessing the environmental impacts arising from these rapid changes is crucial (Prenzel, 2004). Furthermore, scenario predictions that incorporate the temporal evolution of the study area are also significant (Bhatta, 2010). Therefore, historical LULC changes from 1990 to 2020 were conducted in the RMPA since such analyses have not yet been performed for this metropolitan area. In addition, this study also aims to predict the LULC for the years 2030 and 2040 using two different scenarios.

2 Materials and methods

Assessing, observing, and analyzing a LULC change requires substantial data. The availability of satellite data captured by various satellite sensors proves advantageous in LULC studies (Mishra and Rai, 2016). The remote sensing image processing and analysis methods employed in this study include cloud and noise removal, spectral indices generation, Random Forest (RF) classifier parameter tuning, and the generation and accuracy evaluation of LULC classification maps were conducted in the Google Earth Engine (GEE) environment. Afterward, an artificial neural network with a cellular automaton (ANN-CA) was employed to model future LULC scenarios in the QGIS software. This approach relied on space-time transition potential matrices of the LULC classes and independent spatial variables. This study's methodological steps will be detailed in the following subsections and are shown in the flowchart (Figure 1).

2.1 Study area

The Porto Alegre Metropolitan Region (RMPA) is located in the Rio Grande do Sul state in Brazil (Figure 2). The RMPA was created in 1973 by Federal Complementary Law 14/73, currently comprises 34 municipalities with 10,335 km^2, and is Brazil's fifth most populous metropolitan region. The RMPA is a pole of attraction and integration for political and socioeconomic dynamics. Previously, this characteristic was primarily observed in Porto Alegre and the most populous cities, but it has now extended to the surrounding municipalities. The RMPA experiences significant economic expansion as many individuals are drawn to the region by employment opportunities. This flux of people has contributed to the area's robust economic growth within the state over the years (Secretaria de Planejamento, 2020).

2.2 Dataset

In this study, satellite data from Landsat-5 (sensor: TM) for the years 1990 and 2000, Landsat-7 (sensor: TM+) for the year 2010, and Landsat-8 (sensor: OLI) for the year 2020 were chosen between June and October to minimize visual obstruction caused by cloud cover. These datasets were accessed automatically from the United States Geological Survey (USGS) database within the GEE platform.

The independent spatial variables for the CA-ANN model for the future scenarios in this study were constructed using the road, railway network data, the Porto Alegre capital location, the other municipality's downtown locations, and a Digital Elevation Model

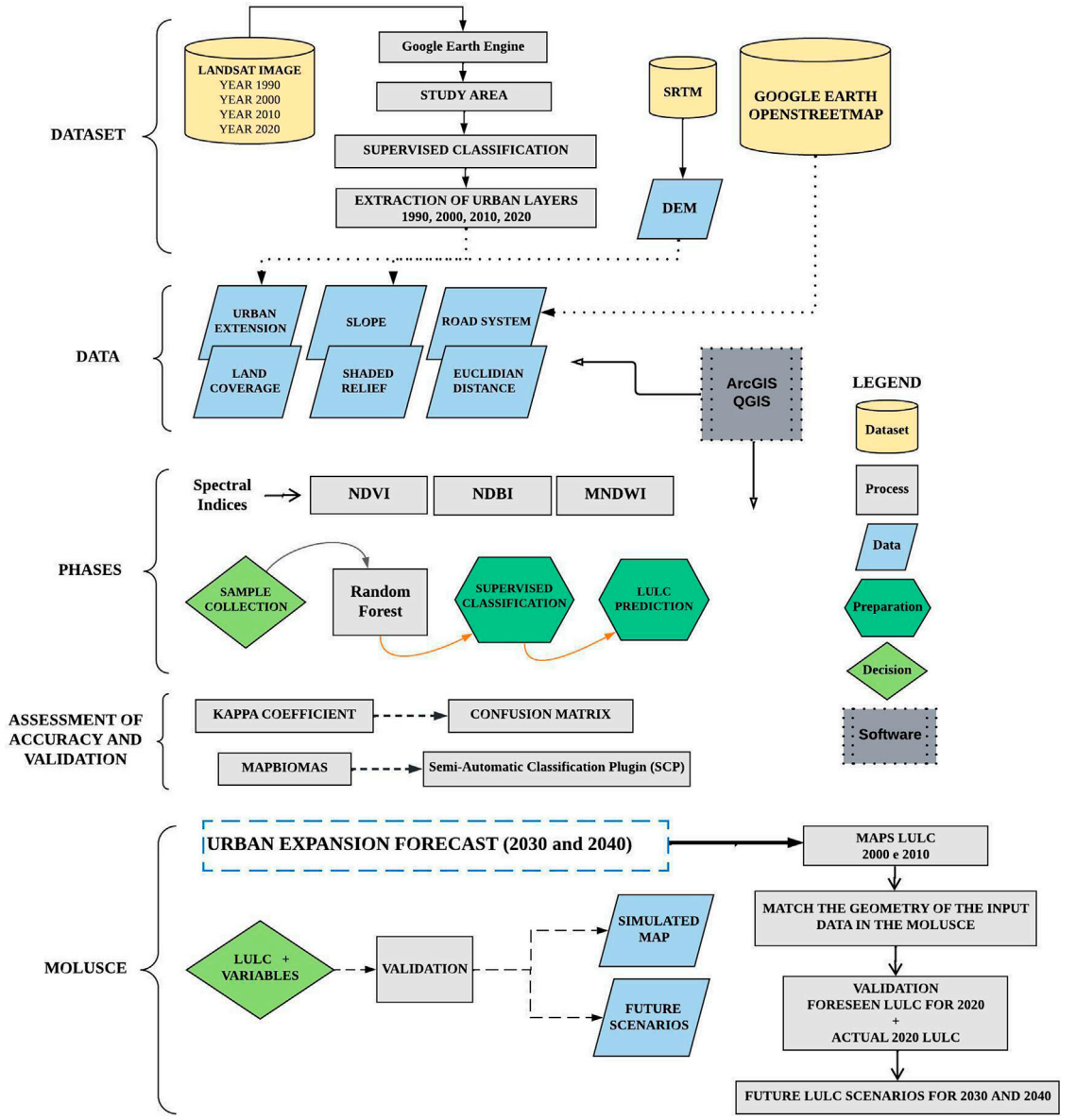

FIGURE 1
Methodology flowchart.

(DEM). These spatial variables were integrated into the model to capture and represent relevant geographical and transportation features of the study area.

This study's declivity (slope) and shaded relief data were derived from the Shuttle Radar Topography Mission (SRTM) Digital Elevation Model at a 30 m spatial resolution. This data was downloaded from the NASA Earth Data website (https://search.earthdata.nasa.gov/) and accessed in June 2022. These data provide information about the slope and the terrain shade, essential variables for analyzing LULC changes in the study area. The vector layers of roads, railway stations, and municipal downtown locations were obtained from the OpenStreetMap project (https://www.openstreetmap.org/), an independent mapping collaborative project which provides freely accessible data.

This study calculated several Euclidian distance maps based on the vector layers, including the distance to the road, railway structures, the city's downtown, and the capital Porto Alegre (Figure 3). Calculating these distances provides valuable spatial information and helps analyze the relationship between LULC changes and their proximity to transportation infrastructure and urban centers. According to Sajan et al. (2022), road and railway stations significantly shape the LULC dynamic conditions. These transportation infrastructure layers can influence LULC changes and patterns in a given area. The roads and railroads can impact accessibility, urban expansion, and the spatial distribution of different land use categories. Therefore, considering their influence is essential in understanding and predicting future LULC dynamics.

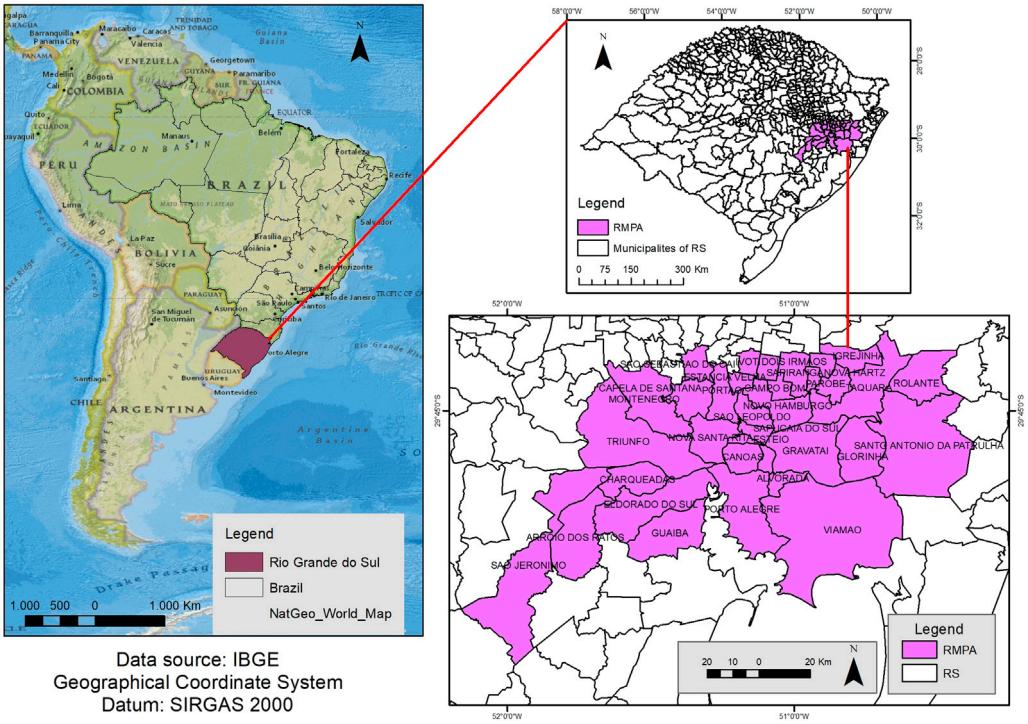

FIGURE 2
Porto Alegre Metropolitan Region (RMPA) location.

2.3 Pre-processing multitemporal satellite data

Cloud masking was employed to remove both cloud coverage and their corresponding shadows from each time series collection. This technique eliminates all contaminated pixels caused by cloudiness or no-data conditions, ensuring that only clear and useable data is retained for further analysis (Langner et al., 2018; Pimple et al., 2018). By eliminating the cloud's influence, the accuracy and reliability of subsequent analyses and interpretations are significantly improved.

Next, the data from multiple sources for each time slot were combined into specific data stacks using the median filter, a common technique used in image processing to reduce noise and preserve spatial data integrity. By applying it, the resulting data stacks represent the median values of the input data, effectively decreasing the outlier's impact and enhancing the dataset's overall quality.

For the supervised classification process, in addition to the conventional bands (B2, B3, B4, and B5 for all the Landsat family sensor collections), spectral indices such as the Normalized Difference Vegetation Index (NDVI), Normalized Difference Built-Up Index (NDBI), and Modified Normalized Difference Water Index (MNDWI) were used.

These spectral indices provide additional information that helps distinguish different LULC classes. The NDVI is commonly used to assess vegetation density and health, with higher values indicating denser and healthier vegetation Eq. 1. The NDBI highlights built-up areas, with higher values indicating a higher proportion of built-up surfaces Eq. 2. The MNDWI is sensitive to water bodies, with higher values indicating the water presence Eq. 3. Although NDWI is widely used to detect water bodies, MNDWI performs better when the water body is mixed with vegetation (Xu, 2006). Therefore, incorporating these indices into the classification process allows a more LULC comprehensive analysis, capturing essential characteristics related to vegetation, built-up areas, and water bodies, which can improve the accuracy and effectiveness of the classification results.

$$\mathrm{NDVI} = \frac{(\mathrm{NIR} - \mathrm{RED})}{(\mathrm{NIR} + \mathrm{RED})} \quad (1)$$

$$\mathrm{NDBI} = \frac{(\mathrm{SWIR1} - \mathrm{NIR})}{(\mathrm{SWIR1} + \mathrm{NIR})} \quad (2)$$

$$\mathrm{MNDWI} = \frac{(\mathrm{GREEN} - \mathrm{SWIR1})}{(\mathrm{GREEN} + \mathrm{SWIR1})} \quad (3)$$

where red (RED), near-infrared (NIR), green (GREEN), and short-wave infrared (SWIR1) are the satellite's bands. These three spectral indices were added as three bands to each image stack. Finally, the new stacked image was then used in the RF classifier.

2.4 Machine learning algorithms

The LULC classes used in this study were Cropland, Built-up, Grasslands, Water, Natural Forest, and Planted Forest. Approximately 300–400 polygonal samples were obtained for each class in the classification process. The samples were divided into two sets: 70% were randomly selected for model training, while the remaining 30% were used to validate the LULC maps. These polygons were uniformly

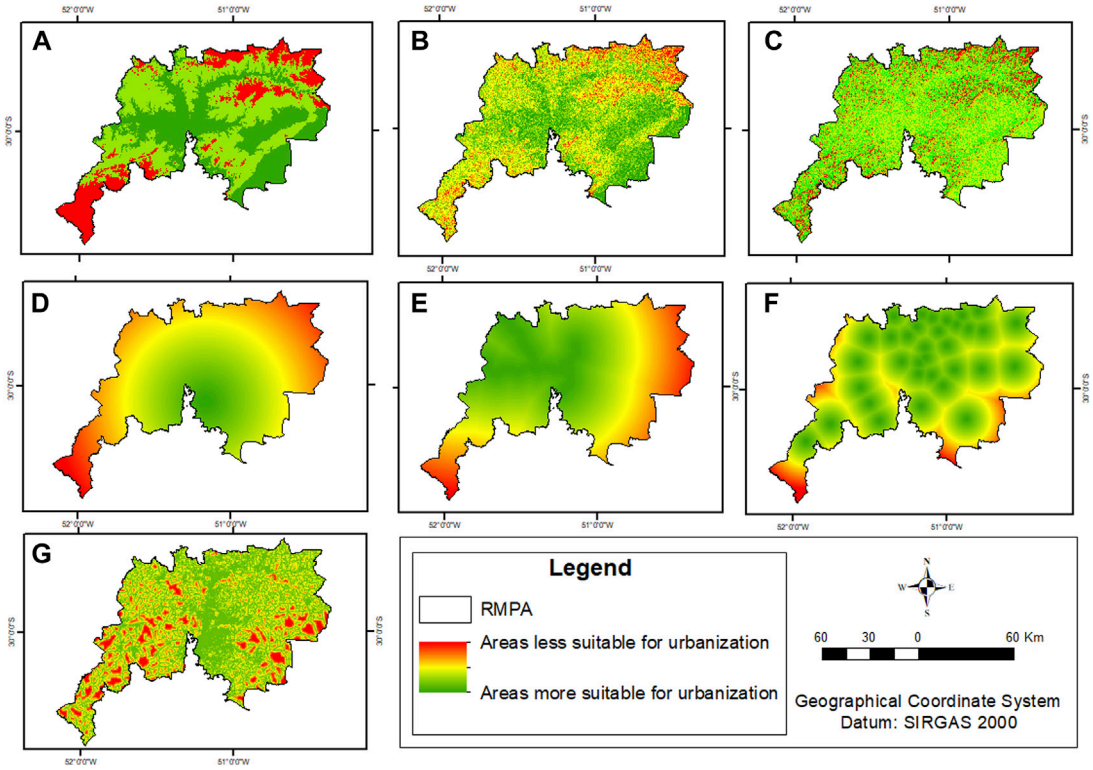

FIGURE 3
(A) altimetry; **(B)** slope; **(C)** shaded relief; **(D)** distance from Porto Alegre; **(E)** distance from railway stations; **(F)** distance from urban centers; **(G)** distance from roads.

selected across the study area, with the assistance of high-resolution Google Earth images.

According to Breiman (2001), the RF classification algorithm is based on an ensemble learning technique that combines multiple independent decision trees into a single model. Each tree in the RF is trained on a random dataset subset, where a data subsample is randomly selected for training. The tree is constructed during the process by recursively partitioning the dataset into smaller subsets based on decision rules derived from the data's features. Each node corresponds to a question about the data, and each branch represents a possible answer. This building tree process enables the model to learn the relationship between the features of the data and their respective classes. During the classification phase, each tree is utilized to classify the image independently, and the final classification is determined by aggregating the results of all the trees and assigning the most common class to each pixel.

In the remote sensing image classification, two adjustable parameters are crucial in the algorithm: the decision trees number to be generated and the minimum number of nodes. These parameters are considered "floating" because their values can be adjusted based on the data-specific characteristics and the desired classification results. Although, studies such as Pelletier et al. (2016) indicate that the change in parameter values interferes little with the final model outcome. In this sense, the decision tree value was set as 50.

After generating the classification results, addressing local noise, commonly referred to as the "salt and pepper" effect, in the pixel-based classification is recommended. This can be achieved by applying a smoothing process using a moving window of size three on the classified image. The smoothing can be performed iteratively in three iterations using the majority vote rule. Therefore, this approach was conducted and helped reduce the impact of isolated misclassifications and improve the overall accuracy of the classification.

2.5 Accuracy assessment

As Huang et al. (2017) described, a contingency or confusion matrix was created using 30% of the sample data reserved for validation to assess the accuracy of the LULC classifications. The confusion matrix compares the predicted classes with the actual classes and comprehensively assesses the classification performance. It consists of cells representing the counts of true positives and negatives, false positives and negatives. By analyzing the values in the matrix, various accuracy metrics can be calculated, such as overall, producer's, and user's accuracies and the Kappa index (K). This evaluation process helps in understanding the quality and reliability of the classification results and identifying areas of improvement if necessary.

A confusion matrix is an algorithm built into GEE, which validates and evaluates the image classification accuracy. With the confusion matrix, the K and overall accuracy (OA) are calculated Eqs 4–6:

$$OA = \frac{\sum_{i=1}^{n} x_{ii}}{N} \times 100\% \quad (4)$$

$$PA = \frac{x_{ii}}{x_{+i}} x100\% \quad (5)$$

$$UA = \frac{x_{ii}}{x_{i+}} \times 100\% \quad (6)$$

where N refers to the rows and columns number in the error matrix, Xii corresponds to the number of observations in row i and column i, xi+ is the row i marginal total, and X + i equals the column i marginal total.

The User Accuracy (UA) for each class is assessed by the proportion of pixels correctly associated with a given class relative to the total number of classified pixels. Similarly, Producer Accuracy (PA) is determined by the ratio of correctly classified pixels to the total number of pixels in the reference data in each LULC class. Proportional error reduction is determined by comparing the errors of a classification class to the errors of a completely random class. Typically, the magnitude ranges from −1 to +1. The coherence level is considered adequate when it is greater than + 0.5. The statistics used to evaluate the accuracy of LULC maps are metrics established in the literature (Jensen and Cowen, 1999; Congalton and Green, 2009).

The Kappa index is widely used for evaluating the LULC classification's accuracy. However, as mentioned in studies such as Foody (2010), it has certain limitations and considerations that should be considered when interpreting its results. It measures the agreement between the observed classifications and the reference data, considering the agreement that could occur by chance. It considers the confusion matrix's diagonal (agreement) and off-diagonal (disagreement) elements. Usually, the K can be influenced by class frequency distribution, sample size, and confusion matrix structure. For example, if a particular class is highly dominant or rare in the dataset, it may disproportionately affect the results. Despite these limitations, the K is still widely used as an indirect indicator of classification accuracy, providing a single value that summarizes the agreement between the classified map and the reference data. However, interpreting it with other accuracy measures and considering the dataset-specific characteristics and classification process limitations is essential.

2.6 ANN-CA model

This study utilized the MOLUSCE plugin, which operates within the QGIS 2.18.10 software, to develop future LULC scenarios for the RMPA region in 2030 and 2040. The prospective model employed the ANN-CA method, which offers several advantages, including its ability to handle complex data, exhibit strong prediction performance, and require minimal pre-processing of input data (Abbas et al., 2021).

2.7 Correlation between geographical variables in the CA-ANN

Pearson's coefficient was estimated to evaluate the linear correlation between the independent geographic variables, LULC spatial-temporal changes conditioners. This coefficient ranges from −1 to +1, where −1 indicates a perfect negative correlation, +1 indicates a perfect positive correlation, and 0 indicates no linear correlation between the variables. After calculating Pearson's coefficient, it was found that the variables with the highest correlation with each other include the distance from stations and roads, urban centers and Porto Alegre, shaded relief and distance from roads, distance from urban centers and shaded relief.

2.8 Transition potential modeling

To correctly develop future scenarios, preparing the input layers must demand special attention from the users since the input layers' inconsistencies in geometry, pixel size, and projection affect the results. Thus, all dependent and independent variables were set to contain the exact spatial resolution of 30 m/pixel and SIRGAS2000 Datum, 23 S UTM zone projection. Among the simulation models, the ANN seeks to establish a sigmoid function *numpy. tanh*, which is responsible for resizing the intervals of the transition categories to (y 1,1) during the configuration of the predictive scenarios (Rahman et al., 2017).

This model encompasses the complex dynamic relationships logic, which has proven to be highly suitable for modeling temporal transformations in land use as described in the works of Perović et al. (2018), and six steps support its execution model, the first being the loading of inputs comprising the LULC layers associated with the RMPA physical-social characterization layers.

In the next step, the level of correlation between the first period and the second period are quantified through the consistency values present in the intersection between the independent variables, which can be calculated through Pearson's equation, Crammer's coefficient, or uncertainty of the joint information. In the third step, the quantitative changes in the area of the use and cover classes between 2000 and 2010 are stipulated, as well as their expansion or retraction process, represented in km^2.

In addition to generating a transition map that is responsible for guiding the next step, focused on modeling the transition potential, being the basis for applying the ANN, MLP, which operates the transition model based on the collection of input variables, guided by additional parameters provided by the user, aiming to optimize the ANN training model to obtain the most reliable result regarding the 2020 usage and coverage scenario, the trial and error process was adopted in the parameter adjustments during the fourth step, getting the following optimized parameters: Iteration rate: 1,000, Learning rate: 0.001, Momentum: 0.03, Neighborhood: 10 px, Hidden layer: 11. The prediction for the 2020 usage and coverage scenario was performed using the CA simulation stage (Hakim et al., 2019).

After generating the projection map for the year 2020, it was compared to the observed LULC map generated by the Randon Forest classifier in the GEE for the same year. This comparison aimed to evaluate the ANN-CA model prediction performance, then the validation assessment was employed to calculate the Histogram Kappa (HisK) Eq. 7, Overall Kappa (OvK) Eq. 8, Location Kappa (LocK) Eq. 9 metrics, and the percentage of correction Eqs 10, 11. These metrics play a crucial role in determining the model's performance.

$$HisK = \frac{iPmax\,i - iP(E)}{1 - iP(E)} \quad (7)$$

Where, HisK is the kappa histogram value for the specific class "i", iPmax i is the maximum observed proportion of agreement for the specific class "i", and iP(E) is the expected proportion of agreement for the specific class " i".

$$OvK = \frac{P(A) - P(E)}{1 - P(E)} \quad (8)$$

Where, OvK is the overall kappa coefficient, P(A) is the observed proportion of agreement, and P(E) is the expected proportion of agreement.

$$LocK = \frac{P(A) - P(E)}{Pmax - P(E)} \quad (9)$$

Where, LocK is the kappa location coefficient, P(A) is the observed proportion of agreement, P(E) is the expected proportion of agreement, and Pmax is the maximum observed proportion of agreement.

$$P(A) = \sum_{(i=1)}^{cPii}, = \sum_{(i=1)}^{cPiT\,PTi} \quad (10)$$

$$P_{Max} = \sum -(i = 1)\,\hat{}\,c[(min\ \ (PiTPTi)] \quad (11)$$

Where, Pii is the proportion of units correctly classified for the specific class "i", PiT is the proportion of units of class "i" observed in the reference classification, PTi is the proportion of units of class "i" observed in the evaluated classification, P(A) is the correction percentage, "c" is the total number of classes, and PMax is the maximum possible value of P(A), considering all classes.

Afterward, the spatial similarity and consistency between them can be assessed by comparing the actual LULC map with the future scenarios generated by the CA-ANN model. The LoK quantifies their spatial similarity relationship, indicating how well they align in spatial distribution. On the other hand, the OvK assesses the simulation performance, considering both spatial and non-spatial comparison aspects. Both cases range between 0 and 1, where values closer to 1 indicate a higher agreement, whereas values closer to 0 show a lower agreement between the compared factors. The procedures were performed iteratively, using the trial and error method. Therefore, several calibrations were tested on the model parameters until the desired accuracy was achieved.

After obtaining the desired accuracy in the validation stage, the future LULC projection scenarios for 2030 and 2040 began the last modeling stage. Initially, the value of "n" in the time transition module was modified to 2 and 3 in the Input tab of the plugin. This adjustment was made to generate predictions when the input was set as 2000 for the initial year and 2010 as the final year. The ANN spatiotemporal model transition was conditioned to be equivalent to 10 years, ensuring a consistent 10-year interval between the predicted years.

2.9 Annual LULC rate change analysis

In order to measure the annual LULC change rate for the scenarios, the magnitude of change between the years of interest was calculated as the difference between the end year and the start year, then divided by the product between the start year and the period covered Eq. 12 (Muhammad et al., 2022).

$$ACR(\%o) = \frac{Fy - Iy}{Iy \times t} \times 100 \quad (12)$$

where, ACR corresponds to the LULC class annual dynamics rate. Iy and Fy comprise the LULC class area volume quantifications for the initial and final year, respectively, and t is the time interval.

3 Results and discussions

3.1 LULC's classifications assessment

Through the "explain" function executed by the GEE cloud platform, each variable relevance level used for the LULC classification scenarios was identified. This function assigns contribution values to the variables based on the classification results, where higher values indicate greater importance (Yang et al., 2008). The normalized indices obtained intermediate scores for all four classification models performed, while a more dynamic relevance behavior is found in the spectral bands.

The LULC classes used in this study were Cropland, Built-up, Grasslands, Water, Natural Forest, and Planted Forest. The Random Forest algorithm was used to classify the LULC features corresponding to 1990, 2000, 2010, and 2020 years based on Landsat data and spectral indices. Each class in square kilometers (km^2) for the RMPA is shown in Table 1, which provides a comprehensive overview of the spatial distribution and LULC changes over time, spatially illustrated in Figure 4. The results of the multitemporal statistical analysis of the LULC spatial dynamics in the RMPA showed that from 1990 to 2020, there was a linear growth of urban area and cropland, as can be seen in Table 1 which shows the area estimates and change statistics of LULC classes for each year under study.

Kappa statistics, producer, consumer and global precision were used to evaluate the LULC maps derived from the supervised classification carried out in the GEE for the years 1990, 2000, 2010 and 2020, which reached an excellent average precision of 0.9. The highest overall accuracy and K were found in 1990, with 0.92 and 0.91, respectively. In 2000, 2010 and 2020, the overall accuracy and K values were 0.90 and 0.88, 0.90 and 0.88, 0.88 and 0.86, respectively. These results are in agreement with those found by Phan et al. (2020), who used the RF classifier to produce LULC maps with "moderate" to "high" accuracy, estimating overall accuracy levels between 0.84 and 0.89, using different satellite data, normalized indices, and radar data. The results observed by Talukdar et al. (2020) evaluate the classification potential of several machine learning and deep learning algorithms RF, SVM, ANN, Fuzzy Adaptive Resonance Theory-supervised predictive Mapping (Fuzzy ARTMAP), spectral angle mapper (SAM) and Mahalanobis Distance (MD), the results indicate that the RF algorithm estimated the highest accuracy levels, with 0.89.

Therefore, the accuracy values estimated in our classification for the RMPA can be considered excellent accordingly (Congalton and Green, 2009). For the commission and omission errors in 1990, the grassland class suffered the most pixel mixing with other classes, mainly cropland, reaching 24%

TABLE 1 LULC areas from 1990 to 2020 in km² and annual change rate (ACR) in percentage.

LULC class	1990		2000		2010		2020		ACR (%)
	km²	%	km²	%	km²	%	km²	%	
Built-up	603.55	5.84	650.08	6.29	742.46	7.18	840.33	8.12	0.94
Cropland	1802.76	17.43	2052.79	19.85	2160.08	20.88	2300.83	22.25	0.72
Water	244.85	2.37	266.83	2.58	261.20	2.53	246.26	2.38	0.02
Grasslands	3799.30	36.73	3937.83	38.07	3313.14	32.03	3134.24	30.30	−0.71
Natural forest	3708.05	35.85	3210.58	31.04	2992.98	28.94	2860.56	27.66	−0.99
Planted Forest	184.43	1.78	224.82	2.17	873.04	8.44	960.69	9.29	2.69

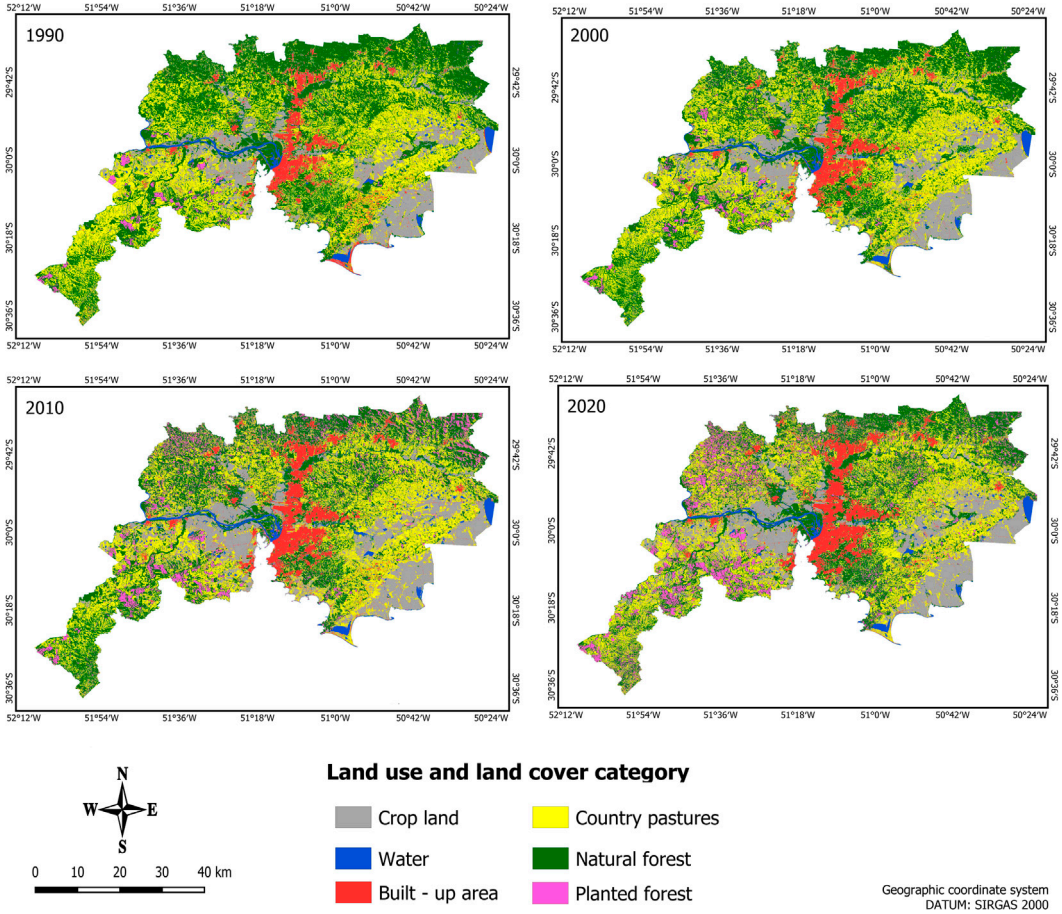

FIGURE 4
Relationship between the 1990–2020 LULC maps.

and 15%, respectively. The same was observed for 2000 and 2010, with 28% and 17%, and 23% and 11%, consumer and producer errors, respectively. However, for 2020, the classes that showed the most pixel mixtures were natural and planted forests, with consumer and producer errors of 23% and 24%.

That way, the LULC classifications were consistent with the field reality. Some questions remained open, especially regarding the more suitable number of samples used in the validation process. In this study, the volume of samples presented in the confusion matrixes comprised 30% of the total volume of the samples collected, reaching from 300 to 400 polygons per class, which is usually used in other studies such as in Loukika et al. (2021), Pech-May et al. (2022). However, in other studies, much larger sample volumes have been used, such as in Yu et al. (2018). Therefore, we recommend that future studies test the accuracy values with different sample volumes to generate LULC validation.

TABLE 2 Temporal changes 1990–2020.

LULC class	1990–2000		2000–2010		2010–2020		1990–2020	
	km²	(%)	km²	(%)	km²	(%)	km²	(%)
Built-up	46.53	7.71	92.38	14.21	97.87	13.18	236.79	39.23
Cropland	250.03	13.87	107.29	5.23	140.75	6.52	498.07	27.63
Water	21.98	8.98	−5.63	−2.11	−14.93	−5.72	1.41	0.58
Grasslands	138.54	3.65	−624.69	−15.86	−178.90	−5.40	−665.05	−17.50
Natural Forest	−497.47	−13.42	−217.59	−6.78	−132.42	−4.42	−847.49	−22.86
Planted Forest	40.39	21.90	648.22	288.33	87.65	10.04	776.26	420.89

3.2 LULC spatial analysis changes between 1990 and 2020

LULC maps for the years 1990, 2000, 2010, and 2020, derived from Landsat TM/ETM+/OLI datasets and spectral NDVI, NDBI, and MNDWI indices, served as a basis for assessing the LULC class's spatial dynamics in the RMPA. The variations and estimated percent area are presented in Table 2. Based on these data, it can be observed that the LULC feature corresponding to the built-up in the RMPA has undergone steady expansion since 1990, with a 0.9% annual increase rate.

The most significant built-up area expansion was found between 2000 and 2010, approximately 14.2%, followed by the decade 2010–2020, 13.1%, and 1990–2000, 7.7%. In the last 30 years, from 1990 to 2020, the overall built-up area expansion was greater than 39.2%. The cropland area showed the most significant growth between 1990 and 2000, with a more than 13.8% increase. While in the two following decades, the area volume increased by 5.2% and 6.5% for the periods 2000 to 2010 and 2010 to 2020, respectively. In general, the cropland area showed an increase bigger than 27.6% from 1990 to 2020 and 0.7% annual rate.

In contrast, natural forests presented a linear decrease, which was most apparent between 1990 and 2000, reaching more than 13.4% suppression, followed by the decade 2010–2020, and 2000–2010, 4.4% and 6.7%, respectively. The native forest overall decrease in the RMPA from 1990 to 2020 was greater than 22.8% and about a 1.0% annual decrease rate. Although a natural forest area reduction has been observed over the decades, the suppression process is still linear, driven by built-up and cropland expansion. The grassland areas decreased significantly between 2000 and 2010, equivalent to approximately 15.8%, followed by the 2010–2020 decade, with a 5.4% decrease. However, it showed a considerable increase of more than 13.4% between 1990 and 2000. Even though the entire period of 1990–2020 presented a 17.5% grassland decrease and 0.7% annual decrease rate. Notably, the grassland areas in the RMPA have been replaced by built-up, cropland, and planted forest areas.

The water bodies are composed mainly of the Jacuí, Gravataí, Caí, and Sinos rivers, and in smaller expression lakes, ponds, and small dams. In this study, the water LULC class has not changed much over the years, which may be related to the precipitation volume in the reference years used to select the satellite images. During 1990 and 2000, the area increased by approximately 8.9%. However, from 2000 to 2010, there was a decrease greater than 2.1%; between 2010 and 2020, this decrease is even more significant, reaching more than 5.7%. In general, the water gain in the RMPA from 1990 to 2020 was only 0.58%, representing only a 0.02% annual rate increase.

In this study, the LULC class called "planted forest" indicated the spaces with Acacia, Eucalyptus, and Pinus forest crops, which are economically important for the Rio Grande do Sul state and Brazil's national territory. The most significant increase occurred between 2000 and 2010, when the planted forest class more than doubled, followed by the 1990–2000 and 2010–2020 periods, with increases of 21.9% and 10.0%, respectively. The overall increase in planted forest from 1990 to 2020 more than quadrupled, and the annual growth rate was around 2.7%. The LULC spatial dynamic transition evaluation between 1990 and 2020 revealed a remarkable expansion in impervious surfaces and cropland to the detriment of forest and grassland (Table 2).

It can be seen that grassland, natural forests, cropland, planted forests, and water contributed 1.41%, 0.98%, 0.85%, 0.03%, and 0.02% to built-up class increase, respectively. The natural forest, along with the grassland, were the ones that contributed the most to the inter-class dynamics between 1990 and 2020. The natural forest lost about 0.98% of its areas to built-up, 2.34% to cropland, while the grassland areas received 4.34%, planted forest received 4.47%, and water body 0.16%. The grassland areas gave up about 1.41% of its areas to urban Infrastructure, 5.02% to cropland, 0.08% to water, 3.45% to natural forest, and 1.87% to planted forest.

If current trends continue, future LULC scenarios indicate that built-up will continue to happen in areas as close as possible to Porto Alegre and municipalities that offer more opportunities. This population and development concentration is driven by proximity to downtown, employment opportunities, and socioeconomic considerations. However, it is essential to conduct further analysis and consider other factors, such as infrastructure capacity, environmental sustainability, and urban planning strategies, to ensure these areas' long-term viability and balanced growth since the results showed a decreasing trend in the natural landscape and an increase in built-up areas in the past and the future.

3.3 Artificial neural network-based modeling (ANN) in LULC change

The transition matrix is critical for monitoring and understanding the LULC spatiotemporal dynamics. It can represent the number of pixels changed from one category to another. The matrix comprises rows and columns representing the LULC classes at the beginning and end of the studied period. The diagonal entries in the matrix are composed of each category stability level, i.e., the number of pixels that remained in the same category over the period studied. The off-diagonal entries represent the transitions from one category to another (Muhammad et al., 2022).

The transition matrix construction approach is especially suited for situations with a lot of ambiguity or challenges in implementing input data. From this process, an index is generated that ranks the landscape from zero to one, producing a consistent result, where values close to 1 in the diagonal entries represent the category stability, while values close to 0 indicate that significant changes during the period analyzed occurred (Sajan et al., 2022).

In the present study, the transition matrix's applicability was essential for analyzing changes in the RMPA landscape over time, allowing the LULC changing pattern identification. The water and natural forest were the most stable in the first period, with change probabilities equivalent to 0.857 and 0.731, respectively. In contrast, grasslands, cropland, and planted forests had their stability levels reduced to 0.725, 0.660, and 0.468. It is worth mentioning that built-up presented a stability level of 0.689, and in the cropland and grassland, the main contributions were 0.047 and 0.027, respectively. In the second period, water and built-up had the highest stability levels, 0.835 and 0.824, respectively. The cropland, grassland, natural, and planted forests had reduced levels of transition stability, 0.647, 0.656, 0.656, and 0.631, respectively.

The classes that contributed the most to built-up remained cropland, 0.035, and grassland, 0.031. In the last period, the transition values for built-up and water were 0.846 and 0.810, respectively. In contrast, the values for cropland, grassland, natural, and planted forest were 0.687, 0.674, 0.665, and 0.419, respectively, similar to the first and second periods. Finally, the LULC classes that contributed the most to built-up were cropland, 0.038, and grassland, 0.029. During the study period, there was significant pressure on the natural forest and grassland areas, which had part of their areas absorbed by other LULC classes. The transition matrix between 1990 and 2000 shows this dynamic, with these being the classes with the lowest stability, 0.579 and 0.564, respectively.

3.4 Forecasting and validation LULC 2020

Based on the LULC changes in historical data between 2000 and 2010, the CA-ANN method was used to project, in the first instance, the 2020 LULC condition with a 10-year phase extension and one iteration. Subsequently, the simulated 2020 LULC scenario was compared to the actual 2020 LULC obtained from the supervised classification using the RF algorithm (Figure 5) and Table 3. After the simulated model accuracy validation, the same CA-ANN framework was used and replicated to estimate the LULC scenarios for 2030 and 2040, presented in Figure 6 and Table 4.

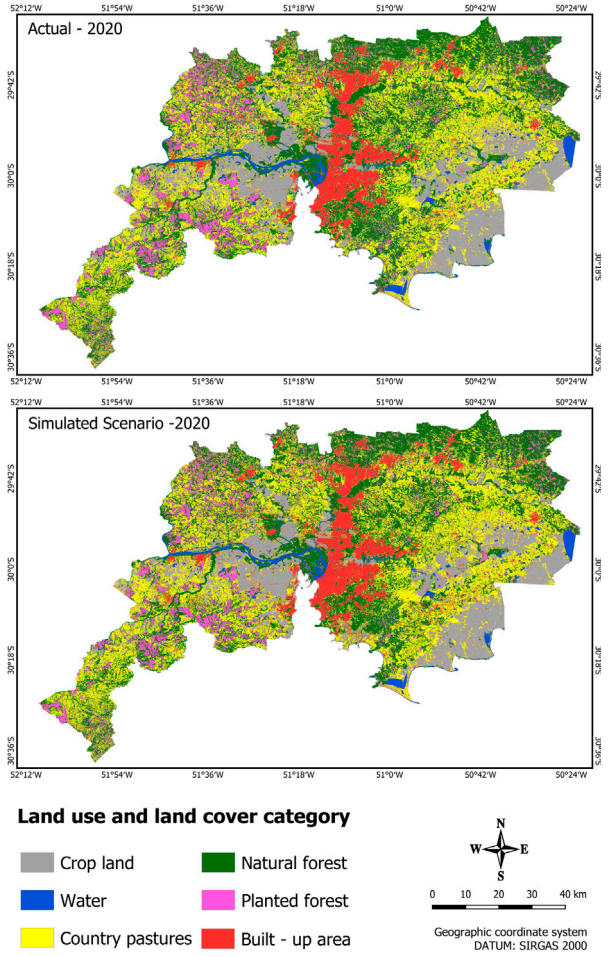

FIGURE 5
Current and projected LULC maps for 2020.

The estimated model accuracy measurement from the comparison between the LULC simulation projected for 2020 and the actual LULC for 2020 presented the HisK, OvK, and LoK of 0.80, 0.65, and 0.80, respectively, and 73.5% of percentage correctness. These results validate the simulation model's suitability for predicting LULC future scenarios for the RMPA. For example, Muhammad et al. (2022) also used the CA-ANN approach in the MOLUSCE to analyze future spatiotemporal changes for Linyi, China, in 2030, 2040, and 2050 and got a LocK of 0.97, an percent of correctness of 65.80%, and an OvK value of 0.48. Another study for future LULC scenarios of 2030, 2040, and 2050 in Guangdong Hong Kong Macau, China got a validation OvK of 0.76, an percent of correctness of 96.25%, and LocK of 0.94 (Abbas et al., 2021). While in Dehingia et al. (2022), the validation indices were: HisK of 0.89, OvK of 0.61, and LocK of 0.69, with a 72.81% percent of correctness to estimate the future condition of 2029 for the Balikpapan City, Indonesia. In Gao et al. (2023), the future LULC scenarios in the Greater Yellow River region obtained an OvK of 0.94, HisK of 0.98, LocK of 0.95, and 96.42% percent of correctness. Therefore, we can infer that our simulation validation results are suitable for estimating the future LULC conditions for 2030 and 2040 in the RMPA.

TABLE 3 Actual and projected LULC for 2020.

LULC class	Actual		Projected		Percent of correctness	Kappa		
	km²	%	km²	%		Overall	Histogram	Location
Built-up	840.33	8.12	1032.70	9.98	73.50%	0.65	0.80	0.80
Cropland	2300.82	22.25	2039.72	19.72				
Water	246.26	2.38	271.53	2.63				
Grasslands	3134.24	30.30	3302.15	31.93				
Natural Forest	2860.56	27.66	2837.83	27.44				
Planted Forest	960.69	9.29	858.96	8.30				

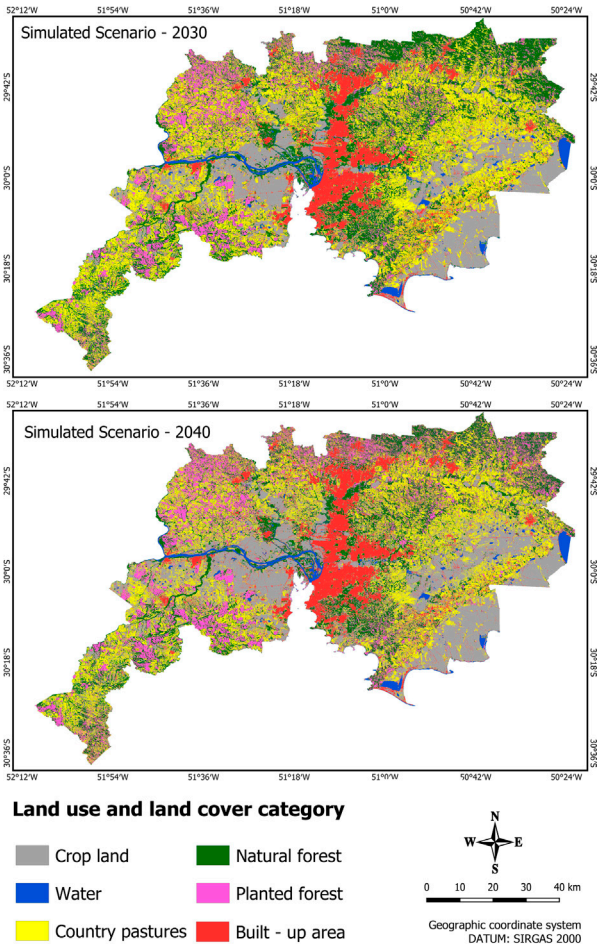

FIGURE 6
Predicted LULC maps for 2030 and 2040.

3.5 Land cover forecast in 2030 and 2040

The future scenario for 2030 and 2040 shows the cropland, built-up, and planted forests as the main LULC expanding classes (Table 5). The results indicate that by 2030, the cropland areas will show an increase of more than 12.0% compared to the 2020 actual scenario, equivalent to a 1.2% annual rate increase. For 2040, cropland areas are projected to still increase, reaching more than 42.1% of the 2020 area, indicating a 2.1% yearly growth rate and a 122.6% increase compared to the 2030 scenario. In addition, for the 2030 to 2040 period, an annual 2.6% growth rate is projected. Similarly, the model predicts a linear expansion for planted forest areas, with a 15.1% expansion for 2030, a 1.5% annual rate, and a 33.9% increase for 2040, reaching about 1.7% yearly growth concerning 2020. It is worth mentioning that planted forests will increase by about 16.3% in 2040 compared to 2030, reflecting a 1.6% annual growth rate between the years.

TABLE 4 Predicted area statistics in 2030 and 2040.

LULC class	2030		2040	
	km²	%	km²	%
Built-up	1,137,484	11.00	1,283,620	12.41
Cropland	2,578,284	24.93	3,270,507	31.62
Water	249,729	2.41	236,851	2.29
Grasslands	2,990,294	28.91	2,375,133	22.96
Natural Forest	2,280,977	22.05	1,890,448	18.28
Planted Forest	1,106,151	10.69	1,286,359	12.44

In turn, built-up areas will also increase in future scenarios, reaching more than 35.3% in 2030, compared to 2020, reaching a 3.5% annual growth rate, the highest recorded for this time series. Whereas in 2040, it will present a 52.7% increase indicating a yearly expansion rate of 2.6%. It is worth noting that despite maintaining a built-up growth trend in 2040, with a positive annual rate of 1.28%, this increase was 12.8%, reaching a 63.6% smaller area advance than that observed from 2020 to 2030.

Regarding the other LULC class's prediction for 2030 and 2040, the most significant decrease occurred for the natural forest, which in 2030 will present an area loss corresponding to 20.2% concerning 2020, reaching a 2.0% annual rate decrease. While in 2040 a loss of natural forest equivalent to 33.9% is estimated compared to the 2020 scenario, getting a 1.70% yearly rate loss for the same period. Following the same trend, the grassland will present a decrease of about 4.6% in its by the year 2030, concerning 2020, keeping a 0.4% annual rate, and for

TABLE 5 LULC temporal changes in 2020 and 2040.

LULC class	2020–2030			2020–2040			2030–2040		
	km²	%	ACR (%)	km²	%	ACR (%)	km²	%	ACR (%)
Built-up	297.15	35.36	3.54	443.29	52.75	2.64	146.14	12.85	1.28
Cropland	277.46	12.06	1.21	969.68	42.14	2.11	692.22	26.85	2.68
Water	3.46	1.41	0.14	−9.41	−3.82	−0.19	−12.88	−5.16	−0.52
Grasslands	−143.95	−4.59	−0.46	−759.11	−24.22	−1.21	−615.16	−20.57	−2.06
Natural Forest	−579.58	−20.26	−2.03	−970.11	−33.91	−1.70	−390.53	−17.12	−1.71
Planted Forest	145.46	15.14	1.51	325.67	33.90	1.69	180.21	16.29	1.63

2040, a 24.2% reduction related to 2020, indicating a 1.2% yearly loss.

For the water, an 1.41% area increase is forecast for 2030 concerning 2020, indicating a 0.14% annual gain. In contrast, for 2040, a loss of 3.8% is estimated, reaching a 0.19% yearly decrease. According to the future scenarios, the LULC changes will adversely impact environmental and socioeconomic structures, mainly with cropland and built-up areas, in contrast with decreased vegetation and water. Similar trends are found in other studies worldwide, such as in Muhammad et al. (2022), Padma et al. (2022), Barwicka and Milecka (2022), Sajan et al. (2022), and Gao et al. (2023). Therefore, indications that the LULC changes behavior obtained for the RMPA follow a similar trend to those observed in other regions around the globe.

Regarding the contribution of LULC in built-up areas for future scenarios from 2030 to 2040 in the RMPA, there was a variation of cultivated area, pasture and natural forest of 1.7%, 0.6% and 1.3% for built-up areas, respectively. In addition, grassland was the class that contributed the most change, reaching 6.1% for cropland, while the natural forest class contributed 2.4% for planted forests increase. Therefore, this study can help formulate a better land use management policy in the Metropolitan Region of Porto Alegre. Furthermore, the study demonstrates the ability of the CA-ANN model to develop future LULC scenarios and understand the spatiotemporal changes. So, combining satellite remote sensing data with GIS has generated much interest due to concerns about the LULC dynamics (Lambin et al., 2001).

4 Conclusion

This research aimed first to determine the spatiotemporal dynamics present in LULC classes between 1990 and 2020 and second to develop future LULC scenarios for 2030 and 2040 for the Metropolitan Region of Porto Alegre (RMPA), located in the Rio Grande do Sul state, Brazil. Therefore, the Random Forest algorithm in the GEE cloud processing environment was used for the first aim to classify LULC conditions for 1990, 2000, 2010, and 2020 from Landsat, TM, ETM+, and OLI data, respectively, reaching an excellent global accuracy of 0.92, 0.90, 0.90, 0.88 for the years under study. Then, the LULC simulation was successfully estimated and validated for 2020, and the CA-ANN model was used to develop the 2030 and 2040 future LULC scenarios in the RMPA in the second aim, reaching a 0.65 overall Kappa index, 0.80 histogram Kappa, 0.80 Location Kappa and 73.50% percentage of correctness.

Thesethe findings in the validation statistics make it possible to infer that the model demonstrates good effectiveness in prospecting the LULC spatial conditions. The future scenarios regarding LULC changes for 2030 and 2040 highlighted that built-up, cropland and planted forests will be together the most representative areas along the RMPA boundaries, reaching 46.6% and 56.4%in 2030 and 2040, respectively. The built-up stands out as having the highest expansion rate in the area, reaching 35.3% and 52.3% increase in 2030 and 2040, respectively. In contrast, in the same period in 2030, natural forests will lose the largest area, suffering an area decline of 20.26%, followed by the grassland that will lose about 4.6% of its area in 2020.

In addition, by 2040, the natural forest loss is expected to be approximately 33.9%, followed by the grassland loss of 24.2% concerning 2020. Therefore, the present study highlights the relevance of monitoring the past and developing future LULC scenarios. Moreover, similar LULC pattern behaviors observed in the RMPA were also found in other regions of the country and the world, indicating that the methodology in this study could be replicated in other metropolitan regions.

The results obtained through modeling and predicting landscape patterns highlighted the need to consider physical elements and factors such as development policies and climatic conditions for a more comprehensive understanding of the LULC transitional dynamics in future studies. Therefore, it is suggested that future research incorporate a wide range of factors and data to deepen the knowledge of the effects of these elements on landscape patterns. Such more comprehensive investigations will be crucial to informing land managers and risk decision-makers, enabling the development of effective plans to mitigate the climate change impact and promote more sustainable use of the environment.

Understanding the built-up sprawl effect is essential to plan and develop better cities. This study took into account significant factors influencing urban sprawl. The variables used in the CA-ANN model were critical determinants as they significantly affected the LULC change mechanism. Based on the results, it is understood that the factors used were shown to be very

influential in the way in which urban sprawl occurred and may continue to occur.

Data availability statement

The raw data supporting the conclusion of this article will be made available by the authors, without undue reservation.

Author contributions

AF and FA conducted the study, prepared the data, performed the analysis, wrote the article, discussed the results and contributed to the final manuscript. VN supervised the project, verified the analytical methods, discussed the results and contributed to the final manuscript. JO checked the methods, discussed the results and contributed to the final manuscript. All authors contributed to the article and approved the submitted version.

Funding

This research was funded by Fundação de Amparo à Pesquisa do Estado de São Paulo (FAPESP) project number (2017/22269-2) and by Global Programme of Action for the Protection of the Marine Environment from Landbased Activities of the United Nations Environment Program (GPA/UNEP, no 2500116256) in support of the project Towards the Establishment of an International Nitrogen Management System (INMS).

Acknowledgments

The authors would like to thank the Coordenação de Aperfeiçoamento de Pessoal de Nível Superior (CAPES) process number (88882.438974/2019-01), the Fundação de Amparo à Pesquisa do Estado de São Paulo (FAPESP) project number (2017/22269-2). The the Global Program of Action for the Protection of the Marine Environment against Land Activities of the United Nations Environment Program (GPA/UNEP, no. 2500116256) in support of the project Towards the Establishment of an International Nitrogen Management System (INMS). The Graduate Program in Remote Sensing at Federal University of Rio Grande do Sul, the Federal University University of ABC in Brazil.

Conflict of interest

The authors declare that the research was conducted in the absence of any commercial or financial relationships that could be construed as a potential conflict of interest.

Publisher's note

All claims expressed in this article are solely those of the authors and do not necessarily represent those of their affiliated organizations, or those of the publisher, the editors and the reviewers. Any product that may be evaluated in this article, or claim that may be made by its manufacturer, is not guaranteed or endorsed by the publisher.

References

Abbas, Z., Yang, G., Zhong, Y., and Zhao, Y. (2021). Spatiotemporal change analysis and future scenario of LULC using the CA-ANN approach: A case study of the greater bay area, China. *Land* 10, 584. doi:10.3390/land10060584

Alam, N., Saha, S., Gupta, S., and Chakraborty, S. (2021). Prediction modelling of riverine landscape dynamics in the context of sustainable management of floodplain: A geospatial approach. *Ann. GIS* 27 (3), 299–314. doi:10.1080/19475683.2020.1870558

Arsanjani, J. J., Kainz, W., and Mousivand, A. J. (2011). Tracking dynamic land-use change using spatially explicit Markov chain based on cellular automata: the case of Tehran. *Int. J. Image Data Fusion* 2 (4), 329–345. doi:10.1080/19479832.2011.605397

Ashaolu, E. D., Olorunfemi, J. F., and Ifabiyi, I. P. (2019). Assessing the spatio-temporal pattern of land use and land cover changes in osun drainage basin, Nigeria. *J. Environ. Geogr.* 12 (1–2), 41–50. doi:10.2478/jengeo-2019-0005

Barwicka, S., and Milecka, M. (2022). The "perfect village" model as a result of research on transformation of plant cover—case study of the puchaczów commune. *Sustainability* 14, 14479. doi:10.3390/su142114479

Batty, M. (1997). Cellular automata and urban form: A primer. *J. Am. Plan. Assoc.* 63 (2), 266–274. doi:10.1080/01944369708975918

Bhatta, B. (2010). *Analysis of urban growth and sprawl from remote sensing data*. Berlin/Heidelberg, Germany: Springer.

Breiman, L. (2001). Random forests. *Mach. Learn.* 45, 5–32. doi:10.1023/A:1010933404324

Chen, Y., Li, X., Liu, X., Ai, B., and Li, S. (2016). Capturing the varying effects of driving forces over time for the simulation of urban growth by using survival analysis and cellular automata. *Landsc. Urban Plan.* 152, 59–71. doi:10.1016/j.landurbplan.2016.03.011

Clarke, K. C., Hoppen, S., and Gaydos, L. (1997). A self-modifying cellular automaton model of historical urbanization in the San Francisco Bay area. *Environ. Plan. B Plan. Des.* 24 (2), 247–261. doi:10.1068/b240247

Congalton, R. G., and Green, K. (2009). *Assessing the accuracy of remotely sensed data: Principles and practices*. Boca Raton: CRC Press.

Dehingia, H., Das, R. R., Abdul Rahaman, S., Surendra, P., and Hanjagi, A. D. (2022). "Decadal transformation of land use land cover and future spatial expansion in Bangalore metropolitan region, India: open-source geospatial machine learning approach," in The International Archives of the Photogrammetry, Remote Sensing and Spatial Information Sciences. XLIII-B3-2022, Nice, France, 6–11 June 2022. doi:10.5194/isprs-archives-XLIII-B3-2022-589-2022

Foody, G. M. (2010). Assessing the accuracy of land cover change with imperfect ground reference data. *Remote Sens. Environ.* 114 (10), 2271–2285. doi:10.1016/j.rse.2010.05.003

Gao, C., Cheng, D., Iqbal, J., and Yao, S. (2023). Spatiotemporal change analysis and prediction of the great Yellow River region (GYRR) land cover and the relationship analysis with mountain hazards. *Land* 12, 340. doi:10.3390/land12020340

Guidigan, M. L. G., Sanou, C. L., Ragatoa, D. S., Fafa, C. O., and Mishra, V. N. (2019). Assessing land use/land cover dynamic and its impact in Benin republic using land change model and CCI-lc products. *Earth Syst. Environ.* 3 (1), 127–137. doi:10.1007/s41748-018-0083-5

Hakim, A. M. Y., Baja, S., Rampisela, D. A., and Arif, S. (2019). Spatial dynamic prediction of landuse/landcover change (case study: tamalanrea sub-district, makassar city). *IOP Conf. Ser. Earth Environ. Sci.* 280, 012023. doi:10.1088/1755-1315/280/1/012023

Haykin, S. S. (2001). *Redes neurais: Princípios e prática*. Bookman Editora, 898.

Hu, Z., and Lo, C. P. (2007). Modeling urban growth in Atlanta using logistic regression. *Comput. Environ. Urban Syst.* 31 (6), 667–688. doi:10.1016/j.compenvurbsys.2006.11.001

Huang, D., Xu, S., Sun, J., Liang, S., and Wang, Z. (2017). Accuracy assessment model for classification result of remote sensing image based on spatial sampling. *J. Appl. Remote Sens.* 11, 1–13. doi:10.1117/1.jrs.11.046023

IBGE (2020). Agência IBGE notícias. Available at: https://agenciadenoticias.ibge.gov.br/agencia-noticias/2012-agencia-de-noticias/noticias/31471-ibge-lanca-colecao-de-mapas-municipais-2020.

Jensen, J. R., and Cowen, D. C. (1999). Remote sensing of urban/suburban Infrastructure and socioeconomic attributes. *Remote Sens. Environ.* 68 (1), 1–3.

Lambin, E. F., Turner, B., Geist, H. J., Agbola, S. B., Angelsen, A., Bruce, J. W., et al. (2001). The causes of land-use and land-cover change: moving beyond the myths. *Glob. Environ. Chang.* 11, 261–269. doi:10.1016/s0959-3780(01)00007-3

Langner, A., Miettinen, J., Kukkonen, M., Vancutsem, C., Simonetti, D., Vieilledent, G., et al. (2018). Towards operational monitoring of forest canopy disturbance in evergreen rain forests: A test case in continental southeast asia. *Remote Sens.* 10 (4), 544. doi:10.3390/rs10040544

Li, X., Lin, J., Chen, Y., Liu, X., and Ai, B. (2013). Calibrating cellular automata based on landscape metrics by using genetic algorithms. *Int. J. Geogr. Inf. Sci.* 27 (3), 594–613. doi:10.1080/13658816.2012.698391

Li, X., and Yeh, A. G. O. (2002). Neural-network-based cellular automata for simulating multiple land use changes using GIS. *Int. J. Geogr. Inf. Sci.* 16 (4), 323–343. doi:10.1080/13658810210137004

Ligtenberg, A., Bregt, A. K., and Van Lammeren, R. (2001). Multi-actor-based land use modelling: spatial planning using agents. *Landsc. Urban Plan.* 56 (1–2), 21–33. doi:10.1016/S0169-2046(01)00162-1

Loukika, K. N., Keesara, V. R., and Sridhar, V. (2021). Analysis of land use and land cover using machine learning algorithms on Google Earth engine for munneru river basin, India. *Sustainability* 13, 13758. doi:10.3390/su132413758

Meraj, G., Kanga, S., Ambadkar, A., Kumar, P., Singh, S. K., Farooq, M., et al. (2022). Assessing the yield of wheat using satellite remote sensing-BasedMachine learning algorithms and SimulationModeling. *Remote Sens.* 14, 3005. doi:10.3390/rs14133005

Mishra, V. N., and Rai, P. K. (2016). A remote sensing aided multi-layer perceptron-Markov chain analysis for land use and land cover change prediction in Patna district (Bihar), India. *Arab. J. Geosci.* 9, 1–18. doi:10.1002/9780470979587.ch22

Muhammad, R., Zhang, W., Abbas, Z., Guo, F., and Gwiazdzinski, L. (2022). Spatiotemporal change analysis and prediction of future land use and land cover changes using QGIS MOLUSCE plugin and remote sensing big data: A case study of Linyi, China. *Land* 11, 419. doi:10.3390/land11030419

Padma, S., Vidhya Lakshmi, S., Prakash, R., Srividhya, S., Sivakumar, A. A., Divyah, N., et al. (2022). Simulation of land use/land cover dynamics using Google Earth data and QGIS: A case study on outer ring road, southern India. *Sustainability* 14, 16373. doi:10.3390/su142416373

Pech-May, F., Santos, R. A., Toledo, G. R., and Duran, J. P. F. P. (2022). Mapping of land cover with optical images, supervised algorithms, and Google Earth engine. *Sensors* 22, 4729. doi:10.3390/s22134729

Pelletier, C., Valero, S., Inglada, J., Champion, N., and Dedieu, G. (2016). Assessing the robustness of Random Forests to map land cover with high resolution satellite image time series over large areas. *Remote Sens. Environ.* 187, 156–168. doi:10.1016/j.rse.2016.10.010

Perović, V., Jakšić, D., Jaramaz, D., Koković, N., Čakmak, D., Mitrović, M., et al. (2018). Spatio-temporal analysis of land use/land cover change and its effects on soil erosion (Case study in the Oplenac wine-producing area, Serbia). *Environ. Monit. Assess.* 190 (11), 675. doi:10.1007/s10661-018-7025-4

Phan, T. N., Kuch, V., and Lehnert, L. W. (2020). Land cover classification using Google Earth engine and random forest classifier-the role of image composition. *Remote Sens.* 12 (15), 2411. doi:10.3390/rs12152411

Pimple, U., Simonetti, D., Sitthi, A., Pungkul, S., Leadprathom, K., Skupek, H., et al. (2018). Google Earth engine based three decadal Landsat imagery analysis for mapping of mangrove forests and its surroundings in the trat province of Thailand. *J. Comput. Commun.* 6, 247–264. doi:10.4236/jcc.2018.61025

Prenzel, B. (2004). Remote sensing-based quantification of land-cover and land-use change for planning. *Prog. Plan.* 61, 281–299. doi:10.1016/s0305-9006(03)00065-5

Rahman, M., Tabassum, F., Rasheduzzaman, M., Saba, H., Sarkar, L., Ferdous, J., et al. (2017). Temporal dynamics of land use/land cover change and its prediction using CA-ANN model for southwestern coastal Bangladesh. *Environ. Monit. Assess.* 189, 565. doi:10.1007/s10661-017-6272-0

Sajan, B., Mishra, V. N., Kanga, S., Meraj, G., Singh, S. K., and Kumar, P. (2022). Cellular automata-based artificial neural network model for assessing past, present, and future land use/land cover dynamics. *Agronomy* 12, 2772. doi:10.3390/agronomy12112772

Saputra, M. H., and Lee, H. S. (2019). Prediction of land use and land cover changes for North Sumatra, Indonesia, using an artificial-neural-network-based cellular automaton. *Sustain. Switz.* 11 (11), 1–16. doi:10.3390/su11113024

Secretaria De Planejamento (2020). Atlas socioeconômico do Rio Grande do Sul. Available at:https://atlassocioeconomico.rs.gov.br/regiao-metropolitana-de-porto-alegre-rmpa.

Shi, W., and Pang, M. Y. C. (2000). Development of Voronoi-based cellular automata—an integrated dynamic model for Geographical Information Systems. *Int. J. Geogr. Inf. Syst.* 14 (5), 455–474. doi:10.1080/13658810050057597

Talukdar, S., Singha, P., Shahfahad, Mahato, S., Praveen, B., and Rahman, A. (2020). Dynamics of ecosystem services (ESs) in response to land use land cover (LU/LC) changes in the lower Gangetic plain of India. *Ecol. Indic.* 112, 106121. doi:10.1016/j.ecolind.2020.106121

Vaz, E., de Noronha, T., and Nijkamp, P. (2014). Exploratory landscape metrics for agricultural sustainability. *Agroecol. Sustain. Food Syst.* 38 (1), 92–108. doi:10.1080/21683565.2013.825829

Wu, F., and Webster, C. J. (2000). Simulating artificial cities in a GIS environment: urban growth under alternative regulation regimes. *Int. J. Geogr. Inf. Sci.* 14 (7), 625–648. doi:10.1080/136588100424945

Xu, H. (2006). Modification of normalised difference water index (NDWI) to enhance open water features in remotely sensed imagery. *Int. J. Remote Sens.* 27 (14), 3025–3033. doi:10.1080/01431160600589179

Yang, Q., Li, X., and Shi, X. (2008). Cellular automata for simulating land use changes based on support vector machines. *Comput. Geosciences* 34 (6), 592–602. doi:10.1016/j.cageo.2007.08.003

Yu, Z., Di, L., Tang, J., Zhang, C., Lin, L., Genong, E., et al. (2018). "Land use and land cover classification for Bangladesh 2005 on Google Earth engine," in 7th International Conference on Agro-geoinformatics (Agro-geoinformatics), Hangzhou, China, August 6-9, 2018, 1–5. doi:10.1109/Agro-Geoinformatics.2018.8475976

Frontiers in
Remote Sensing

Highlights innovation in remote sensing science and its applications

An exciting journal which focuses on physical and quantitative approaches to remote sensing of the land, oceans, biosphere, atmosphere and space at local and global levels.

Discover the latest Research Topics

See more →

Frontiers

Avenue du Tribunal-Fédéral 34
1005 Lausanne, Switzerland
frontiersin.org

Contact us

+41 (0)21 510 17 00
frontiersin.org/about/contact